

AD-A115 188

ENVIRONMENTAL RESEARCH INST OF MICHIGAN ANN ARBOR RA--ETC F/8 17/9

THE UTILITY OF SAR TO MONITOR OCEAN PROCESSES.(U)

NOV 81 R A SHUCHMAN, E S KASISCHKE

N00014-76-C-1048

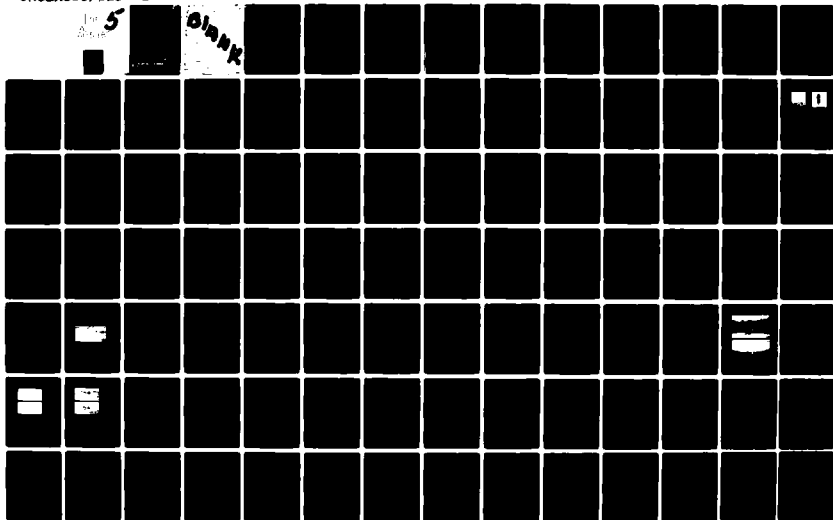
UNCLASSIFIED

ERIN-124300-11-F

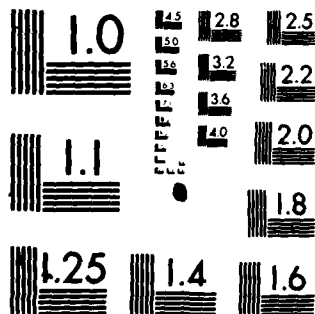
NL

5

0100K



15 18



MICROCOPY RESOLUTION TEST CHART
NATIONAL BUREAU OF STANDARDS-1963-A

124300-11-F

Final Report

AD A115188

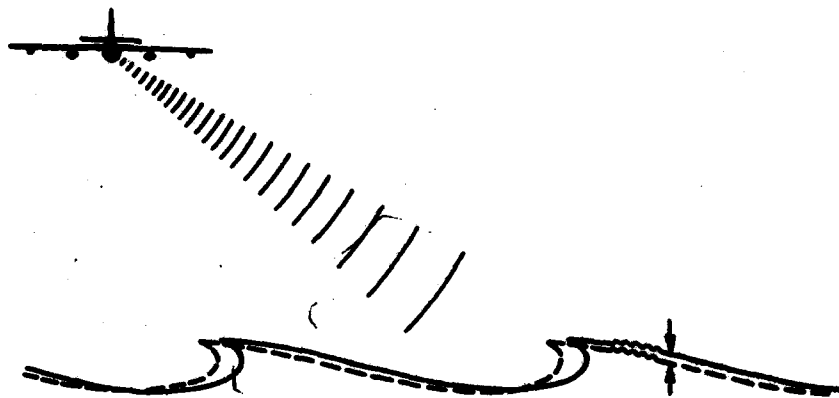
DTIC FILE COPY

THE UTILITY OF SAR TO MONITOR OCEAN PROCESSES

NR 387-132

R.A. SHUCHMAN
E.S. KASISCHKE
G.A. MEADOWS
J.D. LYDEN
D.R. LYZENGA
P.L. JACKSON
A.L. MAFFETT
A. KLOOSTER, Jr.
Radar and Optics Division

NOVEMBER 1981



Ocean Sciences Division
Office of Naval Research
Arlington, Virginia 22217

Contract No. N00014-76-C-1048
Technical Monitor: Hans Dolezalek

ENVIRONMENTAL
RESEARCH INSTITUTE OF MICHIGAN
BOX 8618 • ANN ARBOR • MICHIGAN 48107

DTIC
ELECTE
JUN 7 1982
E

82 06 07 069



Unclassified

SECURITY CLASSIFICATION OF THIS PAGE (When Data Entered)

REPORT DOCUMENTATION PAGE		READ INSTRUCTIONS BEFORE COMPLETING FORM
1. REPORT NUMBER 124300-11-F	2. GOVT ACCESSION NO AD-A115188	3. RECIPIENT'S CATALOG NUMBER
4. TITLE (and Subtitle) THE UTILITY OF SAR TO MONITOR OCEAN PROCESSES		5. TYPE OF REPORT & PERIOD COVERED Final Report Jan. 1980 thru Sept. 1981
7. AUTHOR(s) R. Shuchman, E. Kasischke, G. Meadows, J. Lyden, D. Lyzenga, P. Jackson, A. Maffett, A. Klooster		6. PERFORMING ORG REPORT NUMBER 124300-11-F
9. PERFORMING ORGANIZATION NAME AND ADDRESS Environmental Research Institute of Michigan Radar and Optics Division; P.O. Box 8618 Ann Arbor, MI 48107		8. CONTRACT OR GRANT NUMBER(s) N00014-76-C-1048
11. CONTROLLING OFFICE NAME AND ADDRESS Ocean Sciences Division; Code 422CS (Coastal Sciences); Office of Naval Research Arlington, VA 22217		10. PROGRAM ELEMENT PROJECT TASK AREA & WORK UNIT NUMBERS
14. MONITORING AGENCY NAME AND ADDRESS (if different from Controlling Office)		12. REPORT DATE November 1981
		13. NUMBER OF PAGES
		15. SECURITY CLASS. (of this report) Unclassified
		15a. DECLASSIFICATION/DOWNGRADING SCHEDULE
16. DISTRIBUTION STATEMENT (of this Report) Distribution of this document if unlimited.		
17. DISTRIBUTION STATEMENT (of the abstract entered in Block 20, if different from Report)		
18. SUPPLEMENTARY NOTES The technical monitor for this program is Hans Dolezalek.		
19. KEY WORDS (Continue on reverse side if necessary and identify by block number) Synthetic aperture radar Oceanography Ocean fronts Wind Ship wakes Bottom topography Review paper Oil slicks Sea ice MARSEN'79 Remote sensing Ocean waves Internal waves Radar Maritime remote sensing Ocean currents Surf zone SEASAT		
20. ABSTRACT (Continue on reverse side if necessary and identify by block number) This report investigates the utility of using synthetic aperture radar (SAR) to monitor the earth's oceans. The report consists of three parts which include: (1) a review on the present capability of SARs to monitor ocean processes, (2) a status report on the processing and preliminary analysis of UPD-4 and UPD-6 data collected during the MARSEN'79 Experiment, and (3) a collection of journal articles and symposia papers which resulted from this ONR-funded ERIM research. (continued)		

DD FORM 1473 EDITION OF 1 NOV 65 IS OBSOLETE

Unclassified

SECURITY CLASSIFICATION OF THIS PAGE (When Data Entered)

Unclassified

SECURITY CLASSIFICATION OF THIS PAGE (When Data Entered)

20. ABSTRACT (continued)

The review of the present status of SAR's utility to monitor the oceans includes the detection and measurement of gravity waves, currents, long-period waves, internal waves, frontal boundaries, bottom topographic features, surface winds, surf zone conditions, oil slicks, and sea ice.

In respect to the processing and analysis of X-band MARSEN data, ERIM has precision optically processed all UPD-6 X-band data and a majority of the UPD-4 data. Included in the past year's analysis was an investigation of the effects of using special motion compensation techniques on UPD-4 X-band imagery of ocean gravity waves. (Results of this analysis indicate the UPD-4 X-band SAR imagery is not significantly improved, with regard to visibility of waves on the imagery when motion compensation adjustments are incorporated into the processing of the SAR signal histories. Selected passes of UPD-4 and UPD-6 X-band imagery have been digitized and comparisons between SAR generated wave spectra and surface measured spectra were made. ←

Found in the Appendix to this report are fourteen journal articles and papers given at scientific meetings and symposia. The research which resulted in these papers was sponsored by ONR.

Unclassified

SECURITY CLASSIFICATION OF THIS PAGE (When Data Entered)

PREFACE

The work described in this final report was conducted by the Radar and Optics Division of the Environmental Research Institute of Michigan. This work was supported by the Office of Naval Research, Coastal Sciences (Code 422CS) under Contract No. N00014-76-C-1048. This report covers the contract period 1 January 1980 to 30 September 1981. The Technical Monitor for this work was Hans Dolezalek.

The principal investigator for this project is Robert A. Shuchman. The work performed during this contracting period is reported in most cases as published or submitted journal articles; thus the specific efforts of each ERIM staff member can be identified by authorship on the enclosed articles.

Accession For	
NTIS GRA&I	<input checked="" type="checkbox"/>
DTIC TAB	<input type="checkbox"/>
Unannounced	<input type="checkbox"/>
Justification	
By _____	
Distribution/	
Availability Codes	
Dist	Avail and/or Special
A	

DTIC
COPY
INSPECTED
2

ACKNOWLEDGMENTS

The timely analysis of aircraft and satellite remotely sensed data is never accomplished through the efforts of one person alone. The authors would like to thank Jack Losee, Raja Shounia, and James Marks of ERIM for processing the SAR data and generating the back-scatter values presented in this report.

Walt Brown and Ben Holt of the Jet Propulsion Laboratory are thanked for providing the optical and digital Seasat products used in this report. Robert Stewart of Scripps Institute of Oceanography and John Vesecky of Stanford University are acknowledged for supplying the JASIN sea truth, and allowing ERIM access to the JASIN SAR data set.

Barbara Burns, Ralph Mitchell, Jack Walker and Richard Larson of ERIM are acknowledged for reviewing this report. Lisa Feezell and Karla Amble are thanked for editing and preparing the figures for this report. Finally, the authors gratefully acknowledge the efforts put forth by Lee Walls in typing the manuscript for this report.

TABLE OF CONTENTS

ACKNOWLEDGEMENTS	v
LIST OF FIGURES	ix
LIST OF TABLES	xiii
PREFACE	iii
1. INTRODUCTION	1
2. ERIM PUBLICATIONS SUPPORTED UNDER ONR SPONSORSHIP	3
3. PRESENT CAPABILITIES OF SAR SENSING OF THE OCEAN SURFACE	7
3.1 Introduction	7
3.2 SAR Sensing of Ocean Surface Roughness (Theory)	9
3.3 SAR Monitoring of Gravity Waves	10
3.3.1 Theory	10
3.3.2 Extraction of Gravity Wave Information from SAR Data	12
3.3.3 SAR Versus Sea Truth Spectral Comparisons	21
3.3.4 Limitations of SAR in Detecting Gravity Waves	26
3.4 Sar Detection of Ocean and Coastal Currents	32
3.4.1 SAR Doppler Effects	33
3.4.2 Wave Refraction Effects	35
3.5 SAR Detection of Long-Period Waves	36
3.6 SAR Detection of Internal Waves	39
3.7 SAR Sensing of Frontal Boundaries	42
3.8 SAR Detection of Bottom Topographic Features	46
3.9 SAR Measurement of Surface Winds	51
3.10 Observation of Surf Zone Conditions	53
3.11 Detection of Oil Slicks	54
3.12 SAR Detection and Classification of Sea Ice	56
3.13 Conclusions and Recommendations	56
4. ANALYSIS OF MARSEN UPD-4 AND UPD-6 SAR WAVE DATA	61
4.1 Data Description	62
4.2 Motion Compensation Adjustments	67
4.2.1 Range Telerotation Adjustments	72
4.2.2 Azimuth Focus Shifts	73
4.2.3 Combination Focus Shifts and Telerotation Adjustments	79

Table of Contents (concluded):

4.2.4	Integration Time Measurements	82
4.2.5	Dependence of Wave Visibility on SAR Look Direction	85
4.3	Further Analysis of Motion Induced Perturbations on SAR Imagery	85
4.3.1	Theory	88
4.3.2	Azimuth Image Scans of Selected Wave Imagery	89
4.3.3	Orbital Motion Measurements	95
4.4	SAR Versus Sea Truth Spectral Comparisons	99
4.4.1	Data Set	105
4.4.2	Comparisons	109
4.5	Summary and Recommendations for Additional Analysis of MARSEN X-band Data	119
REFERENCES	123
APPENDIX	131
TABLE A1:	Papers in Appendix	132

LIST OF FIGURES

1. SEASAT SAR Image of Ocean Gravity Waves and Their Resultant Two-Dimensional Fourier Transforms, SEASAT Rev. 762, 19 August 1978	14
2. One-Dimensional Representations of FFT-Derived Spectra from Rev. 762	15
3. Two-Dimensional Spectral Estimates from SEASAT SAR Data (L-band 23.5 cm)	17
4. SIFT-Generated Spectral Estimates for Adjacent Areas Collected by SEASAT During JASIN Rev. 1049	19
5. FFT-Generated Spectral Estimate from SAR Wave Data Collected by SEASAT During JASIN Rev. 1049	20
6. Plot of Wavelength, SAR Versus Sea Truth, For L-band SEASAT Data	22
7. Plot of Wave Direction, SAR Versus Sea Truth, For L-band SEASAT Data	22
8. Plot of Wavelength, SAR Versus Sea Truth, For X-band Aircraft Data	24
9. Plot of Wave Direction, SAR Versus Sea Truth, For X-band Aircraft Data	24
10. Plot of Wavelength, SAR Versus Sea Truth, For L-band Aircraft Data	25
11. Plot of Wave Direction, SAR Versus Sea Truth, For L-band Aircraft Data	25
12. Modulation Depth at X-Band and L-Band as a Function of Radar Look Direction	30
13. SAR Derived Two-Dimensional Spectral Estimate (Near-Shore)	37
14. Schematic of the Structure of Progressive Internal Wave Motion Along a Sharp Thermocline Illustrating Alteration of Surface Roughness	41

List of Figures (continued):

15. Sketch of Frontal System Illustrating Convergent Surface Currents and Surface Roughness Effects	43
16. SAR Image (X-band) of Mouth of Chesapeake Bay Illustrating Ocean Frontal Type Features (10 October 1980)	44
17. Schematic Diagram of Current, Wind, and Capillary Wave Interactions	49
18. Simultaneously Obtained X- and L-band Images of a Crude-Oil Spill Off the East Coast of the United States	55
19. L-band Parallel and Cross Polarized SAR Imagery of Ice in the Beaufort Sea. (Also Shown on the Figure is a Transect of Received Power Across the Image.)	57
20. X-band Parallel and Cross Polarized SAR Imagery of Ice in the Beaufort Sea. (Also Shown on the Figure is a Transect of Received Power Across the Image.)	58
21. Map of Southeastern North Sea Showing Locations of Noordwijk and Nordsee Test Sites	63
22. Summary of Peak-to-Background Measurement	71
23. Wave Contrast (PBR) as a Function of Range Telerotation Adjustments Using UPD-4 X-band SAR Data Collected During MARSEN	75
24. A) Wave Contrast (PBR) as a Function of Azimuth Focus Shifts Using UPD-4 X-band SAR Data Collected During MARSEN (Lines 7 and 10)	77
B) Wave Contrast (PBR) as a Function of Azimuth Focus Shifts Using UPD-4 X-band SAR Data Collected During MARSEN (Line 12)	78
25. Wave Contrast (PBR) as a Function of Combined Azimuth Focus and Telerotation Adjustments Using UPD-4 X-band SAR Data Collected During MARSEN	81
26. Wave Contrast (PBR) as a Function of Integration Time Using UPD-4 X-band SAR Data Collected During MARSEN	84

List of Figures (concluded):

27. Wave Contrast (PBR) as a Function of Radar Look Direction Using UPD-4 X-band SAR Data Collected During MARSEN	87
28. Image Intensity Scan of a Breaking Wave	90
29. UPD-4 X-Band SAR Imagery Collected During MARSEN Illustrating Azimuthal Streaking	91
30. Effects of Observation Time on Azimuth Displacement	93
31. Azimuth Position Shift of Velocity Component	94
32. Effects of Sequential Azimuth Spectral Bands on Velocity Component	96
33. Relative Intensity Scan of a Breaking Wave	97
34. SAR Image of Floating Fishnet Buoys Collected During the MARSEN Experiment	98
35. Illustration of Position of a Particle in a Moving Gravity Wave Field	100
36. Relative Intensity Scan of a Floating Fishnet Buoy	101
37. Relative Intensity Scan of a Floating Fishnet Buoy	102
38. Relative Intensity Scan of a Floating Fishnet Buoy	103
39. Relative Intensity Scan of a Floating Fishnet Buoy	104
40. FFT-Generated Spectral Estimates for all Four Sub-Swaths from UPD-4 Imagery of Line 12, Pass 3	107
41. Optically Processed UPD-4 Imagery from Line 12, Pass 3	108
42. Comparison of Surface-Measured and SAR-Derived Spectral Estimates from Slyt Target Pass, Line 12	112
43. Comparison of Surface-Measured and SAR-Derived Spectral Estimates from Pass 1, Line 12	113
44. Comparison of Surface-Measured and SAR-Derived Spectral Estimates from Pass 2, Line 12	114
45. Comparison of Surface-Measured and SAR-Derived Spectral Estimates from Pass 3, Line 12	115
46. Representative Scatterplot of $\log_{10} \left(\frac{E(f)_{\text{radar}}}{E(f)_{\text{surface}}} \right)$ vs. $\log_{10}(f)$	118

LIST OF TABLES

1. Summary of Journal Articles Resulting from ONR-Sponsored Research	4
2. Summary of Papers Presented at Scientific Meetings and Symposia Resulting from ONR-Sponsored Research	5
3. Technical Reports and Masters Thesis Resulting from ONR-Sponsored Research	6
4. Summary of Wavelength, Height, and Direction Data for JASIN Test Area	27
5. Comparison Between the Long-Period SAR-Derived Spectral Estimates and the <u>In Situ</u> Sea Truth	38
6. Summary of UPD-4 Wave Data Collected During MARSEN and Processed at ERIM	65
7. Summary of UPD-6 Wave Data Collected During MARSEN	66
8. Summary of Environmental Conditions During MARSEN Experiment	68
9. Summary of Telerotation Adjustments Versus Peak-to-Background Ratios (PBRs)	74
10. Summary of Azimuth Focus Shifts Versus Peak-to-Background Ratios (PBRs)	76
11. Summary of Combined Focus Shifts and Telerotation Adjustments Versus Peak-to-Background Ratios (PBRs)	80
12. Summary of Integration Time Versus Peak-to-Background Ratios (PBRs)	83
13. Summary of Line 7 Peak-to-Background Ratios (PBRs)	86
14. Summary of SAR-Generated Estimates of Dominant Wavelength and Direction from MARSEN, Line 10, Sub-Swath A	110
15. Summary of SAR-Generated Estimates of Dominant Wavelength and Direction from MARSEN, Line 12, Sub-Swath A	111
16. Comparison of SAR-Derived and Surface-Measured Spectral Estimates for Lines 10 and 12	116
17. Summary of α Estimates for Lines 10 and 12	120

THE UTILITY OF SAR TO MONITOR OCEAN PROCESSES

1
INTRODUCTION

Beginning in 1976, the Environmental Research Institute of Michigan (ERIM) has conducted research for the Office of Naval Research (ONR) on the use of Synthetic Aperture Radar (SAR) to monitor ocean processes. Some of the ocean processes considered include: 1) the propagation of gravity waves; 2) the formation of ocean fronts; 3) the variability of surface winds on the ocean; and 4) the variability of currents. During the past two years ONR has contracted ERIM under Contract No. N00014-76-C-1048/NR387-132 to process and analyze SAR data collected during the MARSEN '79 experiment for the Coastal Sciences group (Code 422CS) and to also process and analyze Seasat SAR data collected during the JASIN experiment for the Physical Oceanography group (Code 422PO) of ONR.

The purpose of this report is three-fold: 1) to present a compendium of journal articles, symposia papers, technical reports and a Master's Thesis which have been written during the past two years as a result of ONR-funded research; 2) to present a review of the present capability of SAR to monitor oceanographic features; and 3) provide a summary of the MARSEN analysis which is presently being prepared for journal submission. This report covers research conducted under ONR sponsorship between January 1980 and September 1981.

In Section 2, a list of ONR funded articles and technical reports is presented. In Section 3, a summary is given on the present capability of SAR to monitor ocean processes. Found in this section are discussions on SAR sensing of ocean surface roughness, SAR monitoring of gravity waves, and SAR detection of ocean and coastal currents, long-period waves, internal waves, frontal boundaries, bottom topographic features, surface winds, surf zone conditions, oil slicks and sea ice. Each sub-section of Section 3 will briefly review the

present capability of SAR for that particular application and provide sufficient references for the reader to obtain more information on each topic if desired.

The results from the ONR sponsored MARSEN SAR analysis are reported in Section 4. Found with the MARSEN analysis are discussions dealing with focusing corrections.

2
ERIM PUBLICATIONS SUPPORTED UNDER
ONR SPONSORSHIP

There are three classes of documents published by ERIM during the past year that resulted from research which were entirely, or in part, sponsored by the Office of Naval Research. The first class includes refereed journal articles, which are summarized in Table 1. The second class includes papers presented at major scientific meetings or symposia; these are summarized in Table 2. The third class includes ERIM technical reports and a Master's Thesis; and these are summarized in Table 3. Many of the findings of these publications are summarized in Section 3, and most of the journal articles and symposia papers are included in the Appendix to this report.

TABLE 1
SUMMARY OF JOURNAL ARTICLES RESULTING
FROM ONR-SPONSORED RESEARCH

*Jackson, P.L. and R.A. Shuchman, A New High Resolution Two-Dimensional Spectral Estimation Technique for SAR Ocean Wave Analysis, submitted to J. Geophys. Res., 1981.

*Kasischke, E.S., R.A. Shuchman, J.D. Lyden, R.H. Stewart, J.F. Vesecky and H.M. Assal, Seasat Observations of Ocean Gravity Waves during the JASIN Experiment, submitted to J. Geophys. Res., 1981.

*McLeish, W., D. Ross, R.A. Shuchman, P.G. Teleki, S.U. Hsiao, O.H. Shemdin, and W.E. Brown, Jr., Synthetic Aperture Radar Imaging of Ocean Waves; Comparison with Wave Measurements, J. Geophys. Res., Vol. 85, pp. 5003-5010, 1980.

*Meadows, G.A., R.A. Shuchman, and J.D. Lyden, Analysis of Long-Period Wave Motions, submitted to J. Geophys. Res., 1981.

*Schwab, D.J., R.A. Shuchman, and P.L. Liu, Wind Wave Directions Determined from Synthetic Aperture Radar Imagery and from a Tower in Lake Michigan, J. Geophys. Res., Vol. 86, pp. 2059-2064, 1981.

*Shuchman, R.A. and G.A. Meadows, Airborne Synthetic Aperture Radar Observations of Surf Zone Conditions, Geophys. Res. Letters, Vol. 7, pp. 857-880, 1980.

*Shuchman, R.A., A.L. Maffett and A. Klooster, Static Modeling of a SAR Imaged Ocean Scene, IEEE J. Oceanic Eng., Vol. OE-6, pp. 41-49, 1981.

*Shuchman, R.A., Processing Synthetic Aperture Radar Data of Ocean Waves, Proceedings of the COSPAR/SCOR/IUCRM Symposium on Oceanography from Space, Plenum Publishing Corp., New York, pp. 477-496, 1981.

*Vesecky, J.F., R.H. Stewart, H.M. Assal, R.A. Shuchman, E.S. Kasischke, J.D. Lyden, Gravity Waves, Large-Scale Surface Features and Ships Observed by Seasat Synthetic Aperture Radar During the 1978 JASIN Experiment, submitted to Science 1981.

*See Appendix for a Reprint of this paper.

TABLE 2
SUMMARY OF PAPERS PRESENTED AT SCIENTIFIC
MEETINGS AND SYMPOSIA RESULTING FROM
ONR SPONSORED RESEARCH

Kasischke, E.S. and R.A. Shuchman, Comparisons of Wave Contrast Measurements made from SAR Data with Selected Oceanographic Parameters, presented at the Symposium on Wave Dynamics and Radio Probing of the Ocean Surface, Miami, FL, May 1981.

*Kasischke, E.S. and R.A. Shuchman, The Use of Wave Contrast Measurements in the Evaluation of SAR/Gravity Wave Models, Proc. Fifteenth Int. Symp. Remote Sens. Env., Ann Arbor, MI, pp. 1187-1210, 1981.

Kasischke, E.S., R.A. Shuchman, J.D. Lyden, R.F. Stewart, J.F. Vesecky, and H.A. Assal, Seasat SAR Observations of Ocean Gravity Waves during the JASIN Experiment, presented at the AGU Spring Meeting, Baltimore, MD, 1981.

*Meadows, G.A., E.S. Kasischke, and R.A. Shuchman, SAR Observations of Coastal Zone Conditions, Proc. Fourteenth Int. Symp. Remote Sens. Env., Ann Arbor, MI, pp. 845-863, 1980.

*Shuchman, R.A., Oceanographic Information Obtainable from Synthetic Aperture Radar, presented at the Symposium on Remote Sensing for Oceanography, Amagi, Japan, September 26-28, 1981.

Shuchman, R.A., E.S. Kasischke, and G.A. Meadows, Detection of Coastal Zone Environmental Conditions using Synthetic Aperture Radar, 1981 International Geoscience and Remote Sensing Symposium Digest, Washington, DC, pp. 756-767, 1981.

*Shuchman, R.A., E.S. Kasischke, J.D. Lyden, and G.A. Meadows, The Use of Synthetic Aperture Radar (SAR) to Measure Ocean Gravity Waves, presented at the National Academy of Sciences Special Conference on Wave Technology, Washington, DC, April 1981.

Vesecky, J.F., H.A. Assal, R.F. Stewart, R.A. Shuchman, E.S. Kasischke, and J.D. Lyden, On the Ability of Synthetic-Aperture Radar to Measure Ocean Waves, presented at the Symposium on Wave Dynamics and Radio Probing of the Ocean Surface, Miami, FL., May 1981.

*See Appendix for a Reprint of this paper.

TABLE 3
TECHNICAL REPORTS AND MASTERS
THESIS RESULTING FROM ONR SPONSORED RESEARCH

Kasischke, E.S., Extraction of Gravity Wave Information from Spaceborne Synthetic Aperture Radar Data, Univ. of Mich. M.S. Thesis, Ann Arbor, MI, 109 pp., 1980.

Shuchman, R.A., K.H. Knorr, J.C. Dwyer, P.L. Jackson, A. Klooster, and A.L. Maffett, Imaging Ocean Waves with SAR - A SAR Ocean Wave Algorithm, ERIM Internal Technical Report 124300-5-T, Ann Arbor, MI, 129 pp., 1979 (revised 1980).

Shuchman, R.A., A. Klooster, J.D. Lyden, and C.L. Liskow, Engineering Evaluation of ERIM-Generated Seasat SAR Data, ERIM Informational Note 151400-1-I, Ann Arbor, MI, 85 pp., 1980 (revised 1981).

3
THE PRESENT CAPABILITIES OF
SAR SENSING OF THE OCEAN SURFACE

This section presents a review of the use of synthetic aperture radars to image the ocean surface and infer sub-surface conditions. The review is not comprehensive, but it does present an overview in respect to the potential of SAR as an ocean remote sensor. Note that the referencing of ERIM studies throughout the review is not to imply that other organizations are not active in the SAR/oceanography field, but merely reflects the prejudice of the authors.

3.1 INTRODUCTION

Considerable effort has been expended during the past decade exploring the potential use of synthetic aperture radar (SAR) to monitor the resources and physical phenomena of the world's oceans and coastal regions. SAR data collected by aircraft and satellite have demonstrated the following information is obtainable from SAR data: detection of gravity waves, determination of the magnitude and direction of surface winds, detection of current velocity and direction, detection of bottom features, identification of oceanic fronts and internal waves, detection of ship wakes, detection of oil slicks, classification of sea ice, and the mapping of coastal wetlands. This interest eventually resulted in the launch of the Seasat satellite which contained a SAR as one of its five instruments, and offered the oceanography community a vast quantity of data which, three years after their collection, are still being studied with great enthusiasm. In addition, numerous oceanographic remote sensing missions have been flown by aircraft SARs.

Synthetic aperture radar is an active imaging device that senses the environment with short electromagnetic waves. As active sensors, radars provide their own illumination in the microwave region of the

electromagnetic spectrum and thus are not affected by temporal changes in emitted or reflected radiation from the earth's surface. Additionally, SARs have the recognized advantage of being able to image the earth's surface independent of weather conditions and to provide synoptic views of the ocean at high resolution. The resolution of aircraft SARs is typically on the order of a few meters while the Seasat satellite SAR had a resolution of approximately 25 meters. Most radars operate in the frequency region of 300 MHz (1 m) to 30 GHz (1 cm), and bandwidths within this region are commonly designated by letters. SARs discussed in this paper are designated as L-band (23.5 cm) or X-band (3.2 cm).

Synthetic aperture radar is a coherent airborne (or spaceborne) radar that uses the motion of a moderately broad physical antenna beam to synthesize a very narrow beam, thus providing fine azimuthal (along-track) resolution (Brown and Porcello, 1969; Harger, 1970). Fine range (cross-track) resolution is achieved by transmitting either very short pulses or longer coded pulses which are compressed by matched-filtering techniques into equivalent short pulses. Usually, the coded pulse is a waveform linearly modulated in frequency.

The data discussed throughout this report were collected by both aircraft and satellite synthetic aperture radars. The aircraft SARs include the ERIM X- and L-band SAR, the UPD-4 X-band SAR, and the JPL L-band SAR. The satellite SAR is the Seasat L-band SAR. For a review of these systems, see Shuchman, et al. (1981), Rawson, et al. (1975), and Jordan (1980).

As an introduction to the SAR/oceanographic applications to be discussed, a theory is presented as to the imaging mechanism which allows SARs to detect a wide variety of ocean surface conditions.

3.2 SAR SENSING OF OCEAN SURFACE ROUGHNESS (THEORY)

The principle behind imaging any surface with a radar is that the backscatter of microwave energy (echo) received by the radar receiver contains information on the roughness characteristics (shapes, dimensions, and orientations) of the reflecting area. The parameters that influence the echo received from the ocean surface include the motion of the scattering surfaces, the so-called speckle effect, system resolution and non-coherent integration as well as primary contributions of scattering attributable to wind, waves, surface currents and surface tension.

Although the SAR ocean imaging mechanism is not completely understood, theories have been developed to explain the radar return from the ocean surface. Most of these theories surround SAR imaging of gravity waves, and these will be addressed in detail below (Section 3.3).

The most widely accepted theory for obtaining microwave backscatter from a water surface is based on Bragg scattering (as proposed by Wright, 1966). Bragg scattering is basically a resonant reflection from a periodic surface of wave number:

$$K_w = 2K_R \sin \theta, \quad (1)$$

where $K_w = 2\pi/L$ and $K_R = 2\pi/\lambda$ are the wave numbers (L and λ are the wavelengths, respectively, of the ocean wave and the radar), and θ is the incidence angle of the radar beam.

For aircraft systems discussed in this section operating with a nominal incidence angle (θ) of 45° , use of Eq. (1) leads to a Bragg water wavelength of approximately 2 cm for X-band ($\lambda = 3.2$ cm) and 17 cm for L-band ($\lambda = 23.5$ cm). For the Seasat L-band system, with an incidence angle (θ) of 20° , use of Eq. (1) leads to approximately a 34 cm wavelength Bragg water wave. These waves represent the capillary and ultra-gravity wave portion of the water wave spectrum.

If the ocean surface on which the Bragg waves are riding is flat, and the viewing angle is not in the specular direction, the amplitude of the radar return from this surface is proportional to the average amplitude of the Bragg scatterers (for the particular radar wavelength) in each SAR resolution element. Many physical oceanic processes result in a variation in the amplitude of the Bragg waves causing a variety of patterns on SAR imagery of the ocean surface. These processes include surface wind, gravity waves, ocean currents, ocean frontal boundaries, internal waves, surface slicks, temperature changes, ship wakes and rain. Selected capillary wave/oceanic process interactions will be discussed in more detail below.

3.3 SAR MONITORING OF GRAVITY WAVES

This section will present a brief summary of some of the theories as to how a SAR images gravity waves. Next, it will summarize current techniques used to extract gravity wave data from SAR imagery. Then, comparisons of SAR wave data to sea-truth wave data will be discussed. Finally, the limitations of SAR systems in monitoring gravity waves, as they are presently understood, will be presented. This section closely follows the work of Shuchman, et al. (1981a); Beal (1980); Elachi and Brown (1977); and Alpers, et al. (1981).

3.3.1 THEORY

The first and most widely accepted theory on SAR imaging of gravity waves is based on Bragg scattering (discussed in the previous section 3.2). It has been suggested by Phillips (1981) and several others that the short capillary and ultra-gravity waves (i.e., the Bragg waves) are modulated by the longer gravity waves, causing a compression of the small waves and an increase in their height in the crest region of the gravity wave and a height decrease and elongation of the shorter waves in the trough region. This compression and expansion is thought to result from the straining of the shorter

waves by the orbital velocity of the gravity wave (Wright, et al., 1980; Alpers and Rufenach, 1979). This compression/expansion of the small waves causes certain portions of the long wave to have a higher amplitude of Bragg (resonant) scatterers than other parts of the wave, resulting in a SAR image modulation closely corresponding to the gravity wave field. Also, from a SAR standpoint, the greater the compression/expansion of the small waves, the higher the contrast (of the gravity wave field) on the SAR imagery. It should be noted that this theory does not explain the appearance of azimuth-traveling waves on SAR imagery, since in this case the Bragg waves are propagating in a direction perpendicular to the long-period gravity waves and are not modulated by those waves.

Other theories that describe aspects of the SAR imaging mechanism of waves include: accounting for the change of the local tilt angle due to the waves; a composite theory which accounts for the local tilt of the surface as well as for Bragg scattering; and a third mechanism which is dependent upon the orbital velocity of the ocean waves (Elachi and Brown, 1977). This last theory, which suggests that the SAR observed radial velocity (produced by the orbital velocity component of the gravity wave motion) produces a periodic azimuthal target displacement, has caused much discussion.

This discussion has centered on the effects of imaging a moving target with a synthetic aperture radar. Synthetic aperture radar signal histories are normally processed assuming there is no movement of the target which was illuminated by the microwave beam. When the target is moving, its signal histories can be displaced, resulting in a defocusing and shifting of the position of that target's image when processed. SAR imaging of ocean gravity waves is a case where there is considerable along-track (azimuth) and cross-track (range) movement and such a situation may result in degradation of the SAR image of these waves.

Various new theories have been formulated that try to explain the dependence of the SAR image on water wave velocity and theoretically describe the SAR ocean image formation process (Raney and Shuchman, 1978; Alpers and Rufenach, 1979; Harger, 1981; Valenzuela, 1980; Jain, 1978; and Shuchman, 1981). The reader is referred to the article by Shuchman (1981) for a detailed discussion of the effects of wave motion on SAR images.

A number of investigators (Shuchman, 1981; Kasischke and Shuchman, 1981; Jain, 1978; and Shuchman and Zelenka, 1978) have designed or evaluated algorithms to enhance, through focusing and other processing procedures (i.e., accounting for water wave motion), SAR imaged gravity waves. Results of these investigations generally agree that detectability of azimuth and range traveling waves can be improved by adjusting the focal distance and rotating the lenses of the cylindrical telescope in the SAR optical processor, respectively. This procedure to enhance of ocean waves has been successfully employed on both Jet Propulsion Laboratory (JPL) L-band and ERIM X- and L-band data (Jain, 1978; Kasischke, et al., 1979; Kasischke and Shuchman, 1981).

Two additional pieces of information can be obtained through image enhancement processes. First they can be used to solve the 180° directional ambiguity of ocean wave propagation, and secondly, they can be used as a rough estimator of the phase velocity associated with these waves. Focusing effects are usually more discernible when using L-band data than X-band (see, for example, Kasischke and Shuchman, 1981). Consequently, X-band data is less useful in providing information on wave direction ambiguity and phase velocity.

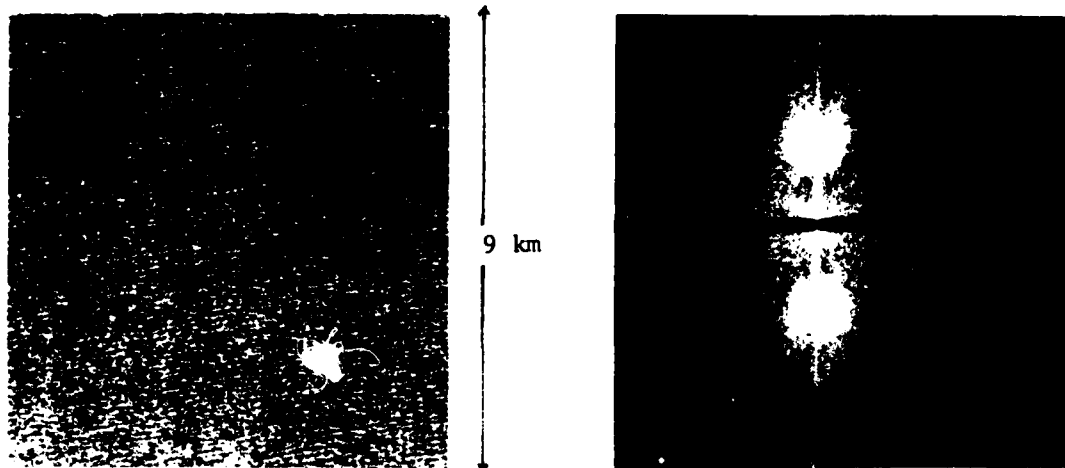
3.3.2 EXTRACTION OF GRAVITY WAVE INFORMATION FROM SAR DATA

There are presently four recognized techniques to extract estimates of wave number and direction of the dominant gravity wave component from SAR data. These include two-dimensional Fourier transforms (both optical and digital), a semicausal spectral estimation

technique, and a one-step spectral estimation routine which extracts the wave number directly from the SAR signal histories.

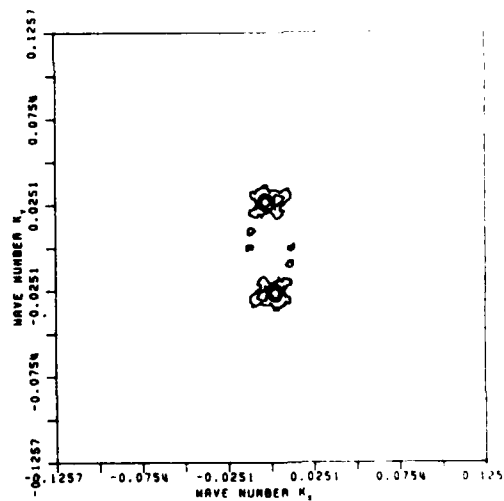
It should be noted that SAR spectral estimates of water gravity waves are wave number spectra of the radar return intensity. The data do not represent wave height information, at least not in a recognizable form. The modulation transfer function (i.e., SAR gravity wave imaging mechanism) is not totally understood at the present time. The determination of this transfer function, as well as determination of wave height using SAR data, will be a major scientific advancement. With that complete, it will be possible to use SAR gravity wave data to obtain power density estimates of the sea surface.

By passing a monochromatic, collimated beam of light through the film image of the gravity waves imaged by the SAR, a two-dimensional optical Fourier transform (OFT) of the image is created (Barber, 1949; Shuchman, et al., 1977). If a digital image is available, a similar process can be accomplished numerically by taking a fast Fourier transform (FFT) of the data. Producing a FFT has an advantage over an OFT in that distributional wave spectra, as a function of wave frequency and direction, can also be generated, as opposed to just dominant wavelength and direction as obtained from an OFT. Figure 1 (after Shuchman, et al., 1981) presents an example of actual Seasat SAR wave imagery and the resulting OFT and FFT generated from these data. These data were collected during the Joint Air/Sea Interaction (JASIN) experiment during Seasat Rev. 762, on 19 August 1978. Surface measurements, made coincident with and near to the SAR ground coverage area, indicate a wave field with a dominant wavelength of 210 meters from 240° True (T) with a significant wave height ($H_{1/3}$) of 5.5 meters. The sea-truth also reported a wind speed of 12 m/sec from 186° (T). Figure 2 presents the one-dimensional wave number and directional spectra produced from the FFT of the data. The one-dimensional wave number plot was produced



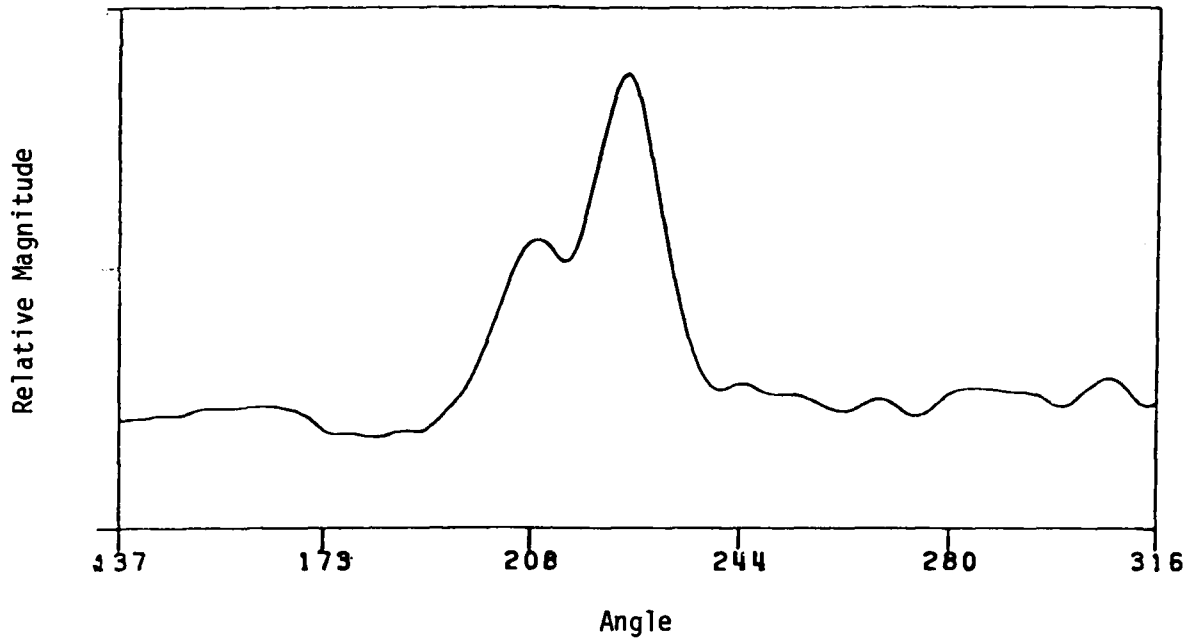
a.) SAR Image

b.) Optical Fourier Transform

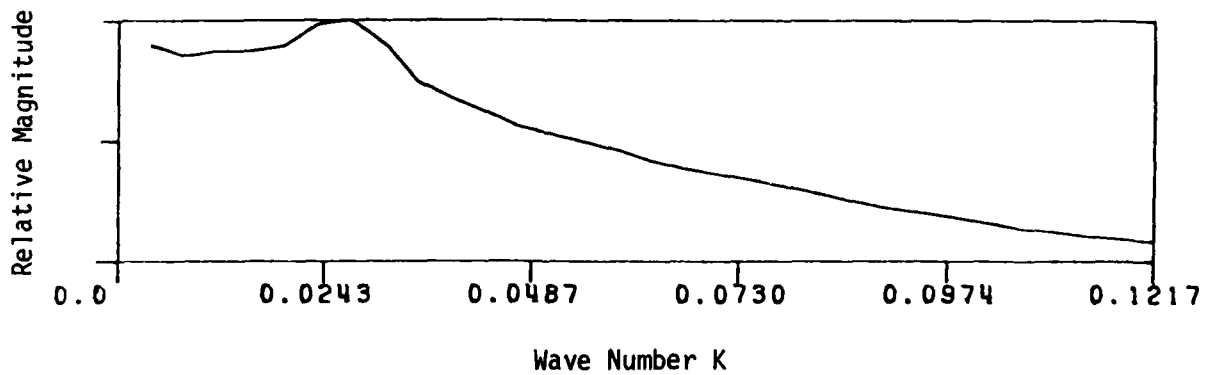


c.) Fast Fourier Transform

FIGURE 1. SEASAT SAR IMAGE OF OCEAN GRAVITY WAVES AND THEIR RESULTANT TWO-DIMENSIONAL FOURIER TRANSFORMS, SEASAT REV. 762, 19 AUGUST 1978 (After Shuchman, et al., 1981).



a) Directional Spread of Energy at 230m Wavelength



b) One-Dimensional Spectrum as a Function of Wave Number

FIGURE 2. ONE-DIMENSIONAL REPRESENTATIONS OF FFT-DERIVED SPECTRA FROM REV. 762.

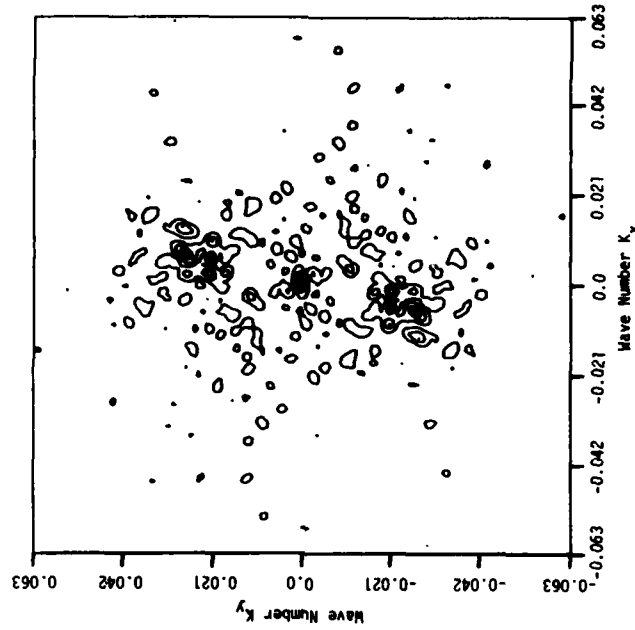
by digitally summing over angles in one-half of the two-dimensional spectrum. A wave direction plot is generated by extracting the values at a specific wave number (usually the peak wave number) as a function of angle. These FFT spectral estimates indicate a dominant wavelength of 259 meters with a direction of propagation of 227° (T).

A new two-dimensional spectral estimation algorithm related to maximum entropy, called the semicausal model (Jain and Ranganath, 1978), has been applied to synthetic aperture radar imagery of ocean waves (Jackson and Shuchman, 1982). These semicausal spectral estimations were compared to FFT estimates of identical data sets and reference functions. Results indicate the semicausal model can successfully produce spectral estimates of truncated data sets (i.e., 1-2 wave cycles). However, similar to the one dimensional maximum entropy, the two-dimensional semicausal model is sensitive to the autoregressive order and to noise, and exhibits spectral splitting in some cases.

Figure 3 (after Jackson and Shuchman, 1982) presents two-dimensional contour plots generated with the semicausal method from digital Seasat SAR wave data collected during Seasat Rev. 1049. This L-band data was collected during the JASIN experiment (Allan and Guymet, 1980). A pitch and roll buoy operating at the time when Rev. 049 was made and identified a wavetrain as swell (12.5 sec period or 244 m) which was traveling in the approximate direction of 264° (T) with a significant wave height of 5.0 meters.

The vertical axis in Figure 3 represents the range dimension of the radar image while the horizontal axis is the azimuth direction or direction of SAR platform motion. The scale of each axis is the wavenumber (K) defined as $2\pi/\lambda$ where λ is the ocean wavelength. In Figure 3, approximately 10 wave cycles were sampled. We can see that the SC model produces a much smoother spectra than the FFT spectra.

FFT 50X50



SC SPECTRUM 50X50

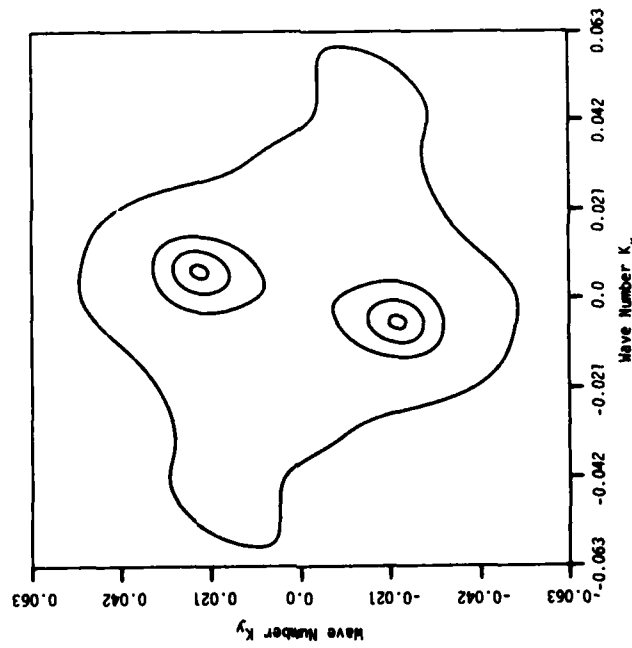


FIGURE 3. TWO-DIMENSIONAL SPECTRAL ESTIMATES FROM SEASAT SAR DATA (L-band, 23.5 cm).

A fourth technique has recently been proposed by Hasselmann (1980) to extract spectral wave information from SAR. Hasselmann has derived a simple method for the determination of the two-dimensional surface image spectrum from the return signal of a SAR without explicitly forming an image. This algorithm, called a signal-image-Fourier transform (SIFT), has recently been programmed on ERIM computers and is undergoing testing and evaluation using Seasat SAR and synthetically generated data.

Figure 4 shows contour plots of two SIFT spectral estimates from the Seasat SAR digital signal data of revolution 1049. The plots represent areas of 4 by 4 km which are adjacent in azimuth. Represented on the figures by a large black dot is the sea truth (i.e., pitch and roll buoy) derived value. Note that the estimate in the lower plot agrees well with the sea truth estimate, while the estimate in the upper plot gives a value which is 100 percent higher in wavenumber. Figure 5 is a contour plot of the two-dimensional fast Fourier transform of an 8 by 8 km area within 25 km of this estimate.

To summarize the present state of this fourth method, Hasselmann has developed a mathematical theory to extract ocean gravity wave spectral estimates from SAR data without explicitly forming an image for both aircraft and satellite SAR data. The satellite case has been programmed on ERIM computers and results are being evaluated. Preliminary results are mixed, suggesting further evaluation is warranted. The data presented in Figure 4 required approximately 10 hours of computer (PDP 11/45) running time to realize the results. The algorithm in its present form is not optimized; the inherent computation speed of the SIFT algorithm should be evaluated relative to the time required to form a 4 by 4 km SAR image from Seasat data and then generate a spectral estimate using conventional fast Fourier transform techniques.

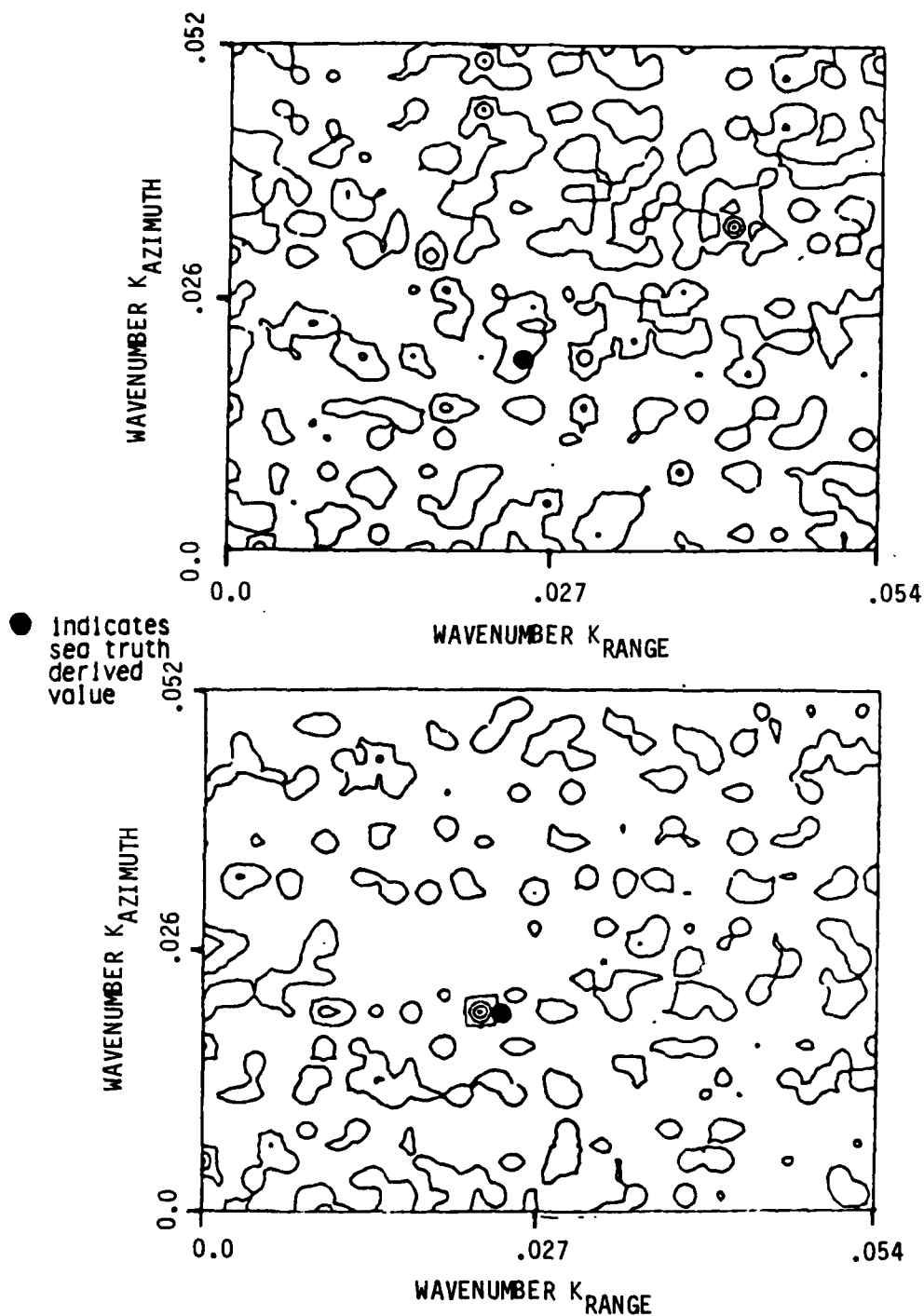


FIGURE 4. SIFT-GENERATED SPECTRAL ESTIMATES FOR ADJACENT AREAS COLLECTED BY SEASAT DURING JASIN REV. 1049.

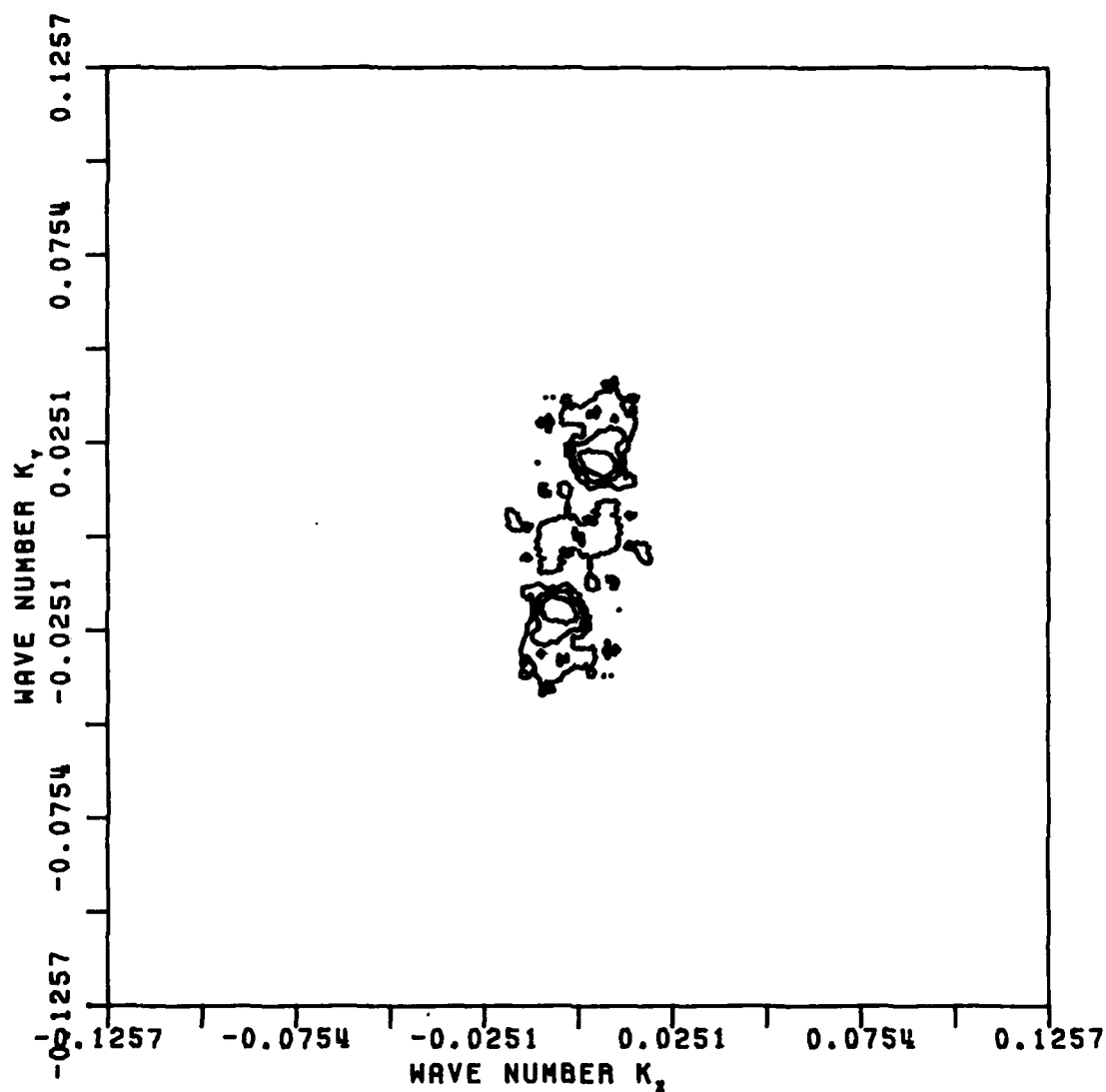


FIGURE 5. FFT-GENERATED SPECTRAL ESTIMATE FROM SAR WAVE DATA COLLECTED BY SEASAT DURING JASIN REV. 1049.

3.3.3 SAR VERSUS SEA TRUTH SPECTRAL COMPARISONS

During the past seven years a series of experiments has been conducted with the partial purpose of demonstrating that SAR data can be used to determine gravity wave direction and wave number. These experiments include: Marineland, West Coast, DUCKEX, GOASEX, JASIN, MARSEN, ARSLOE and a set of Lake Michigan test flights. (These experiments are described in detail by Shemdin, 1980; Shemdin 1980a; Mattie, et al., 1980; Gonzalez, et al., 1981; Allan and Guymer, 1980; Anonymous, 1980; Baer, 1980; and Shuchman and Meadows, 1980 and Schwab, et al., 1981, respectively.) The general consensus of these experiments was that SARs have the capability to produce imagery from which estimates of dominant wave-number and direction can be obtained.

Figure 6 (after Vesecky and Stewart, 1982) is a scatterplot of dominant ocean wavelength information obtained from the Seasat SAR compared to in situ (pitch and roll buoy) ocean sea truth. Note the pitch and roll buoy data have been converted from frequency to wavelength using the dispersion relationship. Figure 7 (after Vesecky and Stewart, 1982) is the dominant direction of wave propagation obtained from the Seasat SAR and again compared to sea truth. Based on this data, Seasat SAR estimates of wavelengths are biased slightly high and the average error is ~12 percent. For wave direction, there appears to be no significant bias and the average error is ~11 degrees. Note directional wave information provided by a SAR has an 180° ambiguity. Selective Doppler processing, as reported earlier (Shuchman and Zelenka, 1978), can resolve this 180° ambiguity in the case of aircraft data, but not Seasat data. The data included in Figures 6 and 7 represent significant wave heights in the 1-5 m range. Ocean wavelengths shorter than approximately 80 m in length were not observed by the Seasat SAR. The wind speed for all the above observations was greater than 3 m/s. To summarize, the analysis indicates dominant wavelength and direction can be measured by

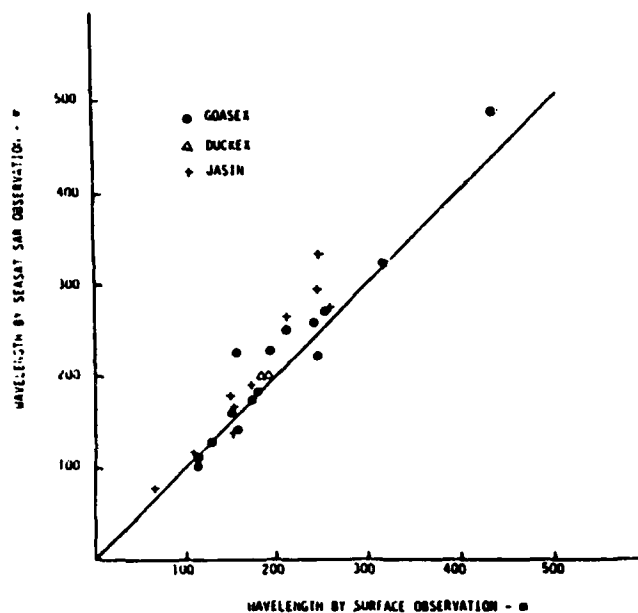


FIGURE 6. PLOT OF WAVELENGTH, SAR VERSUS SEA TRUTH, FOR L-BAND SEASAT DATA (After Vesecky and Stewart, 1981).

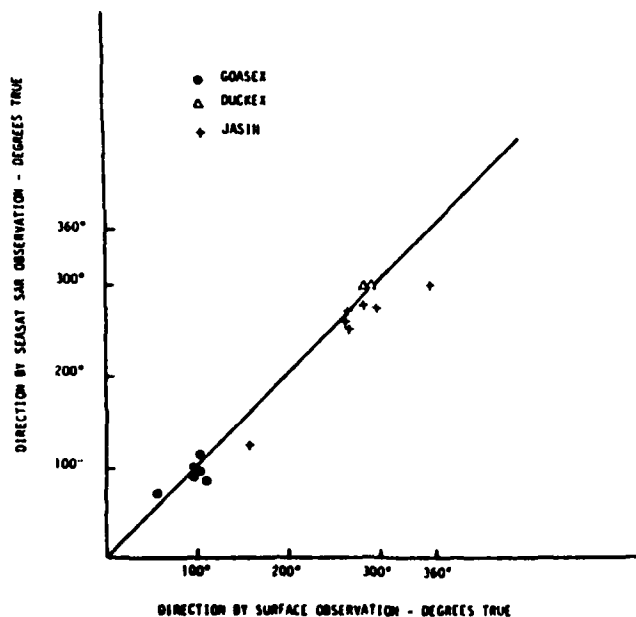


FIGURE 7. PLOT OF WAVE DIRECTION, SAR VERSUS SEA TRUTH, FOR L-BAND SEASAT DATA (After Vesecky and Stewart, 1981).

the Seasat SAR provided the waves in question are visible on the imager (Vesecky, et al., 1981; Kasischke, 1980).

Figures 8, 9, 10, and 11 are scatterplots of aircraft SAR derived estimates of wavelength and direction versus sea truth for X- and L-band data of Marineland, GOASEX (aircraft), and Lake Michigan. These results indicate wavelength information does not appear biased and is accurate to within ~13 percent, while directional information is also not biased and is accurate to within ~10 degrees. It should be noted for the airborne SAR results, the L-band SAR did not detect wind generated waves on every occasion where waves were detected on the X-band imagery. The sea truth for the above aircraft SAR studies was provided by a variety of wave measuring devices, including pitch and roll buoys (Marineland and GOASEX), wave staff, wave rider buoy (Lake Michigan), pressure sensors (Marineland), water level gauges (Lake Michigan), and velocity meter arrays (Lake Michigan).

To assess the potential of using SARs to measure surface gravity wavelength and direction, we must know the accuracy of the SAR system. In determining the accuracy of a measurement, one compares the results obtained from the measuring device against a standard. In determining the accuracy of SAR spectral estimates, we could use the standard oceanographic technique (i.e., pitch and roll buoys, wave rider buoys, etc.) as our standard, but the accuracy of these techniques is not very high. It may be, in fact, that SAR spectral estimates of dominant ocean wavelength and direction are more accurate (in the absolute sense) than present day oceanographic techniques.

There is a "level of uncertainty" associated with SAR spectral measurements which is mainly due to the variability in the wave field being imaged by the SAR and the precision limitations of the devices used to measure wavelength and direction. This level of uncertainty is on the order of ± 2 percent for wavelength and $\pm 1^\circ$ in direction (Kasischke, et al., 1981).

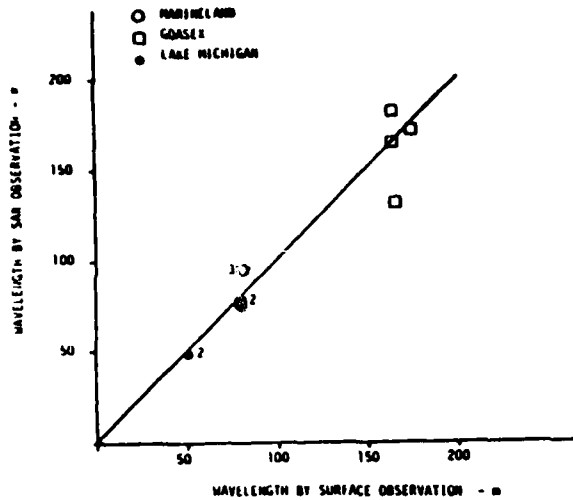


FIGURE 8. PLOT OF WAVELENGTH, SAR VERSUS SEA TRUTH, FOR X-BAND AIRCRAFT DATA.

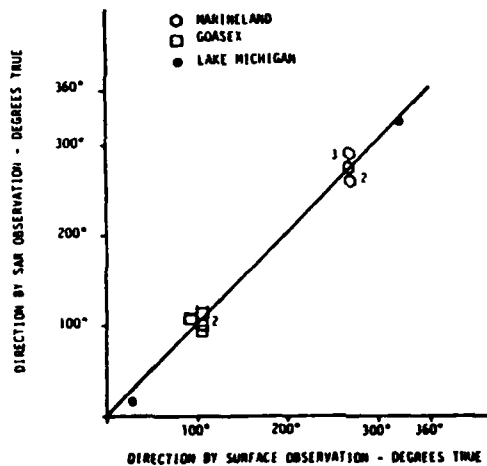


FIGURE 9. PLOT OF WAVE DIRECTION, SAR VERSUS SEA TRUTH, FOR X-BAND AIRCRAFT DATA.

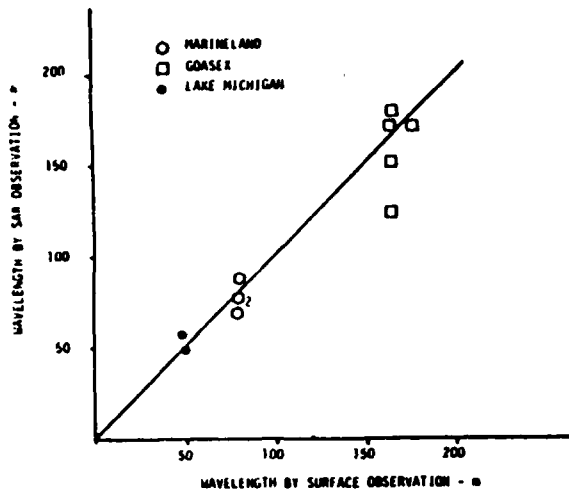


FIGURE 10. PLOT OF WAVELENGTH, SAR VERSUS SEA TRUTH, FOR L-BAND AIRCRAFT DATA.

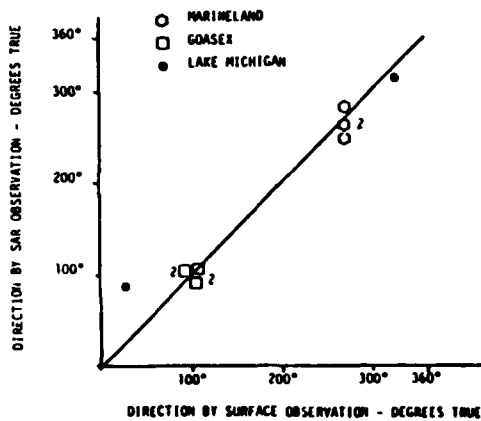


FIGURE 11. PLOT OF WAVE DIRECTION, SAR VERSUS SEA TRUTH, FOR L-BAND AIRCRAFT DATA.

3.3.4 LIMITATIONS OF SAR IN DETECTING GRAVITY WAVES

The limitations of using a SAR to image gravity waves are still under study. The major obstacle in this definition is collecting SAR data under the wide variety of conditions (both atmospheric and oceanic) which naturally occur. Usually, no single SAR data set contains all the environmental variables one would like to evaluate. In addition, even within a single limited SAR data set, it is often difficult to ascertain what parameters are playing an important role determining whether or not a gravity wave field is visible on SAR imagery.

In examining the evidence to date, it appears that the following parameters play a role in SAR imaging of ocean gravity waves:

1. Radar wavelength,
2. Radar look direction relative to wave direction,
3. Number of resolution elements per wavelength,
4. Wind speed, and
5. Wave height.

No single factor taken alone is responsible for determining the degree of SAR detection of gravity waves, but it is usually due to a combination of the above factors. This point can be best illustrated through an example.

During the recent JASIN experiment, the Seasat SAR successfully imaged gravity waves on thirteen out of a possible eighteen opportunities (Vesecky, et al., 1981; Kasischke, 1980). During this experiment, only an L-band SAR was operating (Seasat) and the wind speeds were always above the threshold (~ 3 m/s) for wave detection. Therefore, points (1) and (4) above are not variable factors when determining whether or not the Seasat SAR detected the ocean gravity waves. Table 4 presents the environmental conditions present when the 18 JASIN passes were made. As can be seen in Table 4, in most cases the SAR did not detect gravity waves when two of the three following conditions were met:

TABLE 4
SUMMARY OF WAVELENGTH, HEIGHT, AND DIRECTION
DATA FOR JASIN TEST AREA*

<u>Revolution</u>	<u>Wavelength (meters)</u> <u>(sea truth)</u>	<u>Height (meters)</u>	<u>θ_A^{**} (°True)</u>
<u>No Wave Detection</u>			
590	89-222	1.2	73° - 39°
599	71	1.1	25
633	89	1.1	77
642	169	2.7	14
1006	105	3.6	33
<u>Poor Wave Detection</u>			
556	151	1.5	64
714	182*	-	59*
834	147	2.8	29
958	108	1.4	31
719	164*	-	76*
<u>Fair-to-Good Wave Detection</u>			
547	170	1.6	58
757	256	4.9	23
762	210	5.5	90
792	151	3.1	73
1001	81	2.3	63
1044	244*	5.7	44
1049	244	5.0	57
1087	299*	-	34

All data use sea-truth estimates except for those denoted with an ().

**Relative direction of the wave crests with respect to the radar line-of-sight.

1. Significant wave height ($H_{1/3}$) was less than 1.3 meters;
2. The waves were traveling in nearly an azimuth direction with respect to the radar line-of-sight ($\theta_A < 35^\circ$, where θ_A is the angle between the wave crest orientation and the radar line-of-sight); and
3. The number of resolution cells per wavelength was less than 5 (or the ocean wavelength (λ) was less than 125 meters for the 25 meter resolution Seasat SAR).

From Table 4, it can be seen that in most cases where waves were not detected by the SAR, a minimum of two of the above criteria were met. In only one case where waves were visible on the SAR image were two criteria met (Rev. 958) and here the waves were not very clear on the SAR image.

Of the five original conditions mentioned at the beginning of this section, all have been examined independently. It has been the general consensus within the SAR community that X-band (3.2 cm) SARs detect gravity waves more readily than L-band (23.5 cm) SARs. In measuring the crest-to-trough modulation (or modulation depth) of waves on SAR imagery collected during the Marineland experiment, Kasischke, et al. (1979), showed that X-band imagery of gravity waves had higher modulation depths than L-band imagery. More recently, Kasischke and Shuchman (1981 and 1981a) showed the same result (i.e., higher wave contrast on X-band imagery when compared to L-band imagery) through the use of a SAR image wave contrast measurements, called a peak-to-background ratio (PBR). This latter comparison was based on aircraft SAR data collected over Lake Michigan. From yet unpublished results obtained at ERIM, the same trend was apparent in the GOASEX data.

A possible explanation for the higher quality of X-band surface wave imagery was given by Shuchman and Zelenka (1978) who suggested that X-band data possess a larger depth of focus than L-band, and

therefore, the waves moving in the azimuth direction are not appreciably defocused as commonly occurs on L-band images of comparable resolution. X-band SARs also incorporate a shorter synthetic-aperture length or integration time than L-band systems, hence reducing motion errors. Another possible explanation for the increased X-band image quality is that there are generally more X-band Bragg waves (~2 cm) present on the water surface per unit surface area.

There are several effects of the radar look direction on wave detectability by SARs. First SARs, in general, detect range traveling waves (wave crests perpendicular to radar line-of-sight) more readily than azimuth traveling waves (wave crests parallel to radar line-of-sight); and second, SARs appear to detect waves traveling towards the radar better than those traveling away from the radar.

Teleki, et al. (1978), using Marineland data, indicated that optimum wave images result when the radar is looking essentially up-wave or down-wave; that is, when waves propagate towards or away from the aircraft in the range direction. Figure 12 (after Teleki, et al., 1978) is a graph of modulation (wave crest to trough contrast) versus radar look direction (relative to wave crest orientation) for X- and L-band SAR aircraft data collected from Marineland. Note, from Figure 12, that when the SAR is looking up-wave or down-wave (i.e., SAR line-of-sight perpendicular to the wave crests), higher contrast or more visible waves result. It should be noted that the significant wave height was approximately 1.2 m for the 8-second swell presented in Figure 12. The same result was obtained using MARSEN UPD-4 X-band data as will be discussed in Chapter 4. Range-traveling waves are more clearly discernable on SAR imagery because, in the range direction, the SAR uses a train of very short pulses. Therefore, waves traveling in range appear quasi-stationary relative to the sampling time.

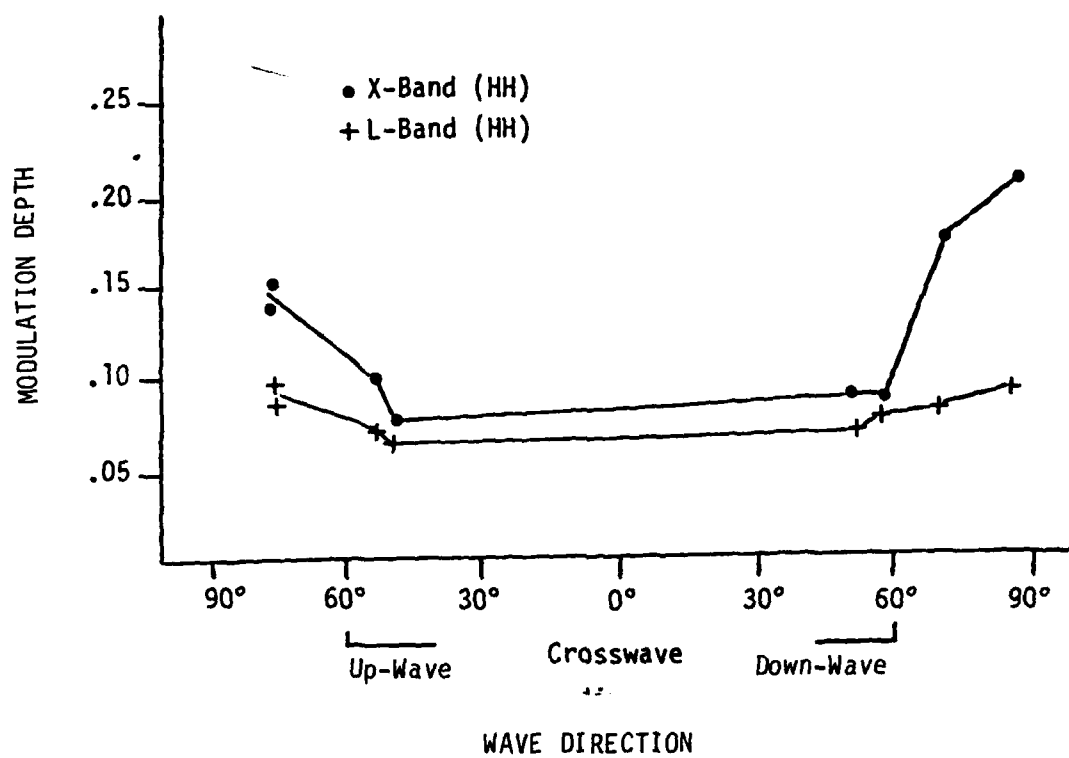


FIGURE 12. MODULATION DEPTH AT X-BAND AND L-BAND AS A FUNCTION OF RADAR LOOK DIRECTION (After Teleki, et al., 1978).

Studies by Kasischke and Shuchman (1981) have shown that SAR (both X- and L-band) images of waves traveling towards the radar have higher contrast (PBR) than SAR imagery of waves traveling away from the radar.

Nyquist sampling theory indicates that at least two samples per wave cycle are necessary to resolve gravity waves on SAR imagery. For real data, the number of samples needed is probably between four and six. The number of samples per wave cycle is dependent on two variables: the spatial resolution of the SAR system and the wavelength of the gravity waves. In general, airborne SARs can detect shorter wavelength wave fields than spaceborne SARs. The lower limit for the Seasat SAR appears to be around 100 meters or approximately 4 resolution elements. Airborne SARs, with their finer resolution, can detect wind driven waves with wavelengths on the order of 35 meters.

As mentioned previously, in order for gravity waves to be detected by SARs, a small scale surface roughness must be present on the longer gravity waves. The small scale surface roughness corresponds to the capillary and ultra-gravity wavelength region waves which are typically abundant in the presence of low to moderate winds. The minimum wind speed necessary for detection of gravity waves is on the order of three meters per second (Beal, 1979). There has been speculation that waves would not be detectable by SARs in the presence of high winds. However, L-band radars have detected waves in hurricanes (Ross, et al., 1974; Brown, et al., 1976; Gonzalez, et al., 1981a).

The final factor which appears to play a significant role in SAR imaging of surface gravity waves is wave height. Recent studies (Kasischke, 1980) involving Seasat SAR imagery collected during the JASIN experiment have shown a significant degree of positive linear correlation ($R = 0.78$ at $\rho = 0.99$) between wave contrast (PBR) and significant wave height ($H_{1/3}$). Furthermore, SARs do not detect

gravity waves when the wave height of the field is below a certain minimum. For the Seasat SAR, this lower bound is approximately one meter. Additionally, the Seasat SAR had greater difficulty in imaging waves with heights less than 1.5 meters than waves higher than 1.5 meters for $H_{1/3}$. Aircraft SARs, however, have routinely imaged gravity waves with heights less than 1.5 meters, and have produced very good images of wave fields with heights approaching one meter (Lake Michigan, $H_{1/3} = 1.0$ to 1.2 m; GOASEX: $H_{1/3} = 1$ m; Marineland: $H_{1/3} = 1.5$ m; MARSEN: $H_{1/3} = 1$ to 1.5 m). The lower limit of wave height for aircraft SARs has not yet been determined, but is probably around 0.75 meters.

3.4 SAR DETECTION OF OCEAN AND COASTAL CURRENTS

There appears to be little question that ocean current boundaries can frequently be observed on SAR images, although the reason for their appearance is not yet understood. Current boundaries were first noted on aircraft SAR imagery by Moskowitz (1973). Since then, currents have been extensively studied by both aircraft SARs (Larson, et al., 1976; Shuchman, et al., 1977a; 1979; Weissman, et al., 1980; Shuchman, et al., 1981b) and spaceborne SARs (Hayes, 1981; Shuchman, et al., 1979; Shemdin, et al., 1980; Mattie, et al., 1980; Cheney, 1981; Lichy, et al., 1981; Shuchman, et al., 1981c). Current velocity gradients (du/dx) on the order of 10^{-3} sec^{-1} appear to be detectable (Larson, et al., 1976), and the sensing of current boundaries apparently occurs for a wide range of wind speeds (3-10 m/s) and air-sea temperature differences ($0.1 - 10^\circ\text{C}$).

The appearance of current boundaries on SAR images was at first thought to be due to a Doppler-induced image displacement (Larson, et al., 1976), but this notion has been discounted by the observation of current boundaries at all radar look direction orientations on Seasat data (Hayes, 1981). Although the Doppler mechanism may be a contributing factor in some cases, it is now felt that the main reason for the appearance of current boundaries on SAR imagery is either

a stress-induced variation in surface roughness in the area of the shear, or a difference in the surface roughness of the water masses.

Research has been conducted not only on the detection of ocean and coastal currents, but also on obtaining velocity information from SAR data. The next two sections will discuss these efforts.

3.4.1 SAR DOPPLER EFFECTS

Measurements of the perturbation of SAR signal histories due to Doppler effects, arising from the radial component of the surface velocity, is a potentially useful technique for measuring currents. This technique has been utilized on X-band aircraft SAR data of several locations (Shuchman, et al., 1979; Gonzalez, et al., 1981b; Shuchman and Meadows, 1980). It takes advantage of the fact that the SAR instrument responds primarily to backscatter from capillary waves which, in conventional SAR processing, are assumed stationary with respect to other time scales of the radar system. However, these scatterers are not stationary; they move with a characteristic phase velocity as well as with velocities due to the presence of currents and longer gravity waves. The radial (line-of-sight) component of the resultant velocity produces a Doppler shift in the temporal frequency of the return signal, which translates to a spatial frequency shift recorded on SAR signal film.

Shuchman, et al. (1979) showed that the radial component of a target velocity (V_r) could be calculated as:

$$V_r = \frac{\Delta f' \lambda V_{AC}}{2P} \quad (2)$$

where $\Delta f'$ is the azimuth spatial frequency shift, λ is the transmitted radar wavelength, V_{AC} is the platform velocity and P is the azimuth packing factor.

This relationship can be used to measure the average radial velocity component of an ocean-wave scattering field relative to a fixed-land scattering field. A shift in the azimuth spatial frequency spectrum between fixed-land and moving-ocean surfaces yields an estimate for $\Delta f'$. Variations in spectrum location due to antenna pointing may be eliminated by choosing imagery having both land and ocean imaged simultaneously.

Seasat data are not well suited to the Doppler perturbation technique because of the high platform velocity (~7 km/sec), the wavelength (L-band = 23.5 cm) and the small incidence angle (~20°) of the Seasat SAR (Shuchman, et al., 1981c). It may be possible, however, to design a satellite system with a more optimal configuration for measuring ocean currents using this technique. Studies are currently being carried out at ERIM to investigate the system parameters which influence a SAR's capability of measuring currents using Doppler methods, which will hopefully lead to new design criteria (Rufenach, et al., 1981). There are a large variety of SAR system configurations which could conceivably lead to an improved capability of measuring ocean currents using Doppler techniques. Among these are systems using specialized antenna designs or multiple antennas, angle diversity or spotlight techniques and multiple frequency techniques. (For a discussion of multiple frequency or ΔK techniques, see McIntosh, 1981.) For this reason, it is felt that Doppler methods have a high potential value for measuring ocean currents, although this potential is not yet fulfilled.

Another technique to measure currents via SAR data was reported by Shemdin, et al. (1980). This technique was applied to Seasat data collected over the mouth of the Columbia River (Oregon); the azimuthal shift of the boundary of the current as it flowed past stationary jetties was measured. Using the relationship:

$$\Delta X = \frac{V_r}{V_{AC}} R \quad (3)$$

where ΔX is the azimuthal displacement, R the range to the target and V_{AC} the platform velocity, the radial line-of-sight velocity (V_r) of the Columbia River was successfully estimated. Although this method may be useful in some cases, in general it is felt that an azimuthal displacement of this kind is difficult to measure accurately, since it is likely to be obscured by brightness variations due to surface roughness or other effects.

3.4.2 WAVE REFRACTION EFFECTS

The interaction of gravity waves with ocean currents may provide a tool for estimating large scale current variations from SAR imagery (Hayes and Shuchman, 1981). This effect has been documented on aircraft SAR data by Hayes (1980), and investigations are currently underway at ERIM and elsewhere to evaluate the usefulness of Seasat data for this purpose (Kasischke, et al., 1981; Meadows, et al., 1981; Mapp, et al., 1981). However, there appear to be several limitations to this method. First, a suitable wave field must exist coincidentally with an ocean current. Second, this technique is not applicable to enclosed or shallow water areas where wave refraction or diffraction may occur through interactions with the shoreline or the ocean floor. Third, existing wave-current models have yet to be thoroughly tested, and questions exist as to their validity (Meadows, et al., 1981). Finally, the angle between the wave train and the current directional vector is critical in determining the degree of refraction the current causes. According to wave-current refraction models (Phillips, 1981; Kenyon, 1971), the amount of refraction that occurs is proportional to the cosine of the angle between the wave direction and the current direction, i.e., when this angle approaches 90° , little refraction occurs and the maximum refraction occurs as this angle approaches some critical angle of total internal reflection (which is dependent on the phase speed of the waves). In the many circumstances where the angle changes due to refraction are

small, it is difficult to detect these changes from SAR data with its present directional resolution.

In summary, the potential exists for the determination of ocean current velocities by observing wave refraction through the current. Research is still being conducted to test this potential.

3.5 SAR DETECTION OF LONG PERIOD WAVES

Recently, SAR oceanographic research has been concerned with the question of whether a two-dimensional transform of a SAR imaged gravity wave field can yield information other than dominant gravity wavelength and direction. One such investigation in this regard has examined SAR images to see if long period (15-300 second) wave information is inherent in SAR signals received from the ocean surface.

Synthetic aperture radar (SAR) has been used to image long period (15 - 300 s) gravity waves in the near-shore region of Lake Michigan (Meadows, et al, 1981a). These long-period waves appear to be a response of the sea surface to forcing by a non-monochromatic, wind-generated, surface wave field. SAR data compared favorably with an in situ wave gauge record. Both one- and two-dimensional fast Fourier transforms were generated from the SAR data of a near and offshore region, each 1.5 x 1.5 km in size. A two-dimensional transform of the SAR data showing low frequency components is presented in Figure 13. The SAR derived near- and off-shore spectral estimates both exhibited low and high frequency wave components. Table 5 is a comparison table between the long period SAR derived spectral estimates and the in situ step resistance wave gauge measurements (sea truth). Classical bathymetrically controlled wave refraction was observed for both the short and the long wave components of the water surface. This Lake Michigan analysis is one demonstration of the ability of X-band SAR to successfully image low amplitude, long period signals. These signals appear to correspond to a "surf beat" generated by the incident wave field.

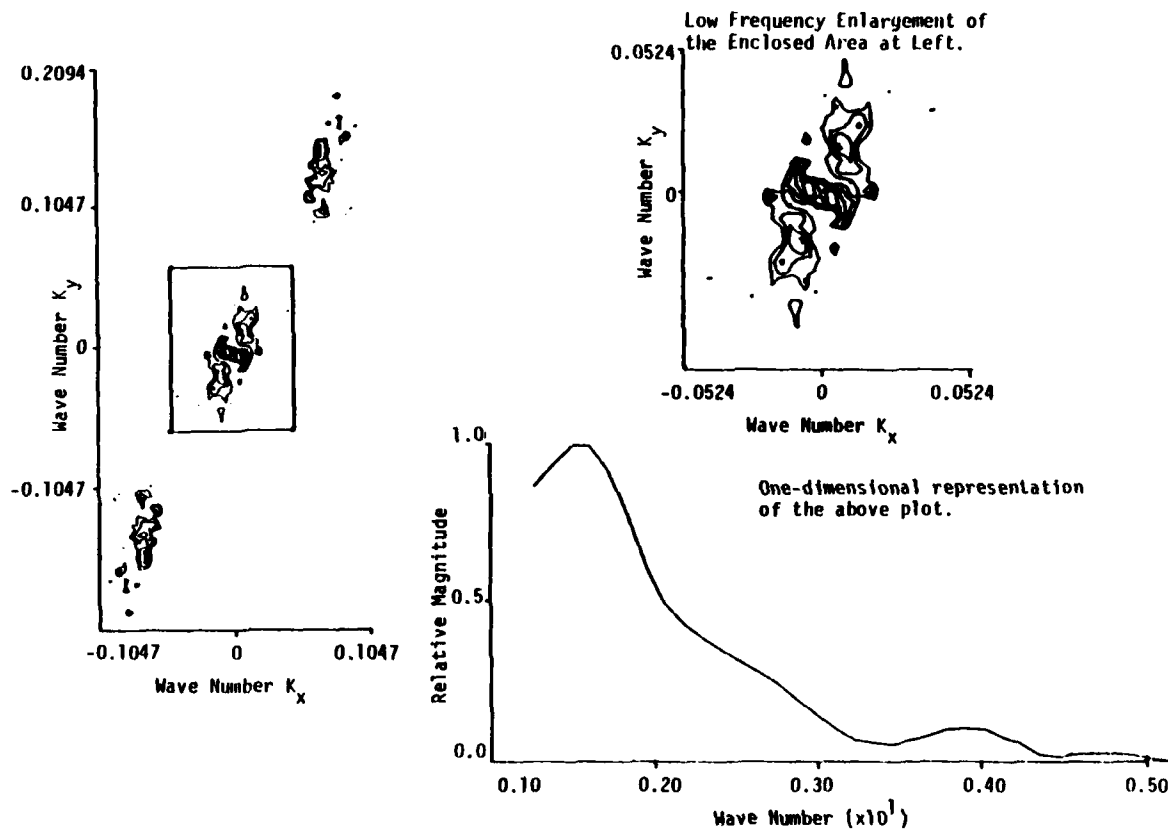


FIGURE 13. SAR DERIVED TWO-DIMENSIONAL SPECTRAL ESTIMATE (Near-Shore).

TABLE 5
COMPARISON BETWEEN THE LONG-PERIOD SAR-DERIVED SPECTRAL
ESTIMATES AND THE IN-SITU SEA TRUTH

Test Area	Distance from Shore (m)	Depth (m)	SAR-Derived		Sea-Truth*	
			Dominant Long-Period Wavelengths (m)	Direction (T°)	Dominant Long-Period Wavelengths (m)	Direction (T°)
A (Nearshore)	2650	16.2	157-167 393-423	35 ± 3	216 406	34 ± 2
B (Offshore)	5800	28.7	498-523	25 ± 3	288 541	28 ± 2

*Actual measurements made at the surf zone, values for test areas A and B are depth corrected.

A proposed physical mechanism for the indirect imaging of "surf beats" by radar backscatter is as follows. A modulated, wind driven, capillary/ultra-gravity wave field exists in conjunction with a shoreward propagating, non-monochromatic, gravity wave field. Non-linear capillary-gravity wave interactions occur which produce increased surface roughness on the crests of the gravity waves and decreased surface roughness in the troughs. Concurrently, similar but slightly different gravity wave components of the non-monochromatic wave field are interacting to form surf beats consisting of groups of high waves separated by groups of low waves. These wave groups produce corresponding depressions and relaxations of the mean water level in response to fluctuations of the applied radiation stress (Longuet-Higgins and Stewart; 1964). Hence, a forced, long-period wave, traveling at the group velocity of the wind wave packet is generated. Bright radar returns, therefore, should correspond to groups of high gravity waves in the troughs of the forced long-period waves. It should be noted that SAR sensing of long period waves is a new research area and much more work is needed to fully define SAR's role.

3.6 SAR DETECTION OF INTERNAL WAVES

Internal wave studies have been a popular subject among oceanographers using aircraft and satellite data since Apel, et al. (1975) reported internal wave patterns on Landsat imagery. Since that time, the study of internal waves using remote sensing data from the optical domain has drawn much attention (Fett and Rabe, 1977; Mollo-Christensen and Mascarenhas, 1979; Osborne and Burch, 1980).

The first SAR image of internal waves was presented by Brown, et al. (1976). Since then, several other authors have presented SAR imagery of internal waves (Elachi, 1978; Gower and Hughes, 1979; Shuchman and Kasischke, 1979; Apel, 1981; Beal, et al., 1981; Trask and Briscoe, 1981; Vesecky and Stewart, 1982). A review of Seasat

SAR data reveals an abundance of internal wave patterns along both the east and west coasts of the U.S., in the coastal waters of the Canadian Pacific and Gulf of Alaska, along the European coast and even in Lake Michigan.

There are several forces believed to be responsible for the generation of internal waves. The most common is tides (Apel, et al., 1975) or tidal currents (Gower and Hughes, 1979). Another force believed to generate internal waves are shear flow instabilities induced by large vertical gradients in ocean currents such as the Gulf Stream (Apel, et al., 1974). When an internal wave is propagating along a density gradient, as is shown in Figure 14 (after LaFond and Cox, 1962), it has its own distinct energy and current fields. These motion fields create areas of surface convergence and divergence, and thus provide the mechanism for their detection by SARs.

At one time it was believed that the alternating rough and smooth bands on the ocean surface associated with internal waves were due to the collection of surface oils at the convergence zones (Lafond and Cox, 1962). Recent theory (Gargett and Hughes, 1972) states that the current fields associated with the internal waves are strong enough to alter the surface capillary and ultra-gravity structure. Recent experiments by Gower and Hughes (1979) support this theory.

The environmental bounds under which internal waves are detected by SARs have yet to be determined. Obviously a capillary and ultra-gravity wave field must first be present, which means that there must be a surface wind. Gower and Hughes (1979) observed internal waves on airborne SAR data which were collected over relatively calm seas (winds of two to three m/sec and surface wave heights of approximately one meter) while Shuchman and Kasischke (1979) observed internal wave patterns on Seasat SAR imagery during a relatively high sea state (winds of 12 m/sec and significant wave heights ($H_{1/3}$) of 5.5 m). Therefore it appears that a SAR can detect internal waves over a wide range of environmental conditions.

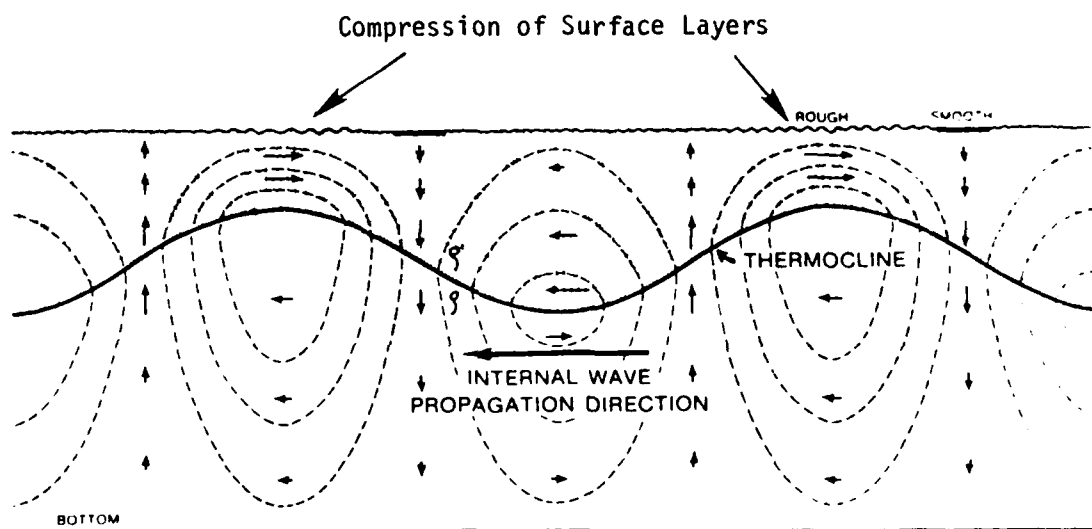


FIGURE 14. SCHEMATIC OF THE STRUCTURE OF PROGRESSIVE INTERNAL WAVE MOTION ALONG A SHARP THERMOCLINE ILLUSTRATING ALTERATION OF SURFACE ROUGHNESS (After Lafond and Cox, 1962).

3.7 SAR SENSING OF FRONTAL BOUNDARIES

With the launch of SEASAT in the summer of 1978, the ability to collect SAR data on a synoptic scale was realized. Among the many interesting features imaged were large radar backscatter discontinuities. These backscatter discontinuities were believed to correlate in location with the boundary of different water masses (i.e., fronts). The detection of these fronts is useful in many applications: sonar propagation, biological activity, and pollution dispersion.

During the fall of 1980, a multi-institutional experiment coordinated by NASA/Langley was conducted to study fronts at the mouth of Chesapeake Bay. Among the sensors flown were an X-band UPD-4 SAR carried aboard a U.S. Marine F-4, an X-L dual polarized SAR housed in a CV-580 and a real aperture X-band SLAR flown in a U.S. Mohawk aircraft.

The fronts found at the entrance to Chesapeake Bay are formed by the mixing of the Atlantic Ocean with various bay water masses. Fronts that are commonly observed in the bay entrance are sometimes accompanied by visible foam lines, slicks, or capillary ripples, but little is known about their stability or temporal and spatial distribution. The maintenance of estuarine fronts such as those found on Chesapeake Bay, is closely influenced by the lateral shear across the interface (Bowman and Iverson, 1978). This lateral shear may be a result of various combinations of bathymetric variation, tidal current, and river discharge. Also, convergent surface currents are typically found at these frontal boundaries, causing buoyant particulate matter as well as debris to collect at the boundary. Figure 15 (from Oertel and Dunstan, 1981) is a typical front found at the mouth of Chesapeake Bay.

Several SAR images of the Chesapeake Bay fronts were collected during the fall of 1980; a typical example is shown as Figure 16.

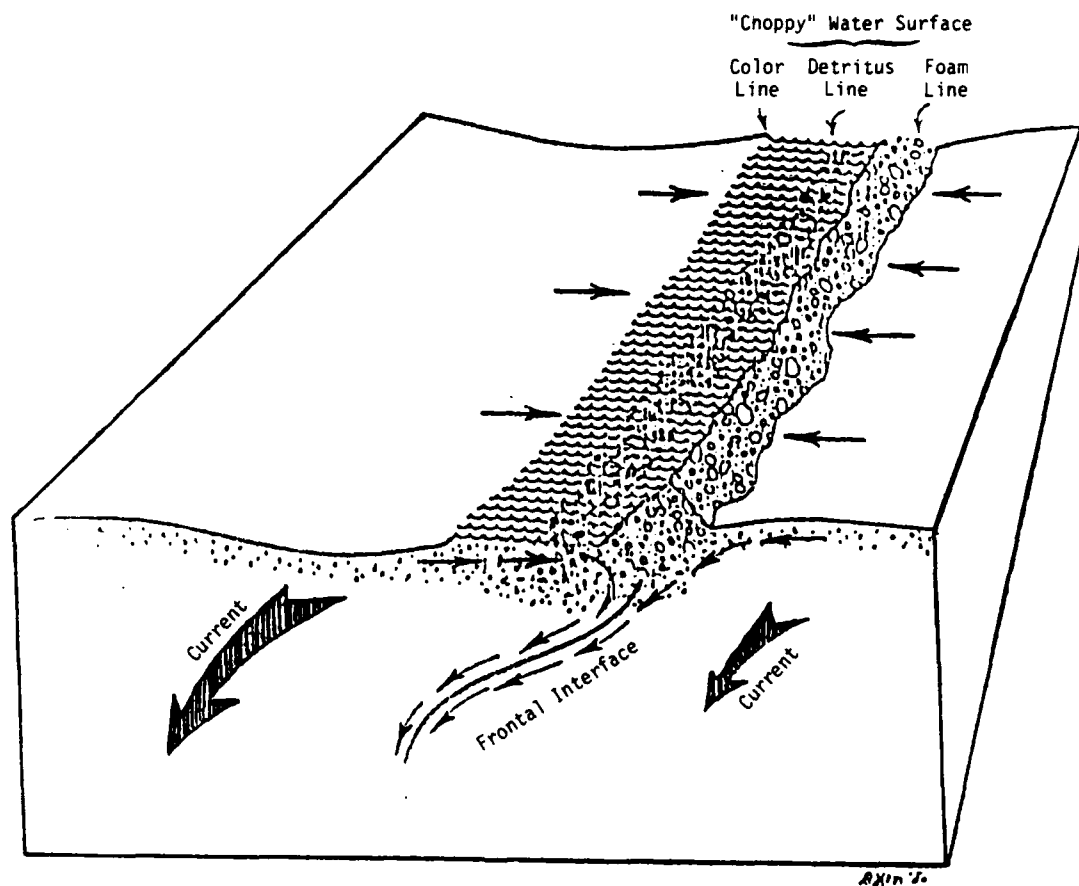


FIGURE 15. SKETCH OF FRONTAL SYSTEM ILLUSTRATING CONVERGENT SURFACE CURRENTS AND SURFACE ROUGHNESS EFFECTS (Adapted From Oertel and Dunstan, 1981).

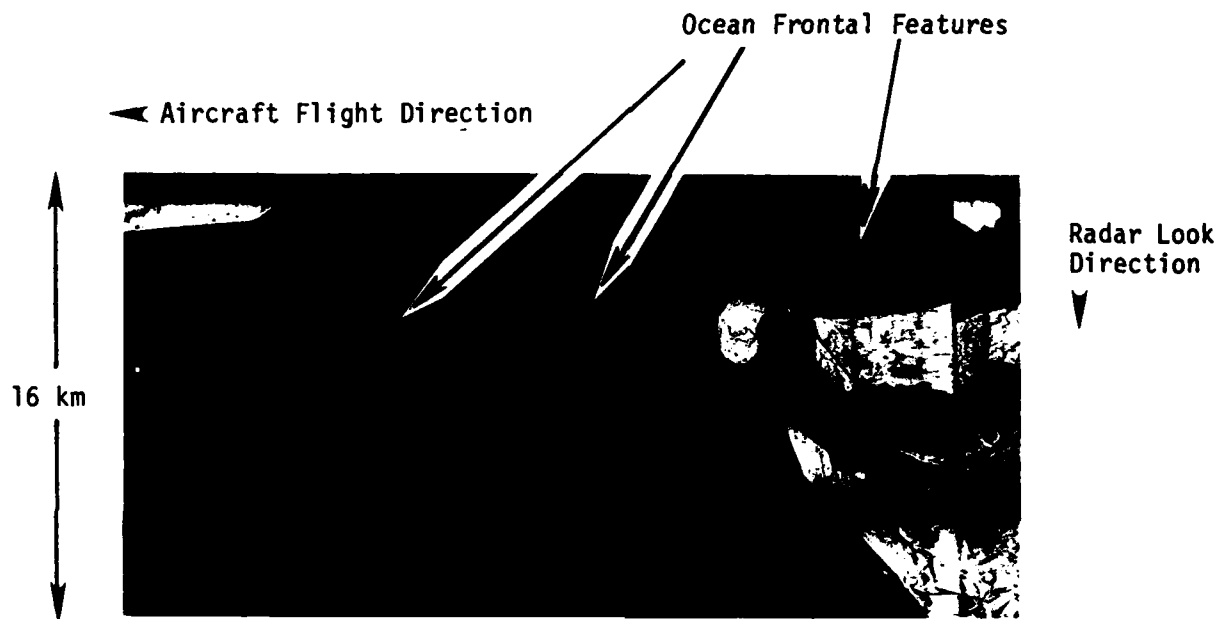


FIGURE 16. SAR IMAGE (X-band) OF MOUTH OF CHESAPEAKE BAY
ILLUSTRATING OCEAN FRONTAL TYPE FEATURES
(10 October 1980).

Recent backscatter measurements made at ERIM on this data show approximately a 2-3 dB increase in radar backscatter at the boundary of the front (Lyden and Shuchman, 1981).

The preliminary analysis of the data collected during this experiment has indicated that imaging radars have the ability to image oceanic fronts. This conclusion was based on repeated observations of frontal features in radar imagery at locations where fronts were known to occur. Direct comparisons between radar imagery and coincident surface observations support this observation.

Fronts were detected with a variety of radar operating parameters; these include: (1) both X- and L-bands, (2) HH and VV polarizations, (3) both synthetic and real aperture radars, and (4) incidence angles ranging from approximately 20° to 85°. Fronts were also imaged under a wide variety of environmental conditions: (1) wind speeds of 1.5 to 16.5 m/sec, (2) all wind directions, and (3) all stages of tide. However, fronts were not always detected within these ranges of conditions; apparently, some particular combination of the various parameters (i.e. tides and winds) is necessary for detection.

Although the radar imaging mechanism for frontal boundaries is not totally understood at the present time, a plausible explanation partially supported by experimental evidence of why fronts are visible on radar imagery has been formulated. Imaging radars are sensitive to the Bragg ocean wave components as discussed earlier. The currents associated with the fronts cause the Bragg waves to refract (i.e. undergo compression or elongation) in direct proportion to the magnitude and direction of the current. The refraction therefore differs from one side of the frontal boundary to the other. The radar detects these subtle changes in the amplitude and wavelength of the primary wave and records these changes in the form of received backscatter.

3.8 SAR DETECTION OF BOTTOM TOPOGRAPHIC FEATURES

A variety of remote sensing techniques have been studied over the past decade for their potential in providing information for updating navigation charts. Remote sensing data can be used to accomplish this goal in three ways: (1) detect the presence of submerged features that are potentially hazardous to ship navigation; (2) accurately locate the geographical position of these hazardous features and underwater topographical surface variations; and (3) provide estimates of water depth.

Recently, ERIM under Defense Mapping Agency funding (Kasischke et al., 1980) began to explore the use of SAR to provide bathymetric information. The SAR energy does not penetrate appreciably into the water surface, thus the features observed on SAR imagery are caused by a hydrodynamic interaction between the bottom feature and surface Bragg waves. The SAR observed topography-related phenomena can be classified into five categories:

1. A change in direction and wavelength of ocean swell as it enters shallow coastal regions;
2. A distinct change in radar backscatter associated with a current flowing over a shallow water (<50 m) bottom feature;
3. A distinct change in radar backscatter associated with an ocean swell propagating over a distinct depth discontinuity;
4. Classic internal wave patterns over continental shelf regions; and
5. Anomalous SAR backscatter signatures found in deep (> 200 m) ocean regions over topographic features (such as guyots and submarine ridges) on the ocean floor.

As gravity waves enter shallow, coastal waters, the wavelengths and directions of the waves begin to change due to interactions with the bottom. The amount the wavelength and direction changes is

proportional to the depth of the water at a given point; therefore, if the change in wavelength and/or direction can be measured, an indirect measure of water depth can be obtained.

This theory was tested in a study by Shuchman, et al. (1979a). Using Seasat SAR data from Rev. 974 (collected on 3 September 1978), dominant wavelengths and directions were obtained (via optical Fourier transforms) for a gravity wave train as it travelled shoreward in the Cape Hatteras, North Carolina, area. Using two simple wave refraction models, water depths were estimated using SAR derived wavelengths and/or directions as inputs. The model derived depths compared favorably to existing hydrographic chart depths.

Several researchers have reported surface signatures on SAR imagery that are the result of a current flowing over a bottom feature in shallow (< 50 m) water. De Loor and Brunsveldt van Hulten (1978) first detected this phenomenon in real aperture radar imagery collected over the North Sea. Using Seasat SAR imagery, Kasischke, et al. (1980) and Kenyon, et al. (1979) have reported detecting sand waves in the southeast corner of the North Sea; McLeish, et al. (1981) reported on sand waves off the Dutch coast detected on real aperture radar imagery; and finally, Kasischke, et al. (1980) reported detecting sand waves and ridges in the Nantucket Shoals region off the Massachusetts coast.

The above features are detected by radar (both real and synthetic aperture) due to an interaction between a current and a bottom feature. Whether or not the SAR signature associated with these features is an increase or decrease in radar backscatter depends on several factors, which include depth of the feature, current speed and direction, and wind speed and direction, as well as radar geometry.

Figure 17 shows a schematic diagram of two scenarios where a current is flowing over a bottom feature. Figure 17a illustrates a situation where the surface capillary waves and current are traveling in the same direction. In this case, the increase in current velocity over the bottom feature causes a "stretching out" of the surface capillary waves, resulting in a decrease in radar backscatter due to the decrease in the amplitude of the Bragg scatterers in this region. If there is a large enough wind component in the same direction, the waves may be regenerated in this region and the wave amplitude "overshoot" in the convergence zone behind the bottom feature. This results in a banded appearance with a dark region on one side of the feature and a bright region on the other side. Another possible case is given in Figure 17b. Here the wind and surface capillary waves are traveling in the opposite direction of the current. This combination results in a bunching of the small surface waves, causing an increase in radar backscatter relative to the surrounding sea surface.

Kasischke, et al. (1980) observed that when an ocean swell propagates over a distinct bottom discontinuity, such as the shallow water area around an island, a distinct change in radar backscatter occurs. This phenomenon has been seen on Seasat SAR imagery of North Rona Rock, Bermuda, and Isle de Gonave (Haiti). The exact cause of this particular type of surface anomaly has yet to be precisely determined. The prevailing theory to explain this phenomenon is based on a non-linear interaction between the gravity wave and the small capillary waves as the gravity wave propagates onto an abruptly changing bottom. In the above examples, there exists a bottom morphology with a very abrupt change in water depth.

Observations of internal waves on Seasat SAR imagery in the vicinity of continental shelf breaks suggest that these waves may be influenced by bottom features. In their early studies of internal waves, Apel, et al. (1975) noted that in the continental shelf

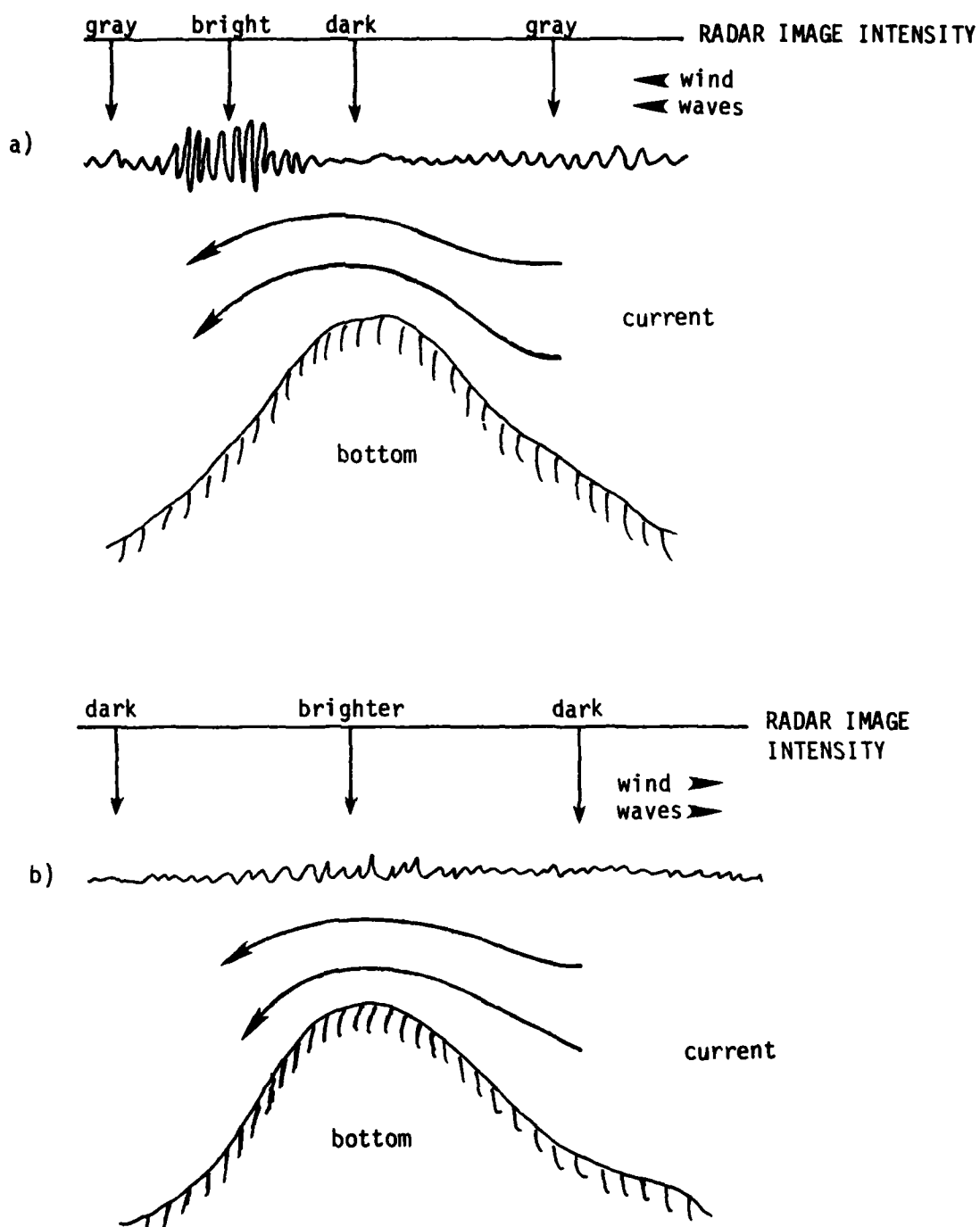


FIGURE 17. SCHEMATIC DIAGRAM OF CURRENT, WIND, AND CAPILLARY WAVE INTERACTIONS.

regions of the U.S., internal waves did not appear on satellite imagery until a minimum depth was reached, and furthermore, once beyond this minimum depth, the internal waves underwent refraction due to the changing water depth. The conclusion which can be drawn from Apel's work is that internal waves on continental shelf regions can be related to the bottom topography.

Finally, in an early study of Seasat SAR imagery, Shuchman and Kasischke (1979) noted the occurrence of numerous "internal wave-like" signatures from data collected over the North Atlantic Ocean. It was discovered that these anomalous signatures occurred over major deep water bottom features, such as the Faeroe Banks and the Wyville-Thomson Ridge (water depth = 300-400 meters).

Recent examination of Seasat SAR imagery collected during the JASIN experiment (Allan and Guymer, 1980) revealed that deep-water, internal wave-like signatures in the North Atlantic always occurred over or near (within 30 kilometers) a deep-water bottom feature (Kasischke, et al., 1982). Furthermore, whenever the Seasat SAR covered the area over one of these deep-water bottom-features, seventy percent of the time an internal wave-like signature appeared on the SAR image.

Further evidence which supports the ability of SAR to detect deep ocean bottom features comes from recent Seasat altimeter studies (Le Schack, et al., 1981; Haxby, 1981), which have determined that there is a significant rise in the mean sea level over guyots and submarine ridges, in some cases as high as 3 to 5 meters. Given the sensitivity of the surface capillary and ultra-gravity wave field to oceanic processes, and the obvious, yet not completely understood, physical processes occurring over these deep water bottom features, it is not surprising that a SAR-detectable surface feature is present.

3.9 SAR MEASUREMENT OF SURFACE WINDS

Knowledge of the synoptic distribution of ocean surface winds is of high importance to oceanographers. Wind speed and direction are important inputs for wave forecasting and hindcasting models (Earle, 1981). These predictions are in turn used as an aid to ship routing, coastal zone management and offshore drilling operations. According to Pierson (1981), wind measurements are required as a function of time and space for periods ranging from three hours down to one minute and over areas of several hundred square kilometers to several square meters. Clearly, the only feasible way to acquire these levels of spatial and temporal coverage is to employ remote sensing techniques.

Wind near a water surface causes small ripples (i.e., capillary waves) to form almost instantaneously. These ripples are therefore highly correlated to the local wind field and microwave measurements sensitive to this scale of roughness can be used to estimate surface winds. This microwave/ripple scattering is governed by the previously discussed Bragg scattering.

Nearly all of the work in microwave wind measurements has employed scatterometers (as reviewed by Moore and Fung, 1979). However, recently the utility of SAR in monitoring surface winds has been explored (Jones, et al., 1981; Weissman, et al., 1980).

An empirical model proposed by Jones and Schroeder (1978) for relating normalized radar cross section (σ_0) to the neutral stability wind vector is:

$$\sigma_0(\text{ratio}) = U_{19.5}^\gamma (1 + \alpha_1 \cos \psi + \alpha_2 \cos 2 \psi) \quad (4)$$

where $U_{19.5}$ = neutral stability wind speed at 19.5 m height,

γ = wind speed exponent,

α_1 and α_2 = anisotropy coefficients, and

ψ = radar azimuth direction relative to upwind.

Typical wind speed exponent (γ) values (obtained from a scatterometer) range from 1.0 to 1.5 at 13 GHz (Moore and Fung, 1979). For an L-band SAR, past studies have indicated that the upwind/downwind anisotropy coefficient (α_1) is negligibly small. This reduces Eq. (4) to:

$$\sigma_0 = U_{19.5}^\gamma (1 + \alpha_2 \cos 2\psi) \quad (5)$$

Present efforts to use SARs to measure surface winds have used this simplified equation.

Although several experiments have employed the use of SAR to detect surface winds (for example, see Ross, 1981; Jones, et al., 1981; Ross and Jones, 1978; Weissman, et al., 1980), this review discusses only data collected during the Duck, N.C. experiment (i.e., DUCKEX), as presented by Jones, et al. (1981).

This experiment utilized SAR data collected by Seasat during orbit 1339. After appropriate corrections and filtering, the L-band scattering model Eq. (5) was applied. The parameters α_2 and γ were then estimated by applying a least-squares fit of the SAR measured power and the surface measured winds. The surface winds used to calibrate the model were determined by a scatterometer operating at 8 km altitude. It was found that the SAR backscatter was nearly isotropic ($\alpha_2 = 0.02$), with a wind speed exponent $\gamma = 0.4$. This is in good agreement with previous L-band airborne radar measurements.

Once these coefficients were determined, the model was tested on an independent data set. Agreement between the Seasat SAR and SASS scatterometer derived winds was excellent (rms of the difference was 0.7 ms^{-1}).

SAR data used for surface wind measurements are generally restricted to areas free of bottom features, currents, or fronts. As previously described, these phenomena act on the wind-generated Bragg

wave field and can therefore affect the accuracy of any wind measurements made from data that include such features. In the case of strong winds, the effects of topography- and current-related modulations may not be of sufficient importance to appear in SAR data.

The use of SAR to measure ocean surface winds appears promising. The advantage of a SAR over a scatterometer is its higher spatial resolution. This allows the measurements to be made over a smaller surface area, and therefore on a fine enough scale to meet the objectives outlined in the introduction to this section.

3.10 OBSERVATION OF SURF ZONE CONDITIONS

Both aircraft and satellite SAR systems have demonstrated an ability to detect various environmental parameters pertaining to the surf zone. Detection abilities include: (1) location of the breaking waves, (2) location of the land/water boundary, (3) measurement of the dominant gravity wave wavelength and direction, (4) measurement of long-shore current strengths and directions, and (5) detection of long-period surf beats.

A SAR sea truth comparison reported by Shuchman and Meadows (1980) and Meadows, et al. (1980) indicated:

1. SAR-derived wavelengths and directions of gravity waves are in good agreement with sea truth,
2. SAR directional spectra taken in various water depths do correlate with predicted wave refraction,
3. The bright lines found on the SAR imagery correspond to the breaker zone as defined by shore observers,
4. Longshore current direction and relative magnitude as obtained from the SAR Doppler history are in reasonable agreement with sea truth, and

5. Low-frequency components observed on SAR spectra seem to correlate with low frequency "surf beat" found in sea truth spectral estimates.

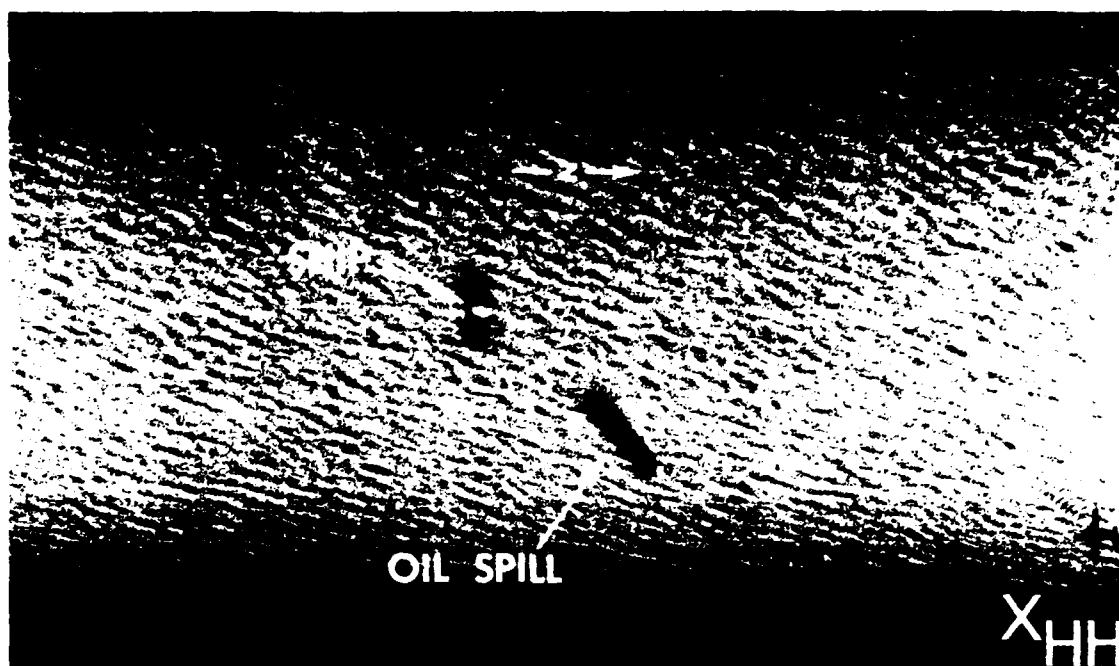
3.11 DETECTION OF OIL SLICKS

The amount of received backscatter from a SAR imaged ocean surface is a function of:

1. The small scale roughness,
2. The mean slope of the water's surface, and
3. The velocity of the ocean scatterers.

The small scale roughness is the most important of the three mentioned factors. A maximum backscatter return is obtained when the small scale ocean roughness satisfies the Bragg roughness criterion of Eq. (1).

The presence of oil on the ocean surface significantly reduces the amplitude of capillary and ultra-gravity ocean waves. Equation (1) predicts that an X-band and L-band SAR imaging the ocean at 45° incidence angle responds to ocean Bragg waves are 2.2 cm and 17 cm in wavelength respectively. Oil films on the ocean surface will damp the X-band Bragg waves more readily than the larger L-band resonant ocean waves. Figure 18 graphically illustrates this concept through an example. Shown in the figure is simultaneously obtained X- and L-band SAR imagery of a crude-oil slick off the east coast of the United States. Note from the figure that the X-band SAR data more clearly delineate the oil slick than the L-band imagery. Rawson and Liskow (1981) calibrated the data shown in the figure and determined that the radar backscatter decreased approximately 3 dB at X-band over the oil slick area, while the radar reflectivity for the L-band data decreased approximately 1.5 dB over that same oil slick area.



Scale = 2.5 km

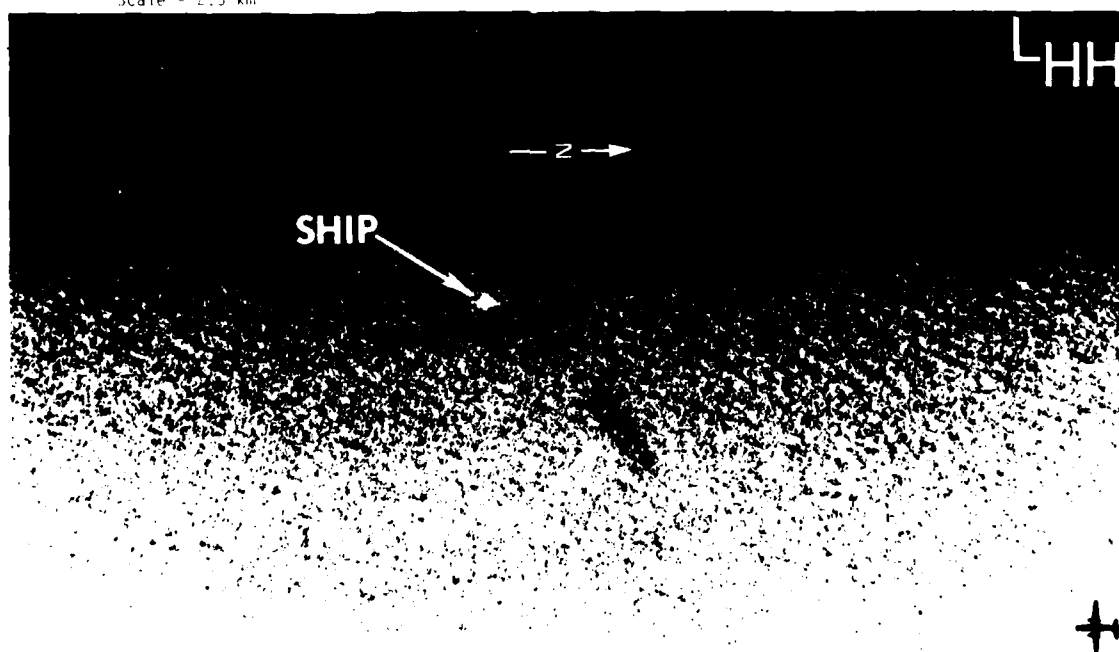


FIGURE 18. SIMULTANEOUSLY OBTAINED X- AND L-BAND IMAGES OF A CRUDE-OIL SPILL OFF THE EAST COAST OF THE UNITED STATES.

3.12 SAR DETECTION AND CLASSIFICATION OF SEA ICE

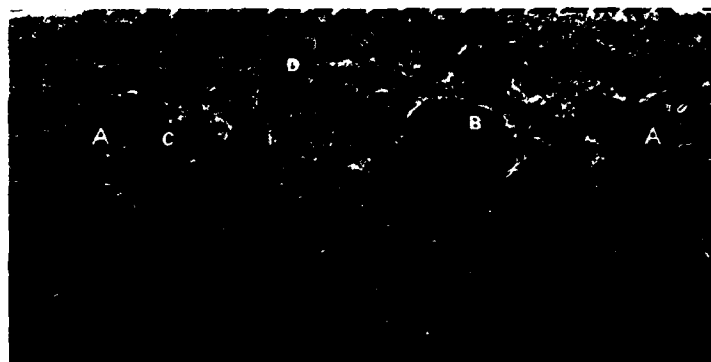
Much research has been done in the area of SAR detection of sea, lake, and river ice (Ketchum and Tooma, 1973; Larson, et al., 1978; 1981). There is general agreement in the community that a high resolution aircraft or satellite SAR operating at an X-band (3 cm) frequency can detect first year and multi-year ice, and open water areas.

Figures 19 and 20 represent simultaneously collected X- and L-band (3 cm and 23.5 cm respectively) parallel and cross polarized sea ice data collected in the Beaufort Sea. Clearly shown on the data is multi-year ice (letter B), first year ice (letter C) and open water or newly formed ice areas (letter D). These data have approximately 3 meter resolution in both range and azimuth, and the incidence angle at near edge is approximately 10° , while at the far edge, the incidence angle is approximately 60° . Also given on the figures are plots of relative intensity across the images along the lines drawn between the letters A and A'. This example of typical SAR ice data indicates that the higher frequency X-band cross polarized data (i.e., transmitted horizontally and received vertically) result in the highest contrast between first year and multiyear ice flows.

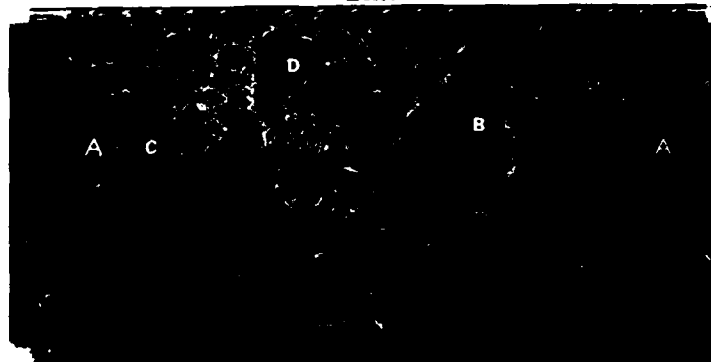
In addition to detecting ice flows, SAR has also been demonstrated to be capable of detecting icebergs. Larson, et al. (1978) showed that X-band cross polarized SAR data resulted in the highest contrast between the iceberg and surrounding ice flow when compared to X-band parallel polarized data and L-band parallel and cross polarized data.

3.13 CONCLUSIONS AND RECOMMENDATIONS

A review of the current capabilities of SAR for oceanographic applications has been presented. SAR data collected by aircraft and satellite have demonstrated the SAR to be capable of the following:



LHH



LHV

B - Multi-Year Ice
C - First-Year Ice
D - Open Water or New Ice

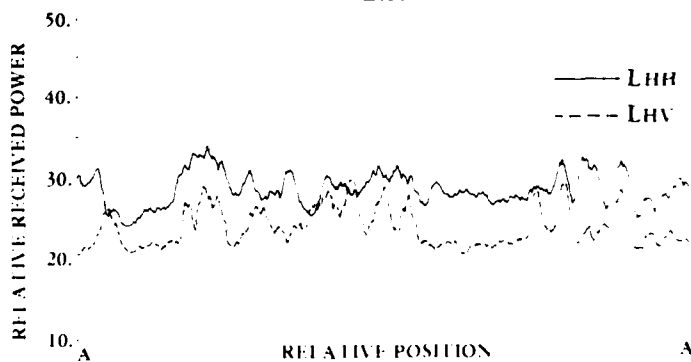


FIGURE 19. L-BAND PARALLEL AND CROSS POLARIZED SAR IMAGERY OF ICE IN THE BEAUFORT SEA. (Also Shown On The Figure Is A Transect Of Received Power Across The Image At The Location Marked A To A'.)

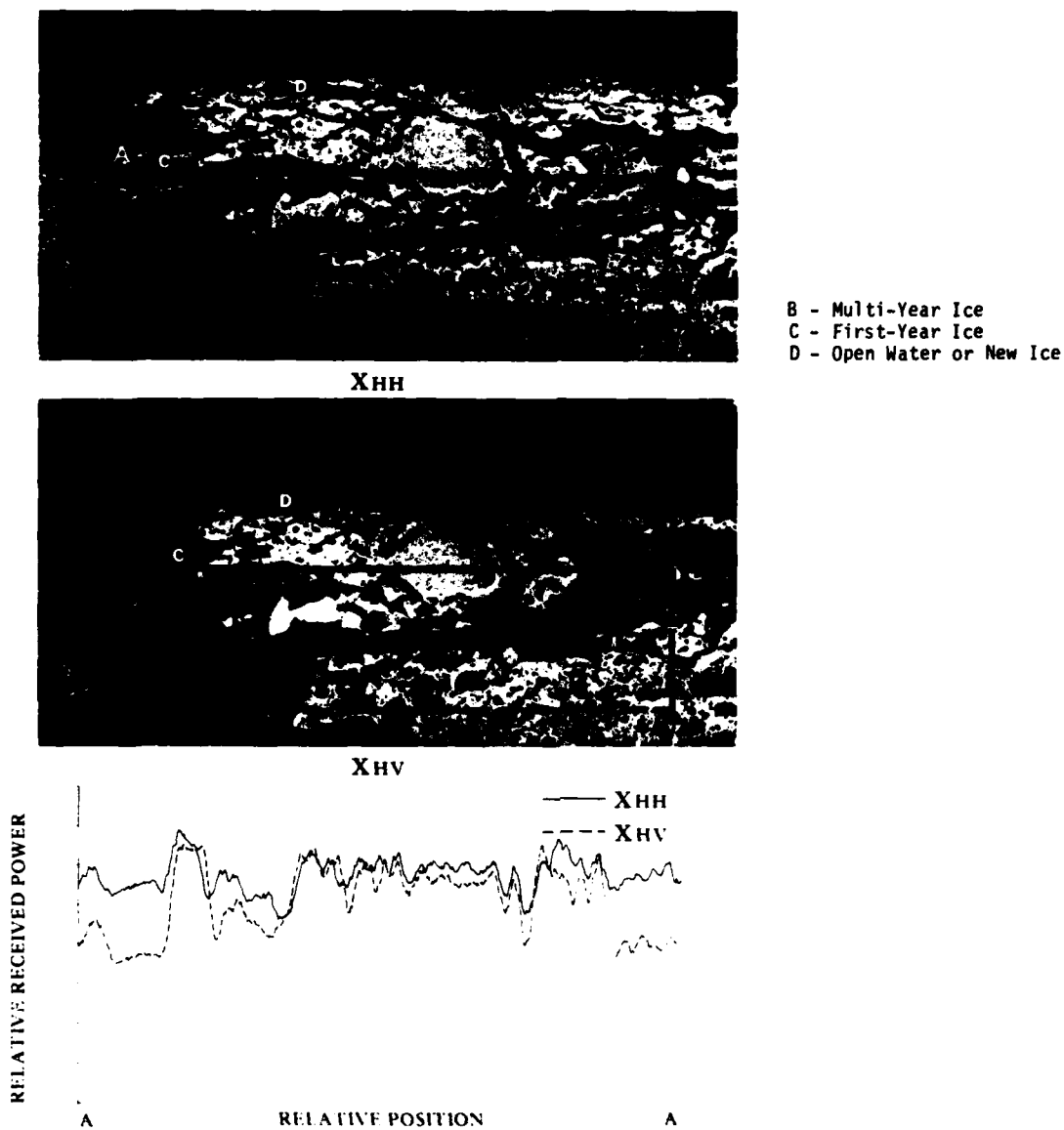


FIGURE 20. X-BAND PARALLEL AND CROSS POLARIZED SAR IMAGERY OF ICE IN THE BEAUFORT SEA. (Also Shown On The Figure Is A Transect Of Received Power Across The Image At The Location Marked A To A'.)

detection of gravity waves, determination of the magnitude and direction of surface winds, detection of current velocity and direction, detection of bottom features, identification of oceanic fronts and internal waves, detection of ship wakes, detection of oil slicks and classification of sea ice. SAR's ability to image the ocean surface independent of sun illumination (day or night), as well as through clouds and moderate rain, makes it an ideal ocean remote sensor.

The SAR spectral estimates of gravity waves discussed are wave number and directional spectra of the radar return intensity. At present, wave height information is not extractable from SAR data. The modulation transfer function (i.e., the SAR gravity wave imaging mechanism) is not totally understood at the present time. The determination of the transfer function as well as determination of wave height using SAR data will be a major scientific advance. At that time it will be possible to use SAR gravity wave data to obtain power density estimates of the sea surface.

The Doppler current measurements discussed are still experimental and the reader is cautioned that this technique to measure currents is far from operational and perhaps a new SAR system will have to be designed to realize the measurement of sea surface currents. Recall that the Doppler method works only on currents in the radial (line-of-sight) direction.

To realize the full utility of SAR in detecting frontal boundaries, bottom topographic features and oil spills, the respective SAR imaging mechanisms underlying the observation of these features need to be quantified. A model that accounts for the hydrodynamics of the subsurface and surface flow of water needs to be developed. The output of the hydrodynamic model should be values for the small scale (Bragg wave) and large scale (slope) roughness of the ocean as they are altered by the hydrodynamics. An electromagnetic model

would then use the hydrodynamic input to predict observed SAR backscatter. Actual SAR imagery should then be used to validate these models.

The ice type classification using SAR data demonstrates the need for development of machine aided analysis techniques and indicates the advantage of a multi-frequency SAR approach.

Perhaps the greatest problem facing SAR oceanographic users is the data handling problem. SAR signal histories must first be processed into image histories (either complex or just intensity) and then undergo rather time consuming additional data processing to extract the useful oceanographic information. Thus, clever data handling schemes such as the SIFT algorithm need to be developed to shorten computational times.

ANALYSIS OF MARSEN UPD-4 AND UPD-6 SAR WAVE DATA

This section summarizes the present progress made on the analysis of UPD-4 and UPD-6 SAR data collected during the MARSEN experiment. (UPD-4 and UPD-6 are model codes for the two types of synthetic aperture radars, produced by Goodyear, used in the Maritime Remote Sensing Experiment (MARSEN) carried out in the North Sea in the summer and fall of 1979. Principal investigator: Klaus Hasselmann; Deputy: Omar Shemdin. More information is obtainable from ONR, Code 422CS.) First a summary of the SAR data utilized in the study is presented, followed by a discussion on the special enhancement and processing performed on the signal history data. Next a section describing scatterer motion artifacts visible on the UPD-4 data is presented. SAR derived spectral estimates of the gravity wave field are then compared to sea truth estimates. Finally, a recommendations section outlining continued analysis for the UPD-4 data set is discussed.

It should be noted that the purpose of this chapter is to present a progress report on the analysis of UPD-4 and UPD-6 SAR data from MARSEN, not discuss the overall experiment or present conclusive results. The reader is referred to the 1980 Pasadena Workshop Report (Anonymous, 1980) for a description of the overall MARSEN experiment. Additionally it should be noted that the ERIM analysis to be presented is a cooperative effort with Dr. Wolfgang Rosenthal of the Geophysical Institute, University of Hamburg, in cooperation with the Max Planck Institute of Meteorology in Hamburg, West Germany. Only representative imagery and spectra are presented in this report. The complete SAR data set is archived at the Jet Propulsion Laboratory and the Max Planck Institute, and a partial set of the imagery and all the generated spectral estimates are stored at ERIM.

4.1 DATA DESCRIPTION

During the Fall of 1979, the UPD-4 and UPD-6 X-band SAR systems were flown over regions of the German Bight of the North Sea. There were two primary test sites (Nordsee Tower and Noordwijk), whose locations are presented in Figure 21. The Nordsee Tower test site was located in 30 m deep water approximately 80 kms due west of the German island of Sylt while the Noordwijk test site was located in 10 m deep water approximately 10 km west of the Dutch coast.

To avoid confusion, we will now discuss the nomenclature used to identify a specific SAR test flight. A specific mission flown by an aircraft is referred to as a LINE of data. Lines of data collected by the UPD-4 system were annotated by a one or two digit number (e.g. line 6 through line 13) while the lines collected by the UPD-6 system had an annotation with a "DA" prefix followed by a three digit number (e.g. line DA187 through line DA240). Within a given LINE, the aircraft changed headings a number of times. Each individual change of direction is referred to as a PASS of data within a LINE. It should be noted the UPD-4 and UPD-6 data were recorded by four different displays (CRTs); therefore the 18.5 km (10 nmi) swath of data consists of four SUB-SWATHS, designated A, B, C, D.

The UPD-4 and UPD-6 are high-resolution airborne side-looking reconnaissance SARs, each carried aboard a U.S. Marine F-4, operating at X-band (3 cm). The UPD-4 and UPD-6 have six modes of operation which provide a variety of standoff distances and also provide both fixed target imagery (FTI) along with moving target imagery (MTI). Imagery can be obtained from either side of the aircraft. For the data presented in this report, the UPD-4 system operated in a right-look only mode while the UPD-6 system operated in a mode where the SAR would look both to the right and to the left.

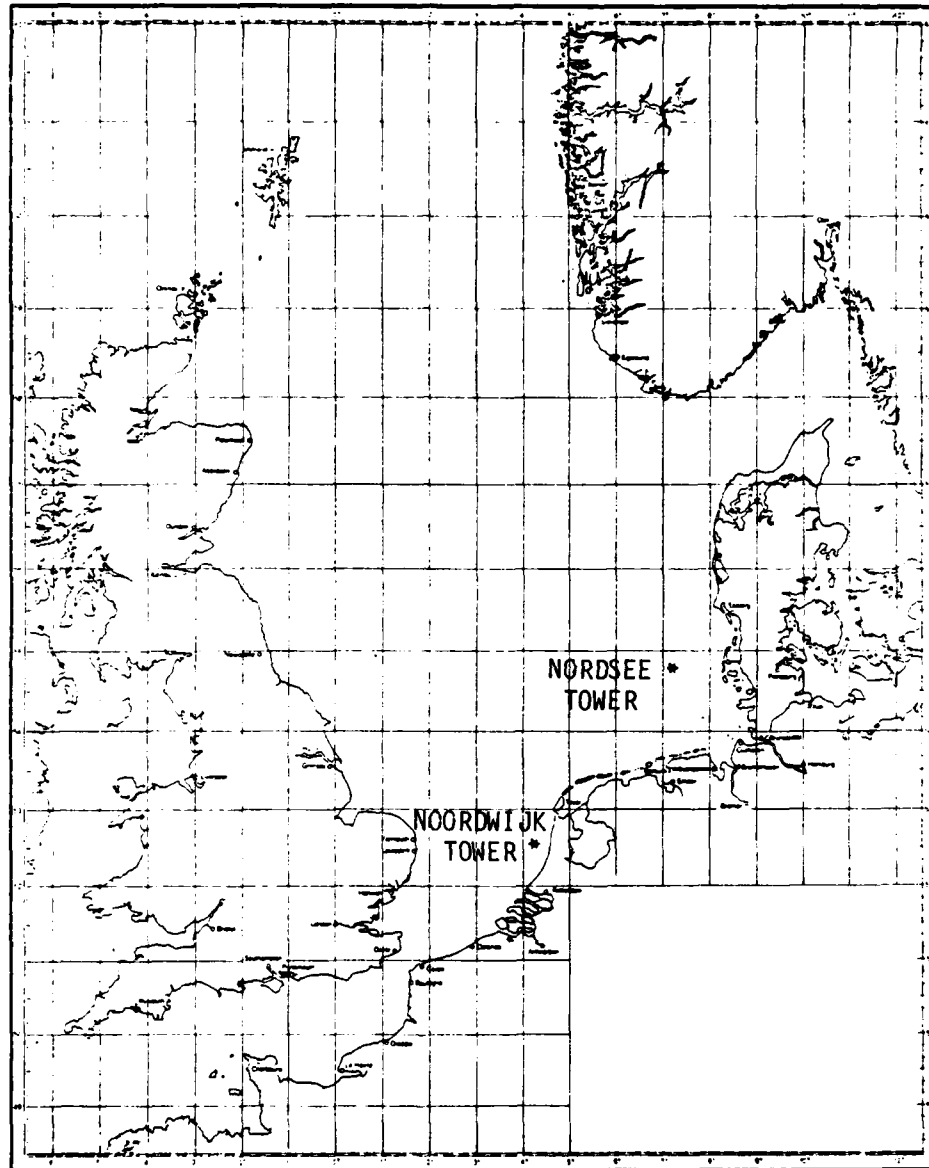


FIGURE 21. MAP OF SOUTHEASTERN NORTH SEA SHOWING LOCATIONS OF NOORDWIJK AND NORDSEE TEST SITES.

FTI is recorded on 24 cm (9.5 inch) film in four channels. Each channel is nominally 4.6 km (2.5 nmi) in width with an additional 0.46 km (0.25 nmi) overlap between adjacent channels. The nominal resolution of the UPD-4 and UPD-6 systems is 3 m. The fixed slant-range distance to the near edge of the recorded data is 4.6 km (2.5 nmi).

For the UPD-4 imagery, the near-edge sub-swath is labeled sub-swath A and the far-edge sub-swath D. For the UPD-6 imagery, the near edge, right-side was labeled sub-swath A; the far-edge right-side, sub-swath B; the near-edge, left-side, sub-swath C; and the far-edge, left-side, sub-swath D. During the MARSEN experiment the UPD-4 imaged over incidence angles ranging from 40° to 82°, while the UPD-6 imaged over angles ranging from 40° to 75°.

UPD-4 SAR imagery of the two test sites collected during seven separate missions was processed at ERIM as summarized in Table 6. ERIM has precision optically processed data from all four sub-swaths of the Lines 6, 7, 10, 12, and 13.

UPD-6 SAR imagery collected over the two test sites during ten separate missions was processed at ERIM, as summarized in Table 7. ERIM has precision optically processed data from all four sub-swaths of all passes of lines DA188, DA235, DA239, and DA240. For the other 6 lines, swaths A of all passes was processed.

The first analysis performed on the UPD-4 and UPD-6 data was to determine the sensitivity of these data to special motion compensation adjustments used during processing of the data. Individual passes of data from UPD-4 lines 7, 10, 12, and 13 were used for this purpose. This analysis is described in detail in Section 4.2. Further experiments designed to study azimuth smearing and orbital motion using MARSEN data are described in the following section (4.3).

TABLE 6
SUMMARY OF UPD-4 SAR WAVE DATA COLLECTED DURING MARSEN
AND PROCESSED AT ERIM

<u>Line</u>	<u>Area</u>	<u>Date</u>
6	Noordwijk	28 September 1979
7	Nordsee	28 September 1979
8	Noordwijk	25 September 1979
10	Nordsee	28 September 1979
11	Noordwijk	27 September 1979
12	Nordsee	27 September 1979
13	Noordwijk	27 September 1979

TABLE 7
SUMMARY OF UPD-6 SAR WAVE DATA COLLECTED DURING MARSEN
AND PROCESSED AT ERIM

<u>Line</u>	<u>Area</u>	<u>Date</u>
DA 187	Noordwijk	27 August 1979
DA 188	Noordwijk	29 August 1979
DA 200	*	*
DA 201	*	*
DA 228	Nordsee	25 September 1979
DA 231	Nordsee	28 September 1979
DA 232	Nordsee	28 Septemer 1979
DA 235	Nordsee	2 October 1979
DA 239	Noordwijk	4 October 1979
DA 240	Noordwijk	4 October 1979

*Data Logs Incomplete.

Finally, selected lines of UPD-4 and UPD-6 data were digitized on ERIM's Hybrid Digitizing Facility (Ausherman, et al., 1975). The digitized data include areas from UPD-4 line 10, passes 1-5, sub-swaths A-D; UPD-4 line 12, passes 1-3 and the Sylt Target pass, sub-swaths A-D; and UPD-6 line DA235, passes 2-6, sub-swaths A and C. The analysis of the SAR derived spectra is presented in Section 4.4. Summarized in Table 8 is the sea truth collected during the MARSEN experiment that is relevant to the present study.

4.2 MOTION COMPENSATION ADJUSTMENTS

The first step in the analysis of UPD-4 and UPD-6 SAR data was to determine the sensitivity of these data to motion compensation adjustments used to process SAR images that include moving scatterers. Previous studies using aircraft SAR data have shown that the visibility or detectability of gravity waves is often sensitive to motion compensation adjustments made during the processing of the SAR signal histories (Kasischke, et al., 1979; Kasischke and Shuchman, 1981). These motion compensation adjustments are inversely proportional to the velocity of the SAR platform. Since the F-4 aircraft has a high velocity (~ 210 m/s), the adjustments, if necessary, are probably quite small and the effect on SAR imagery quite subtle.

The initial work quantifying the effects of target motions on the synthetic aperture radar imaging mechanism was performed by Raney (1971). SARs are sensitive to both the azimuth and range velocity components of moving targets; a SAR image of a moving target will sometimes be degraded.

A velocity in the range (line-of-sight) direction affects the SAR imaging process in several ways. One effect is an azimuthal displacement of the moving target's image relative to a stationary target's image. When a target is accelerating in the range direction, this azimuthal displacement changes during the imaging time, resulting in a smearing in the azimuthal direction. Neither one of these effects is correctable during processing.

TABLE 8
SUMMARY OF ENVIRONMENTAL CONDITIONS DURING MARSEN EXPERIMENT

Line	Date	Area	Period (sec)	Wave Parameters*			Wind Conditions**	
				Frequency (Hz)	Propagation Direction (° True)	Height (m)	Speed (ms ⁻¹)	Direction (° True)
6	28 September	Noordwijk	8.0	0.125	150	1.0	3.5	330
7	28 September	Nordsee	7.0	0.143	150	1.2	7.2	280
8	25 September	Noordwijk	5.0	0.200	055	0.7	5.0	235
10	28 September	Nordsee	7.5	0.133	154	1.2	7.5	270
11	27 September	Noordwijk	5.5	0.182	150	1.0	8.2	290
12	27 September	Nordsee	7.5	0.133	068	1.0	10.3	290
13	27 September	Noordwijk	5.5	0.182	150	1.0	8.2	330

* Direction waves are propagating towards.

** Direction wind is coming from.

A range velocity component will also cause a smearing or defocusing in the range direction due to a rotation of the phase history of the target. This effect can be corrected for during processing of the data by rotating the lenses of the cylindrical telescope in the optical processor (i.e., telerotation) as described below.

Motion of a SAR imaged target in the along track (azimuthal) direction results in a defocusing of the image in the azimuthal direction. This defocusing can be compensated for during processing by adjusting the focal length of the azimuthal lens. For a more detailed discussion of the problems associated with imaging moving targets with a SAR, the reader is referred to an article by Shuchman (1981).

Four motion compensation adjustments were analyzed: 1) Range telerotation adjustments; 2) Azimuth focus shifts; 3) A combination of azimuth focus shifts and telerotation adjustments; and 4) Use of various integration times to process the data. A complete discussion of these motion compensation adjustments is presented in a paper by Shuchman (1981) which is included in the appendix to this report.

To summarize, the adjustment used to correct for a velocity in the range direction is called a telerotation adjustment (ϕ) and is defined as:

$$\phi = \frac{V_r p}{V_{AC} Q} \quad (6)$$

where ϕ is the rotation angle for correction,
 V_r is the line-of-sight velocity of the target,
 V_{AC} is the SAR platform velocity,
 p is the azimuth scale factor, and
 Q is the range scale factor.

The adjustment used to correct for a velocity in the azimuth direction is a shift in azimuth focus length (δF) of the processor and is defined as:

$$\delta F = 2 F_0 \frac{V_A}{V_{AC}} \quad (7)$$

where V_A is the target velocity in the azimuth direction, and

F_0 is the stationary azimuth focus of the SAR processor defined as:

$$F_0 = \frac{R\lambda}{2M^2\lambda_0} \left(\frac{V_F}{V_{AC}} \right)^2 \quad (8)$$

where R is the slant range to the target,

λ is the radar wavelength,

λ_0 is the optical processor wavelength,

M is azimuth demagnification of the optical processor, and

V_F is the velocity of the recording film onboard the aircraft.

The combination adjustment uses both a telerotation adjustment for the velocity vector in the range direction and an azimuth focus shift for the velocity vector in the azimuth direction.

The purpose of the adjustment experiments described below was to determine if the visibility of the gravity waves on the SAR imagery increased when the motion compensation adjustments were used during processing of the data. To measure wave visibility, a recently developed wave crest-to-trough contrast measurement called a peak-to-background ratio (PBR) was used. A peak-to-background ratio is obtained by measuring the peak amplitude of the two-dimensional spectra produced by Fourier transforming the SAR wave image and dividing that peak by the lowest amplitude in the same K-space of that peak (see Figure 22).

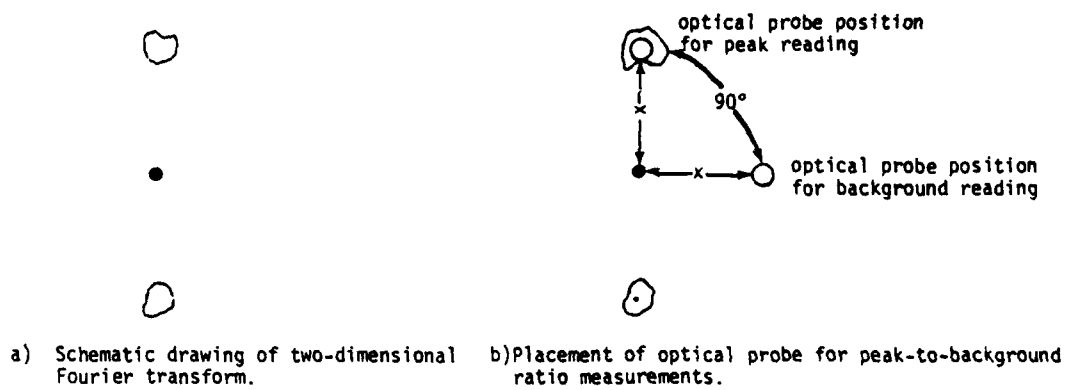


FIGURE 22. SUMMARY OF PEAK-TO-BACKGROUND MEASUREMENT.

For each motion compensation adjustment test, five separate PBR measurements were obtained for each telerotation, focus shift or combination setting. From these five samples, an average PBR can be calculated along with a standard error of the estimate (σ_x), defined as (after Schaeffer, et al., 1979):

$$\sigma_x = \frac{s_x}{\sqrt{n}} \quad (9)$$

where s_x is the standard deviation of the mean, and

n is the sample size.

By running a statistical analysis of variance (ANOVA) (Scheffe, 1959) test on the PBR from a set of motion compensation adjustments, it can be determined if the adjustments resulted in significantly higher PBRs, and hence increased wave visibility on the SAR imagery.

Previous experiments using wave motion compensation adjustments have indicated that the velocity component that SARs appear most sensitive to is the phase speed of the gravity waves (Kasischke, et al., 1979; Kasischke and Shuchman, 1981). Table 8, the summary of wind and wave conditions present during the times UPD-4 data were collected, indicates the existence of an average 6.0 sec wave with a phase speed $c = 9.4$ m/sec. This phase speed was used in the calculation of all motion compensations.

4.2.1 RANGE TELEROTATION ADJUSTMENTS

Using a phase speed of 9.4 m/sec, a set of telerotation adjustments (ϕ) was calculated for line 7, pass 2 and line 13, pass 2 data. The telerotation adjustments were -3ϕ , -2ϕ , $-3/2\phi$, $-\phi$, $-1/2\phi$, 0 , ϕ , and 2ϕ , for line 7, pass 2 and -2ϕ , $-\phi$, 0 , $1/2\phi$, ϕ , $3/2\phi$, 2ϕ , and 3ϕ for line 13, pass 2. A positive (+) telerotation is an adjustment for waves moving towards the radar, while a minus (-) telerotation is a setting for waves moving away. In line 7, pass 2, the waves

were moving away from the SAR and in line 13, pass 2, the waves were moving towards the SAR. The telerotation adjustments and their resultant peak-to-background ratios are summarized in Table 9 and Figure 23.

An analysis of variance (ANOVA) of the line 7, pass 2 data reveals no significant difference between the average PBRs (wave contrast) on the SAR imagery that was processed using the various telerotation adjustments. However, from Figure 23a, we can see there is a definite bias in the data, with the curve skewed to the minus telerotation adjustments.

An ANOVA of the line 13, pass 2 average PBRs reveals that the positive telerotation adjustments consistently result in higher PBRs than the minus telerotations. The curve in Figure 23b is definitely skewed to the positive telerotation adjustments.

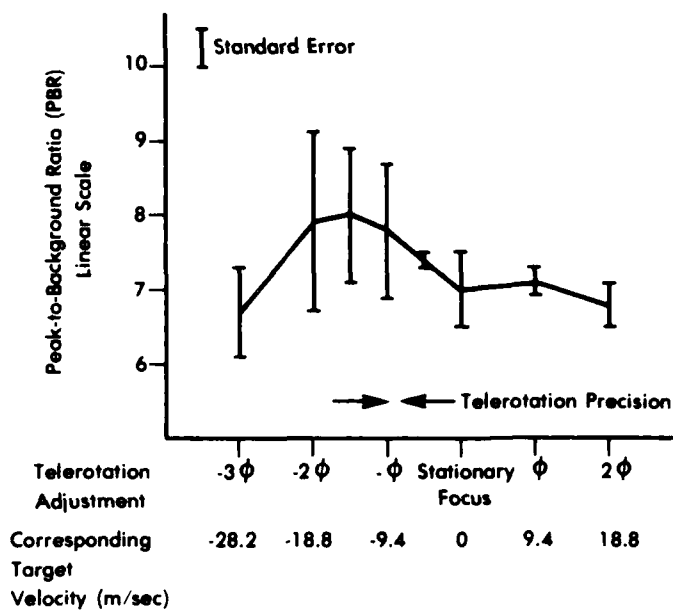
4.2.2 AZIMUTH FOCUS SHIFTS

Using a phase speed of 9.4 m/sec, a set of azimuth focus shifts ($\delta F = P$) were calculated for the line 7, pass 4, line 10, pass 4 and line 12, pass 2 data. The focus shifts were $-3P$, $-2P$, $-3/2P$, $-P$, $-1/2P$, 0 , $+P$, $+2P$. A positive (+) focus is an adjustment for waves moving in the same direction as the SAR platform, where a minus (-) focus shift is for waves moving the opposite direction. In all our examples, the waves were moving in the opposite direction as the aircraft.

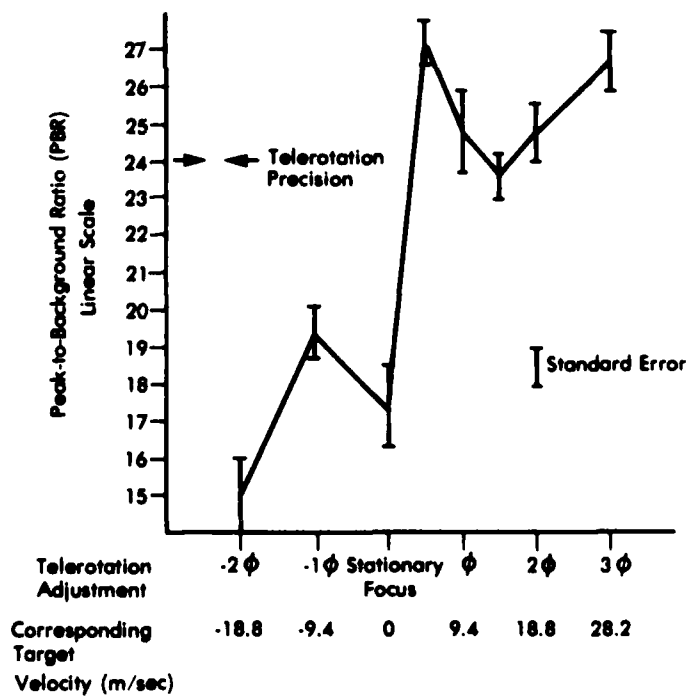
Table 10 and Figure 24 summarize the PBR versus azimuth focus shift calculations. An ANOVA of the line 7 and line 10 data revealed no significant differences in the PBRs from the various focus shifts. The ANOVA of the line 12 data indicated that the 0 , $-1/2P$ and $-P$ focus shifts resulted in higher PBRs than the other adjustments. However, in the context of wave visibility on SAR imagery, a 0.3 PBR difference can hardly be considered significant.

TABLE 9
SUMMARY OF TELEROTATION ADJUSTMENTS
VERSUS PEAK-TO-BACKGROUND RATIOS (PBRs)

Telerotation	Equivalent Phase Speed	Line 7 Pass 2		Line 13 Pass 2	
		Average PBR	Standard Error	Average PBR	Standard Error
3 ϕ	28.2 m/s			26.7	0.8
2 ϕ	18.8 m/s	6.8	0.7	24.8	0.8
3/2 ϕ	14.1 m/s			23.6	0.6
ϕ	9.4 m/s	7.1	0.2	24.8	1.1
1/2 ϕ	4.7 m/s			27.2	0.6
0	0 m/s	7.0	0.5	17.4	1.1
-1/2 ϕ	-4.7 m/s	7.4	0.2		
- ϕ	-9.4 m/s	7.8	3.1	19.4	0.7
-3/2 ϕ	-14.1 m/s	8.0	0.9		
-2 ϕ	-18.8 m/s	7.9	1.2	15.0	1.0
-3 ϕ	-28.2 m/s	6.7	0.6		



LINE 7 — PASS 2

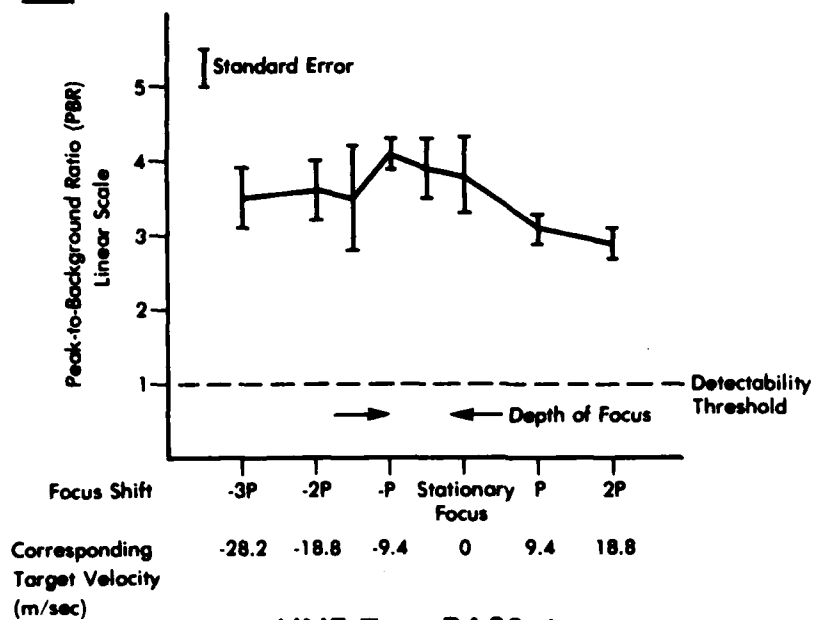


LINE 13 — PASS 2

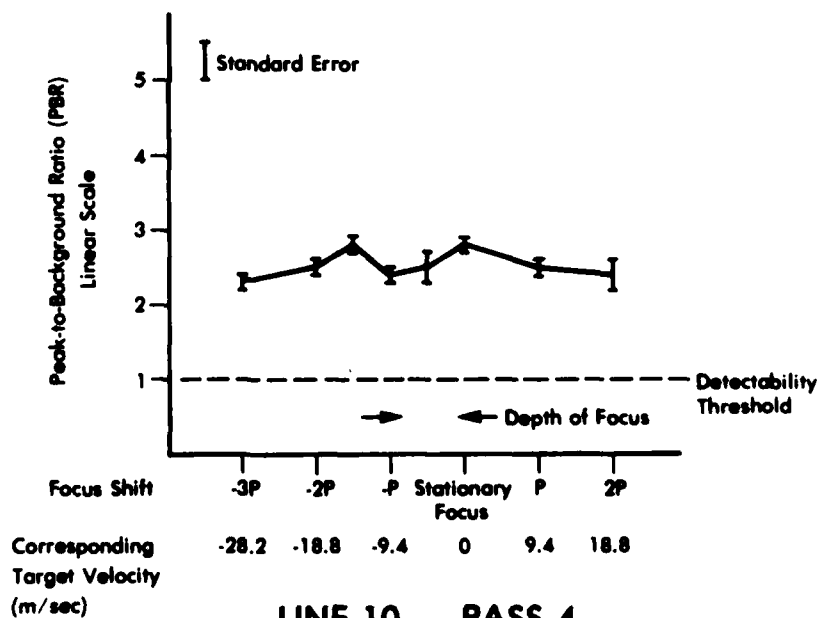
FIGURE 23. WAVE CONTRAST (PBR) AS A FUNCTION OF RANGE TELEROTATION ADJUSTMENTS USING UPD-4 X-BAND SAR DATA COLLECTED DURING MARSEN.

TABLE 10
SUMMARY OF AZIMUTH FOCUS SHIFTS VERSUS
PEAK-TO-BACKGROUND RATIOS (PBRs)

Focus Setting	Equivalent Phase Speed	Line 7 Pass 4		Line 10 Pass 4		Line 12 Pass 2	
		Average PBR	Standard Error	Average PBR	Standard Error	Average PBR	Standard Error
-3 P	-28.2 m/s	3.5	0.4	2.3	0.1	1.8	0.1
-2 P	-18.8 m/s	3.6	0.4	2.5	0.1	1.7	0.1
-3/2 P	-14.1 m/s	3.5	0.7	2.8	0.1	1.9	0.1
-P	-9.4 m/s	4.1	0.2	2.4	0.1	2.0	0.1
-1/2 P	-4.7 m/s	3.9	0.4	2.5	0.2	2.0	0.1
0	0	3.8	0.5	2.8	0.1	2.0	0.1
P	9.4 m/s	3.1	0.2	2.5	0.1	1.7	0.1
2 P	18.8 m/s	2.9	0.2	2.4	0.2	1.6	0.1



LINE 7 — PASS 4



LINE 10 — PASS 4

FIGURE 24-A. WAVE CONTRAST (PBR) AS A FUNCTION OF AZIMUTH FOCUS SHIFTS USING UPD-4 X-BAND SAR DATA COLLECTED DURING MARSEN.

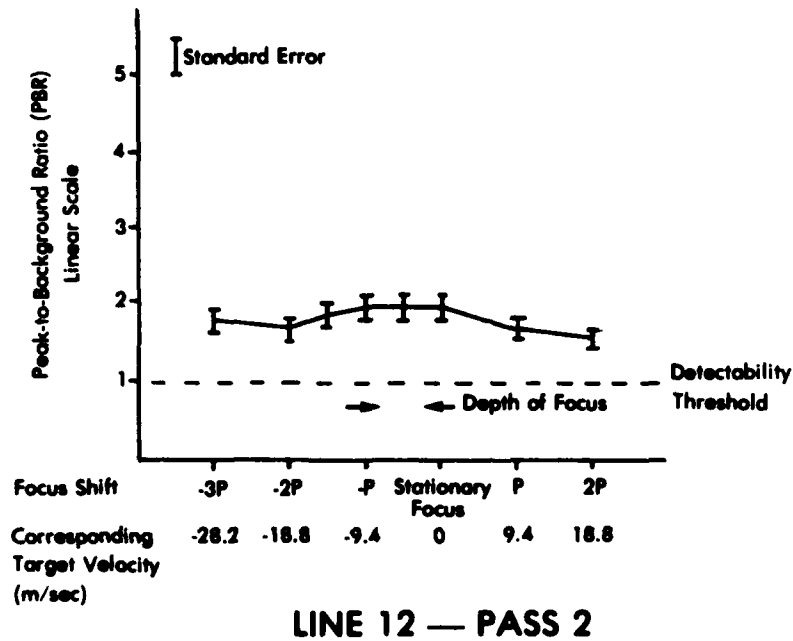


FIGURE 24-B. WAVE CONTRAST (PBR) AS A FUNCTION OF AZIMUTH FOCUS SHIFTS USING UPD-4 X-BAND SAR DATA COLLECTED DURING MARSEN.

As with the range telerotation adjustments, there appears to be a bias in the data towards those focus shifts which adjust for the direction the waves are moving. In Figure 24, we can see that the PBRs for minus focus shifts have slightly greater values than those for the positive focus shifts. Remember, for the data examined, the waves were moving in the opposite direction as the aircraft, indicating a minus focus shift would be necessary to correct the data.

4.2.3 COMBINATION FOCUS SHIFTS AND TELEROTATION ADJUSTMENTS

When waves are somewhere between azimuth and range traveling on the SAR imagery, a combination motion adjustment may have to be used. This combination adjustment has both a focus shift component (proportional to the velocity vector in the azimuth direction) and a telerotation component (proportional to the velocity vector in the range direction).

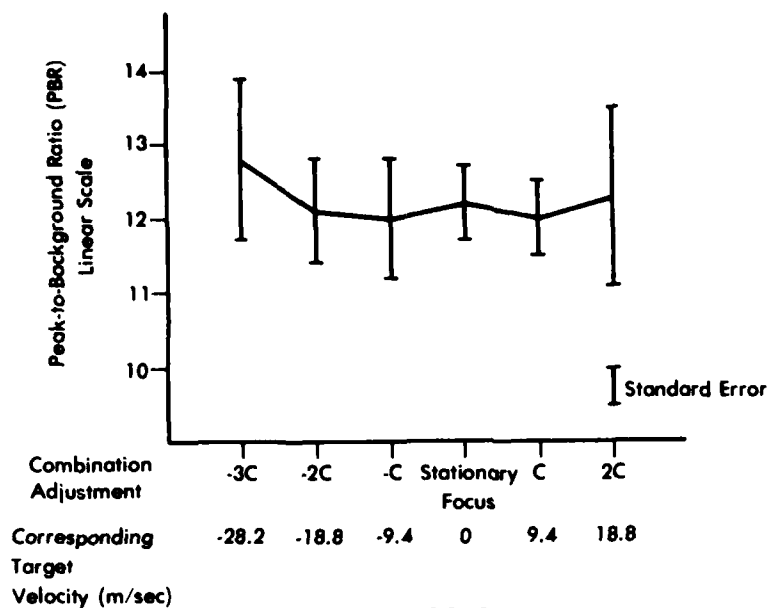
Using the phase speed of 9.4 m/sec, a set of combination adjustments (C) was calculated for line 7, pass 3 and line 10, pass 3 data. The combination adjustments were 3C, 2C, C, 0, -C, -2C. A plus adjustment is for waves moving towards the SAR and a minus adjustment is for waves moving away from the SAR. In the SAR images processed for this study, the waves were moving towards the SAR.

Table 11 and Figure 25 summarize the PBR versus combination motion adjustment PBRs. The statistical ANOVA of the line 7 PBRs indicates no significant differences in wave visibility as a function of the combination adjustments, while the ANOVA of the line 10 data indicates the 3C, 2C and C adjustments produced higher PBRs than the other settings.

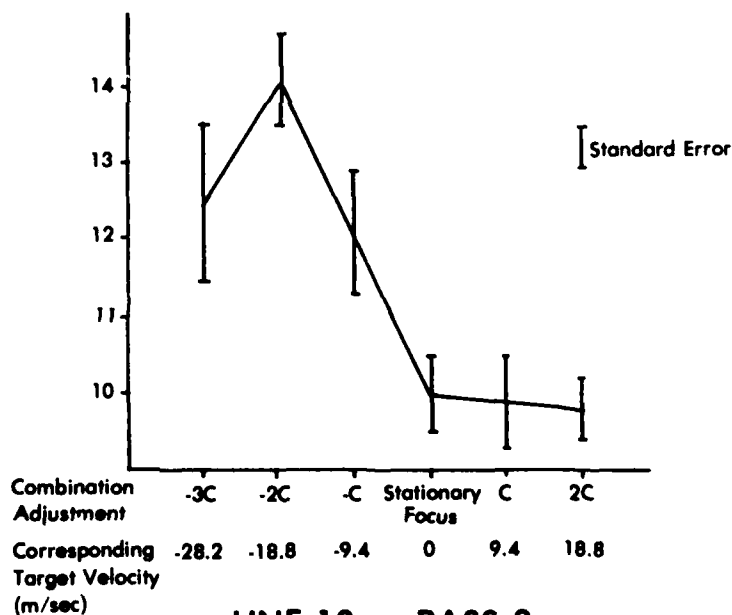
In summary, it appears the UPD-4 X-band imagery was relatively insensitive to azimuth focus shifts and somewhat sensitive to range telerotation adjustments. This is most likely a result of the high platform velocity of the F-4 aircraft (210 m/s). In most cases, a graph of either ϕ , P or C versus PBR gave an indication of what

TABLE 11
SUMMARY OF COMBINED FOCUS SHIFTS AND TELEROTATION
ADJUSTMENTS VERSUS PEAK-TO-BACKGROUND RATIOS (PBRs)

Combination Adjustment	Equivalent Phase Speed	Line 7 Pass 3		Line 10 Pass 3	
		Average PBR	Standard Error	Average PBR	Standard Error
3 C	28.2 m/s	12.8	0.9	12.5	1.0
2 C	18.8 m/s	12.1	0.7	14.1	0.6
C	9.4 m/s	12.0	0.8	12.1	0.8
0	0	12.2	0.5	10.0	0.5
- C	- 9.4 m/s	12.0	0.5	9.9	0.6
-2 C	-18.8 m.s	12.3	1.2	9.8	0.4



LINE 7 — PASS 3



LINE 10 — PASS 3

FIGURE 25. WAVE CONTRAST (PBR) AS A FUNCTION OF COMBINED AZIMUTH FOCUS AND TELEROTATION ADJUSTMENTS USING UPD-4 X-BAND SAR DATA COLLECTED DURING MARSEN.

direction the waves are heading because the curve is skewed in that direction.

4.2.4 INTEGRATION TIME MEASUREMENTS

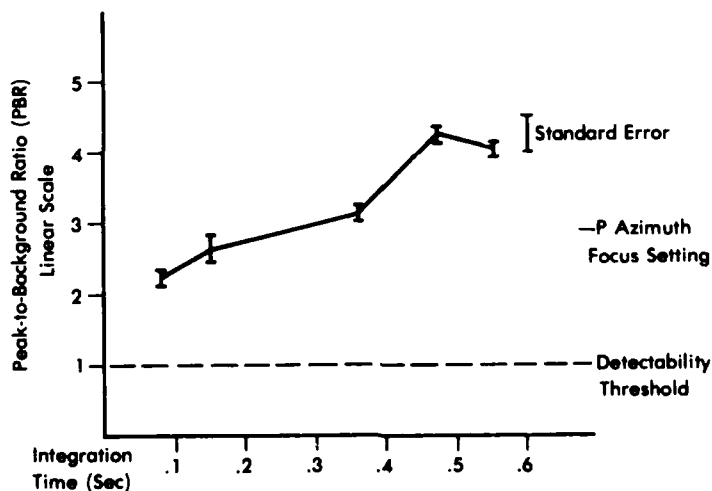
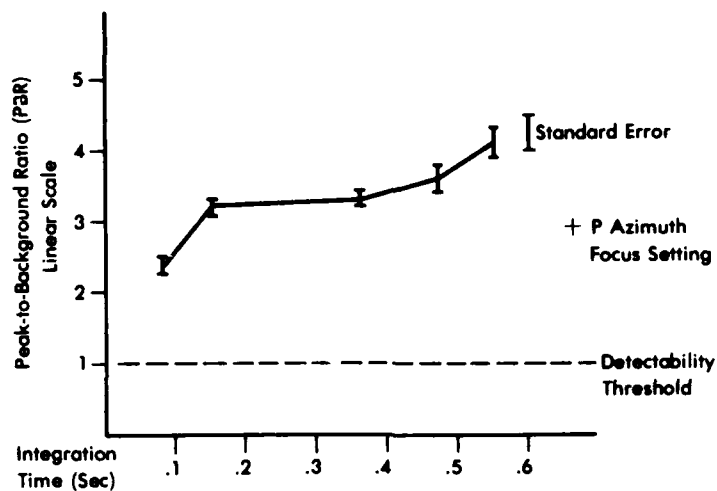
The purpose of the integration time measurement was to answer the question of whether the coherence time (or lifetime of the SAR scatterers) should be of concern to SAR scientists studying gravity waves. Raney and Shuchman (1978) using data from Trunk (1970) reported that the average X-band Bragg ocean scatterer has a lifetime of approximately 0.10 to 0.15 seconds and suggested that using integration times longer than this scatterer lifetime would not result in a higher contrast of wave imagery but rather would result in degraded imagery. Thus, it was suggested by Raney and Shuchman (1978) that the SAR integration time (and corresponding azimuth resolution) be matched to the coherence time of the scatterer and the remaining SAR bandwidth information be utilized in a non-coherent manner to reduce the speckle of the images.

This concept was evaluated using line 7, pass 4 data where the waves were traveling in the azimuth direction. Both -P focus shift and +P focus shift data were processed using five different integration times (0.08 sec, 0.16 sec, 0.27 sec, 0.48 sec and 0.55 sec). The integration times and average PBRs are summarized in Table 12 and Figure 26.

An ANOVA of this data reveals that the trend is significant. The longer the integration time the greater the PBR or wave contrast. The results of this experiment suggest the coherence time for X-band ocean Bragg waves maybe longer than the reported 0.10 to 0.15 seconds indicated by Trunk.

TABLE 12
SUMMARY OF INTEGRATION TIME VERSUS PEAK-TO-BACKGROUND
RATIOS (PBRs)

Integration Time	<u>-P Focus Shift</u>		<u>+P Focus Shift</u>	
	Average PBR	Standard Error	Average PBR	Standard Error
0.08 sec	2.4	0.1	2.2	0.1
0.16 sec	3.2	0.1	2.6	0.2
0.27 sec	3.3	0.1	3.1	0.1
0.48 sec	3.6	0.2	4.2	0.1
0.55 sec	4.1	0.2	4.0	0.1



LINE 7 — PASS 4

FIGURE 26. WAVE CONTRAST (PBR) AS A FUNCTION OF INTEGRATION TIME USING UPD-4 X-BAND SAR DATA COLLECTED DURING MARSEN.

AD-A115 186

ENVIRONMENTAL RESEARCH INST OF MICHIGAN ANN ARBOR RA--ETC F/G 17/9

THE UTILITY OF SAR TO MONITOR OCEAN PROCESSES.(U)

NOV 81 R A BRUCHMAN, E S KASISCHKE

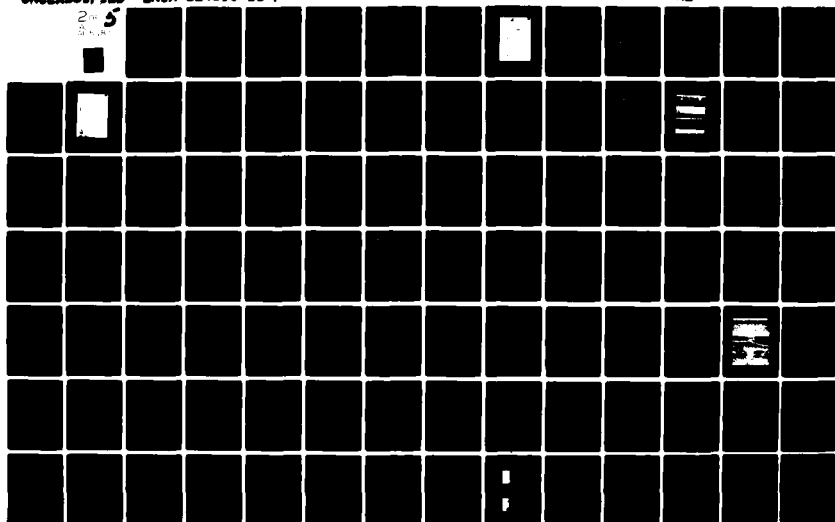
N00014-76-C-1048

ERIM-124300-11-F

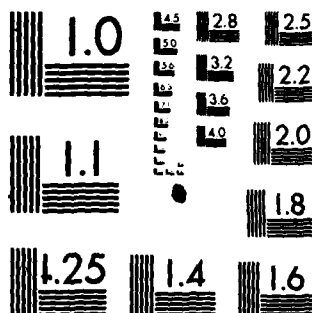
ML

UNCLASSIFIED

2
5



15 18



MICROCOPY RESOLUTION TEST CHART
NATIONAL BUREAU OF STANDARDS-1963-A

4.2.5 DEPENDENCE OF WAVE VISIBILITY ON SAR LOOK DIRECTION

In examining the data in Figures 23 through 25, it became apparent that the highest wave contrast was from SAR images of range traveling waves and the lowest from azimuth waves. It has long been speculated (see Teleki, et al., 1978) that SARs will image range traveling waves better than they will image azimuth traveling waves. The MARSEN data set offers an opportunity to further examine this question.

Line 7 data were used in this study. Five peak-to-background ratio measurements were obtained from swath-A in the same general location around the Nordsee Tower. The average PBRs are summarized in Table 13 along with the wave orientation relative to the radar look direction. Also indicated on the table is whether the SAR was looking at waves propagating towards the aircraft (up-wave) or away from the aircraft (down-wave). These results are also presented graphically in Figure 27. Analysis of Figure 27 and Table 13 indicates the SAR images range traveling waves better than azimuth traveling waves. By comparing pass 1 to pass 5 and pass 2 to pass 3, we can see another trend in the data; the SAR images waves more clearly when they are moving towards the SAR than when they are moving away from the SAR. This same trend was observed by Kasischke and Shuchman (1981) when they analyzed SAR data of wind-generated waves on Lake Michigan.

It should be noted that although higher PBRs were obtained from certain radar look directions over others, the UPD-4 X-band SAR imaged gravity waves regardless of radar look direction.

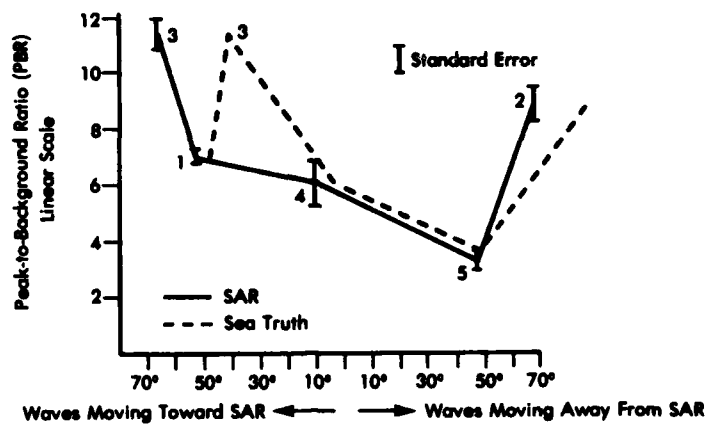
4.3 FURTHER ANALYSIS OF MOTION INDUCED PERTURBATIONS ON SAR IMAGERY

In examination of SAR imagery collected over coastal regions, azimuth streaks are often noticed on the images. It is believed that this streaking is a motion induced artifact. This phenomenon was examined using MARSEN UPD-4 X-band SAR data.

TABLE 13
SUMMARY OF LINE 7 PEAK-TO-BACKGROUND RATIOS (PBRs)

Pass	Direction of Waves*	PBR	
		Average PBR	Standard Error
1	53° up-wave	7.0	0.1
2	68° down-wave	8.9	0.6
3	67° up-wave	11.5	0.4
4	11° up-wave	6.1	0.8
5	47° down-wave	3.3	0.3

*Up-wave means the SAR is looking at a wave propagating towards the SAR; down-wave, at a wave moving away from the SAR.



LINE 7

FIGURE 27. WAVE CONTRAST (PBR) AS A FUNCTION OF RADAR LOOK DIRECTION USING UPD-4 X-BAND SAR DATA COLLECTED DURING MARSEN.

4.3.1 THEORY

Synthetic aperture radar uses precise sequential measurements of target range to locate targets in the along track (or azimuth) dimension. Relative measurements of range, each representing small fractions of a radar wavelength are recorded to establish the range history (phase history) for each object imaged by the radar. For stationary objects, the range to that object changes in a highly predictable way if the radar platform moves in a straight line. For this case the range (R) to the target is given by

$$R = [R_0^2 + (x - x_0)^2]^{1/2} \quad (10)$$

where R_0 = the minimum target range

and x_0 = the position of the platform when $R = R_0$

If the object is not stationary, the range history is perturbed and an uncertainty in the objects along track location is introduced. When the object motion is a uniform radial velocity, V_r , the image of the object at the output of the radar processor will appear to be shifted in the along track direction a distance, Δx , which is computed as (Raney, 1971):

$$\Delta x = \frac{V_r R}{V_{AC}} \quad (11)$$

where V_{AC} is the SAR platform velocity. If the object is initially stationary as it enters the radar beam and then accelerates to a maximum velocity V_r as it leaves the beam, the image will be smeared an amount Δx as given above. Conversely, any azimuth smearing of the radar image may be attributed to a range of radial target velocities given by:

$$\Delta V_r = \frac{\Delta x V_{AC}}{R} \quad (12)$$

Thus, the extent of azimuth image defocusing or smear may be used to indicate the limits on the effective radial velocity spread of the target. Note that the displacement or smear of Δx is independent of the radar wavelength, antenna beamwidth and target illumination time.

SAR imagery of the ocean surface often shows substantial azimuth smearing of breaking waves. This is most apparent in imagery of the near shore surf zone where, because of azimuth smear, the waves always appear to be traveling in the cross-track direction. Similar effects are noted in the open ocean where cresting seems to be directly proportional to the radar range and is not dependent on the wavelength of the radar. This suggests that the smearing may be the result of a radial velocity distribution characteristic of the backscatter from the breaking wave. A number of measurements of image smear observed in the MARSEN radar data suggest that the waves imaged have an effective radial velocity distribution between 2.5 and 3 m/s.

4.3.2 AZIMUTH IMAGE SCANS OF SELECTED WAVE IMAGERY

A Precision Optical Processor (POP) was used to image breaking waves from pass 3, line 6 of the MARSEN UPD-4 radar data. A Gamma Scientific scanner was set up at the output plane of the SAR optical processor to record the azimuth smear of the breaking waves observed in Swath 4. Figure 28 is an azimuth scan of the breaking wave identified as "A" in Figure 29. The signal film aperture was set to illuminate 4 seconds of data and the frequency plane was opened to pass the full azimuth Doppler bandwidth. The measured azimuth smear is about 255 m. We presume that the actual extent of the breaker was much smaller than this. Then the effective radial velocity range may be found from Eq. (12)

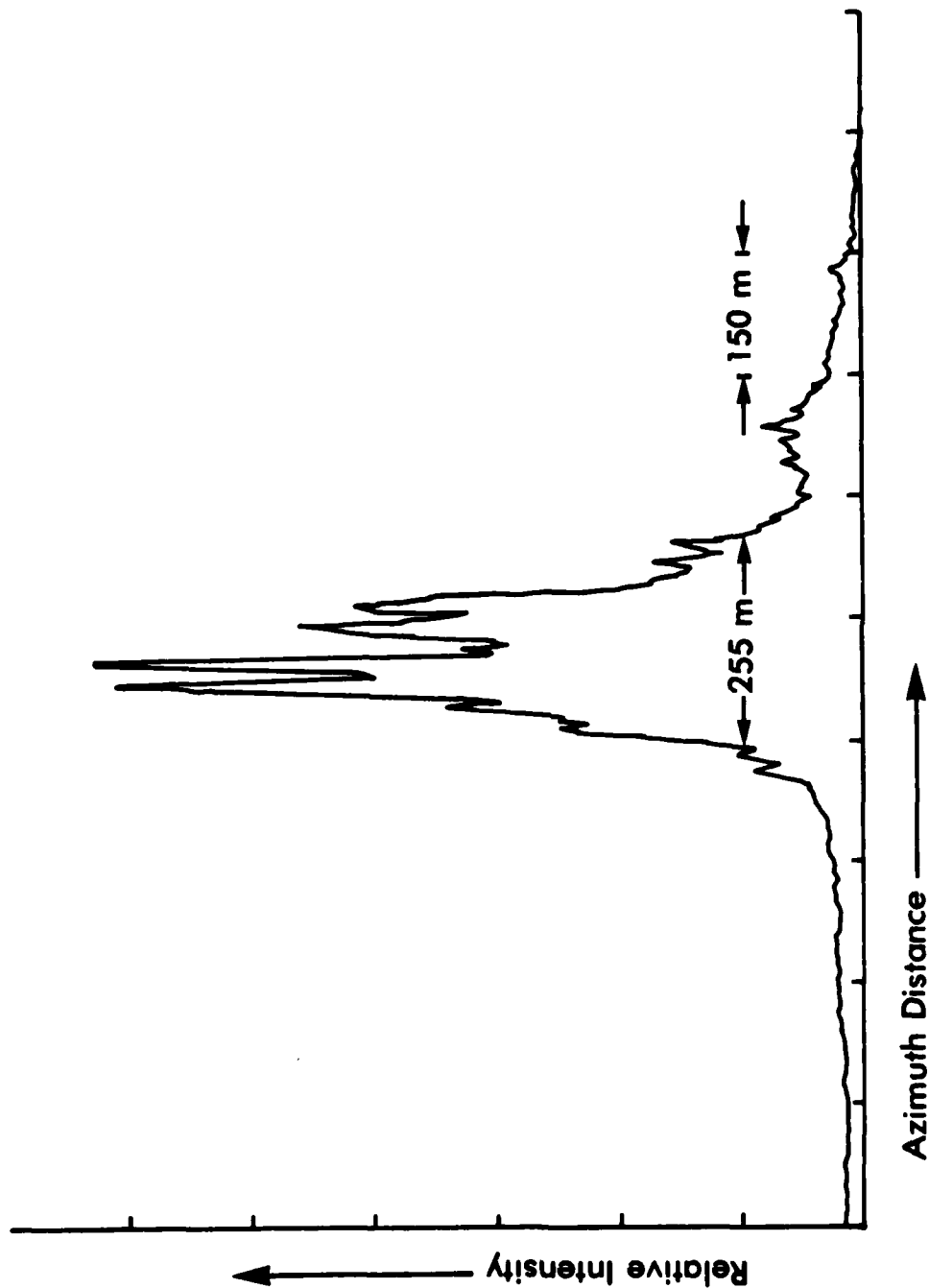


FIGURE 28. IMAGE INTENSITY SCAN OF A BREAKING WAVE.

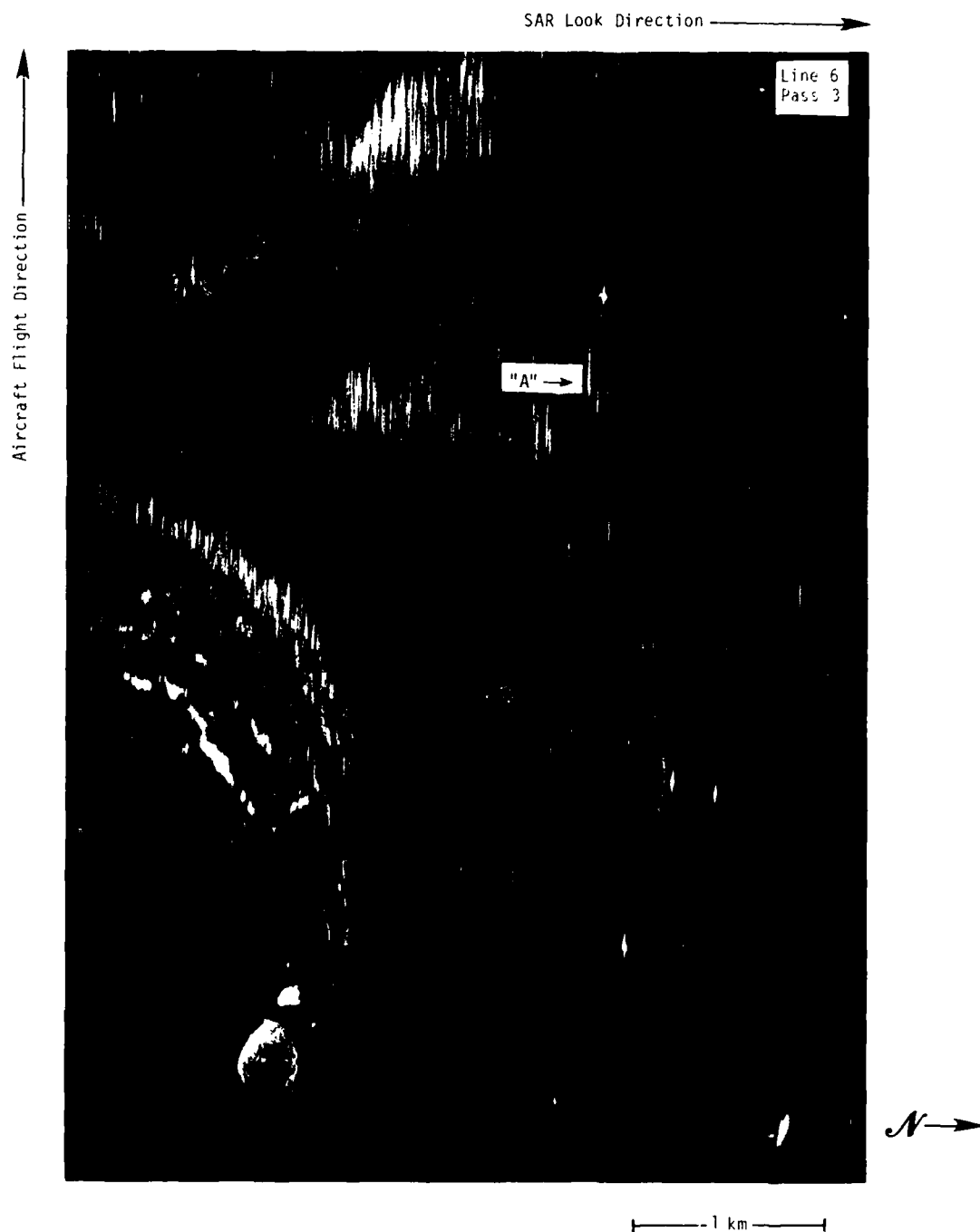


FIGURE 29. UPD-4 X-BAND SAR IMAGERY COLLECTED DURING MARSEN ILLUSTRATING AZIMUTHAL STREAKING (Position A Is Where Azimuth Intensity Scans Were Made).

$$\Delta V_r = \frac{\Delta x V_{AC}}{R} . \quad (13)$$

Where $\Delta x = 255$ m,
 $V_{AC} = 213$ m/sec, and
 $R = 21,500$ m,

$$\Delta V_r = \frac{255 \times 213}{21,500} = 2.5 \text{ m/sec.}$$

The effect of observation time on the azimuth displacement was investigated by limiting the along track signal film illumination to increments of 1/3 second illumination intervals. The resulting scans are shown in Figure 30. The scan labeled "0" was made with a 5.5 mm aperture centered on the optical axis of the processor. This scan shows an image spread of about 225 m. The scans above the "0" represent 1/3 second intervals earlier in time and those below later time. Note that the smear for 1/3 second before the zero has a spread of ~ 300 m corresponding to a ΔV_r of about 3 m/sec. This result is essentially the same as that for the 4 second data interval, suggesting that the effective velocity distribution producing the smearing is fully developed within the 1/3 second observation time. Note also that the distribution has an apparent shift toward the end of the pass with later observation times. This shift might be due to a real azimuth velocity of the breaking part of the wave. A measurement of this shift is shown in Figure 31. The image appears to shift about 120 m while the aircraft moves 481.6 m. It can be shown that an azimuth velocity of 26.5 m/sec would produce the given shift. The shift may also be explained as a shift in the average radial velocity over the time of observation. In this case the average velocity of the breaking wave appears to shift about 1/2 m/sec over a 2.3 second interval.

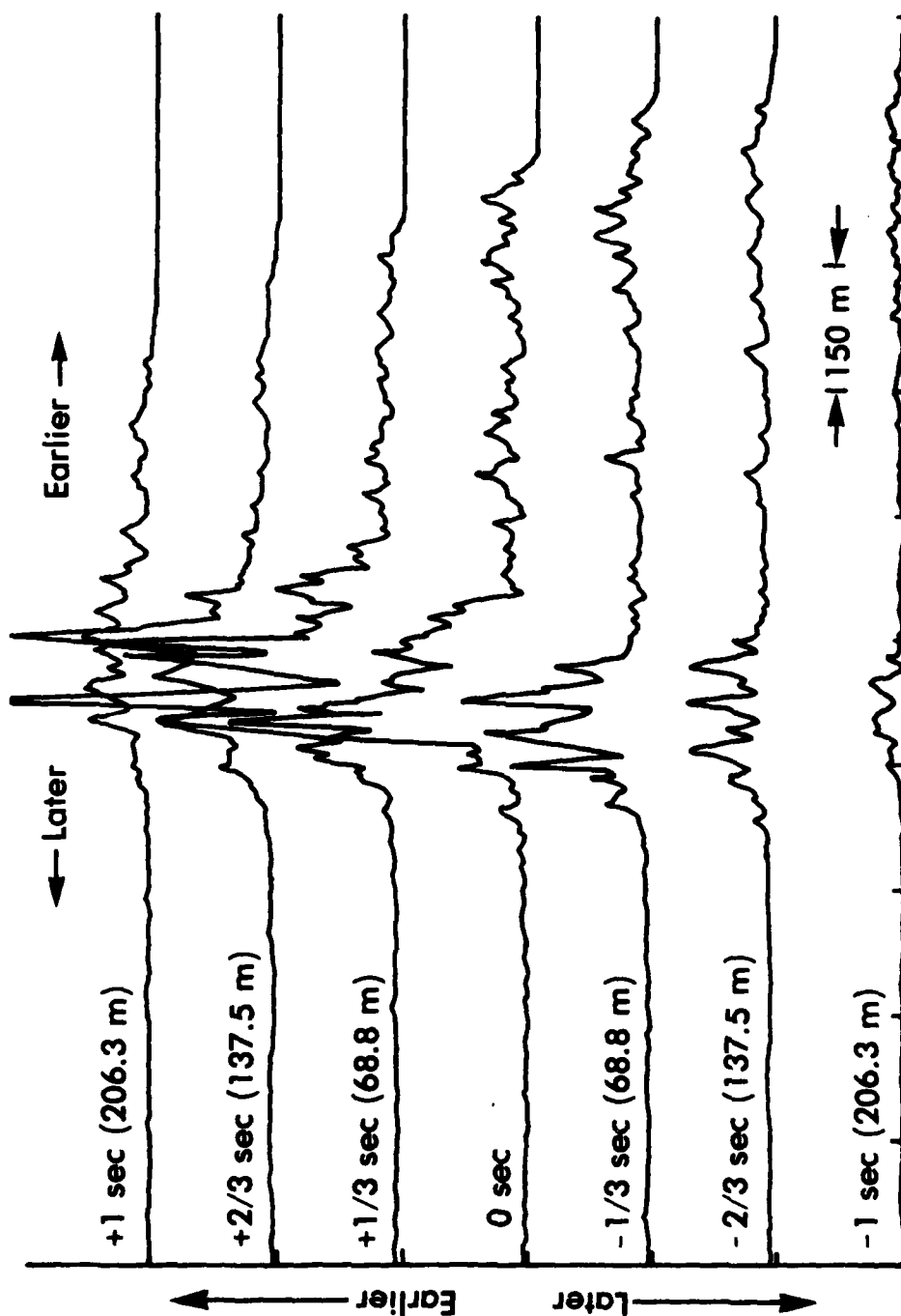


FIGURE 30. EFFECTS OF OBSERVATION TIME ON AZIMUTH DISPLACEMENT.

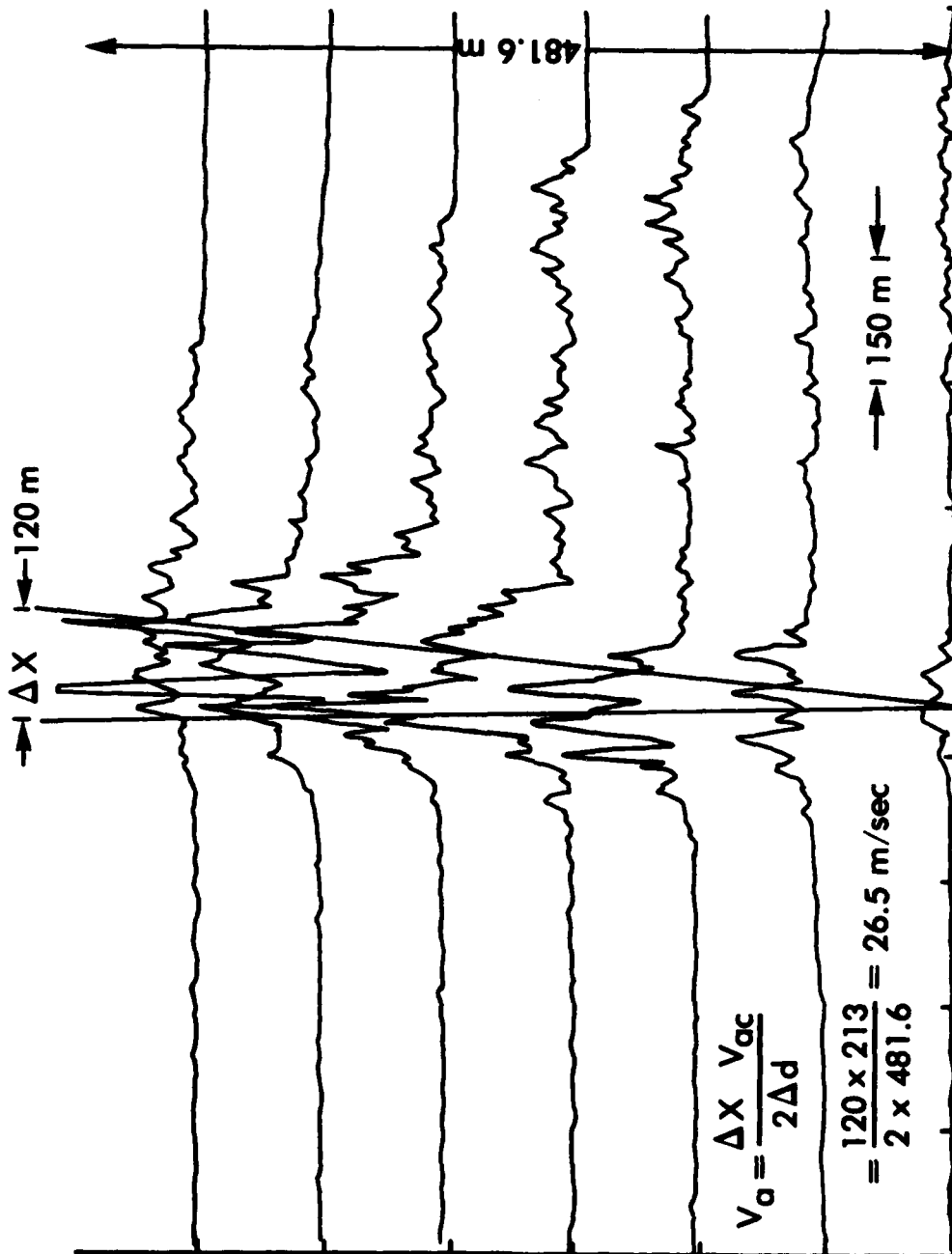


FIGURE 31. AZIMUTH POSITION SHIFT OF VELOCITY COMPONENT.

Figure 32 shows the result of scanning the image using sequential azimuth spectral bands. The frequency bandwidth was chosen to represent what would be expected from a stationary target at a given range over a 1/3 second interval. The scans are similar although not identical to those made with the 1/3 second signal plane aperture.

An azimuth scan of a second breaking wave is shown in Figure 33. This wave is located near the one identified previously and shows a spread of about 300 m indicating a ΔV_r of ~ 3 m/sec.

4.3.3 ORBITAL MOTION MEASUREMENTS

Noted throughout pass 3 of line 6 is the presence of what appears to be lines of floats attached to fish nets (see Figure 34). The images of these floats show azimuth spreading effects. If the motion of a float is not restricted by the presence of the fishing net it may be expected to follow the orbital motion of passing ocean swells. The azimuth spread of the image may then be used to measure the orbital velocities of the waves if the waves are traveling in the range direction.

The sea truth for line 6 indicates the presence of swells of 1 m wave height with a period of 8 seconds. The orbital velocity (tangential) is thus

$$V_o = \frac{\pi H}{T} \quad (14)$$

or

$$V_o = \frac{\pi \times 1}{8} = 0.393 \text{ m/sec.}$$

Since the illumination time is less than 8 seconds, the full spread of ± 0.393 m/sec will not be effective in producing image smear; however, we may limit the signal film illumination to a 2 second interval and observe various degrees of smearing depending on the phase of the orbital motion. For an 8 second wave a 2 second observation

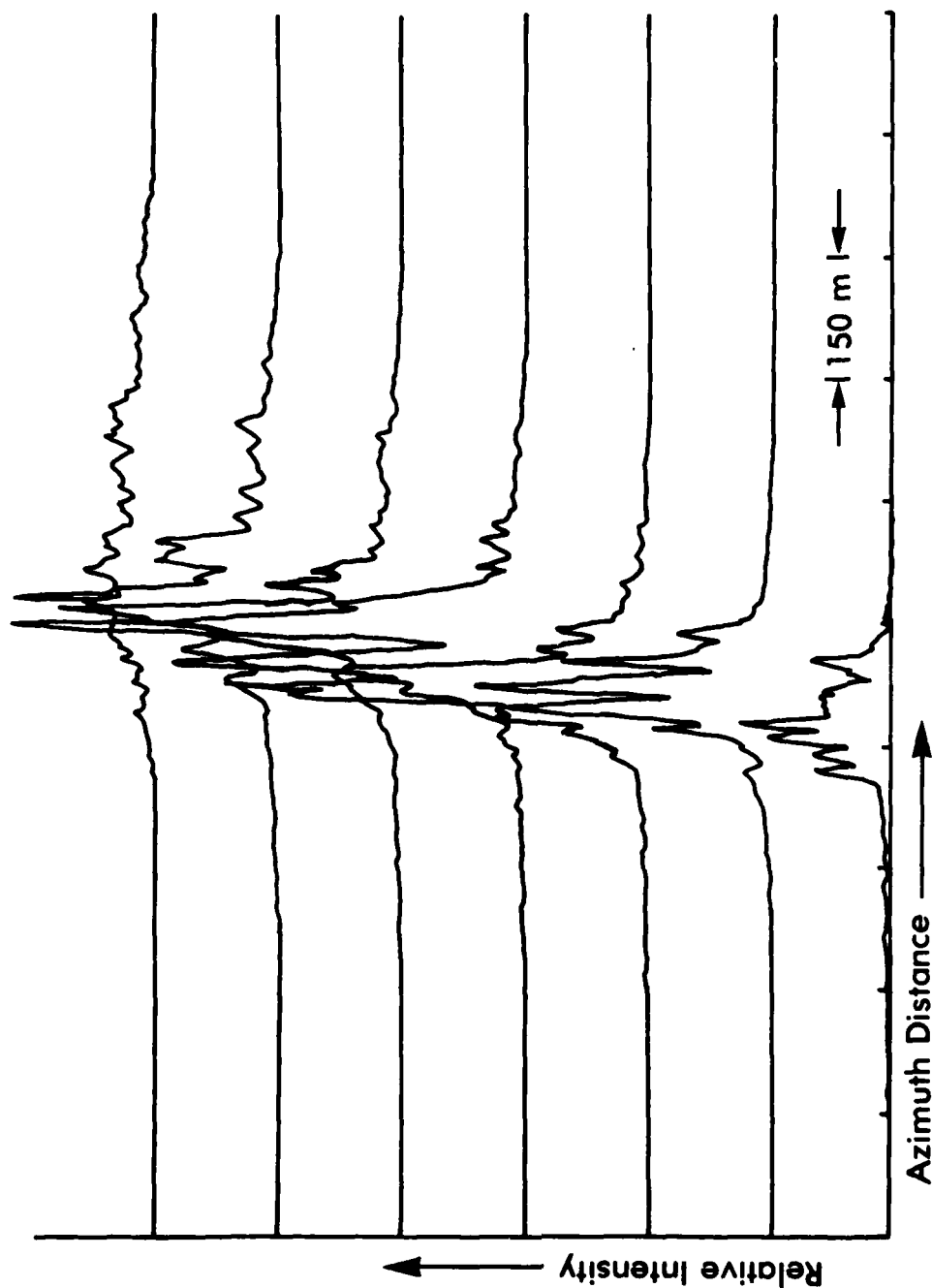


FIGURE 32. EFFECTS OF SEQUENTIAL AZIMUTH SPECTRAL BANDS ON VELOCITY COMPONENT.

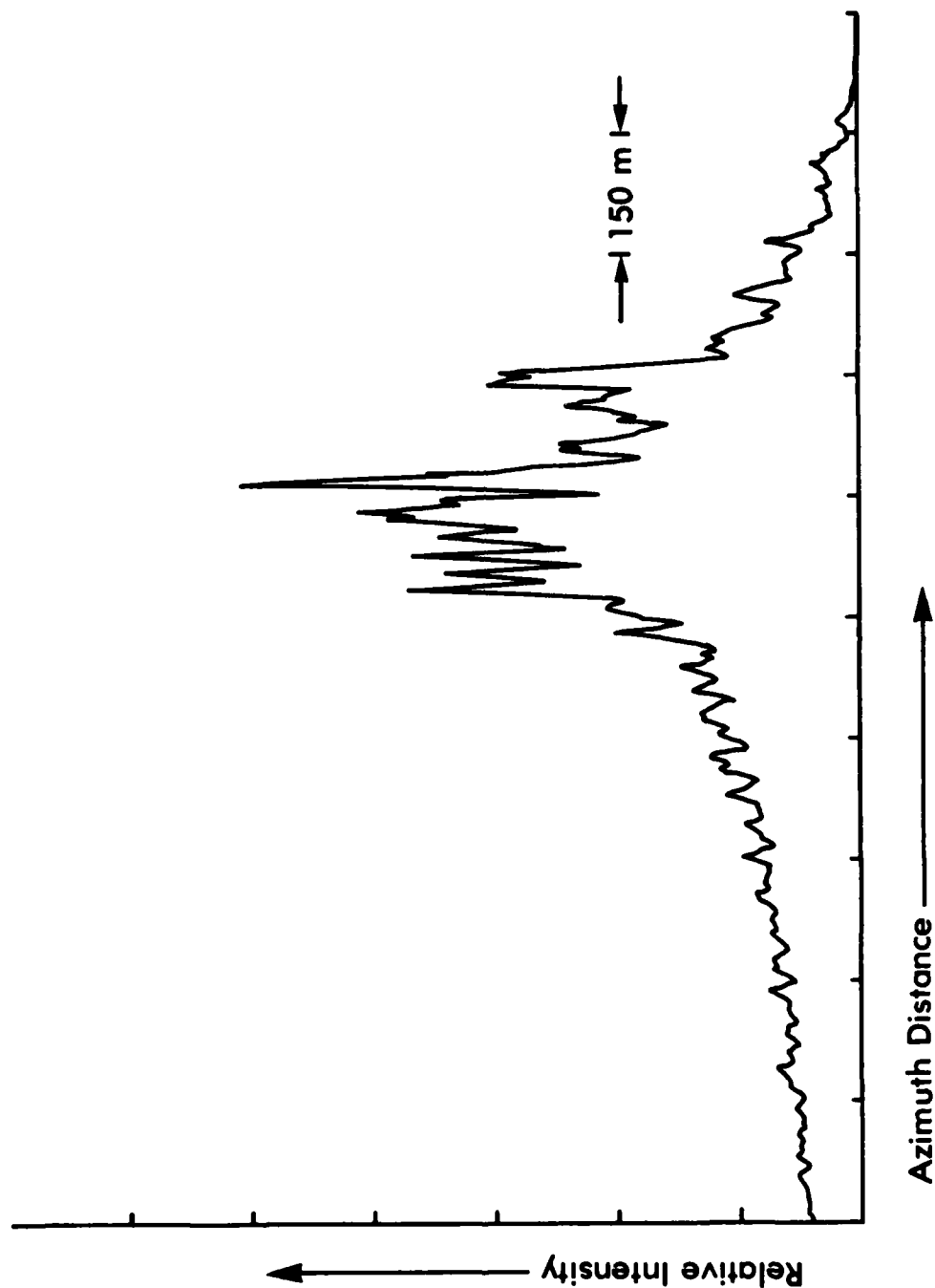


FIGURE 33. RELATIVE INTENSITY SCAN OF A BREAKING WAVE.

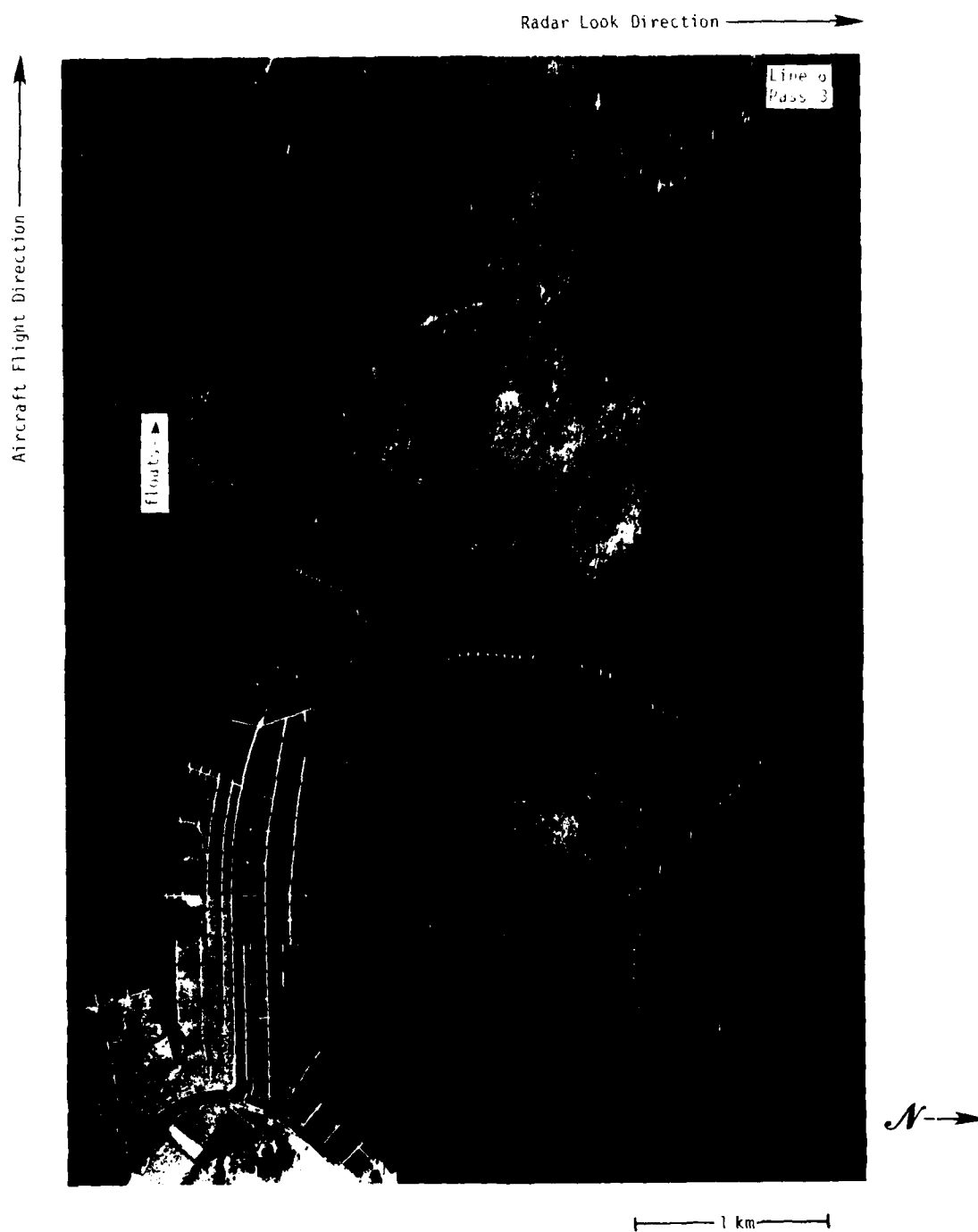


FIGURE 34. SAR IMAGE OF FLOATING FISHNET BUOYS COLLECTED DURING THE MARSEN EXPERIMENT.

will record one quarter of a cycle of orbital motion. If the orbital velocity component in direction of the radar is described by a sine function, the maximum change in velocity for a 1/4 cycle interval occurs between -45° and $+45^\circ$ (see Figure 35). Thus the maximum velocity spread will be given by

$$\Delta V_r = 2 \sin 45^\circ \times V_o = 2 \times \sin 45^\circ \times 0.393 = 0.56 \text{ m/sec.}$$

The minimum smear occurs between $+45^\circ$ and 135° and is given by

$$\Delta V_r = (1 - \sin 45^\circ) \times V_o = (1 - \sin 45^\circ) 0.393 = 0.115 \text{ m/sec.}$$

If we choose an observation range of 20 km, the expected image smear is given by Eq. (10)

$$\Delta x = \frac{\Delta V_r R}{V_{AC}} = \frac{\Delta V_r \times 20,000}{213} = 93.9 \Delta V_r .$$

Thus the expected float image smear will be between

$$93.9 \times 0.115 = 10.8 \text{ m}$$

and

$$93.9 \times 0.56 = 52.6 \text{ m.}$$

The experimental results are shown in Figures 36 to 39. The observed values of image smear of the fishing floats for the four examples are: 31.5 m, 48 m, 50 m, and 42 m, respectively. These values are all quite near the theoretical maximum of 52.6 m and therefore may well be the result of orbital wave motion.

4.4 SAR VERSUS SEA TRUTH SPECTRAL COMPARISONS

This section of the report considers comparisons between SAR-derived and surface measured wave spectra. Past studies have typically only compared the dominant peaks of SAR-derived and surface measured spectra for both wavelength and directional information. In this study, we have begun to investigate the relationship between

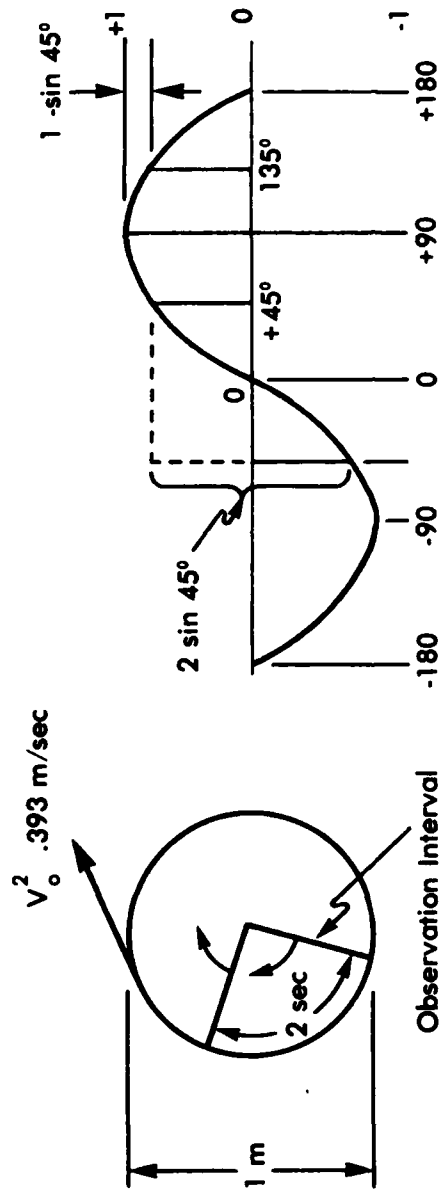


FIGURE 35. ILLUSTRATION OF POSITION OF A PARTICLE IN A MOVING GRAVITY WAVE FIELD.

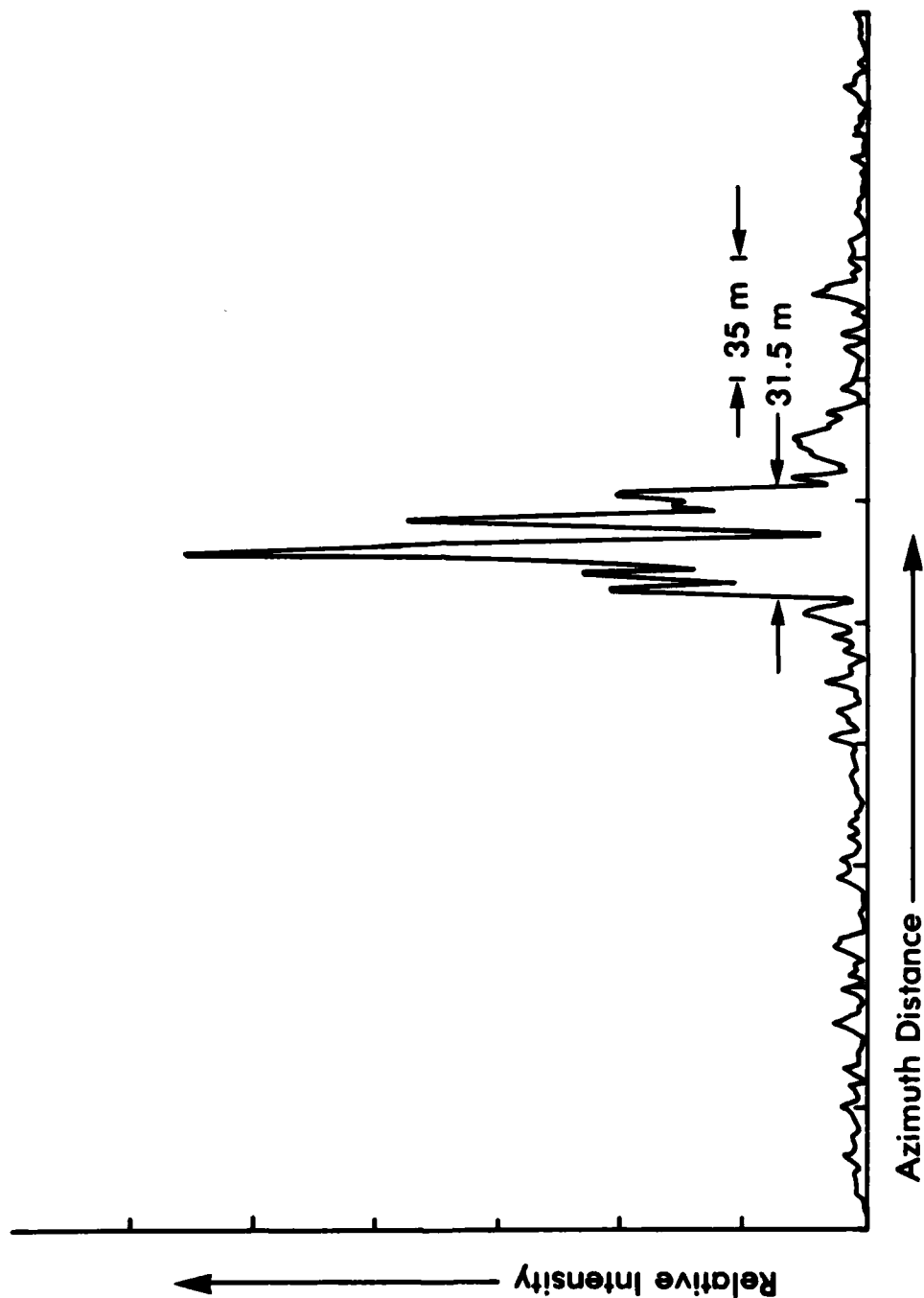


FIGURE 36. RELATIVE INTENSITY SCAN OF A FLOATING FISHNET BUOY.

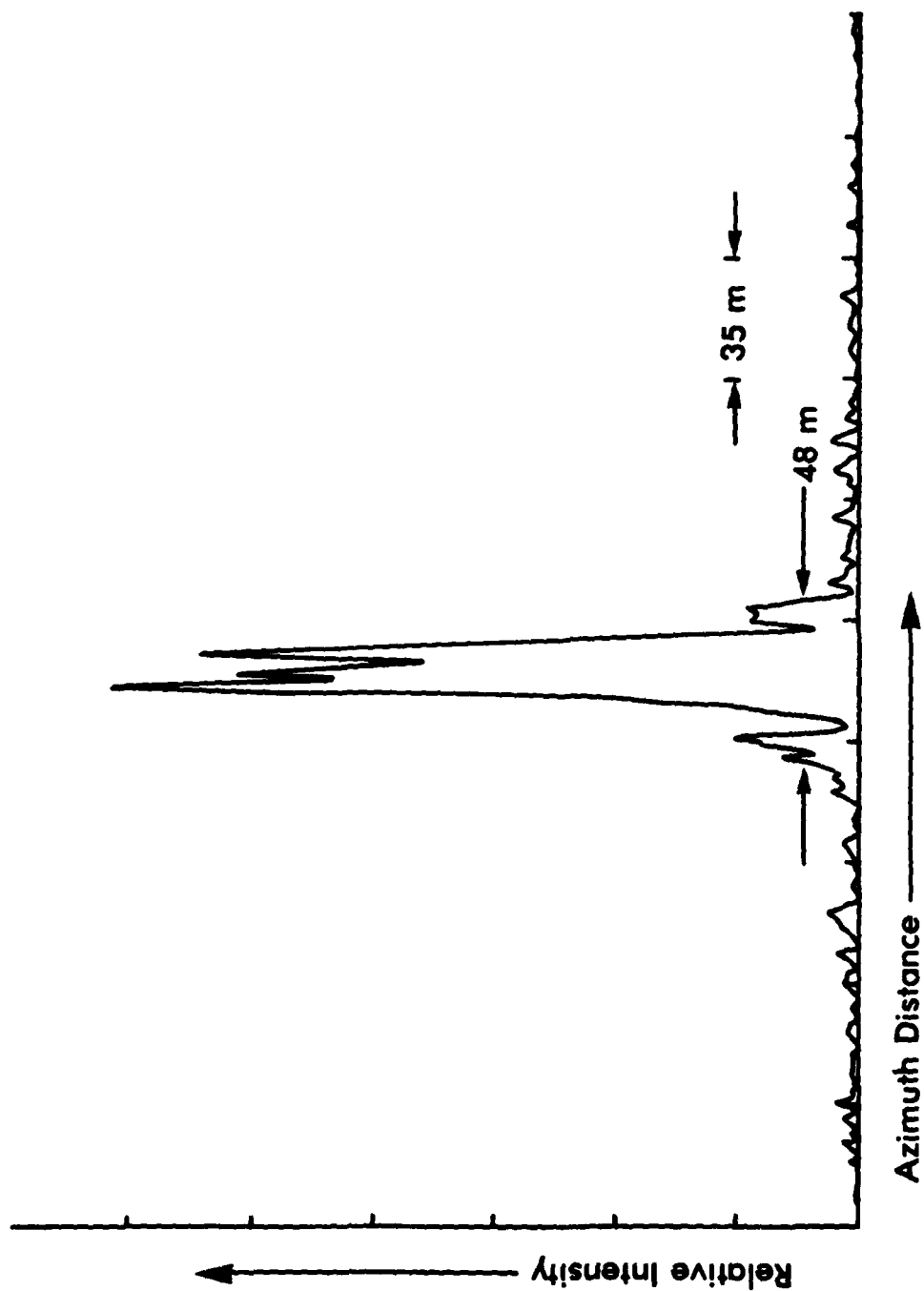


FIGURE 37. RELATIVE INTENSITY SCAN OF A FLOATING FISHNET BUOY.

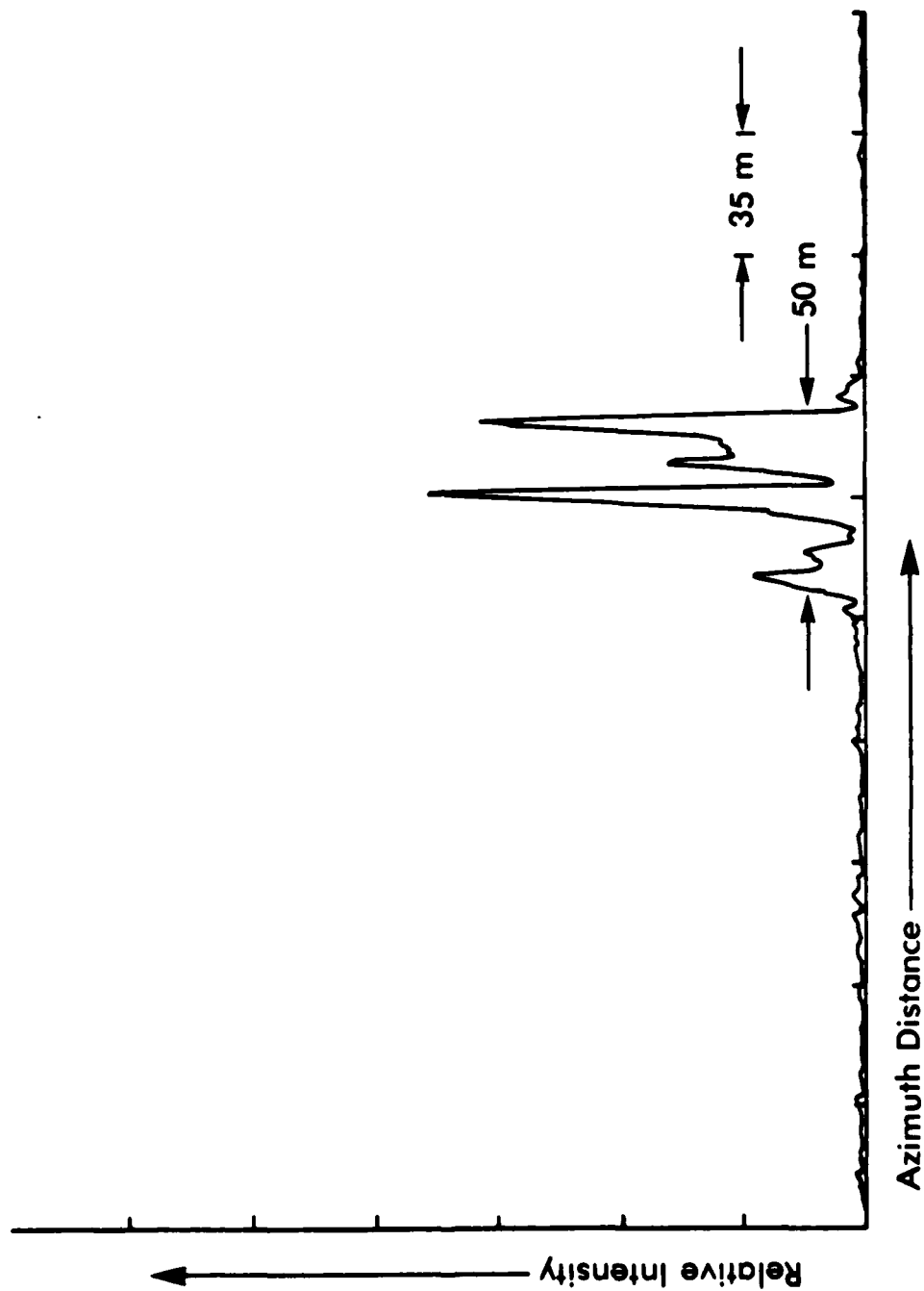


FIGURE 38. RELATIVE INTENSITY SCAN OF A FLOATING FISHNET BUOY.

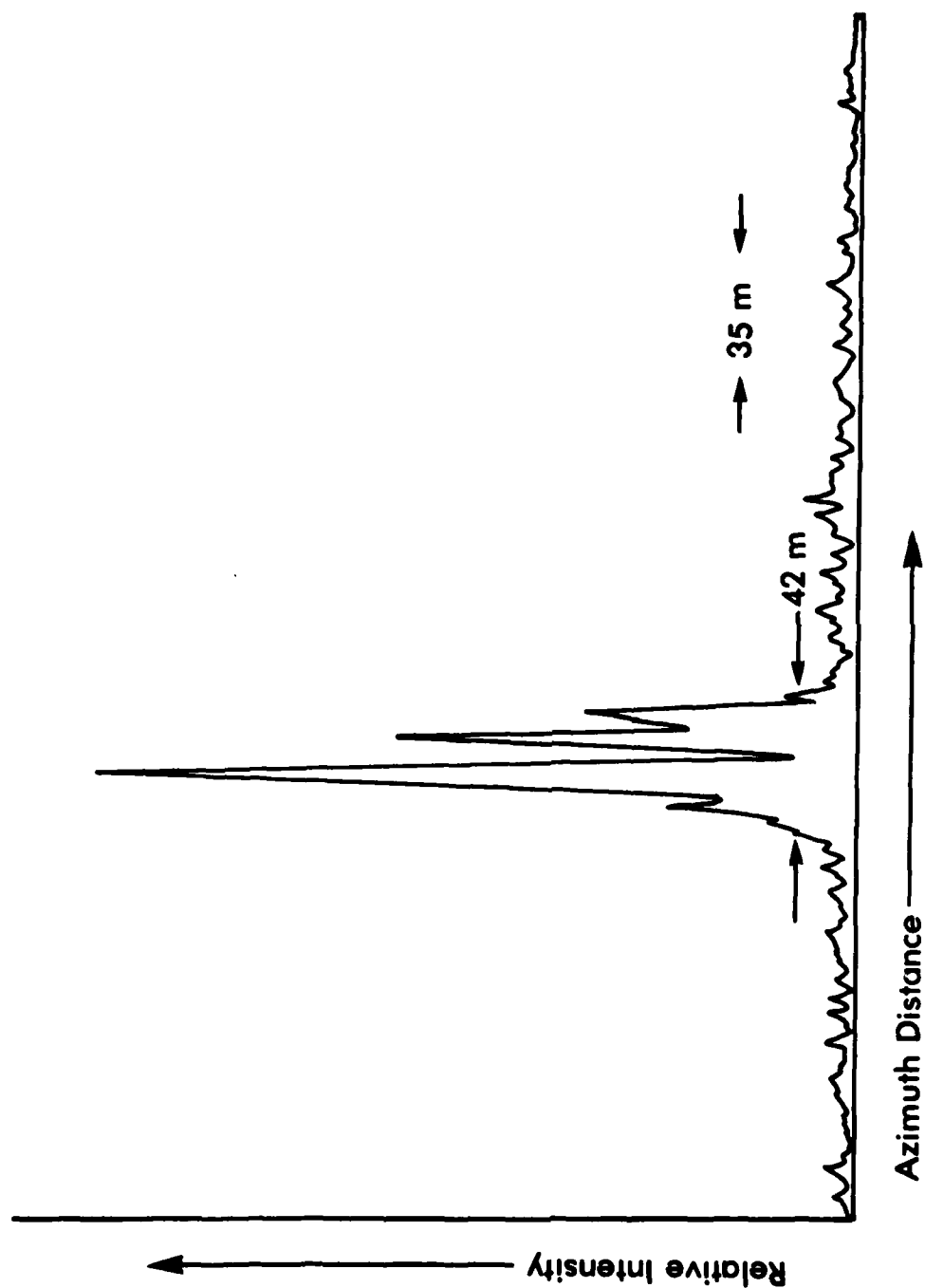


FIGURE 39. RELATIVE INTENSITY SCAN OF A FLOATING FISHNET BUOY.

the two spectra not only in the dominant or peak energy region, but also in the frequency ranges above and below this peak. The purpose of this investigation is two-fold: 1) To compare SAR derived dominant wavelength and direction to surface measurements as a function of SAR parameters and varying wind and wave conditions; and 2) To investigate the relationship between the SAR and sea truth spectra to try to determine the transfer function between the two instruments. Solving problem two would allow calculation of the wave power spectrum from the SAR-derived spectra, and thus, an estimate could be made of the wave height. It should be noted that results from this study are preliminary and no definite conclusions have been reached at present.

4.4.1 DATA SET

The SAR data used in this study were collected during six passes from line 10 and four passes from line 12 by the X-band UPD-4 system housed in United States Air Force of Europe (USAFE) F-4 aircraft. Environmental conditions for these passes were given previously in Table 8.

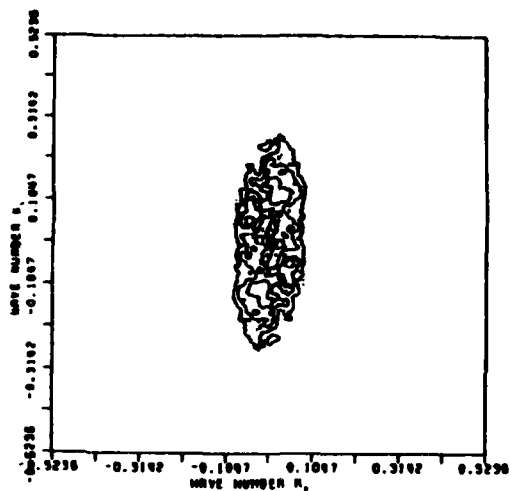
The SAR data collected during lines 10 and 12 were precision optically processed, digitized, and 512 x 512 pixel subsets were extracted and spectrally analyzed using fast Fourier transform (FFT) techniques as described by Shuchman, et al. (1979b).

The 3 m pixel digitized SAR images were converted to 6 m resolution by 4 pixel averaging to increase coherence in the image. The average value of each azimuthal line was subtracted from the line to remove the trend of intensity falloff with increasing range distance. Two-dimensional fast Fourier transforms were performed on each 256 x 256 cell subsection to yield raw directional wave number spectra each with a Nyquist wave number of 0.52 m^{-1} . The raw spectra were smoothed by replacing each value with the average of the surrounding

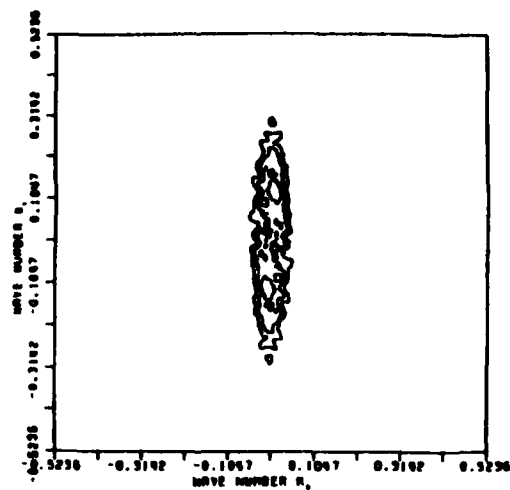
5 x 5 cell. The approximate number of degrees of freedom for the resulting spectrum is 142 (Kinsman, 1965, p. 464). The 99 percent confidence limits are then ± 1.5 dB (Jenkins and Watts, 1968).

An example of the contour plots produced from these transforms is shown in Figure 40 for all four sub-swaths of line 12, pass 3 wave data. Each contour on these plots represents a 3 dB (50 percent) decrease in spectral intensity from the previous one. On the two-dimensional plots the azimuth direction is the horizontal direction while the vertical axis is the range direction. It should be apparent from these plots, that a range-traveling artifact becomes more pronounced as the range to the ocean surface increases (i.e., swath A to swath D). In fact, the spectra in swaths C and D are completely dominated by this artifact. This is not a result of the digital processing techniques employed, as witnessed by the corresponding optical imagery shown for all four sub-swaths in Figure 41. Clearly, azimuth-oriented streaks can be seen becoming more pronounced as range increases. Over this same interval, the gravity waves of interest become less visible. The azimuth-oriented streaks lead to a perceived range-traveling wave. The exact cause of this streaking is not known at this time but as previously discussed in Section 4.3, it appears to be a motion artifact. Due to these streaks being present on all MARSEN UPD-4 imagery, and the relative fading (decreased contrast) of imaged gravity waves with range, accurate wave estimates could only be extracted from sub-swath A.

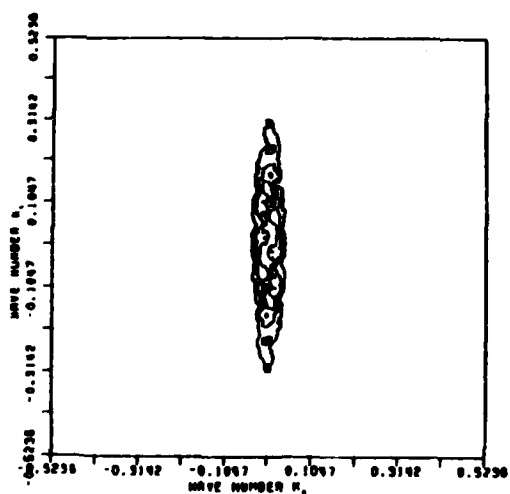
The surface-based spectra were obtained by processing measurements collected by an array of resistance wave staffs operating coincidentally with the SAR overflights. Recall that these measurements produce spectra as a function of frequency, the SAR-derived spectra however is in wavenumber space, the SAR spectra has to be converted to the frequency domain prior to any direct comparisons between the two.



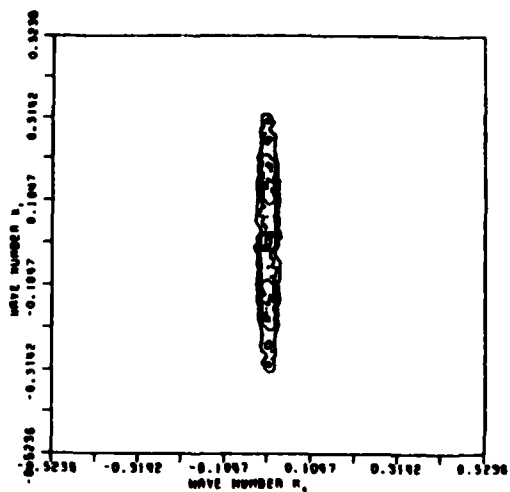
Sub-Swath A



Sub-Swath B



Sub-Swath C



Sub-Swath D

FIGURE 40. FFT-GENERATED SPECTRAL ESTIMATES FOR ALL FOUR SUB-SWATHS FROM UPD-4 IMAGERY OF LINE 12, PASS 3.

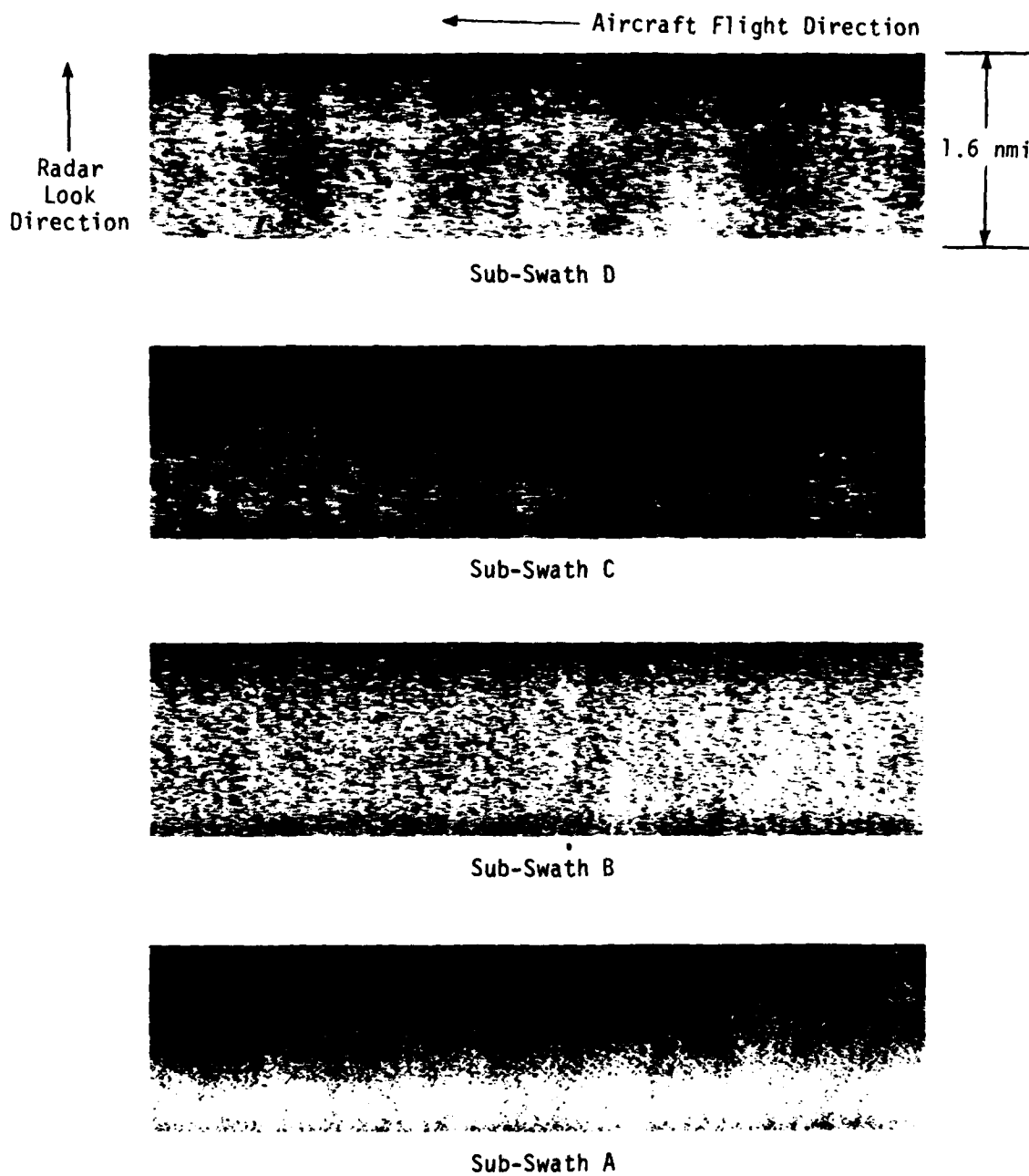


FIGURE 41. OPTICALLY PROCESSED UPD-4 IMAGERY FROM LINE 12, PASS 3.

4.4.2 COMPARISONS

The first analysis of the MARSEN data was to compare the estimates of dominant wavelength and direction obtained from the SAR data to the sea-truth estimates. Table 14 summarizes the results obtained from line 10, sub-swath A data. The estimates of dominant wave direction produced by the SAR are in good agreement with the estimate produced by the surface measurements (154°T). The estimates of dominant wavelength produced by the SAR were generally higher than the surface measurements which indicate a wave of 57 m.

Table 15 summarizes the results obtained from line 12, sub-swath A data. The SAR estimates compare well with the sea truth estimates of dominant wavelength (64 m) and wave direction (068°T) for this date. It is interesting to note that two dominant wavelengths and directions were detected on passes 2 and 3.

The two-dimensional digital transforms produced from lines 10 and 12 were further processed to produce one-dimensional wave number and wave direction plots. To generate a one-dimensional wave number plot, one-half of the two-dimensional FFT spectrum is integrated over all angles. A one-dimensional wave direction plot is generated by extracting values for a given wave number as a function of angle. The wave number plots were converted to frequency space using a simple deep water dispersion relationship for frequencies ranging from 0.086 to 0.273 Hz. Both sets of spectral intensity were normalized to 1 and plotted together. Mean directions from each were also plotted. Figures 42 to 45 show these plots for the four passes from line 12.

From the results summarized in Table 16, it appears that in the peak gravity wave region, the two spectra compare extremely well in the 0.1 - 0.15 Hz peak region (typically, frequencies ± 0.015 Hz, directions $\pm 24^{\circ}$). At frequencies greater and less than this peak, there is very little agreement between the two. It is this "dis-

TABLE 14
SUMMARY OF SAR GENERATED ESTIMATES OF DOMINANT
WAVELENGTH AND DIRECTION FROM MARSEN UPD-4 DATA,
LINE 10, SUB-SWATH A

Pass	OFT		FFT			
	Wavelength (m)	Wave Number (k) (m ⁻¹)	Propagation Direction (° True)	Wavelength (m)	Wave Number (k) (m ⁻¹)	Propagation Direction (° True)
1	87	0.072	144	90	0.070	142
2	74	0.085	131	82	0.077	130
3	83	0.076	119	98	0.064	119
4	85	0.074	129	124	0.051	141
5(a)	92	0.068	157	110	0.057	151
5(b)	92	0.068	153	123	0.051	151

TABLE 15
SUMMARY OF SAR GENERATED ESTIMATES OF DOMINANT
WAVELENGTH AND DIRECTION FROM MARSEN UPD-4 DATA, LINE 12, SUB-SWATH A

Pass	OFT			FFT		
	Wavelength (m)	Wave Number (k) (m ⁻¹)	Propagation Direction (°True)	Wavelength (m)	Wave Number (k) (m ⁻¹)	Propagation Direction (°True)
Sylt Tgt (a)	72	0.087	61			
Sylt Tgt (b)	72	0.087	65	75	0.084	49
1	87	0.072	56	99	0.063	50
2(a)	55	0.114	118			
2(b)	55	0.114	113	75	0.084	79
				57	0.110	118
3(a)	72	0.087	61	89	0.071	68
	44	0.143	108	57	0.110	108
3(b)	83	0.076	61			
	47	0.134	109			
3(c)	83	0.076	64			
	55	0.114	107			

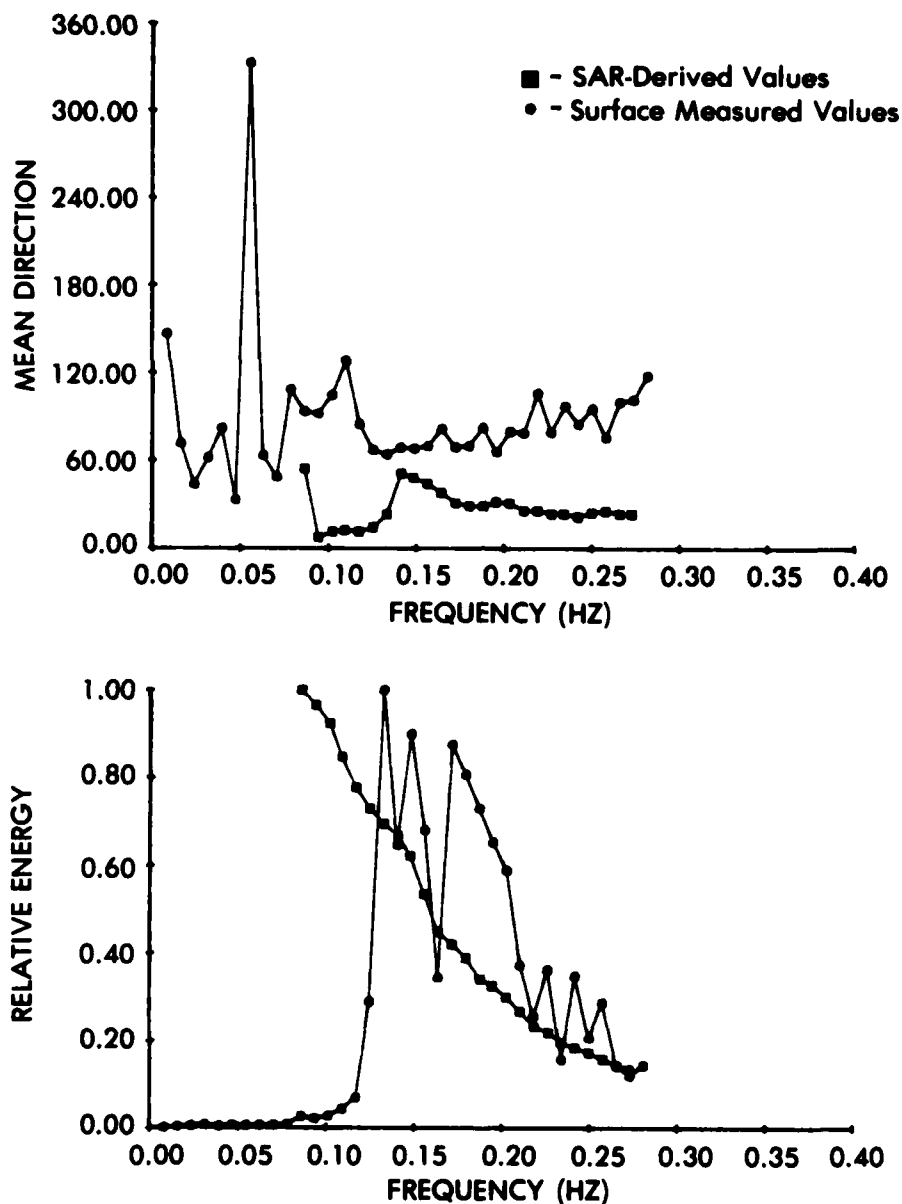


FIGURE 42. COMPARISON OF SURFACE-MEASURED AND SAR-DERIVED SPECTRAL ESTIMATES FROM SYLT TARGET PASS, LINE 12.

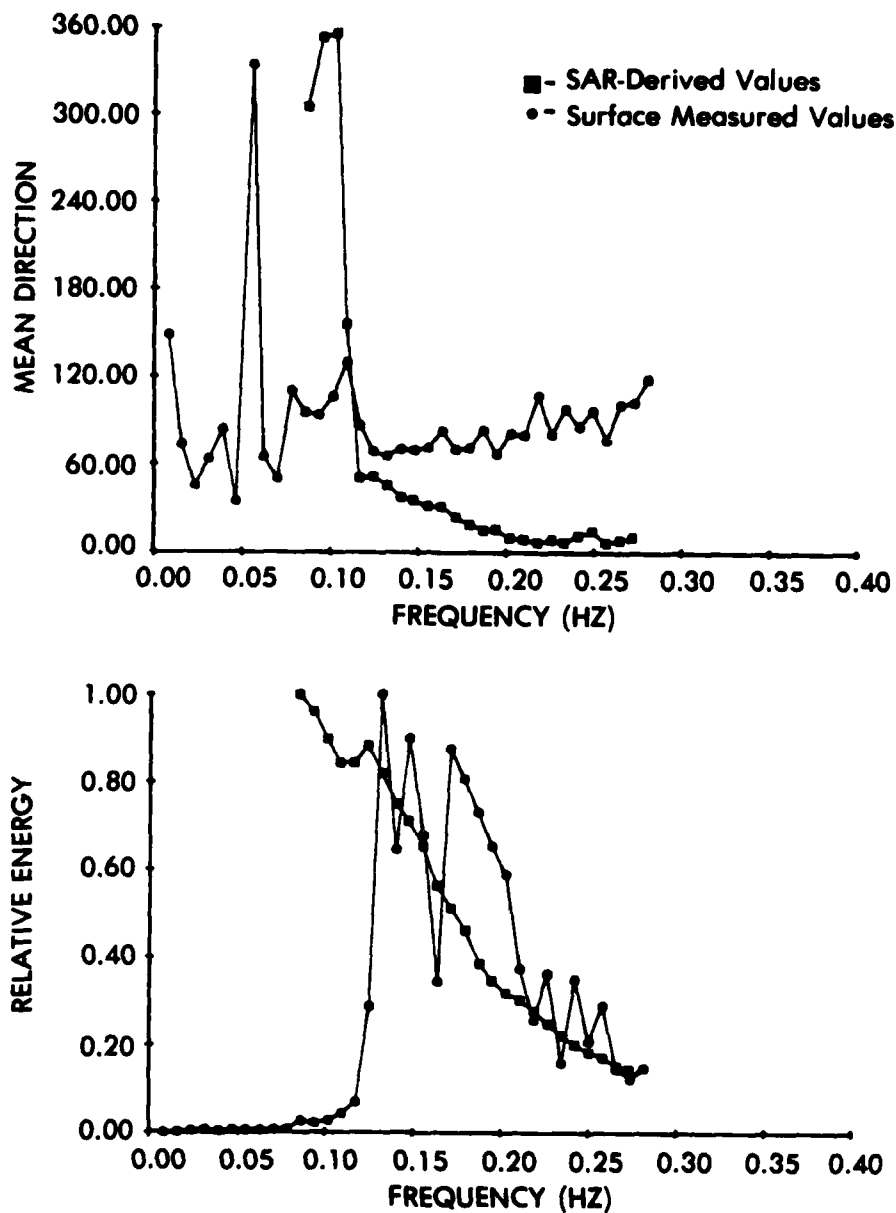


FIGURE 43. COMPARISON OF SURFACE-MEASURED AND SAR-DERIVED SPECTRAL ESTIMATES FROM PASS 1, LINE 12.

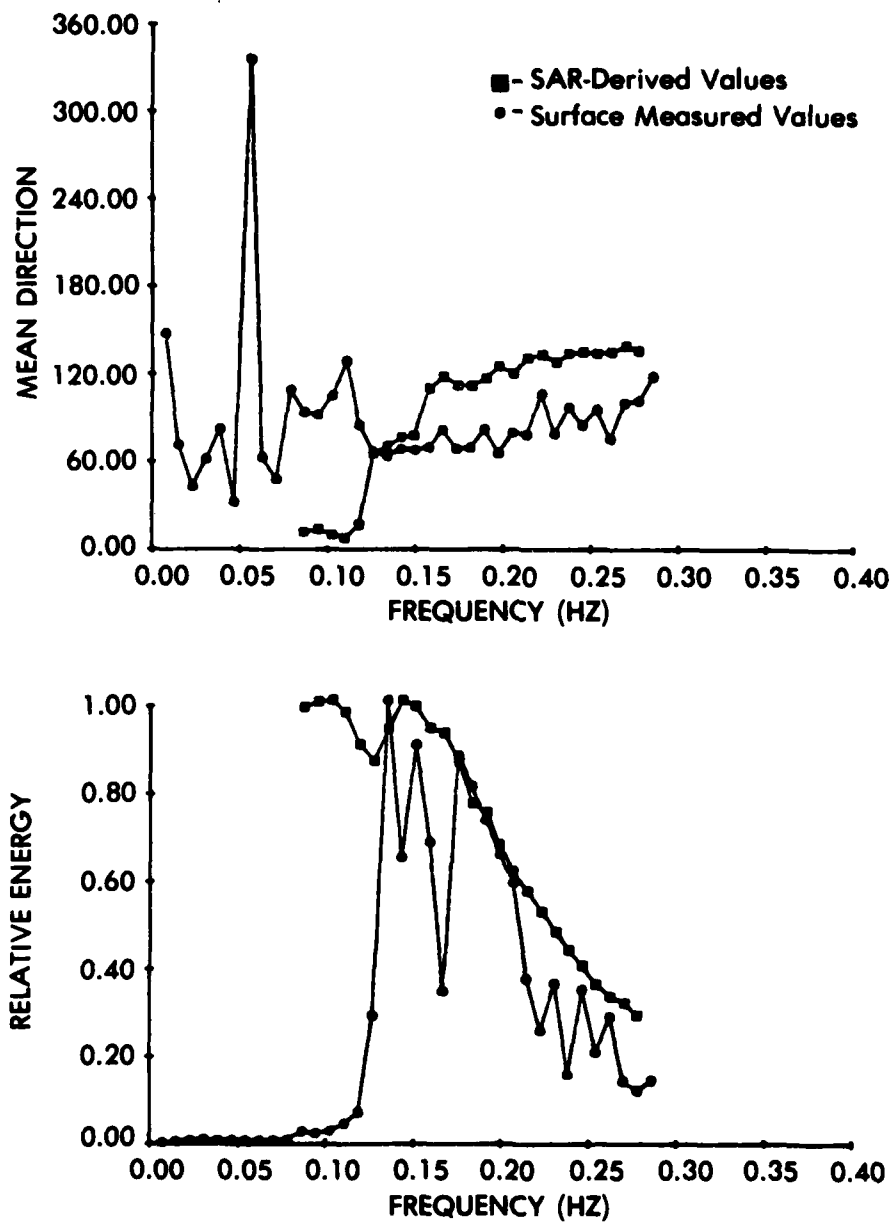


FIGURE 44. COMPARISON OF SURFACE-MEASURED AND SAR-DERIVED SPECTRAL ESTIMATES FROM PASS 2, LINE 12.

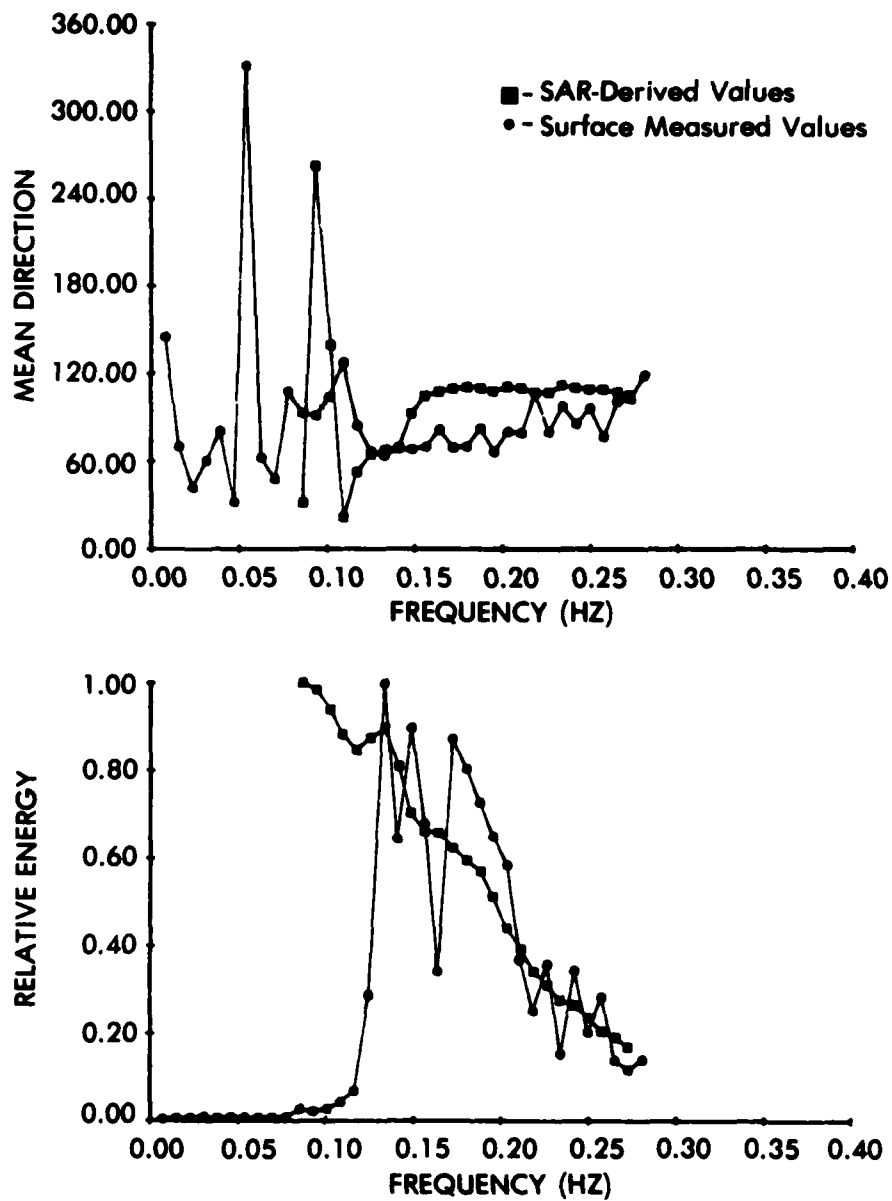


FIGURE 45. COMPARISON OF SURFACE-MEASURED AND SAR-DERIVED SPECTRAL ESTIMATES FROM PASS 3, LINE 12.

TABLE 16
COMPARISON OF SAR-DERIVED AND SURFACE-MEASURED SPECTRAL ESTIMATES FOR LINES 10 AND 12

Line	Pass	Radar Look Direction *	Surface-Measured			SAR-Derived (OFT)			SAR-Derived (FFT)		
			f (Hz)	λ (m)	θ (°True)	f (Hz)	λ (m)	θ (°True)	f (Hz)	λ (m)	θ (°True)
10	1	Up-Wave (39°)	0.133	88	154	0.134	87	144	0.132	90	142
	2	Down-Wave (8°)				0.145	74	131	0.138	82	130
	3	Up-Wave (53°)				0.137	83	119	0.126	98	119
	4	Up-Wave (83°)				0.135	85	129	0.112	124	141
	5(a)	Down-Wave (38°)				0.130	92	157	0.119	110	151
12	5(b)	Down-Wave (38°)				0.130	92	153	0.113	123	151
	Sylt	Down-Wave (41°)	0.133	88	68	0.147	72	63	0.144	75	49
	1	Down-Wave (55°)				0.134	87	56	0.126	99	50
	2	Down-Wave (78°)				0.168	55	115	0.144	75	79
	3	Up-Wave (31°)				0.137	83	61	0.132	89	68

*The value in parenthesis is the angular difference between the radar look direction and directly up-wave or down-wave.

**The surface-measured wavelengths and SAR-derived frequencies were obtained assuming the deep water dispersion relationship was valid.

agreement" that we would like to identify and quantitatively evaluate in hopes that a transfer function could be found which relates the spectra. The benefits of such a function would be the ability to calculate a wave height estimate from a SAR-derived spectrum.

To attempt to determine the relationship between the two spectra, a model of the form

$$E(f)_{\text{Radar}} = E(f)_{\text{Surface}} \times f^{\alpha} \quad (15)$$

was proposed where $E(f)_{\text{Radar}}$ and $E(f)_{\text{Surface}}$ are the unnormalized spectral intensities at frequency f , and α is an unknown constant. Simple mathematical transformations reduce (15) to

$$\log_{10} \left(\frac{E(f)_{\text{Radar}}}{E(f)_{\text{Surface}}} \right) = \alpha \log_{10}(f) \quad (16)$$

The significance of Eq. (16) is that if a constant α exists which satisfies Eq. (15), there will be a linear relationship between the left side of Eq. (16) and $\log_{10}(f)$, this relationship can be examined through simple linear regression analysis.

To test this theory, a scatterplot was produced of the left side of Eq. (16) versus $\log_{10}(f)$ for line 10, pass 4, as shown in Figure 46. At first inspection there does not appear to be a linear relationship over this frequency range (0.086 - 0.273 Hz). Upon closer examination, there does appear to be linear trends at frequencies higher and lower than that of the inflection point clearly visible in Figure 46. Performing a regression analysis on either side results in α estimates of -5.8 and 1.46 with correlation coefficients of 0.9 and 0.79 for the left (0.086 - 0.164 Hz) and right (0.164 - 0.273 Hz) sides respectively.

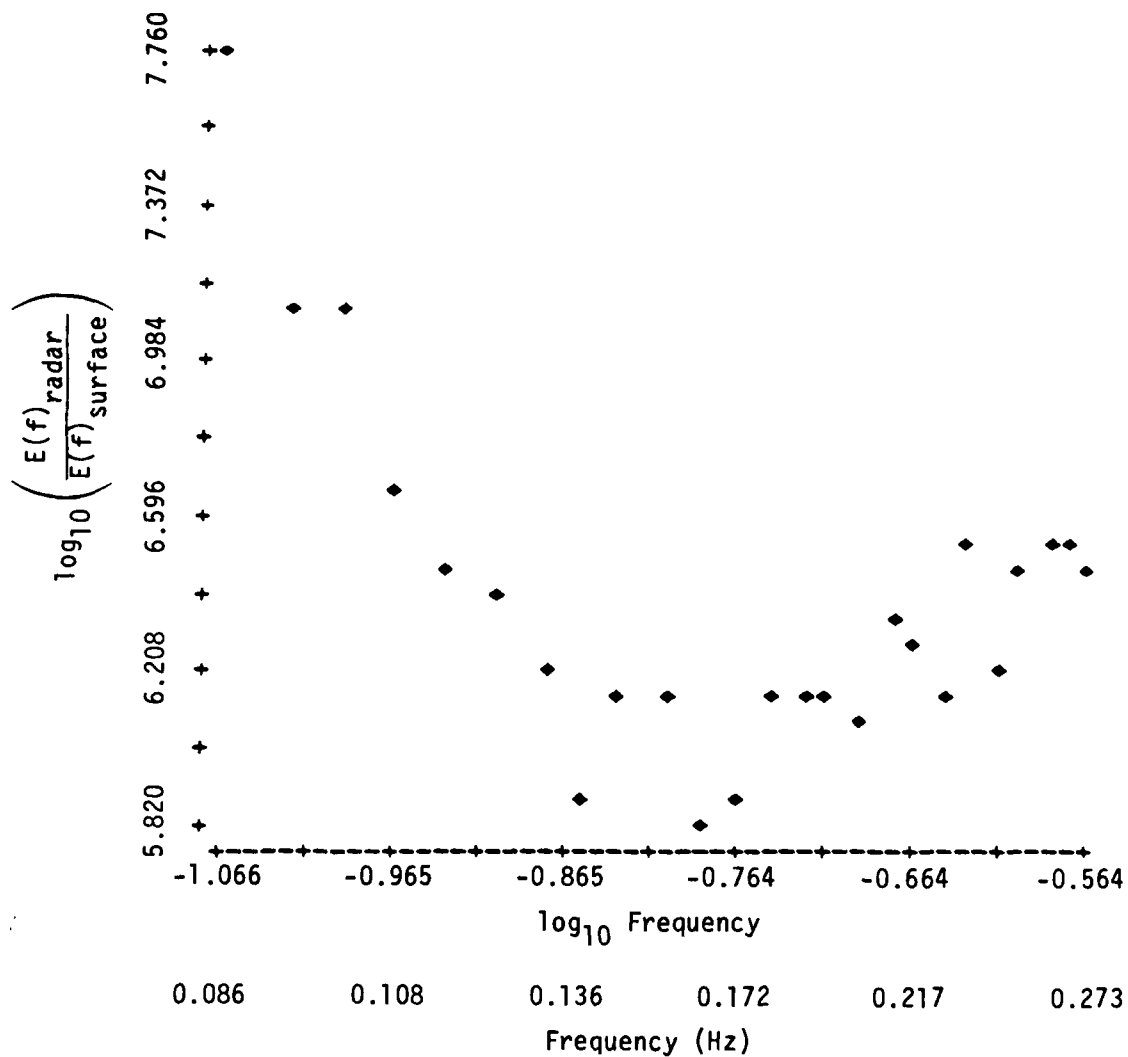


FIGURE 46. REPRESENTATIVE SCATTERPLOT OF
 $\log_{10} \left(\frac{E(f)_{\text{radar}}}{E(f)_{\text{surface}}} \right)$ VS. $\log_{10}(f)$.

This approach was followed for the six passes of line 10, and the four passes of line 12. These areas exhibited similar characteristics to the example above; the results are summarized in Table 17. It appears from these results that there exists a predictable relationship between the SAR-derived and surface-measured spectral estimates at frequencies lower than that of the inflection point. Frequencies above this do not have such linear behavior. These results are not applicable between data sets due to the digitization and data handling processes.

The application of the above results has not yet been thoroughly analyzed. Probably the key questions that need to be addressed include: (1) Do other data sets exhibit characteristics similar to Figure 46? (2) What procedures should be followed to insure normalization in the digitization process? and (3) How would one use the derived relationship to infer wave height? In any case a rigorous analysis should be undertaken to investigate the three questions posed above.

4.5 SUMMARY AND RECOMMENDATIONS FOR ADDITIONAL ANALYSIS OF MARSEN X-BAND DATA

This preliminary analysis has indicated the UPD-4 SAR system successfully imaged the dominant gravity wave component present during the MARSEN experiment. The shape of the SAR-derived spectrum of the wave field does not correspond to the shape of the wave spectrum produced by surface measurements. A transfer function to relate SAR derived spectral information to surface measurements is presently under development. Further analysis of the MARSEN data set indicates only the first or near range subswath of the UPD-4 and UPD-6 system produces reliable wave estimates. Dominant wavelength and directional information was obtainable independent of the radar look direction (in respect to wave crest), although range traveling waves are more clearly visible on the imagery than azimuth traveling gravity waves.

TABLE 17
SUMMARY OF α ESTIMATES FOR LINES 10 AND 12

Line	Pass	Lower Frequencies			Higher Frequencies		
		α	(Hz)	R^2	α	(Hz)	R^2
10	1	-5.4	0.086-0.133	0.89	1.2	0.133-0.273	0.45
	2	-5.6	0.086-0.133	0.88	1.3	0.133-0.273	0.44
	3	-5.4	0.086-0.133	0.89	1.3	0.133-0.273	0.47
	4	-5.8	0.086-0.133	0.92	1.5	0.133-0.273	0.52
	5	-6.5	0.086-0.133	0.92	1.4	0.133-0.273	0.50
	6	-5.8	0.086-0.133	0.92	1.4	0.133-0.273	0.48
12	SYLT	-7.2	0.086-0.180	0.88	1.7	0.188-0.273	0.35
	1	-6.9	0.086-0.180	0.87	1.5	0.188-0.273	0.29
	2	-6.4	0.086-0.172	0.81	1.8	0.180-0.273	0.44
	3	-7.0	0.086-0.172	0.85	1.2	0.180-0.273	0.27

The analysis has also indicated that the UPD-4 and UPD-6 systems are relatively insensitive to wave image enhancement performed during the SAR processing. The enhancement adjustment, which is inversely proportional to the SAR platform velocity, accounts and corrects for the motion of the ocean waves during the SAR observation time. Although the UPD-4 and UPD-6 SAR systems are insensitive to the wave motion correction algorithms, numerous motion artifacts are visible on the data. These artifacts, which appear as azimuth streaks on the imagery, are more pronounced in the far sub-swaths. They appear to be range dependent and are caused by velocity variations of the ocean scatterers. One possible cause of these image artifacts is breaking waves.

Five topics of investigation in regard to the X-band SAR MARSEN data will be pursued during 1982. The five topics are listed below:

1. Continue the development of the transfer function of SAR-derived spectral estimates to surface measurements. This effort will be performed jointly with Dr. Rosenthal of the University of Hamburg.
2. Further quantify the motion induced artifacts (i.e., azimuth streaks) observed on the data. A theory explaining their origins will be developed and the question as to which wave component causes the streaks will be answered if possible. Additionally the correlation of these artifacts with breaking waves will be evaluated.
3. Evaluate the utility of the UPD-4 system to provide information on the magnitude and direction of surface winds. In particular the stability of the system to yield quantifiable radar backscatter values will be assessed. The MARSEN SAR data set also offers the unique ability to ascertain the isotropic or anisotropic nature of X-band Bragg waves.

4. Evaluate the utility of the UPD-4 system to detect currents and frontal boundaries. Both Doppler as well as radar backscatter measurements will be utilized in this investigation.
5. Explore the utility of the X-band SAR to detect sub-surface bottom features via a change in observed backscatter.

REFERENCES

- Allan, T.D. and T.H. Guymr, Seasat and JASIN, Int. J. Remote Sensing, 1, pp. 261-267, 1980.
- Alpers, W.R. and C.L. Rufenach, The Effect of Orbital Motions on Synthetic Aperture Radar Imagery of Ocean Waves, IEEE Trans. Antennas Propagat., AP-27, pp. 685-690, 1979.
- Alpers, W.E., D.B. Ross, and C.L. Rufenach, On the Detectability of Ocean Surface Waves by Real and Synthetic Aperture Radar, J. Geophys. Res., 86, 6481-6498, 1981.
- Anonymous, MARSEN Data Analysis and Research Plan, Pasadena, 1980.
- Apel, J.R., R.L. Charnell and R.J. Blackwell, Ocean Internal Waves Off the North American and African Coasts from ERTS-1, Proc. Ninth Int. Symp. Remote Sens. Environ., Ann Arbor, MI, pp. 1345-1354, 1974.
- Apel, J.R., H.M. Byrne, J.R. Proni and R.L. Charnell, Observations of Oceanic Internal and Surface Waves from the Earth Resources Technology Satellite, J. Geophys. Res., 80, pp. 865-881, 1975.
- Apel, J., Non-Linear Features of Internal Waves as Derived from the Seasat Imaging Radar, in Oceanography from Space, ed. by J.F.R. Gower, Plenum Publishing Co., New York, pp. 525-534, 1981.
- Auserman, D.A., W.D. Hall, J.N. Latta, and J.S. Zelenke, Radar Data Processing and Exploitation Facility, Proceedings IEEE International Radar Conference, Washington, D.C., 1975.
- Baer, L., Informal Proceedings of the Atlantic Remote Sensing Land Ocean Experiment Data and Analysis Workshop, Virginia Beach, VA, 1981.
- Barber, N.F., A Diffraction Analysis of a Photograph of the Sea, Nature, 164, p. 485, 1949.
- Beal, R.C., The Seasat SAR Wind and Ocean Wave Monitoring Capabilities, JHU/APL Report No. 79U-019, Laurel, MD, 42 p., 1979.
- Beal, R.C., Spaceborne Imaging Radar: Monitoring of Ocean Waves, Science, 204, pp. 1373-1375, 1980.
- Beal, R.C., P.S. DeLeonibus and I. Katz (eds.), Spaceborne Synthetic Aperture Radar Imagery for Oceanography, Johns Hopkins Univ. Press, Baltimore, MD, 215 pp., 1981.
- Bowman, M.J. and R.L. Iverson, Estuarine and Plume Fronts, in Oceanic Fronts in Coastal Processes, Bowman and Esais (eds.), Springer-Verlag, New York, 1978.
- Brown, W.J. and L. Porcello, An Introduction to Synthetic Aperture Radar, IEEE Spectrum, 6, pp. 52-66, 1969.

Brown, W.E., Jr., C.E. Elachi and T.W. Thompson, Radar Imaging of Ocean Surface Patterns, J. Geophys. Res., 81, pp. 2657-2667, 1976.

Cheney, R.E., A Search for Cold Water Rings with Seasat, in Spaceborne Synthetic Aperture Radar for Oceanography, ed. by R.C. Beal, P.S. DeLeonibus and I. Katz, Johns Hopkins Univ. Press, Baltimore, MD, pp. 161-170, 1981.

De Loor, G.P. and H.W. Brunsveltdt van Hulten, Microwave Measurements Over the North Sea, Boundary-Layer Meteorol., 13, pp. 119-131, 1978.

Earle, M.D., Problems in Ocean Wave Hindcasting, in Spaceborne Synthetic Aperture Radar for Oceanography, ed. by R.C. Beal, P.S. DeLeonibus, and I. Katz, Johns Hopkins Univ. Press, Baltimore, MD, pp. 78-109, 1981.

Elachi, C., Radar Imaging of the Ocean Surface, Boundary-Layer Meteorol., 13, pp. 165-179, 1978.

Elachi, C. and W.E. Brown, Models of Radar Imaging of the Ocean Surface Waves, IEEE Trans. Antenna Propagat., AP-25, pp. 84-95, 1977.

Fett, R. and R. Rabe, Satellite Observation of Internal Wave Refraction in the South China Sea, Geophys. Res. Ltrs., 4, 189-191, 1977.

Gargett, A.E. and B.A. Hughes, On the Interaction of Surface Internal Waves, J. Fluid Mech., 52, pp. 179-192, 1972.

Gonzalez, F.I., R.A. Shuchman, D.B. Ross, C.L. Rufenach and J.F.R. Gower, Synthetic Aperture Radar Wave Observations During GOASEX, in Oceanography from Space, ed. by J.F.R. Gower, Plenum Publishing Co., New York, pp. 459-468, 1981.

Gonzalez, F.I., T.W. Thompson, W.E. Brown, Jr., and D.E. Weissman, Seasat Wind and Wave Observations of North Pacific Tropical Storm Iva (Abstract), Trans. Amer. Geophys. Union, 62, pp. 29, 1981a.

Gonzalez, F.I., C.L. Rufenach, and R.A. Shuchman, Surface Current Detection Using SAR Data, in Oceanography from Space, ed. by J.F.R. Gower, Plenum Publishing Co., New York, pp. 511-524, 1981b.

Gower, J.F.R. and B.A. Hughes, Radar and Ship Observations of Coastal Sea Surface Roughness Patterns in the Gulf of Georgia, Proceedings of the Thirteenth International Symposium on Remote Sensing of Environment, Ann Arbor, Michigan, pp. 103-115, 1979.

Harger, R.O., Synthetic Aperture Radar Systems, Academic Press, New York, NY, 240 pp., 1970.

Harger, R.H., SAR Ocean Imaging Mechanisms, in Spaceborne Synthetic Aperture Radar for Oceanography, ed. by R.C. Beal, P.S. DeLeonibus, and I. Katz, Johns Hopkins Univ. Press, Baltimore, MD, pp. 41-52, 1981.

Hasselmann, K., A Simple Algorithm for the Direct Extraction of the Two-Dimensional Surface Image Spectrum from Return Signal of a Synthetic Aperture Radar, Int. J. Rem. Sens., 1, pp. 219-240, 1980.

Haxby, W.F., Sensitivity of Seasat Altimetry Data to Seafloor Topography (Abstract), Trans. Amer. Geophys. Union, 62, pp. 257, 1981.

Hayes, J.G., Ocean Current Wave Interaction Study, J. Geophys. Res., 85, pp. 5025-5031, 1980.

Hayes, R.M., SAR Detection of the Gulf Stream, in Spaceborne Synthetic Aperture Radar for Oceanography, ed. by R.C. Beal, P.S. DeLeonibus and I. Katz, Johns Hopkins Univ. Press, Baltimore, MD, pp. 146-160, 1981.

Hayes, J.G. and R.A. Shuchman, Seasat SAR Ocean Surface Current and Shallow Water Wave Refraction, in Oceanography from Space, ed. by J.F.R. Gower, Plenum Publishing Company, New York, pp. 469-476, 1981.

Jackson, P.L. and R.A. Shuchman, High Resolution Spectral Estimation of SAR Ocean Wave Imagery, submitted to J. Geophys. Res., 1982.

Jain, A.K., Focusing Effects in Synthetic Aperture Radar Imaging of Ocean Waves, J. Appl. Phys., 15, pp. 323-333, 1978.

Jain, A.K. and S. Ranganath, Two-Dimensional Spectral Estimation, Proc. of the RADC Spectrum Estimation Workshop, 1978.

Jenkins, A.M. and D.G. Watts, Spectral Analysis and Its Applications, Holden-Day, San Francisco, Calif., 525 pp., 1968.

Jones, W.L. and L.C. Schroeder, Radar Backscatter from the Ocean: Dependence on Surface Friction Velocity, Boundary-Layer Meteorol., 13, pp. 133-149, 1978.

Jones, W.L., V.E. Delnore, and E.M. Bracalente, The Study of Mesoscale Ocean Winds, in Spaceborne Synthetic Aperture Radar for Oceanography, ed. by R.C. Beal, P.S. DeLeonibus, and I. Katz, Johns Hopkins Univ. Press, Baltimore, MD, pp. 87-94, 1981.

Jordan, R.L., The Seasat-A Synthetic Aperture Radar System, IEEE J. Oceanic Eng., OE-5, pp. 154-164, 1980.

Kasischke, E.S., Extraction of Gravity Wave Information from Synthetic Aperture Radar Data, Univ. of Mich. M.S. Thesis, 108 pp., 1980.

Kasischke, E.S., A. Klooster and R.A. Shuchman, Verification of Synthetic Aperture Radar Focusing Algorithms, Proc. Thirteenth Int. Symp. Remote Sensing Environ., Ann Arbor, MI, pp. 1077-1092, 1979.

Kasischke, E.S., R.A. Shuchman and J.D. Lyden, Detection of Bathymetric Features Using SEASAT Synthetic Aperture Radar - A Feasibility Study, ERIM Final Report No. 135900-2-F2, 77 pp., 1980.

Kasischke, E.S. and R.A. Shuchman, The Use of Wave Contrast Measurements in the Evaluation of SAR/Gravity Wave Models, Proceedings of the Fifteenth International Symposium on Remote Sensing of Environment, Ann Arbor, MI, pp. 1187-1209, 1981.

Kasischke, E.S. and R.A. Shuchman, Comparisons of Wave Contrast Measurements made from SAR Data with Selected Oceanographic Parameters, presented at the Symposium on Wave Dynamics and Radio Probing of the Ocean Surface, May 1981a.

Kasischke, E.S., R.A. Shuchman, G.A. Meadows, P.L. Jackson, Y. Tseng, and J.D. Lyden, Further Seasat Coastal Ocean Wave Analysis, ERIM Final Report No. 138600-6-F, 138 pp., 1981.

Kasischke, E.S., R.A. Shuchman, D.R. Lyzenga, B. Termaat, Y. Tseng, and B.A. Burns, The Use of Synthetic Aperture Radar to Detect and Chart Submerged Navigation Hazards, ERIM Final Report 155200-6-F, 155 pp., 1982.

Kenyon, K.E., Wave Refraction in Ocean Currents, Deep-Sea Res., 18, pp. 1023-1034, 1971.

Kenyon, N.H., R.H. Belderson, A.H. Stride and M.A. Johnson, Offshore Tidal Sand Boules as Indicators of Net Sand Transport and as Potential Deposits, in Holocene Marine Sedimentation in the North Sea Basin, Selected Papers from the IAS Meeting, Texel, Netherlands, ed. by S.D. Nio, R.T.E. Schuttenhelm and T.C.E. Van Weering, IAS Spec. Pub. 5., Sept. 1979.

Ketchum, R.D. and S.G. Tooma, Analysis and Interpretation of Airborne Multi-Frequency Side-Looking Radar Sea Ice Imagery, J. Geophys. Res., 78, pp. 520-538, 1973.

Kinsman, B., Wind Waves - Their Generation and Propagation on the Ocean Surface, Prentice-Hall, Englewood Cliffs, N.J., 676 pp., 1965.

LaFond, E.C. and C.S. Cox, Internal Waves, The Sea, Vol. 1, M.N. Hill (ed.), Interscience Publishers, New York, pp. 731-763, 1962.

Larson, T.R., L.I. Moskowitz and J.W. Wright, A Note on SAR Imagery of the Ocean, IEEE Trans. Antenna Propag., AP-24, pp. 393-394, 1976.

Larson, R.W., R.A. Shuchman, R.F. Rawson and W.D. Worsfold, The Use of SAR Systems for Iceberg Detection and Characterization, Proceedings of the Twelfth International Symposium on Remote Sensing of Environment, Ann Arbor, MI, pp. 1127-1147, 1978.

Larson, R.W., J.D. Lyden and R.A. Shuchman, An Analysis of Four-Channel Synthetic Aperture Radar Data of Sea Ice, presented at the Symposium on Signature Problems in Microwave Remote Sensing, Lawrence City, Kansas, 1981.

Le Schack, A.R., A.R. LaZarewicz and R.V. Sailor, Limits on Seamount Detectability from Seasat Altimetry Data (Abstract), Trans. Amer. Geophys. Union, 62, pp. 256-257, 1981.

Lichy, D.E., M.G. Mattie and L.J. Mancini, Tracking of a Warm Water Ring Using Synthetic Aperture Radar, in Spaceborne Synthetic Aperture Radar Imagery for Oceanography, ed. by R.C. Beal, P.S. DeLeonibus, and I. Katz, Johns Hopkins Univ. Press, Baltimore, MD, pp. 171-182, 1981.

Longuet-Higgins, M.S. and R.W. Stewart, Radiation Stresses in Water Waves in a Physical Discussion, with Applications, Deep Sea Research, 11, pp. 529-562, 1964.

Lyden, J.D. and R.A. Shuchman, Detection of Chesapeake Bay Oceanic Fronts with Imaging Radar, ERIM Final Report No. 151800-11-F, 110 pp., 1981.

McIntosh, R.E., Feasibility of Mapping Ocean Surface Currents Using ΔK Microwave Radars Mounted on Geostationary Satellite Platforms, 1981 Int. Geoscience and Remote Sensing Symposium Digest, Washington, D.C., pp. 1083-1088, 1981.

McLeish, W., D.J.P. Swift, R.B. Long, D. Ross and G. Merrill, Ocean Surface Patterns Above Seafloor Bedforms as Recorded by Radar, Southern Bight of North Sea, Mar. Geol., 43, pp. M1-M8, 1981.

Mapp, G.R., J.C. Munday and C.S. Welch, Wave Refraction by Warm Core Rings (Abstract), Trans. Amer. Geophys. Union, 62, p. 2951, 1981.

Mattie, M.G., D.E. Lichy and R.C. Beal, Seasat Detection of Waves, Currents and Inlet Discharge, Int. J. Remote Sensing, 1, pp. 377-398, 1980.

Meadows, G.A., E.S. Kasischke and R.A. Shuchman, SAR Observations of Coastal Zone Conditions, Proceedings of the Fourteenth International Symposium on Remote Sensing of Environment, Ann Arbor, MI., pp. 845-863, 1980.

Meadows, G.A., R.A. Shuchman, E.S. Kasischke Y. Tseng, and J.D. Lyden, The Observation of Gravity Wave - Current Interactions Using Seasat Synthetic Aperture Radar, submitted to J. Geophys. Res., 1981.

Meadows, G.A., R.A. Shuchman and J.D. Lyden, Analysis of Remotely Sensed Long-Period Wave Motions, submitted to J. Geophys. Res., 1981a.

Mollo-Christensen, E. and A.D.S. Mascarenhas, Jr., Heat Storage in the Oceanic Upper Mixed Layer Inferred from Landsat Data, Science, 203, pp. 653-654, 1979.

Moore, R.K. and A.K. Fung, Radar Determination of Winds at Sea, Proc. of IEEE, 67, pp. 1504-1521, 1979.

Moskowitz, L.I., The Feasibility of Ocean Current Mapping via Synthetic Aperture Radar Methods, Proc. Amer. Soc. of Photogrammetry, Part II, pp. 760-771, 1973.

Oertel, G.F. and W.M. Dunstan, Suspended Sediment Distribution and Certain Aspects of Phytoplankton Production Off Georgia, USA, J. Mar. Geol., 40, pp. 171-197, 1981.

Osborne, A.R. and T.L. Burch, Internal Solitons in the Andaman Sea, Science, 208, pp. 451-460, 1980.

Phillips, O.M., The Structure of Short Gravity Waves on the Ocean Surface, in Spaceborne Synthetic Aperture Radar for Oceanography, ed. by R.C. Beal, P.S. DeLeonibus, and I. Katz, Johns Hopkins Univ. Press, Baltimore, MD, pp. 24-31, 1981.

Pierson, W.J., The Variability of the Winds Over the Ocean, in Spaceborne Synthetic Aperture Radar for Oceanography, ed. by R.C. Beal, P.S. DeLeonibus, and I. Katz, Johns Hopkins Univ. Press, Baltimore, MD, pp. 56-74, 1981.

Raney, R.K., Synthetic Aperture Radar and Moving Targets, IEEE Trans. Aerospace Elect. Syst., AES-7, pp. 499-505, 1971.

Raney, R.K. and R.A. Shuchman, SAR Mechanism for Imaging Waves, Proc. Fifth Canadian Symp. on Remote Sensing, Victoria, B.C., 1978.

Rawson, R., F. Smith and R. Larson, The ERIM X- and L-Band Dual Polarized Radar, IEEE 1975 International Radar Conference, p. 505, 1975.

Rawson, R.F. and C.L. Liskow, Radar Reflectivity Measurements of Ocean Surface with and Without a Surface Look of Oil, IEEE International Geoscience and Remote Sensing Symposium Digest, Washington, D.C., pp. 1268-1273, 1981.

Ross, D., B. Au, W. Brown and J. McFadden, A Remote Sensing Study of Pacific Hurricane Ava, Proceedings of the Ninth International Symposium on Remote Sensing of Environment, Ann Arbor, MI, pp. 163-180, 1974.

Ross, D.B. and W.L. Jones, On the Relationship of Radar Backscatter to Wind Speed and Fetch, Boundary-Layer Meteorol., 13, pp. 151-163, 1978.

Ross, D.B., The Wind Speed Dependency of Ocean Microwave Backscatter, in Spaceborne Synthetic Aperture Radar for Oceanography, ed. by R.C. Beal, P.S. DeLeonibus, and I. Katz, Johns Hopkins Univ. Press, Baltimore, MD, pp. 75-86, 1981.

Rufenach, C.L., R.A. Shuchman, and D.L. Lyzenga, Interpretation of Synthetic Aperture Radar Measurements of Ocean Currents, submitted to J. Geophys. Res., 1981.

Schaeffer, R.L., W. Mendenhall, and L. Ott, Elementary Survey Sampling, 2nd Ed., Duxburg Press, North Scituate, Mass., 278 pp., 1979.

Schwab, D.J., R.A. Shuchman and P.L. Liu, Wind Wave Directions Determined from Synthetic Aperture Radar Imagery and from a Tower in Lake Michigan, J. Geophys. Res., 86, pp. 2059-2064, 1981.

Sheffe, H., The Analysis of Variance, John Wiley and Sons, Inc., New York, 477 pp., 1959.

Shemdin, O.H., The Marineland Experiment: An Overview, Trans. Amer. Geophys. Union, 61, pp. 625-626, 1980.

Shemdin, O.H., The West Coast Experiment: An Overview, Trans. Amer. Geophys. Union, 61, pp. 649-651, 1980.

Shemdin, O.H., A. Jain, S.V. Hsiao and L.W. Gatto, Inlet Current Measured with Seasat-1 Synthetic Aperture Radar, Shore and Beach, 48, pp. 35-39, 1980.

Shuchman, R.A., Processing Synthetic Aperture Radar Data of Ocean Waves, in Oceanography from Space, ed. by J.F.R. Gower, Plenum Publishing Co., New York, pp. 477-496, 1981.

Shuchman, R.A., P.L. Jackson and G.B. Feldkamp, Problems of Imaging Ocean Waves with Synthetic Aperture Radar, ERIM Interim Technical Report No. 124300-1-I, Ann Arbor, MI, 111 pp., 1977.

Shuchman, R.A., R.F. Lawson and E.S. Kasischke, Analysis of Synthetic Aperture Radar Ocean Wave Data Collected at Marineland and Georges Banks, ERIM Report No. 123000-11-F, 129 pp., 1977a.

Shuchman, R.A. and J.S. Zelenka, Processing of Ocean Wave Data from a Synthetic Aperture Radar, Boundary-Layer Meteorol., 13, pp. 181-191, 1978.

Shuchman, R.A. and E.S. Kasischke, The Detection of Oceanic Bottom Topographic Features Using SEASAT Synthetic Aperture Radar Imagery, Proc. Thirteenth Int. Symp. Rem. Sens. Environ., pp. 1277-1292, 1979.

Shuchman, R.A., C.L. Rufenach and F.I. Gonzalez, The Feasibility of Measurement of Ocean Surface Currents Using Synthetic Aperture Radar, Proceedings of the Thirteenth International Symposium on Remote Sensing of Environment, Ann Arbor, MI, pp. 93-102, 1979.

Shuchman, R.A., E.S. Kasischke, A. Klooster, and P.L. Jackson, SAR Coastal Ocean Wave Analysis - A Wave Refraction and Diffraction Study, ERIM Final Report No. 138600-2-F, Ann Arbor, MI, 1979a.

Shuchman, R.A., K.H. Knorr, J.C. Dwyer, P.L. Jackson, A. Klooster, and A.L. Maffett, Imaging Ocean Waves with SAR - A SAR Ocean Wave Algorithm Development, ERIM Interim Technical Report No. 124300-5-T, Ann Arbor, MI, 123 pp., 1979b.

Shuchman, R.A. and G.A. Meadows, Airborne Synthetic Aperture Radar Observations of Surf Zone Conditions, Geophys. Res. Ltrs., 7, pp. 857-860, 1980.

Shuchman, R.A., E.S. Kasischke, J.D. Lyden and G.A. Meadows, The Use of Synthetic Aperture Radar (SAR) to Measure Ocean Gravity Waves, Proceedings of the National Academy of Sciences Special Conference on Wave Technology (in press), April 1981.

Shuchman, R.A., A.L. Maffett and A. Klooster, Static Modeling of a SAR Imaged Ocean Scene, IEEE J. Oceanic Eng., OE-6, pp. 41-49, 1981a.

Shuchman, R.A., E.S. Kasischke and G.A. Meadows, Detection of Coastal Zone Environmental Conditions Using Synthetic Aperture Radar, IEEE International Geoscience and Remote Sensing Symposium Digest, pp. 756-767, 1981b.

Shuchman, R.A., D.R. Lyzenga, and A. Klooster, Exploitation of SAR Data for Measurement of Ocean Currents and Wave Velocities, ERIM Final Report No. 137600-1-F, 84 pp., 1981c.

Teleki, P.G., R.A. Shuchman, W.E. Brown, Jr., W. McLeish, D. Ross and M. Mattie, Ocean Wave Detection and Direction Measurements with Microwave Radars, Oceans '78, IEEE/MTS, pp. 639-648, 1978.

Trask, R.P. and M.G. Briscoe, Surface Expressions of Internal Waves Detected by Seasat's SAR (Abstract), Trans. Amer. Geophys. Union, 1981.

Trunk, G.V., Non-Rayleigh Sea Clutter: Properties and Detection of Targets, NRL Report 7986, p. 81, 1976.

Valenzuela, G.R., An Asymptotic Formulation for SAR Images of the Dynamical Ocean Surface, Radio Science, 15, 1980.

Vesecky, J.F. and R.H. Stewart, The Observation of Ocean Surface Phenomena Using Imagery from the Seasat Synthetic Aperture Radar - An Assessment, J. Geophys. Res. (in press), 1982.

Vesecky, J.F., R.H. Stewart, H.M. Assal, R.A. Shuchman, E.S. Kasischke and J.D. Lyden, Gravity Waves, Large-Scale Surface Features and Ships Observed by Seasat During the 1978 JASIN Experiment, submitted to Science, 1981.

Weissman, D.E., T.W. Thompson and R. Legeckis, Modulation of Sea Surface Radar Cross Section by Surface Stress: Wind Speed and Temperature Effects Across the Gulf Stream, J. Geophys. Res., 85, pp. 5032-5042, 1980.

Wright, J.W., Backscattering from Capillary Waves with Application to Sea Clutter, IEEE Trans. Antenna Propagat., AP-14, pp. 749-754, 1966.

Wright, J.W., W.J. Plant, W.C. Keller and W.L. Jones, Ocean Wave-Radar Modulation Transfer Functions from the West Coast Experiment, J. Geophys. Res., 85, pp. 4957-4966, 1980.

APPENDIX

Contained in this Appendix are a series of papers which are the result of ONR funded research conducted during the 1980 calendar year. These articles are presented in alphabetical order, according to first author, as summarized in Table A1. The figures contained in this appendix are xerox prints, not half-tone prints. Anyone wishing to obtain higher quality reprints should contact ERIM.

TABLE A1
PAPERS IN APPENDIX

- A. Jackson, P.L. and R.A. Shuchman, High Resolution Spectral Estimation of SAR Ocean Wave Imagery, submitted to J. Geophys. Res., 1982.
- B. Kasischke, E.S. and R.A. Shuchman, The Use of Wave Contrast Measurements in the Evaluation of SAR/Gravity Wave Models, Proceedings of the Fifteenth International Symposium on Remote Sensing of Environment, Ann Arbor, MI, pp 1187-1209, May 1981.
- C. Kasischke, E.S., R.A. Shuchman, J.D. Lyden, R.H. Stewart, J.F. Vesecky, and H.M. Assal, Seasat Observation of Ocean Gravity Waves During the JASIN Experiment, Submitted to J. Geophys. Res., 1981.
- D. McLeish, W., D. Ross, R.A. Shuchman, P.G. Teleki, S.V. Hsiao, O.H. Shemdin and W.E. Brown, Synthetic Aperture Radar Imaging of Ocean Waves: Comparison with Wave Measurements, J. Geophys. Res., 85, pp. 5003-5011, 1980.
- E. Meadows, G.A., E.S. Kasischke and R.A. Shuchman, SAR Observations of Coastal Zone Conditions, Proceedings of the Fourteenth International Symposium on Remote Sensing of Environment, Ann Arbor, MI., pp. 845-863, 1980.
- F. Meadows, G.A., R.A. Shuchman and J.D. Lyden, Analysis of Remotely Sensed Long-Period Wave Motions, submitted to J. Geophys. Res., 1981.
- G. Schwab, D.J., R.A. Shuchman and P.L. Liu, Wind Wave Directions Determined from Synthetic Aperture Radar Imagery and from a Tower in Lake Michigan, J. Geophys. Res., Vol. 86, pp. 2059-2064, 1981.
- H. Shuchman, R.A., Processing Synthetic Aperture Radar Data of Ocean Waves, Oceanography from Space, ed. by J.F.R. Gower, Plenum Publishing Company, New York, pp. 477-496, 1981.
- I. Shuchman, R.A., Oceanographic Information Obtainable from Synthetic Aperture Radar, presented at the Symposium on Remote Sensing for Oceanography, Amagi, Japan, September 26-28, 1981.
- J. Shuchman, R.A. and G.A. Meadows, Airborne Synthetic Aperture Radar Observations of Surf Zone Conditions, Geophys. Res. Ltrs., Vol. 7, pp. 857-860, 1980.
- K. Shuchman, R.A., A.L. Maffett and A. Klooster, Static Modeling of a SAR Imaged Ocean Scene, IEEE J. Oceanic Eng., Vol. OE-6, pp. 41-49, 1981.
- L. Shuchman, R.A., E.S. Kasischke and G.A. Meadows, Detection of Coastal Zone Environmental Conditions Using Synthetic Aperture Radar, IEEE International Geoscience and Remote Sensing Symposium Digest, pp. 756-767, 1981.

- M. Shuchman, R.A., E.S. Kasischke, J.D. Lyden and G.A. Meadows, The Use of Synthetic Aperture Radar to Measure Ocean Gravity Waves, Paper presented at the National Academy of Sciences Special Conference on Wave Technology, Washington, D.C., March 1981.
- N. Vesecky, J.F., R.H. Stewart, H.M. Assal, R.A. Shuchman, E.S. Kasischke and J.D. Lyden, Gravity Waves, Large-Scale Surface Features and Ships Observed by Seasat During the 1978 JASIN Experiment, submitted to Science, 1981.

HIGH RESOLUTION SPECTRAL ESTIMATION OF SAR OCEAN WAVE IMAGERY

P.L. Jackson*

Geological Sciences Department
The University of Michigan
Ann Arbor, Michigan 48109

and

R.A. Shuchman

Radar and Optics Division
Environmental Research Institute of Michigan
Ann Arbor, Michigan 48107

ABSTRACT

A new two-dimensional spectral estimation procedure, termed semicausal, is applicable to analysis of ocean wave gravity waves. Spectral estimates of both reference functions and actual synthetic aperture radar (SAR) data of ocean waves have been generated using semicausal techniques and compared to Fast Fourier Transform estimates of identical data sets. The semicausal method can successfully generate spectral estimates of truncated data sets and data sets with two closely spaced frequency components. The semicausal estimate is sensitive to the autoregressive order and exhibits spectral splitting in some cases. Its noise sensitivity is similar to that of the Fourier transform.

INTRODUCTION

The wave number and propagation direction of ocean gravity waves are readily computed from digitized imagery by two-dimensional spectral estimation. A commonly used type of wave spectra display, where the distance of peak values from the origin is proportional to the wave number, is shown in Figure 1. Peak values are shown by the contour levels. Propagation direction is along a line between the

*Also an ERIM consultant.

origin and the peak contour values, which are a direct but as yet undetermined function of wave height. Note, there is a 180° ambiguity with respect to direction of wave propagation. In present practice, ocean wave spectral estimates are produced by both digital (FFT) and optical (OFT) two-dimensional Fourier transforms (Shuchman, et al., 1979).

The limited resolution of the Fourier transform, however, impairs its usefulness in discriminating between two waves whose wave numbers are closely spaced, and in spectral estimation using truncated data sets. Since wave refraction produces curved wave fronts, the spectrum of severely truncated sets must be estimated. Truncation approximates a linear wave front, which enables accurate assessment of propagation direction at a specific location. Overcoming the restrictions of Fourier transform resolution would aid in more accurate determination of wave spectra.

Many investigators are involved in overcoming Fourier transform limitations. Since the introduction of autoregressive (AR) techniques by Parzen (1967) and the similar maximum entropy (MEM) by Burg (1967, 1975), contributions have been and are being made to the development of new high resolution spectral estimation. One-dimensional spectral estimation methods have been made more accurate and reliable. Frequency shifts have been reduced, and line-splitting eliminated (Marple, 1980). More two-dimensional high resolution spectral estimation methods are also being introduced (Roucos and Childers, 1980). A recent workshop by the Acoustics, Speech and Signal Processing Society of IEEE (Proceedings of the First ASSP Workshop on Spectral Estimation, 1981) demonstrated the wide extent and rapid development of this field.

To compare the semicausal method (SCM) and the FFT, both were used to obtain spectral estimations of SAR ocean wave imagery, and also of synthesized data for which the frequency components were

accurately known. The high resolution technique was developed by Jain and Ranganath (1979) and termed "semicausal," which we abbreviate to SCM. Jain (1981) also has described the SCM configuration in an image enhancement context. The SCM employs two-dimensional AR and is representative of the new high resolution techniques at this stage of development. The method does exhibit frequency shifts and line splitting. Its sensitivity to noise is illustrated in this paper. As the above publications by Jain and Ranganath are not readily accessible and do not fully describe the derivation, this AR algorithm and its derivation will be described here.

Of approximately 200 experiments on reference functions and approximately 30 on ocean wave data, a selection from those which most clearly compare the FFT with the SCM are presented here. The results of the comparison, which indicate the SCM can improve resolution over the FFT, are shown in the form of contour plots.

ALGORITHM

A two-dimensional AR scheme is employed in which the selection of data samples to form the AR order is "semicausal." This term refers to the two-dimensional treatment as an initial value problem (causal) in one direction and a boundary value problem (non-causal) in the perpendicular direction.

The algorithm can be developed as follows: We wish to find an AR sequence in a zero-mean two-dimensional random field U to predict a sample value $\hat{u}_{i,j}$. The mean square error between the actual value $u_{i,j}$ and $\hat{u}_{i,j}$ should be a minimum. The AR sequence will then enable spectral estimation by an all-pole rather than an all-zero model as in the FFT (Ulrych, 1972).

For the AR sequence, data samples are chosen which are interior to a window W as shown in Figure 2. Then,

$$u_{i,j} = \hat{u}_{i,j} + \epsilon_{i,j} \quad (1)$$

where $u_{i,j}$ is the datum, $\hat{u}_{i,j}$ the predicted value, and $\epsilon_{i,j}$ the prediction error.

Substituting for $\hat{u}_{i,j}$, Eq. (1) becomes

$$u_{i,j} = \sum_{m=-p}^p a_{m,0} u_{i-m,j} + \sum_{m=-p}^p \sum_{n=1}^q a_{m,n} u_{i-m,j-n} + \epsilon_{i,j} \quad (2)$$

where the predicted $\hat{u}_{i,j}$ is written as a linear combination of samples within the window. The $a_{m,n}$ can be found from a mean-square-error criterion, which implies the observations are orthogonal to the error.

For any k, ℓ within the window, Eq. (1) can be multiplied by $u_{i-k,j-\ell}$ and expected values taken:

$$\begin{aligned} E(u_{i,j} u_{i-k,j-\ell}) &= \sum_{\substack{m=-p \\ m \neq 0}}^p a_{m,0} E(u_{i-m,j} u_{i-k,j-\ell}) \\ &+ \sum_{n=-p}^p \sum_{n=1}^q a_{m,n} E(u_{i-m,j-n} u_{i-k,j-\ell}) \\ &+ E(\epsilon_{i,j} u_{i-k,j-\ell}) \end{aligned} \quad (3)$$

If the data are stationary, Eq. (2) becomes

$$\gamma(k, \ell) = \sum_{\substack{m=-p \\ m \neq 0}}^p a_{m,0} \gamma(k-m, \ell) + \sum_{m=-p}^p \sum_{n=1}^q a_{m,n} \gamma(k-m, \ell-n) + 0, \quad (4)$$

since $E(\epsilon_{i,j} u_{i-k,j-\ell}) = 0$ by orthogonality. $\gamma(k, \ell)$ is the two-dimensional autocovariance function.

At $k = \ell = 0$, Eq. (4) becomes

$$\gamma(0,0) = \sum_{\substack{m=-p \\ m \neq 0}}^p a_{m,0} \gamma(-m,0) + \sum_{m=-p}^p \sum_{n=1}^q a_{m,n} \gamma(-m,-n) + E(\epsilon_{i,j} u_{i,j}), \quad (5)$$

where

$$E(\epsilon_{i,j} u_{i,j}) = E(\epsilon_{i,j} [\hat{u}_{i,j} + \epsilon_{i,j}]) = E(\epsilon_{i,j}^2), \quad (6)$$

as $E(\hat{u}_{i,j} \epsilon_{i,j}) = 0$ by the orthogonality principle. By definition,

$$E(\epsilon_{i,j}^2) = \beta^2, \quad (7)$$

is the variance of the prediction error.

Combining Eq. (4), (5), (6), and (7),

$$\gamma(k,\ell) - \sum_{\substack{m=-p \\ m \neq 0}}^p a_{m,0} \gamma(k-m,\ell) - \sum_{m=-p}^p \sum_{n=1}^q a_{m,n} \gamma(k-m,\ell-n) = \beta^2 \delta_{k,0} \delta_{\ell,0} \quad (8)$$

where $\delta_{k,0} \equiv 1$ when $k = 0$ and $\delta_{k,0} \equiv 0$ otherwise, $\delta_{\ell,0} \equiv 1$ when $\ell = 0$ and $\delta_{\ell,0} \equiv 0$ otherwise, so that $\beta \equiv 0$ except at $k = \ell = 0$.

If $a_{0,0}$ is brought within the window and set equal to -1, effectively subtracting the actual value $u_{i,j}$ from the predicted value $\hat{u}_{i,j}$, then

$$\sum_{m=-p}^p \sum_{n=0}^q a_{m,n} \delta(k-m,\ell-n) = -\beta^2 \delta_{k,0} \delta_{\ell,0} \quad (9)$$

where it is clear that β^2 is the error in prediction of $u_{i,j}$.

In matrix notation, Eq. (9) can be written as

$$\underline{R} \underline{a} = -\beta^2 \underline{1} \quad (10)$$

where \underline{a} and \underline{l} are column matrices of $(2p + 1)(q + 1)$ elements each, which is the number of elements within the window W plus one. \underline{a} is the AR sequence of coefficients. \underline{l} is a string of zeros except for the $(pq + p + 1)$ entry, which is unity, and represents $\delta_{k,0}\delta_{l,0}$ of Eq. (9). R is a block Toeplitz matrix of $[(2p + 1)(q + 1)]^2$ elements.

Equation (10) can be restated as

$$\underline{a} = -\beta^2 R^{-1} \underline{l} \quad (11)$$

Since $a_{0,0} = -1$

$$-1 = -\beta^2 [R^{-1}]_{(pq+p+1, pq+p+1)},$$

or

$$\beta^2 = 1/[pq+p+1, pq+p+1 \text{ element of } R^{-1}], \quad (12)$$

and

$$\underline{a} = -\beta^2 [(pq+p+1) \text{ column of } R^{-1}] \quad (13)$$

Since the column vector \underline{a} represents the least-mean-squares estimate of the AR coefficients, we have the samples to make an AR all-pole spectral estimation.

The algorithm to find the two-dimensional AR coefficients is straightforward except for some detailed bookkeeping to select the correct elements of the matrix R :

1. Obtain the covariance (autocorrelation) through the FFT.
2. Form the block Toeplitz matrix R from the $(2p+1)(q+1)$ elements of the window W on the autocovariance function. $s(0,0)$ is located in an analogous position to $u_{i,j}$ in Figure 2.
3. Invert the matrix R to obtain R^{-1} .

4. Select elements from R^{-1} which represent $-\beta^2$ and \underline{a} .
5. With $-\beta^2$ and \underline{a} , compute the power spectra estimation by the 2-D analog of the one-dimensional AR method (Ulrych, 1972).

$$S(k, \ell) = \frac{\beta^2 \sum_{m=-p}^p a_{m,0} \exp(-irmk)}{\sum_{m=-p}^p \sum_{n=0}^q a_{m,n} \exp(-ir[mk+n\ell])^2} \quad (14)$$

where $S(k, \ell)$ is the 2-D power spectrum, $i = \sqrt{-1}$, and $r = 2\pi/s$ where s is the number of samples in one period.

WAVE ANALYSIS BY SPECTRAL ESTIMATION

Background

A two-dimensional spectral estimation of SAR images of ocean waves shows the direction and wavelength of the waves. However, when waves are refracted, a range of directions is estimated if the image includes many wavelengths. A directional smearing in the spectral estimation prevents the assignment of a wave direction to a specific location. Since the amount of wave refraction reveals water depth, it is desirable to specify wave directions at specific locations. These specifications require spectral estimations of data sets truncated to a wavelength or less. As the main lobe of the FFT is inversely proportional to the size of the data sample, the lobe becomes large when data is severely truncated, and resolution is thereby degraded. Discrimination between two similar waves is also degraded because of the merging of FFT main lobes produced by each wave train.

Recent spectral estimation developments have concentrated on reducing the main lobe to improve resolution, and to reduce sidelobes. Historically, improved resolution has come with limitations:

spectral splitting, and frequency shifts. As noted above, limitations have been addressed and improvements made in the one-dimensional case (Marple, 1980). Spectral estimation by the SCM produces much narrower main lobes than the FFT, but shares in the above limitations.

Spectral Estimation of Wave Data

Spectral estimates of SAR ocean wave data from the 1975 Marineland Experiment (Shemdin, et al., 1978) and from the SEASAT JASIN Experiment (Allan and Guymer, 1980) were produced by both the FFT and the SCM. An example of Marineland imagery is shown in Figure 3. The spectral estimates are shown in Figures 4 and 5, where the wave number k is $2\pi/\lambda$ and λ is the ocean wavelength.

The vertical axis on the spectra in Figures 4 and 5 corresponds to the range dimension on the radar image while the horizontal axis is in the direction of the SAR platform motion. The angles of the frequency components with respect to the origin (at the center) indicate, with 180° ambiguity, the direction of ocean wave propagation.

In the 1975 Marineland Experiment, ocean waves were imaged with a SAR X-band (3 cm radar wavelength) aircraft system. A pitch and roll buoy operating at the time of data collection indicated a wave train identified as a swell (8 second period or 80 m wavelength, $k = 0.08$) was traveling in the approximate direction of 270° with respect to true north. The significant wave height ($H_{1/3}$) was 1.5 - 1.8 m. A complete comparison between the pitch and roll spectra and SAR derived spectra (utilizing FFT techniques) is given by McLeish, et al., (1980).

L-band (23.5 cm wavelength) SAR satellite data from SEASAT was collected during the JASIN Experiment (Allan and Guymer, 1980). A pitch and roll buoy was also operating during the JASIN SAR data collection (SEASAT Revolution 1049) and a wave train identified as swell (12.5 sec period or 244 m wavelength) was traveling in the approximate direction of 264° with respect to true north. The

significant wave height ($H_{1/3}$) for the JASIN case was approximately 5.0 meters. SEASAT SAR data have a resolution of approximately 25 meters while the aircraft data have a finer resolution of 3 meters.

Figures 4 and 5 indicate the SCM spectrum corresponds closely to the FFT spectrum and to data gathered at the ocean surface. Note that the ocean surface measurements of the gravity wave field as obtained from pitch and roll buoys are indicated on Figures 4 and 5 as crosses. Figure 4 illustrates the FFT and SCM spectrum for a short truncation (1.5 cycles) of ocean wave data. The SCM spectrum has definite peaks closely approximating the ocean surface measurements, and has no peak at the origin. The corresponding FFT has a peak at the origin, two lower peaks (one of which corresponds to ocean surface measurements), and has a more diffuse pattern.

In Figure 5, the spectral estimation of a comparatively large region of SAR ocean data shows different results with the two methods; the FFT appearing mottled. These data from SEASAT SAR represent 10 wave cycles. In the FFT, much energy goes into zero frequency, even when the bias has been removed from the data. A similar mottled appearance throughout the FFT frequency plane has been found in the approximately 50 FFT spectra of SAR ocean wave imagery which we have processed. It is necessary to look for clustering of small peaks to establish the dominant wave in the FFT. The pitch and roll data indicated only the major frequency component shown in the SCM spectrum.

Spectral Estimation of Synthetic Data

To evaluate the comparative attributes of SCM and FFT, synthetic data were also generated and spectrally estimated. Comparative spectral estimation of data characterized by short truncation, narrowly separated components, and various signal-to-noise ratios are shown in the power spectra of Figures 6 and 7. The synthetic data are sine waves generated with initial shifts of $\pi/4$.

Figure 6 illustrates the comparative resolution of a single sine wave of less than 1 cycle with 10 dB SNR. Note the widths of the main lobes of the SCM are significantly smaller than those of the FFT.

In Figure 7, two closely spaced frequency components are separated in the SCM spectrum but merged in the FFT. One component is 1.43 cycles, the other 2 cycles long. The ratio of the frequencies is 1.4, which is closely approximated by the SCM spectrum.

One of the limitations of the new high resolution spectral estimation is occasional spectral splitting, where two peaks are formed for one frequency component. An example is shown in Figure 8. As spectral splitting has recently been eliminated in one-dimensional spectral estimation, probably a similar advance in two-dimensional spectral estimation can be expected.

Noise Effects

Experiments on severely truncated synthetic data show the main lobes of the SCM estimation significantly smaller than those of the FFT under additive noise conditions. Both fail to discriminate the synthesized frequency at and below a signal-to-noise ratio (SNR) of about -5 dB. The synthetic data were generated with sample intervals of 1/8 of a period. A total of 6 samples were used, giving a data length of 5/8 of a period. Initial phase was $\pi/4$. For these synthetic data, Figure 9 compares the -3 dB levels of main lobes of spectrum estimations for both the SCM and FFT at four SNR levels.

The FFT is sensitive to phase (Jackson, 1967; Marple, 1976), and the SCM was also found to be sensitive to phase, similar to the one-dimensional maximum entropy method (Chen and Stegen, 1974). In addition, noise individuality can cause moderate differences in the spectral estimation between two or more estimations at identical SNR levels, as is well known. The effects of phase, noise variations and AR orders, which are beyond the scope of this paper, remain

within a reasonable range and do not substantially alter the results illustrated in Figure 9. The AR orders used for the illustrated spectral estimations were $p = 4$ $q = 2$ (see Figure 2).

SUMMARY

Examples of spectral estimation of SAR ocean imagery show that a new high resolution autoregression method can be used to obtain the wavelength and propagation direction of ocean gravity waves. The algorithm is termed the "semicausal method" (SCM). More pronounced spectral peaks, less mottling, and less energy at zero frequency were found with this method than with the commonly used FFT.

Synthetic data were generated to compare the SCM with the FFT. With a truncation of less than a single wavelength, the new method produces a main lobe significantly smaller than the width of the FFT main lobes. Also, two closely spaced sine wave components were discriminated where the FFT failed to discriminate.

Noise sensitivity was demonstrated by the comparative sizes of main lobes under different SNR conditions. For severe data truncations, the SCM main lobe continue to be smaller than that of the FFT for SNR conditions down to approximately -5 dB. Below -5 dB, both the FFT and the SCM fail to produce valid spectrums under conditons of severe data truncations.

High resolution frequency analysis using autoregression, moving-averages, maximum entropy and other concepts is a swiftly developing field in which many investigators are offering insights and improvements. The algorithm described and demonstrated here is representative of new techniques in this field. These techniques were developed to achieve high resolution and accuracy, and improvements in accuracy are being made. The SCM algorithm shows two limitations at this stage of development: spectral splitting and frequency shifts. These are well-known limitations in one-dimensional AR estimations and are being reduced or eliminated with new algorithms.

For short data truncations and for discriminating two similar wave trains, this algorithm can be an aid in specifying the wavelength and direction of ocean waves from airborne or satellite imagery.

ACKNOWLEDGEMENTS

This analysis was supported by Code 480 of the Office of Naval Research (ONR). The contract number was N00014-76-C-1048. The technical monitor for the ONR contract was Mr. Hans Dolezalek. The authors appreciate the assistance, comments, and suggestions of James Lyden of ERIM in preparing this paper.

REFERENCES

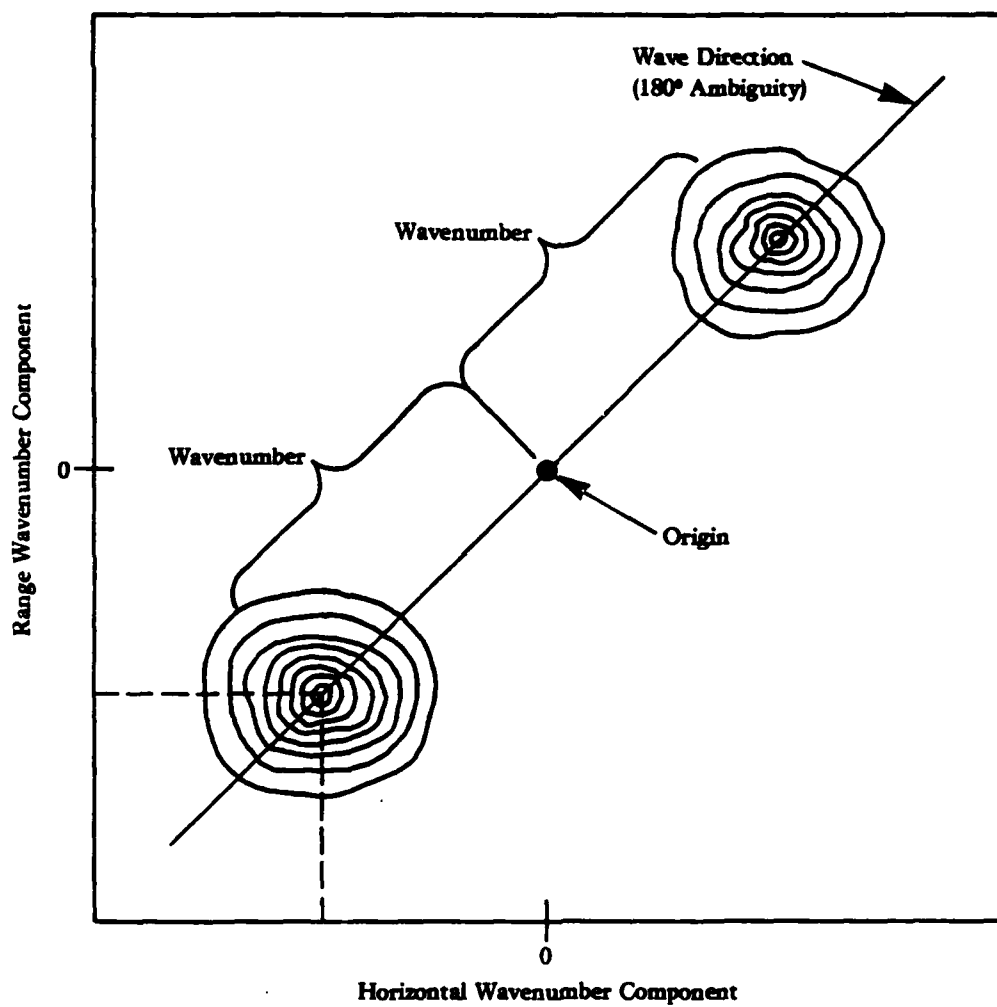
- Allan, T.D. and T.H. Guymer, Seasat and JASIN, Int. J. Remote Sensing, 1, pp. 261-267, 1980.
- Burg, J.P., Maximum entropy spectral analysis, paper presented at the 37th Annual International Meeting, Society of Exploration Geophysicists, Oklahoma City, Oklahoma, 1967.
- Burg, J.P., Maximum entropy spectral analysis, Ph.D Thesis, Stanford University, Xerox Microfilms No. 75-25-499, Ann Arbor, MI, 1975.
- Chen, W.Y. and G.R. Stegen, Experiments with maximum entropy power spectra of sinusoids, J. Geophys. Res., 79, pp. 3019-3022, 1974.
- Jackson, P.L., Truncations and phase relationships of sinusoids, J. Geophys. Res., 72, pp. 1400-1403, 1967.
- Jain, A.K., Advances in mathematical models for image processing, Proc. of the IEEE, 69, pp. 502-529, 1981.
- Jain, A.K. and S. Ranganath, Two-dimensional spectral estimation, Proc. of the RADC Spectrum Estimation Workshop, May 1978.
- Marple, L., Conventional Fourier, autoregressive, and special ARMA methods of spectrum analysis, Degree of Engineering Thesis, Stanford University, 1976.
- Marple, L., A new autoregressive spectrum analysis algorithm, IEEE Trans. on Acoustics, Speech, and Signal Processing, ASSP-28, pp. 441-454, 1980.
- McLeish, W., D. Ross, R.A. Shuchman, P.G. Teleki, S.V. Hsiao, O.H. Shemdin, and W.E. Brown, Synthetic aperture radar imaging of ocean waves: comparison with wave measurements, J. Geophys. Res., 85, pp. 5003-5011, 1980.
- Parzen, E., Statistical spectral analysis (single channel case) in 1968, Department of Statistics, Technical Report No. 11, Stanford University, Stanford, California, 1968.
- Roucos, S.E. and D.G. Childers, A two-dimensional maximum entropy spectral estimator, IEEE Trans. on Information Theory, IT-26, pp. 554-560, 1980.
- Shemdin, O.H., W.E. Brown, F.G. Staudhammer, R. Shuchman, R. Rawson, J. Zelenka, D.B. Ross, W. McLeish, and R.A. Berles, Comparison of in-situ and remotely sensed ocean waves off Marineland, Florida, Boundary-Layer Meteorology, 13, pp. 193-202, 1978.
- Shuchman, R.A., E.S. Kasischke, A. Klooster, and P.L. Jackson, SEASAT SAR coastal ocean wave analysis - a wave refraction and diffraction study, ERIM Final Report to NOAA, Report No. 138600-2-F, November 1979.
- Ulrych, T.J., Maximum entropy power spectrum of truncated sinusoids, J. Geophys. Res., 82, p. 1051, 1972.

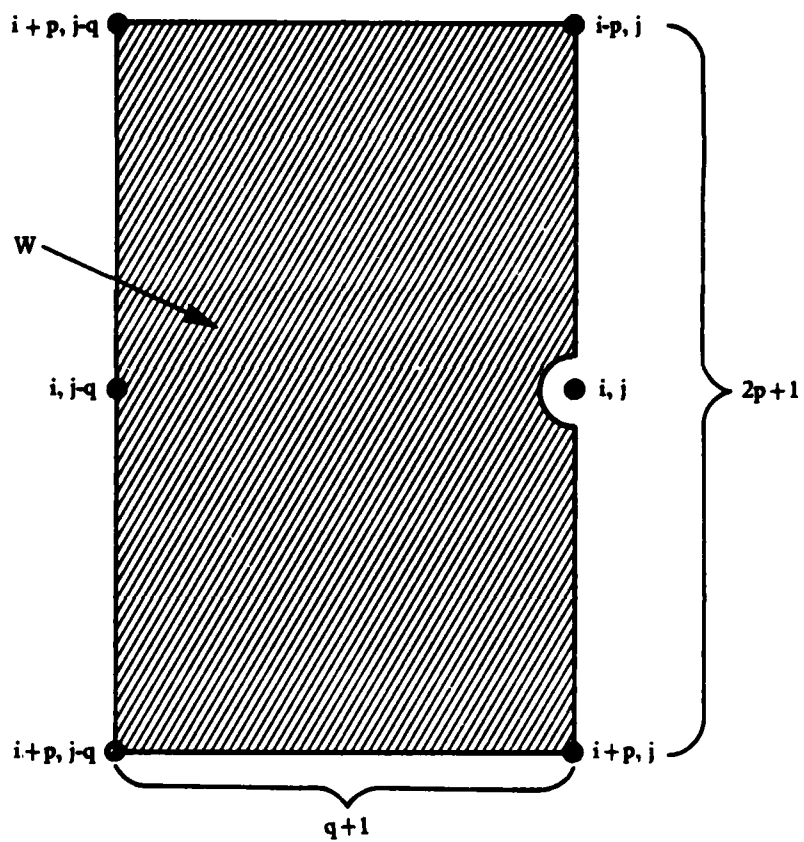
TABLE 1

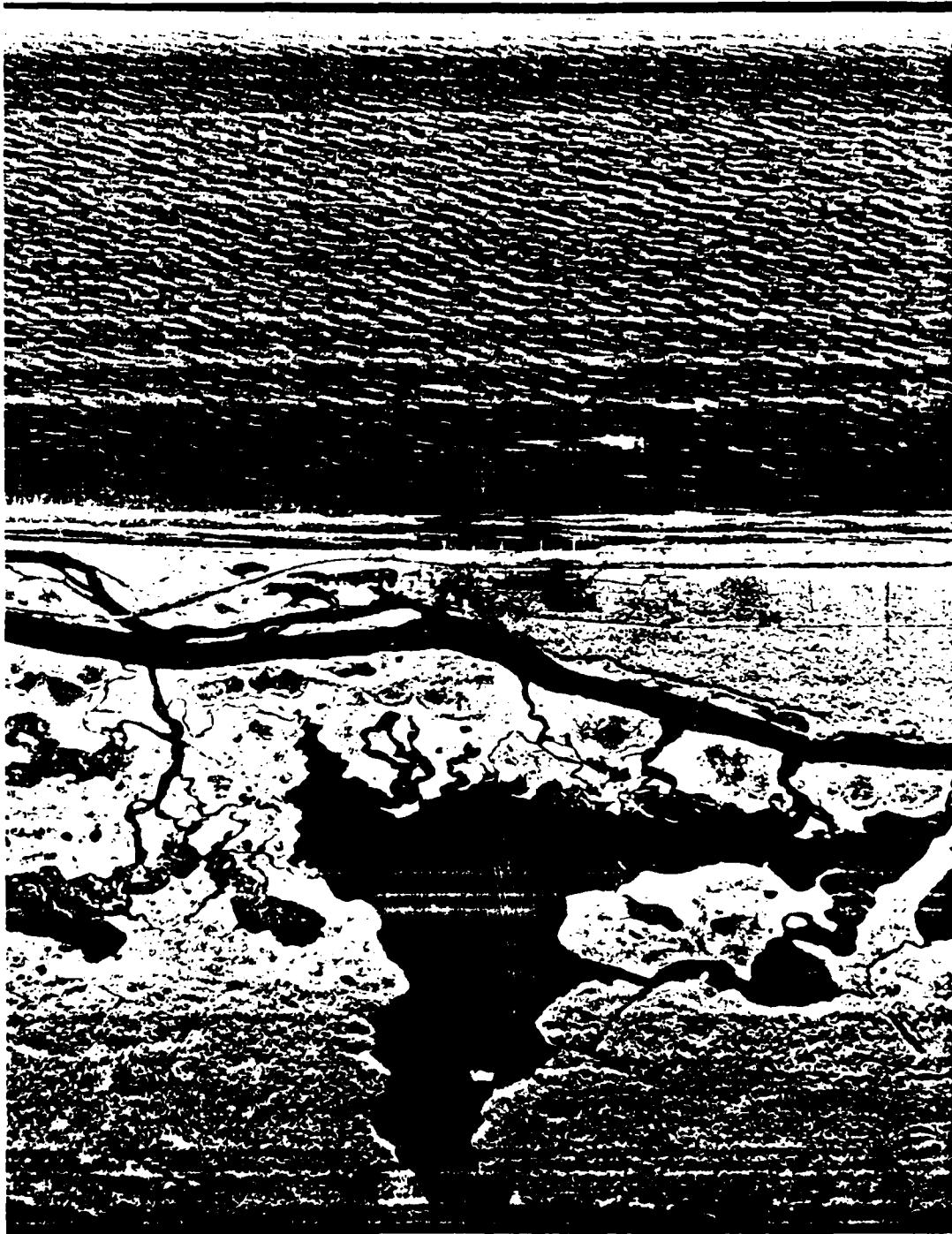
		<u>Wave Number</u>	<u>Wave Direction</u>
Marineland Experiment	SCM Pitch and Roll Buoy	0.15	266° (86°)
SEASAT	SCM	0.08	270°
JASIN	Pitch and	0.026	262° (80°)
	Roll Buoy	0.026	264°

FIGURES LIST

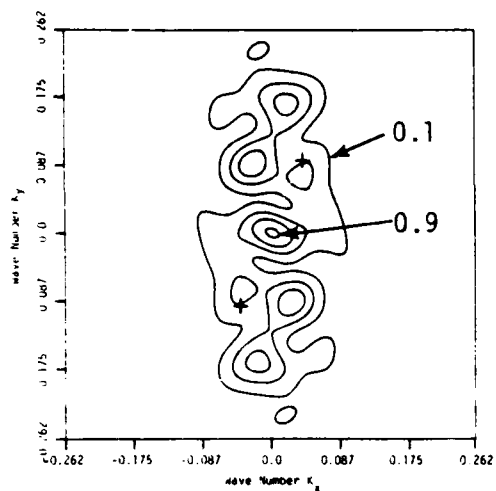
1. Two-dimensional spectral estimation of ocean waves
2. Window of two-dimensional field U , used to predict a sample value $\hat{U}_{i,j}$ based on interior samples
3. Radar image from Marineland experiment (X-band, 3 cm)
4. Two-dimensional spectral estimates of Marineland SAR data (X-band, 3 cm)
5. Two-dimensional spectral estimates of SEASAT SAR data (L-band, 23.5 cm)
6. Spectral estimations of reference function with single frequency truncated to 2/3 of one cycle
7. Spectral estimations of reference function with two closely spaced frequency components
8. Example of SCM spectral splitting with single frequency reference function.
9. Spectral estimations of reference function truncated to 5/8 of one cycle with various SNR levels



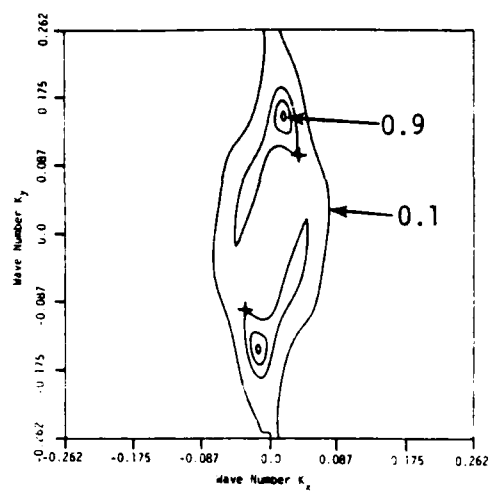




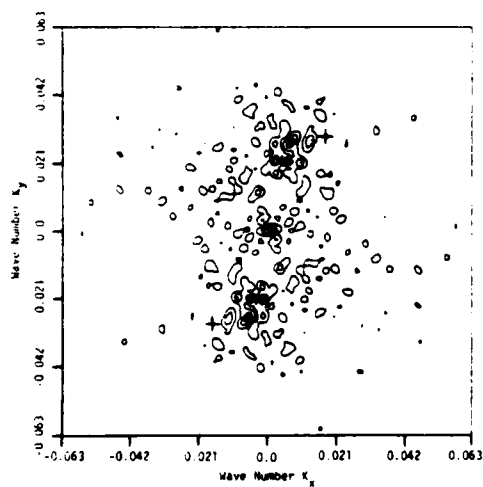
FFT 10X10



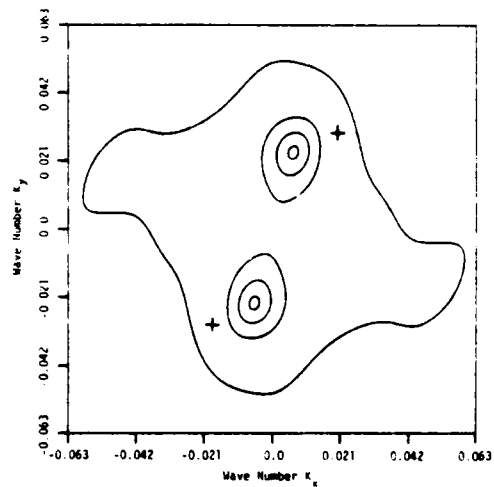
SC SPECTRUM 10X10

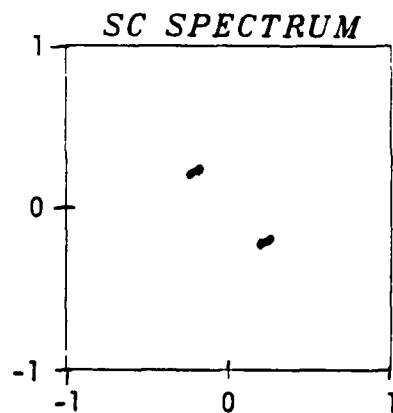
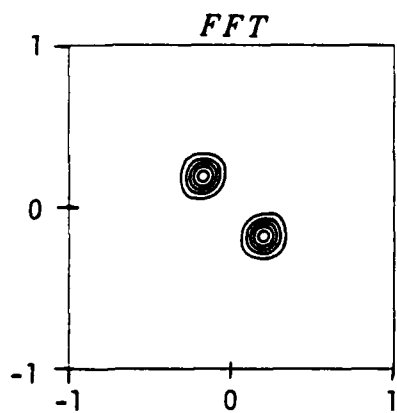
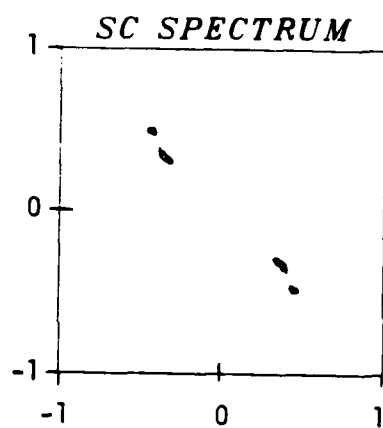
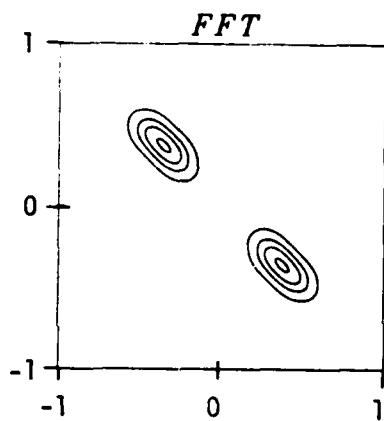
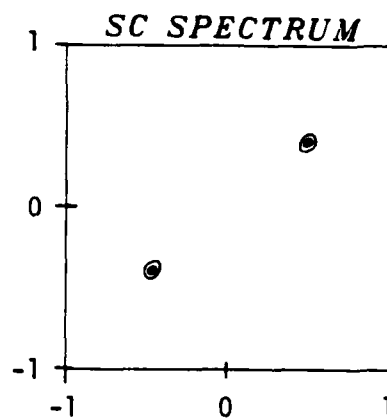
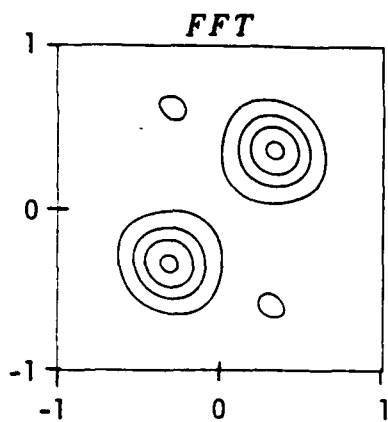


FFT 50X50

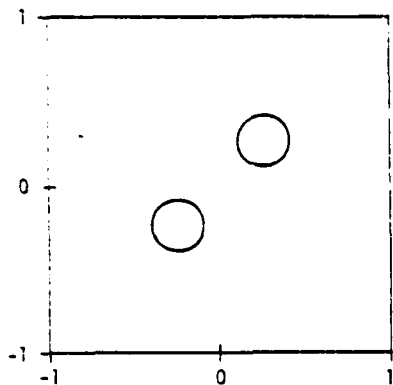


SC SPECTRUM 50X50

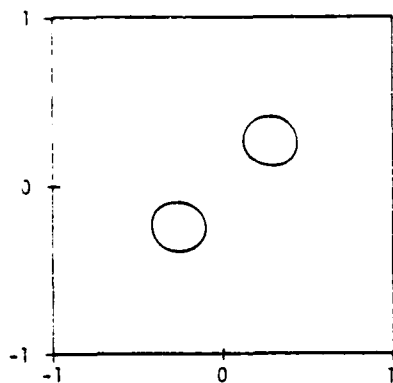




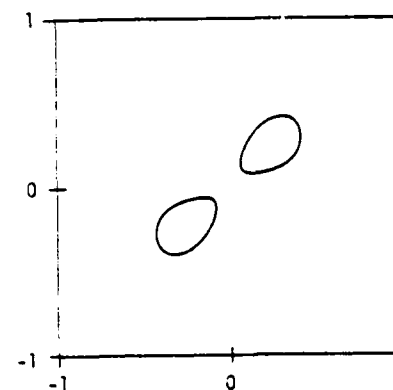
FFT



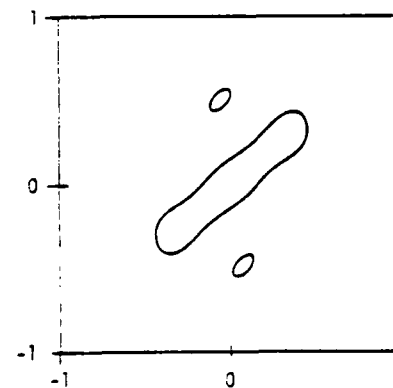
SNR = 12 dB



SNR = 0 dB

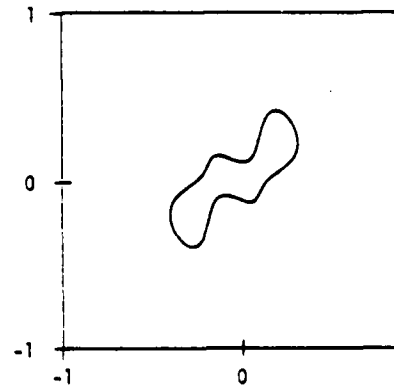
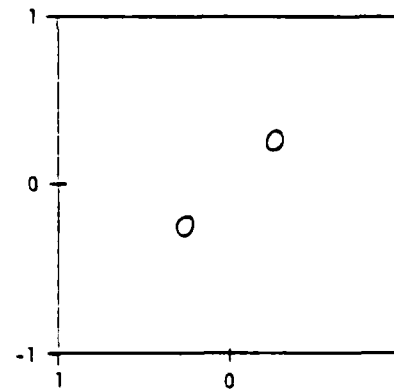
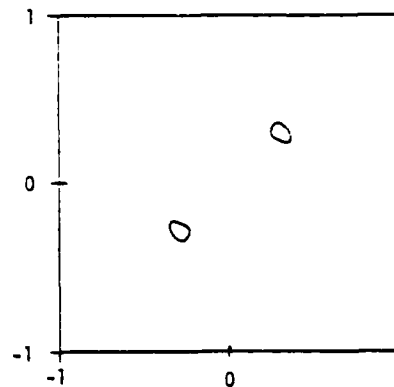
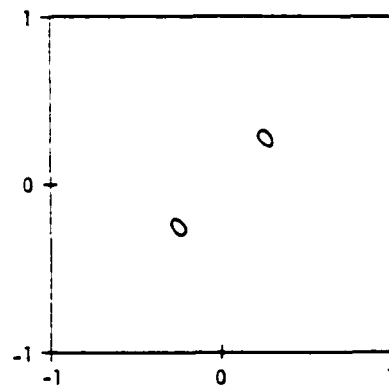


SNR = -3 dB



SNR = -6 dB

SC



THE USE OF WAVE CONTRAST MEASUREMENTS IN THE
EVALUATION OF SAR/GRAVITY MODELS*

E.S. Kasischke and R.A. Shuchman

Radar and Optics Division
Environmental Research Institute of Michigan
Ann Arbor, Michigan 48107

ABSTRACT

A new method to measure the detectability of gravity waves imaged by a synthetic aperture radar (SAR) has been developed. This new method is called a peak-to-background ratio (PBR). The PBR was used in studying two different SAR data sets. X- and L-band aircraft SAR data collected over a Lake Michigan test site were used to study the effects of changing SAR processing parameters (telerotation adjustments and integration time) on wave visibility. A second data set was collected by the Seasat L-band SAR over the JASIN test array and was used to correlate PBRs to various wind and wave parameters. Results of this study indicate the peak-to-background ratio is an effective means to correlate SAR/oceanography theory with actual SAR data sets.

1. INTRODUCTION

Synthetic aperture radar (SAR) is an active imaging device that senses the environment with short electromagnetic waves. As active sensors, radars provide their own illumination in the microwave region of the electromagnetic spectrum and thus are not affected by temporal changes in emitted or reflected radiation from the earth's surface. Additionally, SARs have the recognized advantages of being able to image the earth's surface independent of weather conditions and also, to provide synoptic views of the ocean at high resolution. The resolution of aircraft SARs are typically on the order of a few meters while the Seasat satellite SAR had a resolution of approximately 25 meters. Most radars operate in the frequency region of 300 MHz (1 m) to 30 GHz (1 cm), and bandwidths within this region are commonly designated by letters. SARs discussed in this paper are designated as L-band (23.5 cm) or X-band (3.2 cm).

Additionally, synthetic aperture radar is a coherent airborne or space-borne radar that uses the motion of a moderately broad physical antenna beam to synthesize a very narrow beam thus providing fine azimuthal (along-track) resolution (Brown and Porcello, 1969; Harger, 1970). Fine range (cross-track) resolution is achieved by transmitting either very short pulses or longer coded pulses which are compressed by matched-filtering techniques into equivalent short pulses.

During the past decade, much research has centered on the use of SARs to monitor the earth's oceans. Among the oceanographic features which can be

*Presented at the Fifteenth International Symposium on Remote Sensing of Environment, Ann Arbor, MI, May 1981.

sensed by a SAR are ocean gravity waves, surface currents and fronts, surf zone conditions, sea ice, and surface wind speed and direction (for a review, see Shuchman, et al., 1981). This paper will center on using SARs to image ocean gravity waves.

Several recent experiments have been designed specifically to test SAR's ability to image ocean gravity waves. These include the Marineland Experiment (Shemdin, 1980), the West Coast Experiment (Shemdin, 1980a), the Lake Michigan Experiment (Schwab, et al., 1981; Shuchman and Meadows, 1980), the MARSEN Experiment (Anonymous, 1979), the Gulf of Alaska Seasat Experiment (Gonzalez, et al., 1979; 1981), the East Coast Experiment (Beal, 1980), and the Joint Air/Sea Interaction Experiment (Allan and Guymer, 1980). The general consensus of all these studies is that accurate estimates of dominant wavelength and wave direction can be obtained from SAR images of gravity waves.

It was recognized during the early phases of SAR/oceanographic research that certain conditions exist under which a SAR will not produce high quality images of gravity waves. Much research has centered on developing theories which explain why a SAR does or does not see ocean gravity waves. Relatively little research has been conducted on testing these theories. The primary reason for not evaluating these mathematical models on SAR images of gravity waves in the past has been twofold. First, there was a lack of well documented (sea-truthed) SAR data sets; and second, an efficient method to quantify the concept of wave detectability on SAR imagery was not developed. Thus, the purpose of this paper is to describe a technique where wave contrast on SAR imagery can be quantified and to illustrate how this measurement can be used in SAR models of ocean gravity waves.

2. SAR MODELS ON IMAGING OCEAN GRAVITY WAVES

In developing a model which defines the conditions under which a SAR will image gravity waves, it is first necessary to identify and describe the elements responsible for the microwave backscatter from the ocean's surface (i.e., their shape, orientation, etc.). It is then necessary to describe the manner in which gravity waves alter these scattering elements causing gravity waves to appear on SAR imagery as a series of light and dark bands. Additionally, SAR data are normally processed assuming the targets being imaged are stationary. Because the SAR signal histories are a result of Doppler frequency changes caused by the SAR platform, any movement of the target will result in a shift of its signal histories and the image of that target will be displaced and defocused. Any model which describes SAR imaging of gravity waves must account for the effects of moving targets or scatterers.

The study of interactions between microwave energy and the ocean's surface has generally been treated in two ways: static modeling, which assumes no target motion; and dynamic modeling, which includes the above mentioned Doppler effects (Brown, et al., 1976; Shuchman, et al., 1978). Three basic static models have been proposed: the facet or tangent plane model, the Rayleigh scattering model and the Bragg-Rice-Phillips model.

The facet or tangent plane model (Brown, et al., 1976) is based upon the reflection of electromagnetic energy from areas whose slopes are oriented perpendicular to the line of sight of the radar. This model assumes that the radius of curvature of these reflectors is nearly everywhere larger than the wavelength and that shadowing and multiscattering effects are negligible. This model predicts that radar backscatter is largest for small surface angles.

The Rayleigh scattering model theorizes that the radar backscatter from the sea is composed of many fluctuating individual scatterers (Skolnik, 1970). These scatterers are said to be represented by segments of spheres or complex spheres which are small relative to the radar wavelength. According to this

model, radar backscatter is relatively insensitive to look direction because it is assumed that the scatterers are moving randomly and isotropically.

The Bragg-Rice-Phillips model (as described by Shuchman, et al., 1978; see also Wright, 1966) states that the ocean surface is composed of a combination of periodic surfaces, and the dominant radar backscatter will match some portion of the ocean spectra. This model assumes the heights of the elements producing the radar backscatter are small relative to the radar wavelength and that they are isotropically distributed. According to Wright (1966), the maximum radar return occurs when:

$$K_w = 2K_L \sin \theta \quad (1)$$

where $K_w = 2\pi/\lambda$ (λ is the wavelength of the capillary or ultra-gravity wave),
 $K_L = 2\pi/L$ (L is the wavelength of the radar), and
 θ = the incidence angle of the radar beam.

For the radar wavelengths and incidence angles of typical SARs, the Bragg wave number (K_w) corresponds to the short capillary and ultra-gravity waves present on the ocean's surface.

Shuchman, et al. (1978) evaluated the ability of the facet model and the Bragg-Rice-Phillips model to explain radar backscatter from a large surface area of the ocean and concluded that the Bragg-Rice-Phillips model best explained the large area backscatter from the sea indicating that the scatterers responsible for microwave backscatter from the sea's surface are the capillary and ultra-gravity waves.

Once the structures responsible for radar backscatter from the ocean's surface are identified, it is necessary to define how these scatterers are altered so that gravity waves are imaged by a SAR. There are several theories regarding the processes responsible for changing the small scale capillary and ultra-gravity waves. One states that the sea-surface tilt caused by the long waves produces variations in the local incidence angle, resulting in a change or modulation of the cross section of the smaller waves (Elachi and Brown, 1977). The effect of this "tilt modulation" is at a maximum for range waves and at a minimum for azimuth waves. Another theory holds that the shorter capillary and ultra-gravity waves are being modulated by the longer gravity waves, causing an increase in the wave height and number of the capillary waves in the crest region of the waves and a decrease in the capillary wave height and number in the trough of the waves (Phillips, 1981). Finally, a third theory proposes that the capillary and ultra-gravity wave structure of the waves are changed due to wind stress (Evans and Shemdin, 1980).

In order to produce a comprehensive SAR-gravity wave theory, the above static models need to be incorporated with dynamic models that account for shifts in Doppler frequencies. The initial work studying the relationships between moving targets and the synthetic aperture radar imaging mechanism responsible for imaging them was performed by Raney (1971). SARs are sensitive to both the azimuth and range velocity components of moving targets. A target with a non-constant velocity being imaged by the SAR will result in a degraded image of that target. This image degradation can be partially corrected during optical processing of the SAR signal histories by making adjustments in the optical processor (Shuchman and Zelenka, 1978; Shuchman, et al., 1978a). Shuchman and Zelenka (1978) produced equations to calculate compensations to use during processing of the signal histories for the range and azimuth velocity components present in gravity waves. These velocity adjustments are directly proportional to the velocity of the target and indirectly proportional to the velocity of the SAR platform.

The problem of computing the corrections to compensate for wave movement is not easily solved because of the physical characteristics of the waves being imaged. Ocean waves have three distinct velocity components: orbital, group and phase. Therefore, it may be necessary to calculate at least three distinct focus corrections for a given wave image. This allows an additional question to be explored in an analysis of wave velocities on SAR imagery: does the image enhancement correction selected correspond most closely to the orbital, group or phase velocity component of the imaged wave?

This last point was examined by Kasischke, et al. (1979) in a study using data collected during the Marineland experiment. Not only did they confirm that higher contrast wave imagery was obtained using image enhancement corrections during optical processing, but they also concluded that the corrections which produced the best SAR wave imagery were proportional to the phase velocity of the waves.

Recent works (Swift and Wilson, 1979; Alpers and Rufenach, 1979) have suggested that the SAR imaging mechanism should also be sensitive to the orbital velocity of the waves (which is an order of magnitude lower than the phase velocity) when a SAR is imaging azimuth traveling waves. The basic premise behind this work is a concept called "velocity bunching" of the small capillary and ultra-gravity waves. In this theory, the small waves are bunched due to the orbital velocities of the gravity waves and the SAR image will detect a strong line of return because of this bunching. The theory also notes that this strong line of return has been shifted and defocused an amount proportional to the orbital velocity of the gravity wave. This theory has yet to be tested on actual SAR data. An interesting prediction of this theory is that under certain conditions, two bunching lines will occur for each wave (Swift and Wilson, 1979); therefore, the SAR should produce a wave image which has half the period of the actual gravity wave. No such SAR image has been reported to date.

The point has been reached where many models exist which attempt to explain how a SAR images gravity waves, as is evidenced by the above discussion. The time has come to evaluate the various models and, at the same time, determine under what conditions a SAR will and will not image gravity waves. There are numerous SAR data sets which include gravity waves and the present need is to link this data with the models.

3. PEAK-TO-BACKGROUND RATIO MEASUREMENTS

In order to be able to properly evaluate the various SAR/gravity wave models on actual SAR imagery, it is first necessary to derive a method to evaluate the visibility of wave fields on the SAR images. Using this visibility criterion, it is then necessary to compare various sets of SAR imagery against what we would expect to see under the environmental conditions at the time of the SAR data collection.

The concept of determining the degree of wave detectability on SAR imagery first arose when studying the effects of focusing algorithms on SAR data collected at Marineland. During this study, wave crest-to-trough contrast was calculated in a time-consuming process which resulted in a measurement called a modulation depth. Modulation depths were obtained by placing a recording photomultiplier in the output plane of the optical processor used to correlate the signal film. By placing a photomultiplier in place of an imaging film, a wave modulation scan resulted with the waves themselves modulating the scan. The scan in Figure 1 was obtained by scanning in the direction of wave propagation with an aperture slit corresponding to 500 meters along the crest and 50 meters in the propagation direction. The normalized distance between a maxima (A) and minima (B) on Figure 1 is a modulation depth (for a more in-depth discussion of this topic, see Kasischke, et al., 1979).

A new method of measuring wave contrast was developed during the course of this study, and is referred to as a peak-to-background ratio (PBR). PBRs can be obtained through three separate, but similar techniques. The first technique involves positioning a microscopic optical probe attached to a Gamma Scientific Model 2900 Auto-Photometer in the Fourier transform plane of the Fraunhofer diffraction setup used to generate optical Fourier transforms (OFTs) from SAR gravity wave data observed in the view finder of the probe. The optical probe is used to measure the intensity of the peak of the power spectra of the OFT as it appears in the transform plane. Next, the optical probe is rotated to a point 90° from the peak position, and a second reading is taken as a background measurement. The ratio of these two readings is referred to as the peak-to-background ratio. This concept is illustrated in Figure 2.

The second technique to obtain a PBR is essentially equivalent to the first. Optical Fourier transform spectra were recorded on Polaroid film negatives. The optical density of these negatives is measured using a MacBeth TD504 densitometer using a one millimeter circular aperture. First, the densitometer is placed over the film image of the peak power spectra and a density reading taken. Next, the film negative is rotated 90°, and a background reading taken. Again, the ratio of these two readings results in a PBR.

A third technique not presented here utilizes data contained in a fast Fourier transform (FFT) of the digitized SAR data. Using software available at ERIM (see Shuchman, et al., 1979), two-dimensional Fourier transforms can be generated. From these two-dimensional transforms, one-dimensional wave number and wave direction SAR energy distributions can be generated, and from these, peak intensities and background readings can be obtained.

4. LAKE MICHIGAN DATA ANALYSIS

On October 6, 1977, at approximately 1130h EST, the Environmental Research Institute of Michigan (ERIM) X- and L-band dual-polarized imaging radar (described by Rawson, et al., 1975) made two passes over Lake Michigan at approximately 43°10' north latitude. During the first pass, the aircraft was heading due west (270°) and during the second pass, due east (90°). Surface measurements at the time of the SAR overflight indicate that the waves had a peak frequency of 0.211 Hz and a peak direction of 300° (Schwab, et al., 1981). From the surface measurements, it can be determined the waves were traveling in a nearly range direction with respect to the radar line-of-sight, as is seen in Figure 3. Comparisons made between SAR estimates of dominant wavelength and direction and sea-truth values were in good agreement (Schwab, et al., 1981).

Two analyses were performed on the Lake Michigan SAR data which involved making adjustments during the optical processing of the signal histories. The first adjustment was a telerotation correction and the second was a change in the integration time.

Studies by Raney (1971) and Shuchman and Zelenka (1978) indicate that a target moving with a radial (line-of-sight) velocity will become defocused when imaged by a SAR if its range velocity is sufficiently large relative to the SAR platform velocity. This motion distortion can be compensated for during optical processing of the raw SAR signal histories by rotating a lens within the processor an amount directly proportional to the line-of-sight velocity of the target and inversely proportional to the velocity of the SAR platform. According to Shuchman and Zelenka (1978):

$$\phi = \frac{V_r P}{V_{AC} Q} \quad (2)$$

where ϕ is the rotation angle for correction,
 V_r is the line-of-sight velocity of the target,
 V_{AC} is the SAR platform velocity, and
 P and Q are SAR processing parameters.

According to this theory, SAR imagery of gravity waves should have the highest contrast when the correction in Eq. (2) is used during processing of the SAR signal histories. Previous studies by Kasischke, et al. (1979) showed that higher wave detectability (as indicated by modulation depths) were obtained from SAR data collected at the Marineland Experiment (when the waves were range traveling) when a telerotation correction was used which adjusted for the phase speed of the waves. The purpose of the Lake Michigan data was to further examine the effects of telerotation adjustments on the wave contrast obtained from the SAR imagery.

The first step of the analysis was to calculate the theoretical telerotation (ϕ) necessary to correct for the range-phase velocity present in the data collected over Lake Michigan. It should be noted that although ϕ is the same magnitude for each pass, it is in the opposite direction for each because, with respect to the radar line of sight, the waves are traveling towards the SAR during the westbound pass and away from the SAR during the eastbound pass (i.e., ϕ for the westbound pass would equal $-\phi$ on the eastbound pass). The reader should also note that the telerotation adjustment is dependent on the SAR wavelength.

SAR data were processed for the October 6 Lake Michigan flight using a variety of different telerotation settings ($-\phi$, $-1/2\phi$, 0 , $1/2\phi$, ϕ , $3/2\phi$ and 2ϕ). Both X_{HH} (X-band, horizontally polarized transmitted and horizontally polarized received) and L_{HH} data were processed. Peak-to-background measurements were taken for each band at each telerotation setting and peak-to-background ratios calculated. These PBRs are summarized in Table 1 and Figure 4. Each PBR is an average of three separate readings.

A statistical analysis of variance (Scheffe, 1959) was performed on each of the four data sets. For the X-band, Pass 3 data, the analysis of variance (ANOVA) indicated that the telerotation proportional to the phase velocity of the gravity waves (ϕ) resulted in the highest wave contrast ($p > 0.99$). For the X-band, Pass 4 data, the statistical ANOVA revealed that the $3/2\phi$ telerotation adjustment resulted in significantly higher wave contrasts ($p > 0.95$).

For both L-band data sets, the ANOVA indicated that there was no significant differences between the wave contrast measurements when either a ϕ or $1/2\phi$ telerotation setting was used, but both of these settings resulted in significantly higher PBRs than the other settings, ($p > 0.99$).

An additional ANOVA revealed that regardless of radar wavelength, the higher wave contrasts were when the SAR was looking at waves propagating towards the plane (Pass 3) than when the SAR was looking downwave (Pass 4).

In addition to the telerotation corrections, a test was run using the Lake Michigan SAR data to evaluate the effects of varying integration time on wave detectability. The integration time of a SAR is defined as the time required to collect the synthetic aperture data. In this case, it is the amount of time the SAR observes the moving waves in order to form their image. If movement of the gravity wave during the integration time is significant, then degraded imagery results.

Integration time (T) can be calculated as:

$$T = \frac{\lambda R}{2V_{AC} \rho_a \cos \theta} \quad (3)$$

where λ is the radar wavelength;
 H is the SAR platform altitude,
 θ is the incident angle,
 V_{AC} is the sensor platform velocity, and
 ρ_a is the azimuth resolution.

From Eq. (3), note that integration time is radar wavelength dependent; to obtain the same resolution in L-band imagery as X-band imagery requires an integration time which is approximately 7-8 times longer.

Table 2 summarizes the integration times needed to achieve a specific azimuth resolution for the Lake Michigan X- and L-band SAR data. From this table, we can see:

1. The integration times for L-band are larger than those for X-band for a given resolution;
2. The far edge portion of the radar swath requires a longer integration time than the near edge portion (because of the greater distance); and
3. The finer the azimuth resolution, the longer the integration time.

SAR data from the westbound pass of the 6 October Lake Michigan data were processed using different integration times to achieve different azimuth resolutions. Peak-to-background ratios were obtained from these data, and are summarized in Table 3 and Figure 5. For both the X- and L-band data, it is clear that as resolution improves, so does the degree of wave contrast on the SAR imagery. A statistical ANOVA on the two data sets indicates the trends present in the data and are significant ($P > 0.99$). There does not appear to be any difference between the wave contrast obtained for the L-band fifteen and thirty feet data. Again, note that the higher PBRs were obtained for the X-band data.

The following conclusions can be drawn from the analysis of the Lake Michigan data:

1. For the X-band SAR data, the highest wave contrast was obtained when a telerotation adjustment proportional to the phase speed or 3/2 the phase speed of the gravity waves was used.
2. For the L-band SAR data, the optimum imagery was obtained when a telerotation adjustment between the phase speed and one-half the phase speed of the gravity waves was made.
3. The X-band data had higher contrast wave imagery than the L-band data.
4. Higher wave contrasts (PBRs) were obtained when the SAR was looking upwave (hence, upwind) than where the SAR was looking downwave (downwind).
5. Higher PRBs were obtained on both X-band and L-band imagery by using longer integration times (i.e., higher resolutions) during processing of the data.

5. JOINT AIR/SEA INTERACTION EXPERIMENT DATA ANALYSIS

Data used in this portion of the study were collected during the Joint Air-Sea Interaction (JASIN) experiment. The JASIN experiment was proposed in 1966 as part of the Global Atmospheric Research Project and was sponsored and organized by the Royal Society of the United Kingdom. The primary aims of

the JASIN experiment were to "observe and distinguish between the physical processes causing mixing in the atmospheric and oceanic boundary layers and relate them to mean properties of the layers; and to examine and quantify aspects of the momentum and heat budgets in the atmospheric and oceanic boundary layers and fluxes across and between them" (Royal Society, 1979). To this end, fifty principal investigators from nine countries collaborated on an intensive experiment from mid-July to mid-September, 1978. Fourteen oceanographic research vessels were on site during this period. The study of gravity waves represented a small portion of the overall JASIN experiment which took place in the North Atlantic, in an area just west of Scotland, as is shown in Figure 6. Most of the gravity wave observations were made within the Oceanographic Intensive Area (OIA) (the large "dashed-line," circle in Figure 6), but ships operating in the large triangular region made gravity wave observations as well. Wave data were obtained from visual observations from these ships, from wave recorders mounted on the ships, from wave buoys deployed by the ships, and from permanently anchored wave rider buoys. The wave rider buoys were anchored within the OIA.

Seasat, launched just prior to the JASIN experiment, offered investigators a unique opportunity to collect satellite data over a well instrumented test site. A Seasat SAR receiving station had been set up at Oakhanger, England for the European Space Agency and radar data were collected on twenty different occasions when Seasat passed over or near the JASIN study area. Eighteen of those passes form the basis for part of the present study (data from the other two passes were of too poor quality to process). The surface measurements collected during the JASIN experiment which are of interest to the present study include wave height ($H_{1/3}$), length and direction, and wind speed and direction. These data allow an examination of what factors might be important in the SAR imaging process of ocean gravity wave through a comparison with the wave contrast measurement.

The portion of the Seasat pass chosen for the peak-to-background measurement was the area closest to the sea-truth observation and not necessarily the area closest to the Oceanographic Intensive Area (OIA) as the ships which deployed the pitch and roll buoys were often outside the OIA. Previous studies (see Kasischke, 1980; Vesecky, et al., 1981) have shown that the estimates of dominant wavelength and direction obtained from the Seasat SAR data agreed quite well with those collected by sea truth sources.

Table 4 summarizes the SAR and sea truth data for the 18 JASIN passes. Table 4 contains the following data in fourteen columns:

1. Pass	SEASAT revolution number
2. Date	Date data collected
3. Time	Time data collected
4. Satellite Heading	
5. STS	Sea truth source
6. Distance between sea truth and SAR. The line of sight distance (in kilometers) between the position of the sea truth source and the position where PBRs were produced.	
7. θ_T	Sea truth wave direction
8. λ	Sea truth wavelength
9. $H_{1/3}$	Significant wave height

- | | |
|---------------------|----------------------------|
| 10. U | Wind speed |
| 11. α_T | Wind direction |
| 12. θ_T -OFT | Wave direction -- from OPT |
| 13. λ -OFT | Wavelength -- from OPT |
| 14. PBR | Peak-to-background ratio |

Several special circumstances in Table 4 should be noted. For Rev. 757, there was no sea-truth wave direction information available. Since Rev. 762 was collected eight hours after Rev. 757, the wave direction for Rev. 762 was used as an estimate for Rev 757. The reliability of the sea-truthed wavelength and wave direction information provided for Rev. 1044 were suspect. Therefore, the corresponding values from Rev. 1049, collected eight hours later, were substituted.

Even with the selection criteria used for sea-truth, we were still left with two sea-truth values for wavelength and wave direction for Rev. 590 (see Table 4). To eliminate one estimate in favor of the other would be biasing the data set. Therefore, whenever these data were used, two separate analyses were conducted.

Peak-to-background ratios for the JASIN data were obtained by measuring the optical density on the film negative produced from the Polaroid picture of the optical Fourier transform. From Table 4, it can be seen that the PBRs for the Seasat data are considerably lower than the PBRs for the Lake Michigan L-band data. This occurs because of the different techniques used to obtain PBRs for the different data sets. By recording the Fourier transform spectra on film, a compression of the data occurs. The density on the film is proportional to the log of the light intensity, i.e., a compression of the data has occurred.

Wave data and sea-truth estimates were processed using standard oceanographic techniques at the Scripps Institute of Oceanography and provided to the authors in summary form. Included in this sea-truth data set were estimates of dominant wavelength and direction, wave height ($H_{1/3}$), and surface wind speed and direction. The ocean wave frequency spectra, $F(\theta, \omega)$ obtained from the buoys and wave recorders were converted to wave number spectra using the Jacobian approximation (g^2/ω^3 , where g is the gravitational acceleration) appropriate to deep water waves (Vesecky, et al., 1981a).

Because several of the test dates had more than one set of sea-truth, it was necessary to decide which value to use for comparison to the OPT value. Available sea-truth was, therefore, ranked according to the desirability of the data source, as follows:

- BEST
1. Atlantis II Pitch and Roll Buoy or Discovery Pitch and Roll Buoy.
 2. Moored OIA Wave Rider Buoy.
 3. John Murray Wave Recorder or Discovery Wave Recorder.
- WORST
4. John Murray Visual Readings.

If no sea-truth data were available using the most desirable category, then the next highest category which contained the desired sea-truth data was used.

From the data in Table 5, other parameters were calculated to compare against the peak-to-background ratios. These new parameters are summarized in Table 5 and include:

1. Pass SEASAT revolution number
2. Wave slope Defined as $\lambda/H_{1/3}$
3. v_0 Orbital velocity of deep water wave (after Kinsman, 1965):

$$v_0 = K_w A_0 \quad (4)$$
 v_0 = orbital velocity
 K_w = wave number
 A_0 = wave amplitude
4. $\sin \theta_{AC} v_0$ Normalized orbital velocity
5. θ_A - sea truth Relative radar look direction/sea truth wave direction is from 0° to 179°
 0° - traveling in same direction as radar platform
 90° - traveling perpendicular to radar platform
 179° - waves traveling in opposite direction as radar platform
6. θ_A - OFT Relative radar look direction -- OFT
7. θ_{AC} - sea truth Normalized relative radar look direction, sea truth
For $0-90^\circ$, $\theta_{AC} = \theta_A$
For $91-180^\circ$, $\theta_{AC} = \theta_A - 180^\circ$
8. θ_{AC} - OFT Normalized relative radar look direction, OFT
9. α_{SAR} Wind direction relative to the radar look direction when wind is blowing towards the same direction radar is looking, $\alpha_{SAR} = 0^\circ$, opposite, $\alpha_{SAR} = 180^\circ$, perpendicular, $\alpha_{SAR} = 90^\circ$ or 270°
10. α_{WV} Wind direction relative to wave direction

Linear correlations (Draper and Smith, 1960) were calculated between the sea truth parameters and PBR and are given in Table 6. Note that these linear correlations do not imply a cause-effect relationship between a sea truth parameter and wave detectability; they only suggest where a relationship might exist. Significant linear correlations existed between PBR and wavelength, wave height and orbital velocity of the waves. Multiple linear correlation coefficients were calculated using a combination of these parameters and are presented in Table 7. By correlating wavelength, orbital velocity, and

significant wave height against wave contrast, a correlation coefficient of 0.96 was obtained.

An interesting relationship from the correlation studies was the apparent relationship between wave contrast and wave height ($R = 0.78$). Here-to-fore in SAR wave analysis, it has not been possible to obtain wave height information. Although there are obviously many other factors involved, the plot of PBR versus $H_{1/3}$ in Figure 7 reveals a definite trend: the higher the wave height, the larger the PBR. A further analysis revealed that if wave height was correlated to PBR and wavelength (from optical Fourier transforms), a correlation coefficient of 0.88 resulted. Because these results are from a limited data set ($n = 10$), it would be premature to conclude that wave height information can be obtained from SAR data in this manner. These results do suggest that further research is warranted.

6. DISCUSSION

Analysis of the 6 October Lake Michigan data revealed that the best SAR wave imagery was achieved using a range telerotation adjustment proportional to the phase velocity of the gravity waves. This observation supports the theories of Raney (1971) and Shuchman and Zelenka (1978) that SAR imagery of range traveling waves will be distorted unless special telerotation adjustments are made during the processing of the data. These results also support the observations of Kasischke, et al. (1979) that the necessary telerotation adjustment (ϕ) is approximately proportional to the phase speed of the gravity waves. It should be noted that by changing the telerotation to a distance 2ϕ away from the optimum setting, the waves were still evident on the X-band SAR imagery, but not distinct on L-band imagery.

Another observation made on the October 6 Lake Michigan data was higher peak-to-background ratios were obtained on X-band imagery. It has been noted by some authors (Shuchman and Meadows, 1980) that X-band SARs image waves when L-band SARs do not. This present study supports this observation.

The final observation made on the telerotation SAR data was that higher peak-to-background ratios were obtained from data when the SAR was looking upwave (and upwind) compared to downwave (downwind) data. This was true for both L-band and X-band data. This observation is difficult to interpret. The initial conclusion to be drawn is that the downwave situation presents the preferred orientation of the capillary waves with respect to the radar line-of-sight. The question which cannot be answered using the Lake Michigan data is what is the driving force behind this preferred orientation, wind or waves?

The intended purpose of the integration time measurements was to answer the question whether the coherence time (or lifetime of the SAR scatterers) should be of concern to SAR scientists studying gravity waves. Raney and Shuchman (1978) reported that the average X-band Bragg ocean scatterer has a lifetime of approximately 0.15 seconds and suggested that using integration times longer than this scatterer lifetime would not result in a higher contrast of wave images. Thus, it was suggested by Raney and Shuchman that the SAR integration time (and corresponding azimuth resolution) be matched to the coherence time of the scatterer and the remaining SAR bandwidth information be used in a non-coherent manner to reduce the speckle of the images. However, the graph presented does not support this hypothesis, but rather it suggests that finer resolution SAR images of 50 meter wind generated gravity waves have higher crest-to-trough contrasts than lower resolution images.

In the statistical analysis of PBR and various environmental parameters using JASIN data, significant linear correlations were found between wave contrast (PBR) and wavelength, significant wave height and orbital velocity of

the waves. These correlations can also be studied in their context to SAR-gravity wave models.

It has been suggested by Phillips (1981), and others that short capillary and ultra-gravity waves are modulated by longer gravity waves. Phillips (1981) suggests that gravity waves are moving faster than capillary and ultra-gravity waves causing compression of the small waves and an increase in their height in the crest region of the gravity wave and a height decrease and elongation of the shorter waves in the trough region. This compression and expansion is thought to result from the straining of the shorter waves by the horizontal component of the orbital velocity of the gravity wave (Wright, et al., 1980).

A force which could be responsible for the compression/expansion of small waves is the horizontal component of the orbital velocity (Swift and Wilson, 1979; Alpers and Rufenach, 1979). From Eq. (3), we can see that orbital velocity is directly proportional to wave height; therefore, the higher the wave, the greater the orbital velocity (for a given wavelength), and thus the greater the potential for compression/expansion of small-scale waves. Therefore, the higher the wave, the greater the wave contrast in a SAR image of that wave field. Field experiments by Evans and Shemdin (1980) support this general concept, and brought forth the idea that the shortest of the shorter waves are modulated least. The correlation between wave contrast and wavelength does not present such a straightforward analysis. The positive correlation between wave contrast and wavelength does not necessarily indicate that the longer the wavelength, the higher the wave contrast that wave field will produce. An examination of Eq. (3) reveals that the relationship between wavelength and orbital velocity is an inverse one; the longer the wavelength, the lower the orbital velocity. This indicates that for a constant wave height, wave contrast should decrease for an increase in wavelength (if we are to go by the previous argument made for the relationship between wave contrast and orbital velocity). Therefore, the correlation between wave contrast and wavelength is possibly a secondary effect due to the positive correlation between wave height and wavelength which can be found in the JASIN data. Another interesting aspect of the JASIN data set is the relationship between wave height and wave contrast. It has been proposed by several researchers (Jain, 1977; Shuchman, et al., 1978) that SAR data when properly processed and interpreted, should be able to produce wave height information. Up until now, a practical method of accomplishing this has not emerged. The linear correlation between wave contrast and wave height found in this study suggests that wave contrast measured through a peak-to-background ratio provides a way to extract wave height information from SAR data. When PBR was coupled with wavelength information (also available from SAR data), even higher correlations were observed. Caution should be observed in interpreting these results, however, because of the small sample size in the JASIN data. These relationships could be coincidental to the JASIN data, and certainly should be examined using other data sets before any general conclusions are drawn.

7. SUMMARY

Numerous models have been developed that attempt to explain the synthetic aperture radar (SAR) mechanism responsible for the imaging of ocean gravity waves. However, very little experimental work has been done on the testing of these models due, in part, to the lack of well documented (sea-truthed) SAR ocean data sets and a method of efficiently quantifying the concept of wave detectability.

This paper reports on a technique whereby a numerical representation of wave contrast (detectability) can be quickly and efficiently obtained. By measuring the intensity of the peak of the power spectra produced by either optical or digital Fourier transforms of the SAR image of gravity waves and dividing that value by a background intensity of the same transform, a

peak-to-background ratio (PBR) can be obtained. It has been found that this PBR value is proportional to the wave crest-to-trough contrast which was previously calculated using a time consuming wave-modulation depth measurement technique.

Data sets of SAR imagery where sufficient sea truth existed were analyzed using PBR measurements. These data sets include satellite (SEASAT) and aircraft SAR data.

Peak-to-background ratios were used in three ways:

1. To explore existing SAR imaging mechanism models by performing statistical analyses on the relationship between PBR and various oceanographic parameters such as wave height, orbital velocity, wave slope, wind speed and direction;
2. To explore the possibility of PBR values being used to directly obtain an ocean parameter (i.e., wave height); and
3. To verify existing SAR imaging mechanism models' ability to predict when a SAR images ocean waves.

Aircraft SAR data (both L-band and X-band) data collected over an instrumented test site in Lake Michigan were examined using PBRs. Peak-to-background ratios were used to study the effect of altering radar system parameters (telerotation adjustments and mixed integration time) or wave visibility on SAR imagery. Results of this study indicated the best SAR imagery of the wind driven waves was obtained when a telerotation proportional to the phase velocity of the waves was used. X-band imagery had higher wave contrast than L-band imagery. Higher PBRs were obtained when the SAR was looking up-wave (and upwind) as opposed to downwave (downwind) as opposed to downwave (downwind). Mixed integration time studies showed that, in general, the coarser the azimuth resolution, the lower the wave contrast (PBR).

Using SEASAT data from JASIN, an examination of the correlation coefficients between PBR and various sea truth parameters (wavelength, wave direction, wave height, wind speed, and wind direction) showed a significant linear correlation between wave contrast (PBR) and wave height, the orbital velocity of the waves, and the dominant wavelengths of the waves. The linear correlation between PBR and wave height for the JASIN data implies that through the study of the relationship between these two factors, a technique might evolve where wave height can be obtained from SAR data.

8. ACKNOWLEDGEMENTS

The ERIM analysis performed for this study was supported by the Office of Naval Research (ONR) Contract N00014-76-C-1048. The Lake Michigan analysis was supported by Code 460 funding while the JASIN analysis was supported by Code 481 funding. The technical monitor for this ONR contract is Mr. Hans Dolezalek. The authors would like to acknowledge Mr. Alex Klooster and Ms. Raja Shounia, both of ERIM, for assisting them in processing the SAR data.

Finally, Dr. Robert H. Stewart of the Scripps Institute of Oceanography provided the JASIN sea truth data to the authors in summary form.

9. REFERENCES

- Allan, T.D. and T.H. Guymer, Seasat and JASIN, Int. J. Remote Sensing, 1, pp. 261-267, 1980.
- Alpers, W.R. and C.L. Rufenach, The Effect of Orbital Motions on Synthetic Aperture Radar Imagery of Ocean Waves, IEEE Trans. Antennas Propagat., Vol. AP-27, pp. 685-690, 1979.
- Anonymous, MARSEN Data Analysis and Research Plan, Pasadena, 1980.
- Beal, R.C., Spaceborne Imaging Radar: Monitoring of Ocean Waves, Science, 204, pp. 1373-1375, 1980.
- Brown, W.E., Jr., C.E. Elachi, and T.W. Thompson, Radar Imaging of Ocean Surface Patterns, J. Geophys. Res., 81, pp. 2657-2667, 1976.
- Brown, W.J. and L. Porcello, An Introduction to Synthetic Aperture Radar, IEEE Spectrum, 6, pp. 52-66, 1969.
- Draper, N.R. and H. Smith, Applied Regression Analysis, John Wiley and Sons, Inc., New York, 407 pp., 1966.
- Elachi, C. and W.E. Brown, Models of Radar Imaging of the Ocean Surface Waves, IEEE Trans. Antenna Propagat., Vol. AP-25, pp. 84-95, 1977.
- Evans, D.D. and O.H. Shemdin, An Investigation of the Modulation of Capillary and Short Gravity Waves in the Ocean, J. Geophys. Res., 85, pp. 5019-5024, 1980.
- Gonzalez, F.I., R.C. Beal, W.E. Brown, P.S. DeLeonibus, J.W. Sherman, J.F.R. Gower, D. Lichy, D.B. Ross, C.L. Rufenach, and R.A. Shuchman, Seasat Synthetic Aperture Radar: Ocean Wave Detection Capabilities, Science, 204, pp. 1418-1421, 1979.
- Gonzalez, F.I., R.A. Shuchman, D.B. Ross, C.L. Rufenach, and J.F.R. Gower, Synthetic Aperture Radar Wave Observations During GOASEX, Proceedings of the COSPAR/SCOR/IUCRM Symposium on Oceanography from Space, Plenum Press (in press), 1981.
- Harger, R.O., Synthetic Aperture Radar Systems, Academic Press, New York, NY, 240 pp., 1970.
- Jain, A., Determination of Ocean Wave Height from Synthetic Aperture Radar Imagery, Appl. Phys., 13, pp. 371-382, 1977.
- Kasischke, E.S., Extraction of Gravity Wave Information from Spaceborne Synthetic Aperture Radar Data, Univ. of Mich. M.S. Thesis, Ann Arbor, MI, 108 pp., 1980.
- Kasischke, E.S., A. Klooster, and R.A. Shuchman, Verification of Synthetic Aperture Radar Focusing Algorithms on Ocean Waves, Proceedings of the Thirteenth International Symposium on Remote Sensing of Environment, Ann Arbor, MI, pp. 1077-1092, 1979.
- Kinsman, B., Wind Waves - Their Generation and Propagation on the Ocean Surface, Prentice-Hall, Englewood Cliffs, NJ, 676 pp., 1965.

- Phillips, O.M., The Structure of Short Gravity Waves on the Ocean Surface, in Spaceborne Synthetic Aperture Radar for Oceanography, ed. by R.C. Beal, P.S. DeLeonibus and I. Katz, Johns Hopkins Univ. Press, Baltimore, MD, pp. 24-31, 1981.
- Rawson, R., F. Smith, and R. Larson, The ERIM Simultaneous X- and L-Band Dual Polarized Radar, IEEE 1975 International Radar Conference, p. 505, 1975.
- Raney, R.K., Synthetic Aperture Radar and Moving Targets, IEEE Trans. Aerospace Elect. Syst., Vol. AES-7, pp. 499-505, 1971.
- Raney, R.K. and R.A. Shuchman, SAR Mechanism for Imaging Waves, Proceedings of the Fifth Canadian Symposium on Remote Sensing, Victoria, B.C., 1978.
- Royal Society, Air-Sea Interaction Project: Summary of the 1978 Field Experiment, The Royal Society, London, England, 139 pp., 1979.
- Schwab, D.J., R.A. Shuchman, and P.L. Liu, Wind Wave Directions Determined from Synthetic Aperture Radar Imagery and from a Tower in Lake Michigan, J. Geophys. Res., Vol. 86, pp. 2059-2064, 1981.
- Sheffe, H., The Analysis of Variance, John Wiley and Sons, Inc., New York, NY, 477 pp., 1959.
- Shemdin, O.H., The Marineland Experiment: An Overview, Trans. Amer. Geophys. Union, Vol. 61, No. 38, pp. 625-626, 1980.
- Shemdin, O.H., The West Coast Experiment: An Overview, Trans. Amer. Geophys. Union, Vol. 61, No. 40, pp. 649-651, 1980a.
- Shuchman, R.A. and J.S. Zelenka, Processing of Ocean Wave Data from a Synthetic Aperture Radar, Boundary-Layer Meteorol., 13, pp. 181-191, 1978.
- Shuchman, R.A., A. Klooster, and A.L. Maffett, SAR Mechanisms for Imaging Ocean Waves, Proceedings of the EASTCON '78 Record, IEEE Electronics and Aerospace Systems Convention, pp. 128-134, 1978.
- Shuchman, R.A., E.S. Kasischke, and A. Klooster, Synthetic Aperture Radar Ocean Wave Studies, ERIM Final Report No. 131700-3-F, Ann Arbor, MI, 99 pp., 1978a.
- Shuchman, R.A., E.S. Kasischke, A. Klooster, and P.L. Jackson, SAR Coastal Ocean Wave Analysis - A Wave Refraction and Diffraction Study, ERIM Final Report No. 138600-2-F, Ann Arbor, MI, 1979.
- Shuchman, R.A. and G.A. Meadows, Airborne Synthetic Aperture Radar Observations of Surf Zone Conditions, Geophysical Letters, Vol. 7, pp. 857-860, 1980.
- Shuchman, R.A., E.S. Kasischke, and G.A. Meadows, Detection of Coastal Zone Environmental Conditions Using Synthetic Aperture Radar, 1981 International Geoscience and Remote Sensing Symposium Digest, Washington, D.C., pp. 756-767, 1981.
- Skolnik, M.I., Sea-Echo, in Radar Handbook, McGraw-Hill, New York, vp., 1970.
- Swift, C.T. and L.R. Wilson, Synthetic Aperture Radar Imaging of Moving Ocean Waves, IEEE Trans. Antennas Propag., Vol. AP-27, pp. 725-729, 1979.

Vesecky, J.F., R.H. Stewart, H.M. Assal, R.A. Shuchman, E.S. Kasischke, and J.D. Lyden, Gravity Waves, Large-Scale Surface Features and Ships Observed by Seasat Synthetic Aperture Radar During the 1978 JASIN Experiment, submitted to Science, 1981.

Vesecky, J.F., H.M. Assal, and R.H. Stewart, Remote Sensing of Ocean Waveheight Spectrum Using Synthetic-Aperture-Radar Images, Proceedings of the COSPAR/SCOR/IUCRUM Symposium on Oceanography from Space, Plenum Press (in press), 1981a.

Wright, J.W., Backscattering from Capillary Waves with Application to Sea Clutter, IEEE Trans. Antenna Propagat., Vol. AP-14, pp. 749-754, 1966.

Table 1. Summary of Peak-to-Background Ratios for Telerotation Adjustments on Lake Michigan SAR Data.

Telerotation	<u>X-Band</u>		<u>Eastbound Flight</u>	
	<u>Westbound Flight</u>		<u>(Pass 4)</u>	
	<u>(Pass 3)</u>		<u>PBR</u>	
	<u>Avg.</u>	<u>S.D.*</u>	<u>Avg.</u>	<u>S.D.*</u>
2 ϕ			62.2	2.9
3/2 ϕ	120.5	8.6	89.6	9.8
ϕ	138.8	11.4	78.5	9.7
1/2 ϕ	89.3	7.8	68.0	2.3
0	91.3	6.4	48.0	4.2
- ϕ	31.8	1.6	37.3	0.5
	<u>L-Band</u>			
2 ϕ	1.9	0.2	2.6	0.2
3/2 ϕ	5.0	0.3	3.8	0.5
ϕ	12.3	1.4	5.0	0.5
1/2 ϕ	13.1	2.6	5.1	0.2
0	7.1	0.2	3.3	0.2
-1/2 ϕ	1.5	0.1	1.9	0.1
- ϕ	1.0	0.0	1.5	0.0

*S.D. = Standard Deviation

Table 2. Azimuth Resolution versus Integration Time for
X- and L-Band Imagery.

Frequency (range)	Azimuth Resolution:	7 feet	15 feet	30 feet	50 feet
L-Band (near edge)*		2.41	1.12	0.56	0.28
L-Band (far edge)**		5.62	2.62	1.31	0.79
X-Band (near edge)		0.31	0.15	0.07	
X-Band (far edge)		0.73	0.34	0.17	

*near edge = 11,800 feet

**far edge = 27,500 feet

Table 3. Summary of Peak-to-Background Ratios for Different
Integration Times (Azimuth Resolution), Lake Michi-
gan SAR Data (Pass 4).

Azimuth Resolution	PBR			
	L-Band		X-Band	
	avg.	std. deviation	avg.	std. deviation
50'	7.7	0.7		
30'	8.4	0.2	18.9	0.5
15'	14.7	1.10	27.8	1.0
7'			40.4	3.5

Table 5. Derived Sea Truth Parameters for JASIN Experiment.

Pass	Wave Slope	v_0	$\sin \theta_{AC}$	v_0	θ_A Sea Truth	θ_A OFT	θ_{AC} Sea Truth	θ_{AC} OFT	α_{SAR}	α_{wv}
547	0.009	0.339	0.288	122	119	58	61	189	112	
556	0.010	0.338	0.305	64	58	64	58	270	100	
590	0.054	0.223	0.213	107	---	73	--	129	120	
	0.013	0.352	0.224	39	---	39	--	129	008	
599	0.015	0.362	0.153	155	---	25	--	249	354	
633	0.012	0.323	0.315	77	---	77	--	277	290	
642	0.016	0.575	0.142	166	---	14	--	036	320	
714	---	---	---	---	59	--	59	---	---	
719	---	---	---	---	104	--	76	---	---	
757	0.019	0.848	0.334	23	36	23	36	---	---	
762	0.026	1.051	1.046	96	90	84	90	290	056	
791	0.021	0.699	0.696	85	107	85	73	349	354	
834	0.019	0.640	0.314	151	126	29	54	046	345	
958	0.013	0.373	0.192	149	81	31	81	---	---	
1001	0.037	0.803	0.718	117	87	63	87	351	325	
1006	0.034	0.973	0.524	147	---	33	--	248	011	
1044	0.023	1.011	0.705	44	38	44	38	---	---	
1049	0.020	0.887	0.743	123	103	57	77	---	---	
1087	---	---	---	---	34	--	34	---	---	

Table 6. Linear Correlations between Wave Contrast (PBR) and Environmental Parameters for JASIN Seasat Data.

Parameter	Linear Correlation
Wave Height	0.78*
Wavelength (Sea Truth)	0.74*
Wavelength (OFT)	0.60**
Wave Slope	0.24
Wave Direction Relative to Radar Look Direction (Sea Truth)	0.36
Wave Direction Relative to Radar Look Direction (OFT)	-0.14
Normalized Orbital Velocity	0.76*
Wind Direction Relative to SAR Look Direction	0.43
Wind Direction Relative to Wave Direction	0.26
Wind Speed	0.11

* Significant at $p = 0.99$.** Significant at $p = 0.95$

Table 7. Multiple Linear Correlation Coefficients.

Parameter	PBR
$H_{1/3} \cdot \lambda$	0.84**
$H_{1/3} \cdot \sin \theta_{AC} \cdot v_0$	0.82*
$\lambda \cdot \sin \theta_{AC} \cdot v_0$	0.93*
$\lambda \cdot \sin \theta_{AC} \cdot v_0 \cdot H_{1/3}$	0.96*

* Significant at $p < 0.01$
 ** Significant at $p < 0.05$

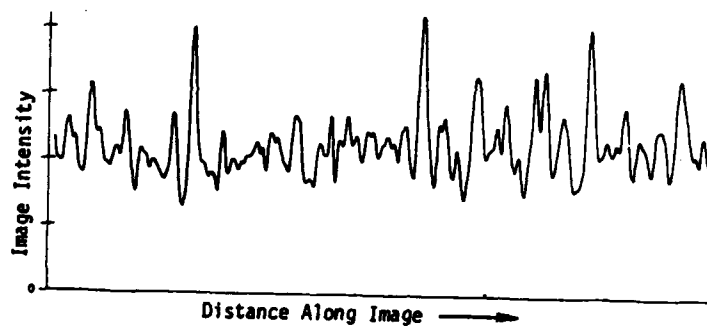


Figure 1. Example of Wave Scan Used in Modulation Depth Calculations.

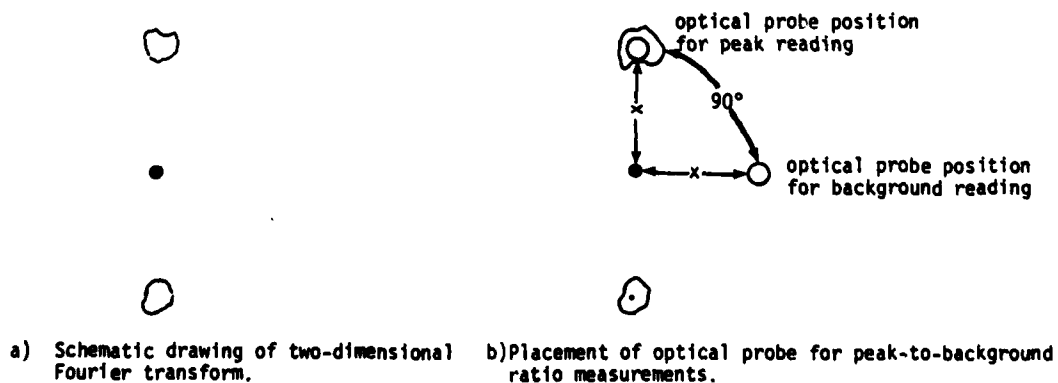


Figure 2. Summary of Peak-to-Background Measurement.

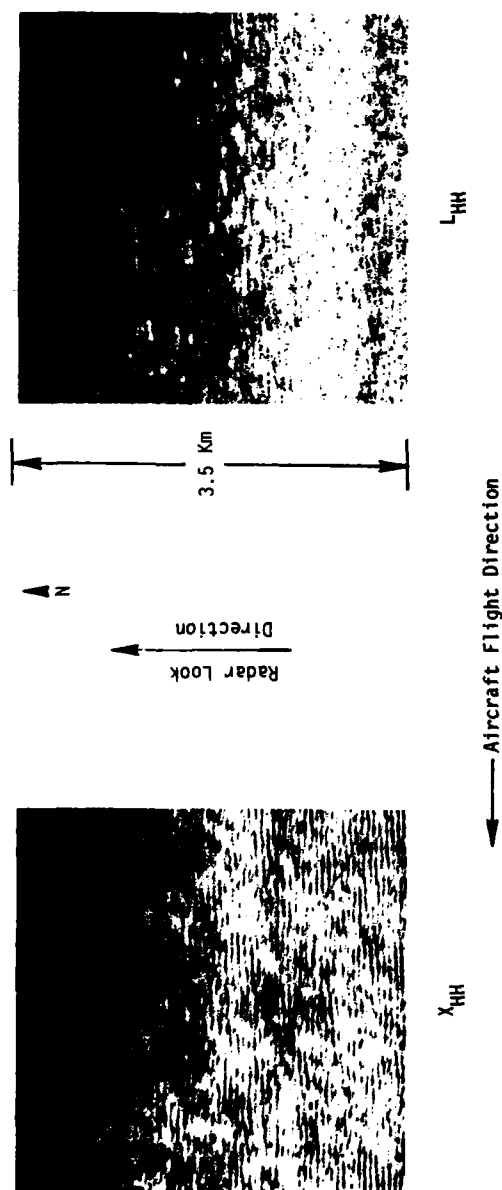


Figure 3. ERIM X- and L-Band (horizontally transmitted, horizontally received) SAR Imagery of Wind Waves in Lake Michigan near Muskegon, Michigan, 6 October 1977.

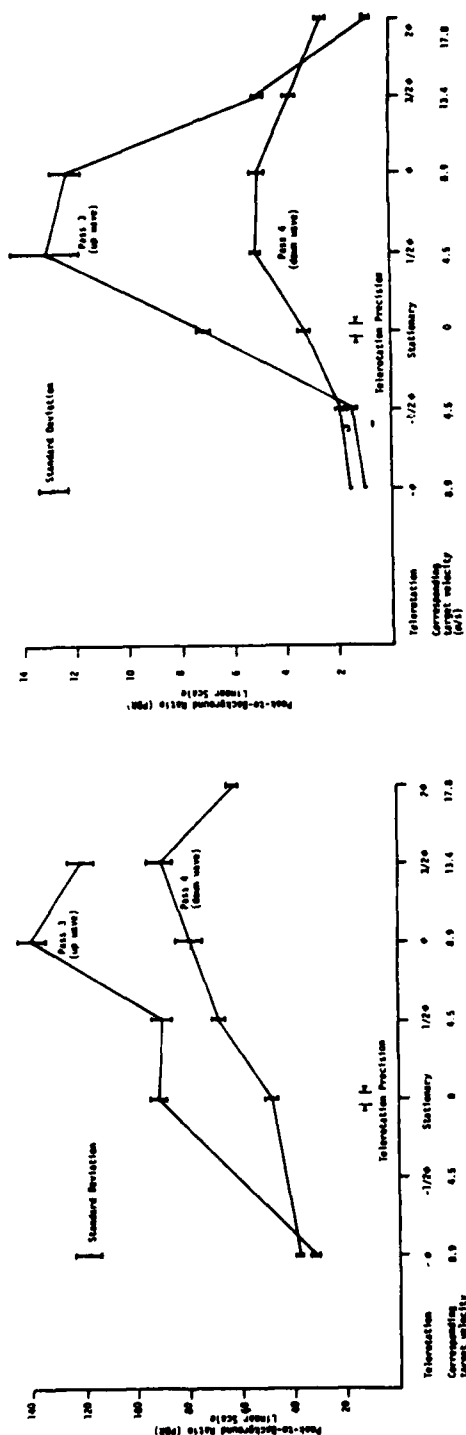


Figure 4. Summary of Peak-to-Background Ratios (PBRs) for Lake Michigan Telerotation Experiments.

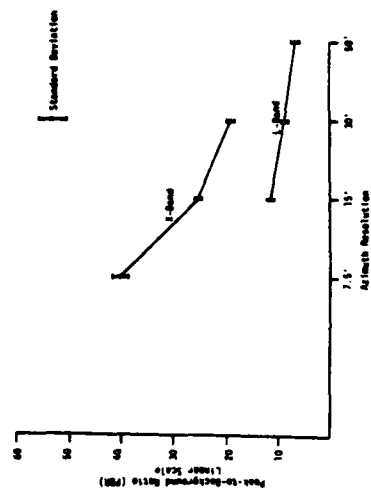


Figure 5. Summary of Peak-to-Background Ratios for Lake Michigan Integration Time Experiments.

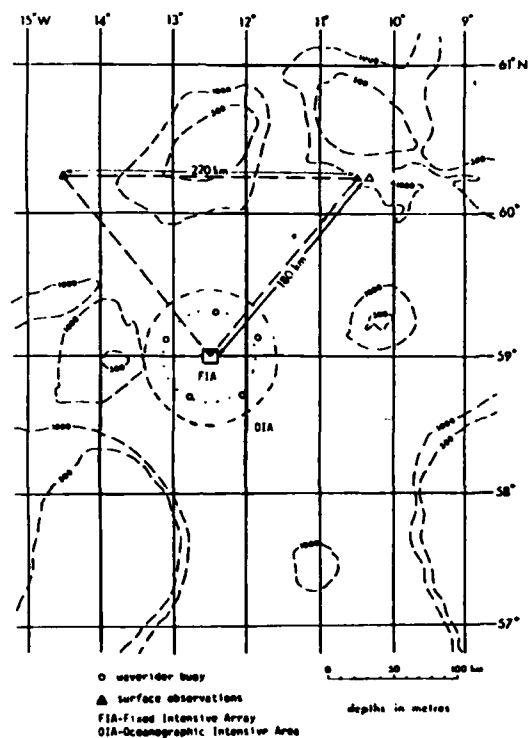


Figure 6. Locations of Joint Air-Sea Interaction Experiment

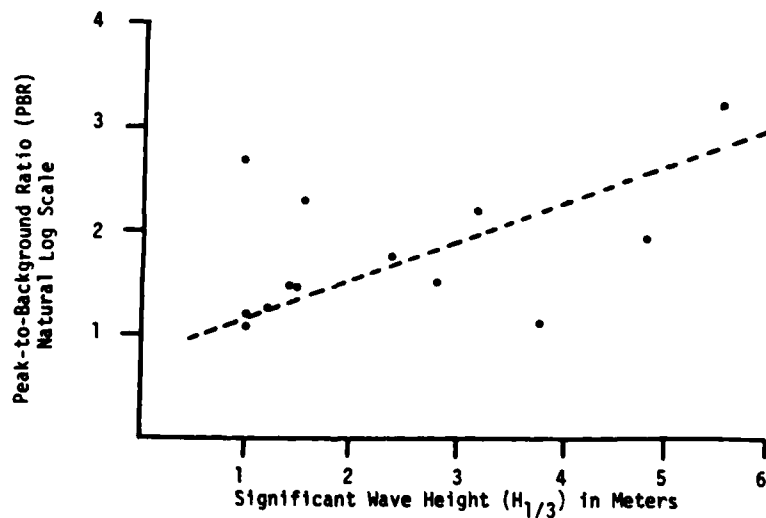


Figure 7. Significant Wave Height versus Peak-to-Background Ratio for JASIN Data.

SEASAT OBSERVATIONS OF OCEAN GRAVITY WAVES
DURING THE JASIN EXPERIMENT

E.S. Kasischke, R.A. Shuchman
and J.D. Lyden

Radar and Optics Division
Environmental Research Institute of Michigan
Ann Arbor, Michigan 48107

R.H. Stewart

Scripps Institute of Oceanography
LaJolla, California 92093

J.F. Vesecky and H.M. Assal

Stanford Center for Radar Astronomy
Stanford University
Stanford, California 94305

ABSTRACT

The Joint Air-Sea Interaction (JASIN) experiment permitted the comparison of wavelength and wave direction data collected simultaneously by both the Seasat synthetic aperture radar (SAR) and surface-based ship and buoy measurements. The Seasat satellite made 18 passes over an instrumented test site and imaged waves on 13 occasions. A comparison of the wave spectra derived from the SAR image to the sea truth indicates that the Seasat SAR produces good estimates of wavelength and wave direction. The environmental conditions under which the SAR failed to image waves have been carefully examined and summarized. A technique has been developed to measure the degree of wave detectability on SAR imagery. This wave detection measurement was statistically compared to oceanographic parameters (wave direction, length and height, wind speed and direction) to further investigate the limitations of the Seasat SAR in imaging ocean gravity waves. A significant, positive linear correlation between wave detectability and wave height ($H_{1/3}$), wavelength and orbital velocity of the wave was found. Also studied were special radar

processing techniques to enhance images of gravity waves obtained by a SAR. Results of this study indicate that for Seasat SAR data, special image enhancement adjustments to correct for motion of gravity waves do not change the estimate of dominant ocean wavelength and direction generated from SAR data and do not significantly improve the wave imagery.

1. INTRODUCTION

The summer of 1978 marked the culmination of two oceanographic research efforts in the United States and England: the launching of the Seasat satellite on 28 June 1978 and the Joint Air/Sea Interaction (JASIN) experiment in the North Atlantic from July through September of 1978. The inter-relation between these two efforts was the study of surface gravity waves.

The Seasat satellite contained four microwave remote sensing instruments: a scatterometer, a microwave radiometer, an altimeter and a synthetic aperture radar (for a description of these instruments, see Barrick and Swift, 1980). The main purpose of the synthetic aperture radar (SAR) was to image gravity waves and other physical oceanic processes visible on the ocean surface. For a review of SAR-oceanographic applications, see Vesecky and Stewart (1981) or Shuchman, et al. (1981).

The Seasat SAR system operated at a central frequency of 1.275 GHz (23.5 cm) and is described in detail by Jordan (1980). Seasat operated for over 100 days (collecting some 450 orbits of SAR data) when, on October 10, 1978, it suffered a catastrophic power failure. Seasat orbited the earth eighteen times a day at an altitude of 800 kilometers. The Seasat SAR had an incident angle of about 20 degrees and covered a swath 100 kilometers wide and up to 4000 kilometers long with a 25 by 25 meter ground resolution. By telemetry, the satellite was linked to one of five ground receiving stations

(Goldstone, California; Merrit Island, Florida; Fairbanks, Alaska; Shoe Cove, Newfoundland; and Oakhangar, England).

The JASIN experiment was sponsored and organized by the Royal Society of the United Kingdom and was conducted during the June through September time frame of 1978 in the North Atlantic. (See also Figure 1. For a more complete discussion of JASIN, the reader is referred to Allan and Guymer, 1980.) The study of gravity waves represented a small portion of the overall JASIN experiment. Most of the gravity wave observations were made within the Oceanographic Intensive Area (OIA) (the large, "dashed-line," circle in Figure 1), but ships operating in the large triangular region made gravity wave observations as well. Seasat, launched just prior to the JASIN experiment, offered a unique opportunity to collect satellite data over this well instrumented test site. A Seasat SAR receiving station was in operation at Oakhangar, England for the European Space Agency and radar data were collected on twenty different occasions when Seasat passed over or near the JASIN study area. Eighteen of those passes form the basis for the present study (data from two passes were of too poor quality to produce usable SAR imagery).

2. STUDY OBJECTIVES

There are three objectives in the present study:

1. To compare estimates of dominant wavelength and wave direction obtained from Seasat SAR data to estimates obtained from surface instrumentation;
2. To examine the environmental conditions under which the Seasat SAR did and did not image ocean gravity waves; and
3. To determine if Seasat SAR images of waves are sensitive to the same motion compensation techniques as are aircraft SAR data.

AD-A115 188

ENVIRONMENTAL RESEARCH INST OF MICHIGAN ANN ARBOR RA--ETC F/6 17/9

THE UTILITY OF SAR TO MONITOR OCEAN PROCESSES. (U)

NOV 81 R A SMUCHMAN, E S KASISCHKE

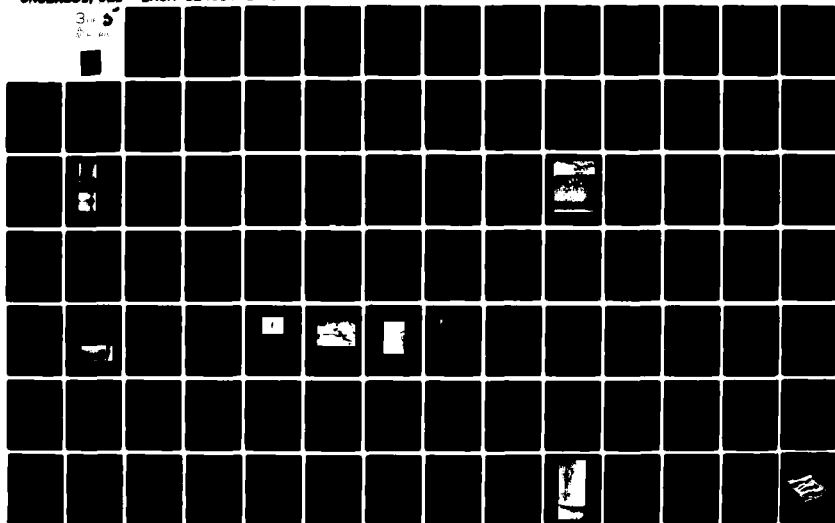
N00014-76-C-1048

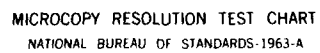
ERIM-124300-11-F

NL

UNCLASSIFIED

3-5
5-1-81





MICROCOPY RESOLUTION TEST CHART
NATIONAL BUREAU OF STANDARDS-1963-A

As previously mentioned, the primary purpose in placing a SAR on Seasat was to image surface gravity waves. A number of experiments have been conducted to test SAR's ability to measure wavelength and direction, including several aircraft and two Seasat experiments (see Shemdin, 1980a and 1980b; Shuchman and Meadows, 1980; Schwab et al., 1980; Gonzalez, et al., 1981; Beal, 1980). If the results of all these experiments are combined, the overall conclusion which emerges is that SAR-derived wave estimates compare favorably to surface measured values. Yet, even when all these previous experiments are considered together, one shortcoming is still apparent: the range of the sea and weather conditions is relatively limited. The JASIN-SAR data set was collected over a much wider range of environmental conditions than previous experiments and therefore represents a unique opportunity to study SAR imaging of gravity waves.

To be able to assess SAR's value in providing wave data, an understanding of the system's limitations (i.e., when a SAR will or will not image surface gravity waves) is a goal of SAR oceanographers. Because the JASIN experiment covered a time span where a wide range of surface wave and wind conditions occurred, an examination of this data set should add greatly to this goal.

A SAR uses the phase histories of backscattered radar signals to produce the SAR image of a target. Movement of a target when it is being imaged by a SAR system may cause a degradation of that target's image. Numerous theoretical papers (Shuchman and Zelenka, 1978; Alpers and Rufenach, 1979; Raney and Shuchman, 1978; Shuchman, 1981) have approached the problem of imaging moving waves with a SAR, but all analyses of these theories have involved using aircraft SAR data (Jain, 1978; Kasischke, et al., 1979; Kasischke and Shuchman, 1981). Data collected during the JASIN experiment were used to study the effects of motion compensation adjustments on Seasat SAR data of gravity waves during the present study. Specifically, two questions were addressed: (1) Is the contrast on Seasat SAR imagery of ocean

gravity waves significantly improved when image enhancement techniques are employed? and (2) Do the estimates of dominant wavelength and direction change significantly when image enhancement techniques are implemented?

3. METHODS

a. Sea-Truth Versus SAR Comparison

The Seasat SAR signal histories collected over the JASIN test site were processed into images using standard optical processing techniques (Cindrich, et al., 1980). This imagery film was then further analyzed to obtain estimates of dominant ocean wavelength and wave direction. Estimates of wavelength and direction can be obtained from SAR imagery by taking two-dimensional Fourier transforms of the data. This can be done either optically or digitally. For the SAR versus sea truth comparison portion of the study, estimates of dominant wavelength and direction were obtained from optical Fourier transforms (OFTs) of the SAR wave imagery (Barber, 1949). Examples of SAR imagery of gravity waves collected during the JASIN experiment are presented in Figure 2. The resulting digital fast Fourier transforms (FFT) from these data are presented in Figures 6 and 8.

The portion of the Seasat pass used to produce the OFT was the area closest to the nearest sea-truth observation for that date. Note, the locations of the OFTs were not necessarily the area closest to the Oceanographic Intensive Area. This was because the ships which deployed the pitch and roll buoys (discussed below) were often outside this area. An aperture setting equivalent to an ocean area of 25 km by 25 km was used during the generation of the OFTs.

During the JASIN experiment, surface truth (wave data) were collected by a variety of different instruments. This instrumentation included pitch and roll buoys (Stewart, 1977) deployed from the R/V Atlantis II and R/V Discovery, a set of moored wave rider buoys which

were within the Oceanographic Intensive Area, wave recorders onboard the R/V John Murray and R/V Discovery and visual readings made from the R/V John Murray. The exact location of the research vessels varied day to day depending on what experiments they were participating in, but all obtained wave data at the time of the Seasat overpass, or at worst, within an hour or two of it. The wave rider buoys were all located within the Oceanographic Intensive Area (their exact locations are marked by Figure 1) and the data from these were collected at the times of the Seasat overpasses.

Wave data and sea-truth estimates were processed using standard oceanographic techniques at the Scripps Institute of Oceanography. Included in this sea-truth data set were estimates of dominant wavelength and direction, wave height ($H_{1/3}$) and surface wind speed and direction. The two-dimensional ocean wave frequency spectra, $F(\omega, \theta)$ obtained from the buoys and wave recorders were converted to wave number spectra using the Jacobian approximation (g^2/ω^3 , where g is the gravitational acceleration and ω is the wave frequency) appropriate to deep water waves (Vesecky, et al., 1981).

Because several of the test dates had more than one available set of sea-truth, it was necessary to decide which value to use to compare to the OFT value. Available sea-truth was therefore ranked according to the desirability of the data source, as follows:

- | | |
|-------|--|
| BEST | 1. <u>Atlantis II</u> Pitch and Roll Buoy or <u>Discovery</u> Pitch and Roll Buoy. |
| | 2. Moored OIA Wave Rider Buoy. |
| | 3. <u>John Murray</u> Wave Recorder or <u>Discovery</u> Wave Recorder. |
| WORST | 4. <u>John Murray</u> Visual Readings. |

If no sea-truth data were available using the most desirable category, then the next highest category which contained the desired sea-truth data was used.

Finally, the SAR estimates of wavelength and direction were statistically compared to the sea-truth values by linear correlation to determine if the two estimates compared favorably.

b. SAR Detection of Gravity Waves

In determining whether a spaceborne SAR system will be an effective tool for gathering wave data, an area of important consideration is the understanding of those conditions under which a SAR will and will not image gravity waves. The JASIN data set provides a valuable opportunity to examine this question because not only were a wide variety of surface measurements made which can be examined against the SAR data, but also because a wide spectrum of environmental conditions were encountered during the time span of the JASIN study.

As mentioned in the previous section, wave measuring instruments collected wave period and directional data at or near the areas where SAR data were collected. From these wave data, significant wave heights ($H_{1/3}$) were also calculated. Other surface measurements of potential interest are surface wind speed (U) and direction.

From these surface measures, a group of derived variables can also be calculated. When examining directional data (wind or wave), it is important to know how the waves (or wind) are traveling with respect to the radar look direction. The following directional variables were calculated:

1. θ_A : Normalized wave direction. When $\theta_A = 0^\circ$, the waves are traveling in the same direction as the SAR platform; when $\theta_A = 180^\circ$, the opposite direction
2. θ_{AC} : Wave direction normalized to a 0° to 90° range (where 0° is an azimuth traveling wave and 90° is a range traveling wave)
3. α_s : Wind direction relative to the platform travel direction (normalized to a 0° - 90° range, where 90° would be a wind blowing perpendicular to the SAR look direction)

4. α_w : Wind direction relative to wave direction (normalized to a 0° - 90° range, where 90° would be a wind blowing perpendicular to the wave direction of travel).

It has been theorized that factors which might affect SAR imaging of gravity waves include the local tilt of the water surface (Elachi and Brown, 1977) and the orbital velocity of the gravity waves which cause bunching of the smaller capillary and ultra-gravity waves (Alpers and Rufenach, 1979; Phillips, 1981).

Wave slope (S) can be defined as:

$$S = H_{1/3}/\lambda \quad (1)$$

where λ = the dominant wavelength.

Kinsman (1965) defines the orbital velocity of a gravity wave (v_o) as:

$$v_o = k_w A_o \quad (2)$$

where k_w = wave number = $2\pi/\lambda$, and

A_o = amplitude of the waves = $2.83 H_{1/3}$.

A normalized orbital velocity (v_n) defined as the orbital velocity in the direction of radar line-of-sight, can be calculated as:

$$v_n = v_o \sin \theta_{AC} \quad (3)$$

The surface measurements and derived variables were compared to the Seasat SAR data in both a qualitative and quantitative manner. For the qualitative comparison, the SAR data was subjectively divided into three visibility categories, and common denominators within these categories for surface measurements were determined. For the quantitative analysis, a wave crest-to-trough contrast measurement was used as a numerical indicator of visibility of waves on SAR imagery and statistically correlated to the various surface measurements and derived variables.

The SAR imagery collected over the JASIN area was visually examined and classified as having waves in one of three categories: (1) GOOD imagery, where gravity waves are clearly visible on the SAR image; (2) POOR imagery, where gravity waves are present, but detected only upon close inspection; and (3) NONE imagery, where no gravity wavelike patterns are visible on the SAR image. Upon categorizing the imagery, the surface measurements and derived data for each category were examined to determine if a trend could be detected.

The data set was then more rigorously analyzed by statistically comparing the surface measurements and derived variables to a recently developed wave crest-to-trough contrast measurement known as a peak-to-background ratio (Kasischke and Shuchman, 1981). The peak-to-background ratio (PBR) is measured as follows: First, the peak intensity of the Fourier transform spectrum is extracted (either measured from an optical Fourier transform or digitally derived from a fast Fourier transform). Next, a minimum intensity from the same k-space of the peak intensity is extracted. The ratio of these two intensities (i.e., peak/minimum) is defined as the peak-to-background ratio. For this portion of the study, the peak and minimum intensities were measured as film densities of the photographic negative of the spectrum obtained from an optical Fourier transform of the wave data.

The peak-to-background ratios for the eighteen JASIN SAR overpasses were linearly correlated (Draper and Smith, 1966) to the various surface measurements and derived variables (such as wave slope, orbital velocity and normalized orbital velocity) to determine where a relationship might exist. It should be noted that a linear correlation does not imply that a cause/effect relationship exists between two variables in an a posteriori examination of the data such as is presented here, it only suggests where such a relationship might exist.

c. SAR Motion Corrections

Because the imaging mechanism employed by the synthetic aperture radar is dependent upon the phase history of the target being imaged, any motion in that target can result in a degraded SAR image. This phenomena was first reported on by Raney (1971) and more recently Shuchman and Zelenka (1978) and Shuchman (1981). Shuchman (1981) produced a set of equations which can be used to calculate the adjustments necessary to compensate for these motion distortions when processing the SAR signal histories.

Studies using aircraft SAR data have shown that the visibility or detectability of gravity waves is often sensitive to motion compensation adjustments made during the processing of the SAR signal histories (Kasischke, et al., 1979; Kasischke and Shuchman, 1981). Because these motion compensation adjustments are inversely proportional to the velocity of the SAR platform, it was theoretically determined by early Seasat investigators that the motion adjustments may be necessary for optimum contrast wave imagery if the SAR data is processed to full resolution. Furthermore, it was determined by Shuchman and Zelenka (1978) that the adjustment, if necessary, would be quite small and the effect on the SAR wave imagery quite subtle.

The purpose of the present investigation was to determine the degree of sensitivity of Seasat SAR data to motion compensation adjustments. This was accomplished in two separate experiments. First, wave detectability or contrast was measured as a function of both the range telerotation adjustment and azimuth focus shift adjustment. Next, SAR imagery with various telerotation and focus adjustments were digitized and fast Fourier transformed to determine if the spectral estimates varied.

To summarize, a velocity in the range (line-of-sight) direction affects the SAR imaging process in several ways. One such effect is an azimuthal displacement of the moving target's image relative to a

stationary target's image. When a target is accelerating in the range direction, this azimuth displacement changes during the imaging time, resulting in a smearing in the azimuthal direction. Neither one of these effects is correctable during processing.

A range velocity component will also cause a smearing or defocusing in the range direction due to a rotation of the phase history of the target. This effect can be corrected for during correlation of the data by rotating the lenses in the optical processor as described below.

Motion of a SAR imaged target in the along track direction results in a defocusing of the image in the azimuth direction. This defocusing can be compensated for during processing by adjusting the focal length of the azimuthal lens. For a more detailed discussion of the problems associated with imaging moving targets with a SAR, the reader is referred to articles by Shuchman (1981) or Shuchman, et al. (1981).

Shuchman (1981) presented equations to calculate adjustments to use during processing of the signal histories for the range and azimuth velocity components present in gravity waves. These velocity adjustments are directly proportional to the velocity of the SAR platform. The motion compensation adjustments are of two types: telerotation adjustments which compensate for motion in the range (line-of-sight) direction and focus shifts which compensate for motion in the azimuth direction.

The telerotation adjustment (Shuchman, 1981) is:

$$\phi = \frac{v_r P}{v_{AC} Q} \quad (4)$$

where v_r is the line-sight velocity of the target,
 v_{AC} is the SAR platform velocity, and
 P and Q are SAR processing parameters.

In a similar fashion, an adjustment can also be made to compensate for azimuth velocity distortions in the SAR data. As derived by Shuchman and Zelenka (1978), the focal length (F_0) for SAR processing is defined as:

$$F_0 = \frac{R\lambda}{2M^2\lambda_0} \left(\frac{v_f}{V_{AC}} \right)^2 \quad (5)$$

where R is the slant range to the target,

λ is the radar wavelength,

λ_0 is the optical processor wavelength,

M is azimuth demagnification of the optical processor, and

v_f is the film velocity.

Using the focal length (F_0) calculated in Eq. (5), the shift in focal length (δF) produced by a moving target is defined as

$$\delta F = 2F_0 \frac{v_A}{V_{AC}} \quad (6)$$

where v_A is the target velocity parallel to the SAR platform direction.

It can be seen that both adjustments are inversely proportional to the velocity of the SAR platform. For the velocity of the Seasat satellite (~ 7800 m/s), the adjustments needed to correct for the phase velocity of the gravity waves are very much smaller than those needed for an aircraft SAR ($v_{AC} = 150$ m/s).

Range telerotation adjustments were made on Seasat SAR data from Revolution 762. Surface measurements indicated the dominant wavelength at this time was 210 meters ($C = 18.1$ m/s) and the SAR data indicated a 241 meter ($C = 19.4$ m/s) dominant wave was present. The telerotation adjustment (ϕ) calculated for the Revolution 762 SAR data assumed a 19.4 m/s dominant wave was present. SAR imagery of waves from Revolution 762 were processed using the following

telerotation adjustments: -9ϕ , -7ϕ , -5ϕ , -3ϕ , -2ϕ , $-\phi$, $0 + \phi$, $+2\phi$, $+3\phi$, $+5\phi$, $+7\phi$, and $+9\phi$. A negative (-) telerotation assumes the waves are moving away from the SAR and a positive (+) telerotation assumes the waves are moving towards the SAR. During Rev. 762, the waves were moving towards the SAR.

Seasat SAR imagery from Revolution 1087 was optically processed using a variety of different azimuth focus shifts. No sea-truth was collected for this pass, but it is clear from Figure 2 that the waves are nearly azimuth traveling. The optical Fourier transform of this data indicates a 299 meter dominant wave is present ($C = 21.2$ m/sec). A focus shift, P , was calculated assuming the waves had a phase speed of 21.2 m/sec. Revolution 1087 data were processed using the following focus shifts: $-4P$, $-3P$, $-2P$, $-P$, 0 , P , $2P$, $3P$, $4P$. A negative (-) focus shift assumes the waves are moving in the same direction as the SAR platform while a positive (+) correction assumes the waves are moving in the opposite direction. Since no sea truth was available, the assumption was made that the waves were propagating towards the Scottish Coast, therefore opposite the SAR platform direction.

To explore the question of whether or not the telerotation adjustments significantly alter the SAR derived estimates of wavelength and direction, digital analysis techniques were employed. SAR imagery from both Revolutions 762 and 1087 were digitized using ERIM's Optical Hybrid Digitizing Facility (see Ausherman, et al., 1975). For Revolution 762, imagery from the -2ϕ , $-\phi$, 0 , $+\phi$ and $+2\phi$ telerotation settings were digitized. For Revolution 1087, imagery from the $-2P$, $-P$, 0 , $+P$ and $+2P$ azimuth focus shifts were digitized. These digital data were then fast Fourier transformed and the resultant one-dimensional wave number and wave direction plots examined.

4. RESULTS

Table 1 summarizes the coincident surface measured wave and wind data along with the SAR-derived estimates of dominant wavelength and direction and wave contrast for the eighteen SAR overpasses made during the JASIN experiment. Included in Table 1 are the Seasat pass number, the date and time the SAR data were collected, the source of the sea truth used to compare to the SAR data, the distance between the SAR and surface observations, the surface measured values for dominant wave direction (θ_T), dominant wavelength (λ), significant wave height ($H_{1/3}$), wind speed (U) and wind direction (α_T) and SAR derived estimates of wave direction (θ_T -OFT and θ_T -FFT), wavelength (λ -OFT and λ -FFT) and wave contrast (PBR).

First, a comparison was made between the surface measured estimates to those obtained from Seasat SAR OFT estimates. Figure 3 presents a scatter plot of SAR-derived versus surface measured values of dominant wavelength. Figure 4 is a scatter plot of the two estimates of dominant wave direction. From these two plots, we can see the two methods of measuring waves compare favorably.

Next, a qualitative assessment of the factors which might be important in determining whether or not a SAR successfully images gravity waves was made.

Table 2 lists wavelength (λ), wave height ($H_{1/3}$) and radar look direction normalized to the direction of wave travel (θ_{AC}) for the three classes of SAR wave imagery (i.e., GOOD, POOR and NONE). For θ_{AC} , a 0° reading means the waves are traveling parallel to the radar line-of-sight and a 90° reading indicates the waves are traveling perpendicular to the radar line-of-sight. An examination of Table 2 reveals that one of two conditions existed when waves were not visible on the SAR imagery: (1) the wave height ($H_{1/3}$) was less than 1.3 meters; or (2) the waves were traveling nearly parallel to the radar line-of-sight ($\theta_{AC} < 35^\circ$). For the POOR wave imagery,

we can also see that one of the above limits was being approached on three out of the five cases.

Table 3 summarizes the derived variables which were calculated to supplement the surface measured data. Included in this table is wave slope, orbital velocity (v_o), normalized orbital velocity (v_n), two estimates of wave direction relative to the SAR look direction (θ_A -sea truth and θ_A -OFT), normalized relative radar look direction (θ_s -sea truth and θ_w -OFT) and two normalized wind directions (σ_{SAR} and σ_{WV}). The surface measured and derived variables were then linearly correlated to the wave contrast peak-to-background ratio (PBR).

Table 4 summarizes the linear correlations between the peak-to-background ratio and the various surface measurements and derived variables. Significant ($p < 0.05$) linear correlations existed between the wave contrast measurement and wavelength (both λ -sea truth and λ -OFT), wave height ($H_{1/3}$), orbital velocity (v_o) and normalized orbital velocity ($\sin \theta_{AC} v_o$). Table 5 summarizes multiple linear regression coefficients calculated between combinations of λ , $H_{1/3}$ and $\sin \theta_{AC} v_o$. Again, these coefficients are all significant ($p < 0.05$).

The final investigation performed on the JASIN-SAR comparison was to determine if Seasat SAR could be improved by using motion compensation adjustments during processing of the SAR data. Figure 5 and Table 6 summarize the results of the wave contrast versus telerotation measurements. Note on Figure 5 that a positive telerotation is compensating for wave motion away from the radar line-of-sight while a negative telerotation adjusts for motion towards the radar. Each point on the curve represents an average of five separate measurements.

The trend in Figure 5 is clear. Telerotation adjustments do not appear to appreciably degrade Seasat SAR imagery within $\pm 30^\circ$ of the

stationary focus setting. Studies of aircraft SAR data have shown that waves become undetectable on SAR imagery when a telerotation of $\pm 2\phi$ from the optimum setting is used (see Kasischke, et al., 1979; Kasischke and Shuchman, 1981).

Figure 6 illustrates the two-dimensional spectra generated by conducting a fast Fourier transform of the digitized SAR data from Revolution 762, for three telerotation adjustments (-2ϕ , 0, $+2\phi$). Figure 6 also presents the one-dimensional wave direction and wave number spectra generated from the fast Fourier transform. We can see that the spectral estimates change very little when a non-zero range telerotation is used.

Table 6 and Figure 7 summarize the results of the wave contrast versus the azimuth focus shift adjustments. Again, each point represents an average of five points. It can be seen that the highest wave contrast was obtained when a land (0) focus setting was used. With the azimuth focus shifts, it appears that the Seasat SAR wave imagery was not significantly degraded until a focus shift greater than $\pm 2P$ was used.

Figure 8 illustrates the two-dimensional spectra generated from the Revolution 1087 data. For the three azimuth focus settings ($-2P$, 0, $+2P$), Figure 8 also presents the one-dimensional wave direction and wave number spectra from these data. From Figure 8, we can see that the spectral estimates generated using different azimuth focus settings change very little when non-stationary settings are used.

5. DISCUSSION OF RESULTS

The telerotation and focus shift adjustment portion of this study shows that Seasat SAR data is relatively insensitive to motion adjustment techniques which compensate for wave motion in both the range and azimuth direction. This insensitivity is true for both

the visibility of waves on SAR imagery and the estimates of dominant wavelength and wave direction obtained from digital fast Fourier transforms of the digital data. This result indicates that when processing spaceborne SAR data of ocean gravity waves, special motion compensation processing techniques will not have to be used if a stationary (0) focus can be established.

The present study of SAR wave imagery collected during the JASIN experiment has added greatly to the evaluation of the utility of SAR to monitor gravity waves. The comparison of dominant wavelength and wave direction estimates obtained from SAR data to those collected by a variety of surface instruments indicates the Seasat SAR was indeed accurately imaging the dominant wave field present on the ocean's surface of the time of the SAR overflights. This argument is strengthened when the JASIN data is combined with other Seasat data, such as that collected during the GOASEX and DUCKEX studies (see Vesecky and Stewart, 1981).

The combined surface truth and Seasat SAR data also allowed an examination of the conditions when the SAR did and did not image gravity waves. A qualitative assessment of the data reveals two factors to be important: the height of the waves and the direction of the waves with respect to the SAR look direction. A quantitative evaluation of the data revealed significant statistical linear correlations between wave contrasts (measured as a peak-to-background ratio) and wave height, wavelength and orbital velocity of the gravity waves.

There is a general consensus that SARs will image gravity waves traveling perpendicular to the radar line-of-sight (i.e., range traveling waves) better than waves traveling parallel to the line-of-sight (i.e., azimuth waves). Using aircraft SAR data collected off of Marineland, Florida, Teleki, et al. (1978) found higher crest-to-trough wave contrast in range waves. This same general trend was found in the JASIN data, using a qualitative examination of the data.

The inter-relationship found between wavelength and wave contrast in the JASIN data supports the present consensus of SAR investigators on this subject. Sampling theory (Nyquist) states that at least two samples per wave cycle are necessary to resolve gravity waves on SAR imagery. In reality, the number of samples is probably between four and six. The number of samples per wave cycle is dependent on two variables: the spatial resolution of the SAR system and the wavelength of the surface waves. It has been determined that given Seasat's 25 meter ground resolution, it should be able to observe 80 meter or longer gravity waves (Beal, 1980). The JASIN data set supports this concept, with the shorter period waves in the data set being less readily detected than the longer period waves.

The relationship between wave height and detection of waves by SARs has yet to be examined in detail. It is known from the East Coast experiment (Beal, 1981) that the Seasat SAR had difficulty imaging waves which had significant heights of less than approximately 1.0 meter. This observation was supported by the JASIN data set in that the cases when the Seasat did not detect gravity waves were generally low wave heights and also the positive linear correlation between wave contrast and wave height ($H_{1/3}$).

The relationship between orbital velocity and wave contrast is perhaps the most interesting from a theoretical standpoint as to why a SAR images gravity waves in the first place. It has been suggested by Phillips (1981), and others that short capillary and ultra-gravity waves are modulated by longer gravity waves. Phillips (1981) suggests that gravity waves are moving faster than capillary and ultra-gravity waves causing compression of the small waves and an increase in their height in the crest region of the gravity wave and a height decrease and elongation of the shorter waves in the trough region. This compression and expansion is thought to result from the straining of the shorter waves by the horizontal component of the orbital velocity of the gravity wave (Wright, et al., 1980). The positive

linear correlation between orbital velocity and wave contrast found in the JASIN data supports this theory.

6. CONCLUSIONS

An examination of Seasat SAR imagery collected during the JASIN experiment has proven beneficial in several ways. First, a comparison of estimates of dominant wavelength and direction produced from SAR data to those produced from surface instrumentation has added to the growing body of evidence that SARs can be used to accurately produce these wave statistics.

The present study has shown that Seasat SAR-wave imagery is not as sensitive to motion compensation techniques as is aircraft SAR data. This result indicates that to produce optimal images of gravity waves from spaceborne SAR data will not require special processing. This is not always the case when processing data collected by aircraft-mounted SARs. The insensitivity to motion effects noticed in Seasat SAR images is true in terms of both detectability of waves on SAR imagery and the estimates of dominant wavelength and direction obtained from the SAR data.

Finally, the JASIN data set has given additional insight to the question of when a SAR will or will not image gravity waves. The data support the present theories that a spaceborne SAR has difficulty imaging azimuth traveling waves and waves with significant wave heights less than approximately 1.0 meter or wavelengths greater than 80 meters. It was also shown that a positive linear correlation existed between wave contrast on the SAR imagery and the orbital velocity of the waves.

ACKNOWLEDGEMENTS

Funds for this project were provided by the Office of Naval Research (Code 480) through Contract N00014-76-C-1048. Particular thanks go to J. Losee, R. Shounia and A. Klooster who processed the SAR data at the Environmental Research Institute of Michigan. We also gratefully acknowledge H. Carlson of the Deuches Hydrographisches Institute and T. Guymen and D. Webb of the Institute of Oceanographic Sciences (IOS) U.K. for their help in obtaining wind and wave data collected during the JASIN experiment.

REFERENCES

- Allan, T.D. and T.H. Guymer, Seasat and JASIN, Int. J. Remote Sensing, Vol. 1, pp. 261-267, 1980.
- Alpers, W.R. and C.L. Rufenach, The Effect of Orbit Motions on Synthetic Aperture Radar Imagery of Ocean Waves, IEEE Trans. Antennas Propagat., Vol. AP-27, pp. 685-690, 1979.
- Barber, N.F., A Diffraction Analysis of a Photograph of the Sea, Nature, 164, p. 485, 1949.
- Barrick, D.E. and C.T. Swift, The Seasat Microwave Instruments in Historical Perspective, IEEE J. Oceanic Eng., Vol. OE-5, pp. 72-79, 80.
- Beal, R.C., The Seasat SAR Wind and Ocean Wave Monitoring Capabilities, Johns Hopkins Univ., 42 p., 1979.
- Cindrich, I., C. Dwyer, A. Klooster and J. Marks, Optical Processing of Seasat-A SAR Data, Published in the Proceedings of a Working Group Meeting, Esrin, Frascati, Italy, 13-14 December, 1979, ESA SP-1031, pp. 43-74, 1980.
- Draper, N.R. and H. Smith, Applied Regression Analysis, John Wiley and Sons, Inc., New York, 407 pp., 1966.
- Elachi, C. and W.E. Brown, Models of Radar Imaging of the Ocean Surface Waves, IEEE Trans. Antenna Propagat., Vol. AP-25, pp. 84-95, 1977.
- Gonzalez, F.I., R.A. Shuchman, D.B. Ross, C.L. Rufenach and J.F.R. Gower, Synthetic Aperture Radar Wave Observations During GOASEX, Proceedings of the COSPAR/SCOR/IUCRM Symposium on Oceanography from Space, Plenum Press (in press), 1981.
- Jain, A., Focusing Effects in Synthetic Aperture Radar Imaging of Ocean Waves, J. Appl. Phys., Vol. 15, pp. 323-333, 1978.
- Jordan, R.L., The Seasat-A Synthetic Aperture Radar System, IEEE J. Oceanic Eng., Vol. OE-5, pp. 154-164, 1980.
- Kasischke, E.S., Extraction of Gravity Wave Information from Synthetic Aperture Radar Data, Univ. of Mich. M.S. Thesis, 108 pp., 1980.
- Kasischke, E.S. and R.A. Shuchman, The Use of Wave Contrast Measurements in the Evaluation of SAR/Gravity Wave Models, Proceedings of the Fifteenth International Symposium on Remote Sensing of Environment (in press), May 1981.
- Kinsman, B., Wind Waves - Their Generation and Propagation on the Ocean Surface, Prentice-Hall, Englewood Cliffs, N.J., 676 pp., 1965.

McLeish, W., D. Ross, R.A. Shuchman, P.G. Teleki, S.V. Hsiao, O.H. Shemdin and W.E. Brown, Synthetic Aperture Radar Imaging of Ocean Waves: Comparison with Wave Measurements, J. Geophys. Res., 85, pp. 5003-5011, 1980.

Phillips, O.M., The Structure of Short Gravity Waves on the Ocean Surface, in Spaceborne Synthetic Aperture Radar for Oceanography, ed. by R.C. Beal, P.S. DeLeonibus, and I. Katz, Johns Hopkins Univ. Press, Baltimore, MD, pp. 24-31, 1981.

Raney, R.K., Synthetic Aperture Radar and Moving Targets, IEEE Trans. Aerospace Elect. Syst., Vol. AES-7, pp. 499-505, 1971.

Raney, R.K. and R.A. Shuchman, SAR Mechanism for Imaging Waves, Proc. Fifth Canadian Symp. on Remote Sensing, Victoria, B.C., 1978.

Schwab, D.J., R.A. Shuchman and P.L. Liu, Wind Wave Directions Determined from Synthetic Aperture Radar Imagery and from a Tower in Lake Michigan, J. Geophys. Res., Vol. 86, pp. 2059-2064, 1981.

Shemdin, O.H., The Marineland Experiment: An Overview, Trans. Amer. Geophys. Union, Vol. 61, No. 38, pp. 625-626, 1980a.

Shemdin, O.H., The West Coast Experiment: An Overview, Trans. Amer. Geophys. Union, Vol. 61, No. 40, pp. 649-651, 1980b.

Shuchman, R.A. and G.A. Meadows, Airborne Synthetic Aperture Radar Observations of Surf Zone Conditions, Geophysical Research Letters, Vol. 7, pp. 857-860, 1980.

Shuchman, R.A., Processing Synthetic Aperture Radar Data of Ocean Waves, Proceedings of the COSPAR/SCOR/IUCRUM Symposium on Oceanography from Space, Plenum Press (in press), 1981.

Shuchman, R.A. and J.S. Zelenka, Processing of Ocean Wave Data from a Synthetic Aperture Radar, Boundary-Layer Meteorol., 13, pp. 181-191, 1978.

Shuchman, R.A., E.S. Kasischke and G.A. Meadows, Detection of Coastal Zone Environmental Conditions Using Synthetic Aperture Radar, IEEE International Geoscience and Remote Sensing Symposium Digest, pp. 756-767, 1981.

Stewart, R.H., A Discus-Hulled Wave Measuring Buoy, Ocean Engng., 4, pp. 101-107, 1977.

Vesecky, J.F. and R.H. Stewart, The Observation of Ocean Surface Phenomena Using Imagery from the Seasat Synthetic Aperture Radar - An Assessment, submitted to J. Geophys. Res., 1981.

Vesecky, J.F., H.M. Assal and R.H. Stewart, Remote Sensing of Ocean Waveheight Spectrum Using Synthetic-Aperture-Radar Images, Proceedings of the COSPAR/SCOR/IUCRUM Symposium on Oceanography from Space, Plenum Press (in press), 1981.

Wright, J.W., W.J. Plant, W.C. Keller, and W.L. Jonse, Ocean Wave-Radar Modulation Transfer Functions from the West Coast Experiment, J. Geophys. Res., 85, pp. 4957-4966, 1980.

TABLE 1. SEA TRUTH AND SEASAT SATELLITE PARAMETERS FOR JASIN DATA.

Satellite Data				Sea Truth Data				SAR-Derived Estimates							
Pass	Date	Time (GMT)	Satellite Heading	Distance Between Sea Truth and SAR (km)	STS*	θ_T (T°)	λ (E)	$H_{1/3}$ (m)	U (m/s)	α_T (°T)	θ_T		λ		PBR
											OFT (°T)	FFT (°T)	OFT (m)	FFT (m)	
547	4 Aug. 78	0615	321	a	10	263	170	1.6	4.7	007	260	261	189	187	1.45
556	4 Aug. 78	2135	216	a	65	280	151	1.5	3.6	017	274	273	157	141	1.15
590	7 Aug. 78	0622	323	a	15	250	222	1.2	7.3	352	---	---	---	---	1.00
599	7 Aug. 78	2143	215	b/f	145	20	89	1.2	7.3	352	---	---	---	---	---
633	10 Aug. 78	0629	323	a	58	220	89	1.1	6.9	356	---	---	---	---	1.00
642	10 Aug. 78	2150	214	a	210	200	169	2.7	9.2	145	---	---	---	---	1.00
714	15 Aug. 78	2235	217	---	---	---	---	---	13.6	146	---	---	---	---	1.00
719	16 Aug. 78	0643	323	---	---	---	---	---	---	---	276	---	182	---	1.08
757	18 Aug. 78	2240	215	b	10	240**	256	4.9	7.6	304	248	---	164	---	1.16
762	19 Aug. 78	0641	324	d/f	45	240	210	5.5	15.2	186	253	---	275	---	1.21
791	21 Aug. 78	0724	325	b/f	35	230	151	3.1	12.0	186	234	227	241	231	2.17
834	24 Aug. 78	0730	324	a	55	295	147	2.8	13.0	235	252	252	174	169	1.81
958	1 Sept. 78	2354	215	c/b	32	354	108	1.4	10.7	271	271	---	180	---	1.16
1001	5 Sept. 78	0006	219	a	30	155	63	2.3	7.2	255	296	---	120	---	1.00
1006	5 Sept. 78	0815	322	a	70	109	105	3.6	13.5	111	125	---	81	---	1.47
1044	8 Sept. 78	0018	220	e/c	30	264**	244**	5.7	12.1	110	---	---	---	---	1.00
1049	8 Sept. 78	0827	323	c/e	30	264	244	5.0	11.5	195	257	264	344	321	2.56
1087	11 Sept. 78	0030	221	---	---	---	---	---	6.3	263	246	254	308	307	2.22
				---	---	---	---	---	13.2	040	253	---	299	---	1.88

* a. Atlantis II, pitch and roll buoy

b. Moored OIA, wave rider buoy

c. Discovery, pitch and roll buoy

d. John Murray, wave recorder

e. Discovery, wave recorder

f. John Murray, visual readings

** Estimate

TABLE 2. SUMMARY OF WAVELENGTH, HEIGHT, AND DIRECTION
DATA FOR JASIN DATA*

<u>Revolution</u>	<u>λ</u>	<u>$H_{1/3}$</u>	<u>θ_{AC}</u>
<u>None</u>			
590	89-222	1.2	73° - 39°
599	71	1.1	25°
633	89	1.1	77°
642	169	2.7	14°
1006	105	3.6	33°
<u>Poor</u>			
556	151	1.5	64°
714	182*	---	59°*
834	147	2.8	29°
958	108	1.4	31°
719	164*	---	76°*
<u>Good</u>			
547	170	1.6	58°
757	256	4.9	23°
762	210	5.5	90°
791	151	3.1	73°
1001	81	2.3	63°
1044	244*	5.7	44°
1049	244	5.0	57°
1087	299*	---	34°

* All data use sea truth estimates except for those denoted with an (*).

TABLE 3. DERIVED SEA TRUTH PARAMETERS FOR JASIN EXPERIMENT.

Pass	Wave Slope	v_0	$\sin \theta_{AC} v_0$	θ_A Sea Truth	θ_A OFT	θ_{AC} Sea Truth	θ_{AC} OFT	α_{SAR}	α_{wv}
547	0.009	0.339	0.288	122	119	58	61	44	76
556	0.010	0.338	0.305	64	58	64	58	71	83
590	0.054	0.223	0.213	107	---	73	--	61	78
	0.013	0.352	0.224	39	---	39	--	---	---
599	0.015	0.362	0.153	155	---	25	--	51	24
633	0.012	0.323	0.315	77	---	77	--	88	75
642	0.016	0.575	0.142	166	---	14	--	22	34
714	---	---	---	---	59	--	59	---	---
719	---	---	---	---	104	--	76	19	56
757	0.019	0.848	0.334	23	36	23	36	61	36
762	0.026	1.051	1.046	96	90	84	90	47	36
791	0.021	0.699	0.696	85	107	85	73	0	5
834	0.019	0.640	0.314	151	126	29	54	37	24
958	0.013	0.373	0.192	149	81	31	81	50	89
1001	0.037	0.803	0.718	117	87	63	87	18	44
1006	0.034	0.973	0.524	147	---	33	--	58	1
1044	0.023	1.011	0.705	44	38	44	38	65	69
1049	0.020	0.887	0.743	123	103	57	77	30	1
1087	---	---	---	---	34	--	34	86	57

TABLE 4. LINEAR CORRELATIONS BETWEEN WAVE CONTRAST (PBR) AND ENVIRONMENTAL PARAMETERS FOR JASIN SEASAT DATA.

<u>Parameter</u>	<u>Linear Correlation</u>
Wave Height	0.69**
Wavelength (Sea Truth)	0.55**
Wavelength (OFT)	0.71*
Wave Slope	0.02
Wave Direction Relative to Radar Look Direction (Sea Truth)	0.38
Wave Direction Relative to Radar Look Direction (OFT)	-0.05
Normalized Orbital Velocity	0.81*
Wind Direction Relative to SAR Look Direction	-0.07
Wind Direction Relative to Wave Direction	-0.18
Wind Speed	0.19

* Significant at $p = 0.99$
 ** Significant at $p = 0.95$

TABLE 5. MULTIPLE LINEAR CORRELATION COEFFICIENTS.

<u>Parameter</u>	<u>PBR</u>
$H_{1/3}, \lambda$	0.70**
$H_{1/3}, \sin \theta_{AC} v_0$	0.94*
$\lambda, \sin \theta_{AC} v_0$	0.88*
$\lambda, \sin \theta_{AC} v_0, H_{1/3}$	0.94*

* Significant at $p < 0.01$

** Significant at $p < 0.05$

TABLE 6. PEAK-TO-BACKGROUND (PBR) RATIO VERSUS TELEROTATION ADJUSTMENT AND AZIMUTH FOCUS SHIFT. (SEASAT SAR Revs. 762 and 1087, respectively)

<u>Telerotation Setting</u>	<u>PBR</u>	<u>S.D. *</u>
+9 ϕ	6.7	0.6
+7 ϕ	11.1	1.1
+5 ϕ	17.1	1.0
+3 ϕ	23.3	3.0
+2 ϕ	30.4	3.9
+ ϕ	31.2	2.3
0 (Stationary Target)	33.3	3.0
- ϕ	33.3	3.2
-2 ϕ	28.9	6.7
-3 ϕ	25.3	3.5
-5 ϕ	12.1	0.7
-7 ϕ	8.2	1.6
-9 ϕ	2.9	0.2

<u>Focus Shift</u>	<u>PBR</u>	<u>S.D. *</u>
+4P	5.9	1.3
+3P	10.2	1.4
+2P	12.7	2.3
+P	11.8	0.8
0 (Stationary Target)	18.4	2.6
-P	14.7	2.8
-2P	13.5	1.8
-3P	8.3	0.9
-4P	6.0	0.9

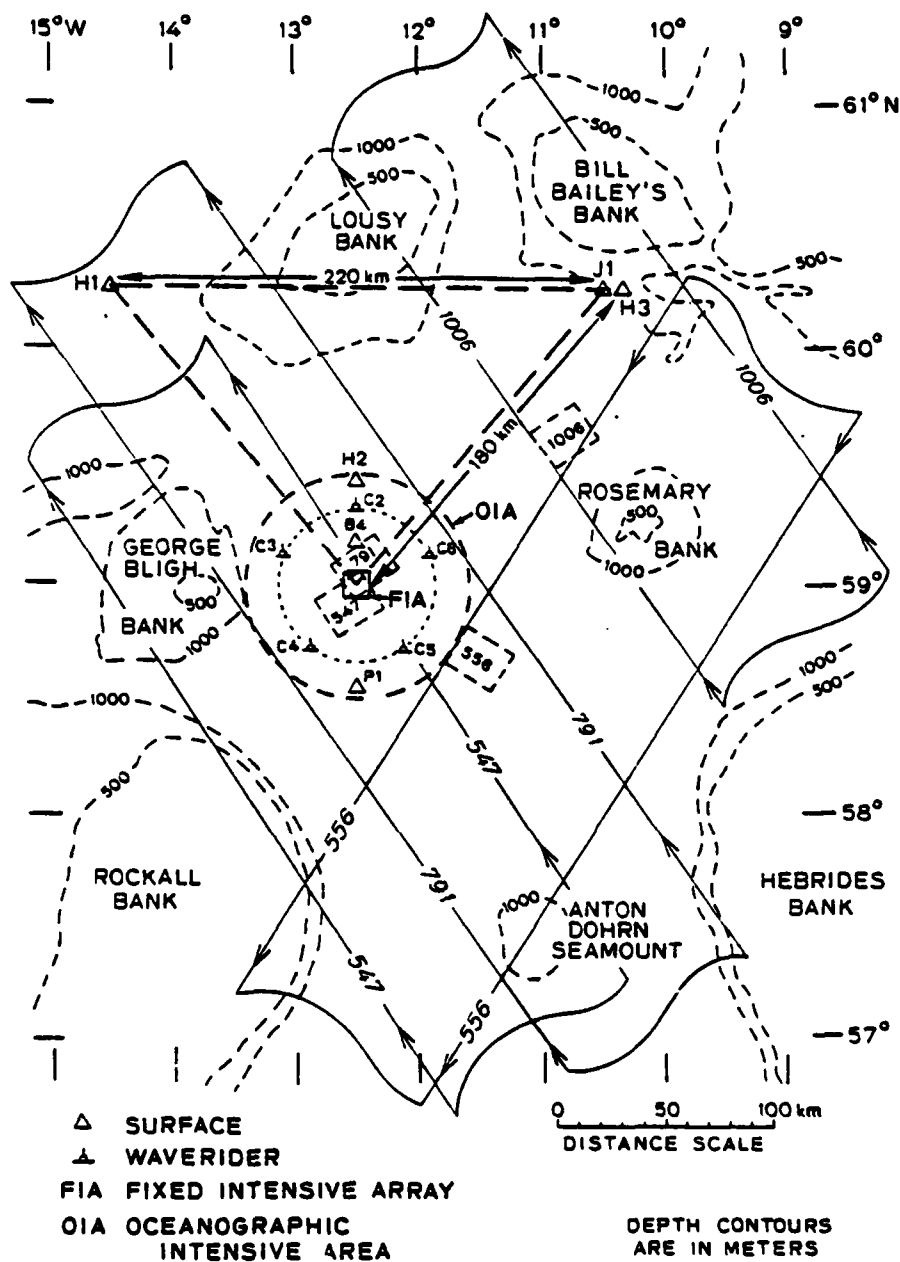
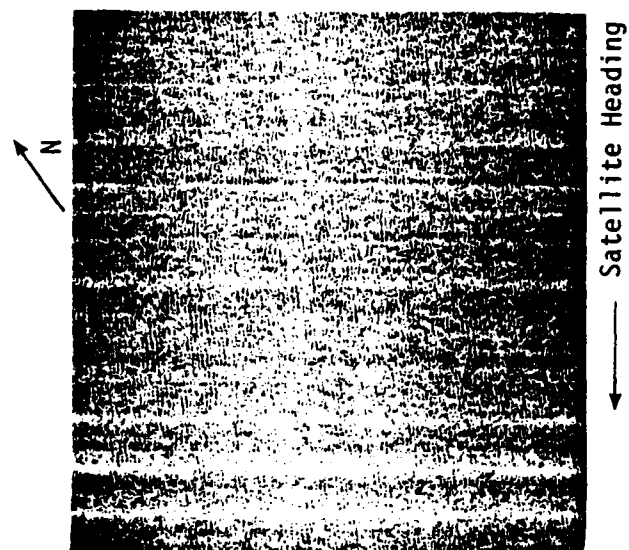


FIGURE 1. JOINT AIR-SEA INTERACTION (JASIN) EXPERIMENT AREA SHOWING TYPICAL SEASAT SAR IMAGE SWATHS AND SECTIONS OF IMAGES USED FOR WAVE ANALYSIS. (THE PERMANENTLY ANCHORED WAVERIDER BUOYS ARE DENOTED C2 THROUGH C6. THE SHIP DEPLOYED PITCH AND ROLL BUOYS WERE TYPICALLY SET IN THE FIA AREA. AFTER VESECKY, ET. AL., 1981.)



Revolution 762
19 August 1978
Wavelength(Wave Recorder) = 210 m.
Wave Direction = 2400 T

FIGURE 2. OPTICALLY PROCESSED SEASAT SAR DATA COLLECTED OVER THE JASIN TEST AREA (PROCESSED BY THE ENVIRONMENTAL RESEARCH INSTITUTE OF MICHIGAN).

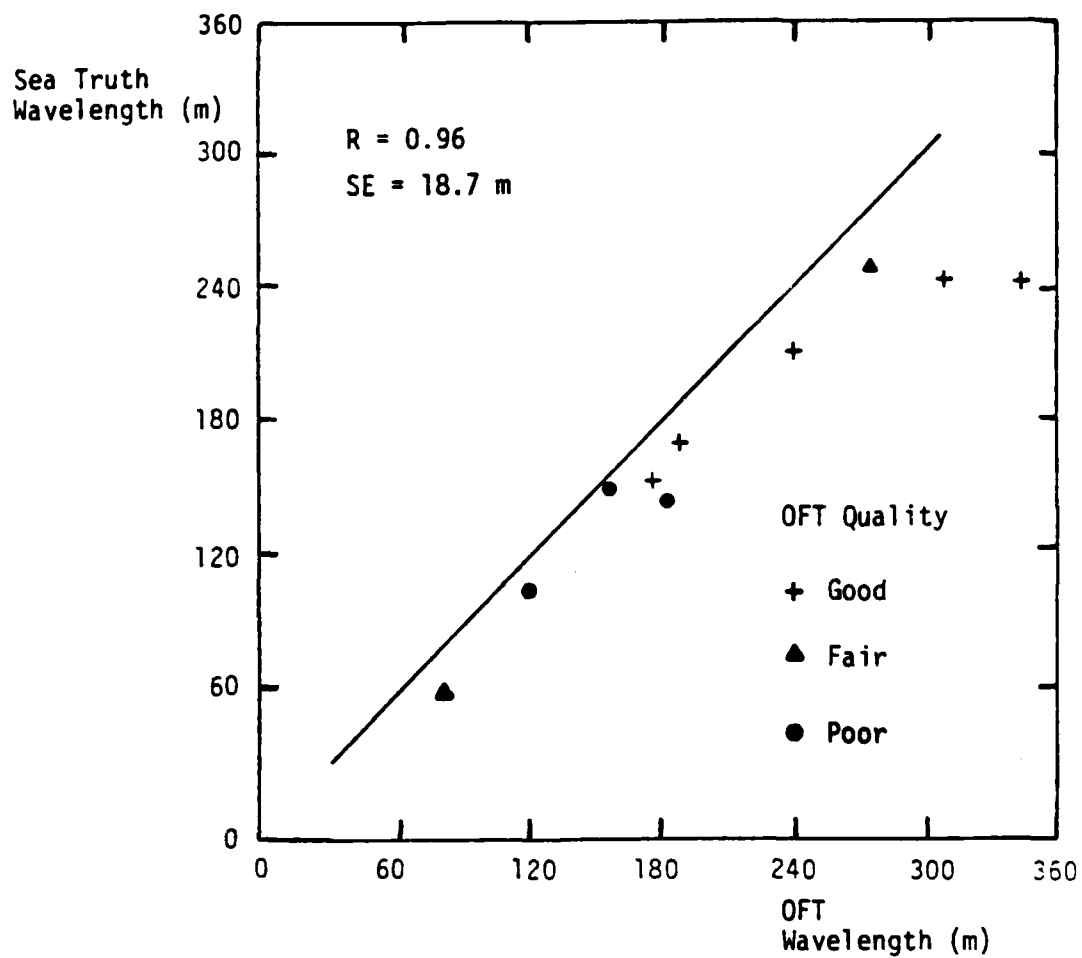


FIGURE 3. PLOT OF WAVELENGTH, SEA-TRUTH VERSUS OFT, FOR JASIN SEASAT DATA.

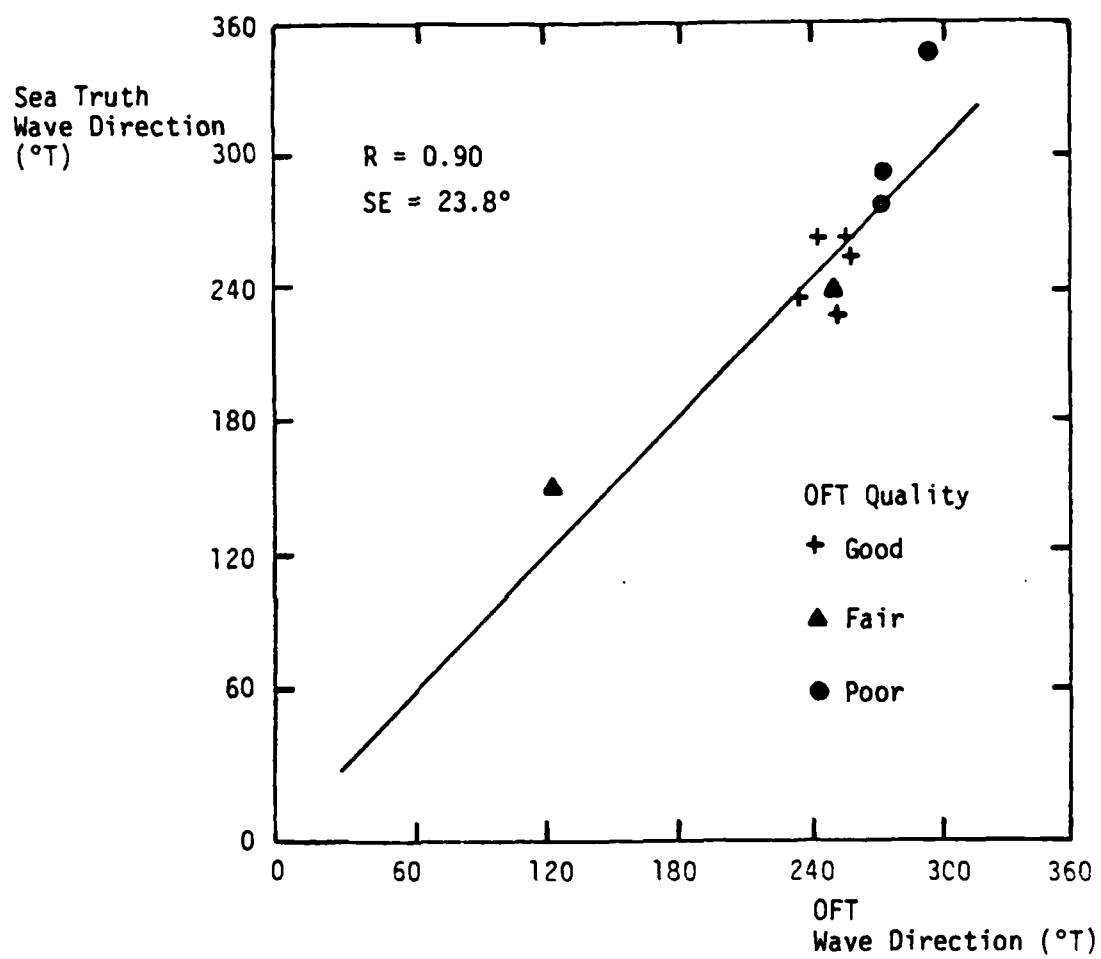


FIGURE 4. PLOT OF WAVE DIRECTION, SEA-TRUTH VERSUS OFT, FOR JASIN SEASAT DATA.

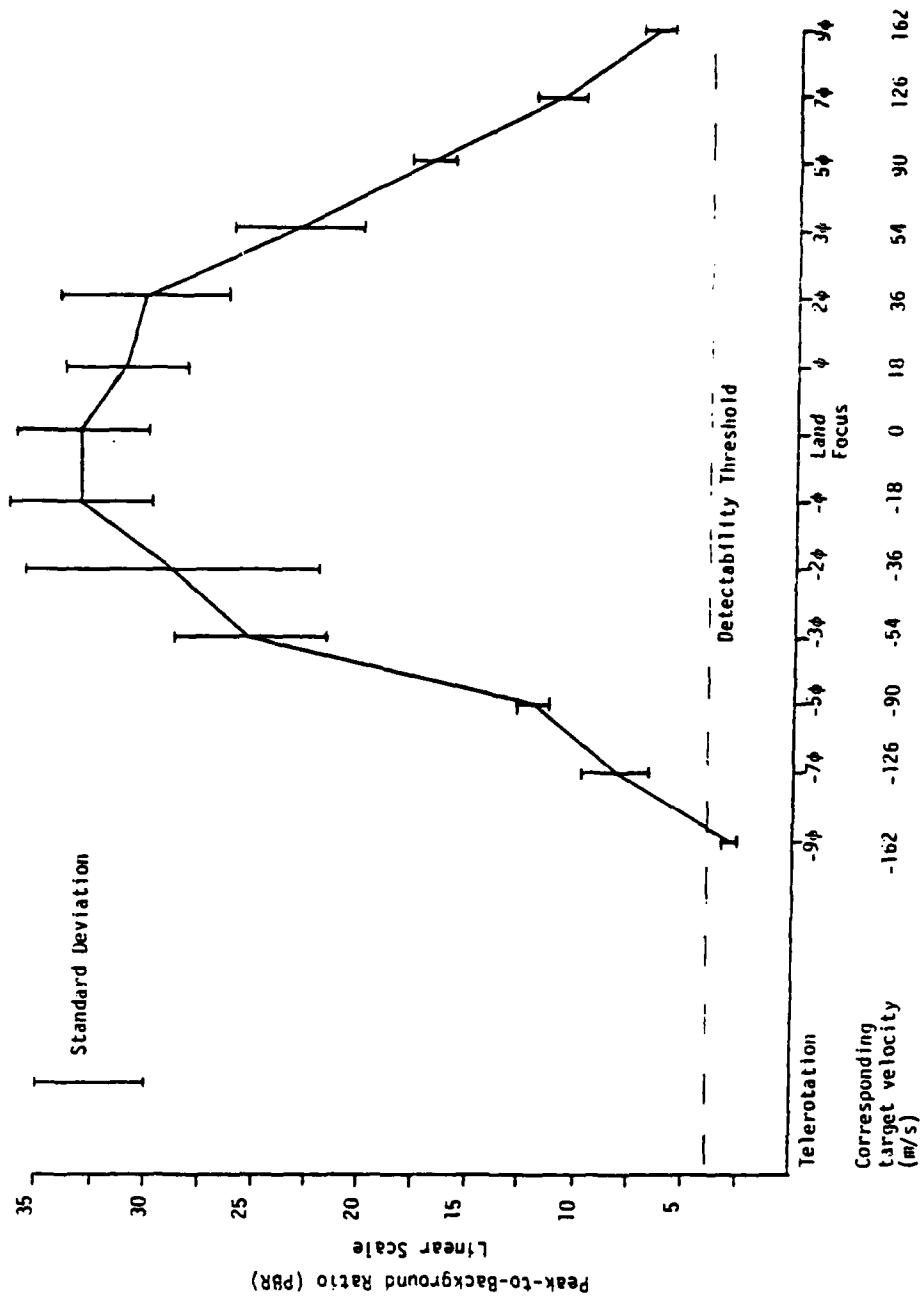


FIGURE 5. PEAK-TO-BACKGROUND RATIO VERSUS TELEROTATION ADJUSTMENT, SEASAT REV. 762.

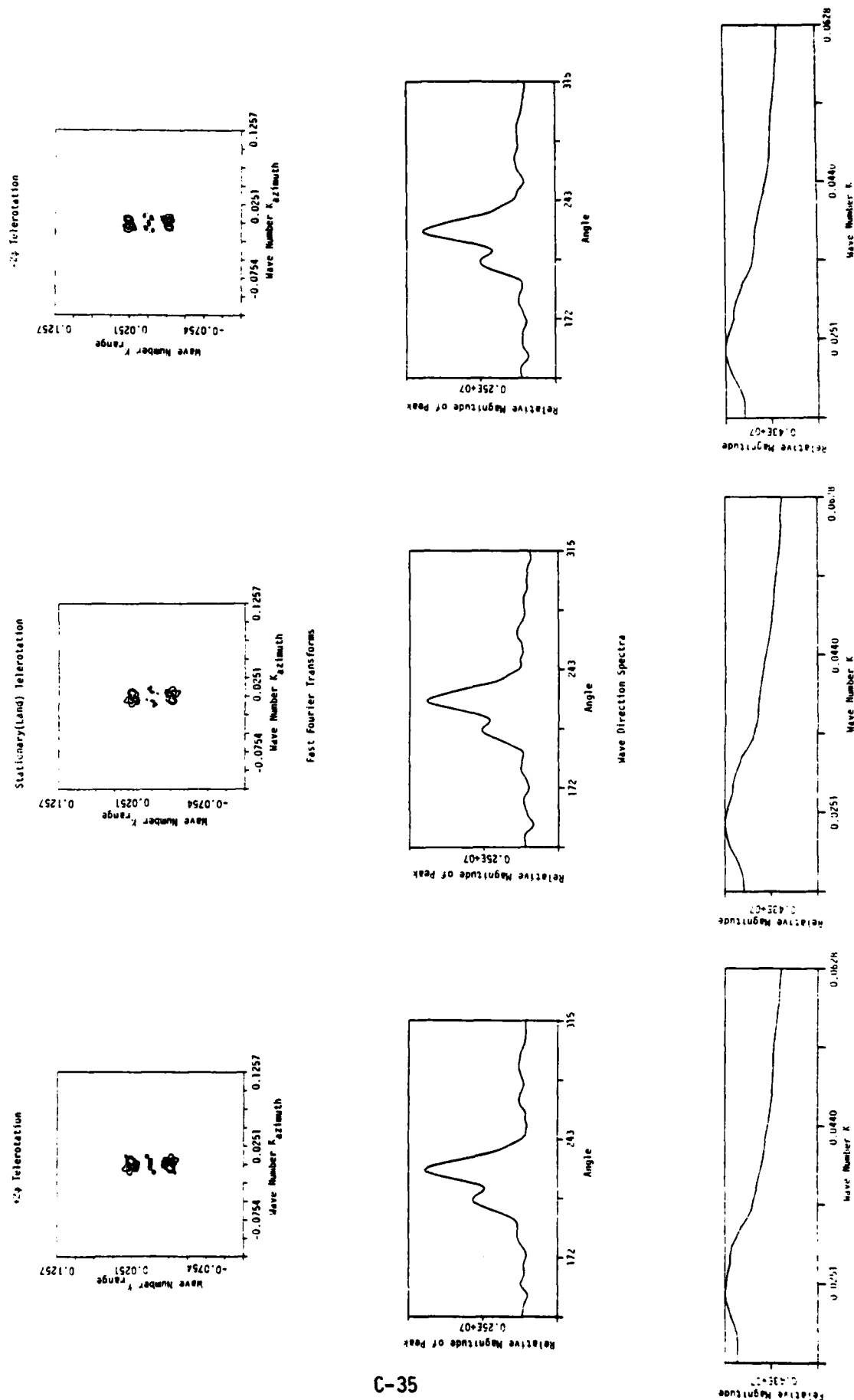


FIGURE 6. TWO-DIMENSIONAL FAST FOURIER TRANSFORMS AND ONE-DIMENSIONAL WAVE DIRECTION AND WAVE NUMBER SPECTRA VERSUS TELEROATION ADJUSTMENTS FOR SEASAT REV. 762 DATA.

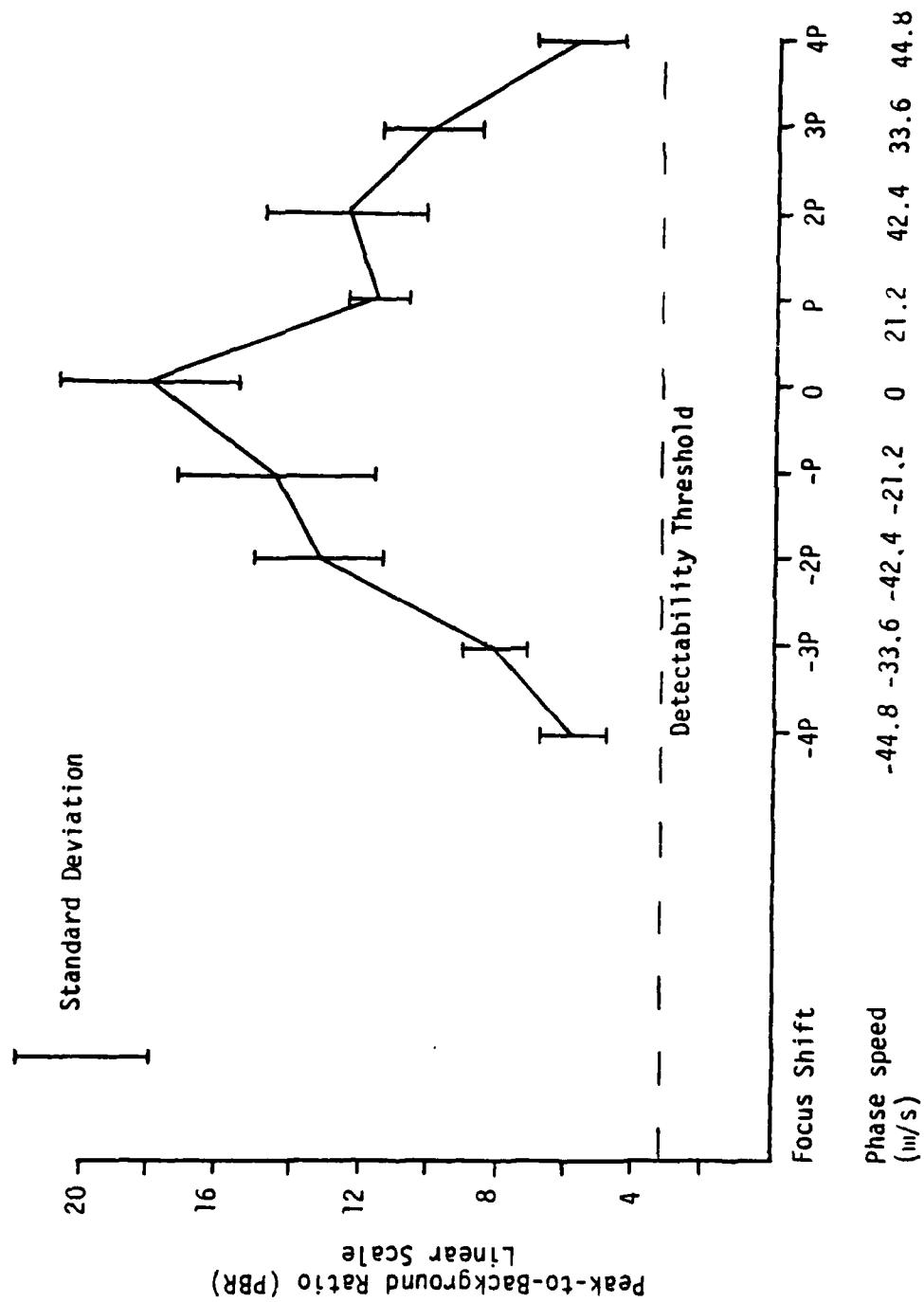


FIGURE 7. PEAK-TO-BACKGROUND RATIO VERSUS AZIMUTH FOCUS SHIFT, SEASAT REV. 1087.

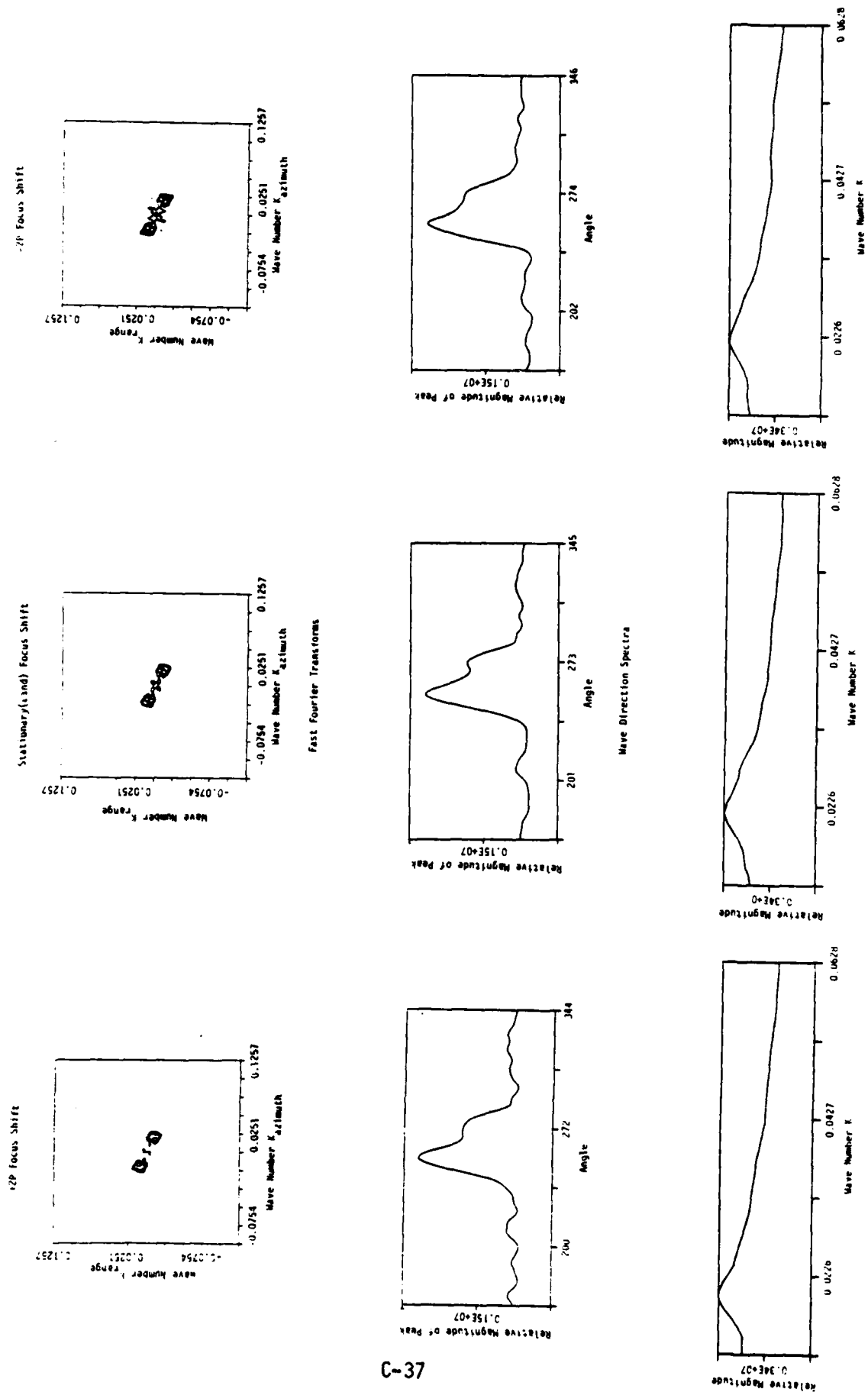


FIGURE 8. TWO-DIMENSIONAL FAST FOURIER TRANSFORMS AND ONE-DIMENSIONAL WAVE DIRECTION AND WAVE NUMBER SPECTRA VERSUS TELEROTATION ADJUSTMENTS FOR SEASAT REV. 1087 DATA.

Synthetic Aperture Radar Imaging of Ocean Waves: Comparison With Wave Measurements

WILLIAM MCLEISH,¹ DUNCAN ROSS,¹ ROBERT A. SHUCHMAN,² PAUL G. TELEKI,³
S. VINCENT HSIAO,⁴ O. H. SHEMDIN,⁴ AND W. E. BROWN, JR.⁴

Synthetic aperture radar images of ocean waves were obtained in conjunction with reference wave data near Marineland, Florida, December 14, 1975. Each of the various types of measurements were processed into a form that allowed direct comparisons with the others. Maxima of radar spectra occurred at the same frequencies as the maxima of reference wave height spectra. In a comparison of a radar spectrum with observed spectra of wave height, wave orbital velocity, and surface slope the high-frequency portion of the radar spectrum lay near and between the wave height and the orbital velocity spectra but differed significantly from the surface slope spectrum. The radar-derived mean directions and model-fitted directional spreads of wave energy were close to the values from a directional wave buoy and indicated the accuracy of radar measurements of wave direction. However, a directional plot of a radar spectrum near shore at the frequency of the maximum showed a sharper peak than such a plot of a fitted spectrum derived from reference data. The high directional resolution of the radar, in addition to its making observations at different locations, allowed radar images to provide information about ocean waves not available from the other instruments. As a swell propagated across the continental shelf, it was scattered in direction, apparently by the irregularities of the bottom, and very little of its energy reached shore. The shorter sea waves had a narrow directional distribution when first observed offshore that may have been sharpened by interaction with the Gulf Stream. Radar images showed effects of bottom refraction on the sea waves as they moved into progressively shallower water.

INTRODUCTION

The ability to obtain nearly synoptic directional wave information on a relatively large spatial scale is a goal actively pursued by some in the ocean research community. One approach to obtaining such information is through the use of imaging radar. *Crombie* [1955] was the first to associate radar backscatter with ocean waves with a wavelength of one-half the wavelength of the incident radar. *Wright* [1968] and *Bass et al.* [1968] proposed a composite theory wherein the level of backscatter was a function of the amplitude of the short (Bragg) waves and their local tilt due to the presence of an underlying longer wave. Thus if a radar beam properly scans the surface, theory predicts that the underlying waves will be imaged.

Indeed, real aperture radars have been in use since the mid-1950's by the Dutch to observe swell patterns at the entrances to harbors, and airborne systems have been utilized both by the Dutch [*De Loor and Brunsveld Van Hulten*, 1978] and in the USSR [*Bondarenko et al.*, 1972] since the early 1970's. Airborne synthetic aperture radar has been used to observe waves generated by hurricanes at L band [*Ross et al.*, 1974], while X band systems have observed features of the Gulf Stream [*Wright et al.*, 1976].

The Seasat A satellite was the first attempt to obtain wave imagery from space. Preliminary results from its data [*Gonzalez et al.*, 1979; *Teleki et al.*, 1979] show that useful imagery can be obtained.

The Seasat A results and previous studies were principally

concerned with wavelength and direction information. The results are encouraging, but it must be noted that the majority of waves imaged appear to have been swell and the limitations of the synthetic aperture approach in imaging local sea is not known.

According to the theory of synthetic aperture systems, as discussed by *Brown and Porcello* [1969], the location of a reflecting element on the earth's surface is determined by tracking the Doppler phase history of the returned signal. For a fixed surface, there is a unique Doppler relationship for the received radar signal from a given earth location. If the surface is in motion, however, as in the case of ocean waves, the Doppler history of the earth location is distorted, and the resulting image becomes 'defocused.' The amount of defocusing varies with the speed of the motions [*Alpers and Rufenach*, 1979].

In this paper we examine synthetic aperture imagery of ocean waves and compare characteristics of the derived radar spectra with wave spectra obtained from in situ instrumentation. Thus the frequency and directional properties of radar spectra are compared with those of height, orbital velocity, and slope spectra obtained from a buoy, orthogonally oriented current meters, pressure transducers, and an airborne laser wave profilometer. The different instruments were assembled in a joint experiment held off Marineland, Florida, in December 1975. The waves on that date had been generated over a fetch of 500-1000 km by a nearly steady east wind with a speed of about 10 m/s offshore and 3 m/s near the coast. Thus the offshore waves were in the downwind portion of an extended generating area, whereas those near shore had begun a modification toward swell under the decreased wind speeds. Propagation through the Gulf Stream and in shallow water caused additional changes in the waves.

The results of the study are both encouraging and inconclusive. The transfer function relating variations in the radar return signal to ocean waves depends in an as yet undetermined manner on several variables, including the state of the

¹ Sea-Air Interaction Laboratory, National Oceanic and Atmospheric Administration, Miami, Florida 33149.

² Environmental Research Institute of Michigan, Ann Arbor, Michigan 48107.

³ U.S. Geological Survey, Reston, Virginia 22092.

⁴ Jet Propulsion Laboratory, California Institute of Technology, Pasadena, California 91103.

This paper is not subject to U.S. copyright. Published in 1980 by the American Geophysical Union.



Fig. 1. Radar image of ocean waves near shore and reference wave measuring instruments: (1) ship operating pitch-roll buoy, (2) UF wave-recording tower, (3) ship operating wave tower, (4) ship recording background data, and (5) surf and five groins extending from the beach. The sea sled was inshore of the pitch-roll buoy. The 15 squares are the regions of individual radar spectra, where each side represents 683 m.

sea, the aspect angle from which the waves are viewed, and the operating characteristics of the radar. Thus no single study is likely to provide a satisfactory knowledge of the function. We are, however, more knowledgeable than we were before

and believe that the cumulative results will lead to the capability of observing remotely the complete two-dimensional wave energy spectrum when in conjunction with a reference airborne wave-measuring instrument.

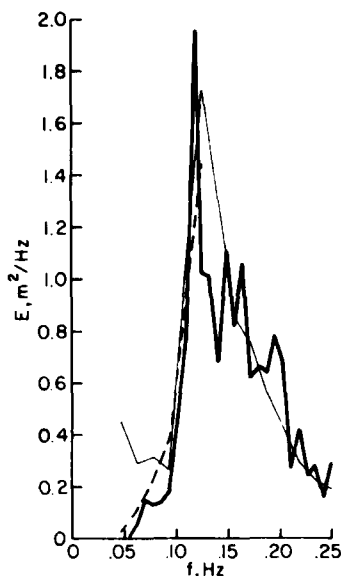


Fig. 2. Intercomparison among reference wave height spectrum measurements: pitch-roll buoy (light solid curve), UF tower (heavy solid curve), and sea sled (dashed curve). E is variance density.

Preliminary portions of the present results were included in the studies by Shemdin *et al.* [1978a], Hsiao [1978], and Teleki *et al.* [1978].

RADAR WAVE MEASUREMENTS

Images of ocean waves were recorded by an X and L band airborne synthetic aperture radar viewing the sea surface at large depression angles [Shemdin *et al.*, 1978a]. In the present study, only horizontally polarized X band ($\lambda = 3.2$ cm) radar data obtained on December 14, 1975, are examined. The radar images showed that the ocean waves were traveling in a direction about 20° – 30° from the range direction. Theoretical considerations suggest that range-traveling waves give optimum patterns on synthetic aperture radar images [Shuchman and Zelenka, 1978]. The radar image in Figure 1 shows ocean waves near shore, the areas of radar image analysis, and the locations of the reference instruments. Since the waves in the areas of radar analysis appear to be similar to those at the locations of the reference instruments, comparison of the results is considered to be appropriate.

An image film was obtained from the radar signal film through an optical Fourier transform [Shuchman and Zelenka, 1978]. Measurements of the optical transmissivity of the image film over the areas marked in Figure 1 produced sets of digital data. An offset weighted filter was used to correct for the distortion resulting from the slant range-ground range difference.

Two-dimensional Fourier transforms of geometry-corrected digital data were calculated by a fast Fourier transform technique after the method of Rabiner and Gold [1975]. According to this method the transforms are given by

$$F(k_1, k_2) = \sum_m \sum_n A_{mn} e^{i k_1 x_m} e^{i k_2 y_n} \quad (1)$$

where k_1 and k_2 are orthogonal components of wave number k , $k_1^2 + k_2^2 = k^2$, $k = 2\pi/L$, L is the wavelength, and each A_{mn}

is the optical transmissivity at an image location. Wave number spectra were obtained with

$$S(k_1, k_2) = |F(k_1, k_2)|^2 / (\Delta k_1 \Delta k_2) \quad (2)$$

The propagation of waves while they are being scanned by a moving sensor may introduce a significant distortion into the record. The effects of wave motion on spectra derived from several types of measurements were examined by Long [1979]. The wind caused a lateral motion of the aircraft, but its effect on the results of the radar measurements was negligible in the present experiment. Under these conditions, Long's equations show that each component of the spectrum is shifted aft by a distance

$$\Delta k_1 = -k \cdot (c/v) \quad (3)$$

where c is the phase speed of the waves at that wave number and water depth and v is the aircraft speed. The change in the wave number of an estimate causes a change in the density of that estimate given by

$$\Delta S/S = \frac{1}{2}(c/v) \cos \alpha \quad (4)$$

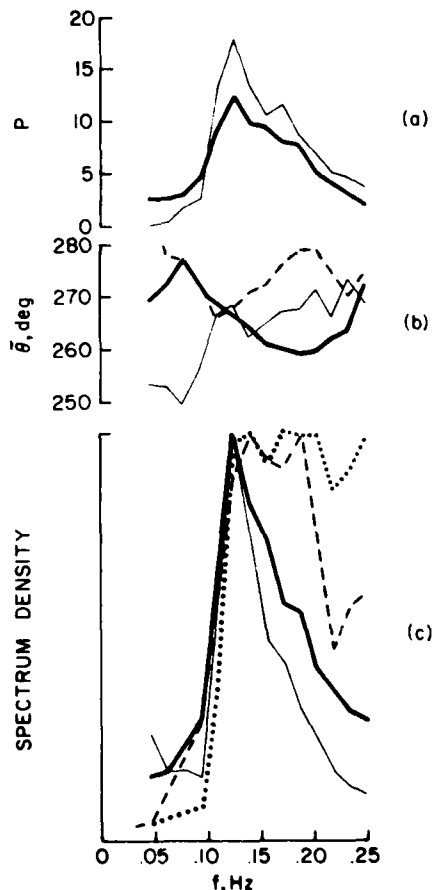


Fig. 3. Calculations from radar data (heavy solid curves) compared with those from reference instruments. (a) Cosine spread exponent factor $P(f)$. (b) Mean direction $\theta(f)$, same instrument designation as below. (c) Wave height spectrum from pitch-roll buoy acceleration (light solid curve), peak at $1.73 \text{ m}^2/\text{Hz}$; orbital velocity spectrum from sea sled (dashed curve), peak value is $1.30 \text{ cm}^2 \text{ s}^{-2} \text{ Hz}^{-1}$; and surface slope spectrum from pitch-roll buoy tilt (dotted curve), peak value is $0.0127 \text{ rad}^2/\text{Hz}$.

where α is the angle between aircraft and wave propagation directions. These two effects were removed prior to further calculation.

One-dimensional wave number spectra were calculated with

$$S(k) = \sum_{n=1}^{179} S(k, \theta_n) k \Delta \theta \quad (5)$$

where $S(k, \theta_n) = S(k_1, k_2)$ with $k_1 = k \sin \theta_n$, $k_2 = k \cos \theta_n$, $\theta_n = \theta_{n-1} + \Delta \theta$, and $\Delta \theta = 1^\circ$. The initial values of θ_n were selected in order to include those portions of the two-dimensional spectra that occurred within 90° of selected dominant wave directions.

Frequency spectra were obtained from wave number spectra by using the transformation

$$S(f) = S(k) \Delta k / \Delta f \quad (6)$$

where Δk and Δf are the differences between the boundaries of spectrum estimates. More stable spectra were obtained by combining the results of 15 adjacent squares in each image. The amplitudes of these spectra were normalized with respect to those of the reference spectra at the peak frequencies.

Directional properties of the waves recorded by the radar were examined following the approach given by *Longuet-Higgins et al.* [1963]. For each value of f evaluated, the first two Fourier harmonics of $S(k, \theta_n)$ were calculated by direct transformation with

$$a_1 + ib_1 = \frac{1}{T} \sum_{n=1}^{179} S(k, \theta_n) \cos \theta_n + \frac{i}{T} \sum_{n=1}^{179} S(k, \theta_n) \sin \theta_n \quad (7)$$

$$a_2 + ib_2 = \frac{1}{T} \sum_{n=1}^{179} S(k, \theta_n) \cos 2\theta_n + \frac{i}{T} \sum_{n=1}^{179} S(k, \theta_n) \sin 2\theta_n \quad (8)$$

where

$$T = \sum_{n=1}^{179} S(k, \theta_n)$$

A smoothed directional distribution function was calculated with

$$G(\theta) = \frac{1}{2} + \frac{1}{2} (a_1 \cos \theta + b_1 \sin \theta) + \frac{1}{2} (a_2 \cos 2\theta + b_2 \sin 2\theta) \quad (9)$$

and the mean direction was obtained with

$$\bar{\theta} = \tan^{-1}(b_1/a_1) \quad (10)$$

The exponent factor of a cosine fit to the directional distribution of the form

$$E(\theta) = \cos^{2P(\theta)} \{(\theta - \bar{\theta})\} \quad (11)$$

was approximated following *Mitsuyasu et al.* [1975] with

$$P(f) = 1/[1 - (a_1^2 + b_1^2)^{1/2}] - 1 \quad (12)$$

REFERENCE WAVE MEASUREMENTS

A pitch-roll buoy similar to one described by *Longuet-Higgins et al.* [1963] was operated on December 14, 1975, in approximately 10-m water depth at the location shown in Figure 1. A series of nine consecutive 34-min records were processed. During the 5 hours of measurement, no significant changes in the wave properties were found; hence the data were com-

bined in one calculation. Estimates at groups of adjacent frequencies were averaged to produce a spectrum with more than 500 degrees of freedom. The filtered acceleration spectrum was divided by the radian frequency to the fourth power to give a wave height spectrum [*Cartwright*, 1963]. The sum of the pitch spectrum and the roll spectrum constituted a spectrum of surface slope. Directional Fourier coefficients of the first two harmonics were calculated as given by *Longuet-Higgins et al.* [1963] and elaborated on by *Cartwright and Smith* [1964]. Directional parameters were calculated from the coefficients as was done in the previous section with radar measurements.

A sea sled provided measurements of pressure and horizontal water velocity components at a height of 1 m above the bottom [*Teleki et al.*, 1975]. A series of 4½-min records at different depths was used to generate spectra with 24 degrees of freedom. The mean water velocity varied between records, but values outside the surf line averaged about 10 cm/s to the south. A wave height spectrum was obtained from the 8.2-m depth pressure spectrum by using equations for linear waves [*Kinsman*, 1965], but only the low-frequency portion of this spectrum is considered to be accurate. The sum of the spectra of the two velocity components in that record was taken as an orbital velocity spectrum and corrected for depth. The mean direction $\bar{\theta}$ at each frequency was calculated from the spectra of velocity components as $\tan^{-1}(S_1(f)/S_2(f))^{1/2}$.

A second pressure sensor was mounted on a tower in shallow water operated through the University of Florida (see Figure 1). A combination of four short records taken during 3½ hours gave a pressure spectrum with about 22 degrees of freedom. The pressure spectrum was converted to a wave height spectrum as described above.

A Spectra Physics laser profilometer aboard the NASA CV-990 aircraft was operated farther offshore. Each record was processed with the assumption that the waves traveled in deep water in a single direction determined from the corresponding radar image [see *Long*, 1979]. Averages of spectra of contiguous records gave 56 and 98 degrees of freedom.

Figure 2 shows wave height spectra obtained from concurrent records from three of the reference instruments, and they seem to be in good agreement. Wave acceleration becomes small at low frequencies, and wave height spectra derived from acceleration records are less accurate in that frequency region. However, pressure-derived spectra are highly accurate in that region. The combined instruments provide an accurate representation of the wave conditions at the Marine-land site.

COMPARISONS OF WAVE HEIGHT SPECTRA

A normalized one-dimensional frequency spectrum derived from the radar image in Figure 1 is compared in Figure 3c with corresponding reference spectra of wave height, orbital velocity, and surface slope. The radar spectrum is a corrected version of that presented by *Shemdin et al.* [1978a] and *Teleki et al.* [1978]. Figures 4a and 4b contain spectra from two radar images at distances of 90 and 30 km from shore in water depths of 60 and 22 m, respectively, normalized to and compared with wave height spectra derived from the laser profilometer data. In each case the frequency of the peak of the radar spectrum is in good agreement with that of the wave height spectrum, although the frequency of the peak changed

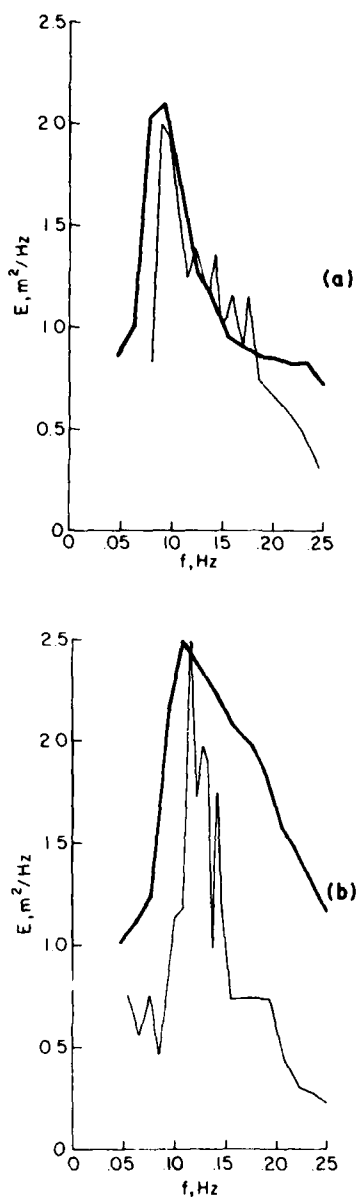


Fig. 4. Comparison of normalized radar spectra (heavy curves) at depths of (a) 60 m and (b) 22 m with the nearest laser profilometer wave height spectra (light curves). E is variance density.

with distance offshore. All of the spectra have steep slopes at lower frequencies.

The slope of the high-frequency portion of the radar spectrum in Figure 3 is much different from the same region of the surface slope spectrum. The radar slope will depend on the signal transfer function relating the data values used in the spectrum calculation to the original radar signal intensities. Since the photographic stages in the initial signal processing were not calibrated, it has not been possible to determine this relationship accurately. However, the difference in slope between the radar and surface slope spectra shows that the present radar images of large waves did not result predominantly from the slopes of those waves. Such a result might be expected with the large depression angles of the radar beam that

were used. Although the high-frequency portion of the radar spectrum in Figure 3 lies between the spectra of wave height and of orbital velocity, the high-frequency parts of the radar spectra in Figure 4 do not show a consistent relationship with the reference spectra. Nevertheless, the slope of this region of a radar spectrum generally does lie close to that of the wave height or orbital velocity spectrum, which suggests that a dependence on some aspect of the wave spectrum exists.

A few limited studies of the slopes of the high-frequency regions of radar wave spectra have been reported in the literature. In an early experiment, Myers [1958] compared spectra from vertically and horizontally polarized radar power signals with a wave height spectrum from a wave gage. The slopes in the high-frequency regions of the radar spectra varied considerably. In general, however, the vertically polarized radar spectra tended to lie close to the reference spectra, but the high-frequency portions of the horizontally polarized radar spectra decreased at a rate less steep than that of the reference. Zamaryev and Kalmykov [1969] considered that their non-scanned radar signals at a shallow depression angle represented the slopes of water waves traveling in one direction. A wave height spectrum derived from the radar matched a reference spectrum and supported their assumption of wave slope effects.

A single sea state will give radar wave height spectra with different high-frequency slopes under different operating conditions. The different conditions can call into play different mechanisms of radar response by ocean waves to much different extents. Within the range of variability that the differences between mechanisms introduce, the present wave height spectrum comparisons are considered to be consistent with the previous studies. However, the present spectra appear not to have been produced by a single mechanism, and the present limited comparison has not evaluated the mechanisms of radar return acting under these conditions.

WAVE DIRECTION MEASUREMENTS

Since the pitch-roll buoy cannot give directional spectra $E(\theta)$ directly, results from the buoy may be examined only with respect to directional wave models that are fit to the data. Two separate models are used: one derived from the pairs of coefficients of the first two harmonics of a directional Fourier transform $G(\theta)$ (Equation (9)) and one consisting of a cosine power function $P(f)$ (Equation (11)). For comparison with the buoy results, then, the radar data were calculated in terms of these two directional spread models.

In Figure 3b the mean wave directions $\theta(f)$ derived from the radar image in Figure 1 through a partial directional Fourier transform (equations (7) and (10)) are compared with the corresponding values from the buoy and from the sea sled. The values from the different instruments are close at those frequencies where significant wave energy is shown in Figure 3c. At other frequencies, however, none of the three curves agree closely.

In Figure 3a the cosine power fit value $P(f)$ (Equation (11)) from the radar is in approximate agreement with the values from the buoy. The difference between the maximum values of 18 from the buoy and 12 from the radar may be attributed to a background noise in the radar data. Also, the directional spectrum $G(\theta)$ at 0.125 Hz reconstituted with Fourier coefficients from radar data near shore is in good agreement with the corresponding spectrum from the buoy (Figure 5). These

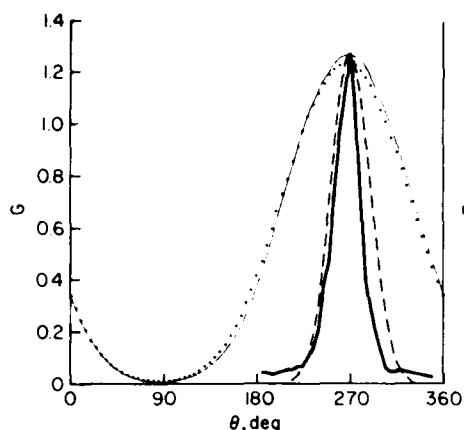


Fig. 5. Directional distribution of wave energy. The function $G(\theta)$ at 0.125 Hz was derived from the buoy (light solid curve) at 10-m depth and from the radar (dotted curve) at 14-m depth. E (dashed curve) was calculated from P (0.125 Hz) derived from the buoy. The normalized energy distribution from the radar two-dimensional spectrum $S(k, \theta n) = E$ (heavy solid curve), with the value of k for a frequency of 0.125 Hz, is shown for comparison.

comparisons demonstrate that radar can furnish directional distribution measurements of ocean waves equivalent to those from a buoy. In addition, to the extent that the two wave direction models that were used represent the ocean wave field the radar and the buoy appear to have recorded the waves similarly. Shuchman and Zelenka [1978] describe a possible directional variation in the transfer function relating radar measurements to ocean waves that would give an emphasis to waves traveling in the range direction. The comparisons indicate that such a directional variation must not have been great in the present radar measurements. Further evidence of the small directional variation of the transfer function in these radar data results from the observation that the radar directional spectra $E(\theta)$ in Figures 5 and 6 are approximately symmetrical even though the peaks of the directional spectra were 20°–30° from the range direction.

The spread of a directional wave spectrum at one frequency may be characterized by a one-half power width representing the difference between the directions at which the energy density is one half of the maximum. Since the quantity $P(f)$ commonly is given as a representation of a directional spectrum of ocean waves, it might be expected that a one-half power width calculated with a value of $P(f)$ from the buoy would match the width observed directly from the radar spectrum. However, the maximum value of $P(f)$ from the buoy gives a width of 45° in Figure 5, while the radar peak $E(\theta)$ shows a width of 30°. That this difference may result from the procedure for calculating $P(f)$ is suggested by the calculation of a width of 55° with a value of $P(f)$ derived from the same radar data that show the 30° width in Figure 5. These greater widths of the fitted models are ascribed to the differences between the possible shapes of the two directional models and the actual wave directional spectrum. In particular, it appears that with narrow peaks the energy density at directions much different from the direction of the maximum can modify the value of $P(f)$ significantly. As a result the present observations provide an example in which the model-fitting techniques used for analysis of buoy data cannot fully describe the directional wave spectrum. In addition, the radar measurements allow a significantly greater directional resolution than do the buoy observations.

Directional properties of waves on the open ocean have been examined through buoy measurements in some previous studies. The directional widths varied with the state of development of the waves, but the widths were more consistent in a generating area than elsewhere and had minimum values at the frequencies of maximum wave energy. Maximum values of $P(f)$ have been reported for waves in a generating area in several of those studies: approximately 7 [Longuet-Higgins *et al.*, 1963], 13 [Cartwright, 1963], 16 [Ewing, 1969], and mostly less than 15 [Mitsuyasu *et al.*, 1975]. The present buoy data yield a maximum value of $P(f)$ of 18. Although the buoy measurements were obtained outside the wave-generating area, in shallow water, and near a shore, the radar directional distributions in Figure 6 show that the waves farther offshore and in the generating area also had narrow directional peaks. The narrow directional spectrum of waves shown by the radar can be understood only if either the buoy techniques do not fully describe the narrowness of wave directional spectra or the waves in the present study for some reason have a unique directional structure. Tayfun *et al.* [1976] calculated changes in the waves having a broad directional spectrum when they encountered a transverse current. The changes led to a sharp peak in the directional distribution. Satellite infrared observations show that the Gulf Stream was east of the locations of the present measurements [Weissman *et al.*, this issue]. If, indeed, waves in a generating area have a wide spread, it seems possible that the narrowness of the directional spectrum of the deepwater waves in Figure 6 should be attributed to refraction by an ocean current.

Tyler *et al.* [1974] obtained directional spectra of waves on the open ocean with a different synthetic aperture radar technique and examined the fine structure within their broad directional distributions. A particular lobe of energy within one range bin was not found to occur at a later time in the appropriate different range bin. In the data of Figure 6 the 60-m depth plot shows a minor lobe of wave energy propagating at about 30° to the right of the main peak, and this lobe is also apparent on the 22-m depth plot. Although the second lobe is

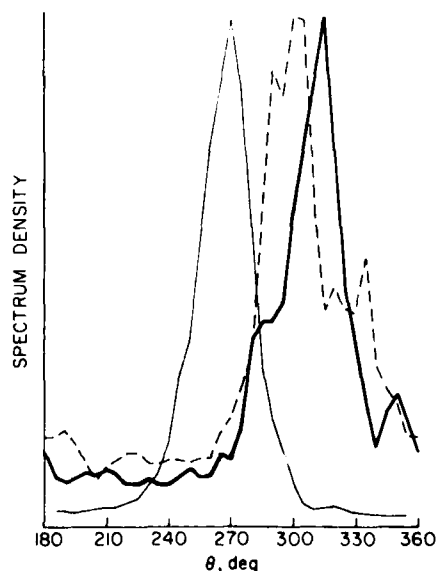


Fig. 6. Directional distribution of wave energy at 0.125 Hz from radar observations at depths of 60 m (heavy solid curve), 22 m (dashed curve), and 14 m (light solid curve). Amplitudes were adjusted to give the same energy at each peak.

not distinguishable from the main lobe nearer the shore, the occurrence of the second lobe at two locations 60 km apart suggests that it is not a random variation in the data. The ability of the present radar images to show wave trains at the same frequency but traveling in different directions is an improvement over the performance of other wave-recording instruments.

The directional spectra at 0.125 Hz from the radar image near shore were averaged at three different depths of water and are shown in Figure 7. The spectral amplitudes were not normalized. The energy distribution in the shallowest water was the narrowest, with a peak value 30% greater than the peak value in the deepest water. In contrast, the small amount of wave energy traveling more than 45° from the shoreward direction of 250° averaged about 30% less in the shallowest water than in the deepest water. The decrease is attributed to the turning of waves traveling largely along the coast toward the shore. The opposite directions of the two differences above cannot both be attributed to the methods of radar image formation or data processing, and the changes with depth appear to represent the effects of bottom refraction. The changes in mean direction shown in Figures 6 and 7 are not examined in this study.

The directional spreads of wave energy as indicated by $P(f)$ derived from three radar images at locations across the continental shelf are shown in Figure 8. There was insufficient wave energy at frequencies less than 0.07 Hz to allow interpretation of the spread calculations. Waves with frequencies greater than 0.14 Hz propagated mostly in deep water, and the spread did not change greatly across the shelf, except that waves in the lower frequencies show a narrower spread at a depth of 14 m. Since the water depths there were about 0.2 times the deepwater wavelength, the change may be attributed to bottom refraction.

In contrast to the directional narrowing near shore the waves with frequencies of 0.07–0.14 Hz show an increase in directional spread between depths of 60 and 22 m. The water depth varies from 0.07 to 0.75 times the deepwater length of these waves. It has been recognized that waves traveling in shallow water can be scattered in direction by irregularities in the bottom. Oakley and Leverette [1979] calculated that under possibly similar conditions of relative water depth and bottom roughness a narrow distribution in wave direction would be widened and the peak value would be reduced in energy by

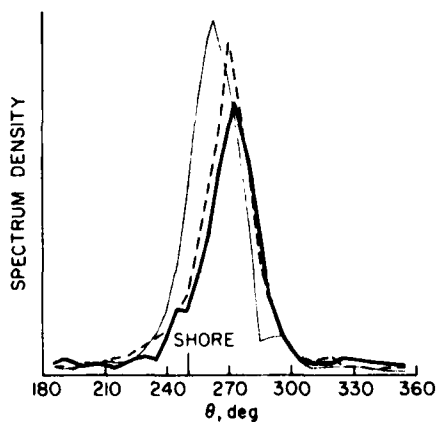


Fig. 7. Directional distribution of wave energy at 0.125 Hz at depths of 16 m (heavy solid curve), 14 m (dashed curve), and 12 m (light solid curve) in a single radar image. The amplitudes were not adjusted in this figure. The direction toward the shore was 250°.

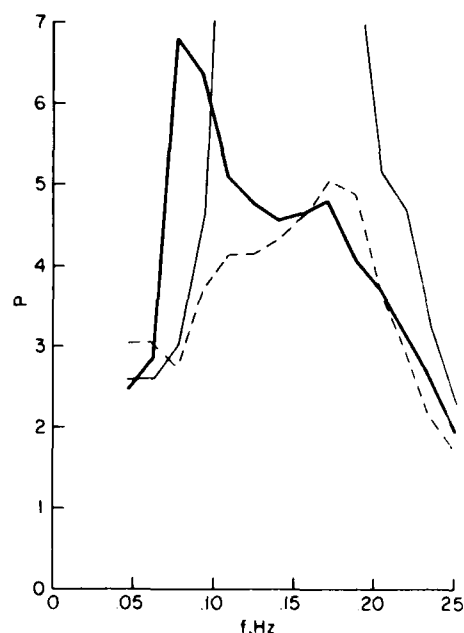


Fig. 8. Cosine spreading exponent $P(f)$ from radar observations at depths of 60 m (heavy solid curve), 22 m (dashed curve), and 14 m (light solid curve). The maximum value of the 14-m plot (off scale) is 12.

one half because of bottom scattering while traveling only 12.5 km. The distance between the present radar images at 60- and 22-m depths is 60 km, and it appears that the widening of the directional spread of these waves might be attributed to bottom scattering. In addition, a comparison of Figures 3c and 4a shows that only 10% of the wave energy at 0.08 Hz survived the passage across the continental shelf. Long [1973] predicted that a scattering in direction of waves by bottom irregularities would eventually cause some energy to be scattered into an offshore direction and lead to a decrease in energy near shore. These data could be an observation of that effect. Other possible causes of the decrease in wave energy were discussed by Hayes [1977] and by Shemdin et al. [1978b].

CONCLUSIONS

Radar images of ocean waves gave values for the frequency and mean direction of the dominant waves in good agreement with reference measurements, although no wave height measurements from the radar were possible. An original goal of the Marineland experiment was to determine the mechanism of formation of radar patterns representing ocean waves by comparison with surface measurements [Shemdin et al., 1975]. The determination was to be accomplished in part through comparison of the high-frequency slopes of the different spectra. Although the comparison showed that the effect of wave slopes was not the dominant mechanism of image formation under the present conditions, these data did not allow the mechanism to be specified further.

When the radar data were calculated in a manner parallel to that used for the buoy data, they gave a directional spectrum close to that from the buoy, except that the directions from the radar contained a 180° ambiguity. However, the radar directional distribution calculated directly had a peak much narrower than the peaks from the fitted models and showed the high directional resolution of the radar. This reso-

lution was apparent in two radar directional spectra that contained peaks in two different directions at a single frequency.

The differences between the fitted models and a directly calculated radar directional spectrum raises a possible question as to the appropriateness of current models in describing a directional distribution of waves on the open ocean. The present observations do not answer this question, but if previous measurements with fitted models do apply to unaltered ocean waves, the directional distribution of deepwater waves observed here may have been made narrower by a transverse ocean current. Waves in shallow water showed further directional narrowing that resulted from bottom refraction. The narrow directional distribution of a swell offshore became much wider as it traversed the continental shelf in relatively shallow water, apparently as a result of bottom scattering, and only a small fraction of its energy reached the coast.

The present observations strongly support the expectation that airborne radar accompanied by an independent airborne means of obtaining absolute wave height information (such as a pulsed radar altimeter or a laser profilometer that measures a one-dimensional wave height spectrum) can give complete two-dimensional spectra of ocean waves. These spectra could be obtained at a number of different locations nearly synoptically in a manner that seldom would be possible with in situ instrumentation.

Acknowledgments. Funds for this study were provided by the NOAA NESS Spacecraft Oceanography Project, the California Institute of Technology Jet Propulsion Laboratory, the Office of Naval Research, and the U.S. Army Corps of Engineers. Radar data were obtained and transformed to images by the Environmental Research Institute of Michigan. Digital values were obtained from the images and corrected for geometric distortion, and two-dimensional Fourier transforms were calculated at the Jet Propulsion Laboratory. The remaining calculations were performed at the Sea-Air Interaction Laboratory. Reference data were collected by the Sea-Air Interaction Laboratory, the U.S. Army Coastal Engineering Research Center, the University of Florida, and the NASA Ames Research Center. The authors are grateful to the many people who assisted in obtaining and processing the data used here. Particular thanks are due to Robert Berles, G. L. Howell, J. Losee, Frank Musialowski, Ron Peterson, R. Rawson, T. W. Thompson, and G. Tober.

REFERENCES

- Alpers, W. R., and C. L. Rufenach, The effect of orbital motions on synthetic aperture radar imagery of ocean waves, *IEEE Trans. Antennas Propagat.*, AP-27, 685-690, 1979.
- Bass, F. G., I. M. Fuchs, A. I. Kalmykov, I. E. Ostrousky, and A. D. Rosenberg, Very high frequency radiowave scattering by a disturbed sea surface, *IEEE Trans. Antennas Propagat.*, AP-16, 554-568, 1968.
- Bondarenko, I. M., A. A. Zagorodnikov, V. S. Loschilov, and K. B. Chelyshov, Relationship between wave parameters and the spatial spectrum of aerial photographs and radar pictures of the sea surface, *Oceanology*, Engl. Transl., 12, 912-919, 1972.
- Brown, W. M., and C. J. Porcello, An introduction to synthetic aperture radar, *IEEE Spectrum*, 6, 57-62, 1969.
- Cartwright, D. E., The use of directional spectra in studying the output of a wave recorder on a moving ship, in *Ocean Wave Spectra*, pp. 203-218, Prentice-Hall, Englewood Cliffs, N. J., 1963.
- Cartwright, D. E., and N. D. Smith, Buoy techniques for obtaining directional wave spectra, in *Buoy Technology*, pp. 112-121, Marine Technology Society, Washington, D. C., 1964.
- Crombie, D. D., Doppler spectrum of sea echo at 13.6 Mc/s, *Nature*, 175, 681-682, 1955.
- De Loor, G. P., and H. W. Brunsvelde Van Hulten, Microwave measurements over the North Sea, *Boundary Layer Meteorol.*, 13, 119-131, 1978.
- Ewing, J. A., Some measurements of the directional wave spectrum, *J. Mar. Res.*, 27, 163-171, 1969.
- Gonzalez, F. I., R. C. Beal, W. G. Brown, P. S. DeLeonibus, J. W. Sherman III, J. R. R. Gower, D. Lichy, D. B. Ross, C. L. Rufenach, and R. A. Shuchman, Seasat synthetic aperture radar: Ocean wave detection capabilities, *Science*, 204, 1418-1421, 1979.
- Hayes, J. G., Ocean current and shallow water wave refraction in an operational spectral ocean wave model, *Tech. Note 77-1*, Fleet Number, Weather Cent., Monterey, Calif., 1977.
- Hsiao, S. V., The comparison between the synthetic aperture radar imagery and the surface truth of ocean waves, in *Ocean '78—The Ocean Challenge*, pp. 385-389, Marine Technology Society, Washington, D. C., 1978.
- Kinsman, B., *Wind Waves—Their Generation and Propagation on the Ocean Surface*, pp. 134 and 144, Prentice-Hall, Englewood Cliffs, N. J., 1965.
- Long, R. B., Scattering of surface waves by an irregular bottom, *J. Geophys. Res.*, 78, 7861-7870, 1973.
- Long, R. B., On surface gravity wave spectra observed in a moving frame of reference, *NOAA Tech. Memo. ERL AOML-38*, equations (6.9) and (6.13), U.S. Government Printing Office, Washington, D. C., 1979.
- Longuet-Higgins, M. S., D. E. Cartwright, and N. D. Smith, Observations of the directional spectrum of sea waves using the motion of a floating buoy, in *Ocean Wave Spectra*, pp. 111-132, Prentice-Hall, Englewood Cliffs, N. J., 1963.
- Mitsuyasu, H., F. Tasai, T. Suhara, S. Mizuno, M. Ohkusu, T. Honda, and K. Rikiishi, Observations of the directional spectrum of ocean waves using a Cloverleaf buoy, *J. Phys. Oceanogr.*, 5, 750-760, 1975.
- Myers, G. F., High-resolution radar, part IV, Sea clutter analyses, *Rep. 5191*, Naval Res. Lab., Washington, D. C., 1958.
- Oakley, O. H., Jr., and S. J. Leverette, Sea bottom spectra and ocean wave scattering, paper presented at BOSS '79 Conference, Mass. Inst. of Technol., London, Aug. 28-31, 1979.
- Rabiner, L. R., and B. Gold, *Theory and Application of Digital Signal Processing*, pp. 448-450, Prentice-Hall, Englewood Cliffs, N. J., 1975.
- Ross, D. B., B. Au, W. Brown, and J. McFadden, A remote sensing study of Pacific hurricane Ava, *Proc. Int. Symp. Remote Sensing Environ.*, 9th, 163-180, 1974.
- Shemdin, O. H., J. E. Blue, and J. A. Dunne, Seasat-A surface truth program: Marineland test plan, *Rep. 622-6*, Jet Propul. Lab., Pasadena, Calif., 1975.
- Shemdin, O. H., W. E. Brown, Jr., F. G. Staudhammer, R. Shuchman, R. Rawson, J. Zelenka, D. B. Ross, W. McLeish, and R. A. Berles, Comparison of in situ and remotely sensed ocean waves off Marineland, Florida, *Boundary Layer Meteorol.*, 13, 193-202, 1978a.
- Shemdin, O., K. Hasselmann, S. V. Hsiao, and K. Herterich, Non-linear and linear bottom interaction effects in shallow water, in *Turbulent Fluxes Through the Sea Surface, Wave Dynamics, and Prediction*, edited by A. Favre and K. Hasselmann, pp. 347-370, Plenum, New York, 1978b.
- Shuchman, R. A., and J. S. Zelenka, Processing of ocean wave data from a synthetic aperture radar, *Boundary Layer Meteorol.*, 13, 181-191, 1978.
- Tayfun, M. A., R. A. Dalrymple, and C. Y. Yang, Random wave-current interactions in water of varying depth, *Ocean Eng.*, 3, 403-420, 1976.
- Teleki, P. G., F. R. Musialowski, and D. A. Prins, Data acquisition methods for coastal currents, in *Proceedings of the Specialty Conference on Civil Engineering in the Oceans III*, pp. 1190-1210, American Society of Civil Engineers, New York, 1975.
- Teleki, P. G., W. McLeish, R. A. Shuchman, D. Ross, W. E. Brown, Jr., and M. Mattie, Ocean wave detection and direction measurements with microwave radar, in *Oceans '78—The Ocean Challenge*, pp. 639-648, Marine Technology Society, Washington, D. C., 1978.
- Teleki, P. G., W. J. Campbell, R. O. Ramseier, and D. Ross, The offshore environment: A perspective from Seasat SAR data, paper presented at Offshore Technology Conference, Houston, Tex., 1979.
- Tyler, G. L., C. C. Teague, R. H. Stewart, A. M. Peterson, W. H. Munk, and J. W. Joy, Wave directional spectra from synthetic aperture observations of radio scatter, *Deep Sea Res.*, 21, 989-1016, 1974.
- Weissman, D. E., T. W. Thompson, and R. Legeckis, Modulation of sea surface radar cross section by surface stress: Wind speed and

- temperature effects across the Gulf Stream, *J. Geophys. Res.*, this issue.
- Wright, J. W., A new model for sea clutter, *IEEE Trans. Antennas Propagat.*, AP-16, 217-223, 1968.
- Wright, J. W., T. R. Larson, and L. I. Moskowitz, A note on SAR imagery of the ocean surface, *IEEE Trans. Antennas Propagat.*, AP-24, 393, 1976.
- Zamarayev, B. D., and A. I. Kalmykov, On the possibility of determining the spatial structure of an agitated ocean by means of radar, *Izv. Acad. Sci. USSR. Atmos. Oceanic Phys.*, Engl. Transl., 5(1), 124-127, 1969.
- (Received December 10, 1979;
revised March 28, 1980;
accepted April 4, 1980.)

SAR OBSERVATIONS OF COASTAL
ZONE CONDITIONS

G.A. Meadows*
E.S. Kasischke
R.A. Shuchman

Radar and Optics Division
Environmental Research Institute of Michigan
Ann Arbor, Michigan 48107

ABSTRACT

Synthetic Aperture Radar (SAR) data collected both from satellite and aircraft systems have been shown to be useful in observing coastal zone conditions. Coastal zone conditions observed by SAR include: gravity wave detection (refraction and diffraction effects), surf zone location, surface currents, and long-period "surf beats". Incident storm generated waves and the resulting near shore circulation within the active surf zone were concurrently observed with both an in-situ sensing array as well as with airborne SAR. Algorithms have been developed to determine significant wave and current parameters from the sea surface backscatter of microwave energy. These algorithms have been successfully tested and are compared with wave and current observations derived from a Lake Michigan sensing array. Incident wave spectra calculated from the SAR information agreed well with observed near shore spectra. Both the dominant incident wind wave components as well as long-period near shore wave phenomena were correctly identified. Use of the Doppler information obtained from the SAR optical correlator allows a rough estimation of near shore surface flow velocities. These estimates of the motion of the scattering surface were in reasonable agreement with both theory and in-situ field observations. SEASAT SAR data collected off the coast of Scotland and Cape Hatteras, North Carolina, was also analyzed with respect to the identification of gravity waves as they propagated toward shore. Classical wave refraction was documented on the Cape Hatteras data. The Scotland SAR data exhibited a calculated 11.6-second swell pattern that could not be explained through wave refraction and bottom topography effects. Instead the wave patterns observed were shown to result from diffraction caused by an island approximately 30 km outside the SAR pass. To further demonstrate the ability of SAR for coastal remote sensing, the radar wave data was reduced using refraction and wavelength comparison methods to extract depth information. This depth information was compared to bathymetry charts. The results demonstrated the utility of SAR in providing measurements concerning shallow water transformations of surface wind waves and swell as well as updates of bathymetric charts of coastal areas.

INTRODUCTION

Recently Synthetic Aperture Radar (SAR) data of coastal waters has been collected and analyzed. Near shore conditions observed by SAR have included:

* (ERIM consultant, Assistant Professor, Department of Atmospheric and Oceanic Science, The University of Michigan, Ann Arbor, Michigan 48109.)

gravity wave detection (refraction and diffraction effects), surf zone location, surface currents, and long-period surf beats. This paper discusses two SAR coastal zone studies. The first study utilized X-band (3 cm) synthetic aperture radar data collected by aircraft over an instrumented site in Lake Michigan, while the second reports an analysis of SEASAT SAR satellite data collected over Cape Hatteras, North Carolina and Cape Wrath, Scotland.

In the Lake Michigan study, incident storm generated waves and the resulting near shore circulation within the active surf zone were concurrently observed with both an in-situ sensing array as well as airborne SAR. The Lake Michigan experiment demonstrated SAR's ability to sense the incident wave spectra, location of the surf zone, surf beats, and provide an estimation of the magnitude and direction of the longshore current.

The SEASAT SAR data collected off Cape Hatteras, North Carolina and Cape Wrath, Scotland were used to study coastal gravity waves as they undergo refraction and diffraction. To further demonstrate the potential of SAR for coastal remote sensing, the SEASAT radar wave data were reduced using refraction and wavelength comparison methods to extract the depth of the water column.

BACKGROUND

Synthetic Aperture Radar (SAR) is an active imaging device that senses the environment with short electromagnetic waves. As active sensors, radars provide their own illumination in the microwave region of the electromagnetic spectrum and thus are not affected by diurnal changes in emitted or reflected radiation from the earth's surface. Additionally SAR's have the recognized advantage of being able to image the earth's surface independent of weather conditions and to provide synoptic views of the ocean at high resolution. Most radars operate in the frequency region of 300 MHz (1 m) to 30 GHz (1 cm), and bandwidths within this region are commonly designated by letters. SAR's discussed in this paper are designated as L-band (23.5 cm) or X-band (3.2 cm).

Synthetic Aperture Radar is a coherent airborne or spaceborne radar that uses the motion of a moderately broad physical antenna beam to synthesize a very narrow beam thus providing fine azimuthal (along-track) resolution (Brown and Porcello, 1968; Harger, 1970). Fine range (cross-track) resolution is achieved by transmitting either very short pulses or longer coded pulses which are compressed by matched-filtering techniques into equivalent short pulses. Usually, the coded pulse is a waveform linearly modulated in frequency.

Typically, the phase history of a scattering point in the scene is recorded on photographic film as an anamorphic (astigmatic) Fresnel zone plate. The parameters of the zone plate are set in the azimuth direction by the Doppler frequencies produced by the relative motion between the sensor and the point scatterer, and in the range direction by the structure of the transmitted pulses. The film image is a collection of superimposed zone plates representing the collection of point scatterers in the scene. This film is used by a coherent optical processor which focuses the anamorphic zone plates into the points which produced the microwave scatter of the scene (Kozma, et al., 1972). Recently, SAR processing has employed digital techniques.

LAKE MICHIGAN STUDY

On 18 October 1978 at approximately 16:35 EST, SAR data was collected along the shoreline of Lake Michigan centered at latitude 43°50'N. The site for this field experiment was the eastern shore of Lake Michigan, between the cities of Ludington and Pentwater, Michigan (see Figure 1). This thirteen-kilometer section of shoreline, extending approximately north-south, is characterized by a multiple-barred bathymetry with nearly straight and parallel contours. The SAR system used to collect the data was the ERIM X- and L-band dual-polarized imaging radar described by Rawson, et al. (1975). The FRIM SAR system records four channel return but we will focus our attention here

on the X-band horizontal-transmit-horizontal-receive channel as this data provided the clearest wave images. The SAR was flown at an altitude of 6100 m and operated with an incident angle from the vertical of 20° , yielding a swath width of 5.6 km. The cross-track or range resolution of SAR is limited by radar frequency and is about 2 m for X-band. A sample of the X-band imagery showing the location of the coastal array (letter A in Figure 1) is shown in Figure 2.

At the same time as the radar flight, the University of Michigan, Department of Atmospheric and Oceanic Science was operating its mobile surf zone, wave and current sensing array (Meadows, 1979). Monitoring of incident wave characteristics and longshore current velocities was conducted through the growth of a storm on Lake Michigan. A detailed discussion of the experimental design is presented in Wood and Meadows (1975) and Meadows (1977). Surface-piercing, step resistance wave probes and bi-directional ducted impeller flow meters were employed to make simultaneous measurements of wave and current conditions. These sensors were oriented on a line perpendicular to shore, extending from the beach through the outer surf zone. Other coastal sensing equipment included a directionally mounted motion picture camera and Lagrangian drifters. A representative portion of the 18-minute record from the outer surf zone resistance wave gauge is shown in Figure 3.

The SAR data shown in Figure 2 was digitized using the ERIM hybrid image/digitizer (Ausherman, 1975). The data was digitized with an approximate resolution of 6 meters (3 m pixels). The range coordinates of the digitized data were analytically corrected for slant-to-range geometry (Feldkamp, 1978). Four 1.5×1.5 km subsections (see Figure 1) with 6 meter resolution were extracted from the digitized data. The four sections are labeled A-D where A is closest to shore.

The 3.0 m pixel digitized SAR images were converted to 6 m resolution by 4 pixel averaging in order to increase coherence in the image. The average value of each azimuthal line was subtracted from the line to remove the trend of intensity falloff with increasing range distance. Two-dimensional fast Fourier transforms were performed on each 256×256 cell subsection to yield raw directional wave number spectra with a Nyquist wave number of 0.52 m^{-1} . The raw spectra were smoothed by replacing each value with the average of the surrounding 5×5 cell.

The longshore current magnitude and directional information was extracted from the SAR data by exploitation of the SAR Doppler history (Shuchman, et al., 1979). This technique takes advantage of the fact that the SAR instrument responds primarily to backscatter from capillary waves, which, in conventional SAR processing, are assumed stationary with respect to other time scales of the radar system. However, these scatterers are not stationary, they move with a characteristic phase velocity as well as with velocities due to the presence of currents and longer gravity waves. The radial (line of sight) component of this resultant velocity produces a Doppler shift in the temporal frequency of the return signal, which translates to a spatial frequency shift recorded on SAR signal film.

The Doppler frequency shift (Δf_D) for a moving target relative to a stationary target in a SAR system is

$$\Delta f_D = \frac{2V_r}{\lambda}, \quad (1)$$

where V_r = radial component of target velocity, and
 λ = transmitted radar wavelength

This temporal frequency shift will produce an azimuth spatial frequency shift of

$$\Delta f' = \frac{f_D P}{V_{AC}}, \quad (2)$$

on the SAR signal film, where P = azimuth packing factor, and V_{AC} = aircraft velocity.

Equations 1 and 2 can be combined to relate radial target velocity to Doppler spectrum shift:

$$V_R = \frac{\Delta f' \lambda V_{AC}}{2P}, \quad (3)$$

Typical values for λ , V_{AC} , and P for the imaging of the Lake Michigan data are 0.032 m, 109 m/s, and 15,000 respectively. This relationship can be used to measure the average radial velocity component of an ocean-wave scattering field relative to a fixed-land scattering field. A shift in the azimuth spatial frequency spectrum between fixed-land and moving-ocean surfaces yields an estimate for $\Delta f'$. Variations in spectrum location due to antenna pointing may be eliminated by choosing imagery having land and ocean imaged simultaneously.

To calculate the wave spectrum at the instrumented surf zone site, the 18-minute analog record shown in Figure 2 was digitized at 0.25 second intervals and analyzed using conventional one-dimensional fast Fourier transform techniques. The directional information was obtained by utilizing data from the directionally mounted camera. The current information was obtained by again using the directionally mounted camera but this time photographing the Lagrangian drifters since, by the time of the radar overflight, the last current meter station had been destroyed.

Figure 4 represents the contour plots for the four test areas (A-D) extracted from the digitized SAR data. Six contour levels are given in 3 dB increments. The data is normalized to the highest value found within the contours and analyzed using conventional one-dimensional fast Fourier transform techniques. The average depth for each of $1.5 \times 1.5 \text{ km}^2$ areas are indicated on Figure 4. Note the large amount of low frequency energy on the contours even though the data was extensively corrected to reduce the DC bias. The reason for these low frequency components will be discussed later. The contour data presented was motion corrected. There is a 180° ambiguity in wave direction measured by SAR which was resolved by assuming the waves were coming from the west and therefore propagating towards the shore.

Close inspection of the contour plots indicates dominant wavelengths of 44, 46, and 55 meters have been resolved by the spectral analysis. The general direction of wave travel in the near shore region is approximately $30^\circ(T)$. Note that wave refraction can be observed when comparing the direction of Area D with the shallow water area, A.

It is important to remember that the energy spectrum derived from SAR imagery is an image intensity (hence, wavelength and directional information) spectrum and not a wave height spectrum. The relationship between SAR image intensity and wave height is still being investigated (Jain, 1977 and Shuchman, et al., 1979). The directional spectrum determined from resistance wave gauge data is a true wave height spectrum.

Figure 5 is a scan of Doppler history for stationary land and the surf zone. Both scans used a $1 \times 1 \text{ km}$ aperture. The surf zone scan was centered approximately 650 meters offshore. Note on Figure 5 how the coastal zone (water) scan is displaced to the left of the stationary (land) target. This indicates a radial motion away from the radar. Recall from Figure 2 that the radar was traveling with a heading of $270^\circ(T)$, thus, the longshore current sensed by the radar was in the northward direction. The $\Delta f'$ frequency change which is used in Equation 3 is indicated on Figure 5. This f' is corrected

for a bias caused by the laser illumination in the SAR optical processor. A Δf of 0.55 lp/mm was detected, which indicates a current velocity of approximately 0.5 m/sec.

A summary of the in-situ measured incident surf zone conditions during the SAR overflight is presented in Table 1. Wave characteristics were obtained by statistical analysis of the 18-minute continuous sea surface elevation record. A representative portion of this surface piercing wave staff record is presented in Figure 2. A one-dimensional wave height spectrum of this wave height data, incident at the outer surf zone, is shown in Figure 6. The dominant frequencies resolved by the spectral analysis are indicated on the figure. In addition, the calculated deep water wave periods and wavelengths are also shown on the figure for each of the major spectral peaks. These correspond to deep water wavelengths of 15, 27, 31, 46 and 55 m, respectively. This analysis indicates the presence of a multi-component incident gravity wave group with dominant periods in the range of 3-6 s. Significant long period wave components have also been identified with the wave group. The periods of these low frequency components are 17 and 33 seconds, respectively and appear to resemble surf beats (Munk, 1949; Tucker, 1950). These results are consistent with measurements of near shore multi-component wave trains reported by Meadows and Wood (1980).

Incident wave direction and longshore current velocity were determined by a frame-by-frame analysis of a synchronous motion picture sequence from the shore based directionally mounted camera. The mean wave angle of attack to the beach was determined to be $57^\circ \pm 5^\circ$ (T) and the mean longshore current velocity midway across the active surf zone was 0.26 m/sec flowing toward the north.

Table 2 provides a comparison between the SAR derived surf zone conditions and the sea truth provided by the surf zone array. The values presented in Table 1 represent surf zone conditions actually measured at the shoreward edge of test area A. The wave directions and wavelengths were then corrected for depth effects using classical linear wave theory. The depths used for the corrections are also indicated on the table. The SAR derived results presented in Table 2 are also corrected for the previously discussed motion distortions. The excellent agreement between SAR observations and the surf zone sea truth shown in the table indicates the following:

1. The dominant surface gravity wave wavelengths and direction are obtainable from the SAR.
2. These observations are in excellent agreement with sea truth, even within the active surf zone.
3. Wave refraction can be observed with SAR and favorably compares to calculated refraction using classical linear wave theory.

The SAR derived radial current velocity measurement of 0.5 m/sec was higher than reported in Table 1 (0.26 m/sec). However, recall that the current measurement derived from the SAR was not taken in the surf zone but was centered 650 m from the shore. Meadows (1977 and 1979) reports that under certain conditions, an increase in longshore current velocity as one moves from the surf zone into deeper water may be expected. As presented earlier, the SAR Doppler measurement is a radial velocity and is denoted by a line of sight. Thus, only rather coarse directional information is obtainable, in this case, a current velocity away from the radar look direction (northward flowing current). Two orthogonal flight headings and resulting current measurements could greatly enhance the directional sensing capability.

The SAR spectrum data presented in Figure 4 are wave number spectrum of the radar intensity. As such, they are not expected to have the same appearance as the one-dimensional spectrum from the resistance wave gauge (Figure 6) which was determined from wave height and period data. Even if the wave number spectrum is converted to a frequency spectrum or vice-versa, it is clear that the SAR spectra examined here cannot be easily transformed to, or

interpreted as, wave height spectra. However, the wave number and direction of the peak energy, determined from SAR spectra, agree very well with in-situ measurements. Synoptic availability of even these parameters is currently unobtainable by conventional ground-based measurements. This addition represents a significant advance in large scale wave data acquisition.

All four of the SAR derived wave spectra presented in Figure 4 exhibit significant low frequency components. These components were observed even after the digital SAR data was extensively smoothed and the intensity fall-off in the range direction was digitally corrected. The low frequency (near zero wave number) components could in fact be real components of the sea surface; the one-dimensional transform derived from the resistance wave gauge record, shown in Figure 6, indicated the presence of 17 and 33 second wave periods.

Preliminary analysis of the four 2-D spectral estimates indicate that the low frequency components corresponding to 17 and 33 seconds as determined from the resistance wave gauge record are identifiable on the radar imagery in wave spectra space. Thus, it appears very likely that the "surf beat" component identified on the resistance wave gauge were also identified on the SAR data. As expected, the direction of these SAR derived low frequency components were also in the 30° (T) direction.

SEASAT COASTAL WAVE ANALYSIS

Historically, aerial photography has been the remote sensing technique used to provide the best evidence of wave refraction in coastal waters, but it has limitations. Aerial photography is rarely possible during storm conditions when wave heights are at a maximum and when a knowledge of wave refraction is most important to coastal engineering studies. Most aerial photographs have ground coverage which extends no further than a few kilometers from shore, and thus generally do not display the early stages of wave refraction. Additionally, successful photography of gravity waves is greatly dependent on the angle of sun illumination (Barber, 1949). Spacecraft photography (Polcyn and Sattinger, 1969) successfully imaged ocean waves and provided sufficient ground coverage to image both deep and shallow water waves, but the availability of this type of imagery, at present and for the foreseeable future, is limited. Passive multispectral scanning systems such as LANDSAT do not have sufficient spatial resolution to image gravity wave fields.

Aircraft SAR systems have some of the same limitations as aircraft aerial photography, i.e., limited area of swath coverage, typically no wider than 10 kilometers*.

The SEASAT satellite, launched in June of 1978, contained an imaging synthetic aperture radar with a wavelength of 23.5 cm, and a resolution of approximately 25 x 25 m. The SAR imagery has a swath width of 100 kilometers and data lengths up to a few thousand kilometers long. The SEASAT SAR thus offers the potential to cover sufficiently broad coastal areas to view wave refraction from deep water to the shore. This section reports on a study that documents wave refraction using SEASAT SAR data.

The purpose of this study was to investigate whether or not the SEASAT SAR imaged gravity waves in coastal areas with sufficient clarity to document wave refraction. This was done by comparing depth measurements derived from models based on classical oceanographic wave refraction theory with "sea truth" depths obtained from available hydrographic charts.

Dominant wavelength and direction estimates were obtained from SEASAT SAR imagery of gravity waves by analyzing spectra produced from optical Fourier

*The U.S. Air Force operates an X-band aircraft SAR with a 50 km swath; additionally, the ERIM X-L system now has a 22 km swath.

transforms. These wavelengths and directions were then used as inputs into two simple theoretical models in an attempt to assess SEASAT's potential for discerning refraction of gravity waves. The theoretical models included a refraction (angle) model and deep to shallow water wavelength comparison model. Both of these models were used to obtain depth estimates. The depths, as derived from the SAR data, were then compared to the depth as obtained from bathymetric charts.

Two areas where SEASAT made overpasses were chosen as study sites. On 3 September 1978, at approximately 02:53 GMT, SEASAT collected data over Cape Hatteras, North Carolina during Revolution 974. This pass was descending; therefore, the satellite was looking at waves propagating away from the line of sight. Sea truth provided by Coastal Erosion Research Laboratory personnel

who operated at Duck, North Carolina (approximately 80 km from Cape Hatteras) reported a dominant wavetrain with a 10.7 second period using Baylor and wave-rider gauges. The wave height was 2-3 meters. This sea truth is consistent with the ERIM OFT-obtained dominant wavetrain (11.0 second swell). On 19 August 1978, SEASAT collected data over Cape Wrath, Scotland during Revolution 762, at approximately 6:46 GMT. Unfortunately, there were no oceanographic sea truth measuring devices present in the test area. However, ship reports did indicate an ocean swell with a 4 m significant wave height and an 11.5 second period. This is again consistent with the ERIM OFT-obtained wave period estimates (11.6 second). Both these data sets contained clearly visible gravity wave fields.

Dominant wavelengths and their resultant wave directions were obtained by analyzing a series of two-dimensional optical Fourier transforms (OFTs). Gonzalez, et al., (1979) used OFTs successfully to obtain dominant wavelength and direction, as compared to sea truth, in the SEASAT Gulf of Alaska Experiment. OFTs are obtained by passing a monochromatic, collimated beam of light through the film image of the waves. Through Fraunhofer diffraction, the light is diffracted proportionally to the frequency of the features in the image in the same direction as the features (Shuchman, et al., 1977). Therefore, OFTs produce an estimate of the dominant wavenumber (or wavelength) and direction of the waves. Figure 7 is an example of an ERIM produced optical Fourier transform.

Given an ocean gravity wavefield which is propagating shoreward in a coastal area (see Figure 8), we know that the deepwater wavelength (L_0), direction (α_0), and celerity (C_0) will all change as the wave begins to feel the effect of the sea floor (approximately at the point where $H/L_0 = 0.5$, where H is the water depth). If we assume that the bottom bathymetric contours are straight and parallel to the shoreline, then at any point towards shore, C_1 (the wave celerity at the shoreward point) can be derived from Snell's Law as:

$$C_1 = C_0 \frac{\sin \alpha_1}{\sin \alpha_0}$$

where α_1 is the angle between the wave and shore. We also can derive any C_1 in terms of wave properties (Neumann and Pierson, 1966) as:

$$C_1 = \frac{gT}{2\pi} \tanh \frac{2\pi H}{L}$$

where H is the water depth and the period (T) is;

$$T = \frac{2\pi L_0}{L}$$

From Eqs. (4), (5), and (6), we can derive the depth of water (H) as:

$$H = \frac{L_0}{4\pi} \ln \frac{2 L_0}{g}$$

where $b = \sin \alpha_1 / \sin \alpha_0$. Therefore, the amount a wave is refracted can be determined if one knows α_0 , L_0 and H.

Similarly, L_1 can be defined in terms of H and L_0 :

$$H = \frac{L_1}{4\pi} \ln \frac{1 + L_1/L_0}{1 - L_1/L_0}$$

By obtaining measurements of α_1 , α_0 , L_1 , and L_0 from OFTS from the SEASAT data, it is possible to calculate an estimate of H, the water depth. If the SEASAT SAR is "seeing" wave refraction, then these predicted depths should be comparable to "sea truth" depths obtained from hydrographic charts.

Therefore, two simple, theoretical models were considered in this study. The wave refraction model [Equation (7)] uses α_1 , α_0 , and L_0 as inputs. The wavelength comparison model [Equation (8)] uses L_0 and L_1 as inputs.

For a complete discussion and derivation of these models, see Shuchman, et al., (1979a). Figure 9 gives a graphical presentation of these two models. The inputs for these models were produced by OFT analysis.

A set of twelve optical Fourier transforms were produced at ERIM from the Rev. 762 data for the Cape Wrath Test area. Wavelengths and wave directions obtained from these two models were then used as inputs into the two theoretical models.

A comparison of predicted depth, using Eq. (7), vs. actual charted depth using the wave refraction model reveals in all cases that the predicted depth was much less than the actual depth. This indicates that the measured angle of wave propagation is much less than it should be, i.e., the waves are being bent to a greater extent than the bottom topography would account for. Therefore, effects other than those of bottom refraction must be working on the waves in this SAR imagery.

In order to explain the change in deep-water wave angles, a diffraction analysis was conducted for the wave pattern shown in the imagery. A deep-water incident wave direction (α_0) of $68^\circ(T)$ (as obtained by an OFT and FFT of deepwater waves on Revolution 762) was assumed. The tip of the barrier was taken to be the Butt of Lewis on the Isle of Lewis, an island 30 kilometers to the southeast of the SEASAT overpass. The diffraction pattern was drawn as a series of arcs centered on the Butt of Lewis. Transposing these diffraction arcs onto the SAR imagery clearly shows that the wave pattern is a result of waves diffracting around the northern end of the Isle of Lewis (see Figure 10).

This diffraction of the waves along with violation of the assumption of straight and parallel bottom contours introduce enough uncertainty into the model as to make it very difficult to estimate depth from wave refraction in this area. Therefore, further wave refraction studies were not conducted on these data.

Two sets of optical Fourier transforms were analyzed for the Cape Hatteras data. One set was produced at ERIM, while the other was produced at the Coastal Engineering Research Center (CERC) of the U.S. Army Corps of Engineers. The ERIM data set contained 26 points, of which 8 were used to calculate an estimate of the deep water wavelength and direction. The CERC data set contained 28 shallow water OFTs. Figure 11 shows the location of the CERC and ERIM OFTs. Figure 12 shows a portion of sub-swath 3 of the JPL (Jet

Propulsion Lab) optically processed SAR imagery from Rev 974. Portions of subswaths 2 and 4 were also used.

Figure 13 represents a plot of predicted depth versus chart depth using the results from the wave refraction model. Although a statistical analysis indicated there was a significant linear correlation present ($R = 0.52$, $p = 0.01$), Figure 13 does not indicate a very good fit in the data. One possible reason for this lack of fit is a violation of the assumption made earlier that the bottom bathymetric contours are straight and parallel to the shoreline. Because the ERIM data were from a wide range of points, this assumption probably does not hold true.

The CERC points, however, were collected over a small area (see Figure 11), and the assumption of straight and parallel contours probably is valid for this smaller data set. A separate analysis of the CERC data above is warranted. Figure 14 summarizes the CERC data from the wave refraction model. For this data set, the linear correlation was 0.76, again significant for a $p = 0.01$.

The results for the wavelength comparison model are summarized in Figure 15. The linear correlation for this data was 0.81, significant at $p = 0.01$. It is felt that of the two models, the wavelength comparison model is the more desirable one. Not only does this model produce better correlation, but its inputs are less sensitive to both SAR imaging and oceanographic constraints. SAR systems are typically quite sensitive to imaging geometry. Wave angles are also sensitive to other oceanographic phenomena such as tides and coastal currents in addition to refraction and diffraction. Wavelengths are also sensitive to these phenomena, but recent studies by Hayes (1980) in the Cape Hatteras area showed that wavelengths are much less sensitive to current effects than wave angles. Both these factors are reflected in a high level of variability in the estimate of the deepwater wave angle. From the ERIM OFTs of deep water points, a deepwater wave angle (α_0), of 49° was calculated, which had a standard deviation of 15.4° , or approximately thirty percent of α_0 . In contrast, the deepwater wavelength (L_0) of 181 meters had a standard deviation of 10.4 meters, or approximately six percent of L_0 . Therefore, as far as inputs into the two models are concerned, those for the wavelength comparison model (L_0 and L_1) are apparently less variable than those for the wave refraction model (α_0 , α_1 , and L_0). Because the inputs to the wavelength comparison model are inherently subjected to less variability, it is felt that this model is the better of the two.

SUMMARY

This paper has demonstrated that both aircraft and satellite SAR data can provide useful near shore wave climate information. Both the fine resolution (3 x 3 meter pixel), narrow swath width (6 km) aircraft data and the coarser resolution (25 x 25 meter pixel), wide swath (100 km) satellite data proved useful in imaging gravity waves. Synthetic aperture radar (SAR) surface gravity wave data of the coastal zone of a portion of Lake Michigan has been compared to in-situ surf zone wavelength, period, direction, and surface current information. The comparisons were favorable, indicating SAR's utility as a tool to remotely sense coastal zone conditions. This could in turn enable oceanographers to synoptically study the entire coastline of large water bodies. This data could then prove useful in mapping not only surface wave climates and currents, but also provide a mechanism for rapid and large scale assessment of changes in coastal conditions.

Specifically, this study has shown:

1. SAR derived wavelengths and directions are in good agreement with sea truth,
2. SAR directional spectra taken in various water depths do correlate with predicted wave refraction,

3. Longshore current direction and relative magnitude as obtainable from SAR Doppler history and are in reasonable agreement with sea truth, and
4. Low-frequency components observed on SAR spectra seem to correlate with low frequency "surf beat" found in sea truth spectral estimates.

It should be mentioned when utilizing SAR data such as presented in this paper, that the SAR spectral estimates presented are wave number-directional spectra of the radar return intensity. The data does not represent wave height information, at least not in a recognizable form. The modulation transfer function (i.e., SAR gravity wave imaging mechanism) is not totally understood at the present time. The determination of the transfer function as well as determination of wave height using SAR data will be a major scientific advance. At that time, it will then be possible to use SAR gravity wave data to obtain power density estimates of the sea surface.

SEASAT SAR data collected off the coast of Scotland and Cape Hatteras, North Carolina, was analyzed in respect to identifying gravity waves as they propagated toward shore. Classical wave refraction was documented on the Cape Hatteras data as an 11-second swell was detected by the SAR and successfully tracked from deep water to the coastline. The Scotland SAR data exhibited an 11.5-second swell pattern that could not be explained through wave refraction and bottom topography effects. Instead the wave patterns observed were shown to be caused by diffraction around an island approximately 30 km outside of the SAR pass. Both optical and digital Fourier transform techniques were utilized in this study. To further demonstrate the ability of SAR for coastal remote sensing, the radar wave data was reduced using refraction and wavelength comparison methods to exact depth information. This depth information was compared to bathymetry charts and the results were very encouraging, indicating the utility of SAR data to update bathymetry charts of coastal areas.

ACKNOWLEDGMENTS

The ERIM analysis of the SAR Lake Michigan gravity wave data was supported by the Office of Naval Research (ONR) Contract N00014-76-C-1048. The technical monitor for this ONR contract is Mr. Hans Dolezalek. The field installation of the mobile wave and current monitoring system, as well as the reduction of the in situ sea truth data, was supported under the University of Michigan research grant no. 387349. The authors would like to thank Alex Klooster and Ken Knorr of ERIM for generating the digital data and running the fast Fourier transforms, respectively. Students of the Department of Atmospheric and Oceanic Science of the University of Michigan are also thanked for their assistance in the field portion of this investigation and for assistance with data reduction and analysis.

The wave SEASAT refraction work reported herein was jointly supported by the National Oceanic and Atmospheric Association (NOAA) and the National Aeronautics and Space Administration (NASA) as part of the SEASAT Announcement of Opportunity Program under Contract No. MO-A01-78-00-4339. The technical monitors were John W. Sherman III and Patrick DeLeonibus of NOAA. The wave refraction study would not have been possible without the cooperation of many people. The authors would like to specifically acknowledge the help of the following individuals: F.I. Gonzalez of the NOAA Pacific Marine Environmental Laboratory (PMEL) for providing oceanographic expertise on the relationships of deep and shallow water gravity waves; D. Lichy of the U.S. Army Corps of Engineers Coastal Engineering Research Center for sharing Revolution 974 data as well as providing optical Fourier transforms of that data; and J. Hammack of the Defense Mapping Agency, Hydrographic Center for providing bathymetric charts of the Cape Hatteras test area. Carl Leonard and Craig Dwyer generated the ERIM optical Fourier transforms presented using ERIM optical processing facilities.

REFERENCES

- Ausherman, D.A., W.D. Hall, J.N. Latta, and J.S. Zelenka, Radar Data Processing and Exploitation Facility, Proceedings IEEE International Radar Conference, Washington, D.C., 1975.
- Barber, N.F., A Diffraction Analysis of a Photograph of the Sea, Nature, Vol. 164, No. 4168, p. 485, 17 September 1949.
- Brown, W.J. and L. Porcello, An Introduction to Synthetic Aperture Radar, IEEE Spectrum 6, pp. 52-66, 1968.
- Feldkamp, G., Correction of SAR-Induced Distortion in SFASAT Imagery, Paper Presented at the SPIE Conference on Applications of Digital Image Processing, San Diego, Calif., August 1978.
- Gonzales, F.I., R.C. Beal, W.E. Brown, P.S. DeLeonibus, J.W. Sherman III, J.F. Gower, D.B. Ross, C.L. Rufenach, and R.A. Shuchman, SEASAT Synthetic Aperture Radar: Ocean Wave Detection Capabilities, Science, Vol. 204, No. 4400, 29 June 1979.
- Harger, R.O., Synthetic Aperture Radar Systems, Academic Press, New York, 1970.
- Hayes, J.G., Ocean Current Wave Interaction Study, Journal of Geophysical Research (Ocean and Atmospheres), In Press, September 1980.
- Jain, A. Determination of Ocean Wave Heights from Synthetic Aperture Radar Imagery, Applied Physics, Vol. 13, p. 371, 1977.
- Kozma, A., E.N. Leith, and N.G. Massey, Tilted Plane Optical Processor, Applied Optics, 11, p.1766, 1972.
- Meadows, G.A., The Wind Driven Component of Surf Zone Circulation (Abstract), Trans. Amer. Geophy. Union, Vol. 60, No. 46, 1979.
- Meadows, G.A., A Field Investigation of the Spatial and Temporal Structure of Longshore Currents, Ph.D Dissertation, Purdue Univ., West Lafayette, Indiana, 1977.
- Meadows, G.A. and W.L. Wood, Long-Period Zone Motions (In Review), 1980.
- Munk, W.H. Surf Beats, Trans. Amer. Geoph. Union, Vol. 30, 1949.
- Neumann, G. and W.J. Pierson, Jr., Principles of Physical Oceanography, Prentice-Hall, Inc., Englewood Cliffs, New Jersey, 1966.
- Polcyn, F.C. and I.J. Sattinger, Water Depth Determinations Using Remote Sensing Techniques, Proceedings of the Sixth International Symposium on Remote Sensing of Environment, 1969, pp. 1017-1028.
- Rawson, R., F. Smith, and R. Larson, The ERIM Simultaneous X- and L-Band Dual Polarized Radar, IEEE 1975 International Radar Conference, 505, 1975.
- Shuchman, R.A., P.L. Jackson, and G.B. Feldkamp, Problems of Imaging Ocean Waves with Synthetic Aperture Radar, FRIM Report No. 124300-1-T, Ann Arbor, Michigan 1977.
- Shuchman, R.A., C.L. Rufenach, and F.I. Gonzalez, The Feasibility of Measurement of Ocean Surface Currents Using Synthetic Aperture Radar, Proceedings of the Thirteenth International Symposium on Remote Sensing of Environment, Ann Arbor, Mich., April 1979.
- Shuchman, R.A., E.S. Kasischke, A. Klooster, and P.L. Jackson, SEASAT SAR Coastal Ocean Wave Analysis: A Wave Refraction and Diffraction Study, ERIM Final Report 138600-2-F, Ann Arbor, Michigan, 1979a.
- Tucker, M.J. Surf Beats: Sea Waves of 1 to 5 Minutes Period, Proc. Roy. Soc., A 207, pp. 565-573, 1950.
- Wood, W.L. and G.A. Meadows, Unsteadiness in Longshore Currents, Geophy. Res. Lett., Vol. 2, No. 11, 1975.

Table 1. Incident Surf Zone Conditions at the Time of the SAR Overflight

SIGNIFICANT WAVE HEIGHT	0.95 (m)
DOMINANT WAVE PERIODS	5.9, 5.3, 4.8, 4.0, 2.9 (s)
DEEP WATER WAVELENGTH	54, 44, 36, 25, 13 (m)
INCIDENT WAVE DIRECTION	$57^{\circ} \pm 5^{\circ}$
LONGSHORE CURRENT VELOCITY	0.26 (m/s)
LONGSHORE CURRENT DIRECTION	NORTH (360° T)
WIND SPEED	7.5-10 m/s
WIND DIRECTION	230° T

Table 2. Comparison Between the SAR Derived Surf Zone Condition and the In Situ Sea Truth

TEST AREA	DISTANCE FROM SHORE (m)	DEPTH (m)	SAR DERIVED		SEA TRUTH*	
			DOMINANT WAVELENGTH (m)	DIRECTION (T°)	WAVELENGTH (m)	DIRECTION (T°)
A	900	10.5	48	35 ± 3	47.72	34 ± 2
			43		43.7	
B	2200	14	55	30 ± 3	53.8	30 ± 2
					43.7	
C	4600	27	55	25 ± 3	55.3	28 ± 2
			43		45.7	
			48			
D	6900	31	55	25 ± 3	55.3	28 ± 2
			48		45.7	

*ACTUAL MEASUREMENTS MADE AT SURF ZONE, VALUES FOR TEST AREAS A-D ARE DEPTH CORRECTED.

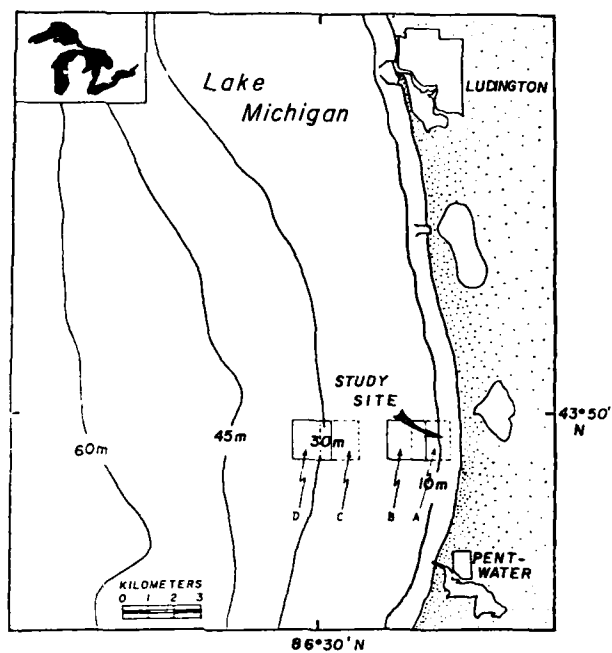


Figure 1. General study area showing nearshore bathymetry and locations of fast Fourier transforms performed on SAR data

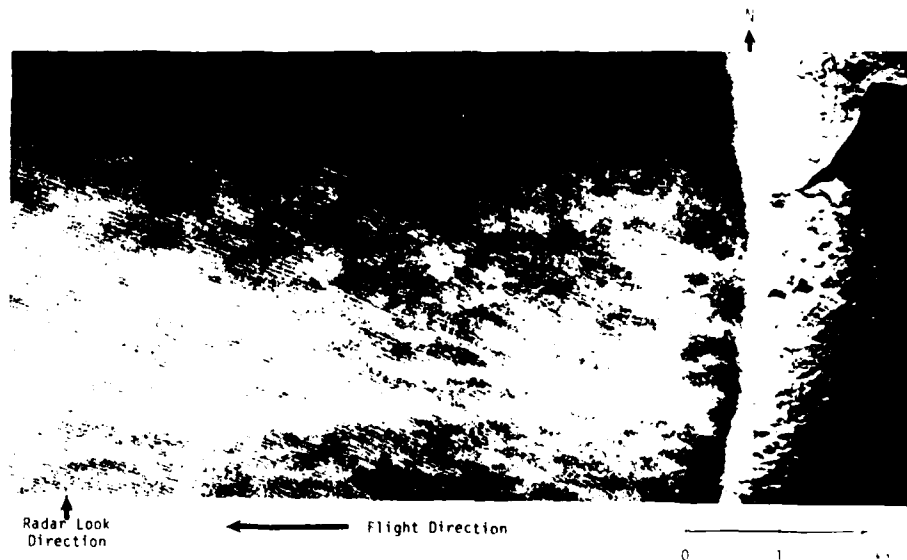


Figure 2. X-Band (HH) SAR data used in study. (The letter A indicates approximate location of surf zone array. Image represents 3 x 3-meter resolution.)

OCTOBER WAVE DATA 1978

25, seconds

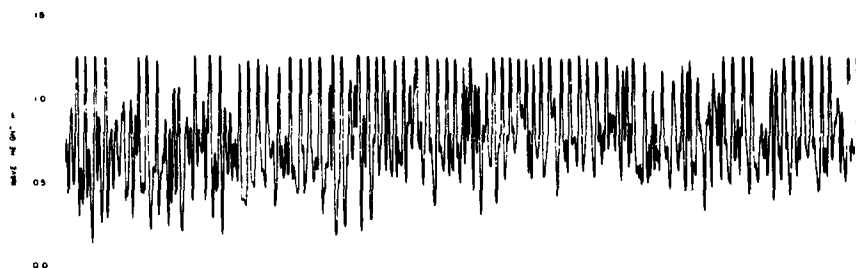


Figure 3. Representative Section of 18 minute time history of water level elevation data from nearshore resistance wave gauge

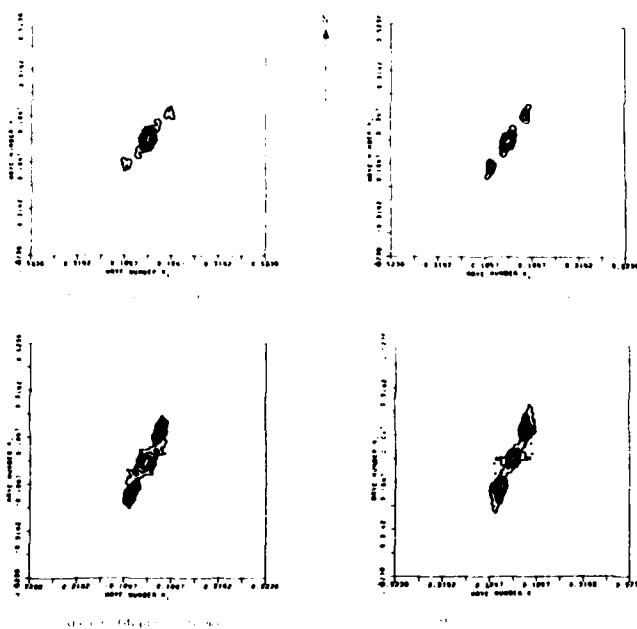


Figure 4. Contour plots of fast Fourier transforms (FFTs) of SAR X-Band Lake Michigan wave data

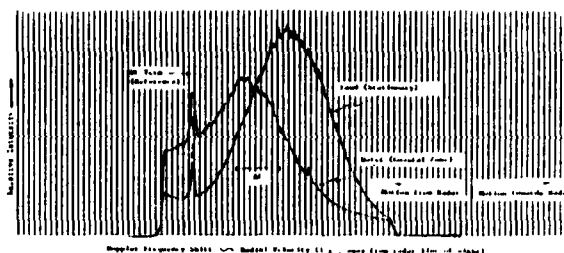


Figure 5. Plot of Doppler displacement caused by radial velocity component of longshore current averaged over 1 km² area

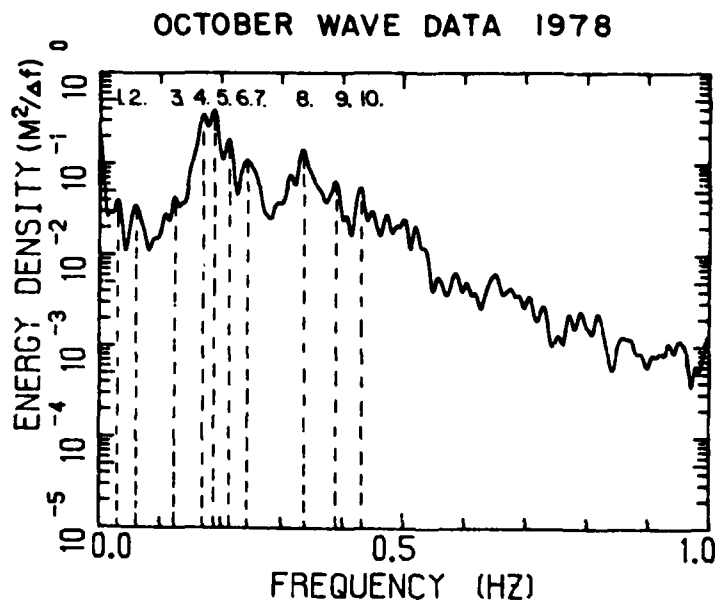


Figure 6. One-dimensional wave height spectrum of water surface elevation time history from resistance wave gauge. Dominant wave periods and wavelengths are as follows: (1) $T = 40.0$ s, $L = 685.9$ m; (2) $T = 17.2$ s, $L = 294.9$ m; (3) $T = 8.1$ s, $L = 138.9$ m; (4) $T = 5.9$ s, $L = 54.3$ m; (5) $T = 5.3$ s, $L = 43.8$ m; (6) $T = 4.8$ s, $L = 35.9$ m; (7) $T = 4.0$ s, $L = 25.0$ m; (8) $T = 2.9$ s, $L = 13.1$ m; (9) $T = 2.6$ s, $L = 10.5$ m; (10) $T = 2.3$ s, $L = 8.25$ m.



Figure 7. Example of ERIM Generated Optical Fourier Transform

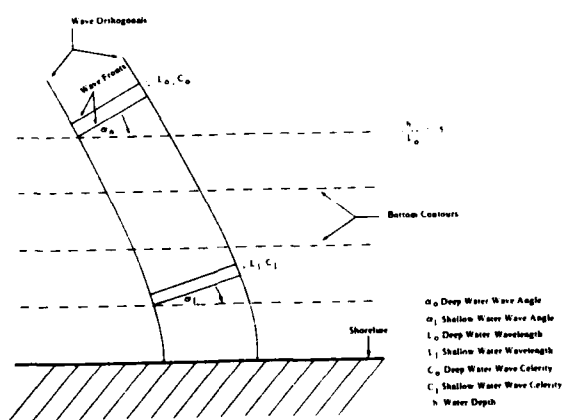


Figure 8. Theoretical Refraction of Gravity Waves

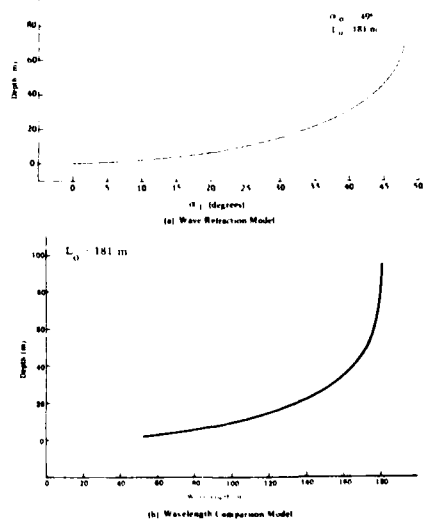


Figure 9. Theoretical Refraction Models

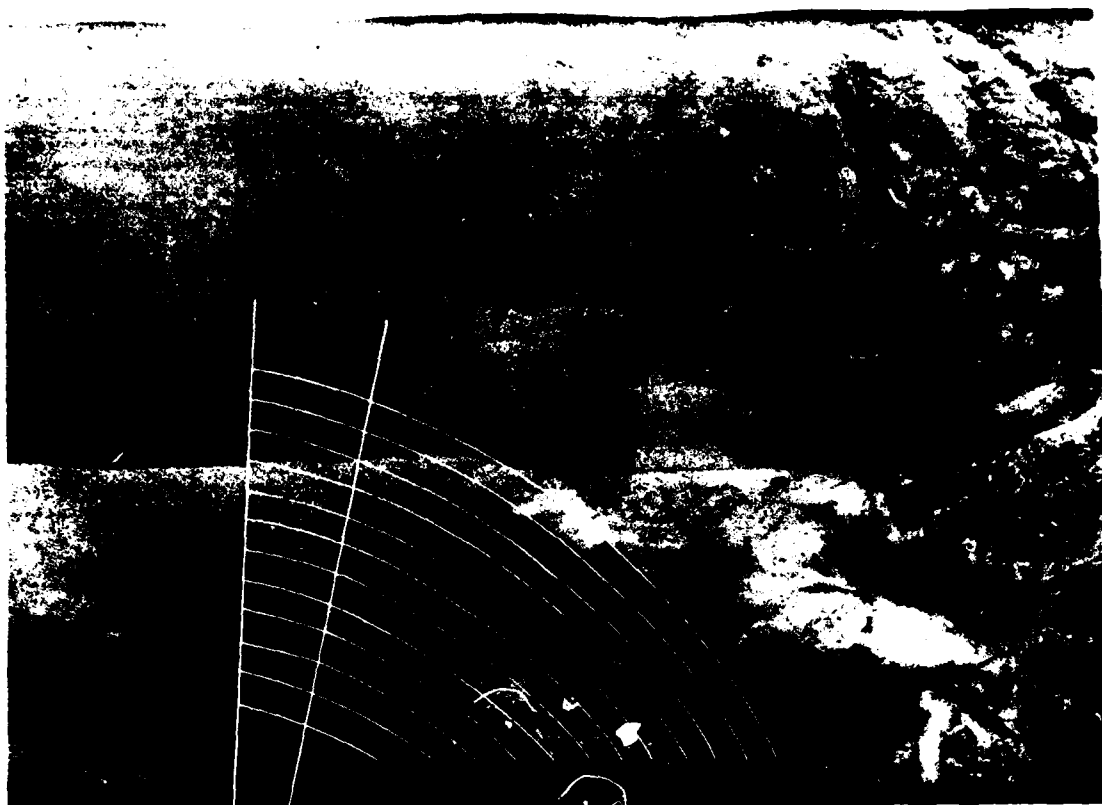
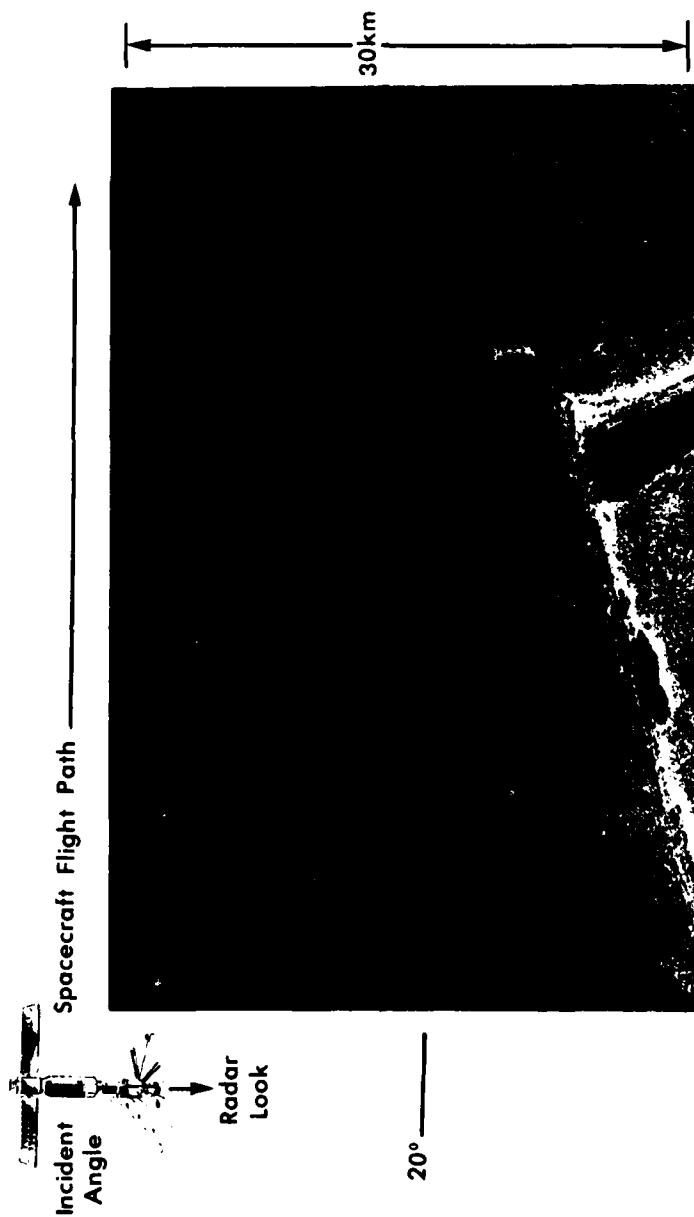


Figure 10. ERIM Processed SAR Imagery, Revolution 762, Show Wave Diffraction

SEASAT SAR



20°

Figure 11. JPL Processed SAR Imagery, Revolution 974, 3 September 1978

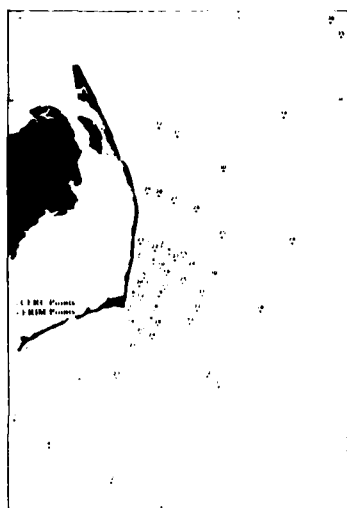


Figure 12. Positions of Optical Fourier Transforms for Revolution 974

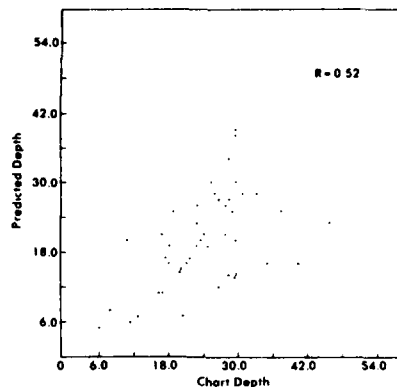


Figure 13. Chart Depth versus Predicted Depth, Wave Refraction Model, ERIM and CERC Points

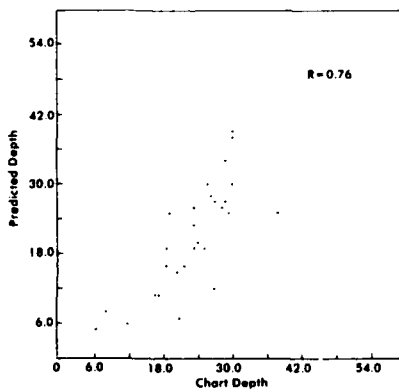


Figure 14. Chart Depth versus Predicted Depth, Wave Refraction Model, CERC Points Only

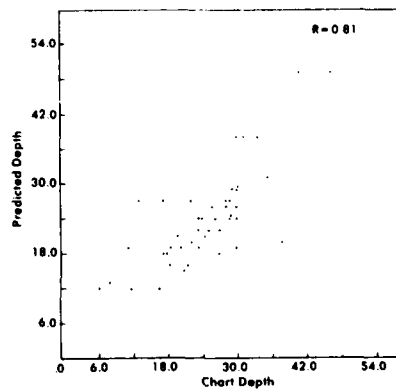


Figure 15. Chart Depth versus Predicted Depth, Wavelength Comparison Model, ERIM and CERC Points

ANALYSIS OF REMOTELY SENSED LONG-PERIOD WAVE MOTIONS

by

G.A. Meadows*

Department of Atmospheric and Oceanic Science
University of Michigan,
Ann Arbor, Michigan 48109

R.A. Shuchman, and J.D. Lyden

Radar and Optics Division
Environmental Research Institute of Michigan
Ann Arbor, Michigan 48107

*Additionally an ERIM consultant.

ABSTRACT

Synthetic aperture radar (SAR) has been used to image long-period (15-200 s) gravity waves in the nearshore region of Lake Michigan. These long-period waves are a response of the sea surface to forcing by a non-monochromatic, wind-generated surface wave field. The SAR data was successfully compared with an in-situ wave gauge record. Both one- and two-dimensional fast Fourier transforms were generated from near and offshore regions of SAR data, 1.5 x 1.5 km size each. Comparison of the SAR derived near and offshore spectral estimates exhibited both low- and high-frequency wave components. Classical bathymetrically controlled wave refraction was observed for both the short as well as long wave components of the sea surface. This paper demonstrates the ability of SAR X-band data to image successfully low amplitude, long-period, signals. The signals appear to correspond to a "surf beat" generated by the incident wind wave field.

Introduction

Since the initial observations of long-period (30-300 s) wave motions by Munk (1949) and Tucker (1950), several conjectures concerning the generation and propagation of "surf beats" have been proposed. The theoretical development of Longuet-Higgins and Stewart (1962) employed interactions of a non-monochromatic sea to generate an amplitude modulated sea surface. Through the use of the calculated increased radiation stress beneath groups of large waves and a corresponding decrease in the stress associated with lower waves, a forced long-period wave is generated at the beat frequency. Meadows (1977) showed that this long-period forced wave propagated at the short wave group velocity and was observable in the nearshore zone. Similarly, Larsen (1979) has observed long-period forced waves in the North Pacific which appeared to have been generated by, and propagated with, the modulated sea surface.

All inferences, as well as previous attempts at field verification of the physical characteristics of these long-period waves, have been based on single point time series measurements. The studies of Meadows (1977) represented the first two-dimensional, synchronous, time series observations of nearshore, long-period wave motions. These studies, however, were still conducted over an offshore spatial interval which was small (order of half the wavelength) compared to the wavelengths of the forced surf beat.

Investigation of the backscatter of microwave energy from the sea surface provides a unique way to view large spatial regions of the sea surface nearly simultaneously. Synoptic coverage of wave characteristics, as available from synthetic aperture radar (SAR), has provided a three-dimensional (two spatial dimensions and radar backscatter modulation) representation of the propagation and physical characteristics of long-period wave motions across the sea surface. Since the intensity of radar backscatter can be related to

the characteristics of ocean wave propagation (Gonzales, et al., 1979; Gower and Hughes, 1979; Shuchman and Meadows, 1980; Schwab, et al., 1981), definitive information is now available concerning the generation and propagation of these wave motions.

SAR sea surface information was collected over a region of Lake Michigan by the Environmental Research Institute of Michigan (ERIM). At the time of the SAR overflight, the University of Michigan, Department of Atmospheric and Oceanic Science was operating its mobile nearshore wave and current monitoring array (Meadows, 1979; Meadows, et al., 1980; Shuchman and Meadows, 1980). The concurrent acquisition of airborne SAR sea surface data with in-situ sea truth has provided a valuable opportunity to investigate the three-dimensional characteristics of a complex nearshore wave field. A previous paper, utilizing this coincident SAR and in-situ wave gauge data (Shuchman and Meadows; 1980), has shown SAR can successfully image the incident wind generated gravity wave field. This paper will concentrate on the long-period (15-200 s) response of the sea surface to forcing by a non-monochromatic, wind-generated surface wave field and the ability of SAR to successfully image these subtle surface wave motions.

Theory of Long-Period Wave Generation

Employing the classic formulation for the linear interaction of two sinusoidal waves of differing radian wavenumbers, k_1 and k_2 , and radian wave frequencies, σ_1 and σ_2 , a solution for the resultant sea surface is possible by simple superposition of these wave components. The resultant sea surface (η) is a function of both space (x) and time (t) and is given by,

$$\eta(x, t) = a \cos(k_1 x - \sigma_1 t) + a \cos(k_2 x - \sigma_2 t), \quad (1)$$

where a is the wave amplitude. As suggested by Kinsman (1965) for the condition when the two component waves are very nearly the same length and period, such that

$$\Delta k \ll k_1, \quad \text{and} \quad \Delta \sigma \ll \sigma_1,$$

where $\Delta k = k_1 - k_2$ and $\Delta \sigma = \sigma_1 - \sigma_2$, then

$$k_1 \approx k_2 \quad \text{and} \quad \sigma_1 \approx \sigma_2.$$

Hence, the amplitude-modulated sea surface, as a function of distance in the propagation direction, may be expressed as

$$\eta(x) \approx 2a \cos\left(\frac{\Delta k}{2} x\right) \cos(kx) \quad (2)$$

and as a function of time as,

$$\eta(t) \approx 2a \cos\left(\frac{\Delta \sigma}{2} t\right) \cos(\sigma t). \quad (3)$$

Since $\Delta k \ll k$ and $\Delta \sigma \ll \sigma$, the spatial and temporal scales of the modulation are very long compared to the individual wave components which comprise the group. This interference pattern results in the generation of groups of large waves separated by groups of small waves (see Figure 1 from Longuet-Higgins and Stewart, 1962). The length of the long-period modulation is given by Kinsman (1965) as

$$L_{\text{mod}} = \frac{4\pi}{\Delta k} \quad (4)$$

while the period of the modulation is

$$T_{\text{mod}} = \frac{4\pi}{\Delta \sigma}. \quad (5)$$

The distance between successive groups of high waves is therefore, $1/2 L_{\text{mod}}$ and the corresponding time interval is $1/2 T_{\text{mod}}$.

Consider a conventional right-handed rectangular coordinate system with the x-axis horizontal and in the direction of wave propagation and the z-axis vertical and upward. Let u , v and w be the velocity components in the x , y and z directions respectively; and let p , ρ and g denote the pressure, density and gravitational acceleration respectively. Also let the free surface be given by the

equation $z = \eta(x, y, t)$, where t is time, and the rigid horizontal bottom by the equation $z = -h$.

When the length of the modulated wave groups are long compared to the local water depth, changes in the mean sea level and the wave mass-transport correspond to those that would result from an applied horizontal force; in this case, the radiation stress (Whitham, 1962; Longuet-Higgins and Stewart, 1962). For this condition, the flux of momentum across an $x = \text{constant}$ vertical plane is given by Longuet-Higgins and Stewart (1960) as

$$S = \overline{\int_{-h}^{\eta} (\rho + \rho u^2) dz} \quad (6)$$

where the radiation stress, (S_x) , is the difference between S and the contribution due to the hydrostatic pressure;

$$\begin{aligned} S_x &= \overline{\int_{-h}^{\eta} (\rho + \rho u^2) dz} - \int_{-h}^{\bar{\eta}} \rho g (\bar{\eta} - z) dz \\ &= S - \frac{1}{2} \rho g (h + \bar{\eta})^2 \end{aligned}$$

which is approximately equal to

$$\approx S - \rho g \left(\frac{1}{2} h^2 + h \bar{\eta} \right) \quad (7)$$

where the over-bars denote time averages. For the condition of long waves in shallow water, the vertical accelerations are assumed negligible; hence, correct to second order

$$S_x = E \left[\frac{2C}{C} g - \frac{1}{2} \right] \quad (8)$$

where E is the wave energy per unit horizontal area and is defined as:

$$E = \frac{1}{2} \rho g a^2;$$

C_g in Eq. (8) denotes the deep water group velocity of the waves, and C is the phase speed of the individual waves.

Conservation of mass and momentum may be expressed as

$$\frac{\partial(\rho\bar{\eta})}{\partial t} + \frac{\partial M}{\partial x} = 0, \quad (9)$$

and

$$\frac{\partial M}{\partial t} + \frac{\partial S}{\partial x} = 0, \quad (10)$$

where M is the mean, vertically integrated horizontal momentum given by

$$M = \overline{\int_{-h}^{\eta} \rho u \, dz}. \quad (11)$$

Substituting for S_x from Eq. (7), the momentum equation may be written as,

$$\frac{\partial M}{\partial t} + gh \frac{\partial}{\partial x} (\rho\bar{\eta}) = - \frac{\partial S_x}{\partial x}. \quad (12)$$

Since the applied force, $-\partial S_x / \partial x$ travels with the group velocity, $\partial/\partial t$ may be replaced with $-C_g \partial/\partial x$ which upon substitution into Eqs. (9) and (12) gives:

$$-\rho C_g \frac{\partial \bar{\eta}}{\partial x} + \frac{\partial M}{\partial x} = 0 \quad (13)$$

and

$$\rho gh \frac{\partial \bar{\eta}}{\partial x} - C_g \frac{\partial M}{\partial x} = - \frac{\partial S_x}{\partial x}. \quad (14)$$

The solution to this set of equations is given by Longuet-Higgins and Stewart (1962) as

$$\rho \frac{\partial \bar{\eta}}{\partial x} = - \left(\frac{1}{gh - c_g^2} \right) \frac{\partial S_x}{\partial x}, \quad (15)$$

$$\frac{\partial M}{\partial x} = - \left(\frac{c_g}{gh - c_g^2} \right) \frac{\partial S_x}{\partial x}. \quad (16)$$

Upon integration, the free surface elevation and mean horizontal momentum become

$$\bar{\eta} = - \frac{S_x}{\rho(gh - c_g^2)}, \quad (17)$$

and

$$M = - \frac{c_g S_x}{(gh - c_g^2)}, \quad (18)$$

respectively.

The interpretation suggested by Longuet-Higgins and Stewart (1962) is as follows:

"It will be noticed that beneath a group of high waves, where S_x and E are both large, $\bar{\eta}$ and \bar{u} are more negative, that is to say there is a relative depression in the mean surface level, coupled with a mean flow opposite to the direction of wave propagation. Beneath a group of low waves, on the other hand, the mean surface level is raised and the flow is positive." (See Figure 1.).

Sea Surface - SAR Interactions

It is generally accepted that the scattering of microwave energy from the sea surface is a Bragg-Rice resonance phenomenon (Wright, 1968), thus making the received radar image particularly sensitive to capillary and short ultra-gravity ocean surface waves. Non-linear interaction of these short waves with longer period wave motions is the subject of much research (Phillips, 1981; Longuet-Higgins and Stewart, 1960, McGoldrick, 1970, 1972). It is generally agreed,

however, that the short wavelengths are increased in the troughs of the long waves and that the correspondingly short wave height is decreased. Conversely, on the wave crest of the long waves, the short wave height is increased and the short wavelength is decreased. Both effects act to increase the sea surface roughness in the crest regions of long waves and correspondingly decrease the roughness in the trough region (Phillips, 1981). The radar backscatter increases as a function of increasing sea surface roughness, thus producing regions of intense radar backscatter from modulated long wave crests and diminished radar return from modulated long wave troughs. Furthermore, it also appears that the existence of a surface capillary or ultra-gravity wave field is a necessary condition to provide radar images of long-period ocean internal wave motions.

The proposed physical mechanism for the indirect imaging of "surf beats" by radar backscatter is as follows. A modulated, wind-driven, capillary/ultragravity wave field exists in conjunction with a shoreward propagating, non-monochromatic, gravity wave field. Non-linear capillary-gravity wave interactions occur which produce increased surface roughness on the crests of the gravity waves and decreased surface roughness in the troughs. Concurrently, similar but slightly different gravity wave components of the non-monochromatic wave field are interacting to form surf beats consisting of groups of high waves separated by groups of low waves. These wave groups produce corresponding depression and relaxations of the mean water level in response to fluctuations of the applied radiation stress. Hence, a forced, long-period wave, travelling at the group velocity of the wind wave packet is generated. Bright radar returns, therefore, should correspond to groups of high gravity waves and corresponding troughs of the forced long-period waves.

Data Description

The synthetic aperture radar (SAR) used to collect the data is the ERIM X- and L-band dual polarized radar described by Rawson et al. (1975). The ERIM SAR system records four channels of radar return but we will focus our attention here on the X-band horizontal-transmit-horizontal-receive (HH) channel as this data provided the clearest wave images. The SAR was flown at an altitude of 6100 m and operated with a center incident angle from the vertical of 20° , yielding a swath width of 5.6 km. The cross-track or range resolution of SAR is limited by radar bandwidth and is about 2 m for X-band. The along-track or azimuth resolution is obtained from the synthetic aperture technique described by Brown and Porcello (1968). For the X-band, the azimuthal resolution is about 2.5 m. This SAR data was processed on the ERIM tilted-plane precision optical processor described by Kozma, et al. (1972).

The SAR data was collected on October 18, 1978, at approximately 16:35 EST. The airborne data was collected along the shoreline of Lake Michigan centered at latitude $43^\circ 50' N$. The site for this field experiment as shown in Figure 2 was the eastern shore of Lake Michigan, between the cities of Ludington and Pentwater, Michigan. This thirteen kilometer section of shoreline, extending approximately north-south, is characterized by a multiple-barred bathymetry with nearly straight and parallel contours.

At the same time as the ERIM flight, the University of Michigan, Department of Atmospheric and Oceanic Science was operating its mobile surf zone, wave and current sensing array (Meadows, 1979). Monitoring of incident wave characteristics and longshore current velocities was conducted through the growth of a major storm on Lake Michigan. A detailed discussion of the experimental design is presented in Wood and Meadows (1975) and Meadows (1977). Surface-piercing, step-resistance wave probes and bi-directional ducted

impeller flow meters were used to make simultaneous measurements of wave and current conditions. These sensors were oriented on a line perpendicular to shore, extending from the beach to the outer surf zone. Other coastal sensing equipment included a directionally mounted motion picture camera and Lagrangian drifters. Unfortunately, high wind and wave action on 17 and 18 October destroyed much of the array; however, sufficient sensors survived to make this comparative study possible.

Methods

The SAR collected data were digitized with an approximate resolution of 6 meters (3 m pixels) using the ERIM hybrid image dissector (Ausherman, 1975). The range coordinates of the digitized data were analytically corrected for slant-to-ground range geometry (Feldkamp, 1978). Two 1.5 x 1.5 km subsections (see Figure 2) with 6 meter resolution were extracted from the digitized data. The two sections are labeled A and B, where A is closest to shore.

The 3.0 m pixel digitized SAR images were converted to 6 m samples by 4 pixel into 2 pixel averaging in order to increase coherence in the image. The average value of each azimuthal line was subtracted from the line to remove the trend of intensity fall-off with increasing range distance. Two-dimensional fast Fourier transforms (FFTs) were performed on each 256 x 256 cell subsection to yield raw directional wavenumber spectra with a Nyquist wave number of 0.5 m^{-1} . The raw spectra were smoothed by replacing each value with the average of the surrounding 5 x 5 cell. The approximate number of degrees of freedom for the resulting spectrum is 142 (Kinsman, 1965). The 99 percent confidence limits are then $\pm 1.5 \text{ dB}$ (Jenkins and Watts, 1968).

In addition to the two-dimensional FFT analysis, five isorange SAR backscatter records 1.5 km long were analyzed using both a one-dimensional spectral analysis and a band-pass filtering program.

This one-dimensional analysis was performed on the SAR data to better quantify the long-period components of the prevalent wave field. To perform this analysis, 5 adjacent isorange lines of data were extracted from the digital image corresponding to the center of both study areas A and B. These lines were then averaged, or in effect, smoothed in the range direction, this was done to reduce the speckled nature of the SAR data. The averaged lines were then plotted in order to characterize the relative backscatter across these study areas. These data were then selectively filtered for wavelengths lying between 177 and 1180 m for study area A and from 249 to 1660 m for study area B. This wavelength filtering corresponds to the temporal region of interest, 15-200 seconds.

To calculate the directional wave spectrum at the instrumented surf zone site, a sixteen-minute analog record was digitized at 0.25 s intervals and analyzed using conventional one-dimensional fast Fourier transform techniques. The directional information was obtained from the directionally mounted camera. One-dimensional spectral analysis using a FFT routine was performed on the total sixteen-minute, outer surf zone water level elevation time history. The smoothed spectrum resulting from this analysis is presented in Figure 3. This spectrum exhibits a well defined broad peak in the wind wave range (2-8 sec), composed of multiple components. This spectrum is characteristic of locally generated seas. In addition, this spectral analysis has also identified significant long-period wave motion at specific periods of 17.2 and 32.3 seconds and a less significant peak at approximately 59 seconds. These near-shore spectral estimates were obtained from a continuous digital record consisting of 3840 equally spaced values at 0.25 second intervals. The 80 percent confidence band lies between 1.42 and 0.62 times the spectral estimate and is indicated on Figure 3 (Kinsman, 1965).

Based upon these results, this total water level elevation record was band-pass filtered to retain only surface wave motions with

periods between 15 and 200 seconds. A representative portion of the original and band-pass filtered, long-period records is presented in Figure 4. It, therefore, appears that significant long-period wave motions are present in the nearshore region with a mean amplitude of approximately 10 percent of that of the incident wind waves. These results agree favorably with the finding of Meadows and Wood (1982) where both progressive as well as standing long-period wave motions were observed in the nearshore region. The question arises, however, as to the generation mechanism of these waves. It is the hypothesis of the authors that these long-period waves are formed as a result of non-linear interactions between the dominant wind-wave components and that they propagate as forced waves at the group velocity of wind generated waves. Hence, it should be anticipated that these wave motions should exist somewhat homogeneously across the sea surface provided that wind waves of sufficient amplitude and prescribed frequency exist.

Analysis

Synthetic aperture radar provides a unique perspective from which to investigate this hypothesis, namely that long-period surf beats are generated by and propagate with the wind wave field. The nearly simultaneous view of a relatively large spatial region of the sea surface provided by either an airborne or spaceborne SAR, affords an ideal measurement tool for these wave motions. To examine this capability, the results of both the SAR two-dimensional and the nearshore in-situ wave gauge data series will be evaluated.

Results of the nearshore step resistance wave gauge spectral analysis have indicated several well defined peaks in the wind wave range. In addition, two long-period peaks at 17.2 and 32.3 seconds respectively, were also well resolved. A poorly resolved spectral peak is also apparent at approximately 59 seconds. Linear combinations of the dominant wind wave components are formed in Table 1 to

produce their respective beat periods. It may be noted that the dominant wind wave components of 5.6, 4.8 and 4.2 seconds combine theoretically, to form beats of 16.8 and 33.6 seconds, respectively. These calculated beat periods are very close to those periods resolved by the spectral analysis of the total sixteen-minute water surface elevation recorded from the nearshore wave gauge. It, therefore appears that forced long-period wave motions were present in the nearshore region resulting from the non-linear interaction of the dominant wind wave components.

The energy associated with these long-period forced waves is an order of magnitude below that of the peak in the wind wave spectra. Theoretical calculations of the maximum mean surface deformation from Eq. (12) suggest a forced wave height of approximately 0.38 m. The energy associated with the forced wave would be approximately a factor of 8.4 less than that associated with the peak wind wave component. It appears that long-period wave motion in the nearshore region is present with both a period and an amplitude close to theoretical predictions.

To further identify these long-period wave motions, the total sixteen-minute water surface elevation record from the nearshore wave gauge was band-pass filtered for periods between 15 and 200 seconds. A representative portion of the original water surface elevation record and its associated long-period component are presented in Figure 4. This series, as well as the data of Meadows (1977) suggest that the mean surface level is 180° out of phase with the wind wave amplitudes. As theoretically suggested, this implies depressions in the water surface are associated with groups of large waves and long-period elevations of the water surface correspond to groups of low waves.

Based upon these considerations, SAR imagery of a relatively large region of the sea surface should also exhibit these long-wave

features. In an effort to investigate this potential of SAR, a manual photo-interpretation of the radar image film was performed. A portion of the X-band (HH) SAR data collected over the Lake Michigan test site is presented in Figure 5. The image extends 7.9 km offshore and is 5.6 km wide. Alternating groups of large and small wind wave packets can be readily seen across this image. At three representative locations across this nearshore imagery, the long-wave length are indicated on the figure. As these long waves, forced by short-wave groups, propagate shoreward, both wave length compression and refraction are plainly observable. The long wavelengths decrease from approximately 510 m (Area B) to approximately 410 m (Area A). These radar observations of the long wave components of surface elevation are in excellent agreement with sea truth measurements made at the outer surf zone.

To further document the existence and propagation characteristics of these SAR-sensed long wave components, a conventional two-dimensional FFT of the radar backscattered energy was performed. One FFT analysis was performed in both the offshore and nearshore regions of the aircraft swath. The SAR FFTs were generated by the algorithm described by Shuchman, et al. (1979). However, in this application, only the long-wave portion of the spectrum is of interest. For a detailed discussion of the total SAR-sensed wave spectra and associated sea truth see Shuchman and Meadows (1980). A summary of the general sea state conditions during this experiment as well as a comparison of the SAR-derived wind generate sea spectral estimates to sea truth are presented in Table 2.

In the offshore region, the SAR-derived spectral analysis resolved a long-wave component with energy concentrated at a wavelength of approximately 511 m, travelling in a direction of $025 \pm 3^\circ T$. Similarly, in the nearshore region, a long-wave component of 408 m wavelength travelling at $035 \pm 3^\circ T$ was resolved. The nearshore and offshore two-dimensional FFTs are shown in Figure 6 and 7 respectively.

Also shown on each of the figures is the one-dimensional plot of the low-frequency components versus relative energy. These estimates of long-wave characteristics exhibit two important properties. First, the long wavelengths are in excellent agreement with the representative offshore wave group dimensions derived from the SAR image film. Second, the degree of observed refraction from the offshore to the nearshore region of these forced long-period wave motions is also in close agreement with the sea truth as well as with the calculated wave refraction for the dominant wind wave components. A comparison of SAR-derived and sea truth wave characteristics are presented in Table 3.

Furthermore, the two directly observed quantities which determine the propagation of these SAR and sea truth sensed long-period wave motions are the length and period of the modulated wave group. The lengths of the dominant long-period waves were obtained from the SAR-derived two-dimensional FFT. Similarly, the periods of the dominant long-wave components were obtained from a one-dimensional spectral analysis of the nearshore wave gauge data. By combining Eqs. (4) and (5), the celerity of these modulated long-period waves may be expressed as:

$$C_{\text{mod}} = \frac{L_{\text{mod}}}{T_{\text{mod}}} . \quad (19)$$

The calculated long-period wave celerity utilizing both the SAR and wave gauge measured dominant long-period wave parameters, results in values of 12.6 ms^{-1} and 15.8 ms^{-1} for areas A and B, respectively. It is interesting to note that assuming these long-period waves are propagating as shallow water waves with celerity given by

$$C = \sqrt{gd} \quad (20)$$

long-period wave celerities of 12.6 ms^{-1} and 16.8 ms^{-1} are calculated for areas A and B, respectively. Based on this close agreement, it

appears that these observed long-period wave motions are propagating as shallow water waves and not as forced waves as suggested from theory. This apparent discrepancy arises from a complex interaction between the relatively short, steep, locally generated waves and the shallow bathymetry of this region. The theoretical formulation employed in this study is based upon the assumption that the character of the SAR-sensed modulated sea surface is a function of ΔK of the wind wave components, and that $\Delta K \ll K_1$. Hence, for limited fetch situations such as the conditions of this study, the two wind wave components separated by ΔK do not explicitly satisfy the mathematical constraint of $\Delta K \ll K_1$. This produces a modulated long-period wave which is not completely "phase locked" with the short wave components, and in fact, appears to propagate as a shallow water wave.

The close agreement between the long-period celerity derived above, and that predicted for a shallow water wave prompted the inclusion of frequency and period axes on the various plots in Figures 6 and 7. Recall that the SAR only provides a spatial measure of waves, therefore, the only "true" axes in Figures 6 and 7 is that for wavenumber. The frequency and period axes are both based on the shallow water wave assumption for a given wavenumber. They are not derived from any physical measurements.

To document further the existence and character of the SAR-sensed long-period wave motions, one-dimensional scans of the raw radar backscatter were obtained. One spatial series consisting of 512 digital values sampled at three meters, was obtained from each of the two regions where the two-dimensional FFT analysis was performed. Area A was centered 2650 meter offshore and Area B was centered at 5800 meters offshore. The total series of radar backscatter as well as their associated band-pass filtered (177-1180 m, Area A and 249-1660 m, Area B) long-period components are presented in Figure 8. Once again long-period oscillations of the radar backscatter intensity are clearly visible, with maximum radar return occurring in

phase with peaks of the long-period oscillations (i.e., groups of large wind waves). These SAR-sensed, long-period oscillations represent approximately a 1.5 dB change in radar backscatter intensity from crest-to-trough. The dynamic range of the total, unfiltered radar backscatter intensity is approximately 5.2 dB. Hence, the energy associated with these radar-sensed long-period oscillations is approximately a factor of 2.3 less than the energy of the radar backscatter associated with the wind wave components of the sea surface structure.

SUMMARY

It appears that a direct correlation exists between the amplitude of these long-period wave motions, as sensed in-situ, and the long-period component of the radar backscatter. From the sea truth measurements, the ratio of short-period wave to long-period wave mean amplitude is 5.4. Similarly for the radar sensed long-period oscillation this ratio is approximately 6.0. Kasischke (1980) has reported a linear relationship between SEASAT SAR modulation depth (crest-to-trough intensity) and wave height.

Investigation of the information contained in the backscatter of microwave energy from the sea surface can provide detailed and nearly synoptic coverage of relatively large portions of the ocean surface. To illustrate this unique capability, a three-dimensional representation of a portion of a SAR-sensed sea surface is presented in Figure 9 which depicts the long-period undulations present in study area B. This plot was produced from the SAR digital data by extracting 6 isorange lines of 5 pixels each, averaging these 5 pixels, in effect, to smooth in the range direction. These lines were then bandpass filtered for wavelengths lying between 249 and 1660 m (15-200 seconds), this filtered output was then used as input to a perspective view plotting program.

It is clear from this plot that long-period waves are present in this area. However, care should be exercised in interpreting what information this plot contains. This is merely a convenient graphical technique that shows the long-period components, not a detailed analysis technique.

This paper has demonstrated that a synoptic remote sensing device such as SAR has the ability to successfully image low-amplitude, long-period signals (surf beats). The analysis techniques utilized to extract this information from the SAR data, include:

1. a manual photographic interpretation;
2. one- and two-dimensional spectral analyses employing FFT techniques; and
3. extraction of band-pass filtered long-period components from radar backscatter plots.

It should be mentioned when utilizing SAR data such as presented in this paper that the spectral estimates presented are wavenumber, directional spectra of the radar return intensity. The data does not represent wave height information in a direct sense. SAR intensities (i.e., crest-to-trough modulation) have been successfully correlated to wave height, but the exact mathematical modulation transfer function (i.e., SAR gravity wave imaging mechanism) is not totally understood at the present time.

ACKNOWLEDGEMENTS

The ERIM analysis of the SAR gravity wave data was supported by the Office of Naval Research (ONR) Contract N00014-76-C-1048. The technical monitor for this ONR contract is Mr. Hans Dolezalek. The field installation of the mobile wave and current monitoring system, as well as the reduction of the in-situ sea truth data, was supported by The University of Michigan Research Contract 387349.

REFERENCES

- Ausherman, D.A., W.D. Hall, J.N. Latta, and J.S. Zelenka, Radar data processing and exploitation facility, Proceedings IEEE International Radar Conference, Washington, D.C., 1975.
- Brown, W.J. and L. Porcello, An introduction to synthetic aperture radar, IEEE Spectrum, 6, pp. 52-66, 1968.
- Feldkamp, G.B., Correction of SAR-induced distortions in SEASAT imagery, Paper presented at SPIE Conference on Applications of Digital Image Processing, San Diego, Calif., August 1978.
- Gonzalez, F.I., R.C. Beal, W.E. Brown, P.S. DeLeonibus, J.S. Sherman, J.F.R. Gower, D. Lichy, D.B. Ross, C.L. Rufenach, and R.A. Shuchman, SEASAT synthetic aperture radar: ocean wave detection capabilities, Science, 204, pp. 1418-1421, 1979.
- Gower, J.F.R. and B.A. Hughes, Radar and ship observations of coastal sea surface roughness patterns in the Gulf of Georgia, Published in the Proceedings of the Thirteenth International Symposium on Remote Sensing of Environment, Ann Arbor, Michigan, pp. 103-115, 1979.
- Jenkins, A.M. and D.G. Watts, Spectral analysis and its applications, Holden-Day, San Francisco, Calif., 525 pp., 1968.
- Kasischke, E.S., Extraction of gravity wave information from space-borne synthetic aperture radar data, Master's Thesis, University of Michigan, Ann Arbor, 1980.
- Kinsman, B., Wind waves - their generation and propagation on the ocean surface, Prentice-Hall, Englewood Cliffs, N.J., 676 pp., 1965.
- Kozma, A., E.N. Leith, and N.G. Massey, Tilted plane optical processor, Applied Optics, 11, p. 1766, 1972.
- Larsen, L.H., An instability of packets of short gravity waves in waters of finite depth, J. Phys. Ocean., 99, pp. 1139-1143, 1979.
- Longuet-Higgins, M.S. and R.W. Stewart, Radiation stress and mass transport in gravity waves, Jour. Fluid Mech., 13, pp. 481-504, 1962.
- Longuet-Higgins, M.S. and R.W. Stewart, Radiation stresses in water waves in a physical discussion, with Applications, Deep Sea Research, 11, pp. 529-562, 1964.
- McGoldrick, L.F., On Wilton's ripples: a special case of resonant interactions, J. Fluid Mech. 42, pp. 193-200, 1970.
- McGoldrick, L.F., On the rippling of small waves: a harmonic non-linear nearly resonant interaction, J. Fluid Mech. 52, pp. 725-51, 1972.

- Meadows, G.A., A field investigation of the spatial and temporal structure of longshore currents, Ph.D. Dissertation, Purdue Univ., West Lafayette, Indiana, 1977.
- Meadows, G.A., The wind driven component of surf zone circulation (Abstract), Trans. Amer. Geophys. Union, Vol. 60, No. 46, 1979.
- Meadows, G.A., E.S. Kasischke, and R.A. Shuchman, SAR observations of coastal zone conditions, Proceedings of the Fourteenth International Symposium on Remote Sensing of Environment, pp. 845-863, 1980.
- Meadows, G.A. and W.L. Wood, Long-period surf zone motions (in review), 1982.
- Munk, W.H., Surf beats, Trans. Amer. Geoph. Union, Vol. 30, 1949.
- Phillips, O.M., The structure of short gravity waves on the ocean surface, in A Symposium to Explore the Potential of Spaceborne Synthetic Aperture Radar for Radio Oceanography, John Hopkins University, Baltimore, MD, 1981.
- Fawson, R., F. Smith, and R. Larson, The ERIM simultaneous X- and L-band dual polarized radar, Proceedings IEEE International Radar Conference, Washington, D.C., 1975.
- Schwab, D., R.A. Shuchman, and D. Liu, Wind wave directions determined from synthetic aperture radar imagery and from a tower in Lake Michigan, Jour. of Geophysical Research, Vol. 86, No. C3, March 1981.
- Shuchman, R.A., K. Knorr, J.C. Dwyer, A. Klooster, and A. I. Maffett, Imaging ocean waves with SAR, ERIM Report No. 124300-2-T, Environmental Research Institute of Michigan, Ann Arbor, MI, 130 pp., 1979.
- Shuchman, R.A. and G.A. Meadows, Airborne synthetic aperture radar observations of surf zone conditions, Geophysical Research Letters, Vol. 7, No. 11, November 1980.
- Tucker, M.J., Surf beats: sea waves of 1 to 5 minutes period, Proc. Roy. Soc., A 207, pp. 565-573, 1950.
- Whitham, G.B., Mass momentum and energy flux in water waves, Jour. of Fluid Mechanics, Vol. 12, 1962.
- Wood, W.L., and G.A. Meadows, Unsteadiness in longshore currents, Geophys. Res. Lett., Vol. 2, No. 11, 1975.
- Wright, J.W., A new model for sea clutter, IEEE Trans. Antennas and Propagation, Vol. AP-16, pp. 195-223, 1968.

TABLE 1
CALCULATED BEAT PERIODS

Input Components (sec)	<u>5.6</u>	<u>4.8</u>	<u>4.2</u>	<u>3.0</u>	<u>2.6</u>
5.6	---	33.6	16.8	6.5	4.9
4.8	---	---	33.6	8.0	5.7
4.2	---	---	---	10.5	6.8
3.0	---	---	---	---	19.5
2.6	---	---	---	---	---

TABLE 2
COMPARISON BETWEEN THE SAR-DERIVED SURF ZONE
CONDITIONS AND THE IN-SITU SEA TRUTH

Distance from Shore (m)	Depth (m)	SAR Derived		Sea Truth*	
		Dominant Short-Period Wavelengths (m)	Direction (T°)	Dominant Short-Period Wavelengths (m)	Direction (T°)
900	10.5	48	35 ± 3	48	34 ± 2
		43		44	
2200	14.0	55	30 ± 3	54	30 ± 2
		44		44	
4600	27.0	55	25 ± 3	55	28 ± 2
		43		46	
		48			
6900	31.0	55	25 ± 3	55	28 ± 2
		48		46	

*Actual measurements made at surf zone; values for test areas are depth corrected (Shuchman and Meadows, 1980).

TABLE 3
COMPARISON BETWEEN THE LONG-PERIOD SAR-DERIVED SPECTRAL
ESTIMATES AND THE IN-SITU SEA TRUTH

Test Area	Distance from Shore (m)	Depth (m)	SAR-Derived		Sea Truth*	
			Dominant Long-Period Wavelengths (m)	Direction (T°)	Dominant Long-Period Wavelengths (m)	Direction (T°)
A (Nearshore)	2650	16.2	157-167 393-423	35 ± 3	216 406	34 ± 2
B (Offshore)	5800	28.7	498-523	25 ± 3	288 541	28 ± 2

* Actual measurements made at the surf zone, values for test areas A and B are depth corrected.

FIGURE LEGEND

1. Schematic Representation of the Forced Long-Period Modulation of the Surface Resulting from Short Wind-Generated Wave Component Interactions (from Longuet-Higgins and Stewart, 1962).
2. General Study Area Showing Nearshore Bathymetry and Location of Fast Fourier Transformed SAR Data.
3. One-Dimensional Wave Height Spectrum of Water Surface Elevation Time History from Resistance Wave Gauge. Dominant Wave Periods are Identified.
4. Representative Section of 16-Minute Time History of Water Elevation Data from Resistance Wave Gauge. Also Shown is the Corresponding 15-200-Second Band-Pass Filtered Data.
(Note the negative correlation [180° phase shift] between the wind wave amplitudes and the mean surface level.)
5. X-Band (HH) SAR Image of Test Site Showing Long-Period Wave Components.
6. SAR-Derived Two-Dimensional Spectral Estimate (Nearshore).
(Note: Negative wave numbers, frequencies, and periods are included due to the symmetric nature of a 2-D FFT. The frequency and period axes assumes shallow water waves, see text for further explanation.)
7. SAR-Derived Two-Dimensional Spectral Estimate (Offshore).
(Note: Negative wave numbers, frequencies, and periods are included due to the symmetric nature of a 2-D FFT. The frequency and period axes assumes shallow water waves, see text for further explanation.)
8. Filtered and Unfiltered Radar Transects for Both Near and Offshore Study Sites.
9. Perspective Plot of Offshore Area B showing Filtered Long-Period Components.

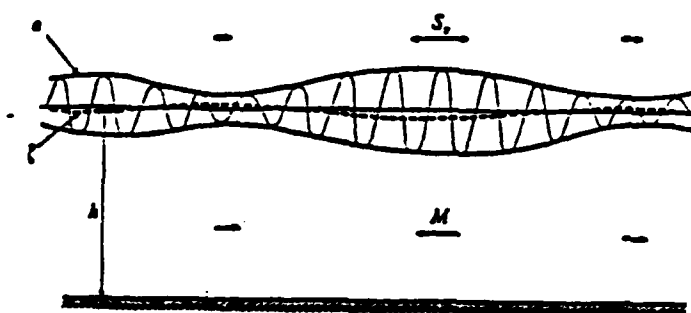


FIGURE 1. SCHEMATIC REPRESENTATION OF THE FORCED LONG-PERIOD MODULATION OF THE SURFACE RESULTING FROM SHORT WIND GENERATED WAVE COMPONENT INTERACTIONS (FROM LONGUET-HIGGINS AND STEWART, 1962)

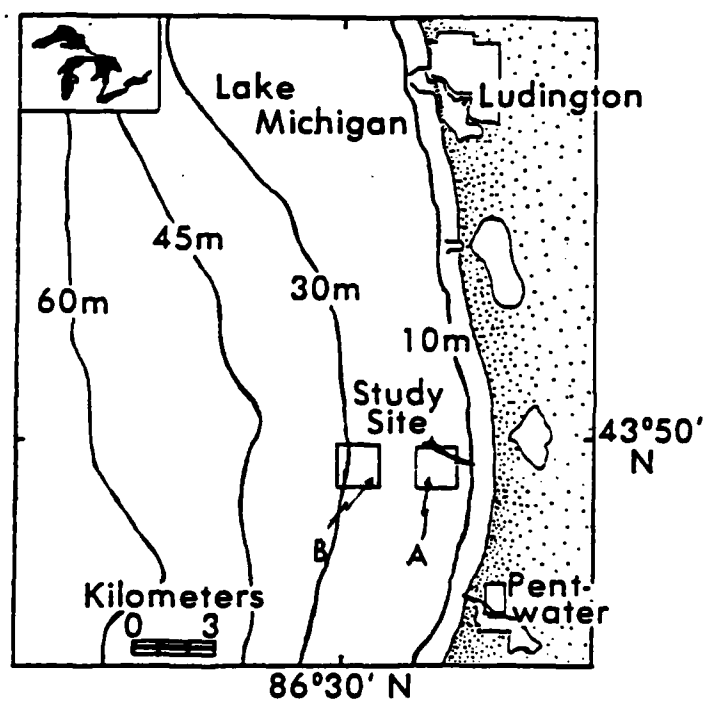


FIGURE 2. GENERAL STUDY AREA SHOWING NEARSHORE BATHYMETRY AND LOCATION OF FAST FOURIER TRANSFORMED SAR DATA.

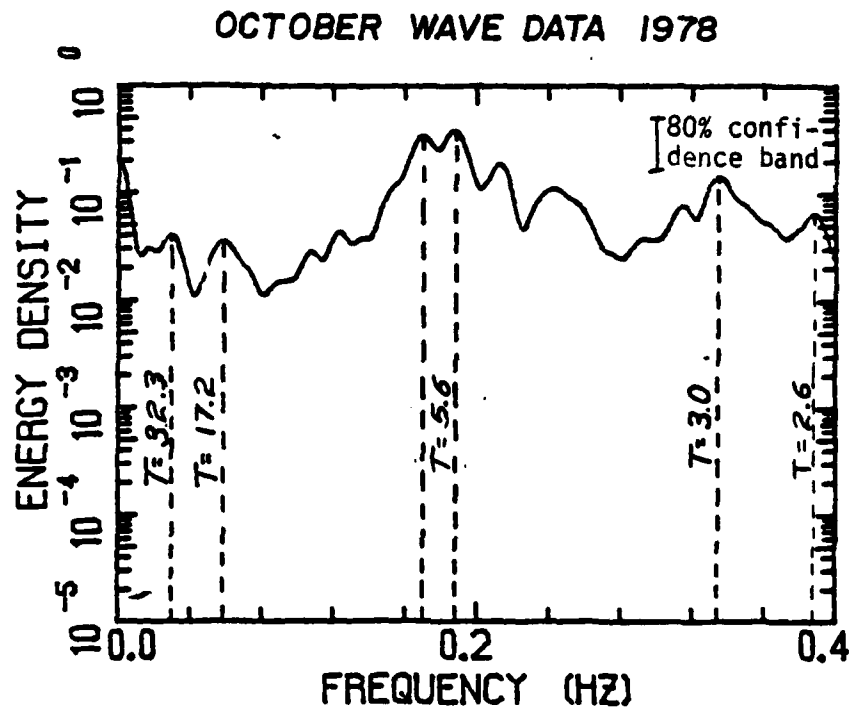


FIGURE 3. ONE DIMENSIONAL WAVE HEIGHT SPECTRUM OF WATER SURFACE ELEVATION TIME HISTORY FROM RESISTANCE WAVE GAUGE. DOMINANT WAVE PERIODS ARE IDENTIFIED.

OCTOBER WAVE DATA 1978

25. SECONDS

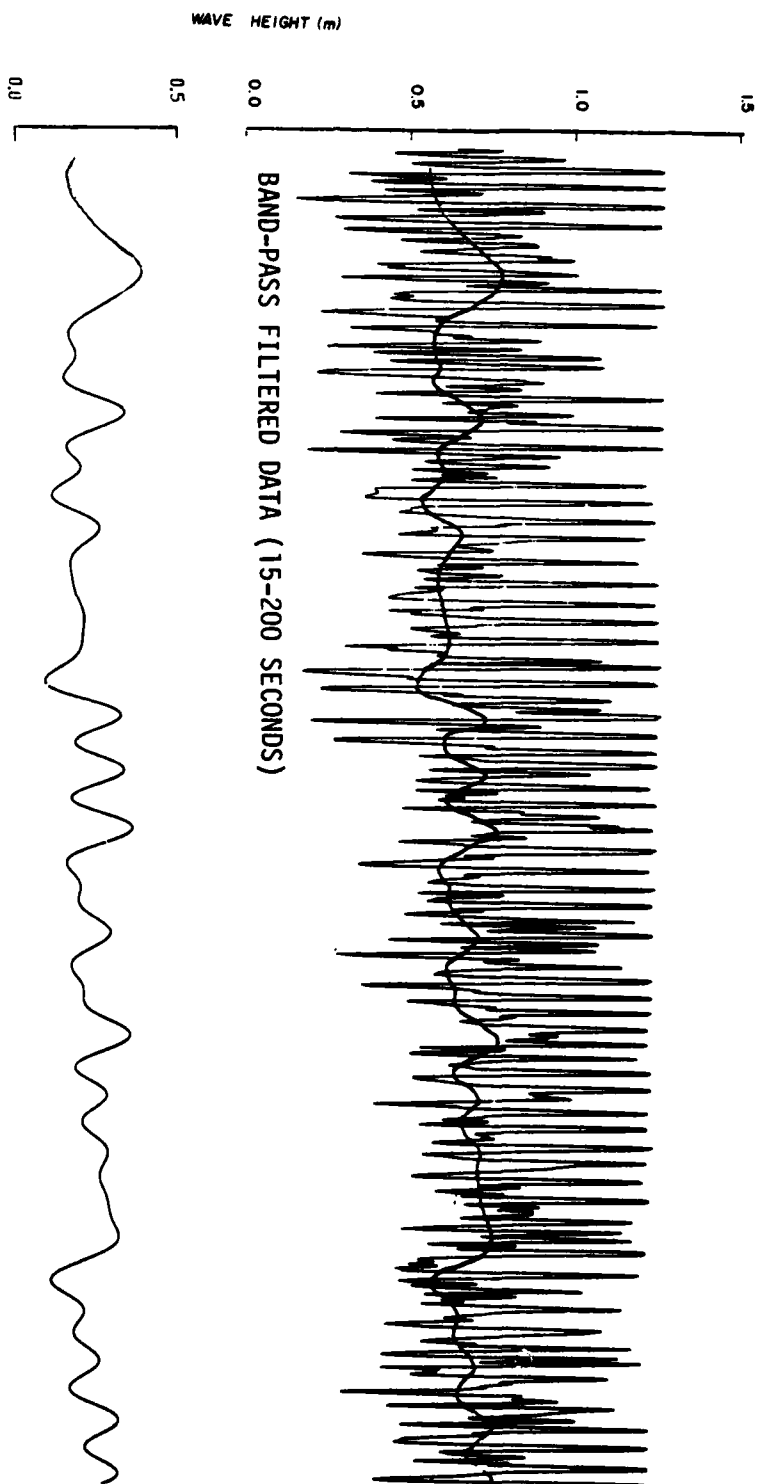


FIGURE 4. REPRESENTATIVE SECTION OF 16-MINUTE TIME HISTORY OF WATER ELEVATION DATA FROM RESISTANCE WAVE GAUGE. ALSO SHOWN IS THE CORRESPONDING 15-200 SECOND BAND-PASS FILTERED DATA.
(Note the negative correlation [180° phase shift] between the wind wave amplitudes and the mean surface level.)

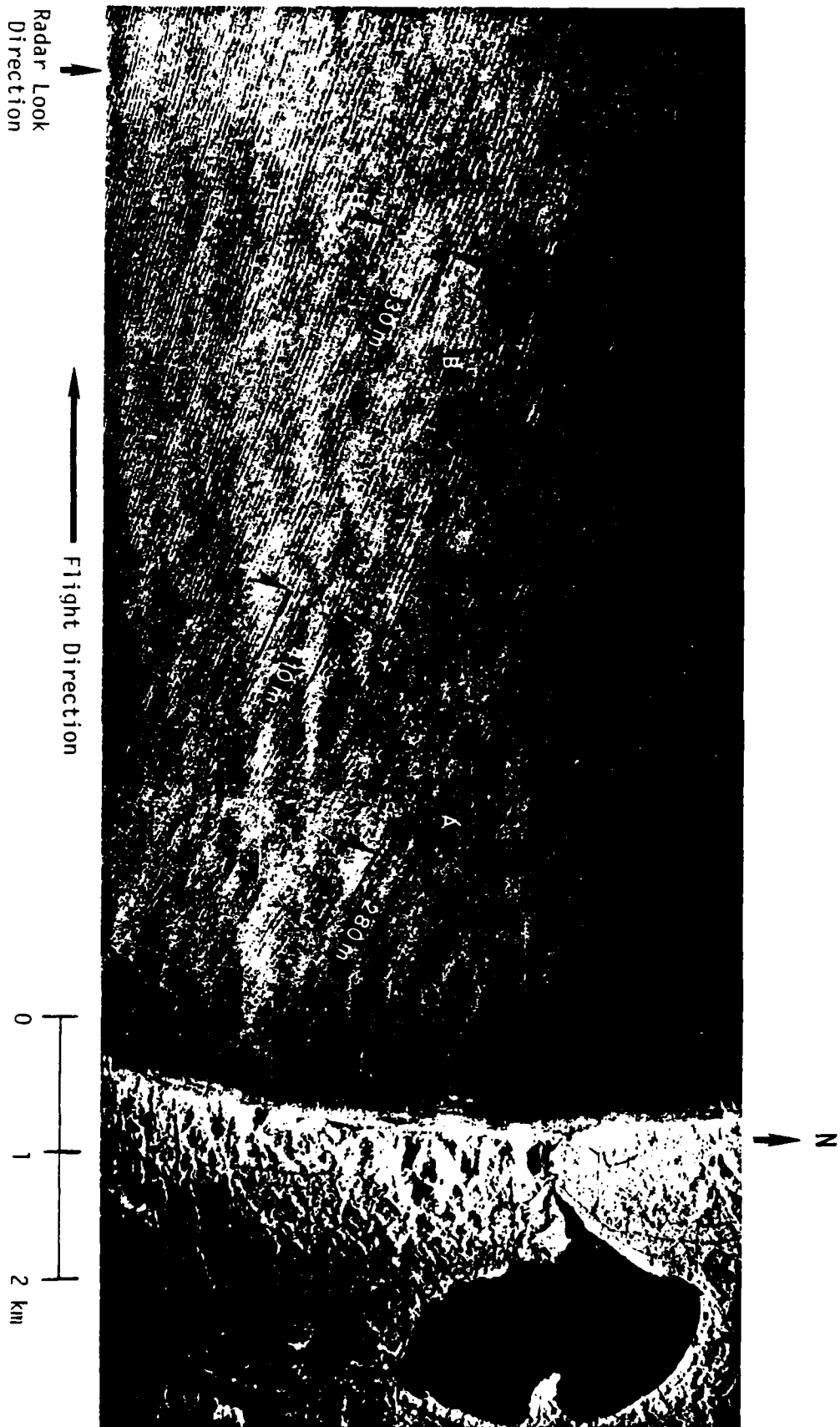


FIGURE 5. X-BAND (HH) SAR IMAGE OF TEST SITE SHOWING LONG-PERIOD WAVE COMPONENTS

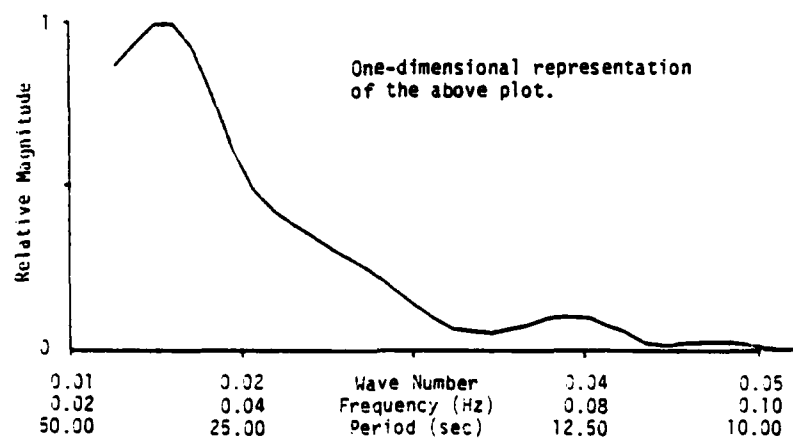
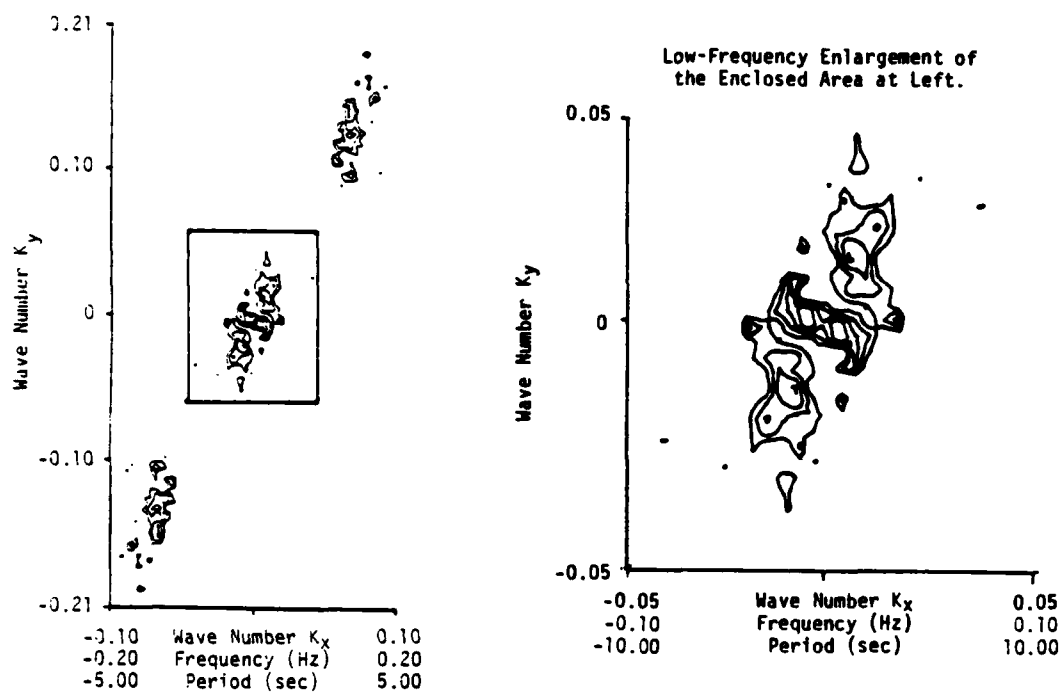


FIGURE 6. SAR-DERIVED TWO-DIMENSIONAL SPECTRAL ESTIMATE (NEARSHORE). (Note: Negative wave numbers, frequencies, and periods are included due to the symmetric nature of a 2-D FFT. The frequency and period axes assumes shallow water waves, see text for further explanation.)

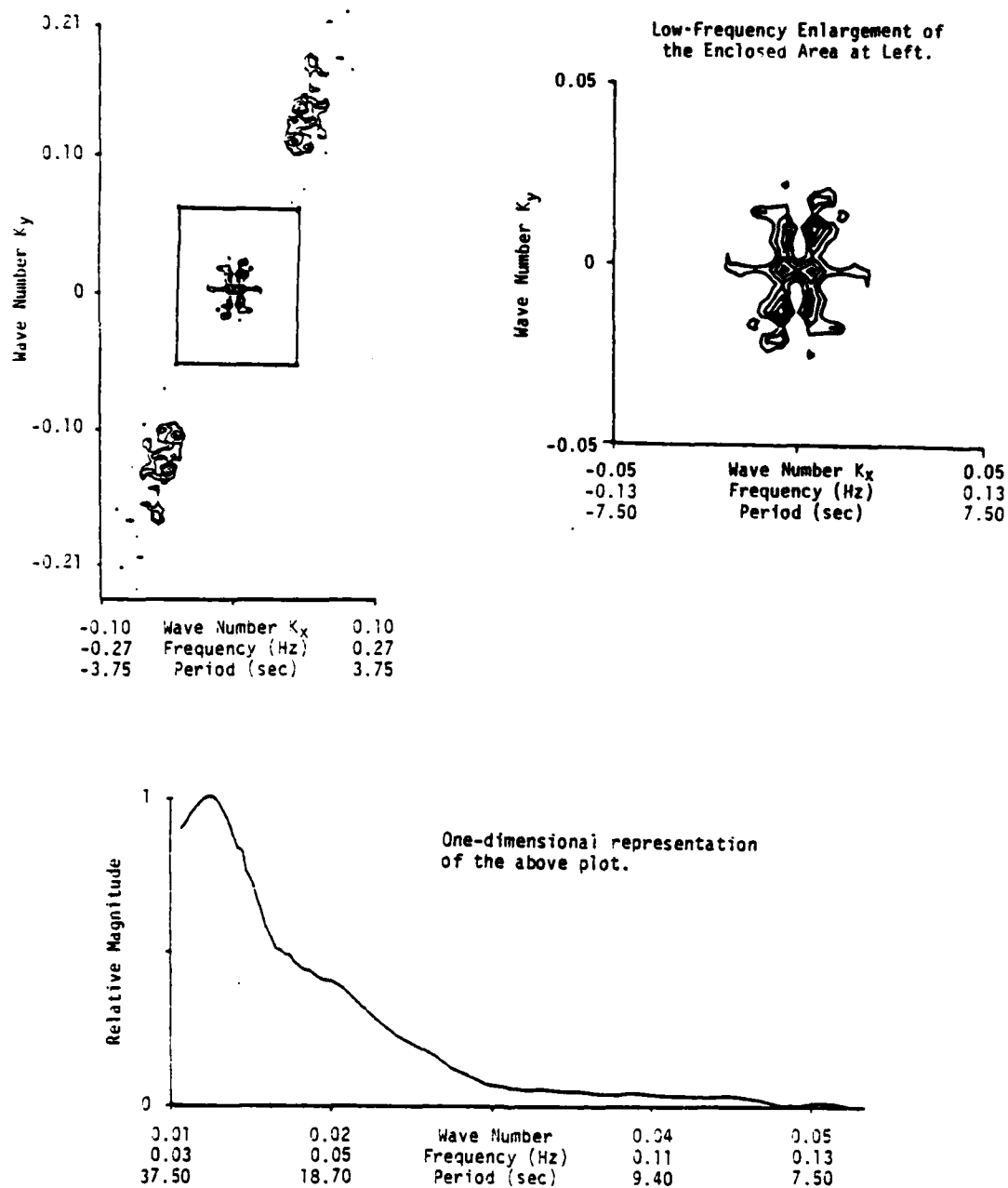


FIGURE 7. SAR-DERIVED TWO-DIMENSIONAL SPECTRAL ESTIMATE (OFFSHORE).
 (Note: Negative wave numbers, frequencies, and periods are included due to the symmetric nature of a 2-D FFT. The frequency and period axes assumes shallow water waves, see text for further explanation.)

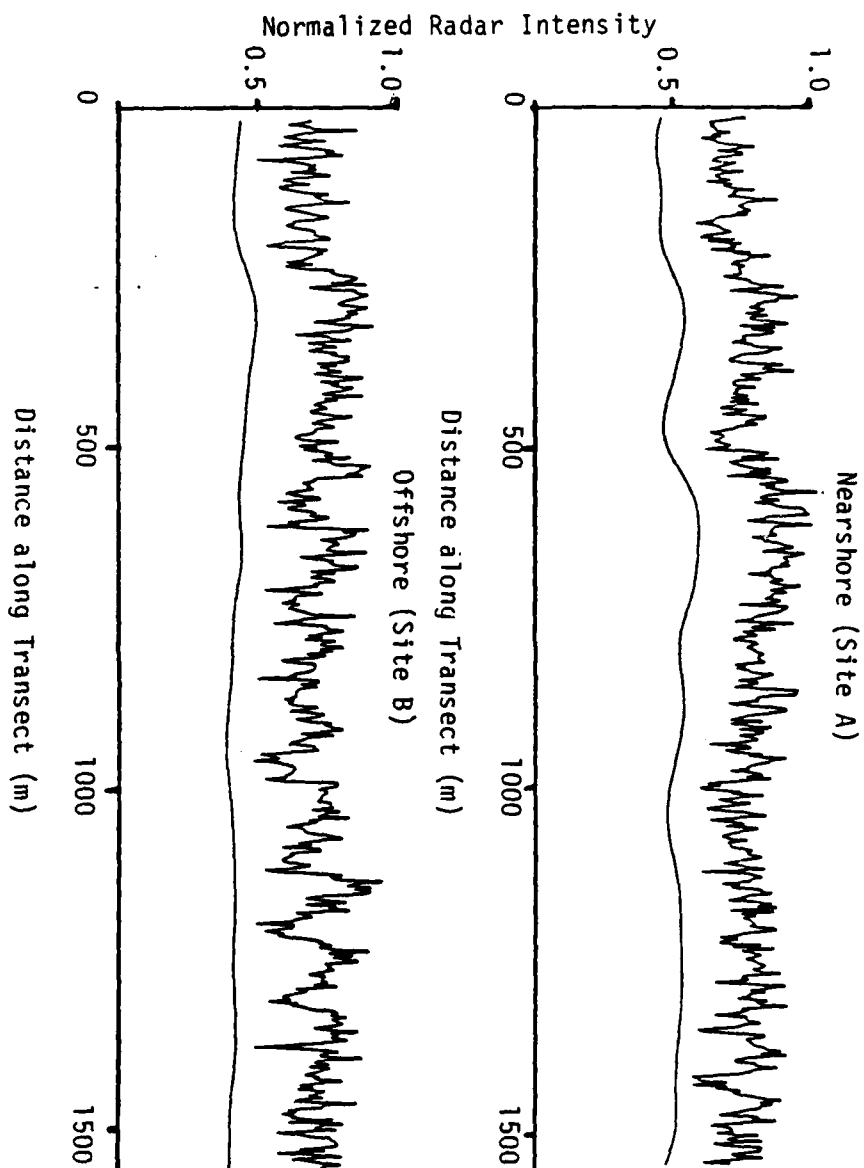


FIGURE 8. FILTERED AND UNFILTERED RADAR TRANSECTS FOR BOTH NEAR AND OFFSHORE STUDY SITES.

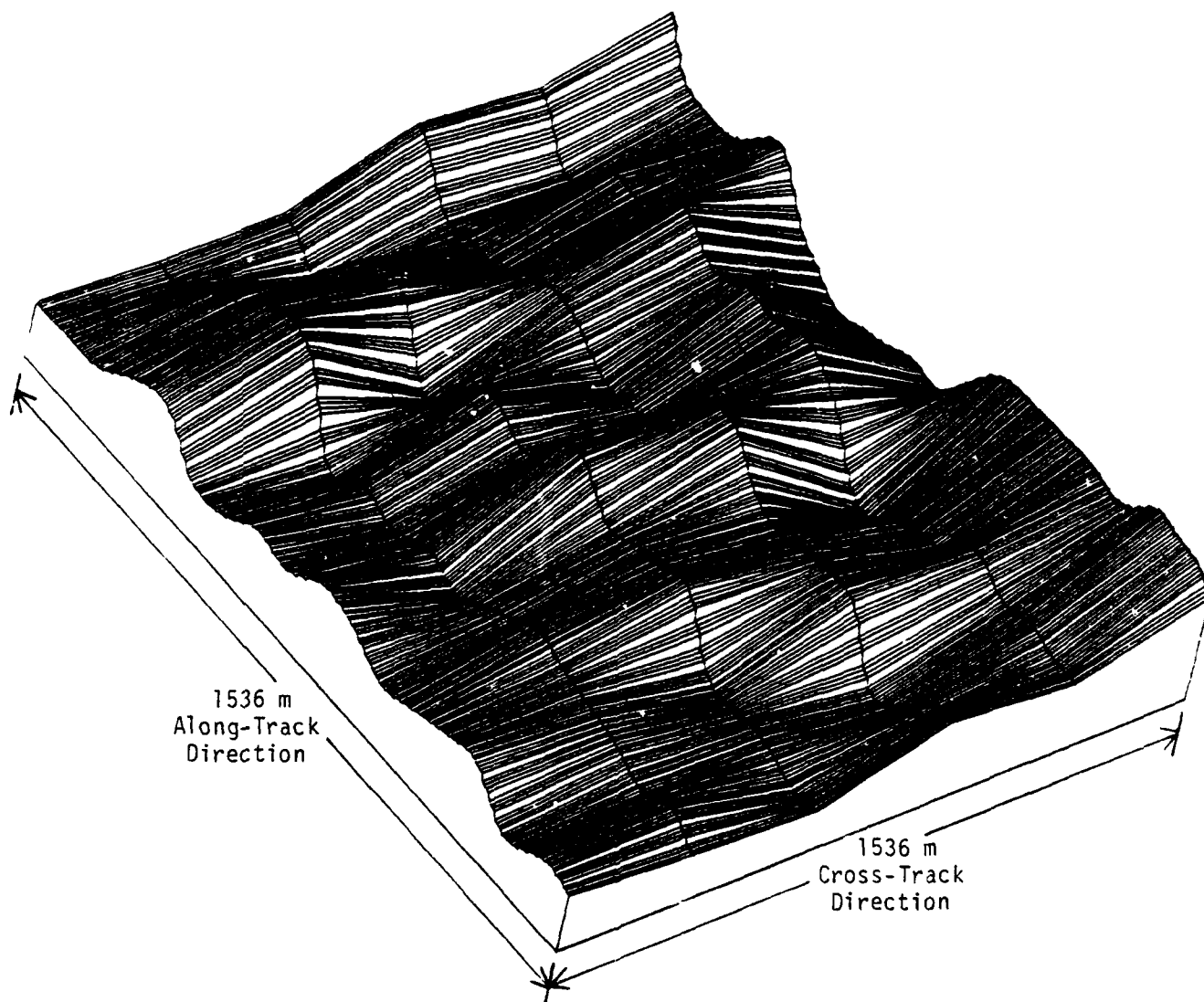


FIGURE 9. PERSPECTIVE PLOT OF OFFSHORE AREA B SHOWING FILTERED LONG-PERIOD COMPONENTS.

AD-A115 188

ENVIRONMENTAL RESEARCH INST OF MICHIGAN ANN ARBOR RA--ETC F/8 17/9
THE UTILITY OF SAR TO MONITOR OCEAN PROCESSES.(U)
NOV 81 R A SMUCHMAN, E S KASISCHKE

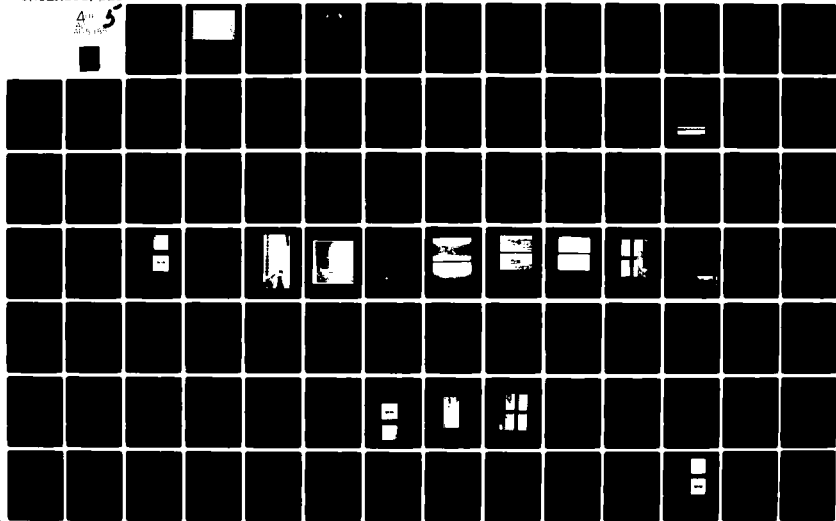
NO0014-76-C-1046

UNCLASSIFIED

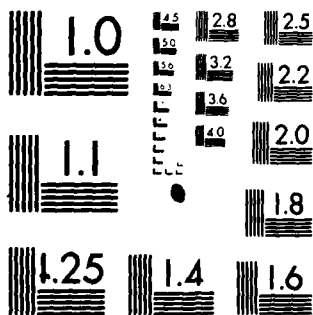
ML

4th
5th

5



15 18



MICROCOPY RESOLUTION TEST CHART
NATIONAL BUREAU OF STANDARDS 1963 A

Wind Wave Directions Determined From Synthetic Aperture Radar Imagery and From a Tower in Lake Michigan

DAVID J. SCHWAB,¹ ROBERT A. SHUCHMAN,² AND PAUL C. LIU¹

Directional wave spectra calculated from digitized synthetic aperture radar (SAR) images of waves on Lake Michigan are compared to a wave directional spectrum determined from measurements taken at a tower and to a one-dimensional spectrum determined from a Waverider buoy. The comparison is within one frequency band for peak energy frequency and within 20° for direction, but the SAR image intensity spectrum does not have the same shape as a wave height spectrum. Wave refraction directions observed in the SAR spectra are within 10° of classical wave refraction calculations.

INTRODUCTION

Directional wave spectra have been measured by a variety of techniques and instruments since the pioneering work of Barber [1954, 1963], Cote *et al.* [1960], and Longuet-Higgins *et al.* [1963]. Early measurements were made with pitch and roll buoys or wave staff arrays. More recently, remote sensing techniques have been used. The principles behind in situ and remote sensing techniques are so different that the two methods have rarely been carefully compared. This paper intends to meet that need.

Synthetic aperture radar (SAR) has been used to image ocean waves over large areas from both conventional aircraft [Elachi, 1976; Shuchman and Zelenka, 1978; Shemdin *et al.*, 1978] and from satellites [Gonzalez *et al.*, 1979]. Image resolution does not depend on antenna aperture size or altitude, as with real aperture radar, or external illumination, as with photography. SAR images have then been used to determine wave direction and wavelength. Although the imaging mechanism has not been explained completely, the forward face and rear face of sufficiently large waves exhibit different scattering characteristics at SAR wavelengths and can be distinguished in SAR imagery.

The Environmental Research Institute of Michigan (ERIM) has been acquiring and processing SAR data from aircraft for several years [Cindrich *et al.*, 1977]. In October 1977 ERIM acquired SAR data on a flight across Lake Michigan between Muskegon, Michigan, and Milwaukee, Wisconsin. At this time the Great Lakes Environmental Research Laboratory (GLERL) was operating a solar-powered research tower 1.8 km off Muskegon capable of measuring and recording wind, temperature, and directional wave information [Schwab *et al.*, 1980]. A sample of the SAR imagery showing the location of the GLERL tower is presented in Figure 1. In addition, a Waverider buoy was deployed 12 km offshore of Muskegon. The purpose of this paper is to compare SAR wave directional measurements to in situ wave directional spectra at the GLERL research tower and one-dimensional spectra at the Waverider buoy and to examine the variability of the directional wave spectrum across the lake. In so doing, we hope to show that the combination of in situ and remotely sensed

wave information is a powerful tool in gaining a better understanding of wave processes.

DATA

On October 6, 1977, at approximately 1130 h EST ERIM's C46 aircraft carrying the X-L band dual polarization imaging radar [Rawson *et al.*, 1975] flew west over Muskegon across Lake Michigan to Milwaukee along a latitude of 43°10'N and then from Milwaukee back to Muskegon. The ground track corresponds to the tails of the numbered arrows in Figure 2. The ERIM SAR system records four channels of radar return, but we will focus our attention here on the X band horizontal-transmit horizontal-receive channel, as these data provided the clearest wave images. L band SAR has been used to image ocean waves from aircraft and the Seasat satellite, but in the present case the wave images from the L band system were not clear enough to warrant further processing. The aircraft flew at 3500 m and operated the radar with an average angle of depression from the horizontal of 30°, yielding a swath width of 5.6 km. The cross-track or range resolution of SAR is limited by radar frequency and is about 2 m for the X band. The along-track or azimuth resolution is obtained from the synthetic aperture technique described by Brown and Porcello [1968] during subsequent processing on the ERIM optical processor. For the X band, the azimuthal resolution is about 2.5 m.

At the same time as the ERIM flight, GLERL was operating a solar powered research tower 1.8 km offshore of Muskegon in 15 m of water [Schwab *et al.*, 1980]. The location is shown in Figure 1 and corresponds to the arrow labeled 1 in Figure 2. The tower operated from July 19, 1977, to October 11, 1977. Sensors on the tower measured wind speed at two levels, wind direction, air and water temperature, and directional wave information from an array of four Zwarts water level gages [Zwarts, 1974]. Data were transmitted to a shore-based recording station at half-second intervals for 30 min out of each hour. The water level gages were deployed at the vertices and center of an equilateral triangle with 3 m sides. The wave gage at the eastern vertex failed on September 2, 1977, so that at the time of the ERIM flight only three gages were operating. The three-gage array can unambiguously determine wave direction for wavelengths greater than about 6 m.

In addition, a Waverider buoy continuously recording wave fluctuations was deployed by GLERL 12 km offshore of Muskegon in 75 m of water. Its location corresponds to the arrow labeled 3 in Figure 2. No directional information is available

¹ National Oceanic and Atmospheric Administration, Great Lakes Environmental Research Laboratory, Ann Arbor, Michigan.

² Radar and Optics Division, Environmental Research Institute of Michigan, Ann Arbor, Michigan.

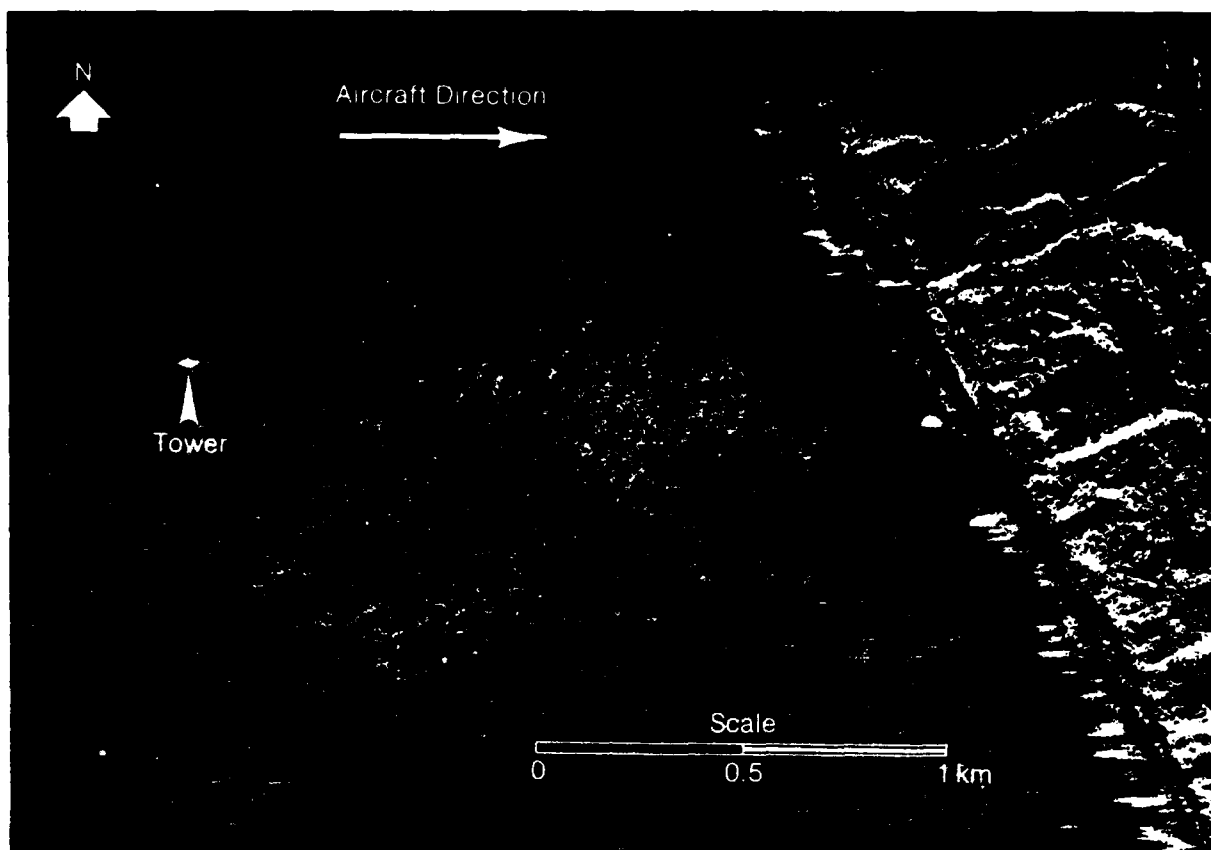


Fig. 1. Synthetic aperture radar imagery of wind waves in Lake Michigan on October 6, 1977, offshore of Muskegon, Michigan.

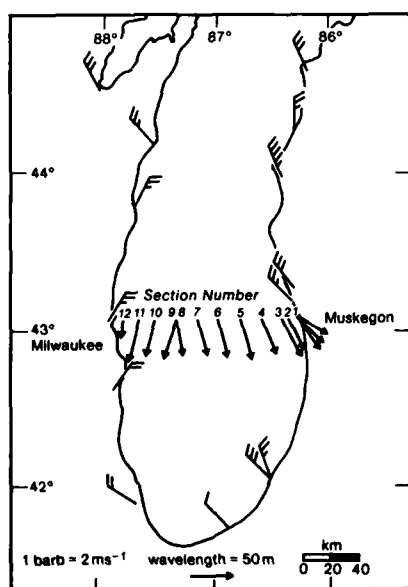


Fig. 2. Wind and wave observations on October 6, 1977, 1200-1300 h EST. Wind speed and direction are from Coast Guard and National Weather Service stations. Wavelength and direction are from directional spectra of the digitized sections of synthetic aperture radar imagery indicated in Tables 1 and 2.

from the buoy, but the one-dimensional wave spectrum can be determined from the recorded water level fluctuations.

METHODS

Twelve sections of SAR images were digitized with an approximate resolution of 3 m (1.5-m pixels). Four sections were from the westbound flight and eight from the eastbound, as indicated in Table 1. The sections are numbered east to west, with sections 8 and 9 overlapping. (See Figure 2). The range coordinate of each section was corrected in a computer program for slant-to-ground range radar geometry [Feldkamp, 1978]. Then 768-m square subsections, with a resolution of 3

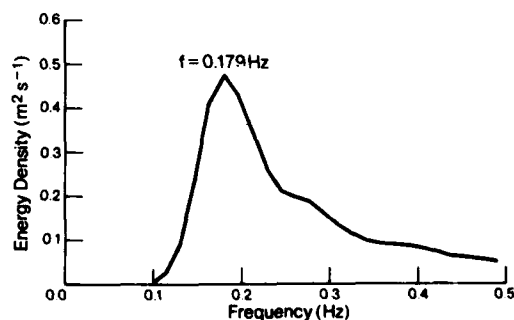


Fig. 3. Wind wave spectrum determined from Waverider buoy data on October 6, 1977, 1200 h EST.

m centered on the coordinates shown in Table 1, were extracted from the digitized sections. Section 1 corresponded to the location of the GLERL tower and section 3 to the location of the Waverider buoy. In section 1, one subsection east of the tower (1a) and one subsection west of the tower (1c) were taken in addition to one centered on the tower (1b) to examine refraction effects.

The 1.5-m pixel digitized SAR images were converted to 3 m resolution by 4 pixel averaging to increase coherence in the image. The average value of each azimuthal line was subtracted from the line to remove the trend of intensity falloff with increasing range distance. Two-dimensional fast Fourier transforms were performed on each 256×256 cell subsection to yield raw directional wave number spectra each with a Nyquist wave number of 1.04 m^{-1} . The raw spectra were smoothed by replacing each value with the average of the surrounding 5×5 cell. The approximate number of degrees of freedom for the resulting spectrum is 142 [Kinsman, 1965, p. 464]. The 99% confidence limits are then $\pm 1.5 \text{ dB}$ [Jenkins and Watts, 1968].

To calculate a directional wave spectrum at the GLERL research tower, wave slopes were determined for 10 min of data as the slopes of the plane passing through the measured locations of the water surface at the three operating gages. Wave height was taken as the average of the measurements of the three gages. Since wave measurements were at $\frac{1}{2}$ -s intervals, the Nyquist frequency for tower spectra was 1 Hz. The first five Fourier coefficients of the angular distribution of energy in 20 frequency bands between 0 and 1 Hz were calculated from the wave height and wave slope records by the method described in Longuet-Higgins *et al.* [1963]. The calculated wave directional spectrum has approximately 120 degrees of freedom with 99% confidence limits of $\pm 1.5 \text{ dB}$.

It is important to remember that the energy spectrum derived from SAR imagery is an image intensity spectrum and not a wave height spectrum. The relationship between SAR image intensity and wave height is still being investigated [Jain, 1977; Shuchman *et al.*, 1979]. The directional spectrum determined from wave staff data, although it may not have the directional resolving power of the SAR spectrum, is a true wave height spectrum.

RESULTS

The wave number and direction corresponding to the peak energy point in each of the 14 SAR spectra are presented in

TABLE 1. Location of SAR Directional Spectra

Section	Flight Leg	Sub-section	Distance From Muskegon Shore, km	Average Water Depth, m	Time, h, EST
1	E	1a	1.01	8	1235
		1b	1.78	15	
		1c	2.55	18	
2	E	2	7.05	35	1233
3	E	3	12.32	66	1232
4	E	4	26.10	110	1230
5	E	5	39.87	103	1227
6	E	6	53.65	96	1224
7	E	7	67.43	83	1221
8	E	8	81.21	75	1218
9	W	9	81.21	75	1146
10	W	10	94.98	82	1149
11	W	11	108.76	96	1152
12	W	12	118.45	75	1154

TABLE 2. Peak Energy Wave Number and Direction from SAR Directional Spectra

Subsection	Wave number, m^{-1}		Direction, °True	
	Uncorrected	Corrected	Uncorrected	Corrected
1a	0.130	0.141	305	303
1b	0.133	0.142	321	317
1c	0.120	0.127	325	321
2	0.147	0.151	342	336
3	0.117	0.123	333	328
4	0.123	0.129	344	339
5	0.117	0.111	350	345
6	0.123	0.126	348	343
7	0.140	0.143	349	344
8	0.150	0.152	354	349
9	0.133	0.136	9	15
10	0.137	0.140	11	16
11	0.123	0.126	8	14
12	0.294	0.296	5	9

Table 2. The SAR process distorts the apparent wavelength of waves moving in the azimuthal direction and distorts the apparent direction of waves with a velocity component in the range direction. A detailed description of these effects and the appropriate corrections can be found in Shuchman *et al.* [1977]. Corrected values of wave number and direction based on the perceived values are also shown in Table 2. Wavelengths range from 21 m at section 12 to 53 m at section 5. There is a 180° ambiguity in wave direction measured by SAR, which was resolved by assuming the waves were coming from the same quadrant as the wind.

A graphical illustration of the results shown in Table 2 is presented in Figure 2, along with wind speed and direction observations from Coast Guard and National Weather Service stations around the lake. Wavelengths in Figure 2 correspond to corrected wave numbers in Table 2, and directions correspond to corrected directions. Wave directions determined from SAR imagery are consistent with observed wind directions. Waves and wind are north-northeast on the western side of the lake and north-northwest on the eastern side. However, the wave direction for section 8 on the eastbound leg of the flight is 26° different from the wave direction determined for the same location (section 9) on the westbound leg. Note, however, that section 8 was imaged 32 min later than section 9.

Wind at the GLERL tower was 288° and 6.5 m/s at 10 m and 5.7 m/s at 5 m. Air temperature was 5.8°C and water temperature 7.1°C , indicating a slightly unstable atmospheric boundary layer over the lake. Significant wave height was 0.99 m. The one-dimensional wind wave spectrum (Figure 3) calculated from Waverider buoy data near section 3 showed an energy peak at 0.179 Hz and a significant wave height of 1.03 m.

The directional frequency spectrum obtained from the GLERL research tower data and the directional wave number spectrum obtained from ERIM SAR imagery are compared in Figure 4. The frequency spectrum shows an energy peak at 0.211 Hz and 300° . As indicated in Table 2, the wave number spectrum has a peak at 0.142 m^{-1} and 317° . Because of the 180° directional ambiguity in analyzing images of waves, the wave number spectrum is symmetric about the origin. The wave number spectrum in Figure 4 is uncorrected for wave motion effects discussed above, but as shown in Table 2, these corrections are small. There is still a large amount of energy at zero wave number owing to imperfect removal of the intensity

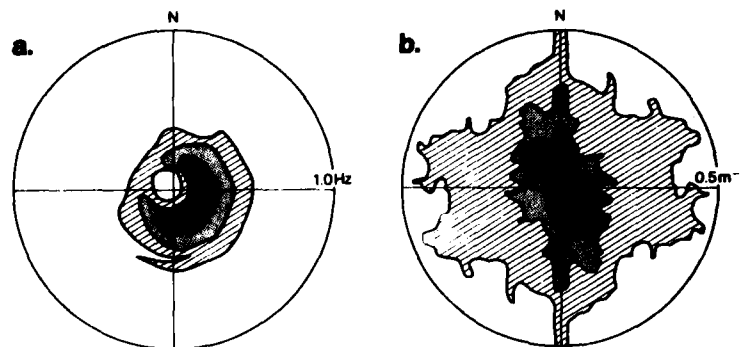


Fig. 4. (a) Directional frequency spectrum of wave height determined from wave research tower measurements, and (b) directional wave number spectrum of image intensity determined from synthetic aperture radar image. Contour levels of the logarithm of spectral density are shown in 5-dB increments relative to the maximum density.

falloff in the range direction. There is also an increase in energy at all wave numbers as the direction approaches the range direction (north-south). The energy lobes in the wave number spectrum are more elongated in the north-south direction than those in the frequency spectrum and show less directional spreading. The reasons for these differences will be discussed in the next section.

DISCUSSION

The peak energy wave number calculated from SAR data at subsection 1b corresponds to a wave frequency of 0.196 Hz. This is within the frequency band of peak energy calculated from the wave gages, 0.185–0.238 Hz. Empirical formulas for the peak energy frequency of fetch limited equilibrium spectra with a fetch of 125 km (appropriate for the wind direction measured at the tower) and 10-m wind speed of 6.5 m/s give 0.178 Hz according to Hasselmann *et al.* [1973] and 0.198 Hz according to Liu [1971]. Measurements from SAR and from tower wave gages are both consistent with these estimates of peak energy frequency. At section 3, the average peak energy wave number determined from the three SAR spectra is 0.124 m⁻¹. The corresponding wave frequency of 0.175 Hz also agrees very well with the peak energy frequency of 0.179 Hz determined from the Waverider spectrum (Figure 3). From these comparisons it is apparent that the frequency of peak energy waves determined from SAR imagery is consistent with both types of in situ measurements.

The discrepancy in peak energy wave direction between SAR and tower systems, 317° versus 300°, is within acceptable directional resolution limits for both the three-gage tower system and the SAR system. The directional spreading of energy in the tower spectrum in Figure 4, which conforms in general to previously published directional wave spectra [e.g., Mitsuyasu *et al.*, 1975], differs somewhat from the spreading in the SAR spectrum. In this case the directional resolution of the SAR system is probably better than a three-gage array, and therefore the SAR spectrum shows less directional spreading. In the SAR spectrum the energy lobes corresponding to waves are elongated in the north-south direction and not spread azimuthally as in the tower spectrum. We believe that this feature is due to range traveling artifacts introduced into the SAR image by multiple-velocity range traveling scatterers. The artifacts appear in the SAR image as bright, east-west (azimuthal) streaks 6–60 m long and rather randomly distributed in space. The effect of this type of noise on a directional spectrum calculated from a digitized image is to introduce energy at all wavelengths and at directions near the range direction, north-south in this case. We speculate that each artifact is due to radar return from a whitecap that appears to the radar as a scatterer with a range of velocities. In the SAR imaging process, a scatterer with a component of velocity in the range direction is displaced on the image in the azimuthal direction by an amount proportional to its range component of velocity [Raney, 1971]. If the scatterer appears to have a vari-

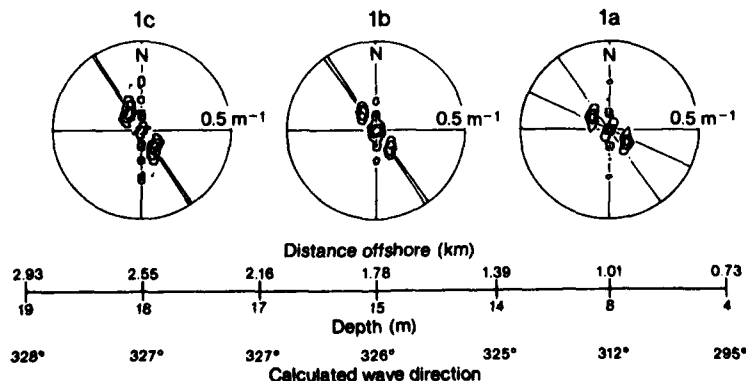


Fig. 5. Contour plots of SAR spectra in 3-dB increments relative to the maximum density for subsections 1a, 1b, and 1c, showing effects of wave refraction. The radial lines on each spectrum correspond to wave directions calculated for the depths at the edges of each subsection.

ety of velocities, its image will be displaced various proportional amounts and will appear as a streak in the azimuthal direction. This is a common feature of SAR images of the breaker zone. The recorded wind speed of 6.5 m/s in an unstable atmosphere is approximately the critical speed for initiation of whitecapping in the Great Lakes according to Monahan [1969]. It appears that the whitecaps are responsible for the resulting range traveling image artifacts and resultant contamination of the wave number spectrum.

If we take 328° true as the mean direction of waves incident on the Muskegon shore (the average direction of section 3) and 0.211 Hz (as measured at the tower) as the wave frequency, wave refraction can be observed in the SAR directional spectra. Contour plots (given in 3 dB levels) of the directional spectra for subsection 1a, 1b, and 1c are shown in Figure 5. Also drawn on the figure are classical refraction directions calculated for depths corresponding to the edges of each subsection. (Kinsman [1965] gives a typical example of refraction calculations on pages 156–167.) For example, the two lines drawn on the contour plot of subsection 1a represent angles of 295° and 325° , the wave directions predicted by classical methods assuming depths of 4 and 14 m, respectively. The entire wave spectrum should be corrected for refraction for a proper comparison, but the spectra in Figure 5 are so peaked that the single component refraction calculations are a good approximation.

Figure 5 indicates that the SAR spectra are sensitive to refraction effects. Also given on the figure is the wave refraction angle assuming the average depth of each of the subsections. When these directions are compared to the Table 2 results, the SAR data have a tendency to show more refraction than was predicted, but the tendency is in the right direction, and 10° can still be considered good agreement.

The SAR wave number spectra shown in Figures 3 and 5 are typical of all 14 SAR spectra. Spectra from the middle of the lake (sections 5–9) have wave energy lobes of somewhat greater magnitude relative to the background noise and show more of the features that appear in the tower wave frequency spectrum, such as a steep forward face and more directional energy spread. The SAR spectrum is of course a wave number spectrum of radar return intensity and is not expected to have the same appearance as the directional frequency spectrum determined from wave heights. Even if the wave number spectrum is converted to a frequency spectrum or vice versa, it is clear that the SAR spectra examined here cannot be easily transformed to or interpreted as wave height spectra. However, the peak energy wave number and direction determined from SAR spectra agree very well with in situ measurements, and the synoptic availability of even these parameters is prohibitively expensive by ground-based measurements.

CONCLUSIONS

Directional spectra calculated from synthetic aperture radar (SAR) data of Lake Michigan have been compared to an in situ directional spectrum from the GLERL research tower and to a one-dimensional spectrum from a Waverider buoy. The comparisons were favorable, indicating SAR's ability to image accurately wind-generated water waves. In addition to data collected over the tower and Waverider buoy, data were continually collected across Lake Michigan in both directions. These data represent a synoptic view of wind waves across the

entire width of Lake Michigan and should prove very useful to those modeling waves on the Great Lakes.

The major caveat about using directional spectra from SAR data is that the SAR spectral estimates are proportional to radar return intensity and not wave energy. The data do not represent wave height information, at least not in a recognizable form. The modulation transfer function (i.e., SAR gravity wave imaging mechanism) is not totally understood at the present time. The determination of the transfer function, as well as determination of wave height, using SAR data will be a major scientific advance, for at that time SAR gravity wave data can be used to obtain power density estimates of the sea surface. Until this is accomplished, SAR wave directional measurements must be accompanied by either in situ (wave staff or Waverider) or remotely sensed (laser altimeter) measurements to give an estimate of wave height.

Acknowledgments. The ERIM contribution to this study was supported by GLERL contract NA79RHA00107. The algorithms used by ERIM to reduce the SAR data and generate spectral estimates were developed under Office of Naval Research support (contract N000-14-1048). The authors thank K. Knorr and K. Amble of ERIM for reducing the SAR data. GLERL contribution 205.

REFERENCES

- Barber, N. F., Finding the direction of travel of sea waves, *Nature*, 174, 1048–1050, 1954.
- Barber, N. F., The directional resolving power of an array of wave detectors, in *Ocean Wave Spectra*, Prentice-Hall, Englewood Cliffs, N. J., 1963.
- Brown, W. J., and L. Porcello, An introduction to synthetic aperture radar, *IEEE Spectrum*, 6, 52–66, 1968.
- Cindrich, I., J. Marks and A. Klooster, Coherent optical processing of synthetic aperture radar data, *Proc. Soc. Photo/Op. Instrum. Eng.*, 128, 1977.
- Cote, L. J., J. O. Davis, W. Marks, R. J. McGough, E. Mehr, W. J. Pierson, Jr., J. F. Ropek, G. Stephenson, and R. C. Vetter, The directional spectrum of a wind generated sea as determined by the Stereo Wave Observation Project, *Meteorol. Pap. 2*, N. Y. Univ. Coll. of Eng., New York, 1960.
- Elachi, C., Wave patterns across the North Atlantic on September 28, 1974, from airborne radar imagery, *J. Geophys. Res.*, 81, 2655–2656, 1976.
- Feldkamp, G. B., Correction of SAR-induced distortion in SEASAT imagery, paper presented at the SPIE Conference on Applications of Digital Image Processing, San Diego, Calif., August 1978.
- Gonzalez, F. I., R. C. Beal, W. E. Brown, P. S. DeLeonibus, J. S. Sherman, J. F. R. Gowere, D. Lichy, D. B. Ross, C. L. Rufenach, and R. A. Shuchman, Seasat synthetic aperture radar: Ocean wave detection capabilities, *Science*, 204, 1418–1421, 1979.
- Hasselmann, K., T. P. Barnett, E. Bouws, H. Carlson, D. E. Cartwright, K. Enke, J. A. Ewing, H. Gienapp, D. E. Hasselmann, P. Kruseman, A. Meerburg, P. Muller, D. J. Olbers, K. Richter, W. Sell, and H. Walden, Measurements of wind-wave growth and swell decay during the Joint North Sea Wave Project (JONSWAP), *Deut. Hydrogr. Z., Suppl. A*, 8, 1973.
- Jain, A., Determination of ocean wave heights from synthetic aperture radar imagery, *Appl. Phys.*, 13, 371–382, 1977.
- Jenkins, A. M., and D. G. Watts, *Spectral Analysis and Its Applications*, Holden-Day, San Francisco, Calif., 1968.
- Kinsman, B., *Wind Waves—Their Generation and Propagation on the Ocean Surface*, Prentice-Hall, Englewood Cliffs, N. J., 1965.
- Liu, P. C., Normalized and equilibrium spectra of wind waves in Lake Michigan, *J. Phys. Oceanogr.*, 1, 249–257, 1971.
- Longuet-Higgins, M. S., D. E. Cartwright, and N. D. Smith, Observations of the directional spectrum of sea waves using the motions of a floating buoy, in *Ocean Wave Spectra*, Prentice-Hall, Englewood Cliffs, N. J., 1963.
- Mitsuyasu, H. F. Tasai, T. Suhara, S. Mizuno, M. Ohkusu, T. Honda, and K. Rikiishi, Observations of the directional spectrum of ocean waves using a cloverleaf buoy, *J. Phys. Oceanogr.*, 5, 750–760, 1975.

SCHWAB ET AL.: BRIEF REPORT

- Monahan, E. C., Fresh water whitecaps, *J. Atmos. Sci.*, 26, 1026-1029, 1969.
- Raney, R. K., Synthetic aperture imaging radar and moving targets, *IEEE Trans. Aerosp. Electron. Syst.*, AES-7, 1971.
- Rawson, R., F. Smith and R. Larson, The ERIM simultaneous X- and L-band dual polarized radar, *IEEE 1975 Int. Radar Conf.*, 505, 1975.
- Schwab, D. J., P. C. Liu, H. K. Soo, R. D. Kistler, H. L. Booker, and J. D. Boyd, Wind and wave measurements taken from a tower in Lake Michigan, *J. Great Lakes Res.*, 6, 76-82, 1980.
- Shemdin, O. H., W. E. Brown, F. G. Standhammer, R. Shuchman, R. Rawson, J. Zelenka, D. B. Ross, W. McLeish, and R. A. Berles, Comparison of in situ and remotely sensed ocean waves off Marine-land, Florida, *Boundary Layer Meteorol.*, 13, 193-202, 1978.
- Shuchman, R. A., and J. S. Zelenka, Processing of ocean wave data from a synthetic aperture radar, *Boundary Layer Meteorol.*, 13, 181-191, 1978.
- Shuchman, R. A., P. L. Jackson, and G. B. Feldkamp, Problems of imaging ocean waves with synthetic aperture radar, *Rep. 124300-1-T*, Environ. Res. Inst. of Mich., Ann Arbor, 1977.
- Shuchman, R. A., K. Knorr, J. C. Dwyer, A. Klooster, and A. L. Maffett, Imaging ocean waves with SAR, *Rep. 124300-2-T*, Environ. Res. Inst. of Mich., Ann Arbor, 1979.
- Zwarts, C. M. G., Transmission line wave height transducer, *Proc. Int. Sym. Ocean Wave Meas. Anal.*, 1, 605-620, 1974.

(Received February 13, 1980;
revised September 19, 1980;
accepted September 29, 1980.)

PROCESSING SYNTHETIC APERTURE RADAR DATA
OF OCEAN WAVES

R.A. Shuchman

Environmental Research Institute of Michigan (ERIM)
Radar and Optics Division
P.O. Box 8618, Ann Arbor, Michigan 48107, U.S.A.

1. ABSTRACT

The usual operation of a Synthetic Aperture Radar (SAR) assumes that the sensor platform moves at a constant velocity along a straight line and that objects to be imaged are stationary. The relative motion between the sensor and the objects produces a systematic set of Doppler frequencies which varies as the objects pass through the radar beam. These Doppler histories are recorded and processed to produce the fine resolution radar image of the objects. Propagating ocean waves as well as surface currents are not stationary and consequently perturb the Doppler histories in the SAR data. These perturbations can be troublesome when imaging gravity waves because the wave images are dispersed and thus defocused in the azimuth (along-track) direction. This defocusing can be compensated in the processor by readjusting the azimuth focus by an amount proportional to approximately the phase velocity of the wave. The perturbations of the Doppler histories can also be useful since they contain information pertaining to wave height and surface currents. Radial (line of sight) motion of ocean waves imaged by a SAR also creates problems in processing. Radial motion causes both an abnormal curvature in the recorded signal histories as well as a shift in the average Doppler frequencies. This effect can be partially compensated in the SAR processing by rotation of the cylindrical lenses by an amount proportional to the radial velocity. Perturbations of the SAR Doppler histories can also be used as a diagnostic tool to aid in the study of the SAR imaging mechanism of ocean surfaces. Adaptive manipulation of Doppler histories can be performed relatively easily in the SAR optical processor and the resulting wave imagery examined.

2. INTRODUCTION

This paper discusses a specialized form of side-looking imaging radar called a Synthetic Aperture Radar (SAR). SAR utilizes the Doppler history (change of phase) associated with the motion of the aircraft, recording both the phase and the amplitude of the back-scattered energy, thus improving the along track or azimuth resolution. The longer the radar data length (i.e. observation time), the greater the improvement in the along track resolution of the system (Brown and Porcello, 1969; Harger, 1970).

The principle in imaging any surface with a radar is that the backscatter of microwave energy (echo) received by the radar receiver contains mainly information on the roughness characteristics (shapes, dimensions and orientations) of the reflecting area. The parameters that influence the echo received from ocean waves include the motion of the scattering surfaces, the so-called speckle effect, system resolution and non-coherent integration as well as contributions attributable to wind, waves, surface currents and surface tension. Also, the orientation of ocean waves to the radar look direction must be considered. When attempting to understand the SAR ocean-wave imaging mechanism, one must also consider factors pertaining to wave orbital velocity, Bragg-scatterer velocity and long (or resolvable) wave phase velocity (Teleki, et al, 1978).

Various theories exist in the literature (Raney and Shuchman, 1978; Alpers and Rufenach, 1978; Rufenach and Alpers, 1979; Harger, 1980, Valenzuela, 1980 and Jain, 1978) that theoretically describe the SAR ocean image formation process. The purpose of this paper is not to present an imaging mechanism theory, but rather to report on measurements made on the SAR optical processor that document motion effects in the SAR scene which affect wave contrast. The SAR observed motions of ocean scatterers can be used as diagnostic tools in better understanding the SAR ocean wave imaging mechanism. Additionally, the motion induced perturbations in the SAR signal history may be potentially exploited to obtain information about the ocean surface such as wave height, wave length and surface current, if present.

3. BACKGROUND

Typically in a SAR system, the phase history of a scattering point in the scene is recorded on photographic film as an anamorphic (astigmatic) Fresnel zone plate. The parameters of the zone plate are set in the azimuth direction by the Doppler frequencies produced by the relative motion between the sensor and the point scatterer, and in the range direction by the structure of the transmitted pulses. The film image is a collection of superimposed zone plates representing the collection of point scatterers in the scene. This film is used by a coherent optical processor which focuses the anamorphic zone plates into the points which produced the microwave

PROCESSING SAR DATA OF OCEAN WAVES

scatter of the scene (Kozma, et al, 1972). Recently, SAR processing has employed digital techniques. Digital processors are sensitive to the same motion effects.

When using a SAR system to image moving targets such as ocean waves, unique problems occur when correlating the signal data. Because moving targets (such as waves) perturb the Doppler frequencies, and hence the phase histories recorded by the signal receiver, conventional processing of these signal histories produces images of the waves that are defocused relative to a stationary target. Defocusing by the along-track (azimuth) velocity of the moving ocean waves can be refocused by readjusting the azimuth focus (cylindrical focus) an amount proportional to the relative velocity of the wave train with respect to the SAR platform velocity.

Similarly, the radial motion of a moving ocean wave imaged by a SAR will also perturb the signal history of a scatterer. Radial wave velocity (motion towards or away from the radar look direction) produces an apparent tilt to the phase history as recorded by the signal receiver. Additionally, the scatterer history will also shift across the signal record. This is referred to as "range walk" and can be compensated for by a rotation of the cylindrical optics in the processing of the signal histories.

4. THEORETICAL FOCUSING ALGORITHMS

Previous work has been presented on the theoretical algorithms needed to focus SAR imagery of a moving target. For an in-depth discussion of this theory, the reader is referred to a paper by Shuchman and Zelenka (1978). The azimuth velocity (V_a) correction is defined as:

$$\delta F = \frac{R\lambda V_a}{P^2 V_{AC} K} \quad (1)$$

where δF is the azimuth focus shift correction (from stationary focus),

λ the radar wavelength,

V_{AC} the SAR platform velocity,

P_{AC} the azimuth scale factor,

K the correlator constant (laser wavelength and magnification factors), and

R the distance to the target.

The radial (range) velocity correction is defined as (Shuchman, et al, 1978):

$$\phi = \frac{V_r P}{V_{AC} Q} \quad (2)$$

where ϕ is the rotation angle for correction,
 V the target velocity in the range direction, and
 Q^r the range scale factor.

The problem of computing the corrections to compensate for wave movement is not a simple one due to the physical characteristics of the wave being imaged. Ocean waves have three distinct velocity components: orbital, group and phase velocity. Therefore, it may be necessary to calculate at least three distinct focus corrections for a given wave image. This, however, allows an additional question to be explored in the analysis: does the focus correction selected correspond most closely to the orbital, group or phase velocity component of the imaged wave?

5. WAVE MOTION VS. FOCUSING OF SEASAT SAR DATA

The relationships between the parameters of the radar system, the SAR processor, and the relative target velocity can be theoretically determined for SEASAT, as reported by Shuchman and Zelenka (1978).

Shuchman and Zelenka showed that the along-track focal length of a moving target can be related to the depth of focus of a SAR image.

A target sensitivity relation can be derived. The relationship indicates:

$$V_a > \frac{2\rho^2 V_{AC}}{\lambda R} \quad (3)$$

where ρ is the azimuth resolution,
 V_{AC} the SAR platform velocity,
 λ the radar wavelength, and
 R the range to the scatterer.

The question arises as to whether imagery obtained from SEASAT is sensitive to wave motion. The SEASAT-A parameters are:

$$\begin{aligned} V_{AC} &= 7868 \text{ m/s,} \\ \rho &= 6.25 \text{ m,} \\ R &= 845 \text{ km, and} \\ \lambda &= 0.235 \text{ m.} \end{aligned}$$

When used in Eq. (3), these give

$$V_a > 3.10 \text{ ms}^{-1}.$$

If the resolution is 25 m for a one-look (fully coherent) image,

PROCESSING SAR DATA OF OCEAN WAVES

$$V_a > 49.53 \text{ ms}^{-1}.$$

If SEASAT uses mixed integration during data processing (i.e. four non-coherently averaged images to produce a four-look 25 m image), a smaller minimum V_a is required than that for a fully coherent case:

$$V_a > 12.38 \text{ ms}^{-1}.$$

This smaller minimum is required because the depth of focus for a mixed integration processor is equal to the geometric mean of the depth of focus corresponding to the full aperture and the depth of focus for the partial aperture (i.e. 6.25 and 25 m).

An experiment was run on actual SEASAT data (Revolution 762) to ascertain focusing sensitivity for waves travelling approximately perpendicular to the SAR flight path (range travelling waves). Five processings of SEASAT Revolution 762 between the coasts of Scotland and Iceland have been made on the ERIM Precision Optical Processor (POP). These entailed small changes in the azimuth focus setting of zero (normal focus setting), ± 0.5 and ± 1.0 mm. The depth of focus of the SEASAT processor is approximately 0.5 mm. The question was: do the changes in focusing produced meaningful changes in the visibility of the wave structures in this imagery?

SAR data from three areas designated "S" (just off the coast of Scotland), "D" (deep water between Scotland and Iceland), and "I" (just off the coast of Iceland) were optically Fourier transformed and the spectral power density of the dominant wave component was measured. The spectral power density of nearby clutter components in the spectrum was also measured for the purpose of normalization.

The results of these measurements are given in Figure 1. The results are plotted in terms of the ratio of the dominant wave spectral power density to clutter spectral power density vs. azimuth focus setting. Note that corresponding velocities/per azimuth focus setting are also indicated on the graph.

A statistical analysis (Shuchman et al, 1979) was applied to the data presented in Figure 1. The analysis indicated that the focusing resulted in no apparent enhancement of the wave spectral estimate. Caution must be used in interpreting these results, however, due to the very limited nature of the data set. The graph does indicate that the deep water waves result in the highest wave-to-clutter spectral power density ratio, but this could be a result of the large aperture used.

An 11.5 second swell was present in the data. The corresponding phase velocity would be approximately 18 m/sec. However, the data presented in Figure 1 was basically a wave traveling in the range

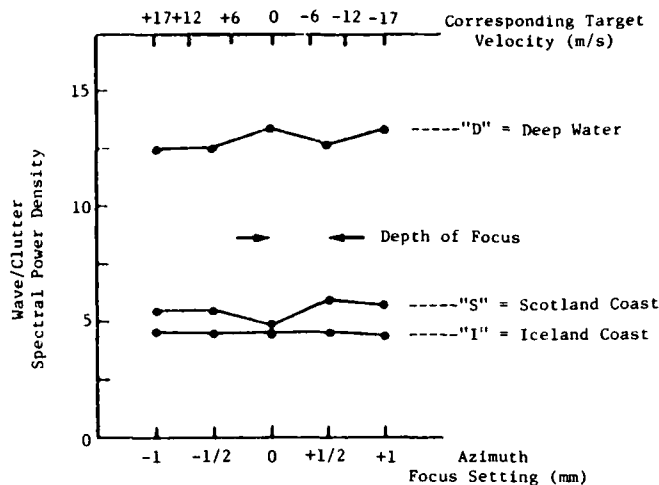


Fig. 1: Wave clutter/spectral power density ratio versus azimuth focus setting.

direction except for the Scotland coastal data (point "S"). To summarize, the focusing sensitivity analysis shows that waves traveling 15-20° off the range axis do not affect the SEASAT-SAR focus setting, given a 10-meter (1-look) azimuth resolution. Additional data sets that consider azimuth-traveling waves will be examined in the proposed follow-on effort. Further work on defocussing effects in SEASAT SAR images is reported by Vesecky et al (this volume).

6. WAVE MOTION VS. FOCUSING OF AIRCRAFT DATA

Azimuth and range wave enhancements were also performed on SAR aircraft data collected during the Marineland experiment. As reported by Kasischke et al (1979), a higher modulation (crest to trough) contrast resulted when the SAR imaged gravity waves were processed assuming a motion near to the phase velocity of the waves.

Figures 2 and 3 show a wave enhancement test performed on azimuth traveling waves at Marineland for L- and X-band SAR data respectively. The December 15th, 1975 Pass 9 data had waves traveling in nearly the azimuth direction and should be sensitive to azimuth motion effects.

Seven focus shifts in the processor (-2.5 mm, -1.5 mm, -0.89 mm, -0.45 mm, 0.0 mm, +0.89 mm and +1.5 mm) were used on the L-band data. Eight focus shifts were used on the X-band data (-15 mm, -9 mm, -1.95 mm, 0.994 mm, 0.0 mm, +0.994 mm, +1.95 mm and +15 mm). The 0.0 mm focus assumes a stationary target and the (+) and (-) values indicate

PROCESSING SAR DATA OF OCEAN WAVES

movement of the azimuth focus toward and away from the frequency plane of the optical processor, with respect to the 0.0 mm focus setting. A 3 x 3 meter resolution setting was used in processing the signal film in the optical processor.

The above numbers reflect focus settings that are nearly proportional to the phase, group and orbital velocity of the gravity waves present on 15 December at the Marineland test site. For the L-band data, the correction for phase velocity corresponds to a -0.89 mm focus shift, while a -0.45 mm shift represents the group velocity correction. The orbital velocity (an order of magnitude lower than the phase velocity) is represented by the 0.0 mm or stationary focus setting, since the azimuthal focus shift for orbital velocity is nearly zero and within the depth of focus of the L-band processor (for a 3 x 3 meter resolution, the L-band depth of focus = ± 0.0502 mm).

The focal shift proportional to phase velocity of the waves for X-band was -1.95 mm, while a -0.994 mm shift corresponds to the focus setting necessary to correct for group velocity of the gravity waves. As in the L-band case, the shift induced by the orbital velocity is most clearly represented by the 0.0 mm setting, again considering the depth of focus of the X-band processor (for a 3 x 3 meter resolution, the X-band depth of focus = ± 0.7804 mm).

Position 9A and 9F on Pass 9 typify the results obtained using azimuth focus shift corrections to refocus wave imagery. Figure 2 indicates for azimuth traveling waves, a greater wave contrast (modulation depth) occurs when the SAR data is adjusted for a target

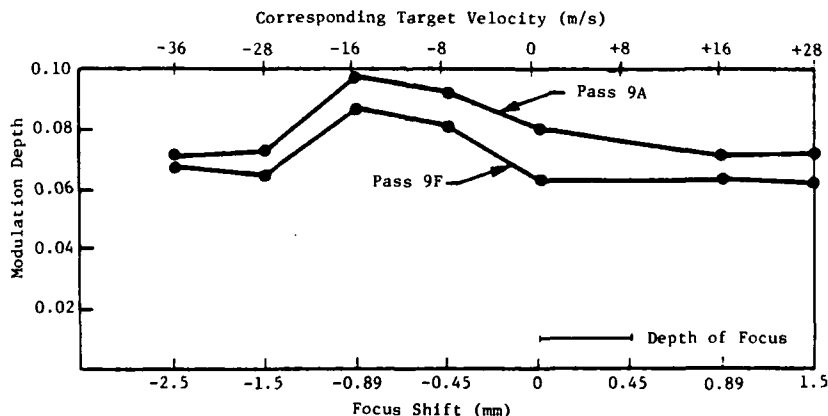


Fig. 2: Graph of modulation depth versus azimuth focus shift, Marineland data, 15 December 1975, Passes 9A and 9F, L-band, azimuth traveling waves.

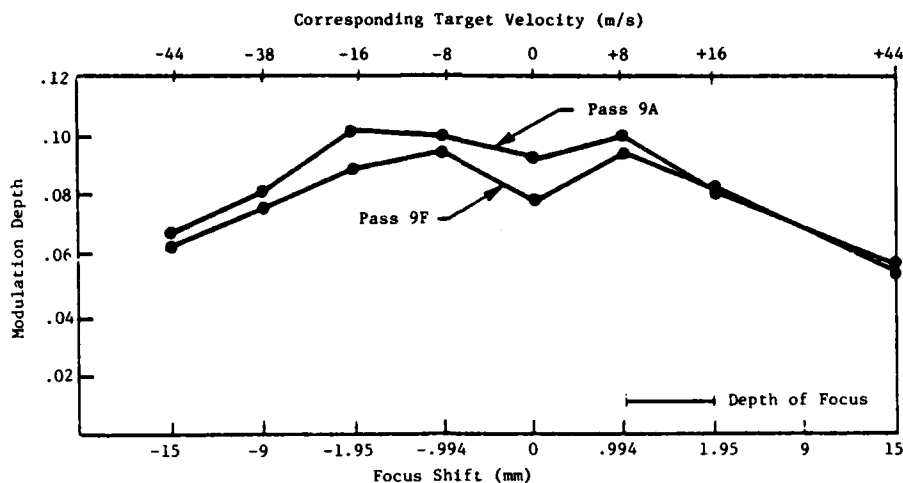


Fig. 3: Graph of modulation depth versus azimuth focus shift, Marineland data, 15 December 1975, Passes 9A and 9F, X-band, azimuth traveling waves.

velocity that is of the same order of magnitude as the phase velocity. The X-band data in Figure 3 does not appear to be motion sensitive due to depth of focus and integration time considerations (Shuchman and Zelenka, 1978; Shemdin et al, 1978).

A similar series of measurements to those made for azimuth-traveling waves were made on range-traveling waves at Marineland. Radial (range) velocity effects can also cause blurring in the resulting SAR imagery. As for the azimuthal velocity, range velocity effects can be partially corrected for in the optical processor. The adjustment needed involves rotating the cylindrical optics of the optical processor (hereafter referred to as telerotation).

Marineland L-band data collected on 15 December 1975 from Passes 2 and 6 were used in this experiment. Both passes have essentially range-traveling waves in them with the aircraft heading varying 180° between the two passes. In Pass 6, the waves are traveling toward the radar (the radar look direction is upwave), and in Pass 2, the radar was looking nearly downwave.

Imaging waves moving away from the aircraft (a downwave radar look direction) requires a negative telerotation while imaging waves moving toward the aircraft (an upwave radar look direction) requires a positive telerotation.

If two sets of waves are imaged, with the only difference being opposite look directions (i.e. 180° apart), the telerotation magni-

PROCESSING SAR DATA OF OCEAN WAVES

tude needed to correct for image distortion due to radial velocity should be the same for each, one being a positive correction (upwave), the other being a negative correction (downwave).

To study this radial velocity phenomenon, wave frequency scans of Pass 2 with seven telerotations from -2.0° to $+1.0^\circ$ and of Pass 6 with seven telerotations from -1.0° to $+2.0^\circ$ were made on the optical processor. Use of Eq. (2) indicates that a -1.0° telerotation for Pass 2 corresponds to the correction needed for the phase velocity of the waves, while a -0.5° setting represents the group velocity adjustment. For Pass 6, $+1.0^\circ$ and $+0.5^\circ$ correspond to the phase and group velocity corrections, respectively. The correction for orbital velocity for both Pass 2 and Pass 6 is best represented by the 0° setting. The average modulation depths for the L-band radial focus corrections are graphically illustrated in Figure 4.

For Pass 2, it can be observed that the highest modulation depth occurred at a telerotation of -1.0° , the telerotation corresponding to the velocity on the order of the phase velocities of the waves, as derived from the theoretical algorithm. The apparent significant differences between the -1.5° and the $+1.0^\circ$ telerotations should not be totally unexpected. While the -1.5° setting is approaching the optimum setting (-1.0°) for the Pass 2 waves, the $+1.0^\circ$ setting is the furthest away from the theoretically correct telerotation setting.

The highest modulation depth obtained for the Pass 6 telerotation

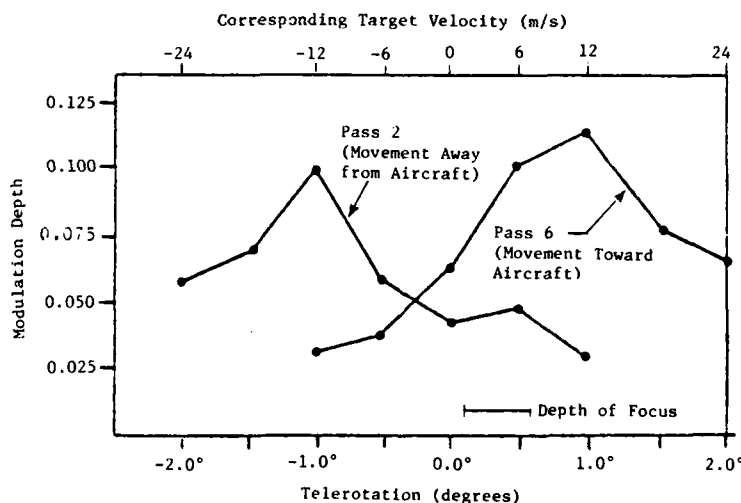


Fig. 4: Graph of modulation depth versus telerotation, L-band, Passes 2 and 6, Marineland data, 15 December 1975, range traveling waves.

settings occurred at $+1.0^\circ$. This was the same magnitude as the optimal setting for the Pass 2 waves. The $+1.0^\circ$ setting corresponds to the correction needed for the phase velocity of the waves, as predicted by the focusing algorithm. The $+1.0^\circ$ setting resulted in apparently significantly higher modulation depths than all other settings except one ($+0.5^\circ$). Again, a setting close to the optimal setting ($+1.5^\circ$) resulted in higher modulation depths than the most defocused settings for Pass 6 (-1.0° , -0.5°). The $+0.5^\circ$ also produced higher modulation depths than the two most defocused settings. The $+0.5^\circ$ telorotation corresponds to the correction calculated for the group velocity component of the wave. Whether or not this is coincidental or insignificant remains yet to be proven.

7. SAR PROCESSOR OBSERVED MOTION OF OCEAN WAVES

A series of motion effects was quantified on the ERIM processor. A model of the individual scatterers and how they are recorded on the SAR signal history was then formulated.

The following points summarize numerous observations made on the ERIM-SAR optical correlator: (Shuchman et al, 1978)

1. Measurements of the azimuth Doppler spectrum shift for a series of range traveling waves indicate a scattering surface velocity, at most, an order of magnitude lower in value than the phase velocity of the waves.
2. Radar image contrast for range traveling waves is maximized when the cylindrical optics used to focus the azimuth signal histories are rotated an amount roughly corresponding to the waves' phase velocity. No shifting of the azimuthal spectrum bandpass is required (see Figure 4).
3. Wave images made from separated Doppler spectral bands show range displacements equal to the wave phase velocity times the equivalent time between the two Doppler spectra for a stationary target at the same radar range.
4. Azimuth traveling waves are defocused an amount equal in magnitude to that produced by radar reflectors moving at roughly the phase velocity of the wave (see Figure 2). Given the same wave velocity, defocusing is more pronounced at L-band than at X-band.

The following discussion utilizes the above mentioned observations and describes how the ocean scatterers are recorded on the SAR signal history.

PROCESSING SAR DATA OF OCEAN WAVES

Range History for a Fixed SAR Target

Consider the geometry of the SAR platform relative to the fixed reflecting point shown in Figure 5. As the antenna beam moves across the reflecting point, the radar range vs. time changes as shown in Figure 6. The slope of the curve is proportional to the relative velocity of the reflecting point and thus the Doppler frequency shift of the reflected radar signal. The reflector is illuminated over the time interval T (integration time of processor) and is at minimum range at time t_0 when the reflector is directly abeam.

Range History for a Target Moving Toward the Flight Line

Suppose the reflector is not stationary, but is moving directly toward the flight line, as shown in Figure 7. The radar range vs. time for this moving reflector is shown in Figure 8. Here, the minimum range no longer occurs at t_0 where the target is directly abeam, but is shifted to the right. The average slope of the curve is no longer zero, as in Figure 6, but is equal to the instantaneous slope at t_0 . Note that the slope of the curve and its corresponding Doppler frequency starts at a higher value and exits at a lower value

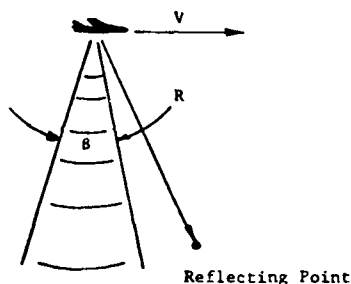


Fig. 5: Radar geometry for stationary reflecting point.

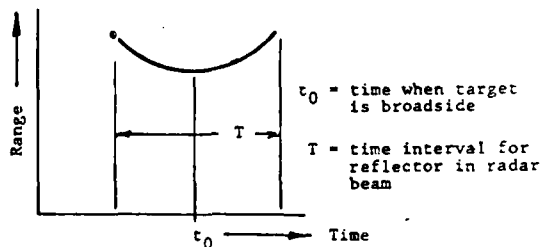


Fig. 6: Range history for stationary point.

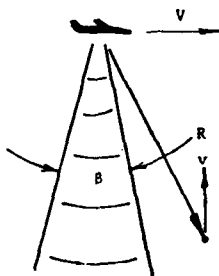


Fig. 7: Radar geometry for moving reflector.

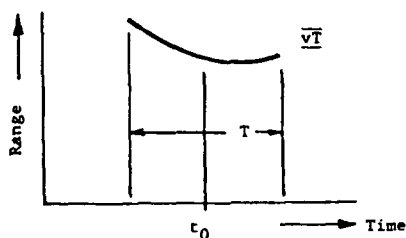


Fig. 8: Range history for moving reflector.

than that for the fixed reflector. Note, also, that the range to the target changes a distance vT between target intercept and drop-out; however, at equal but opposite slopes of the range curve (equal positive and negative Doppler frequencies) the range to the target is identical.

8. THE STATIONARY SURFACE MODEL FOR OCEAN WAVES

Range Traveling Waves

If we presume that a scattering point on the surface of a range traveling wave is moving at the phase velocity of the wave, we should observe a shift in the average Doppler frequency for that point relative to a stationary reflecting point. In addition, no shift in range should be apparent between images formed from equally displaced positive and negative Doppler frequency bands. However, by observations 1 and 3 listed earlier, no Doppler frequency shift is noted and image displacements are observed for symmetrically displaced Doppler bandpassed images of the ocean surface produced by ERIM's X-L Radar. Clearly, the range traveling waves do not behave like simple moving targets.

We will now consider the range history of a series of stationary

PROCESSING SAR DATA OF OCEAN WAVES

reflecting points modulated by the passage of a range traveling wave. Figure 9 shows reflecting points "a-e" at fixed positions on the ocean surface. As the traveling wave progresses toward the flight line, the energy reflected from points "a-e" is modulated to produce a composite range history, as shown in Figure 10. This history has an overall displacement equal to that for the moving reflector shown in Fig. 8, but is discontinuous with each segment having the range vs. time slope of its corresponding stationary reflecting point. The Doppler spectrum of this composite will thus not be shifted with respect to a stationary reflecting field, and is therefore consistent with observation 1. If symmetric Doppler spectra are passed to form an image, such as those corresponding to segments "b" and "d", a displacement corresponding to the wave velocity " v " times the difference in observation times would be observed. This is consistent with observation 3. We then have a model that is consistent with observations 1 and 3. It can also be shown that observation 2 cannot be explained on a basis of the moving reflector model if the processor bandpass is not adjusted to pass only the moving target spectrum. This was not the case for the ERIM data. The stationary surface model predicts a wave displacement over the stationary target spectrum that could be removed by rotation of the processor optics con-

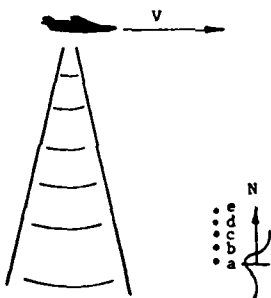


Fig. 9: Radar geometry for range traveling wave.

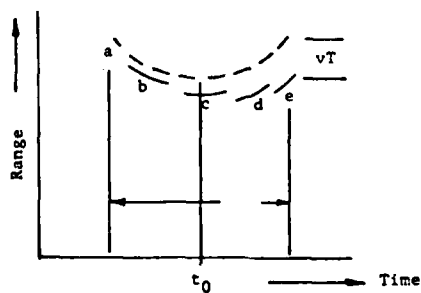


Fig. 10: Range history for range traveling wave.

sistent with observation 2. It remains to be shown that the stationary surface model predicts the same degree of azimuth defocussing as a reflector model that correctly predicts the resulting focus shift.

Range History for a Reflector Moving Parallel to the Flight Line

If the reflecting point is moving parallel to the flight line with the velocity v , as shown in Figure 11, the reflector's range history will have the same variation as that for a stationary point; however, the time the reflector is in the antenna beam will be altered. If the reflector is moving in the same direction as the platform, the time will be increased. For the opposite direction, the time will decrease. For a stationary reflector, the aperture time

$$T = \frac{BR}{V_{AC}} \quad (4)$$

where B is the antenna beamwidth,
 R the range from reflector to the radar, and
 V_{AC} the SAR platform velocity.

For a reflector with velocity v , as shown in Fig. 11, the aperture time

$$T' = \frac{BR}{V_{AC} + v} \quad (5)$$

Figure 12 shows the range histories for the two cases discussed above. Note that for the moving reflector case, the curvature of the range history is increased, the azimuth Doppler FM rate is raised, and the recorded azimuth focal length is reduced. This focal length variation will defocus the image of the moving reflector in the optical processor.

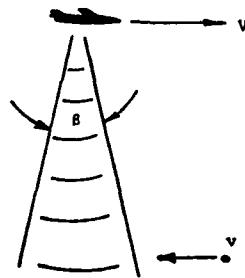


Fig. 11: Radar geometry for reflector with azimuth velocity.

PROCESSING SAR DATA OF OCEAN WAVES

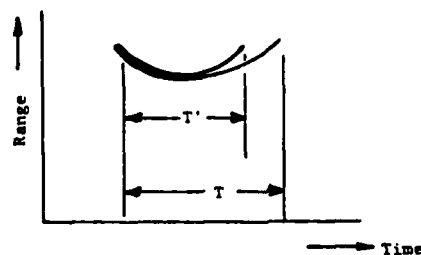


Fig. 12: Range history for reflector moving in azimuth.

Azimuth Traveling Waves

Observation 4 has shown that defocussing of azimuth traveling waves is equal to that of a reflector moving at roughly the phase velocity of the wave. For the stationary surface model to be valid, it must predict an equal degree of defocussing. The discussion below demonstrates that this, indeed, is the case.

Suppose we have a sequence of reflecting points "a-e" to be modulated by an azimuth traveling wave with velocity v , as shown in Figure 13. If point "a" begins reflecting just as the antenna beam first illuminates it, the range history will proceed as shown in Figure 14. Points "b, c, d and e" will reflect, in turn, to produce the segmented range history shown. Each segment will have the azimuth Doppler FM rate of its corresponding stationary reflecting point and will produce an in-focus image at the optical processor output. However, the image of the traveling wave will be blurred if the sequence of reflecting points extends over a substantial part of the ocean wavelength. This blurring may be removed if the processor is refocused to bring each segment to focus at a common point at the processor output. Then each segment will be slightly defocussed,

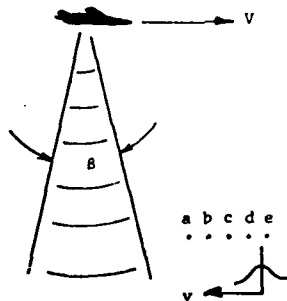


Fig. 13: Radar geometry for azimuth traveling wave.

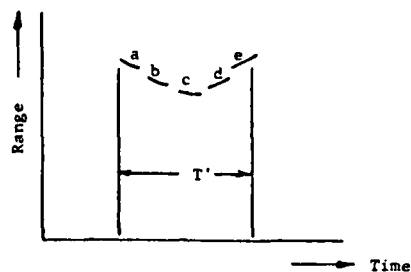


Fig. 14: Range history for azimuth traveling wave.

but the moving wave will have the maximum contrast. The optimum focus setting of the processor would be that which best accommodates the range history shown in Figure 14 as it might have been produced by a single point target. This range history is the same as that for the moving reflecting point shown in Figure 11, except for some small perturbations. Consequently, the processor setting that properly focusses the image for the moving reflector of Figure 11 also produces the best focus of the segmented range history of Figure 14. This is the essential conclusion of observation 4. The stationary surface model is thus shown to be consistent with all of the cited observations.

9. DOPPLER EXPLOITATION AND INTEGRATION TIME CONSIDERATIONS

The radial motion of an ocean current or gravity wave imaged by a SAR will produce an apparent tilt to the phase history as recorded on the signal film. In addition, the scatterer history will also shift across the signal film. Since the synthetic aperture technique utilizes the small range rates of stationary reflecting objects to separate their images in the azimuth coordinate, targets moving in the range direction appear with altered azimuth positions in the processed image, but are still focused. A non-moving target will produce zero Doppler when it is on a line perpendicular to the aircraft track. However, if the reflecting object is moving toward the aircraft, zero Doppler will be produced after the aircraft has passed this perpendicular line, shifting the apparent position of the object in the same direction as the flight direction. Conversely, if the object is moving away from the aircraft, the apparent position will be shifted opposite the flight direction. The use of the SAR to detect surface currents is reported in detail by Gonzalez et al (this volume). This section of the paper discusses the use of Doppler broadening to ascertain wave height.

The Doppler spectrum of radar reflections from the ocean surface may be wider than the spectrum over land if there are substantial surface velocity components in the direction of the radar receiver. The degree of broadening is directly related to the orbital velocity

PROCESSING SAR DATA OF OCEAN WAVES

of the dominant ocean waves imaged by the radar. Over land, the range of radial velocities observed by the radar is approximately equal to

$$V_{AC} \beta \quad (6)$$

where β is the radar antenna azimuth beamwidth and V_{AC} is the SAR vehicle velocity. Observable broadening of the Doppler spectrum is expected when the ocean surface orbital velocities are comparable to $V_{AC} \beta$.

For the SEASAT SAR, V_{AC} is about 7 km/sec and $\beta = 18.7 \times 10^{-3}$ radians. The range of radial velocities in the signal spectrum is $V_{AC} \beta = 7 \times 10^3 \times 18.7 \times 10^{-3} = 131$ meters/sec. For waves with a 10-second period and 5.7 meter wave height, such as those observed on Revolution 1044 over the JASIN site, the velocity of a surface particle is $\pi h/T$ or about 1.8 meters per second. Since this velocity is so much smaller than the velocity bandwidth of the SEASAT SAR any broadening effect may be very difficult to measure. Actual Doppler measurements were made on the SEASAT SAR data to confirm this lack of sensitivity.

The use of aircraft data offers more promise for calculation of orbital velocity of gravity waves. Figures 15 and 16 are Doppler scans of Marineland data that show significant broadening of the ocean scan when compared to the land.

This paper has not discussed the effect of integration time on SAR processing of ocean data (Shemdin et al, 1978). X-band wave data

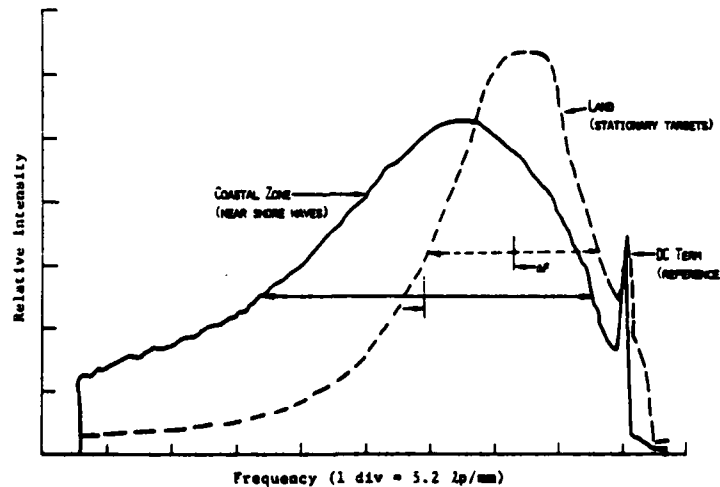


Fig. 15: X-band azimuthal Doppler frequency scans for Pass 3, 14 December 1975.

R. A. SHUCHMAN

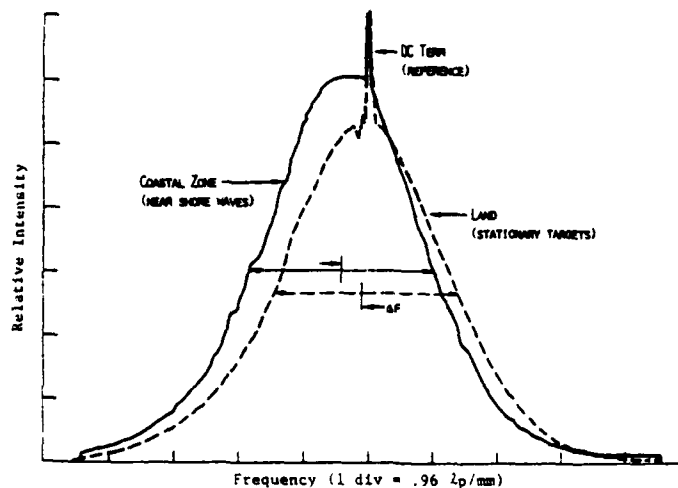


Fig. 16: L-band azimuthal Doppler frequency scan, 14 December 1975.

(shown in Figure 17) shows defocussing or a blurring of the wave data as one goes from near to far range. This X-band data collected at a large incident angle has an integration time that increases by a factor of two from the near to far range. A processing algorithm under development at ERIM will attempt to correct for this effect.

10. SUMMARY

In summary, variation of the azimuth and the range focus indicates the insensitivity of the images of wave components traveling in the along-track direction to azimuth focus, and rather low sensitivity to range focus of wave components traveling in the cross track direction. Detectability of azimuth and range traveling waves can be improved by respective adjustment of focal distance and



Fig. 17: X-band (HH) Lake Michigan wave data showing defocusing of far range waves.

PROCESSING SAR DATA OF OCEAN WAVES

rotation of the cylindrical telescope in the SAR processor. Enhancement of ocean waves as described above has been successfully employed on both Jet Propulsion Laboratory (JPL) L-band and ERIM X- and L-band data (Jain, 1978). The importance of this defocusing effect, due to azimuth and range wave motion, is twofold. First, this effect can be used to determine the direction of ocean wave propagation. Second, it can be used as a rough estimator of the phase velocity associated with these waves. The focusing effects described above are more discernible using L-band data rather than X-band. Consequently, the X-band is less useful in providing information on wave direction and phase velocity.

11. ACKNOWLEDGEMENTS

This paper is intended as a review of the subject of processing synthetic aperture radar data of ocean waves. The work was supported by the Office of Naval Research (ONR), Contract No. N00014-76-C-1408. The ONR technical monitor is Mr. Hans Dolezalek. Many researchers at ERIM contributed to the results presented herein; most notably Mr. Alex Klooster for his processing expertise and Mr. Eric Kasischke for his statistical analysis of the resolution depth measurements.

REFERENCES

- Alpers, W.R. and Rufenach, C.L., 1979, "The Effect of Orbital Motions on Synthetic Aperture Radar Imaging of Ocean Waves," IEEE Trans. Antennas Propagation, AP-27, 685-690.
- Brown, W.M. and Porcello, L.J., 1969, "An Introduction to Synthetic Aperture Radar," IEEE Spectrum, 6, 57-62.
- Harger, R.O., 1970, "Synthetic Aperture Radar Systems," Academic Press, New York.
- Harger, R.O., 1980, "The SAR Seen Sea: A Special Case," submitted to Radio Science for publication.
- Jain, A., 1978, "Focusing Effects in Synthetic Aperture Radar Imaging of Ocean Waves," J. of Applied Physics, 15, 323-333.
- Kasischke, E.S., Klooster, A. and Shuchman, R.A., 1979, "Verification of Synthetic Aperture Radar Focusing Algorithms of Ocean Waves," Thirteenth Intern. Symp. on Remote Sensing of the Environment, Ann Arbor, Michigan.
- Kozma, A., Leith, E.N. and Massey, N.G., 1972, "Tilted Plane Optical Processor," Applied Optics, 11, 1766.
- Raney, R.K. and Shuchman, R.A., 1978, "SAR Mechanism for Imaging Waves," Proc. Fifth Canadian Symp. on Remote Sensing, Victoria, B.C., 495-505.
- Rufenach, C.L. and Alpers, W.R., 1980, "Imaging Ocean Waves by Synthetic Aperture Radars with Long Integration Times," to be submitted to IEEE Antennas and Propagation.
- Shemdin, O.H., Brown, W.E., Jr., Staudhammer, F.G., Shuchman, R.A., Rawson, R.F., Zelenka, J., Ross, D.B., McLeish, W. and Berles, R.A., 1978, "Comparison of In Situ and Remotely Sensed Ocean

R. A. SHUCHMAN

- Waves off Marineland Florida," Boundary-Layer Meteorology, 13, 225-234.
- Shuchman, R.A. and Zelenka, J.S., 1978, "Processing of Ocean Wave Data from a Synthetic Aperture Radar," Boundary-Layer Meteorology, 13, 181-191.
- Shuchman, R.A., Kasischke, E.S. and Klooster, A., 1978, "Synthetic Aperture Radar Ocean Wave Studies," ERIM Final Rept. No. 131700-3-F, Ann Arbor, Michigan.
- Shuchman, R.A., Kasischke, E.S., Klooster, A., Jackson, P.L., 1979, "SEASAT SAR Coastal Ocean Wave Analysis - A Wave Refraction and Diffraction Study," ERIM Final Report 138600-2-F.
- Teleki, P.G., Shuchman, R.A., Brown, W.E. Jr., McLeigh, W., Ross, D. and Mattie, R., 1978, "Ocean Wave Detection and Direction Measurements and Microwave Radars," Oceans, IEEE/MTS, Washington, D.C.
- Valenzuela, G.R., 1980, "An Asymptotic Formulation for SAR Images of the Dynamical Ocean Surface," Radio Science, 15, 105-114.

OCEANOGRAPHIC INFORMATION OBTAINABLE FROM
SYNTHETIC APERTURE RADAR

R.A. Shuchman
Radar and Optics Division
Environmental Research Institute of Michigan (ERIM)
P.O. Box 8618
Ann Arbor, Michigan 48107
USA

ABSTRACT

Oceanographic information obtainable from synthetic aperture radar (SAR) is reviewed. SAR data collected by aircraft and satellite have demonstrated the following information is obtainable from SAR data: detection of gravity waves, determination of the magnitude and direction of surface winds, detection of current velocity and direction, detection of bottom features, identification of oceanic fronts and internal waves, detection of ship wakes, detection of oil slicks, classification of sea ice, and the mapping of coastal wetlands. SAR, with its ability to image the ocean surface independent of sun illumination (day or night), as well as through clouds and moderate rain, makes it an ideal ocean remote sensor.

INTRODUCTION

Considerable effort has been expended during the past decade exploring the potential of using a synthetic aperture radar (SAR) to monitor the resources and physical phenomena of the world's oceans and coastal regions. This interest eventually resulted in the launch of the Seasat satellite which contained a SAR as one of its five instruments; and offered the oceanography community a vast quantity of data which, two years after its collection, is still being studied with great enthusiasm. In addition, numerous oceanographic remote sensing missions have been flown by aircraft SARs.

Synthetic aperture radar is an active imaging device that senses the environment with short electromagnetic waves. As active sensors, radars provide their own illumination in the microwave region of the electromagnetic spectrum and thus are not affected by temporal changes in emitted or reflected radiation from the earth's surface. Additionally, SARs have the recognized advantage of being able to image the earth's surface independent of weather conditions and to provide synoptic views of the ocean at high resolution. The resolution of aircraft SARs is typically on the order of a few meters while the Seasat satellite SAR had a resolution of approximately 25 meters. Most radars operate in the frequency region of 300 MHz (1 m) to 30 GHz (1 cm), and bandwidths within this region are commonly designated by letters. SARs discussed in this paper are designated as L-band (23.5 cm) or X-band (3.2 cm).

Synthetic aperture radar is a coherent airborne or spaceborne radar that uses the motion of a moderately broad physical antenna beam to synthesize a very narrow beam thus providing fine azimuthal (along-track) resolution (Brown and Porcello, 1969; Harger, 1970). Fine range (cross-track) resolution is achieved by transmitting either very short pulses or longer coded pulses which are compressed by matched-filtering techniques into equivalent short pulses. Usually, the coded pulse is a waveform linearly modulated in frequency. The processing of SAR imaged signal histories into an image is described by Kozma, et al. (1972).

Two SAR systems will be discussed in this paper. The first system is an aircraft-borne X- and L-band, dual-polarized imaging radar operated by the Environmental Research Institute of Michigan (ERIM) and is described by Rawson, et al. (1975). The second system was the Seasat L-band imaging radar described by Jordon (1980).

This paper will review a variety of potential uses of SAR data for obtaining oceanographic information. The oceanographic information potentially obtainable include:

1. Detection of gravity waves (wavelength, direction, and height),
2. Determination of the magnitude and direction of surface winds,
3. Detection of current velocity and direction,
4. Detection of bottom features,
5. Identification of oceanic fronts and internal waves,
6. Detection of ship wakes,
7. Detection of oil slicks,
8. Detection of mesoscale features,
9. Classification of sea ice, and
10. Mapping of coastal wetlands.

Detection of Ocean Waves

The main purpose of including a SAR in the Seasat instrument package was to image ocean gravity waves on a fine resolution ocean grid. Figure 1 includes a Seasat image of typical SAR observed gravity waves. Estimates of wave period and direction of the dominant gravity wave can be extracted from this SAR data. Techniques to do this include two-dimensional Fourier transforms (both optical and digital), a semi-causal technique, and a new one-step spectral estimation routine which extracts the wave period directly from the SAR signal histories.

By passing a monochromatic, collimated beam of light through the film image of the gravity waves imaged by the SAR, a two-dimensional optical Fourier transform (OFT) of the image is created (Shuchman, et al., 1977). If a digital image is made, then the same process can be done on a computer by taking a fast Fourier transform (FFT) of data (Shuchman, et al., 1979). Utilizing an FFT has an advantage over an OFT in that distributional wave spectra, as a function of

wave frequency or direction, can also be generated, not just dominant wavelength and direction as obtainable from an OFT. Figure 1 also presents an example of an OFT and FFT generated from the Seasat data.

Advanced data processing techniques for extracting gravity wave information from SAR data also include the use of a semi-causal model and a one-step spectral estimation routine. The semi-causal model is based on maximum entropy techniques and has recently been investigated for the extraction of gravity wavelength and directional data from SAR data (Jackson and Shuchman, 1981). The advantage of the semi-causal model is that it can produce essentially the same estimates as FFTs and OFTs using less SAR data (i.e., a smaller aperture). One-step spectral estimation is another advanced technique which may provide estimates of wavelength and direction through direct processing of raw SAR signal data without first forming an image of the waves (Hasselmann, 1980).

A comparison of estimates of gravity wavelength and direction generated from SAR data collected during the GOASEX (Gulf of Alaska Seasat Experiment) and JASIN (Joint Air-Sea Interaction) experiments were compared to conventional sea truth (i.e., pitch and roll buoy data). From these two experiments, it was verified that accurate wavelength and directional information of gravity wave fields can be obtained from the SAR (Gonzalez, et al., 1979; Kasischke, 1980; and Vesecky, et al., 1981). Linear correlations ($\alpha = 0.01$) between these SAR-derived and sea truth wave spectra estimates were 0.90 to 0.95 for wavelength (Figure 2) and 0.90 for wave direction (Figure 3).

A study by Shuchman and Kasischke (1981) revealed that SAR imagery can be used to document refraction of gravity waves as they enter shallow coastal waters. Wave direction and length from the SAR compared favorably to wave direction and length computed from classical wave refraction techniques. Linear correlations ($\alpha = 0.01$) between SAR-derived and model-derived parameters were 0.76 for wavelength and 0.55 for wave direction. Recent investigations (Meadows,

et al., 1981) indicate that the correlations can be improved significantly if the effect of the Gulf Stream in modifying the characteristics of gravity waves traversing this current is taken into account.

There are limitations in using a SAR to image gravity waves, but these limits have yet to be fully defined. An example is the recent JASIN experiment where the Seasat SAR successfully imaged gravity waves on thirteen out of a possible eighteen opportunities (Vesecky, et al., 1981). A study of the associated sea truth data on those occasions when the Seasat failed to image gravity waves revealed that one of two conditions were present: (1) the waves had a very low significant wave height ($H_{1/3} < 1.3$ m); or (2) the waves were traveling in nearly an azimuth direction with respect to the radar line of sight. Kasischke and Shuchman (1981) found a significant linear correlation between wave contrast (or wave detectability) on the SAR data and wave height. Earlier studies by Teleki, et al. (1978) revealed that on X-band SAR data (collected by an aircraft mounted SAR) gravity waves were clearly more visible when the waves were traveling in a range direction with respect to the radar line of sight.

Surface Currents and Frontal Boundary Detection

SARs have recently been demonstrated to have the capability to detect surface currents and ocean frontal boundaries. The sensing of surface currents with SAR has been through one of three techniques. The first technique reported by Shuchman et al. (1979a) and Gonzalez, et al. (1981) utilizes a measurement of motion-induced Doppler perturbation in the SAR signal history. The technique has been successfully tested on aircraft SAR data collected near Vancouver Island as well as along the Lake Michigan shoreline. This technique takes advantage of the fact that the SAR instrument responds primarily to backscatter from capillary waves which, in conventional SAR processing, are assumed stationary with respect to

other time scales of the radar system. However, these scatterers are not stationary; they move with a characteristic phase velocity as well as with velocities due to the presence of currents and longer gravity waves. The radial (line of sight) component of this resultant velocity produces a Doppler shift in the temporal frequency of the return signal, which translates to a spatial frequency shift recorded on SAR signal film.

Shuchman, et al. (1979) showed that the radial component of a target velocity (V_r) could be calculated as:

$$V_r = \frac{\Delta f' \lambda V_{AC}}{2P} \quad (1)$$

where $\Delta f'$ is the azimuth spatial frequency shift, λ is the transmitted radar wavelength, V_{AC} is the platform velocity and P is the azimuth packing factor.

This relationship can be used to measure the average radial velocity component of an ocean-wave scattering field relative to a fixed-land scattering field. A shift in the azimuth spatial frequency spectrum between fixed-land and moving-ocean surfaces yields an estimate for $\Delta f'$. Variations in spectrum location due to antenna pointing may be eliminated by choosing imagery having land and ocean imaged simultaneously.

A second technique to measure currents via SAR data is reported by Shemdin et al. (1980). This technique applied to Seasat data collected over the mouth of the Columbia River (Oregon) measured the azimuthal shift in the boundary of the current as it flowed past the jetties. Using the relationship:

$$\Delta X = \frac{V_r}{V_{AC}} R \quad (2)$$

where ΔX is the azimuthal displacement, R the range to the target and V_{AC} the platform velocity, the radial line of sight velocity (V_r) of the Columbia River was successfully estimated.

A third technique to measure currents from SAR data is summarized by Hayes and Shuchman (1981), who showed it was possible to calculate the magnitude and direction of the Gulf Stream by observing gravity wave refraction across the stream.

Recently SARs have shown the ability to detect oceanic fronts and freshwater discharge. An experiment to study SAR's ability to monitor ocean fronts was conducted in October of 1980. The frontal boundary of the two water masses at the mouth of Chesapeake Bay is clearly discernible on Figure 4. This SAR data was collected by the UPD-4 X-band SAR operated by the United States Marines. The proposed mechanism for imaging the frontal features is due to a strong current shear modulating the ocean Bragg waves (Wright, 1966) that the radar observes.

Seasat imagery has been used to locate major ocean current boundaries. Hayes (1981) used Seasat imagery to map the northern edge of the Gulf Stream off the eastern U.S. coast. Cheney (1981) tentatively identified the boundary of a cold water ring in the Sargasso Sea using Seasat imagery. Additionally, Lichy, et al. (1981) used Seasat imagery to map warm water rings associated with the Gulf Stream.

Observation of Surf Zone Conditions

Both aircraft and satellite SAR systems have demonstrated an ability to detect various environmental parameters pertaining to the surf zone. These parameters include: (1) location of the breaking waves, (2) location of the land/water boundary, (3) measurement of the dominant gravity wave, (4) measurement of long-shore currents, and (5) detection of long-period surf beats.

A SAR-sea truth comparison reported by Shuchman and Meadows (1980) and Meadows, et al. (1981) indicated:

1. SAR-derived wavelengths and directions are in good agreement with sea truth,

2. SAR directional spectra taken in various water depths do correlate with predicted wave refraction,
3. The breaker zone as defined by shore observers corresponds to the bright lines found on the SAR imagery,
4. Longshore current direction and relative magnitude as obtainable from the SAR Doppler history are in reasonable agreement with sea truth, and
5. Low-frequency components observed on SAR spectra seem to correlate with low frequency "surf beat" found in sea truth spectral estimates.

Detection of Bathymetric Features

The launch of Seasat in 1978 provided a large volume of imagery of the ocean surface showing hitherto unexpected surface detail, some of it apparently correlated with submerged topographic features. As a result of these observations, studies were carried out by Shuchman, et al. and Kasischke, et al. (1980) to quantify the water depth information available in SAR imagery and to evaluate the feasibility of using Seasat SAR data for bathymetry. Some of the results of these continuing investigations are summarized below with the authors' permission.

The appearance of depth-related features in SAR data is due to various hydrodynamic interactions with the ocean bottom which result in surface perturbations visible to the SAR. Five broad categories of depth-related phenomena have been observed in SAR data. These include:

1. Shortening and bending (i.e., refraction) of gravity waves in shallow water,
2. Modulation of surface roughness by currents flowing near bottom features,

3. Generation of internal waves near the edges of continental shelves,
4. Surface manifestations associated with sharp bottom discontinuities in shelf regions, possibly due to current boundaries, and
5. Anomalous features over topographic bumps in deep ocean regions.

An example of a Seasat SAR image showing numerous depth related features is shown in Figure 5. This digitally processed Jet Propulsion Laboratory image represents approximately a 100 x 100 km area of the English Channel. The image was taken on 19 August 1978. At the time of the overpass, a 2 knot (1 m/sec) tidal current was flowing in a southwesterly direction. The features on the SAR image correlate very well to the sand waves present in the English Channel. Figure 6 shows the bathymetry of the area covered in the SAR image.

The features appearing in the SAR image are thought to be due to the interaction of this tidal current with the bottom, causing a modulation of the wind-generated surface roughness. Comparisons of the radar return with the water depth indicate areas of shallower water (i.e., sand waves) have a higher radar reflectivity than surrounding deeper water areas. Although there is apparently a strong correspondence between the radar backscatter and the bathymetry of this region, much work remains to be done before quantitative depth estimates can be made from the surface roughness information recorded in the SAR image.

Detection of Oil Slicks

The amount of received backscatter from a SAR imaged ocean surface is a function of:

1. The small scale roughness,
2. The mean slope, and
3. The velocity of the ocean scatterers.

The small scale roughness is the most important of the three mentioned factors. A maximum backscatter return is obtained when the small scale ocean roughness satisfies the following conditions

$$K_w = 2k \sin \theta \quad (3)$$

where $K_w = 2\pi/L$ and $K = 2\pi/\lambda$ are the wave numbers and L and λ the wavelengths respectively of the capillary waves and the radar, and θ is the incident angle. This roughness criterion is referred to as the Bragg wave equation.

The presence of oil on the ocean surface dampens the capillary and ultra-gravity ocean waves and significantly reduces their amplitude. Equation (3) predicts that a maximum return for an X-band and L-band SAR imaging the ocean at 45° incident angle results when the ocean Bragg waves are 2.2 cm and 17 cm in wavelength respectively. Oil films on the ocean surface will dampen the X-band Bragg waves more readily than the larger L-band resonant ocean waves. Figure 7 graphically illustrates through example this concept. Shown in the figure is simultaneously obtained X- and L-band SAR imagery of a crude-oil slick off the east coast of the United States. Note from the figure that the X-band SAR data more clearly delineates the oil slick than the L-band imagery. Rawson and Liskow (1981) calibrated the data shown in the figure and determined the radar backscatter decreased approximately 3 dB at X-band over the oil slick area, while the radar reflectivity for the L-band data decreased approximately 1.5 dB over that same oil slick area.

Detection and Classification of Sea Ice

Much research has been done in the area of SAR detection of sea, lake, and river ice (Ketchum and Tooma, 1973; Larson, et al., 1978, 1981). There is general agreement in the community that high resolution aircraft or satellite SAR operating at an X-band (3 cm) frequency can detect first year, multi-year, and open water areas.

Figures 8 and 9 represent simultaneously collected X- and L-band (3 cm and 23.5 cm respectively) parallel and cross polarized sea ice data collected in the Beaufort Sea. Clearly shown on the data is multi-year (letter B); first year (letter C) and open water or newly formed ice areas (letter D). This data has approximately 3 meters resolution in both range and azimuth, and the incident angle at near edge is approximately 10° while at the far edge, the incident angle is approximately 60° . Also given on the figures are relative intensity plots of a cross section shown on the figure by the line drawn between the letters A and A'. From this typical SAR ice example, the data indicates the higher frequency X-band data that is cross-polarized (i.e., transmitted horizontally and received vertically) results in the highest contrast between first year and multi-year ice flows.

In addition to detecting ice flows, SAR has also been demonstrated to be capable of detecting icebergs. Larson, et al. (1978) showed that X-band cross polarized SAR data resulted in the highest contrast between the iceberg and surrounding ice flow when compared to X-band parallel polarized data and L-band parallel and cross-polarized data.

Marshland Detection

Figure 10 shows four-channel ERIM SAR imagery of the Marineland test site. The test site was subjected to tidal inundation and therefore primarily composed of tidal marshland. The letter A on Figure 10 indicates the high water mark as well as a relic coastline. Area B represents forest land located on high ground (i.e., not subject to inundation), while region C is an inundated area that is composed of marsh vegetation. Note the differential return between the marsh area (C) on the X- and L-band data. The marshland surrounding the river (D) is also clearly discernible using the X- and L-band data.

The explanation for this differential return is that the X-band radar energy reflects off the tops of the marsh grass, while the longer L-band incident energy penetrates through the vegetation and the L-band return is primarily a specular return from the water. Shuchman and Lowry (1977) used this data set to perform a digital vegetation classification using the four-channel SAR data. The result of that analysis indicated the simple parallelepiped classification (operator interactive) corresponded well to the ground truth available. The study further demonstrated the need to develop more sophisticated digital classification procedures which utilize not only tonal information from the radar, but also texture information.

Summary

It should be mentioned when utilizing SAR data such as presented in this paper, the SAR spectral estimates discussed are wave number-directional spectra of the radar return intensity. The data does not represent wave height information, at least not in a recognizable form. The modulation transfer function (i.e., the SAR gravity wave imaging mechanism) is not totally understood at the present time. The determination of the transfer function as well as determination of wave height using SAR data will be a major scientific advance. At that time, it will then be possible to use SAR gravity wave data to obtain power density estimates of the sea surface.

The Doppler current measurements discussed are still experimental and the reader is warned that this technique to measure current is far from operational and perhaps a new SAR system will have to be designed to realize this type of measurement. Recall that the Doppler method works only in the radial (line of sight) direction.

The ice type and marshland discussions demonstrate the need for development of machine aided analysis techniques and indicate the advantage of a multi-frequency SAR approach.

Perhaps the greatest problem facing SAR oceanographic users is to solve the data handling problem. SAR signal histories must first be processed into image histories (either complex or just intensity) and then undergo rather time consuming additional data processing to extract the useful oceanographic information. Thus, clever data handling schemes need to be developed to shorten computational times.

Acknowledgements

Much of the work mentioned in this review was supported by the Office of Naval Research (ONR) Contract N00014-76-C-1048. The technical monitor for this ONR contract is Mr. Hans Dolezalek. Part of the work summarized in this paper was supported by the National Oceanic and Atmospheric Association (NOAA) and the National Aeronautics and Space Administration (NASA) as part of the Seasat Announcement of Opportunity Program under Contract No. MO-A01-78-00-4339. The technical monitors were John W. Sherman III and Patrick DeLeonibus of NOAA.

References

- Brown, W.J. and L. Porcello, An Introduction to Synthetic Aperture Radar, IEEE Spectrum, 6, pp. 52-66, 1969.
- Cheney, R.E., A Search for Cold Water Rings with Seasat, in Spaceborne Synthetic Aperture Radar for Oceanography, ed. by R.C. Beal, P.S. DeLeonibus and I. Katz, Johns Hopkins Univ. Press (in Press), 1981.
- Gonzalez, F.I., R.C. Beal, W.E. Brown, P.S. DeLeonibus, J.W. Sherman, J.F.R. Gower, D. Lichy, D.B. Ross, C.L. Rufenach, and R.A. Shuchman, Seasat Synthetic Aperture Radar: Ocean Wave Detection Capabilities, Science, 204, pp. 1418-1421, 1979.
- Gonzalez, F.I., C.L. Rufenach, and R.A. Shuchman, Surface Current Detection Using SAR Data, Proceedings of the COSPAR/SCOR/IUCRM Symposium on Oceanography from Space, 1981.
- Harger, R.O., Synthetic Aperture Radar Systems, Academic Press, New York, NY, 240 pp., 1970.
- Hasselmann, K., A Simple Algorithm for the Direct Extraction of the Two-Dimensional Surface Image Spectrum from Return Signal of a Synthetic Aperture Radar, Int. J. Rem. Sens. (in Press), 1980.

Hayes, R.M., SAR Detection of the Gulf Stream, in Spaceborne Synthetic Aperture Radar for Oceanography, ed. by R.C. Beal, P.S. DeLeonibus and I. Katz, Johns Hopkins Univ. Press (in Press), 1981.

Hayes, J.G. and R.A. Shuchman, Seasat SAR Ocean Surface Current and Shallow Water Wave Refraction, Proceedings of the COSPAR/SCOR/IUCRM Symposium on Oceanography from Space (in Press), 1981.

Jackson, P.L. and R.A. Shuchman, A New High Resolution Two-Dimensional Spectral Estimation Technique for SAR Ocean Wave Analysis, submitted to J. Geophys Res., 1981.

Jordan, R.L., The Seasat-A Synthetic Aperture Radar System, IEEE J. Oceanic Eng., Vol. OE-5, pp. 154-164, 1980.

Kasischke, E.S., Extraction of Gravity Wave Information from Synthetic Aperture Radar Data, Univ. of Mich. M.S. Thesis, 108 pp., 1980.

Kasischke, E.S., R.A. Shuchman, and J.D. Lyden, Detection of Bathymetric Features Using Seasat Synthetic Aperture Radar - A Feasibility Study, ERIM Report No. 135900-1-T, Ann Arbor, 1980.

Kasischke, E.S. and R.A. Shuchman, Comparisons of Wave Contrast Measurements Made from SAR Data with Selected Oceanographic Parameters, Proceedings of the Symposium on Wave Dynamics and Radio Probing of the Ocean Surface, Miami, Florida (in Press), 1981.

Ketchum, R.D. and S.G. Tooma, "Analysis and Interpretation of Airborne Multi-Frequency Side-Looking Radar Sea Ice Imagery," J. of Geophys. Res., Vol. 78, No. 3, pp. 520-538, 1973.

Kozma, A., E.N. Leith, and N.G. Massey, Tilted Plane Optical Processor, Applied Optics, 11, p. 1766, 1972.

Larson, R.W., R.A. Shuchman, R.F. Rawson, and W.D. Worsfold, The Use of SAR Systems for Iceberg Detection and Characterization, Proceedings of the Twelfth International Symposium on Remote Sensing of Environment, Ann Arbor, MI, pp. 1127-1147, 1978.

Larson, R.W., J.D. Lyden, and R.A. Shuchman, An Analysis of Four-Synthetic Aperture Radar Data of Sea Ice, presented at the Symposium on Signature Problems in Microwave Remote Sensing, Lawrence City, Kansas, 1981.

Lichy, D.E., M.G. Mattie, and L.J. Mancini, Tracking of a Warm Water Ring Using Synthetic Aperture Radar, in Spaceborne Synthetic Aperture Radar Imagery for Oceanography, ed. by R.C. Beal, P.S. DeLeonibus, and I. Katz, Johns Hopkins Univ. Press (in Press), 1981.

Lyzenga, D.L., Remote Bathymetry Using Active and Passive Techniques, Proceedings of the International Geoscience and Remote Sensing Symposium, Washington, D.C. (in Press), 1981.

Meadows, G.A., E.S. Kasischke, and R.A. Shuchman, SAR Observations of Coastal Zone Conditions, Proceedings of the Fourteenth International Symposium on Remote Sensing of Environment, Ann Arbor, MI., pp. 845-863, 1980.

Meadows, G.A., R.A. Shuchman, E.S. Kasischke, and J.D. Lyden, The Observation of Gravity Wave-Current Interactions Using Seasat Synthetic Aperture Radar Data, submitted to J. Geophys. Res., 1981.

Meadows, G.A., R.A. Shuchman, and J.D. Lyden, Analysis of Remotely Sensed Long-Period Waves, Submitted to J. Geophys. Res., 1981.

Rawson, R.F., F. Smith, and R. Larson, The ERIM Simultaneous X- and L-Band Dual Polarized Radar, IEEE 1975 Radar Conference, p. 505, 1975.

Rawson, R.F. and C.L. Liskow, Radar Reflectivity Measurements of Ocean Surface with and Without a Surface Coat of Oil, IGARSS '81 Proceedings, IEEE Geoscience and Remote Sensing Society, IEEE Catalog No. 81CH1656-8, Washington, DC, June 1981.

Shemdin, O.H., A. Jain, S.V. Hsiao and L.W. Gatto, Inlet Current Measured with Seasat-1 Synthetic Aperture Radar, Shore and Beach, Vol. 48, pp. 35-9, 1980.

Shuchman, R.A. and R.T. Lowry, Vegetation Classification with Digital X-Band and L-Band Dual Polarized SAR Imagery, Proceedings of the Fourth Canadian Symposium on Remote Sensing, Quebec City, pp. 444-459, 1977.

Shuchman, R.A., P.L. Jackson, and G.B. Feldkamp, Problems of Imaging Ocean Waves with Synthetic Aperture Radar, ERIM Interim Technical Report No. 124300-1-T, Ann Arbor, MI, 11 pp., 1977.

Shuchman, R.A., E.S. Kasischke, A. Klooster, and P.L. Jackson, SAR Coastal Ocean Wave Analysis - A Wave Refraction and Diffraction Study, ERIM Final Report No. 138600-2-F, Ann Arbor, MI, 1979.

Shuchman, R.A., C.L. Rufenach, and F.I. Gonzalez, The Feasibility of Measurement of Ocean Surface Currents Using Synthetic Aperture Radar, Proceedings of the Thirteenth International Symposium on Remote Sensing of Environment, Ann Arbor, MI, pp. 93-102, 1979a.

Shuchman, R.A. and G.A. Meadows, Airborne Synthetic Aperture Radar Observations of Surf Zone Conditions, Geophysical Research Letters, Vol. 7, pp. 857-860, 1980.

Shuchman, R.A. and E.S. Kasischke, Refraction of Coastal Ocean Waves as Observed from the Seasat Aperture Radar, in Spaceborne Synthetic Aperture Radar for Oceanography, ed. by R.C. Beal, P.S. DeLeonibus and I. Katz, Johns Hopkins Univ. Press (in Press), 1981.

Teleki, P.G., R.A. Shuchman, W.E. Brown, Jr., W. McLeish, D. Ross, and M. Mattie, Ocean Wave Detection and Direction Measurements with Microwave Radars, Oceans '78, IEEE/MTS, pp. 639-648, 1978.

Vesecky, J.F., H.M. Assal, R.H. Stewart, R.A. Shuchman, E.S. Kasischke and J.D. Lyden, On the Ability of Synthetic Aperture Radar to Measure Ocean Waves, Proceedings of the Symposium on Wave Dynamics and Radio Probing of the Ocean Surface, Miami, Florida (in Press), 1981.

Wright, J.W., Backscattering from Capillary Waves with Application to Sea Clutter, IEEE Trans. Antenna Propag., Vol. AP-14, pp. 749-754, 1966.

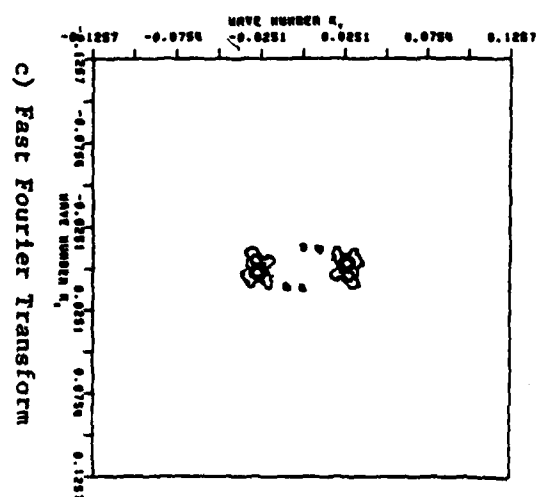
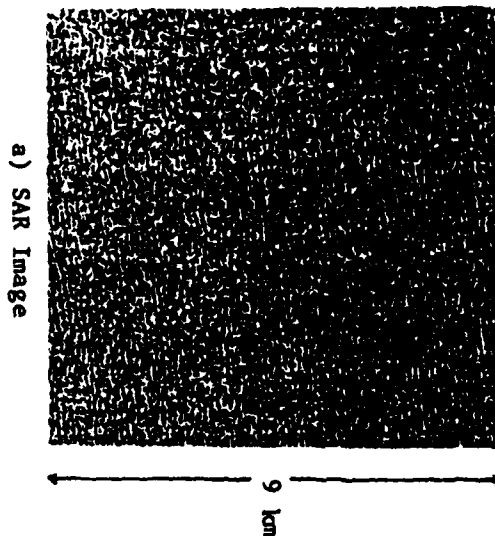


Figure 1. Seasat SAR Image of Ocean Gravity Waves and their Resultant Two-Dimensional Fourier Transforms (Seasat Rev. 762, 19 August 1978).

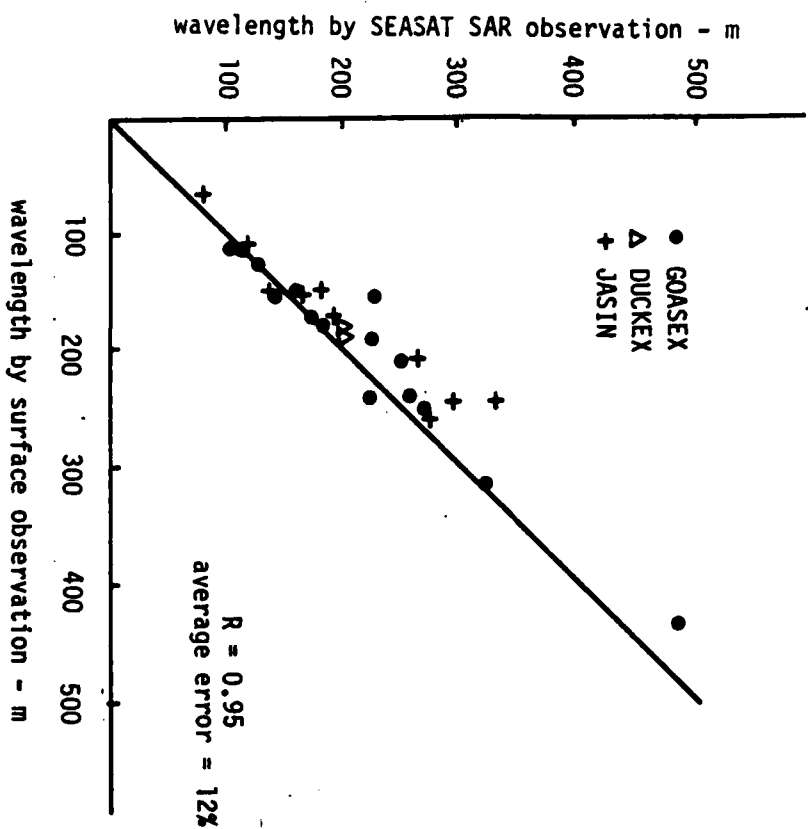


Figure 2. Plot of Wavelength, SAR Versus Sea Truth, for L-band SEASAT Data (after Vesecky and Stewart, 1981).

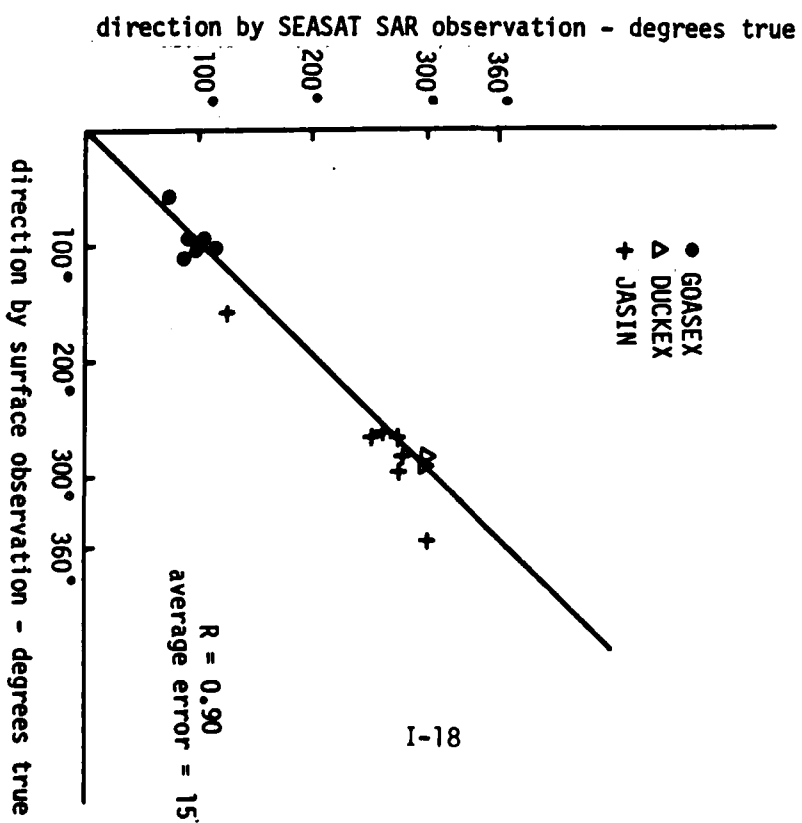


Figure 3. Plot of Wave Direction, SAR Versus Sea Truth, for L-band SEASAT Data (after Vesecky and Stewart, 1981).

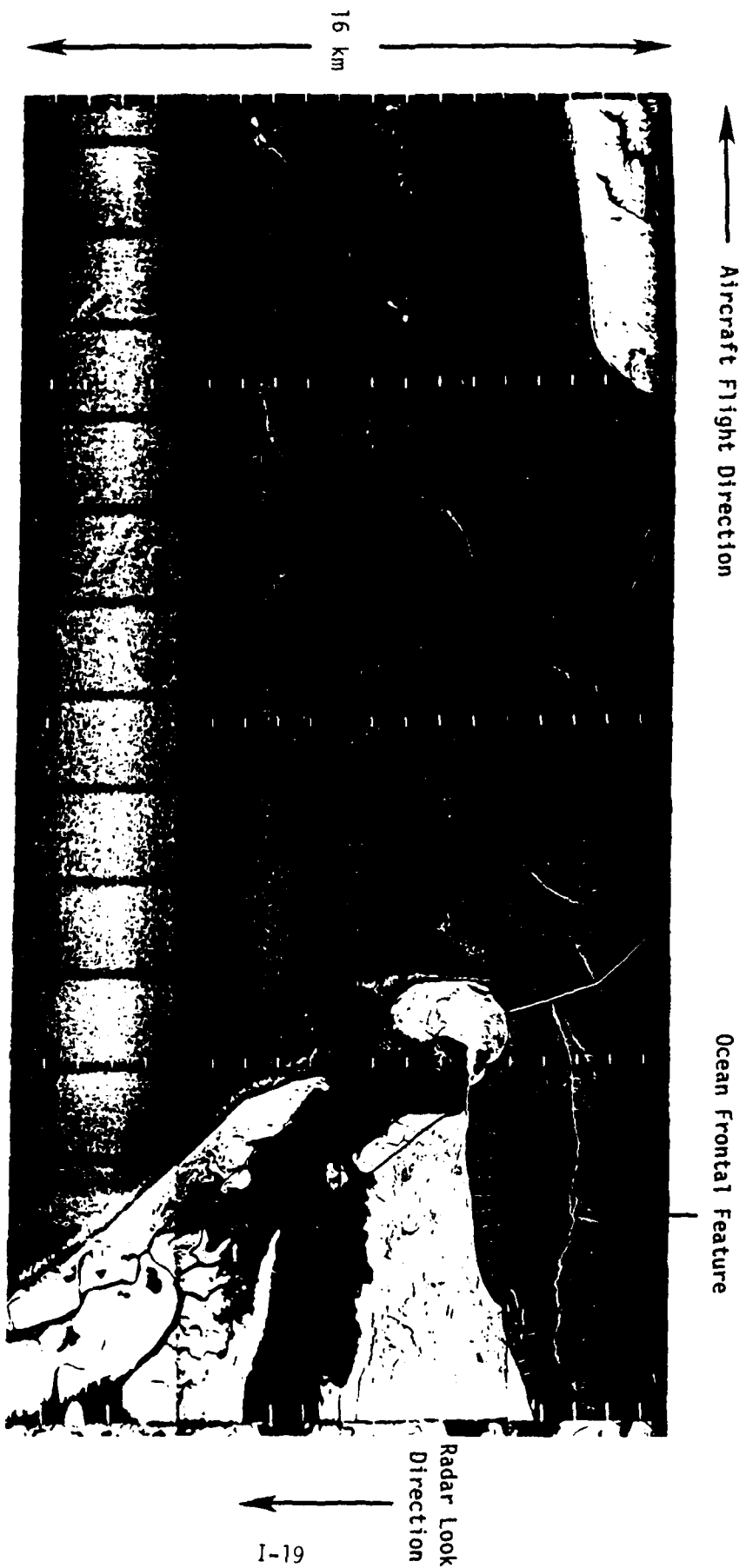


Figure 4. SAR Image (X-band) of Mouth of Chesapeake Bay Illustrating Ocean Frontal Features (10 October 1980).

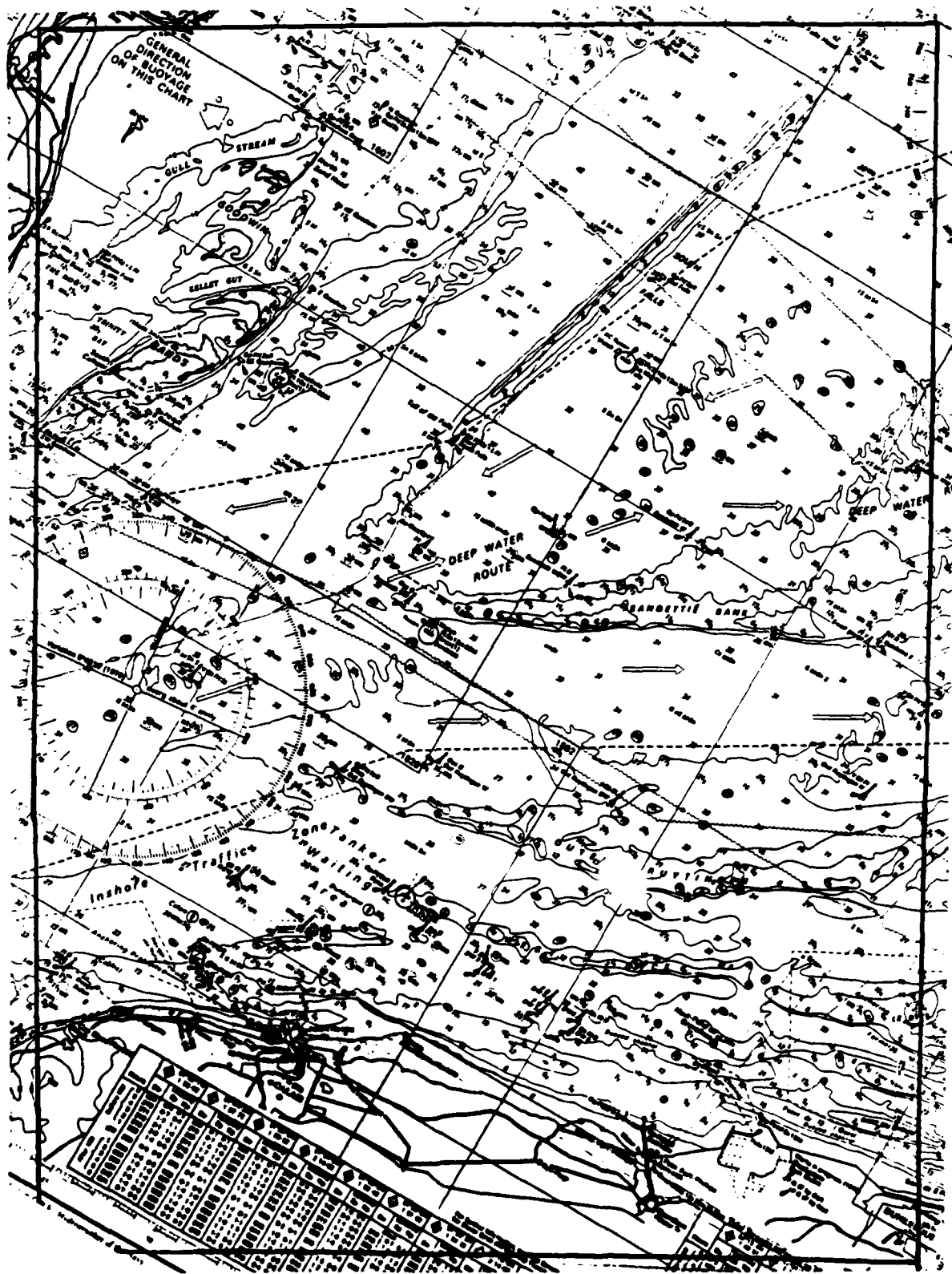


Figure 6. Bathymetry Chart of the English Channel Test Site.

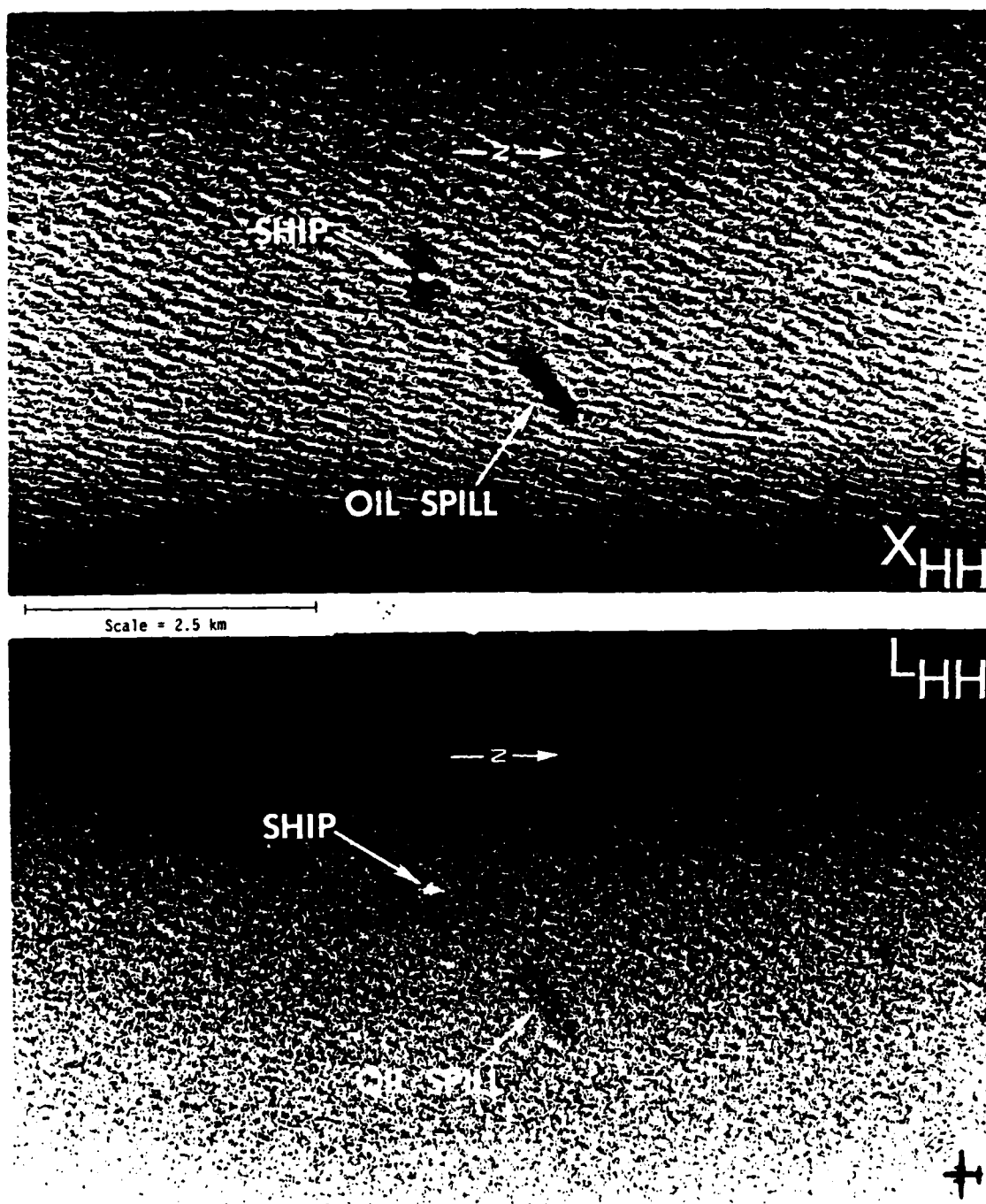


Figure 7. Simultaneously Obtained X- and L-band Images of a Crude-Oil Spill off the east coast of the United States.

B=Multi-Year Ice
C=First-Year Ice
D=Open Water or New Ice



XHH



XHV

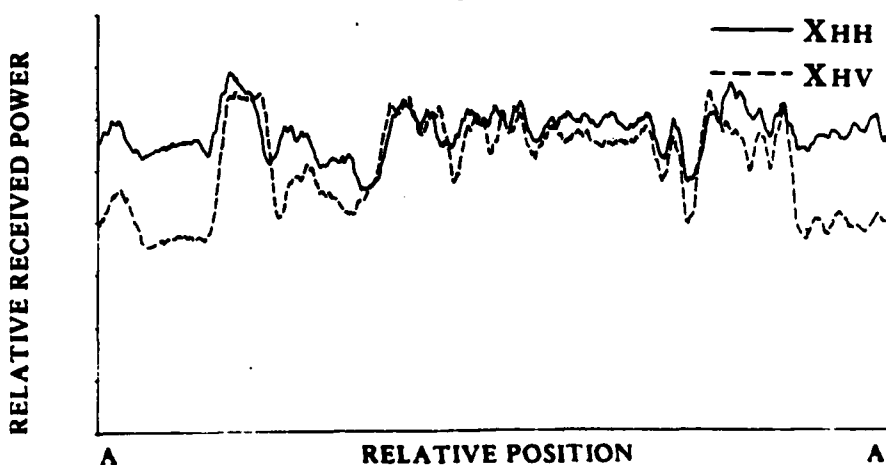
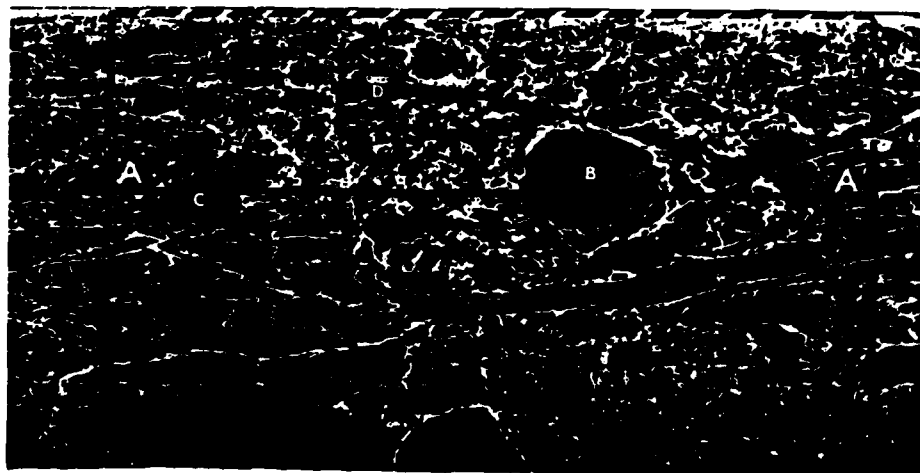
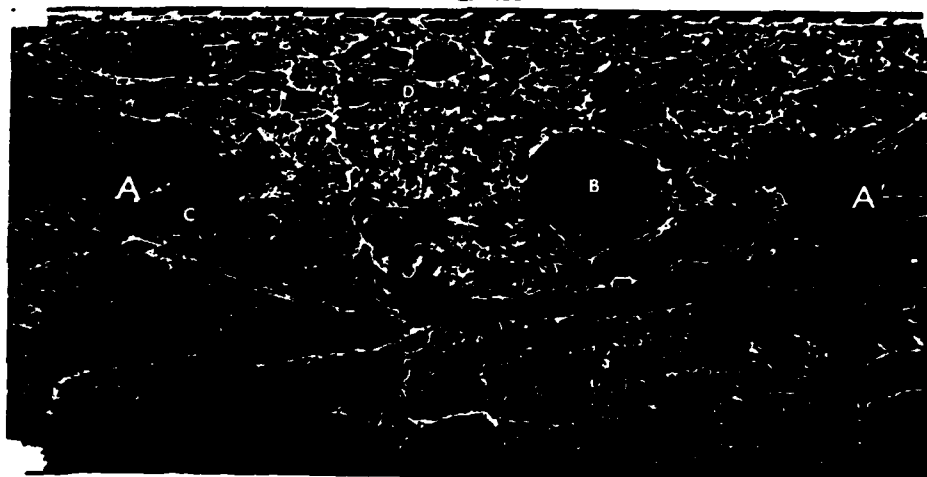


Figure 8. X-band Parallel and Cross Polarized SAR Imagery of Ice in the Beaufort Sea. Also Shown on the Figure is a Transect of Received Power Across the Image at the Location Marked A to A'.

B=Multi-Year Ice
C=First-Year Ice
D=Open Water or New Ice



LHH



LHV

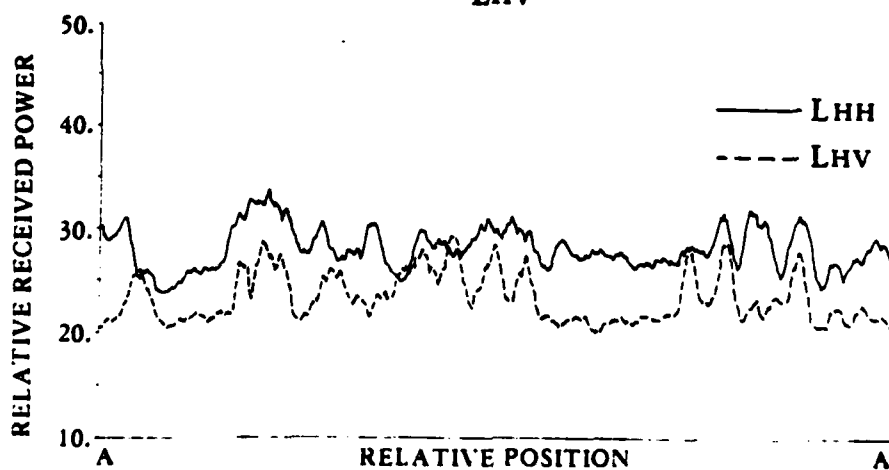


Figure 9. L-band Parallel and Cross Polarized SAR Imagery of Ice in the Beaufort Sea. Also Shown on the Figure is a Transect of Received Power Across the Image at the Location Marked A to A'.

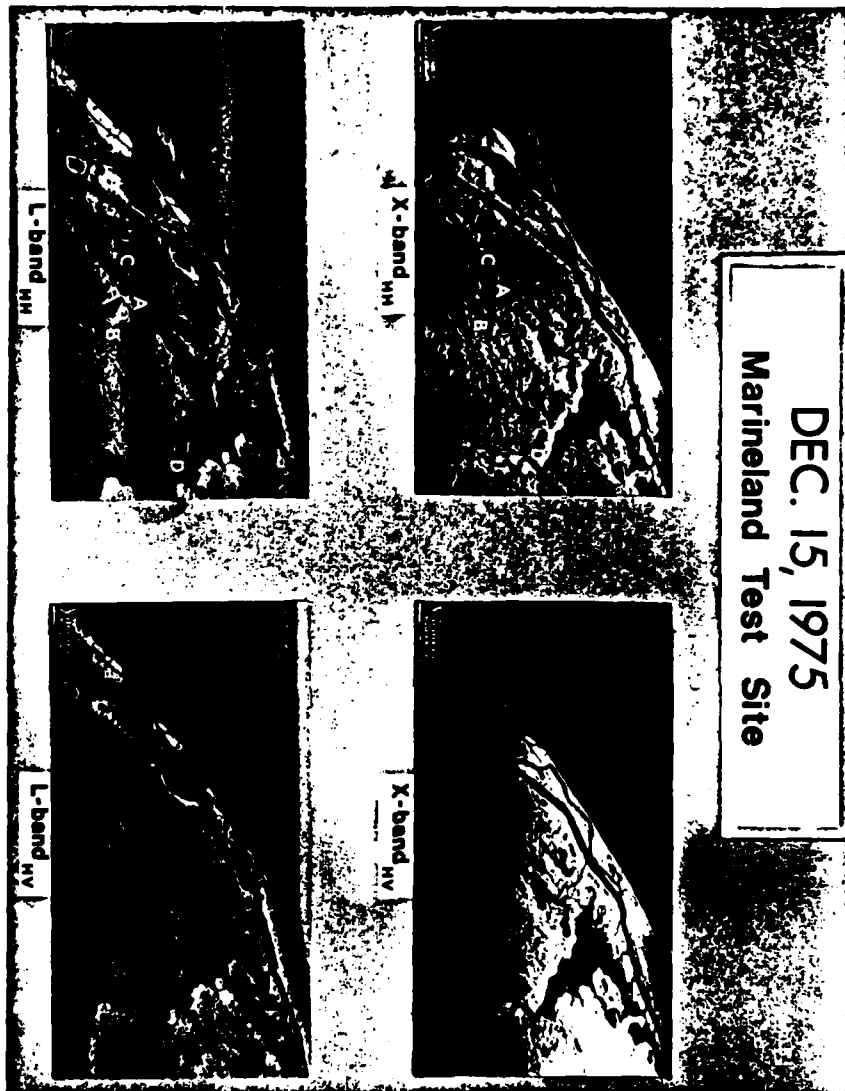


Figure 10. Four Channel SAR Imagery of Atlantic Coastal Zone at Marineland, Florida (15 December 1975).

AIRBORNE SYNTHETIC APERTURE RADAR OBSERVATION OF SURF ZONE CONDITIONS

R. A. Shuchman

Radar and Optics Division, Environmental Research Institute of Michigan, P.O. Box 8618, Ann Arbor, Michigan 48107

G. A. Meadows

Department of Atmospheric and Oceanic Science/ERIM Consultant, University of Michigan, Ann Arbor, Michigan 48109

INTRODUCTION

Synthetic aperture radar (SAR) has been used to image ocean waves over large areas from both conventional aircraft (Elachi, 1976; Shemdin, et al., 1978) and from satellites (Gonzalez, et al., 1979). Imaging is not restricted by platform size or altitude as with real aperture radar, or by external illumination, as with photography. SAR images have then been used to determine surface wave direction and wavelength. Although the imaging mechanism has not been explained completely, the forward face and rear face of sufficiently large waves exhibit different scattering characteristics at SAR wavelengths and can be distinguished in SAR imagery (Shuchman, et al., 1978).

The Environmental Research Institute of Michigan (ERIM) has been acquiring and processing SAR data from aircraft for several years (Cindrich, et al., 1977). In October 1978, ERIM acquired SAR data on a flight along the coast of Lake Michigan approximately half-way between Pentwater and Ludington, Michigan (latitude $43^{\circ}50'N$).

At this time, the University of Michigan's Department of Atmospheric and Oceanic Science was operating a series of resistance wave gauges and ducted impeller current meters in the nearshore zone (Meadows, 1979). This paper compares SAR wave directional spectra measurements to *in situ* wave spectra obtained in the surf zone. Additionally, the SAR Doppler history is exploited to obtain an estimate of surface current magnitude and direction. This SAR derived information is also compared to the *in situ* nearshore surface current sea truth.

The following sections describe the *in situ* sea truth and the ERIM SAR system. Methods of computing wave direction, wavelength, and current information from the SAR are discussed. The comparisons of the SAR derived information with the sea truth are good; indicating remotely sensed surf zone information is a useful tool to oceanographers and coastal engineers. In addition, directions of wave travel, as obtained from the SAR coastal imagery, are shown to be consistent with classical wave refraction calculations.

DATA COLLECTION

On 18 October, 1978 at approximately 16:35 EST, SAR data was collected along the shoreline of Lake Michigan centered at latitude $43^{\circ}50'N$. The site for this field experiment was the eastern shore of Lake Michigan, between the cities of Ludington and Pentwater, Michigan. This thirteen-kilometer section of shoreline, extending approximately north-south, is characterized by a multiple-barred bathymetry with nearly straight and parallel contours. The SAR system used to collect the data was the ERIM X- and L-band dual-polarized imaging radar described by Rawson, et al. (1975). The ERIM SAR system records four channels of radar return but we will focus our attention here on the X-band horizontal-transmit-horizontal-receive channel as this data provided the clearest wave images. The SAR was flown at an altitude of 6100 m and operated with a center incident angle from the vertical of 20° , yielding a swath width of 5.6 km. The cross-track or range resolution of SAR is limited by radar frequency bandwidth and is about 2 m for X-band. The along track or azimuth resolution is obtained from the synthetic aperture technique described by Brown and Porcello (1968). For the X-band, the azimuthal resolution is about 2.5 m. A sample of the X-band imagery showing the location of the coastal array (letter A) is shown in Figure 1. This SAR data was processed on the ERIM processor described by Kozma (1972).

At the same time as the ERIM flight, the University of Michigan, Department of Atmospheric and Oceanic Science was operating its

mobile surf zone, wave and current sensing array (Meadows, 1979). Monitoring of incident wave characteristics and longshore current velocities was conducted through the growth of a significant storm on Lake Michigan. A detailed discussion of the experimental design is presented in Wood and Meadows (1975) and Meadows (1977). Surface-piercing, step resistance wave probes and bi-directional ducted impeller flow meters were employed to make simultaneous measurements of wave and current conditions. These sensors were oriented on a line perpendicular to shore, extending from the beach through the outer surf zone. Other coastal sensing equipment included a directionally mounted motion picture camera and Lagrangian drifters. Unfortunately, increasing wind and wave action on 17 and 18 October, destroyed much of the array, however, sufficient sensors survived to make this comparative study possible. A representative portion of the 18 minute record from the outer surf zone resistance wave gauge is shown in Figure 2.

METHODS

The SAR data shown in Figure 1 was digitized using the ERIM hybrid image digitizer (Ausherman, et al. 1975). The data was digitized with an approximate resolution of 6 meters (3 m pixels). The range coordinates of the digitized data were analytically corrected for slant-to-range geometry (Feldkamp, 1978). Four 1.5×1.5 km subsections (see Figure 3) with 6 meter resolution were extracted from the digitized data. The four sections are labeled A-D where A is closest to shore.

The 3.0 m pixel digitized SAR images were converted to 6 m resolution by 4 pixel averaging in order to increase coherence in the image. The average value of each azimuthal line was subtracted from the line to remove the trend of intensity falloff with increasing range distance. Two-dimensional fast Fourier transforms were performed on each 256×256 cell subsection to yield raw directional wave number spectra with a Nyquist wave number of 0.52 m^{-1} . The raw spectra were smoothed by replacing each value with the average of the surrounding 5×5 cell. The approximate number of degrees of freedom for the resulting spectrum is 142 (Kinsman, 1965). The 99% confidence limits are then $\pm 1.5 \text{ dB}$ (Jenkins and Watts, 1968).

The longshore current magnitude and directional information was extracted from the SAR data by exploitation of the SAR Doppler history (Shuchman, et al., 1979). This technique takes advantage of the fact that the SAR instrument responds primarily to backscatter from

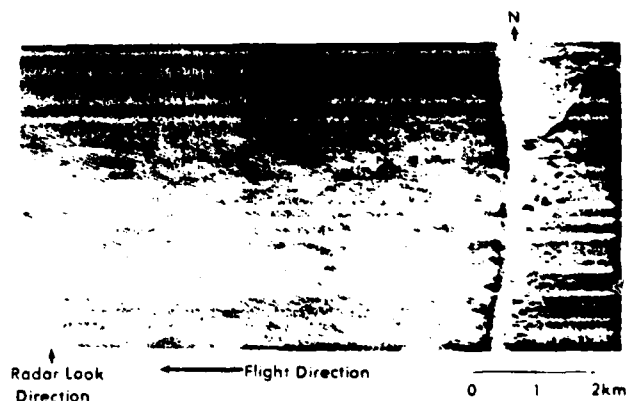


FIGURE 1. X-Band (HH) SAR data used in study. (The letter A indicates approximate location of surf zone array. Image represents 3×3 -meter resolution.)

Copyright 1980 by the American Geophysical Union.

OCTOBER WAVE DATA 1978

25. Seconds

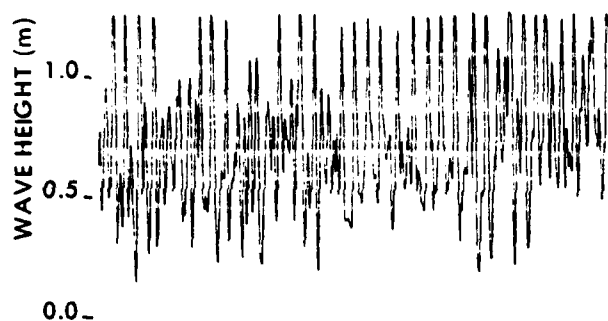


FIGURE 2. Representative Section of 18 minute time history of water level elevation data from nearshore resistance wave gauge

capillary waves, which, in conventional SAR processing, are assumed stationary with respect to other time scales of the radar system. However, these scatterers are not stationary: they move with a characteristic phase velocity as well as with a velocity due to the presence of currents and longer gravity waves. The radial (line of sight) component of this resultant velocity produces a Doppler shift in the temporal frequency of the return signal, which translates to a spatial frequency shift recorded on SAR signal film.

The Doppler frequency shift (Δf_D) for a moving target relative to a stationary target in a SAR system is

$$\Delta f_D = \frac{2V_r}{\lambda} \quad (1)$$

where V_r = radial component of target velocity, and
 λ = transmitted radar wavelength.

This temporal frequency shift will produce an azimuth spatial frequency shift of

$$\Delta f' = \frac{\Delta f_D P}{V_{AC}} \quad (2)$$

on the SAR signal film, where P = azimuth packing factor, and V_{AC} = aircraft velocity.

Equations 2 and 3 can be combined to relate radial target velocity to Doppler spectrum shift:

$$V_r = \frac{\Delta f' \lambda V_{AC}}{2P} \quad (3)$$

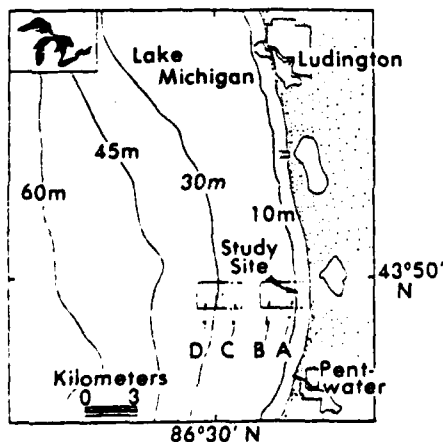


FIGURE 3. General study area showing nearshore bathymetry and locations of fast Fourier transforms performed on SAR data

Typical values for λ , V_{AC} , and P for the imaging of the Lake Michigan data are 0.032 m, 109 m/s, and 15,000 respectively. This relationship can be used to measure the average radial velocity component of an ocean-wave scattering field relative to a fixed-land scattering field. A shift in the azimuth spatial frequency spectrum between fixed-land and moving-ocean surfaces yields an estimate for $\Delta f'$. Variations in spectrum location due to antenna pointing may be eliminated by choosing imagery having land and ocean imaged near simultaneously. An assumption was made that the antenna pointing angle did not change between the land and water measurements. If, however, the antenna angle did change, a slightly higher radial velocity would be calculated.

To calculate the wave spectrum at the instrumented surf zone site, the total 18-minute analog record shown in Figure 2 was digitized at 0.25 s intervals and analyzed using conventional one-dimensional fast Fourier transform techniques. The directional information was obtained by utilizing data from the directionally-mounted camera and the surveyed positions of the array stations. The current information was obtained by again using the directionally-mounted camera but this time photographing the Lagrangian drifters since, by the time of the aerial overflight, the last current meter station had been destroyed.

RESULTS

Figure 4 consists of contour plots of energy density for two test areas (A & D) extracted from the digitized SAR data. Six contour levels are given in 3 dB increments. The data is normalized to the highest value found within the transform. The average depth for each of 1.5 x 1.5 km² areas are indicated on Figure 4. Note the large amount of low frequency energy on the contours even though the data was extensively corrected to reduce the DC bias. The reason for these low frequency components will be discussed later. These contour plots have not been corrected for distortions caused by wave motion. The SAR process distorts the apparent wavelength of waves moving in the azimuthal direction and distorts the apparent direction of waves with a velocity component in the range direction. A detailed description of these effects and the appropriate corrections can be found in Raney and Lowry (1977) and Shuchman, et al. (1979a). The contour data presented was motion corrected and those results will be presented in table form. There is a 180° ambiguity in wave direction measured by SAR which was resolved by assuming the waves were coming from the west and therefore propagating towards the shore.

Close inspection of the contour plots indicates dominant wavelengths of 43, 48, and 55 meters have been resolved by the spectral analysis. Although, spectral energy was resolved at wavelengths as short as 26 m, only the dominant wavelengths have been utilized in the analysis. The general direction of wave travel in the nearshore region is approximately 30°. Note that wave refraction can be observed when comparing the direction obtained in area D with the shallow water area, A.

Figure 5 is a scan of Doppler history for stationary land and the surf zone. Both scans used a 1 x 1 km² aperture. The surf zone scan was centered approximately 650 meters offshore. Note on Figure 5 how the coastal zone (water) scan is displaced to the left of the stationary

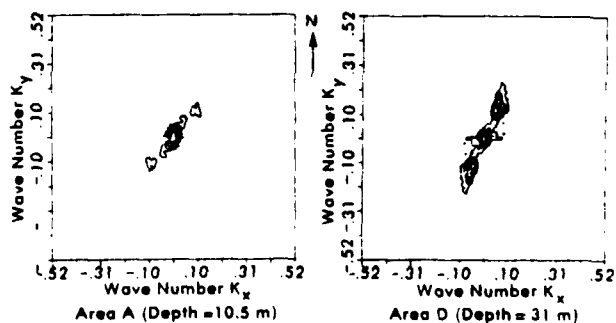


FIGURE 4. Contour plots of fast Fourier transforms (FFT's) of SAR X-Band Lake Michigan wave data

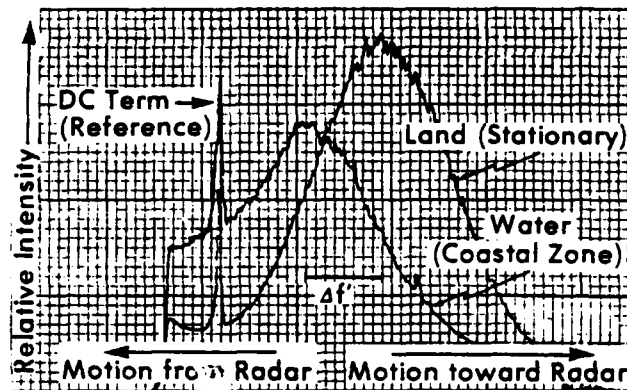


FIGURE 5. Plot of Doppler displacement caused by radial velocity component of longshore current averaged over 1 km² area

(land) target. This indicates a radial motion away from the radar. Recall from Figure 1 that the radar was traveling with a heading of 270°T, thus, the longshore current sensed by the radar was in the northward direction. The Δf frequency which is used in Equation 3 is indicated on the figure. This Δf is corrected for a bias caused by the laser illumination in the SAR optical processor. A Δf of 0.55 lp/mm was detected, which indicates a current velocity of approximately 0.5 m/sec.

A summary of the incident surf zone conditions during the SAR overflight is presented in Table 1. They were obtained by statistical analysis of the 18-minute continuous sea surface elevation record. A representative portion of this surface piercing wave staff record is presented in Figure 2. A one-dimensional spectrum of this wave height data, incident at the outer surf zone, is shown in Figure 6. The dominant frequencies resolved by the spectral analysis are indicated on the figure. In addition, the calculated wave periods and deep water wavelengths are also shown on the figure for each of the major spectral peaks. These correspond to deep water wavelengths of 13, 26, 36, 44 and 54 m, respectively. This analysis indicates the presence of a multi-component incident gravity wave group with dominant periods in the range of 3-6 s. Significant long-period wave components have also been identified with the wave group. The periods of these low frequency components are 17, 40 and a less significant peak at 59 seconds, respectively and appear to resemble surfbeats (Munk, 1949; Tucker, 1950). These results are consistent with measurements of nearshore

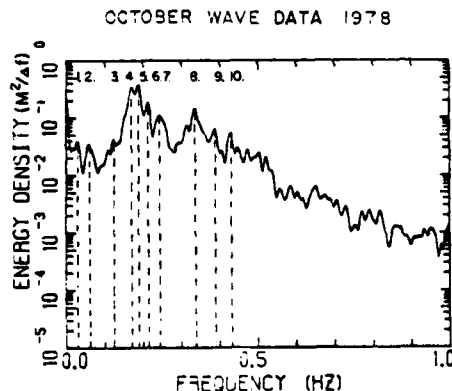


FIGURE 6. One-dimensional wave height spectrum of water surface elevation time history from resistance wave gauge. Dominant wave periods and wavelengths are as follows: (1) T = 40.0 s, L = 685.9 m; (2) T = 17.2 s, L = 294.9 m; (3) T = 8.1 s, L = 138.9 m; (4) T = 5.9 s, L = 54.3 m; (5) T = 5.3 s, L = 43.8 m; (6) T = 4.8 s, L = 35.9 m; (7) T = 4.0 s, L = 25.0 m; (8) T = 2.9 s, L = 13.1 m; (9) T = 2.6 s, L = 10.5 m; (10) T = 2.3 s, L = 8.25 m.

Table 1

Incident Surf Zone Conditions at the Time of the SAR Overflight

Significant Wave Height	0.95 (m)
Dominant Wave Periods	5.9, 5.3, 4.8, 4.0, 2.9 (s)
Deep Water Wavelength	54, 44, 36, 25, 13 (m)
Incident Wave Direction	57° ± 5°
Longshore Current Velocity	0.26 (m/s)
Longshore Current Direction	North (360° T)
Wind Speed	7.5-10 m/s
Wind Direction	230° T

multi-component wave trains reported by Meadows and Wood (1980).

Incident wave direction and longshore current velocity were determined by a frame-by-frame analysis of synchronous motion picture sequence from the shore based directionally-mounted camera. The mean wave angle of attack to the beach was determined to be 57° ± 5° (T) and the mean longshore current velocity midway across the active surf zone was 0.26 m/sec flowing toward the north.

COMPARISON BETWEEN THE SAR AND SURF ZONE MEASUREMENTS

Table 2 provides a comparison between the SAR derived surf zone conditions and the sea truth provided by the surf zone array. The values presented in Table 1 represent surf zone conditions actually measured at the shoreward edge of test area A. The wave directions and wavelengths were then corrected for depth effects using classical linear wave theory. The depths used for the corrections are also indicated on the table. The SAR derived results presented in Table 2 are also corrected for the previously discussed motion distortions. The excellent agreement between SAR observations and the surf zone sea truth shown in the table indicates the following:

1. The dominant surface gravity wave wavelengths and direction are obtainable from the SAR.
2. These observations are in excellent agreement with sea truth, even within the active surf zone.
3. Wave refraction can be observed with SAR and favorably compares to the calculated refraction using classical linear wave theory.

The SAR derived radial current velocity measurement of 0.5 m/sec was higher than reported in Table 1 (0.26 m/sec). However, recall that the current measurement derived from the SAR was not taken in the surf zone but was centered 650 m from the shore. Meadows

Table 2. Comparison Between the SAR Derived Surf Zone Condition and the In Situ Sea Truth

Test Area	Distance from Shore (M)	Depth (M)	SAR Derived		Sea Truth*	
			Dominant Wavelength (M)	Direction (T°)	Wavelength (M)	Direction (T°)
A	900	10.5	48	35 ± 3	47.72	34 ± 2
			43		43.7	
B	2200	14	55	30 ± 3	53.8	30 ± 2
			55		43.7	
C	4600	27	43	25 ± 3	55.3	28 ± 2
			48		45.7	
D	6900	31	55	25 ± 3	55.3	28 ± 2
			48		45.7	

* Actual measurements made at surf zone, values for test areas a-d are depth corrected.

(1977 and 1979), reports that under certain conditions, an increase in longshore current velocity as one moves from the surf zone into deeper water may be expected. As presented earlier, the SAR Doppler measurement is a radial velocity and is denoted by a line of sight. Thus, only rather coarse directional information is obtainable; in this case, a current velocity away from the radar look direction (northward flowing current). Two orthogonal flight headings and resulting current measurements could greatly enhance the directional sensing capability.

DISCUSSION

The SAR spectrum data presented in Figure 4 are wave number spectrum of the radar intensity and as such are not expected to have the same appearance as the one-dimensional spectrum from the resistance wave gauge (Figure 6) which was determined from wave height and period data. Even if the wave number spectrum is converted to a frequency spectrum or vice-versa, it is clear that the SAR spectra examined here cannot be easily transformed to, or interpreted as, wave height spectra. However, the wave number and direction of the peak energy, determined from SAR spectra, agree very well with *in situ* measurements. Synoptic availability of even these parameters is currently unobtainable by conventional ground-based measurements. This addition represents a significant advance in large scale wave data acquisition.

Both of the SAR derived wave spectra presented in Figure 4 exhibit significant low frequency components. These components were observed even after the digital SAR data was extensively smoothed and the intensity falloff in the range direction was digitally corrected. The low frequency (near zero wave number) components could in fact be real components of the sea surface and will be further evaluated in a follow-on study.

SUMMARY

Synthetic aperture radar (SAR) surface gravity wave data of the coastal zone of a portion of Lake Michigan has been compared to *in situ* surf zone wavelength, period, direction, and surface current information. The comparisons were favorable, indicating SAR's utility as a tool to remotely sense coastal zone conditions. This could in turn enable oceanographers to synoptically study the entire coastline of large water bodies. This data could then prove useful in mapping not only surface wave climates and currents, but also provide a mechanism for rapid and large scale assessment of changes in coastal conditions.

Specifically, this study has shown:

1. SAR derived wavelengths and directions are in good agreement with sea truth.
2. SAR spectra taken in various water depths do correlate with predicted wave refraction.
3. Longshore current direction and relative magnitude as obtainable from SAR Doppler history are in reasonable agreement with sea truth, and
4. Low-frequency components observed on SAR spectra seem to correlate with low frequency "surf beat" found in sea truth spectral estimates.

It should be mentioned when utilizing SAR data such as presented in this paper, that the SAR spectral estimates presented are wave number-directional spectra of the radar return intensity. The data does not represent wave height information, at least not in a recognizable form. The modulation transfer function (i.e., SAR gravity wave imaging mechanism) is not totally understood at the present time. The determination of the transfer function as well as determination of wave height using SAR data will be a major scientific advance. At that time, it would then be possible to use SAR gravity wave data to obtain power density estimates of the sea surface.

Acknowledgements. The ERIM analysis of the SAR gravity wave data was supported by the Office of Naval Research (ONR) Contract N00014-76-C-1048. The technical monitor for this ONR contract is Mr. Hans Dolezalek. The field installation of the mobile wave and

current monitoring system, as well as the reduction of the *in situ* sea truth data, was supported under the University of Michigan research grant no. 387349.

REFERENCES

- Ausherman, D. A., W. D. Hall, J. N. Latta, and J. S. Zelenka, Radar Data Processing and Exploitation Facility, Proceedings IEEE International Radar Conference, Washington, D.C., 1975.
- Brown, W. J. and L. Porcello, An Introduction to Synthetic Aperture Radar, *IEEE Spectrum*, 6, pp. 52-66, 1968.
- Cindrich, I., J. Marks, and A. Klooster, Coherent Optical Processing of Synthetic Aperture Radar Data, *Proceedings of the Society of Photo/Optical Instrumentation Engineers*, p. 128, 1977.
- Elachi, C., Wave Patterns Across the North Atlantic on September 28, 1974, from Airborne Radar Imagery, *J. Geophys. Res.*, 81, pp. 2655-2656, 1976.
- Feldkamp, G. B., Correction of SAR-Induced Distortion in Seasat Imagery, Paper Presented at the SPIE Conference on Applications of Digital Image Processing, San Diego, Calif., August 1978.
- Gonzalez, F. I., R. C. Beal, W. E. Brown, P. S. DeLeonibus, J. S. Sherman, J. F. R. Gower, D. Litchy, D. B. Ross, C. L. Rufenach, and R. A. Shuchman, Seasat Synthetic Aperture Radar: Ocean Wave Detection Capabilities, *Science*, 204, pp. 1418-1421, 1979.
- Jenkins, A. M. and D. G. Watts, *Spectral Analysis and Its Applications*, Holden-Day, San Francisco, Calif., 525 pp., 1968.
- Kinsman, B., *Wind Waves—Their Generation and Propagation on the Ocean Surface*, Prentice-Hall, Englewood Cliffs, N.J., 676 pp., 1965.
- Kozma, A., E. N. Leith, and N. G. Massey, Tilted Plane Optical Processor, *Applied Optics*, 11, p. 1766, 1972.
- Meadows, G. A., The Wind Driven Component of Surf Zone Circulation (Abstract), *Trans. Amer. Geophys. Union*, Vol. 60, No. 46, 1979.
- Meadows, G. A., A Field Investigation of the Spatial and Temporal Structure of Longshore Currents, Ph.D. Dissertation, Purdue Univ., West Lafayette, Indiana, 1977.
- Meadows, G. A. and W. L. Wood, Long-Period Surf Zone Motions (In Review), 1980.
- Munk, W. H., Surf Beats, *Trans. Amer. Geoph. Union*, Vol. 30, 1949.
- Raney, R. K. and R. T. Lowry, Oceanic Wave Imagery and Wave Spectra Distortions by Synthetic Aperture Radar, Twelfth International Symposium on Remote Sensing of Environment, Manila, Philippines, 20-29 April 1978.
- Rawson, R., F. Smith, and R. Larson, The ERIM Simultaneous X- and L-Band Dual Polarized Radar, *IEEE 1975 International Radar Conference*, 505, 1975.
- Shemdin, O. H., W. E. Brown, F. G. Standhammer, R. Shuchman, R. Rawson, J. Zelenka, D. B. Ross, W. McLeish, and R. A. Berles, Comparison of In Situ and Remotely Sensed Ocean Waves Off Marineland, Florida, *Boundary-Layer Meteorol.*, 13, pp. 193-202, 1978.
- Shuchman, R. A., C. L. Rufenach, and F. I. Gonzalez, The Feasibility of Measurement of Ocean Surface Currents Using Synthetic Aperture Radar, Published in the Proceedings of the Thirteenth International Symposium on Remote Sensing of Environment, Ann Arbor, Mich., April 1979.
- Shuchman, R. A., K. Knorr, J. C. Dwyer, A. Klooster, and A. L. Maffett, Imaging Ocean Waves with SAR, *ERIM Report No. 124300-2-T*, Environmental Research Institute of Michigan, Ann Arbor, Mich., 130 pp., 1979a.
- Shuchman, R. A., E. S. Kasischke, and A. Klooster, Synthetic Aperture Radar Ocean Wave Studies, *ERIM Final Report No. 131700-3-F*, Ann Arbor, Michigan, 1978.
- Tucker, M. J., Surf Beats: Sea Waves of 1 to 5 Minutes Period, *Proc. Roy. Soc., A* 207, pp. 565-573, 1950.
- Wood, W. L. and G. A. Meadows, Unsteadiness in Longshore Currents, *Geophys. Res. Lett.*, Vol. 2, No. 11, 1975.

(Received February 2, 1980;
accepted March 10, 1980.)

Static and Dynamic Modeling of a SAR Imaged Ocean Scene

ROBERT A. SHUCHMAN, ANDREW L. MAFFETT, AND ALEX KLOOSTER, JR.

Abstract—A number of models exist that attempt to explain wave imagery obtained with a synthetic aperture radar (SAR). These models are of two types: static models that depend on instantaneous surface features and dynamic models that employ surface velocities. Radar backscatter values (σ_0) were calculated from 1.3- and 9.4-GHz SAR data collected off Marineland, FL. The σ_0 data (averaged over many wave trains) collected at Marineland can best be modeled by the Bragg-Rice-Phillips model which is based on roughness variation and the complex dielectric constant of oceans. This result suggests that capillaries on the surface of oceanic waves are the primary cause for the surface return observed by a SAR. Salinity and temperature of the sea at small and medium incidence angles produce little effect upon sea-surface reflection coefficients at X-band, for either of the linear polarizations.

The authors' observation of moving ocean, imaged by the SAR and studied in the SAR optical correlator, support a theory that the ocean surface appears relatively stationary in the absence of currents. The reflecting surface is most likely moving slowly (i.e., capillaries) relative to the phase velocity of the large gravity waves.

I. INTRODUCTION

THIS PAPER discusses a specialized form of side-looking airborne radar (SLAR) called a synthetic aperture radar (SAR). SAR utilizes the Doppler history (change of phase) associated with the motion of the aircraft, recording both the phase and the amplitude of the backscattered energy, thus improving the along-track or azimuth resolution. The longer the radar data length, the greater the improvement in the along-track resolution of the system.

The principle in imaging any surface with a radar is that the backscatter of microwave energy (echo or radar cross section) received by the radar receiver contains information on the roughness characteristics (shapes, dimensions, and orientations) of the reflecting area. These parameters that influence the echo received from ocean waves include the motion of the scattering surfaces, the so-called speckle effect, system resolution, and noncoherent integration, as well as contributions attributable to wind, waves, surface currents, and surface tension. Also, the orientation of ocean waves to the radar look

direction must be considered. When attempting to understand the SAR ocean-wave imaging mechanism, one must also consider factors pertaining to wave orbital velocity, Bragg scatter velocity, and long (or resolvable) wave phase velocity [1], [2].

Several models exist that attempt to explain wave imagery obtained with a SAR. These models are of two types: static models that depend on instantaneous surface features, and dynamic models that employ surface velocities. SAR imagery has been discussed in the literature using both types; though as yet there exists no widely accepted understanding of the imaging mechanism for SAR's. This paper attempts to draw together analytical and experimental results based on a combination of these two types in order to approach a more satisfactory model for SAR ocean-wave imaging.

II. RADAR SYSTEM AND FLIGHT PATTERNS

The experimental observations presented in this paper were obtained with a SAR. These models are of two types: static of Michigan (ERIM) dual-frequency and dual-polarized SAR system. The ERIM X-L system described by [3] consists of a dual-wavelength and dual-polarization SAR [4], [5] that simultaneously images at X-band (3.2 cm) and L-band (23.5 cm). Alternate X- and L-band pulses (chosen to be either horizontally or vertically polarized) are transmitted, and reflections of both polarizations are received; thus four channels of radar imagery are simultaneously obtained. Both polarizations of X-band are recorded on one film, both polarizations of L-band on the other. The Marineland data presented in this paper were obtained from the horizontal-transmit horizontal-receive channel (HH) of both the X- and L-band receivers. The polarization of the electromagnetic radiation is defined by the direction of the electric field intensity vector E . For example, a horizontally polarized wave will have its E vector parallel to the local horizon. Data were calibrated against the return from corner reflectors of known radar cross section.

The SAR ocean data set presented was collected by the ERIM SAR system at Marineland, FL, during mid-December, 1975. The Marineland experiment was conducted to obtain SAR ocean-wave data in support of SEASAT-A with its L-band SAR (launched June, 1978). The specific objectives of the Marineland experiment are outlined in [6]. Wave heights and directions of long waves and slope intensities of capillary and short gravity waves were measured by an array of *in situ* instruments, including a capillary sensor mounted on a wave follower, a pitch-and-roll buoy, and paired orthogonal current meters.

The ERIM radar was flown over the Marineland test area using a flight pattern shown in Fig. 1. This enabled the authors

Manuscript received January 19, 1980; revised February 23, 1981. This work was supported by ONR under Contract N00014-76-C-1048. The ONR technical monitor was Hans Dolczalek. Some aspects of the work reported herein were jointly supported by the Office of Naval Research as well as the National Oceanic and Atmospheric Administration (NOAA). The NOAA work was performed under Contract N07-35328 under the direction of John W. Sherman, III, of the National Environmental Satellite Service of NOAA.

R. A. Shuchman and A. Klooster, Jr., are with the Radar and Optics Division, Environmental Research Institute of Michigan (ERIM), P. O. Box 8618, Ann Arbor, MI.

A. L. Maffett is with the Department of Mathematics, University of Michigan, Dearborn, MI.

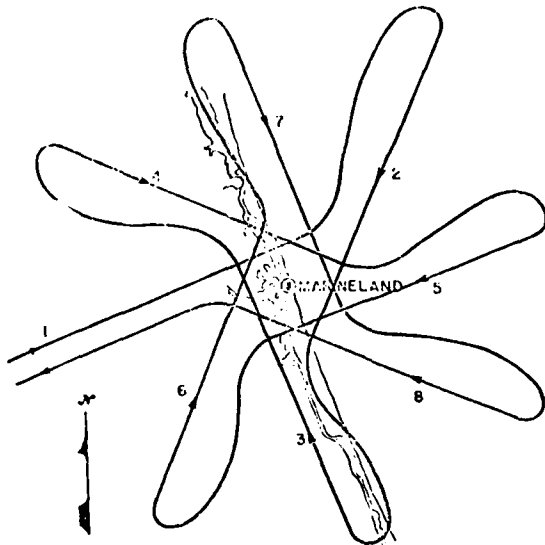


Fig. 1. ERIM flight patterns flown over Marineland test site.

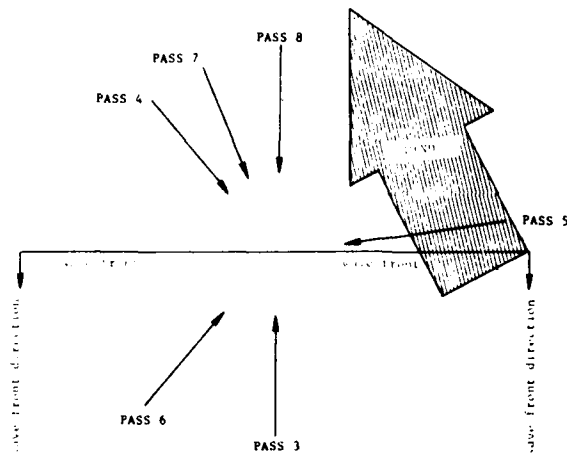


Fig. 2. Radar-look direction with relation to wavefront and wind directions for December 10, 1975.

to study the sensitivity of wave orientation to radar-look direction.

The data discussed in this paper were collected on December 10 and 15, 1975. Fig. 2 summarizes the flight lines, wind, and wave conditions on December 10, 1975. Note from the figure that an off-shore wind existed which was blowing from 310° (true) towards the incoming waves which were propagating towards 340° (true). The wind was blowing at 14-20 knots while the significant wave height was 0.8-1.25 m with a period of 5-6 s. On December 15, a wavetrain identified as swell (8-s period) was traveling in the approximate direction of 275° with respect to true north. The significant wave height ($H_{1/3}$) was 1.5-1.8 m. The wind speed at the site on December 15 was $5-7 \text{ m}\cdot\text{s}^{-1}$ from the east, a direction of 90° with respect to true north.

Propagating ocean wave data collection by a SAR is not necessarily suited to conventional processing techniques which assume stationary objects. Because moving ocean waves may

perturb the Doppler frequencies, and hence the phase histories recorded on the anamorphic zone plate [7], the conventional processing of these zone plates produces images of the waves that are defocused in the azimuth direction relative to stationary terrain. This defocusing by the along-track velocity of the moving ocean waves can be refocused in the processor. This is done by readjusting the azimuth focus (cylindrical focus) an amount proportional to the relative velocity of the wave-trains [8].

The coherently sensed radial motion of a moving ocean wave imaged by a SAR will also perturb the signal history of a scatterer. Radial wave velocity produces an apparent tilt to the phase history as recorded on the signal film. In addition, the scatterer history if coherent will also shift across the signal film. The rotation effect described above is referred to as "range walk" and can be compensated by rotation of the cylindrical optics in the processor. These along-track and radial-velocity effects will be discussed in greater detail in the section dealing with a dynamic model of SAR wave imagery.

III. STATIC MODELS

The three principal static models for the backscatter (σ_0) from the ocean are the facet, Bragg-Rice, and the Rayleigh scattering models. The tangent plane or facet model is based on reflections from areas whose slopes are oriented normal to the line of sight. It is assumed that the surface radius of curvature exceeds the radar's wavelength and that one can neglect multiple scattering and shadowing effects [9]. The radar cross section of the facet model, according to [10], is

$$\sigma_0(\theta) = \cot^2 \beta_0 \exp(-\tan \theta / \tan \beta_0)^2 \quad (1)$$

where θ is the radar incidence angle, and $\tan \beta_0 = 2\sigma/T$, T being the autocorrelation distance for a rough surface whose heights are normally distributed with standard deviations σ .

The Bragg-Rice model uses the concept that the ocean surface can be represented by a combination of periodic surfaces, so that the dominant backscatter will match some portion of the ocean-wave spectrum. The model assumes that the number of favorable additions satisfies the criterion of adequate sample size, that the height and slopes of the backscattering elements are small relative to the incident wavelength, and that their distribution is isotropic. The maximum return, as measured and reported in [11], is obtained when

$$k_w = 2k \sin \theta \quad (2)$$

where $k_w = 2\pi/L$ and $k = 2\pi/\lambda$ are the wavenumbers and L and λ the wavelengths, respectively, of the capillary waves and the radar. For this model, the radar cross section

$$\sigma_0(\theta) = 4\pi k^4 \cos^4 \theta |R(\theta, \psi)|^2 W(k) \quad (3)$$

where $R(\theta, \psi)$ is the reflectivity as a function of the surface electromagnetic properties, the incidence angle θ measured from nadir, and the polarization angle ψ , and where $W(k)$ is the energy density spectrum of surface height variation evaluated at the Bragg resonant condition in (2). The energy density spectrum $W(k)$ can be defined for the high-frequency region of

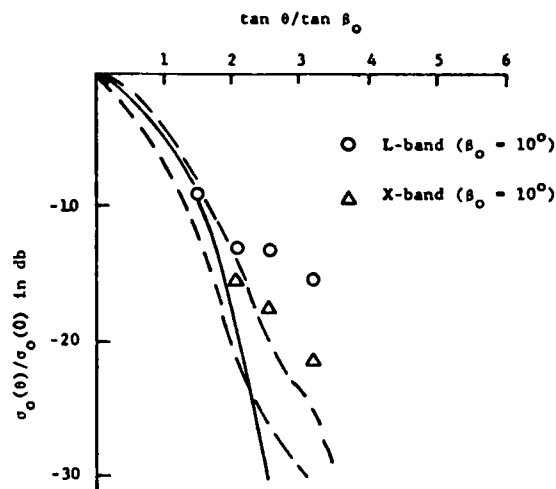


Fig. 3. Comparison of X-band and L-band data obtained at Marineland on December 15, 1975, with the facet model (solid line) and with the range of data reported by [10] (dashed lines).

the spectrum as Bk^{-4} , where reasonable bounding values of B are approximately 6×10^{-3} for gravity waves and 1.5×10^{-2} for capillary waves [12].

Backscatter from the sea is composed of contributions from many fluctuating individual scatterers, which in the Rayleigh scattering model are represented by segments of spheres or complex shapes that are small relative to the radar wavelength. The resultant echo varies in time, reflecting relative phase differences among the echoes received from each of the scattering elements [13]. The resultant radar cross section, which is relatively insensitive to look-direction because the scattering elements are moving randomly and are distributed nearly isotropically, is described by a probability density function. According to [14], the Rayleigh scattering is more sensitive to vertical polarization and more applicable to wide pulse-widths, wherein the received echo contains returns from several breaking waves, added noncoherently.

Two of the static models, the facet and Bragg-Rice scattering models, were evaluated with data from the Marineland experiment as previously mentioned. Analysis indicates the facet model agrees only marginally with the data obtained with the SAR's operated by ERIM. Results shown in Fig. 3 include the range of data reported [16], and X-band ($\lambda = 3.2$ cm) and L-band ($\lambda = 23.5$ cm) measurements normalized to the 12-knot wind speed measured at Marineland (equivalent to $\beta_0 = 10^\circ$).

Alternatively, the Bragg-Rice model discussed in [7] and in [14] offers more promise. For the HH polarization case, the reflection coefficient function R of (3) is given by

$$R_0^- = \frac{\sin \gamma - \sqrt{\epsilon_r - \cos^2 \gamma}}{\sin \gamma + \sqrt{\epsilon_r - \cos^2 \gamma}} \quad (4)$$

where ϵ_r is the relative dielectric constant of the ocean and $\gamma = \pi/2 - \theta$ is the grazing angle (see [14]). The superscript $-$ is used to indicate the HH polarization case. The subscript 0

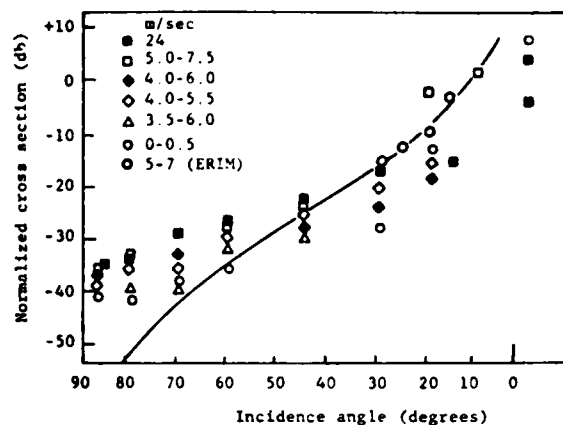


Fig. 4. Variation of the normalized σ_0 (HH) at X-band with incidence angle and wind speed. The line represents the Bragg scattering relationship. Data are from [15] and the ERIM radar.

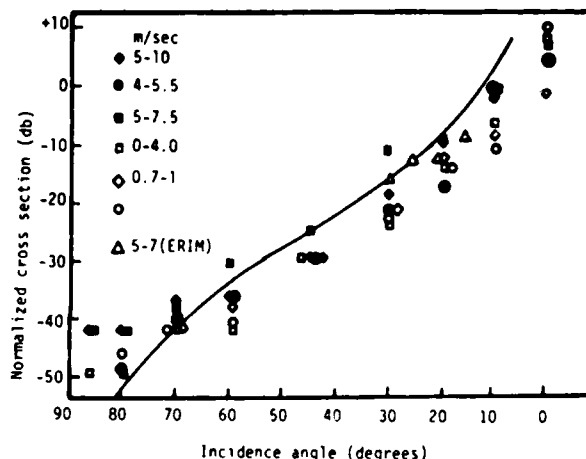


Fig. 5. Variation of the normalized σ_0 (HH) at L-band with incidence angle and wind speed. The line represents the Bragg scattering relationship. Data are from [15] and the ERIM radar.

means that the reflection coefficient is for a smooth surface only. The reflection coefficient R_0^+ for VV polarization differs from (4) by having an additional factor ϵ_r inserted in the first term of both numerator and denominator. Roughness may then be accounted for by a factor ζ , giving complete reflection coefficients $R = \zeta R_0^+$. Now, recalling the Phillips bound for $W(R)$ [12], one finds

$$\sigma_{0HH} = 1.5\pi \times 10^{-3} |R_0^-|^2 \tan^4 \gamma \quad (5)$$

as an upper bound for the Bragg-Rice model. Data summarized in [15], together with data obtained by ERIM on December 15, are shown in Fig. 4 for X-band (using $\epsilon_r = 48.3 - 34.9i$) and in Fig. 5 for L-band (using $\epsilon_r = 73 - 85i$). The Bragg-Rice-Phillips upper bound is shown as a solid line. For the limited range of incidence angles, agreement between theory and data is good.

In summary, the reflectivity of a large area of sea surface observed by a SAR which, when averaged to yield a coarse resolution reflectivity estimate, provides an apparent bright-

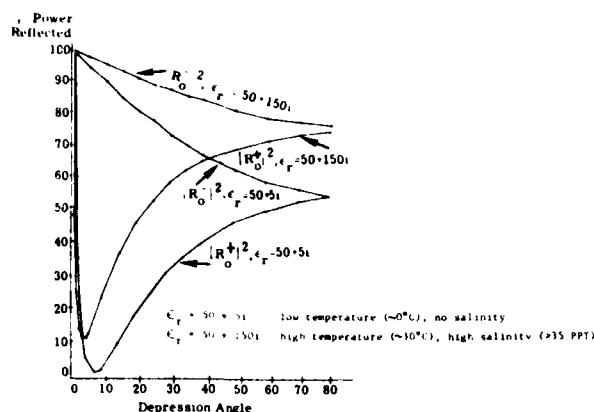


Fig. 6. Reflection coefficient versus depression angle for temperature and salinity ranges at L-band.

ness that approaches the Bragg-Rice-Phillips upper bound. This suggests that capillaries on the surface of the oceanic waves are the primary basis for the surface properties observed by both real and synthetic aperture radar [16].

IV. SEA REFLECTION COEFFICIENT VARIATION WITH TEMPERATURE AND SALINITY

Large σ_0 variations were observed in the SAR data collected near the Gulf Stream during the Marineland experiment. The question then arises to what extent are these σ_0 variations due to temperature and salinity effects upon the reflection coefficient. This query is also germane to the examination of SAR data collected by the SEASAT satellite.

At small and medium incidence angles, the effects of temperature and salinity variations upon sea-surface reflection coefficients for either of the linear polarizations, seem to be of insignificant proportions. At large incidence angles, i.e., near grazing, there is a more pronounced change in the behavior of the vertical polarization reflection coefficient. In fact, in the vicinity of 80° incidence, the ratio of the reflection coefficient for high temperature, high salinity to the reflection coefficient for low temperature, low salinity can take an excursion of as much as 20 dB.

Using values of ϵ' and ϵ'' (real and imaginary parts, respectively, of ϵ_r) representative of cold fresh water ($\sim 0^\circ\text{C}$) and high-temperature sea water ($\sim 30^\circ\text{C}$; 35 ppt salinity) as recorded in [17], expressions for $|R_v^-|^2$ and $|R_h^+|^2$ have been calculated as a function of depression angle γ and are shown in Fig. 6. The value $\epsilon'' = 150$ may seem high for higher temperature sea water; however, Hollinger [17] shows the possibility of very high ϵ'' values for frequencies of 1 GHz and lower. In any case, in going from low-temperature fresh water to high-temperature sea water, the difference in reflection coefficient values for either of the horizontal or vertical polarization cases is not startling, being at most some 25 percent for the vertical polarization reflection coefficient for medium to large depression angles. However, the ratio, particularly of the vertical polarization reflection coefficient values, does attain appreciable size for small depression angles, chiefly because both vertical polarization reflection coefficients take such low values

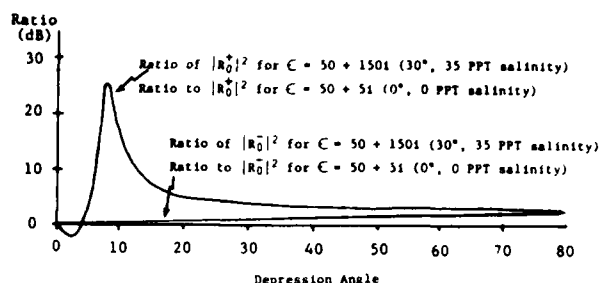


Fig. 7. Behavior of vertical and horizontal polarization reflection coefficients for low and high temperature and salinity conditions at X-band.

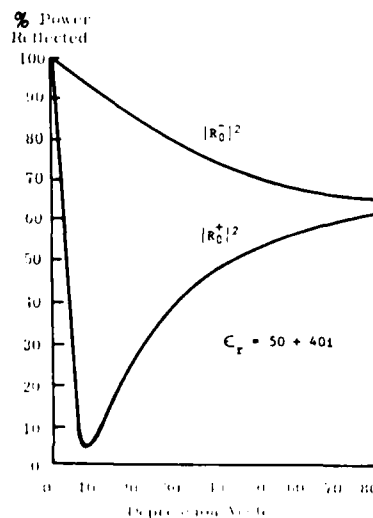


Fig. 8. Reflection coefficient versus depression angle for temperature and salinity ranges at X-band.

at those angles. Fig. 7 shows these ratios plotted in decibels. The horizontal polarization reflection coefficient ratio scarcely budges from 0 dB over the whole angular range. But the vertical polarization reflection coefficient ratio exceeds 20 dB in the vicinity of an 8° depression angle.

The foregoing discussion is pertinent for frequencies in the vicinity of 1 GHz. At 10 GHz, the value of ϵ' should decrease somewhat to about the order of 50. However, the change of ϵ' from 75 to 50 causes an almost imperceptible change in the reflection coefficient values. The value of ϵ'' also changes at 10 GHz to a value of approximately 40. Moreover, at 10 GHz, the value of $\epsilon = 50 + 40i$ is essentially constant for the temperature range 0° to 20°C and for the salinity range 0 to 35. Fig. 8 shows the reflection coefficients $|R_v^+|^2$ and $|R_h^-|^2$ as a function of depression angle at the average permittivity of $\epsilon = 50 + 40i$ for 10 GHz. Note that since the reflection coefficient varies monotonically with ϵ'' , the 10-GHz curve falls within the range of values shown in Fig. 8 for L-band.

In conclusion, changes in smooth-sea reflectivity due to changes in temperature or salinity may be observable at L-band. But it is unlikely that such is the case at X-band (Fig. 7), particularly if the incidence angle is less than 60° (as was the case in the Marineland measurements). It should be noted that

this discussion has only considered the effect of salinity and temperature on the radar reflectivity. The authors, to date, have not considered the effects of temperature and salinity on the surface capillary wave field (i.e., the effects of temperature and salinity on the roughness factor ζ) which could indeed be affected by these two parameters. Thus SAR might be able to detect temperature and salinity differences by detecting subtle differences in the capillary wave field.

V. BACKSCATTER DISTRIBUTION STUDIES

The radar backscatter distributions of Marineland data were examined to ascertain wind and wave propagation sensitivity in respect to the radar-look direction. The results are disappointing in the sense that the distributions display no special features that can be associated with up-, cross-, or down-wave conditions for these data.

Distributions of data sets corresponding to incidence angles of 20° , 30° , 40° , and 50° for Passes 3, 4, 5, 6, 7, and 8 of the Marineland flight of 12/10/75 for X-band HH were examined. The directions of the 6 passes with respect to (ocean) wave-front direction and wind direction were shown in Fig. 2. Pass 8 is down-wave; Passes 3 and 6 are up-wave, with Pass 6 being cross-wind; Pass 3 is with, Pass 8 against, the wind. Pass 5 is both cross-wave and cross-wind. Passes 4 and 7 are down-wave and against the wind.

The film-recorded backscattered return from the sea is digitized in such a way that amplitudes of digitized output are proportional (normalized to an arbitrary level convenient to the digitization process) to square root of power received. The resulting data may be adjusted to account for resolution, range, and antenna pattern, in which case the average level of the data considered for X-band HH corresponds approximately to a σ_0 value of -15 dB. Samples consisting of 12 500 digitized amplitude points were chosen for statistical analysis. These points are obtained from an azimuth swath extending over 100 pixels and a range swath extending over 125 pixels. Each pixel (or sample in a resolution cell) is approximately equivalent to a square 1.5 m on a side.

Of the normal, log-normal [18], and gamma distributions (which includes the well-known Rayleigh distribution as a special case), the digitized data examined are most closely fitted by the log-normal; and this statement remains true for all incidence angles, all wind conditions, and wave-look directions mentioned at the beginning of this section ([15] reports log-normal descriptions for real aperture radar data of ocean surfaces). But, although the type of distribution does not change with changing sea conditions, the parameters of the distribution do change. Fig. 9 shows how the shape (standard deviation) and position (mean) of the distribution may change with wave-look direction for a fixed incidence angle $\theta_i = 20^\circ$. The totality of data distributions examined show that no special features can be associated with up-, cross-, down-wave, or wind conditions. Fig. 10 shows the comparison of distributions as a function of incidence angle for the up-wave condition. Similar relationships also result for the cross- and down-wave conditions. One finds (Fig. 11) a perceptible decrease of standard deviation with increasing incidence angle for the up- and cross-wave conditions. The standard deviation for the

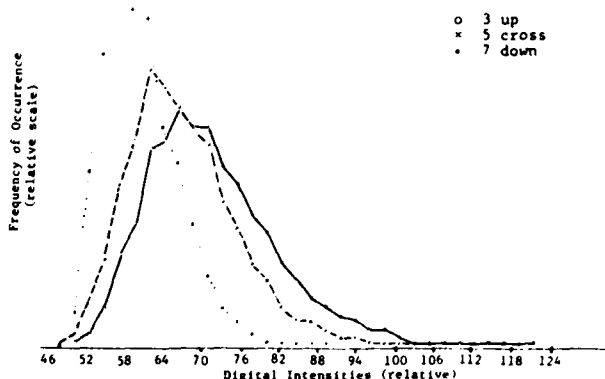


Fig. 9. Comparison of up-, down-, and cross-wave distribution for $\theta_i = 20^\circ$, X_{HH} .

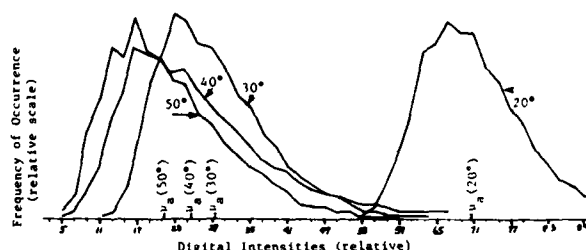


Fig. 10. Comparison of distributions of Marineland X_{HH} Pass 3 data for $\theta_i = 20^\circ, 30^\circ, 40^\circ, 50^\circ$.

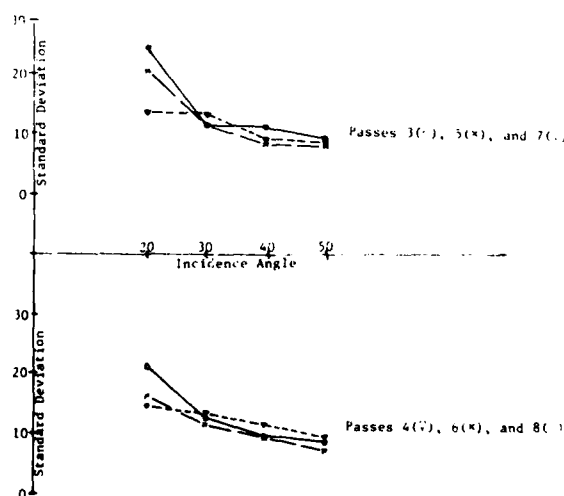


Fig. 11. Adjusted standard deviation versus incidence angle.

down-wave condition is more nearly constant with increasing incidence angle.

To summarize, distributions have been determined for moderate-sized samples of X-band ocean data measured at Marineland for incidence angles of $20^\circ, 30^\circ, 40^\circ$, and 50° and for up-, cross-, and down-wave conditions. Note (Fig. 2) that the Marineland conditions were such that the wind was blow-

ing against the direction of wave travel. The log-normal distribution appears to fit the data histograms better than either the gamma or the normal distributions.

The X-band data distributions do not provide any special features that can be associated with up-, cross-, or down-wave conditions. For example, the trends of the adjusted mean μ_a and standard deviation σ_a for Passes 3 and 7 are reversed for Passes 6 and 4 (the order in both cases being essentially up- and down-wave). This result is in contrast to some preliminary L-band findings for tundra, ice, and mountains. There, the type of distribution appears to change from log-normal for tundra and ice to gamma for mountains for depression angles of 30° . Of course, this same behavior might not be in evidence at X-band, so perhaps we should not expect any special distributional behavior of the up-, cross-, and down-wave data.

The X-band data distributions for a fixed-wave condition do, however, change their mean locations and their shapes (standard deviations) with changes of incidence angle. The trend of the means with incidence angle is similar to the trend of the Bragg-Rice-Phillips theory as presented previously.

VI. DYNAMIC MODELS

Application of static models to non-SAR radars has been reasonably satisfying. However, static models alone cannot be sufficient for SAR's which, by definition, are very sensitive to coherently sensed Doppler velocity components in the scene to be imaged. The effects of motion of wave elements on SAR imagery, in order of importance, include azimuthal displacement, azimuthal image smearing, loss of azimuth focus, reduction of wave contrast, and loss of range focus. The principles of wave motion must be incorporated into the static models to arrive at a more satisfying SAR imaging theory for waves.

Dynamic models, applied to SAR imaging, concentrate on either the phase velocity or on the orbital velocity of ocean waves. Early attempts to explain SAR wave imagery depended on phase velocity effects, and more recent work tends to develop orbital motion models.

The motion of ocean waves imaged by a SAR system may be blurred if the imaged waves move a substantial distance during the time they are in the radar antenna beamwidth. These blurring effects may, in some cases, be removed by compensatory adjustments of the optical correlator processor. In the case of azimuth traveling waves, the correction producing the best azimuth focus may be explained on the basis of a radar scatterer moving at the phase velocity of the ocean wave [8]. This is not the case, however, for range traveling waves where a point scatterer moving at the phase velocity of the wave would displace, but not defocus, the wave image. The observed defocusing can be accounted for if we assume the radar signals are reflected from a nearly stationary scattering surface with variable reflectivity modulated by the passage of a moving ocean wave.

The proposed model presumes that the ocean scattering surface producing visible wave imagery is nearly stationary relative to the phase velocity of the imaged waves. This might be the case where the scatterers producing the wave image were moving at orbital velocity of the wave which is generally an order of magnitude lower than the phase velocity. It would also be true if the scatterers were moving at the phase velocity

of the capillary waves that produce the Bragg-Rice reflections noted in Section III.

In any event, the proposed model does not presume to establish that the scattering surface is absolutely stationary, but that it is moving at velocities an order of magnitude lower than the phase velocity of the imaged waves.

The authors will be showing that a series of measurements and observations made using the ERIM-SAR optical correlator may be explained on the basis of an absolutely stationary surface model. The observations, in fact, would be also consistent with a model that allows for velocities of the scattering surface which are small compared to the phase velocity of the imaged waves.

A stationary surface model is consistent with the following observations:

- 1) Measurements of the azimuth Doppler spectrum shift for a series of range traveling waves indicate a scattering surface velocity, at most, an order of magnitude lower in value than the phase velocity of the waves.

- 2) Radar image contrast for range traveling waves is maximized when the cylindrical optics used to focus the azimuth signal histories are rotated an amount proportional to the waves' phase velocity. No shifting of the azimuthal spectrum bandpass is required.

- 3) Wave images made from separated Doppler spectral bands show range displacements equal to the wave phase velocity times the equivalent time between the two Doppler spectra for a stationary target at the same radar range. For example, if an image is made from the most positive Doppler frequency band corresponding to waves just entering the antenna beam, and another image is made of the waves as they just leave the antenna beam corresponding to the most negative Doppler frequency band, the imaged waves will appear to have moved a distance equal to their phase velocity multiplied by the time of illumination. Note: independent system verification establishes no range walk for stationary targets.

- 4) Azimuth traveling waves are defocused an amount equal in magnitude to that produced by radar reflectors moving at the phase velocity of the wave. Given the same wave velocity, and image resolution, defocusing is more pronounced at L-band than at X-band.

How the model is able to satisfy the above observations will be shown below.

A. Range History for a Fixed SAR Target

Consider the geometry of the SAR platform relative to the fixed-point scatterer shown in Fig. 12. As the antenna beam moves across the reflecting point, the radar range versus time changes as shown in Fig. 13. The slope of the curve is proportional to the relative velocity of the reflecting point and thus the Doppler frequency shift of the reflected radar signal. The reflector is illuminated over the time interval T and is at minimum range at time t_0 when the reflector is directly abeam.

B. Range History for a Target Moving Toward the Flight Line

Suppose the point scatterer is not stationary but is moving directly toward the flight line, as shown in Fig. 14. The radar

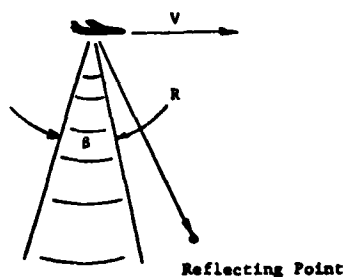


Fig. 12. Radar geometry for stationary reflecting point.

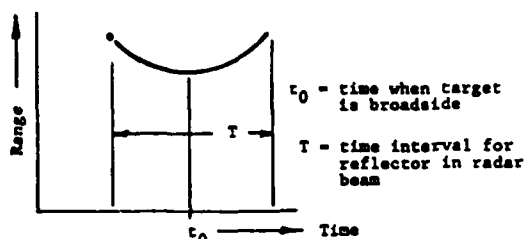


Fig. 13. Range history for stationary point.

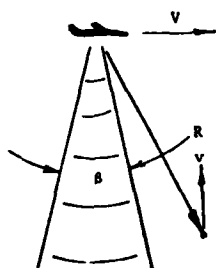


Fig. 14. Radar geometry for moving reflector.

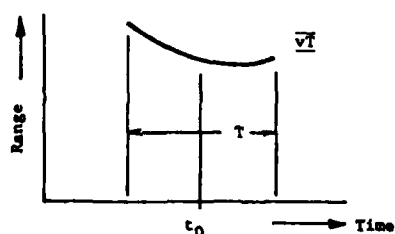


Fig. 15. Range history for moving reflector.

range versus time for this moving reflector is shown in Fig. 15. Here, the minimum range no longer occurs at t_0 where the target is directly abeam, but is shifted to the right. The average slope of the curve is no longer zero, as in Fig. 13, but is equal to the instantaneous slope at t_0 . Note that the slope of the curve and its corresponding Doppler frequency starts at a higher value and exists at a lower value than that for the fixed reflector. Note also, that the range to the target changes a distance vT between target intercept and dropout; however, at equal but opposite slopes of the range curve (equal positive and negative Doppler frequencies) the range to the target is identical.

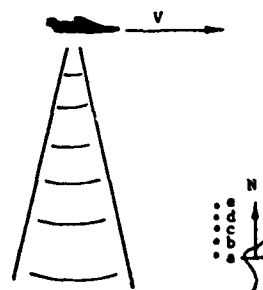


Fig. 16. Radar geometry for range traveling wave.

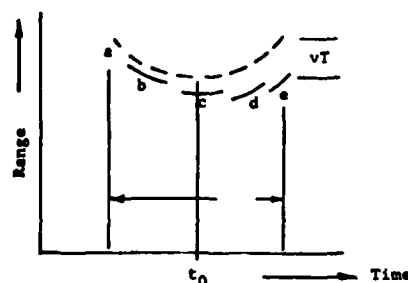


Fig. 17. Range history for range traveling wave.

C. Theoretical Application to Range Traveling Waves

If we presume that a scattering point on the surface of a range traveling wave is moving at the phase velocity of the wave, we should observe a shift in the average Doppler frequency proportional to the phase velocity. In addition, no shift in range should be apparent between images formed from equally displaced positive and negative Doppler frequency bands. However, observations 1) and 3) listed earlier, show no significant Doppler frequency shift, and image displacements are observed for symmetrically displaced Doppler bandpassed images of the ocean surface. Clearly, the range traveling waves do not behave like simple targets moving at phase velocity.

D. Range History of Stationary Reflecting Surface Modulated by a Range Traveling Wave

We will now consider the range history of a series of stationary reflecting points modulated by the passage of a range traveling wave. Fig. 16 shows reflecting points "a-e" at fixed positions on the ocean surface. As the traveling wave progresses toward the flight line, the energy reflected from points "a-e" is modulated to produce a composite range history, as shown in Fig. 17. This history has an overall displacement equal to that for the moving reflector shown in Fig. 15, but is discontinuous with each segment having the range versus time slope of its corresponding stationary reflecting point. The Doppler spectrum of this composite will not be shifted with respect to a stationary reflecting field, and is, therefore, consistent with observation 1). If symmetric Doppler spectra are passed to form an image, such as those corresponding to segments "b" and "d," a displacement corresponding to the wave velocity " v " times the difference in observation times would be observed. This is consistent with observation 3). Then the stationary

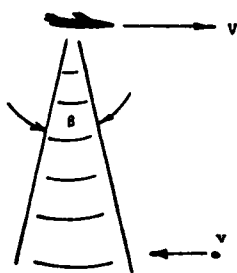


Fig. 18. Radar geometry for reflector with azimuth velocity.

surface model is consistent with both observations 1) and 3). It can also be shown that observation 2) cannot be explained on a basis of a moving reflector if the processor bandpass is not adjusted to pass the moving target spectrum. This was not required for the ERIM data. The stationary surface model predicts a wave displacement over the stationary target spectrum that could be removed by rotation of the processor optics without adjustment of the Doppler bandpass. It remains to be shown that the stationary surface model predicts the same degree of azimuth defocussing as a reflector model that correctly predicts the resulting focus shift.

E. Range History for a Reflector Moving Parallel to the Flight Line

If the reflecting point is moving parallel to the flight line with the velocity v , as shown in Fig. 18, the reflector's range history will have the same variation as that for a stationary point; however, the time the reflector is in the antenna beam will be altered. If the reflector is moving in the same direction as the platform, the time will be increased. For the opposite direction, the time will decrease. For a stationary reflector, the aperture time

$$T = \frac{BR}{V} \quad (6)$$

where

- B antenna beamwidth
- R distance from reflector to flight line, and
- V platform velocity.

For a reflector with velocity v , as shown in Fig. 18, the aperture time

$$T' = \frac{BR}{V + v} \quad (7)$$

Fig. 19 shows the range histories for the two cases discussed above. Note that for the moving reflector point case, the curvature of the range history is changed, the azimuth Doppler FM rate is raised, and the recorded azimuth focal length is reduced. This focal length variation will defocus the image of the moving reflector in the optical processor.

F. Defocussing of Azimuth Traveling Waves

Observation 4) has shown that defocussing of azimuth traveling waves seems to be equal to that of a reflector moving

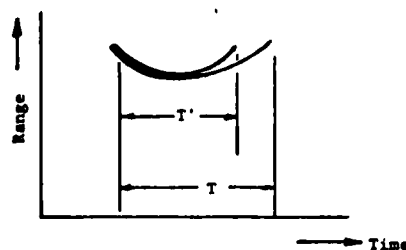


Fig. 19. Range history for reflector moving in azimuth.

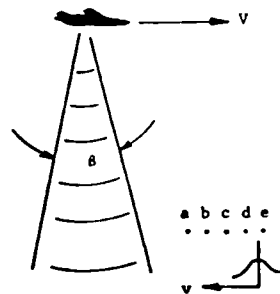


Fig. 20. Radar geometry for azimuth traveling wave.

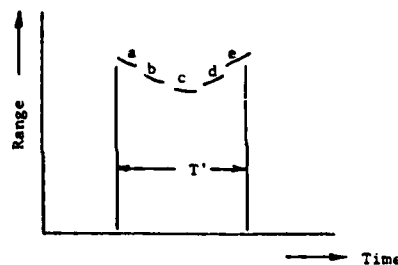


Fig. 21. Range history for azimuth traveling wave.

at the phase velocity of the wave. For stationary surface model to be valid it must predict an equal degree of defocussing. The discussion below demonstrates that this, indeed, is the case.

G. Range History for a Stationary Reflecting Surface Modulated by an Azimuth Wave

Suppose we have a sequence of reflecting points "a-e" to be modulated by an azimuth traveling wave with velocity v , as shown in Fig. 20. If point "a" begins reflecting just as the antenna beam first illuminates it, the range history will proceed as shown in Fig. 21. Points "b, c, d, and e" will reflect, in turn, to produce the segmented range history shown. Each segment will have the azimuth Doppler FM rate of its corresponding stationary reflecting point and will produce an in-focus image at the optical processor output. However, the image of the traveling wave will be blurred if the sequence of reflecting points extends over a substantial part of the ocean wavelength. This blurring may be substantially reduced if the processor is refocused to bring each segment to focus at a common point at the processor output. Then each segment will be slightly defocussed, but the moving wave will have the maximum contrast. The optimum focus setting of the processor would be that which accommodates the range history shown in Fig.

19 produced by the moving reflector. The range history¹ is the same as that for the moving reflecting point shown in Fig. 18, except for some small perturbations. Consequently, the processor setting that properly focusses the image for the moving reflector of Fig. 18 also produces the best focus of the segmented range history of Fig. 21. This is the essential conclusion of observation 4). The stationary surface model is thus shown to be consistent with all of the cited observations.

VII. SUMMARY

The reflectivity of large areas of the sea surface observed by a SAR appear to have a σ_0 brightness that approaches the Bragg-Rice-Phillips upper bound, suggesting that capillaries on the surface of the oceanic waves are the primary basis for the surface return observed by the SAR. However, it should be noted that values presented here represent reflectivity of a large area of sea surface observed by the SAR, averaged to yield a very low resolution highly mixed integrated reflectivity estimate. However, further ERIM measurements indicate that the σ_0 ratio of wave crest to wave trough is a function of orientation of wavetrains in respect to the radar-look direction. This observation could be indicative of a facet model dependency for individual wavetrain detectability or a further confirmation of the importance of wave motion in the SAR formation process as reported by [19].

Future studies of the reflection from capillaries as observed from a SAR should include consideration of 1) the local wave slope effect taking into account windwave directions and the surface interactions that result, and 2) the impact of small scattering cell size to converge on a fine resolution theory of reflectivity.

Distributions have been determined for moderate-sized samples of X-band ocean data measured at Marineland for incidence angles of 20°, 30°, 40°, and 50° and for up-, cross-, and down-wave conditions. The log-normal distribution appears to fit the data histograms better than either the gamma or the normal distributions. Log-normal descriptions have been reported by [14] for real aperture radar data of ocean surfaces.

The X-band data distributions do not provide any special features that can be associated with up-, cross-, down-wave conditions. This result is in contrast to some preliminary L-band findings for tundra, ice, and mountains. There the type of distribution appears to change from log-normal for tundra and ice to gamma for mountains for depression angles of 30° [20]. Of course, this same behavior might not be in evidence at X-band, so perhaps we should not expect any special distributional behavior for the up-, cross-, and down-wave data.

The X-band data distributions for a fixed-wave condition do, however, change their mean locations and their shapes (standard deviations) with change of incidence angle. The trend of the means with incidence angle is similar to the trend of the Bragg-Rice-Phillips theory.

¹ Shown in Fig. 21.

An examination of the effect of salinity and sea temperature at small and medium incidence angles, indicated that their effects upon sea-surface reflection coefficients seem to be insignificant, for either of the linear polarizations. At large incidence angles, i.e., near grazing, there is a more pronounced change in the behavior of the vertical polarization reflection coefficient. In fact, in the vicinity of 80° incidence, the ratio of the reflection coefficient for high temperature, high salinity to the reflection coefficient for low temperature, low salinity can take an excursion of as much as 20 dB.

REFERENCES

- [1] P. G. Teleki, R. A. Shuchman, W. E. Brown, Jr., W. McLeish, D. Ross, and M. Mattie, "Ocean wave detection and direction measurements and microwave radars," in *Oceans* (IEEE/MTS, Washington, DC), 1978.
- [2] D. Evans, "The relationship between ocean surface structure and the synthetic aperture radar imagery of ocean waves," in *Oceans* (IEEE/MTS, Los Angeles, CA), 1979.
- [3] R. Rawson, F. Smith, and R. Larson, "The ERIM X- and L-band data dual polarized radar," in *IEEE 1975 Int. Radar Conf.* (New York), p. 505, 1975.
- [4] W. M. Brown and L. J. Porcello, "An introduction to synthetic aperture radar," *IEEE Spectrum*, vol. 6, pp. 57-62, 1969.
- [5] R. O. Harger, *Synthetic Aperture Radar Systems*. New York: Academic Press, 1970.
- [6] O. H. Shemdin, W. E. Brown, Jr., F. G. Staudhammer, R. Shuchman, R. Rawson, J. Zelenka, D. B. Ross, W. McLeish, and R. A. Berles, "Comparison of in-situ and remotely sensed ocean waves off Marineland, Florida," *Boundary Layer Meteorol.*, vol. 13, pp. 225-234, 1978.
- [7] A. Kozma, E. N. Leith, and N. G. Massey, "Tilted plane optical processor," *Appl. Opt.*, vol. 11, p. 1766, 1972.
- [8] R. A. Shuchman and J. S. Zelenka, "Processing of ocean wave data from a synthetic aperture radar," *Boundary Layer Meteorol.*, vol. 13, 1978.
- [9] W. E. Brown, Jr., C. Elachi, and T. W. Thompson, "Radar imaging of ocean surface patterns," *J. Geophys. Res.*, vol. 81, no. 15, pp. 2657-2667, 1976.
- [10] P. Beckmann and A. Spizzichino, *The Scattering of Electromagnetic Waves from Rough Surfaces*. New York: McMillan, 1963.
- [11] J. W. Wright, "Backscattering from capillary waves with application to sea clutter," *IEEE Trans. Antennas Propagat.*, vol. AP-14, pp. 749-754, 1966.
- [12] O. M. Phillips, *The Dynamics of the Upper Ocean*. London, England: Cambridge Univ. Press, 1966.
- [13] M. I. Skolnik, "Sea echo," in M. I. Skolnik, Ed., *Radar Handbook*. New York: McGraw-Hill, 1970, ch. 26.
- [14] G. V. Trunk, "Non-Rayleigh sea clutter: Properties and detection of targets," *NRL Rep.* 7986, p. 81, 1976.
- [15] N. W. Guinard and J. C. Daley, "An experimental study of a sea clutter model," *Proc. IEEE*, vol. 58, no. 4, pp. 543-555, 1970.
- [16] R. K. Raney and R. A. Shuchman, "SAR mechanism for imaging waves," in *Proc. 5th Canadian Symp. on Remote Sensing*, (Victoria, BC), 1978.
- [17] J. P. Hollinger, "Microwave properties of a calm sea," *NRL Rep.* 7110-2, 1973.
- [18] J. Aitchison and J. A. C. Brown, *The Log-Normal Distribution*. London, England: Cambridge Univ. Press, 1957.
- [19] W. R. Alpers and C. L. Rufenach, "The effect of orbital motions on synthetic aperture radar imaging of ocean waves," *IEEE Trans. Antennas Propagat.*, vol. AP-27, pp. 685-690, 1979.
- [20] A. Maffett, H. Klimach, A. Liskow, R. Rawson, R. Heimiller, and P. Tomlinson, "L-band radar clutter statistics for terrain and ice," *ERIM Rep.* 128900-9-F, vol. 1 (Contract DAAK40-77-C-0012), 1978.

Section of Coastal Zone Environmental
Conditions Using Synthetic Aperture Radar*

by

R.A. Shuchman
E.S. Kasischke
G.A. Meadows

Radar and Optics Division
Environmental Research Institute of Michigan
Ann Arbor, Michigan

*Published in the 1981 International Geoscience and Remote Sensing
Symposium Digest, pp. 756-767.

DETECTION OF COASTAL ZONE ENVIRONMENTAL CONDITIONS USING SYNTHETIC APERTURE RADAR

R.A. Shuchman, E.S. Kasischke, and G.A. Meadows*
Radar and Optics Division
Environmental Research Institute of Michigan
Ann Arbor, Michigan 48107

ABSTRACT

This paper reviews the uses of synthetic aperture radar (SAR) data in monitoring oceanic phenomena and coastal region resources. SAR data collected by aircraft and satellite have been shown to be useful in the detection of ocean waves, surface currents and fronts, surf zone conditions, coastal marshland vegetation and ice. SARs have demonstrated the ability to monitor ocean gravity waves under a variety of sea states. For example, wave refraction was documented in the coastal regions near Cape Hatteras, North Carolina using Seasat SAR data. Various parameters of the surf zone can also be detected by a SAR. These parameters include: surf zone location, measurement of long-shore currents and detection of long-period "surf beats." Long-shore currents have been measured by utilizing Doppler shifts in the SAR signal history. In addition, SARs have recently demonstrated the ability to detect oceanic fronts and freshwater river discharges.

Two frequency X- and L-band SAR aircraft data were shown to be useful in discriminating marshland and the water/land boundary in a test site near Marineland Florida. Distribution and type of sea, lake, and river ice is also mappable using both aircraft and satellite SAR data, thus making SAR a useful tool for reconnaissance of nearshore environmental parameters regardless of geographic location, season, or climate.

Introduction

Considerable effort has been expended during the past decade exploring the potential of using an imaging synthetic aperture radar (SAR) to monitor the resources and physical phenomena of the world's oceans and coastal regions. This interest eventually resulted in the launch of the Seasat satellite which contained a SAR as one of its five instruments; and offered the oceanography community a vast quantity of data which, two years after its collection, is still being studied with great enthusiasm. In addition, numerous coastal remote sensing missions have been flown by aircraft SARs.

Synthetic aperture radar is an active imaging device that senses the environment with short electromagnetic waves. As active

*ERIM consultant, Assistant Professor, Department of Atmospheric and Oceanic Science, The University of Michigan, Ann Arbor, Michigan 48109.

sensors, radars provide their own illumination in the microwave region of the electromagnetic spectrum and thus are not affected by temporal changes in emitted or reflected radiation from the earth's surface. Additionally, SARs have the recognized advantage of being able to image the earth's surface independent of weather conditions and to provide synoptic views of the ocean at high resolution. The resolution of aircraft SARs are typically on the order of a few meters while the Seasat satellite SAR had a resolution of approximately 25 meters. Most radars operate in the frequency region of 300 MHz (1 m) to 30 GHz (1 cm), and bandwidths within this region are commonly designated by letters. SARs discussed in this paper are designated as L-band (23.5 cm) or X-band (3.2 cm).

Synthetic aperture radar is a coherent airborne or spaceborne radar that uses the motion of a moderately broad physical antenna beam to synthesize a very narrow beam thus providing fine azimuthal (along-track) resolution (Brown and Porcello, 1969; Harger, 1970). Fine range (cross-track) resolution is achieved by transmitting either very short pulses or longer coded pulses which are compressed by matched-filtering techniques into equivalent short pulses. Usually, the coded pulse is a waveform linearly modulated in frequency. The processing of SAR imaged signal histories into an image is described by Kozma, et al. (1972).

Two SAR systems will be discussed in this paper. The first system is an aircraft-borne X- and L-band, dual-polarized imaging radar operated by the Environmental Research Institute of Michigan (ERIM) and is described by Rawson, et al. (1975). The second system was the Seasat L-band imaging radar described by Jordon (1980).

This paper will review a variety of uses of synthetic aperture radar data for detecting coastal zone environment conditions. These include SAR detection of gravity waves, surface currents and fronts, surf zone conditions and coastal vegetation. Another paper in these proceedings (see Lyzenga, 1981) describes the potential of using a SAR to provide nearshore bathymetry information.

Detection of Ocean Waves

The main purpose of including a SAR in the Seasat instrument package was to image ocean gravity waves on a fine resolution ocean grid. Figure 1 includes a Seasat image of coastal gravity waves. Estimates of wave period and direction of the dominant gravity wave can be extracted from this SAR data. Techniques to do this include two-dimensional Fourier transforms (both optical and digital), a semi-causal technique, and a new one-step spectral estimation routine which extracts the wave period directly from the SAR signal histories.

By passing a monochromatic, collimated beam of light through the film image of the gravity waves imaged by the SAR, a two-dimensional optical Fourier transform (OFT) of the image is created (Shuchman, et al., 1977). If a digital image is made,

then the same process can be done on a computer by taking a fast Fourier transform (FFT) of data (Shuchman, et al., 1979). Producing a FFT has an advantage over an OFT in that distributional wave spectra, as a function of wave frequency or direction, can also be generated, not just dominant wavelength and direction as obtainable from an OFT. Figure 1 also presents an example of an OFT and FFT generated from the Seasat data.

Advanced data processing techniques for extracting gravity wave information from SAR data also include the use of a semi-causal model and a one-step spectral estimation routine. The semi-causal model is based on maximum entropy techniques and has recently been investigated for the extraction of gravity wavelength and directional data from SAR data (Jackson and Shuchman, 1981). The advantage of the semi-causal model is that it can produce essentially the same estimates as FFTs and OFTs using less SAR data (i.e., a smaller aperture). One-step spectral estimation is another advanced technique which may provide estimates of wavelength and direction through direct processing of raw SAR signal data without first forming an image of the waves (Hasselmann, 1980).

A comparison of estimates of gravity wavelength and direction generated from SAR data collected during the GOASEX (Gulf of Alaska Seasat Experiment) and JASIN (Joint Air-Sea Interaction) experiments were compared to conventional sea truth (i.e., pitch and roll buoy data). From these two experiments, it was verified that accurate wavelength and directional information of gravity wave fields can be obtained from the SAR (Gonzalez, et al., 1979; Kasischke, 1980; and Vesecky, et al., 1981). Linear correlations ($\alpha = 0.01$) between these SAR-derived and sea truth wave spectra estimates were 0.90 to 0.95 for wavelength and 0.90 for wave direction.

A study by Shuchman and Kasischke (1981) revealed that SAR imagery can be used to document refraction of gravity waves as they enter shallow coastal waters. Wave direction and length from the SAR compared favorably to wave direction and length computed from classical wave refraction techniques. Linear correlations ($\alpha = 0.01$) between SAR-derived and model-derived parameters were 0.76 for wavelength and 0.55 for wave direction. Recent investigations (Meadows, et al., 1981) indicate that the correlations can be improved significantly if the effect of the Gulf Stream in modifying the characteristics of gravity waves traversing this current are taken into account.

There are limitations in using a SAR to image gravity waves, but these limits have yet to be fully defined. An example is the recent JASIN experiment where the Seasat SAR successfully imaged gravity waves on thirteen out of a possible eighteen opportunities (Vesecky, et al., 1981). A study of the associated sea truth data on those occasions when the Seasat failed to image gravity waves revealed that one of two conditions were present: (1) the waves had a very low significant wave height ($H_{1/3} < 1.3$ m); or (2) the waves were traveling in nearly an azimuth

direction with respect to the radar line of sight. Kasischke and Shuchman (1981) found a significant linear correlation between wave contrast (or wave detectability) on the SAR data and wave height. Earlier studies by Teleki, et al. (1978) revealed that on X-band SAR data (collected by an aircraft mounted SAR) gravity waves were clearly more visible when the waves were traveling in a range direction with respect to the radar line of sight.

Surface Currents and Frontal Boundary Detection

SARs have recently been demonstrated to have the capability to detect surface currents and ocean frontal boundaries. The sensing of surface currents with SAR has been through one of three techniques. The first technique reported by Shuchman et al. (1979a) and Gonzalez, et al. (1981) utilizes a measurement of motion-induced Doppler perturbation in the SAR signal history. The technique has been successfully tested on aircraft SAR data collected near Vancouver Island as well as along the Lake Michigan shoreline. This technique takes advantage of the fact that the SAR instrument responds primarily to backscatter from capillary waves which, in conventional SAR processing, are assumed stationary with respect to other time scales of the radar system. However, these scatterers are not stationary; they move with a characteristic phase velocity as well as with velocities due to the presence of currents and longer gravity waves. The radial (line of sight) component of this resultant velocity produces a Doppler shift in the temporal frequency of the return signal, which translates to a spatial frequency shift recorded on SAR signal film.

Shuchman, et al. (1979) showed that the radial component of a target velocity (V_r) could be calculated as:

$$V_r = \frac{\Delta f' \lambda V_{AC}}{2P} \quad (1)$$

where $\Delta f'$ is the azimuth spatial frequency shift, λ is the transmitted radar wavelength, V_{AC} is the platform velocity and P is the azimuth packing factor.

This relationship can be used to measure the average radial velocity component of an ocean-wave scattering field relative to a fixed-land scattering field. A shift in the azimuth spatial frequency spectrum between fixed-land and moving-ocean surfaces yields an estimate for $\Delta f'$. Variations in spectrum location due to antenna pointing may be eliminated by choosing imagery having land and ocean imaged simultaneously.

A second technique to measure currents via SAR data is reported by Shemdin et al. (1980). This technique applied to Seasat data collected over the mouth of the Columbia River (Oregon) measured the azimuthal shift in the boundary of the current as it flowed past the jetties. Using the relationship:

$$\Delta X = \frac{V_r}{V_{AC}} R \quad (2)$$

where ΔX is the azimuthal displacement, R the range to the target and V_{AC} the platform velocity, the radial line of sight velocity (V_r) of the Columbia River was successfully estimated.

A third technique to measure currents from SAR data is summarized by Hayes and Shuchman (1981), who showed it was possible to calculate the magnitude and direction of the Gulf Stream by observing gravity wave refraction across the stream.

Recently SARs have shown the ability to detect oceanic fronts and freshwater discharge. An experiment to study SAR's ability to monitor ocean fronts was conducted in October of 1980. The frontal boundary of the two water masses at the mouth of Chesapeake Bay are clearly discernible on Figure 2. This SAR data was collected by the UPD-4 X-band SAR operated by the U.S. Marines. The proposed mechanism for imaging the frontal features is due to a strong current shear modulating the ocean Bragg waves (Wright, 1966) that the radar observes.

Seasat imagery has been used to locate major ocean current boundaries. Hayes (1981) used Seasat imagery to map the northern edge of the Gulf Stream off the eastern U.S. coast. Cheney (1981) tentatively identified the boundary of a cold water ring in the Sargasso Sea using Seasat imagery. Additionally, Lichy, et al. (1981) used Seasat imagery to map warm water rings associated with the Gulf Stream.

Observation of Surf Zone Conditions

Both aircraft and satellite SAR systems have demonstrated an ability to detect various environmental parameters pertaining to the surf zone. These parameters include: (1) location of the breaking waves, (2) location of the land/water boundary, (3) measurement of the dominant gravity wave, (4) measurement of long-shore currents, and (5) detection of long-period surf beats.

A SAR-sea truth comparison reported by Shuchman and Meadows (1980) and Meadows, et al. (1981) indicated:

1. SAR-derived wavelengths and directions are in good agreement with sea truth,
2. SAR directional spectra taken in various water depths do correlate with predicted wave refraction,
3. The breaker zone as defined by shore observers corresponds to the bright lines found on the SAR imagery,
4. Longshore current direction and relative magnitude as obtainable from the SAR Doppler history are in reasonable agreement with sea truth, and
5. Low-frequency components observed on SAR spectra seem to correlate with low frequency "surf beat" found in sea truth spectral estimates.

Marshland Detection

Figure 3 shows four-channel ERIM SAR imagery of the Marine-land test site. The test site was subjected to tidal inundation and therefore primarily composed of tidal marshland. The letter A on Figure 3 indicates the high water mark as well as a relic coastline. Area B represents forest land located on high ground (i.e., not subject to inundation), while region C is an inundated area that is composed of marsh vegetation. Note the differential return between the marsh area (C) on the X and L-band data. The marshland surrounding the river (D) is also clearly discernible using the X- and L-band data.

The explanation for this differential return is that the X-band radar energy reflects off the tops of the marsh grass, while the longer L-band incident energy penetrates through the vegetation and the L-band return is primarily a specular return from the water. Shuchman and Lowry (1977) used this data set to perform a digital vegetation classification using the four-channel SAR data. The result of that analysis indicated the simple parallel-epiped classification (operator interactive) corresponded well to the ground truth available. The study further demonstrated the need to develop more sophisticated digital classification procedures which utilize not only tonal information from the radar, but also texture information.

Summary

This paper has reviewed the potential uses of synthetic aperture radar (SAR) data to monitor ocean phenomena and coastal region resources. SAR data collected by aircraft and satellites have been shown to be useful in the detection of ocean waves, surface currents and fronts, surf zone conditions, coastal marshland vegetation and ice.

This paper has not specifically addressed the question of detection of sea, lake, and river ice with SAR; however, much research has been done in this area (Ketchum and Tooma, 1973; Larson, et al., 1978, 1981) and there is general agreement in the community that high resolution aircraft or satellite SAR operating at an X-band frequency can detect first year, multi-year, and open water areas.

It should be mentioned when utilizing SAR data such as presented in this paper, the SAR spectral estimates discussed are wave number-directional spectra of the radar return intensity. The data does not represent wave height information, at least not in a recognizable form. The modulation transfer function (i.e., the SAR gravity wave imaging mechanism) is not totally understood at the present time. The determination of the transfer function as well as determination of wave height using SAR data will be a major scientific advance. At that time, it will then be possible to use SAR gravity wave data to obtain power density estimates of the sea surface.

The Doppler current measurements discussed are still experimental and the reader is warned that this technique to measure current is far from operational and perhaps a new SAR system will have to be designed to realize this type of measurement. Recall that the Doppler method works only in the radial (line of sight) direction.

The marshland discussions demonstrate the need for development of machine aided analysis techniques and indicate the advantage of a multi-frequency SAR approach.

Acknowledgements

The ERIM analysis was supported by the Office of Naval Research (ONR) Contract N00014-76-C-1048. The technical monitor for this ONR contract is Mr. Hans Dolezalek. Part of the work summarized in this paper was supported by the National Oceanic and Atmospheric Association (NOAA) and the National Aeronautics and Space Administration (NASA) as part of the Seasat Announcement of Opportunity Program under Contract No. MO-A01-78-00-4339. The technical monitors were John W. Sherman III and Patrick DeLeonibus of NOAA.

References

- Brown, W.J. and L. Porcello, An Introduction to Synthetic Aperture Radar, IEEE Spectrum, 6, pp. 52-66, 1969.
- Cheney, R.E., A Search for Cold Water Rings with Seasat, in Spaceborne Synthetic Aperture Radar for Oceanography, ed. by R.C. Beal, P.S. DeLeonibus and I. Katz, Johns Hopkins Univ. Press (in Press), 1981.
- Gonzalez, F.I., R.C. Beal, W.E. Brown, P.S. DeLeonibus, J.W. Sherman, J.F.R. Gower, D. Lichy, D.B. Ross, C.L. Rufenach, and R.A. Shuchman, Seasat Synthetic Aperture Radar: Ocean Wave Detection Capabilities, Science, 204, pp. 1418-1421, 1979.
- Gonzalez, F.I., C.L. Rufenach, and R.A. Shuchman, Surface Current Detection Using SAR Data, Proceedings of the COSPAR/SCOR/IUCRM Symposium on Oceanography from Space, 1981.
- Harger, R.O., Synthetic Aperture Radar Systems, Academic Press, New York, NY, 240 pp., 1970.
- Hasselmann, K., A Simple Algorithm for the Direct Extraction of the Two-Dimensional Surface Image Spectrum from Return Signal of a Synthetic Aperture Radar, Int. J. Rem. Sens. (in Press), 1980.
- Hayes, R.M., SAR Detection of the Gulf Stream, in Spaceborne Synthetic Aperture Radar for Oceanography, ed. by R.C. Beal, P.S. DeLeonibus and I. Katz, Johns Hopkins Univ. Press (in Press), 1981.
- Hayes, J.G. and R.A. Shuchman, Seasat SAR Ocean Surface Current and Shallow Water Wave Refraction, Proceedings of the COSPAR/SCOR/IUCRM Symposium on Oceanography from Space (in Press), 1981.

Jackson, P.L. and R.A. Shuchman, A New High Resolution Two-Dimensional Spectral Estimation Technique for SAR Ocean Wave Analysis, submitted to J. Geophys Res., 1981.

Jordan, R.L., The Seasat-A Synthetic Aperture Radar System, IEEE J. Oceanic Eng., Vol. OE-5, pp. 154-164, 1980.

Kasischke, E.S., Extraction of Gravity Wave Information from Synthetic Aperture Radar Data, Univ. of Mich. M.S. Thesis, 108 pp., 1980.

Kasischke, E.S. and R.A. Shuchman, Comparisons of Wave Contrast Measurements Made from SAR Data with Selected Oceanographic Parameters, Proceedings of the Symposium on Wave Dynamics and Radio Probing of the Ocean Surface, Miami, Florida (in Press), 1981.

Ketchum, R.D. and S.G. Tooma, "Analysis and Interpretation of Airborne Multi-Frequency Side-Looking Radar Sea Ice Imagery," J. of Geophys. Res., Vol. 78, No. 3; pp. 520-538, 1973.

Kozma, A., E.N. Leith, and N.G. Massey, Tilted Plane Optical Processor, Applied Optics, 11, p. 1766, 1972.

Larson, R.W., R.A. Shuchman, R.F. Rawson, and W.D. Worsfold, The Use of SAR Systems for Iceberg Detection and Characterization, Proceedings of the Twelfth International Symposium on Remote Sensing of Environment, Ann Arbor, MI, pp. 1127-1147, 1978.

Larson, R.W., J.D. Lyden, and R.A. Shuchman, An Analysis of Four-Synthetic Aperture Radar Data of Sea Ice, presented at the Symposium on Signature Problems in Microwave Remote Sensing, Lawrence City, Kansas, 1981.

Lichy, D.E., M.G. Mattie, and L.J. Mancini, Tracking of a Warm Water Ring Using Synthetic Aperture Radar, in Spaceborne Synthetic Aperture Radar Imagery for Oceanography, ed. by R.C. Beal, P.S. DeLeonibus, and I. Katz, Johns Hopkins Univ. Press (in Press), 1981.

Lyzenga, D.L., Remote Bathymetry Using Active and Passive Techniques, Proceedings of the International Geoscience and Remote Sensing Symposium, Washington, D.C. (in Press), 1981.

Meadows, G.A., E.S. Kasischke, and R.A. Shuchman, SAR Observations of Coastal Zone Conditions, Proceedings of the Fourteenth International Symposium on Remote Sensing of Environment, Ann Arbor, MI., pp. 845-863, 1980.

Meadows, G.A., R.A. Shuchman, E.S. Kasischke, and J.D. Lyden, The Observation of Gravity Wave-Current Interactions Using Seasat Synthetic Aperture Radar Data, submitted to J. Geophys. Res., 1981.

Meadows, G.A., R.A. Shuchman, and J.D. Lyden, Analysis of Remotely Sensed Long-Period Waves, Submitted to J. Geophys. Res., 1981.

Rawson, R.F., F. Smith, and R. Larson, The ERIM Simultaneous X- and L-Band Dual Polarized Radar, IEEE 1975 Radar Conference, p. 505, 1975.

Shemdin, O.H., A. Jain, S.V. Hsiao and L.W. Gatto, Inlet Current Measured with Seasat-1 Synthetic Aperture Radar, Shore and Beach, Vol. 48, pp. 35-9, 1980.

Shuchman, R.A. and R.T. Lowry, Vegetation Classification with Digital X-Band and L-Band Dual Polarized SAR Imagery, Proceedings of the Fourth Canadian Symposium on Remote Sensing, Quebec City, pp. 444-459, 1977.

Shuchman, R.A., P.L. Jackson, and G.B. Feldkamp, Problems of Imaging Ocean Waves with Synthetic Aperture Radar, ERIM Interim Technical Report No. 124300-1-T, Ann Arbor, MI, 11 pp., 1977.

Shuchman, R.A., E.S. Kasischke, A. Klooster, and P.L. Jackson, SAR Coastal Ocean Wave Analysis - A Wave Refraction and Diffraction Study, ERIM Final Report No. 138600-2-F, Ann Arbor, MI, 1979.

Shuchman, R.A., C.L. Rufenach, and F.I. Gonzalez, The Feasibility of Measurement of Ocean Surface Currents Using Synthetic Aperture Radar, Proceedings of the Thirteenth International Symposium on Remote Sensing of Environment, Ann Arbor, MI, pp. 93-102, 1979a.

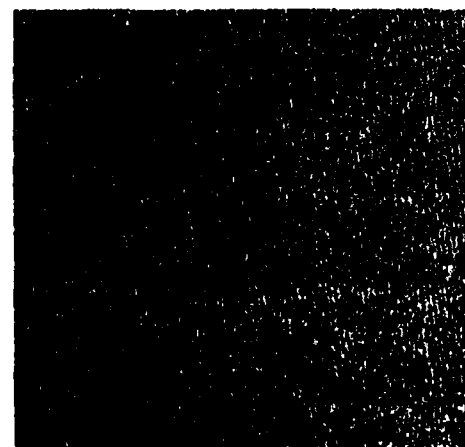
Shuchman, R.A. and G.A. Meadows, Airborne Synthetic Aperture Radar Observations of Surf Zone Conditions, Geophysical Research Letters, Vol. 7, pp. 857-860, 1980.

Shuchman, R.A. and E.S. Kasischke, Refraction of Coastal Ocean Waves as Observed from the Seasat Aperture Radar, in Spaceborne Synthetic Aperture Radar for Oceanography, ed. by R.C. Beal, P.S. DeLeonibus and I. Katz, Johns Hopkins Univ. Press (in Press), 1981.

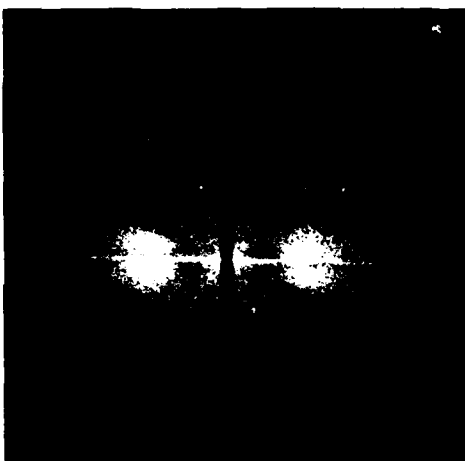
Teleki, P.G., R.A. Shuchman, W.E. Brown, Jr., W. McLeish, D. Ross, and M. Mattie, Ocean Wave Detection and Direction Measurements with Microwave Radars, Oceans '78, IEEE/MTS, pp. 639-648, 1978.

Veseky, J.F., H.M. Assal, R.H. Stewart, R.A. Shuchman, E.S. Kasischke and J.D. Lyden, On the Ability of Synthetic Aperture Radar to Measure Ocean Waves, Proceedings of the Symposium on Wave Dynamics and Radio Probing of the Ocean Surface, Miami, Florida (in Press), 1981.

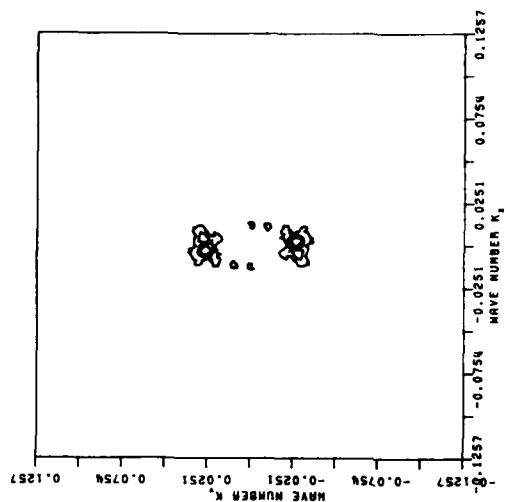
Wright, J.W., Backscattering from Capillary Waves with Application to Sea Clutter, IEEE Trans. Antenna Propag., Vol. AP-14, pp. 749-754, 1966.



a) SAR Image



b) Optical Fourier Transform



c) Fast Fourier Transform

Figure 1. Seasat SAR Image of Ocean Gravity Waves and their Resultant Two-Dimensional Fourier Transforms (Seasat Rev. 762, 19 August 1978).

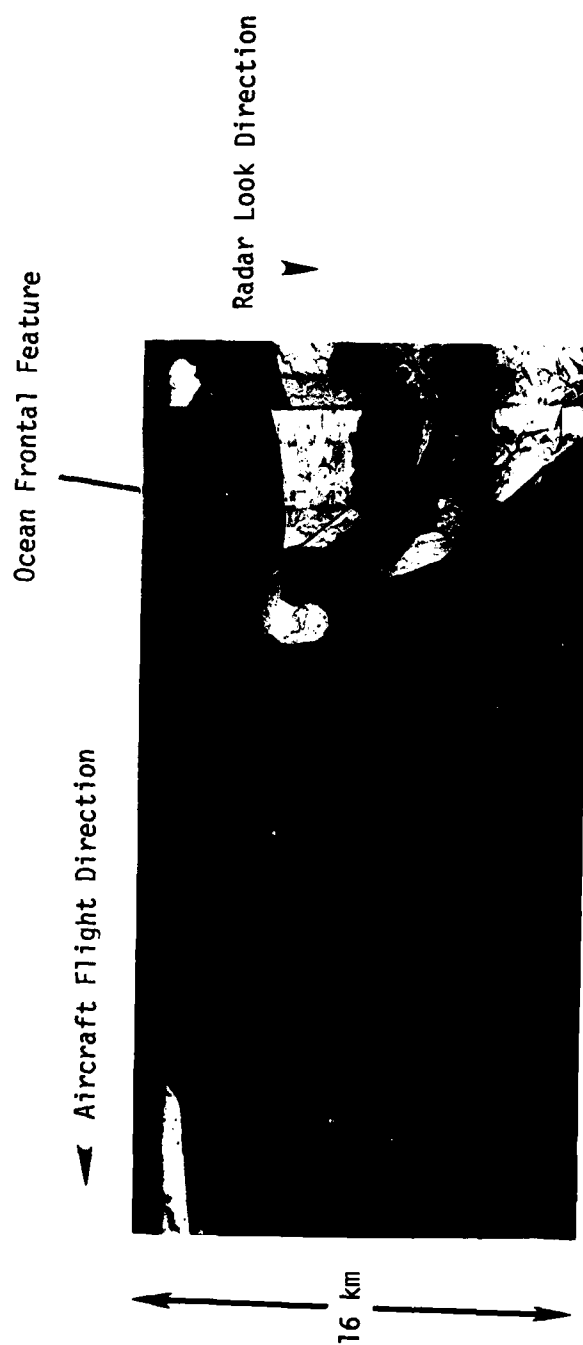


Figure 2. SAR Image (X-Band) of Mouth of Chesapeake Bay Illustrating Ocean Frontal Type Features (10 October 1980).

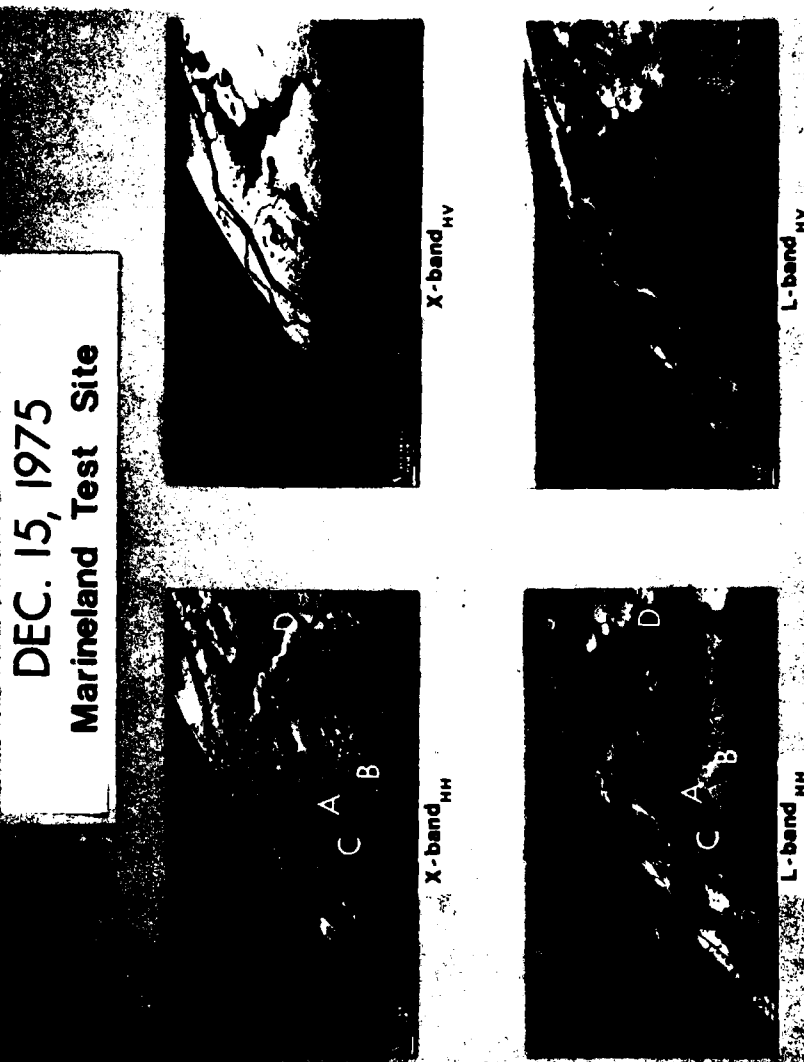


Figure 3. Four Channel SAR Imagery of Atlantic Coastal Zone at Marineland, Florida (15 December 1975).

THE USE OF SYNTHETIC APERTURE RADAR (SAR) TO MEASURE OCEAN GRAVITY WAVES

R.A. Shuchman
E.S. Kasischke
J.D. Lyden
G.A. Meadows*

Radar and Optics Division
Environmental Research Institute of Michigan
Ann Arbor, Michigan 48107

Abstract

This paper reviews the use of synthetic aperture radar (SAR) to detect water gravity waves. SAR data collected by aircraft and satellite have been shown to be capable of measuring gravity water waves under a variety of sea states. For example, wave refraction was successfully documented in the coastal regions near Cape Hatteras, North Carolina using SEASAT SAR satellite data. SAR has also been shown to be capable of detecting internal gravity waves and long period "surf beats." Several parameters determine the visibility of gravity waves on SAR images, including the radar wavelength and polarization, radar incident angle, and radar look direction (relative to the wave propagation direction), as well as the ocean wavelength, wave height, wind speed and direction. In general, waves traveling towards or away from the SAR line of sight are better imaged than waves traveling in a direction perpendicular to the SAR line of sight.

1. INTRODUCTION

Considerable research has been performed during the past decade exploring the utility of synthetic aperture radar (SAR) to detect

*ERIM Consultant, Assistant Professor, Department of Atmospheric and Oceanic Science, University of Michigan 48109.

gravity waves on the oceans and Great Lakes. The purpose of this paper is to review this research and identify areas where additional study efforts are needed.

Synthetic aperture radar (SAR) is a coherent airborne (or space-borne) radar that uses the motion of a moderately broad physical antenna beam to synthesize a very narrow beam, thus providing fine azimuthal (along-track) resolution (Brown and Porcello, 1969; Harger, 1970). Fine range (cross-track) resolution is achieved by transmitting either very short pulses or longer coded pulses which are compressed by matched-filtering techniques into equivalent short pulses. Usually, the coded pulse is a waveform linearly modulated in frequency.

The phase history of a scattering point in the scene is either recorded on photographic film as an anamorphic (astigmatic) Fresnel zone plate or on digital tapes. The parameters of the phase histories are set in the azimuth direction by the Doppler frequencies produced by the relative motion between the sensor and the point scatterer, and in the range direction by the structure of the transmitted pulses. The optical SAR phase history is a collection of superimposed zone plates representing the collection of point scatterers in the scene. SAR optical processing is described by Kozma, et al. (1972) while digital processing techniques are reviewed by Ausherman (1980).

The principle in imaging any surface with a radar is that the backscatter of microwave energy (echo) received by the radar receiver contains mainly information on the roughness characteristics (shapes, dimensions, and orientations) of the reflecting area. The parameters that influence the echo received from ocean waves include the motion of the scattering surfaces, the so-called speckle effect, system resolution and non-coherent integration as well as contributions attributable to wind, waves, surface currents and surface tension.

Also, the orientation of ocean waves to the radar look direction must be considered. When attempting to understand the SAR ocean-wave imaging mechanism, one must also consider factors pertaining to wave orbital velocity, Bragg-scatterer velocity, and long (or resolvable) wave phase velocity (Teleki, et al., 1978).

This review paper discusses the use of both aircraft and space-borne synthetic aperture radar. The aircraft data to be presented were collected by the ERIM X-L SAR flown in an ERIM owned C-46 and presently installed in the Canada Centre for Remote Sensing (CCRS) CV-580 aircraft. This X-L system, described by Rawson, et al. (1975), consists of a dual-wavelength and dual-polarization synthetic aperture radar that simultaneously images at X-band (3.2 cm) and L-band (23.5 cm). Alternate X- and L-band pulses (chosen to be either horizontally or vertically polarized) are transmitted, and reflections of both polarizations received; thus, four channels of radar imagery are simultaneously obtained. Both polarizations of X-band are recorded on one film, while both polarizations of L-band on another.

The data presented in this paper were obtained from the horizontal-transmit, horizontal-receive channel (HH) of both the X- and L-band receivers. Polarization effects have not been analyzed. The polarization of the electromagnetic radiation is defined by the direction of the electric field intensity, E, vector. For example, a horizontally polarized wave will have its E vector parallel to the local horizon. The resolution of the ERIM aircraft SAR system is approximately 3 m in range and azimuth. The swath width of the X-L system is approximately 6 km.

Two other aircraft SAR systems routinely collect ocean gravity wave information. The first is an X-band military system (UPD-4) flown in an F4. This Goodyear built system has similar characteristics to the X-band part of the ERIM SAR system, except the swath

width is 16 km. The Jet Propulsion Laboratory (JPL) also operates an L-band SAR for gravity wave detection (Shemdin, 1980 and 1980a). This system has a resolution of approximately 15 m and has 10 km swath capability.

A spaceborne SAR system specifically designed to image water gravity waves was launched in June of 1978 as part of the NASA SEASAT* satellite (Jordan, 1980). This SAR operated at L-band with a ground resolution of 25 x 25 m. The SEASAT SAR imagery had a swath width of 100 km and data lengths up to a few thousand kilometers long.

2. THEORY

Although the SAR wave imaging mechanism is not completely understood, several theories have been proposed that appear to adequately explain the modulation of the radar backscatter, which leads to the wave-like patterns we observe on SAR images.

The first and most widely accepted theory was proposed by Wright (1966) and is founded on Bragg scattering. Bragg scattering is basically a resonant reflection from surface ocean waves of wave number:

$$K_w = 2K_R \sin \theta, \quad (1)$$

where $K_w = 2\pi/L$ and $K_R = 2\pi/\lambda$ are the wave numbers; L and λ the wavelengths, respectively of the ocean wave and the radar; and θ is the incident angle. For the X- (3.2 cm) and L-band (23.5 cm) SAR considered in this study, with a nominal incidence angle of 45° . Eq. (1) leads to Bragg water waves of 2 and 17 cm (for the X- and L-bands respectively). These correspond to the capillary and

*The entire SEASAT satellite system unfortunately suffered a catastrophic power loss approximately 100 days after launch.

ultra-gravity wavelength regions which are typically abundant in the presence of low to moderate strength wind fields.

It has been suggested by Phillips (1981) and several others that the short capillary and ultra-gravity waves are modulated by the longer gravity waves. Phillips suggests that the gravity waves cause a compression of the small waves and an increase in their height in the crest region of the gravity wave and a height decrease and elongation of the shorter waves in the trough region. This compression and expansion is thought to result from the straining of the shorter waves by the orbital velocity of the gravity wave (Wright, et al., 1980; Alpers and Rufenach, 1979).

From a SAR standpoint, the greater the compression/expansion of these small wave structures, the higher the contrast on the SAR imagery. This results from the fact that this compression/expansion would cause certain portions of the long wave to contain a higher amplitude of Bragg (resonant) scatterers than at other parts of the wave. This would lead to an image modulation that should closely correspond to the prevalent gravity wave field.

Other theories that attempt to describe the SAR imaging mechanism of waves include: accounting for the change of the local tilt angle due to the waves, a composite theory which accounts for both the local tilt of the surface as well as for Bragg scattering, and a theory which is dependent upon the orbital velocity of the ocean waves (Elachi and Brown, 1977). This last theory, which indicates the radial velocity produced by the orbital component of the gravity wave produces a periodic azimuthal target displacement, has caused much controversy.

As a result of this controversy, various new theories have been formulated that discuss the dependence of the SAR image on water wave velocity and theoretically describe the SAR ocean image formation process (Raney and Shuchman, 1978; Alpers and Rufenach, 1979; Harger,

1981; Valenzuela, 1980; Jain, 1978; and Shuchman, 1981). The following paragraphs, as reported by Shuchman (1981), summarize the effect of wave motion on SAR images.

When using a SAR system to image moving targets such as ocean waves, unique problems occur when correlating the signal data. Because moving targets perturb the Doppler frequencies, and hence the phase histories recorded by the signal receiver, conventional processing of these signal histories produces images of the waves that are defocused relative to a stationary target. Defocusing by the along-track (azimuth) velocity of the moving ocean waves can be refocused by readjusting the azimuth focus (cylindrical focus) an amount proportional to the relative velocity of the wave train with respect to the SAR platform velocity.

Similarly, the radial motion of a moving ocean wave imaged by a SAR will also perturb the signal history of a scatterer. Radial wave velocity (motion towards or away from the radar look direction) produces an apparent tilt to the phase history as well as azimuthal shift in the image. Essentially, the scatterer history shifts across the signal record. This is referred to as "range walk" and can be compensated for by a rotation of the cylindrical optics in the processing of the signal histories. The azimuthal image shift is not correctable.

A number of investigators (Shuchman, 1981; Shuchman et al., 1979; Jain, 1978; and Shuchman and Zelenka, 1978) designed and evaluated algorithms to enhance through focusing, (i.e., accounting for water wave motion) SAR imaged gravity waves. The above mentioned investigations generally agree that detectability of azimuth and range traveling waves can be improved by respective adjustment of focal distance and rotation of the cylindrical telescope in the SAR processor. Enhancement of ocean waves as described above has been successfully employed on both Jet Propulsion Laboratory (JPL) L-band

and ERIM X- and L-band data (Jain, 1978; Kasischke, et al., 1979). The importance of this defocusing effect, due to azimuth and range wave motion, is twofold. First this effect can be used to determine the direction of ocean wave propagation. Second, it can be used as a rough estimator of the phase velocity associated with these waves. The focusing effects described above are more discernible using L-band data rather than X-band. Consequently, the X-band is less useful in providing information on wave direction and phase velocity.

3. ANALYSIS TECHNIQUES TO EXTRACT GRAVITY WAVE INFORMATION FROM SAR DATA

It should be noted that SAR spectral estimates of water gravity waves are wave number-directional spectra of the radar return intensity. The data does not represent wave height information, at least not in a recognizable form. The modulation transfer function (i.e., SAR gravity wave imaging mechanism) is not totally understood at the present time. The determination of this transfer function, as well as determination of wave height using SAR data, will be a major scientific advancement. At that time, it would be possible to use SAR gravity wave data to obtain power density estimates of the sea surface.

There are four recognized techniques to extract from SAR data estimates of wave period and direction of the dominant gravity wave. These include two-dimensional Fourier transforms (both optical and digital), a semi-causal technique, and a new one-step spectral estimation routine which extracts the wave period directly from the SAR signal histories.

By passing a monochromatic, collimated beam of light through the film image of the gravity waves imaged by the SAR, a two-dimensional optical Fourier transform (OFT) of the image is created (Barber, 1949; Shuchman, et al., 1977). If a digital image is made, the same process can be accomplished on a computer by taking a fast Fourier

transform (FFT) of the data (Shuchman, et al., 1979). Producing a FFT has an advantage over an OFT in that distributional wave spectra, as a function of wave frequency or direction, can also be generated, not just dominant wavelength and direction as obtained from an OFT. Figure 1 presents an example of actual SEASAT SAR wave images and the resulting OFT and FFT generated from this data.

A new two-dimensional spectral estimation algorithm related to maximum entropy, called the semicausal model (Jain and Ranganath, 1978) has been applied to synthetic aperture radar (SAR) imagery of ocean waves (Jackson and Shuchman, 1981). These semicausal spectral estimations were compared to FFT estimates of identical data sets and reference functions. Results indicate the semicausal model can successfully produce spectral estimates of truncated data sets (i.e., 1-2 wave cycles). However, similar to the one dimensional maximum entropy, the two-dimensional semicausal model is sensitive to the autoregressive order, to noise, and exhibits spectral splitting in some cases.

A new technique has been proposed by Hasselmann (1980) to extract spectral wave information from SAR. Hasselmann has derived a simple method for the determination of the two-dimensional surface image spectrum from the return signal of a SAR without explicitly forming an image. This algorithm called a signal-image-Fourier transform (SIFT) has recently been programmed on ERIM computers and is undergoing testing and evaluation using SEASAT SAR data.

4. SAR VERSUS SEA TRUTH SPECTRAL COMPARISONS

During the past seven years a series of experiments whose purpose was to demonstrate that SAR data can be used to determine gravity wavelength and direction has been conducted. The experiments include: Marineland, West Coast; DUCKEX; GOASEX; JASIN; MARSEN; and ARSLOE. (These experiments are described in detail by Shemdin, 1980;

Shemdin 1980a; Mattie, et al., 1980; Gonzalez, et al., 1981; Allan and Guymer, 1980; Anonymous, 1980; and Baer, 1980, respectively.) Figure 2 (after Vesecky and Stewart, 1981) is a scatterplot of ocean wavelength information obtained from the SEASAT SAR compared to in situ (pitch and roll bouy) ocean wavelength sea truth. Figure 3 (after Vesecky and Stewart, 1981) is the direction of wave propagation obtained from the SEASAT SAR and again compared to sea truth. Based on this data, SEASAT SAR estimates of wavelengths are biased slightly high and the average error is ~12 percent. For wave direction, there appears to be no significant bias and the average error is ~15 degrees. To summarize, the SEASAT SAR wave analysis indicates dominant wavelength and direction can be measured by the SEASAT SAR provided the waves in question are evident in the SAR image (Vesecky, et al., 1981). Note directional wave information provided by a SAR has an 180° ambiguity. Selective Doppler processing, as reported earlier (Shuchman and Zelenka, 1978) can resolve this 180° ambiguity. The data included in Figures 2 and 3 represent significant wave heights in the 1-5 m range. Ocean wavelengths shorter than 100 m in length were not observed by the SEASAT SAR. The wind speed for all the above observations exceeded 3 m/s..

Figures 4-7 are scatterplots of aircraft SAR derived estimates of wavelength and direction versus sea truth for X- and L-band data of Marineland, GOASEX (aircraft), and Lake Michigan. These results indicate wavelength information does not appear biased and is accurate to ~13 percent, while directional information is also not biased and accurate to within ~10 degrees.

5. WAVE REFRACTION AND LONG PERIOD GRAVITY WAVE DETERMINATION

Recently completed work by Shuchman and Kasischke (1981) has revealed that SEASAT SAR imagery can be used to document refraction of gravity waves as they enter shallow coastal waters near Cape Hatteras, N. Carolina. Wave direction and length from the SAR

compared favorably to wave direction and length computed from classical wave refraction techniques. Linear correlations between SAR-derived and model-derived parameters were 0.76 for wavelength and 0.55 for wave direction (significant at $p = 0.99$). Recent investigations (Meadows, et al., 1981) indicate that the correlations can be improved significantly if the effect of the Gulf Stream in modifying the characteristics of gravity waves traversing this current are taken into account.

Additional studies by Schwab, et al. (1981) and Shuchman and Meadows (1980) have shown that aircraft generated SAR directional spectra taken in decreasing water depths off the Lake Michigan shoreline do correlate with predicted wave refraction.

SAR data has also been demonstrated to be capable of discriminating long period internal waves off the coast of southern California (Apel, 1981) as well as in every major ocean basin imaged by SEASAT. Recent work by Meadows, et al. (1981a), has demonstrated the ability of SAR X-band data to successfully image low amplitude long period signals. The signals appear to correspond to a "surf beat" generated by the incident wind wave field.

6. LIMITATIONS OF SAR IN DETECTING GRAVITY WAVES

There are limitations in using a SAR to image gravity waves, but these limits are still in the definition stage. An example is the recent JASIN experiment where the SEASAT SAR successfully imaged gravity waves on thirteen out of a possible eighteen opportunities (Vesecky, et al., 1981). A study of the associated sea truth data on those occasions when the SEASAT failed to image gravity waves revealed that one of two conditions were present: (1) the waves had a very low significant wave height ($H_{1/3} < 1.3$ m); or (2) the waves were traveling in nearly an azimuth direction with respect to the radar line of sight. Additionally the wind speed and direction with

respect to the gravity wave appears to be a factor. Kasischke and Shuchman (1981) found a significant linear correlation between wave contrast (or wave detectability) on the SAR data and wave height. Earlier studies by Teleki, et al. (1978) revealed that on X-band SAR data (collected by an aircraft mounted SAR) gravity waves were clearly more visible when the waves were traveling in a range direction with respect to the radar line of sight.

Work has also been done on determining the sensitivity of various radar parameters on the ability to discriminate gravity waves. The important radar parameters include the radar wavelength, the SAR platform velocity, the radar look direction, polarization, and incident angle. Teleki, et al. (1978), using Marineland data, indicated that optimum wave images result when the radar is looking essentially up-wave or down-wave; that is, when waves propagate towards or away from the aircraft in the range direction. Figure 8 (after Teleki, et al., 1978) is a graph of modulation (wave crest to trough contrast) versus radar look direction for X- and L-band SAR aircraft data collected from Marineland. Note from Figure 8 that when the SAR is looking up-wave or down-wave (i.e., SAR line of sight perpendicular to the wave crests), higher contrast or more visible waves result. It should be noted that the significant wave height was approximately 1.2 m for the 8-second swell presented in Figure 8. Range traveling waves are more clearly discernable on SAR imagery because, in the range direction, the SAR uses a train of very short pulses. Therefore, waves traveling in range appear quasi-stationary relative to the sampling time. Differences in modulation depth of range traveling waves (Figure 8) also indicate that better quality wave images can be generated with X-band (HH) than with L-band (HH) radar. Consequently, wave spectral peaks derived from X-band images can usually be more accurately defined than those from L-band.

A possible explanation for the higher quality of X-band imagery was given by Shuchman and Zelenka (1978) who suggested that X-band

data have a larger depth of focus than L-band, and therefore the waves moving in the azimuth direction are not appreciably defocused as commonly occurs on L-band images of comparable resolution. The X-band also incorporates a shorter synthetic-aperture length or integration time than L-band, hence reducing motion errors.

A further X- and L-band comparison is given in Figure 9. Figure 9 represents a two-dimensional fast Fourier transform (FFT) of simultaneously obtained X- and L-band SAR data from GOASEX. The data, all collected within 30 minutes, represents a 10.2-second swell with a 2.5 m significant wave height. Note from the figure that for this higher wave height and longer ocean wavelength, SAR imaging of the gravity waves is less sensitive to frequency and radar look direction (compared to the Marineland data). Figure 10 represents one-dimensional direction distributions (180°) of the relative magnitude of energy at the dominant wavenumber of the data presented in Figure 9. Also plotted are the wavenumbers immediately above and below this peak/value. Figure 10 indicates there is no significant change in the directional spectral width of the six SAR-derived ocean spectra.

7. SUMMARY AND RECOMMENDATIONS

This paper has presented evidence that both aircraft and space-borne SARs have the capability to detect gravity wavelength and direction. It should be mentioned when utilizing SAR data such as presented in this paper that the spectral estimates presented are wave number and directional spectra of the radar return intensity. The data do not represent wave height information in a direct sense. SAR intensities (i.e., crest to trough modulation) have been successfully correlated to wave heights, but the exact mathematical modulation transfer function (i.e., SAR gravity wave imaging mechanism) is not totally understood at the present time. Obviously, a mathematical expression describing the SAR imaging needs to be developed.

In general, when ocean waves are visible on the SAR imagery, they represent the dominant wavelength and direction that the in situ sea truth indicates. The accuracy of the SAR estimate of dominant wavelength is typically within 15 percent and the direction of propagation is accurate to within 15°.

The ability of SAR to successfully image gravity waves is dependent on both the oceanographic environmental parameters as well as SAR system (imaging) parameters. Generally, waves propagating either towards or away from the radar line of sight are most easily detected by the SAR.

More research is needed exploring the use of SAR to detect wave height so that true power density spectra can be obtained from the SAR. Presently the spectrum of the SAR intensity is not being fully utilized. The spectrum shape as reported by McLeish, et al. (1980) and Vesecky, et al. (1981a) appears to most closely resemble a wave height spectrum than a slope spectrum. A mathematical expression for the SAR imaging mechanism would be quite useful in better explaining the SAR-derived ocean spectrum.

SAR's have the potential to remotely sense dominant ocean gravity wave and direction of propagation throughout the ocean basins. Presently, SAR's have a prohibitively large data rate when operated from satellites. Techniques need to be explored such as the Hasselmann SIFT algorithm to potentially lower these data rates.

ACKNOWLEDGEMENTS

The majority of the work reported in this paper was supported by ONR under Contract N00014-76-C-1048. The ONR technical monitor is Hans Dolezalek.

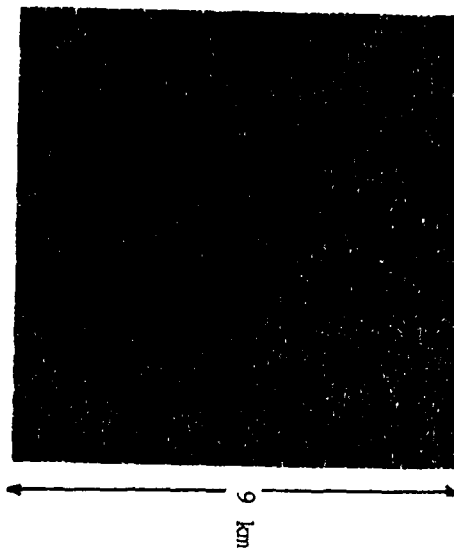
REFERENCES

- Allan, T.D. and T.H. Guymet, Seasat and JASIN, Int. J. Remote Sensing, Vol. 1, pp. 261-267, 1980.
- Alpers, W.R. and C.L. Rufenach, The Effect of Orbit Motions on Synthetic Aperture Radar Imagery of Ocean Waves, IEEE Trans. Antennas Propagat., Vol. AP-27, pp. 685-690, 1979.
- Anonymous, MARSEN Data Analysis and Research Plan, Pasadena, 1980.
- Apel, J., Paper Presented at the COSPAR/SCOR/IUCRUM Symposium on Oceanography from Space, Plenum Press (in press), 1981.
- Ausherman, D.A., Digital Versus Optical Techniques in Synthetic Aperture Radar (SAR) Data Processing, Optical Eng., Vol. 19, pp. 157-167, 1980.
- Baer, L., Informal Proceedings of the Atlantic Remote Sensing Land Ocean Experiment Data and Analysis Workshop, Virginia Beach, VA, 1981.
- Barber, N.F., A Diffraction Analysis of a Photograph of the Sea, Nature, 164, p. 485, 1949.
- Brown, W.J. and L. Porcello, An Introduction to Synthetic Aperture Radar, IEEE Spectrum, 6, pp. 52-66, 1969.
- Elachi, C. and W.E. Brown, Models of Radar Imaging of the Ocean Surface Waves, IEEE Trans. Antenna Propagat., Vol. AP-25, pp. 84-95, 1977.
- Gonzales, F.I., R.A. Shuchman, D.B. Ross, C.L. Rufenach, and J.F.R. Gower, Synthetic Aperture Radar Wave Observations During GOASEX, Proceedings of the COSPAR/SCOR/IUCRM Symposium on Oceanography from Space, Plenum Press (in press), 1981.
- Harger, R.O., Synthetic Aperture Radar Systems, Academic Press, New York, NY, 240 pp., 1970.
- Harger, R.H., SAR Ocean Imaging Mechanisms, in Spaceborne Synthetic Aperture Radar for Oceanography, ed. by R.C. Beal, P.S. DeLeonibus, and I. Katz, Johns Hopkins Univ. Press, pp. 41-52, 1981.
- Hasselmann, K., A Simple Algorithm for the Direct Extraction of the Two-Dimensional Surface Image Spectrum from Return Signal of a Synthetic Aperture Radar, Int. J. Rem. Sens. (in press), 1980.
- Jackson, P.L. and R.A. Shuchman, A New High Resolution Two-Dimensional Spectral Estimation Technique for SAR Ocean Wave Analysis, submitted to J. Geophys. Res., 1980.
- Jain, A., Focusing Effects in Synthetic Aperture Radar Imaging of Ocean Waves, J. Appl. Phys., Vol. 15, pp. 323-333, 1978.
- Jain, A.K. and S. Ranganath, Two-Dimensional Spectral Estimation, Proc. of the RADC Spectrum Estimation Workshop, 1978.

- Jordan, R.L., The Seasat-A Synthetic Aperture Radar System, IEEE J. Oceanic Eng., Vol. OE-5, pp. 154-164, 1980.
- Kasischke, E.S., A. Klooster, and R.A. Shuchman, Verification of Synthetic Aperture Radar Focusing Algorithms, Proc. Thirteenth Int. Symp. Remote Sensing Environ., Ann Arbor, MI, pp. 1077-1092, 1979.
- Kasischke, E.S. and R.A. Shuchman, The Use of Wave Contrast Measurements in SAR/Gravity Wave Models, Paper Presented at the Fifteenth International Symposium on Remote Sensing of Environment, Ann Arbor, MI, 1981.
- Kozma, A., E.N. Leith, and N.G. Massey, Tilted Plane Optical Processor, Applied Optics, 11, p. 1766, 1972.
- Mattie, M.G., D.E. Lichy, and R.C. Beal, Seasat Detection of Waves, Currents and Inlet Discharge, Int. J. Remote Sensing, Vol. 1, pp. 377-398, 1980.
- McLeish, W., D. Ross, R.A. Shuchman, P.G. Teleki, S.V. Hsiao, O.H. Shemdin, and W.E. Brown, Synthetic Aperture Radar Imaging of Ocean Waves: Comparison with Wave Measurements, J. Geophys. Res., 85, pp. 5003-5011, 1980.
- G.A. Meadows, R.A. Shuchman, E.S. Kasischke, and J.D. Lyden, The Observation of Gravity Wave - Current Interactions Using Seasat Synthetic Aperture Radar, submitted to J. Geophys. Res., 1981.
- Meadows, G.A., R.A. Shuchman, and J.D. Lyden, Analysis of Remotely Sensed Long-Period Wave Motions, submitted to J. Geophys. Res., 1981.
- Phillips, O.M., The Structure of Short Gravity Waves on the Ocean Surface, in Spaceborne Synthetic Aperture Radar for Oceanography, ed. by R.C. Beal, P.S. DeLeonibus, and I. Katz, Johns Hopkins Univ. Press, pp. 24-31, 1981.
- Raney, R.K. and R.A. Shuchman, SAR Mechanism for Imaging Waves, Proc. Fifth Canadian Symp. on Remote Sensing, Victoria, B.C., 1978.
- Rawson, R., F. Smith, and R. Larson, The ERIM X- and L-Band Dual Polarized Radar, IEEE 1975 International Radar Conference, p. 505, 1975.
- Schwab, D.J., R.A. Shuchman, and P.L. Liu, Wind Wave Directions Determined from Synthetic Aperture Radar Imagery and from a Tower in Lake Michigan, J. Geophys. Res., 1980.
- Shemdin, O.H., The Marineland Experiment: An Overview, Trans. Amer. Geophys. Union, Vol. 61, No. 38, pp. 625-626, 1980.
- Shemdin, O.H., The West Coast Experiment: An Overview, Trans. Amer. Geophys. Union, Vol. 61, No. 40, pp. 649-651, 1980a.

- Shuchman, R.A., Processing Synthetic Aperture Radar Data of Ocean Waves, Proceedings of the COSPAR/SCOR/IUCRUM Symposium on Oceanography from Space, Plenum Press (in press), 1981.
- Shuchman, R.A. and J.S. Zelenka, Processing of Ocean Wave Data from a Synthetic Aperture Radar, Boundary-Layer Meteorol., 13, pp. 181-191, 1978.
- Shuchman, R.A. and G.A. Meadows, Airborne Synthetic Aperture Radar Observations of Surf Zone Conditions, Geophys. Res. Letters, Vol. 7, pp. 857-860, 1980.
- Shuchman, R.A. and E.S. Kasischke, Refraction of Coastal Ocean Waves as Observed from the Seasat Aperture Radar, in Spaceborne Synthetic Aperture Radar for Oceanography, ed. by R.C. Beal, P.S. DeLeonibus and I. Katz, Johns Hopkins Univ. Press, pp. 128-135, 1981.
- Shuchman, R.A., P.L. Jackson, and G.B. Feldkamp, Problems of Imaging Ocean Waves with Synthetic Aperture Radar, ERIM Interim Technical Report No. 124300-1-T, Ann Arbor, MI, 111 pp., 1977.
- Shuchman, R.A., K.H. Knorr, J.C. Dwyer, P.L. Jackson, A. Klooster, and A.L. Maffett, Imaging Ocean Waves with SAR - A SAR Ocean Wave Algorithm Development, ERIM Interim Technical Report No. 124300-5-T, Ann Arbor, MI, 123 pp., 1979.
- Teleki, P.G., R.A. Shuchman, W.E. Brown, Jr., W. McLeish, D. Ross, and M. Mattie, Ocean Wave Detection and Direction Measurements with Microwave Radars, Oceans '78, IEEE/MTS, pp. 639-648, 1978.
- Valenzuela, G.R., An Asymptotic Formulation for SAR Images of the Dynamical Ocean Surface, Radio Science, Vol. 15, 1980.
- Vesecky, J.F. and R.H. Stewart, The Observation of Ocean Surface Phenomena Using Imagery from the Seasat Synthetic Aperture Radar - An Assessment, submitted to J. Geophys. Res., 1981.
- Vesecky, J.F., R.H. Stewart, H.M. Assal, R.A. Shuchman, E.S. Kasischke, and J.D. Lyden, Gravity Waves, Large-Scale Surface Features and Ships Observed by Seasat During the 1978 JASIN Experiment, submitted to Science, 1981.
- Vesecky, J.F., H.M. Assal, and R.H. Stewart, Remote Sensing of Ocean Waveheight Spectrum Using Synthetic-Aperture-Radar Images, Proceedings of the COSPAR/SCOR/IUCRUM Symposium on Oceanography from Space, Plenum Press (in press), 1981a.
- Wright, J.W., Backscattering from Capillary Waves with Application to Sea Clutter, IEEE Trans. Antenna Propagat., Vol. AP-14, pp. 749-754, 1966.
- Wright, J.W., W.J. Plant, W.C. Keller, and W.L. Jonse, Ocean Wave-Radar Modulation Transfer Functions from the West Coast Experiment, J. Geophys. Res., 85, pp. 4957-4966, 1980.

a) SAR Image



b) Optical Fourier Transform



c) Fast Fourier Transform

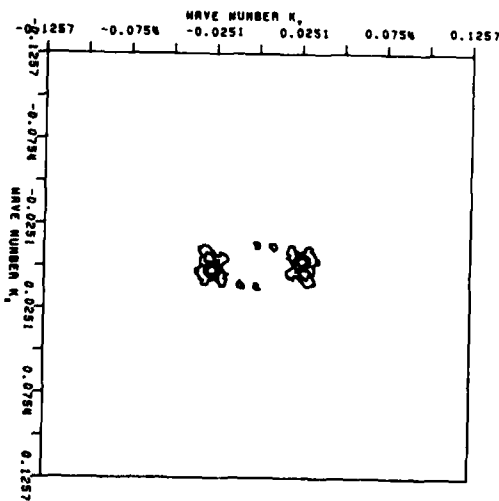


Figure 1. Seasat SAR Image of Ocean Gravity Waves and their Resultant Two-Dimensional Fourier Transforms (Seasat Rev. 762, 19 August 1978).

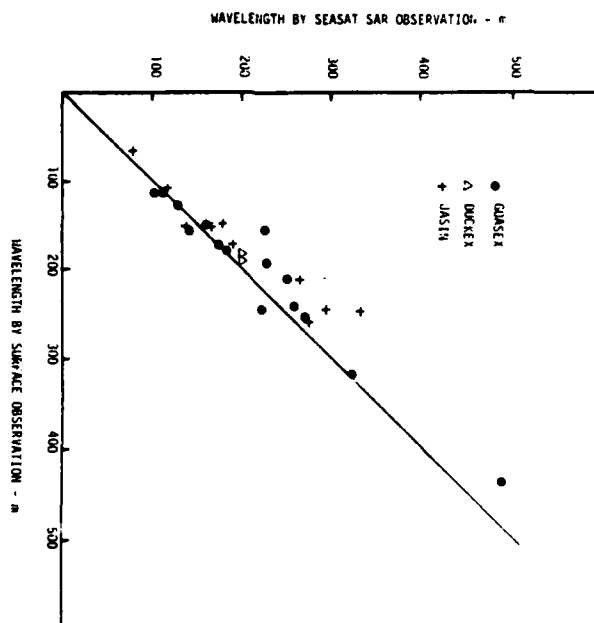


Figure 2. Plot of Wavelength, SAR Versus Sea Truth, for L-Band SEASAT Data (after Vesecky and Stewart, 1981).

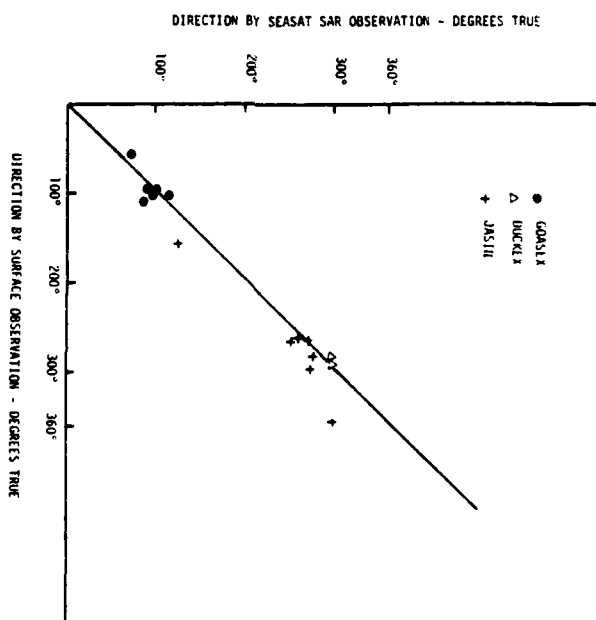


Figure 3. Plot of Wave Direction, SAR Versus Sea Truth, for L-Band SEASAT Data (after Vesecky and Stewart, 1981).

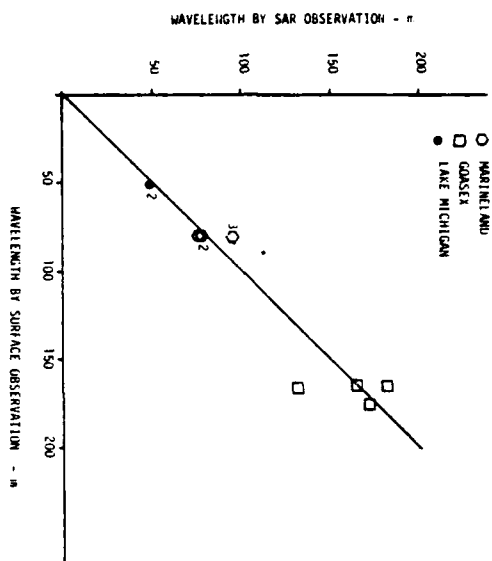


Figure 4. Plot of Wavelength, SAR Versus Sea Truth, for X-Band Aircraft Data.

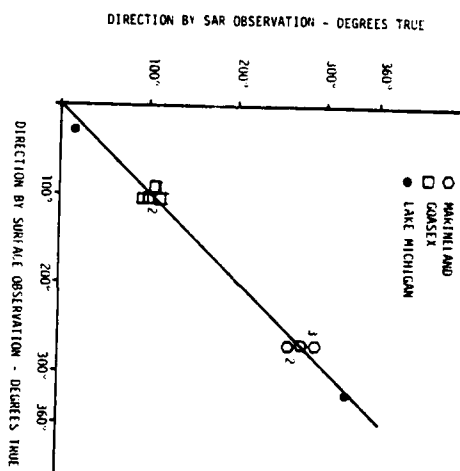


Figure 5. Plot of Wave Direction, SAR Versus Sea Truth, for X-Band Aircraft Data.

ENVIRONMENTAL RESEARCH INST OF MICHIGAN ANN ARBOR RA--ETC F/8 17/9
THE UTILITY OF SAR TO MONITOR OCEAN PROCESSES. (U)
NOV 81 R A SHUCHMAN; E S KASISCHKE N00014-76-C-1048
ERL-124300-11-7 NL

NO0014-76-C-1042

N

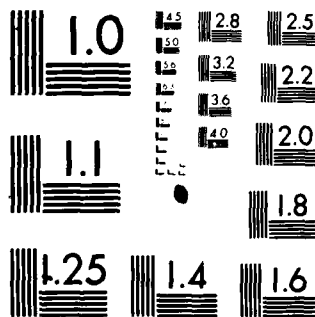
50

END

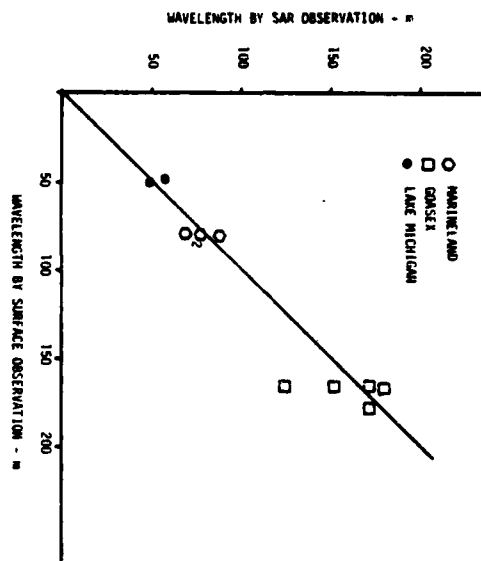
DATE _____

FILMED

15 18



MICROCOPY RESOLUTION TEST CHART
NATIONAL BUREAU OF STANDARDS-1963-A



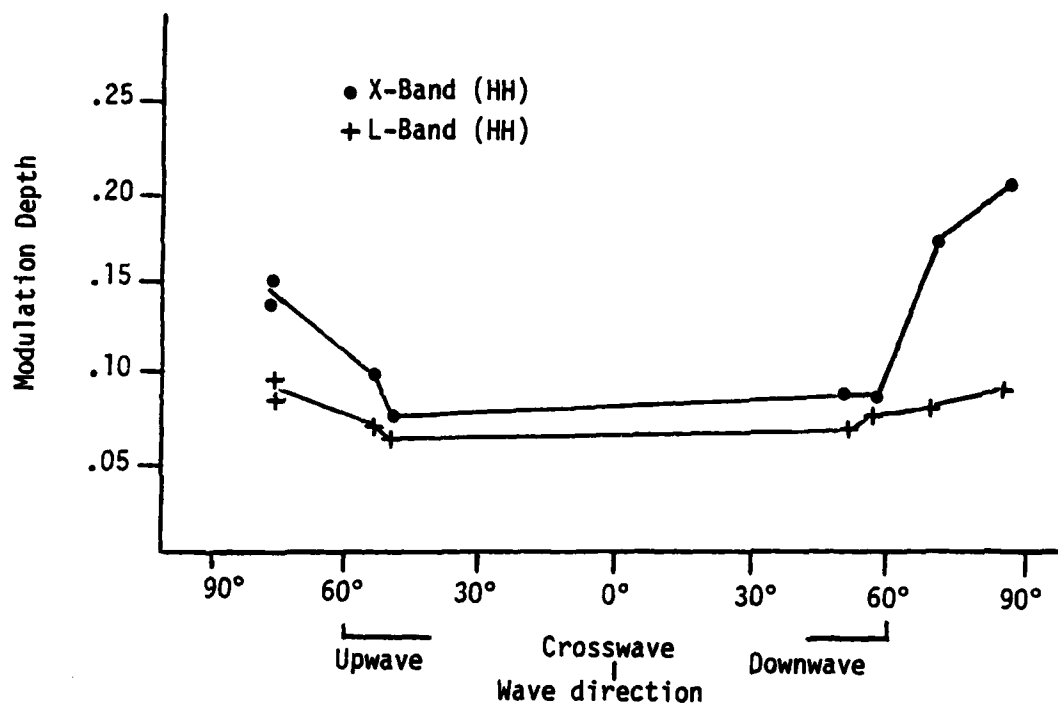
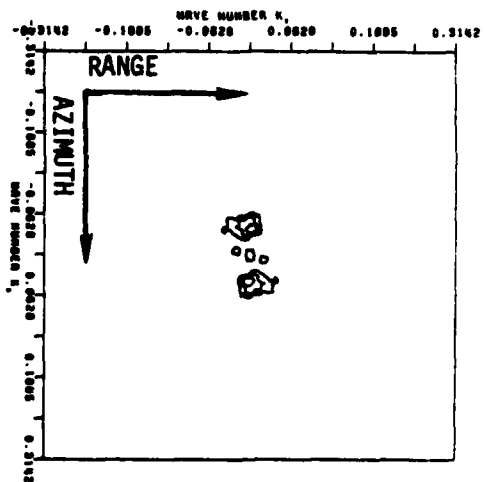
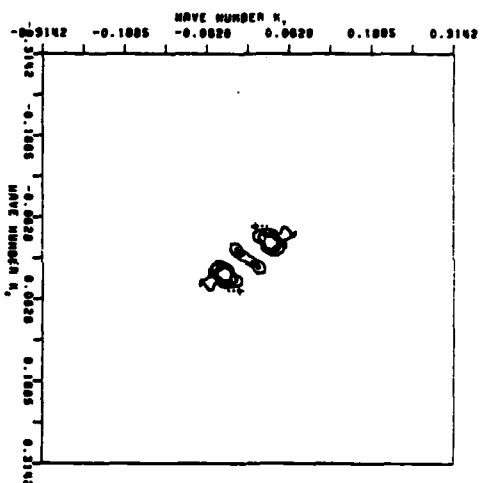


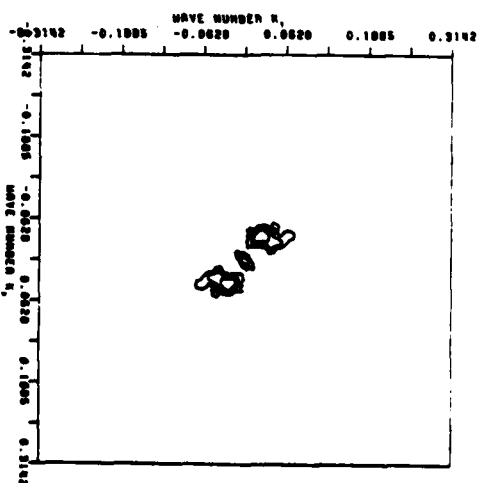
Figure 8. Modulation Depth at X-Band and L-Band as Function of the Direction of Wave Propagation.



X-BAND(HH)

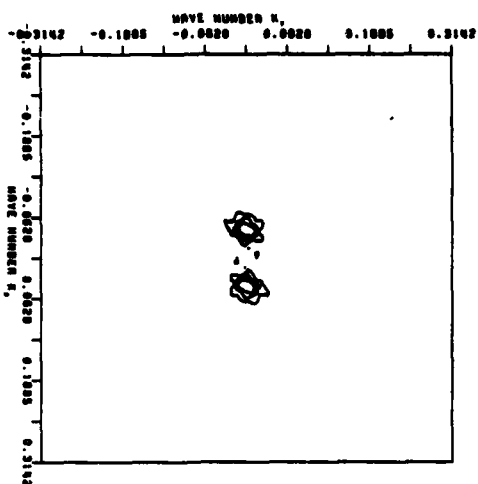


X-BAND(HH)

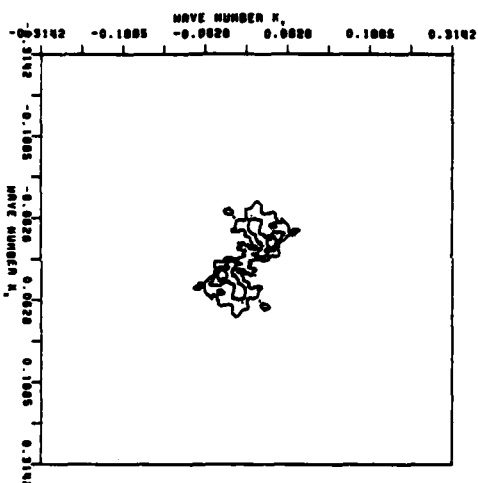


X-BAND(HH)

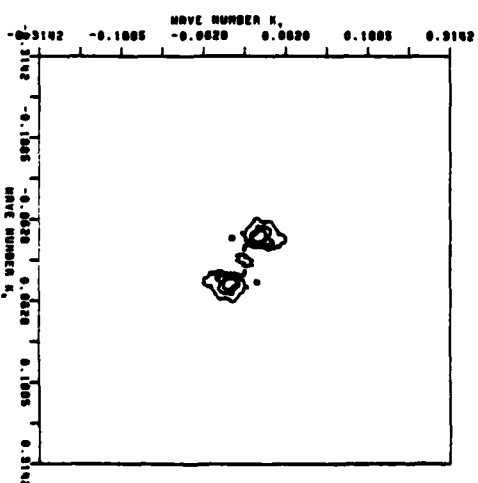
NOTE: Each vertical pair is simultaneously obtained.



L-BAND(HH)



L-BAND(HH)



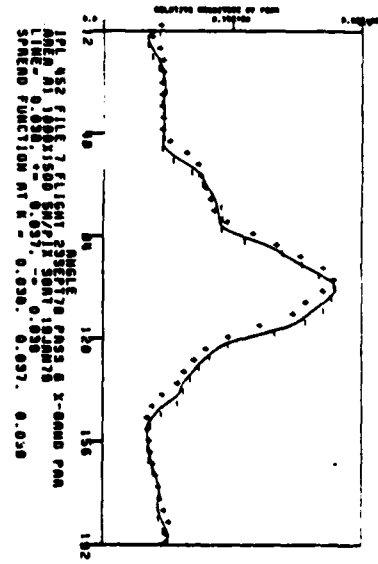
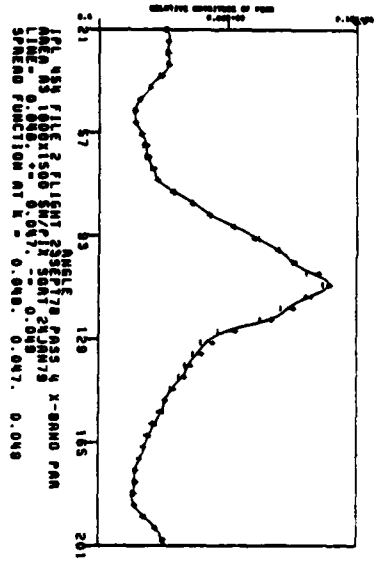
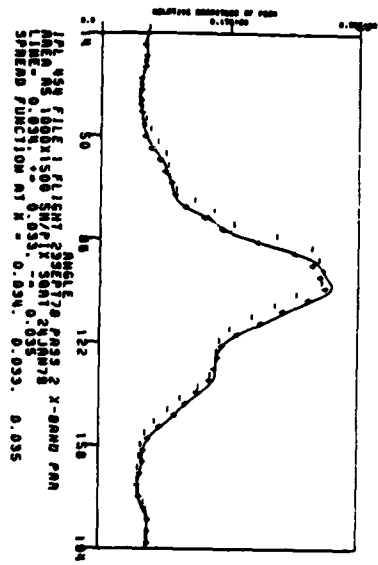
L-BAND(HH)

CROSS WAVE

NEARLY DOWNWAVE

NEARLY UPWAVE

Figure 9. 2-D Fast Fourier Transforms (FFTs) of Simultaneously Collected X- and L-Band (HH) SAR Wave Data From GOASEX (Sept. 23, 1978)



NOTE: Each vertical pair is simultaneously obtained.

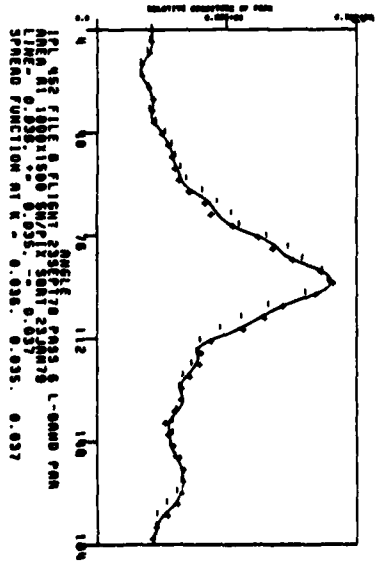
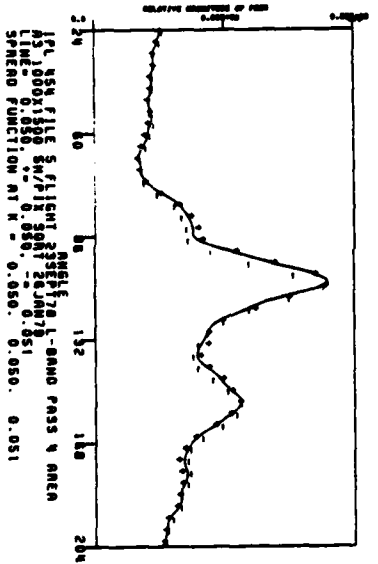
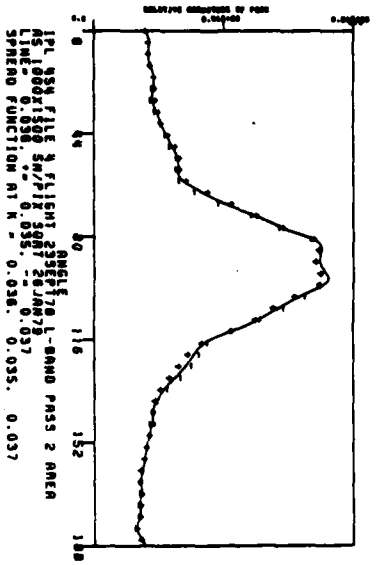


Figure 10. One-Dimensional Directional Distributions (180°) of FFTs Presented in Figure 9.

Sar-ocean:15

Gravity Waves, Large-Scale Surface Features and Ships observed by
SEASAT Synthetic Aperture Radar during the 1978 JASIN Experiment

(to be submitted to Science)

J.F. Vesecky¹, R.H. Stewart², R.A. Shuchman³, H.M. Assal¹,
E.S. Kasischke³, J.D. Lyden³

ABSTRACT

The 23 cm wavelength synthetic aperture radar (SAR) carried aboard the SEASAT satellite collected ~ 25 to 40 m resolution radar images of the ocean in 100 km wide swaths ranging in length from ~ 300 to 3000 km. Here we report results from the 18 SEASAT SAR passes during the Joint Air-Sea Interaction (JASIN) experiment conducted off the west coast of Scotland in summer, 1978. These many SAR images; when coupled with the intensive ship, buoy and aircraft measurements of the JASIN experiment; provide a unique opportunity to assess the ability of satellite SAR to measure ocean surface phenomena, particular surface wave fields. In this study we use only optically processed SAR images. Although gravity waves of length ~ 80 to 300 m are often seen in SAR imagery, they are not always seen. We find that waveheight, SAR resolution and wind velocity are important criteria for determining wave visibility. Comparisons between SAR and buoy

1. Stanford Center for Radar Astronomy, Stanford, CA 94305
2. Scripps Institution of Oceanography, LaJolla, CA 92093 and Jet Propulsion Lab, Pasadena, CA 91103
3. Environmental Research Institute of Michigan, Ann Arbor, MI 48107

estimates of dominant wavelength and direction agree to within about $\pm 15\%$ and $\pm 11^\circ$ respectively. We use a focus sharpness algorithm to resolve the 180° directional ambiguity of SAR image directional estimates. SAR estimates of omnidirectional waveheight variance spectra agree more closely with waveheight than waveslope spectra measured by buoys. By noting that buoy measurements of significant waveheight ($H_{1/3}$) correlate with peak signal to noise in Fourier transforms of the SAR images, we can measure $H_{1/3}$ to an accuracy of $\pm 3/4$ m. In the images studied here no bold large scale (\sim few km) features persisted over time intervals of 8 and 15 hours. Ephemeral features resembling internal waves were almost always found over seamounts and at the edge of the continental shelf. An image from orbit 1006 shows the first clear observation of roll vortices in the surface boundary layer over the ocean. A preliminary search for stationary or slowly moving oceanographic ships suggests that such ships are difficult or impossible to detect for moderate seas and wind speeds $> 3.5 \text{ ms}^{-1}$.

Introduction: The 23 cm wavelength synthetic aperture radar (SAR) carried aboard the SEASAT satellite collected ~ 25 to 40 m resolution radar images of the ocean in 100 km wide swaths ranging in length from ~ 300 to 3000 km. A description of the instrument is given by Jordan (1980) and preliminary results from all SEASAT instruments were given in the June 29, 1979 issue of Science. Here we report results from SEASAT SAR observations during the Joint Air-Sea Interaction (JASIN) experiment. During this experiment (June-September, 1978) many surface observations were made by ships, buoys and aircraft, particularly observations of the wind and wave conditions which are pertinent to evaluating the SAR images (Pollard, 1979). During August and September, 1978 SEASAT SAR imaged the JASIN area on 18 different occasions. Examples of the areas imaged, and their relationship to the surface observation are illustrated in Fig. 1. These many images, when coupled with the intensive surface measurements, provide a unique opportunity to assess the ability of satellite radar to measure surface wave fields.

SAR is capable (under suitable conditions) of sensing a large variety of ocean surface phenomena including long gravity waves (with wavelength Λ greater than about twice the SAR resolution), winds, surface currents, internal waves, ocean fronts, underwater topography, slicks, ships and their wakes (Beal, et al., 1981 and Gower et al., 1981). The SAR image is basically a high resolution map of the radar reflectance (backscatter) of the ocean surface modified by surface motion effects. Because the dielectric properties of the ocean surface are relatively uniform, variations in reflectance are due primarily to variations in the surface roughness. In particular the reflectance is due to resonant scatter of 23 cm radar waves from ocean waves with $\Lambda \sim 30$ cm. The resonance is typical of radiation scattered from a lattice and is usually called Bragg scatter (Bragg, 1933). Because SAR uses

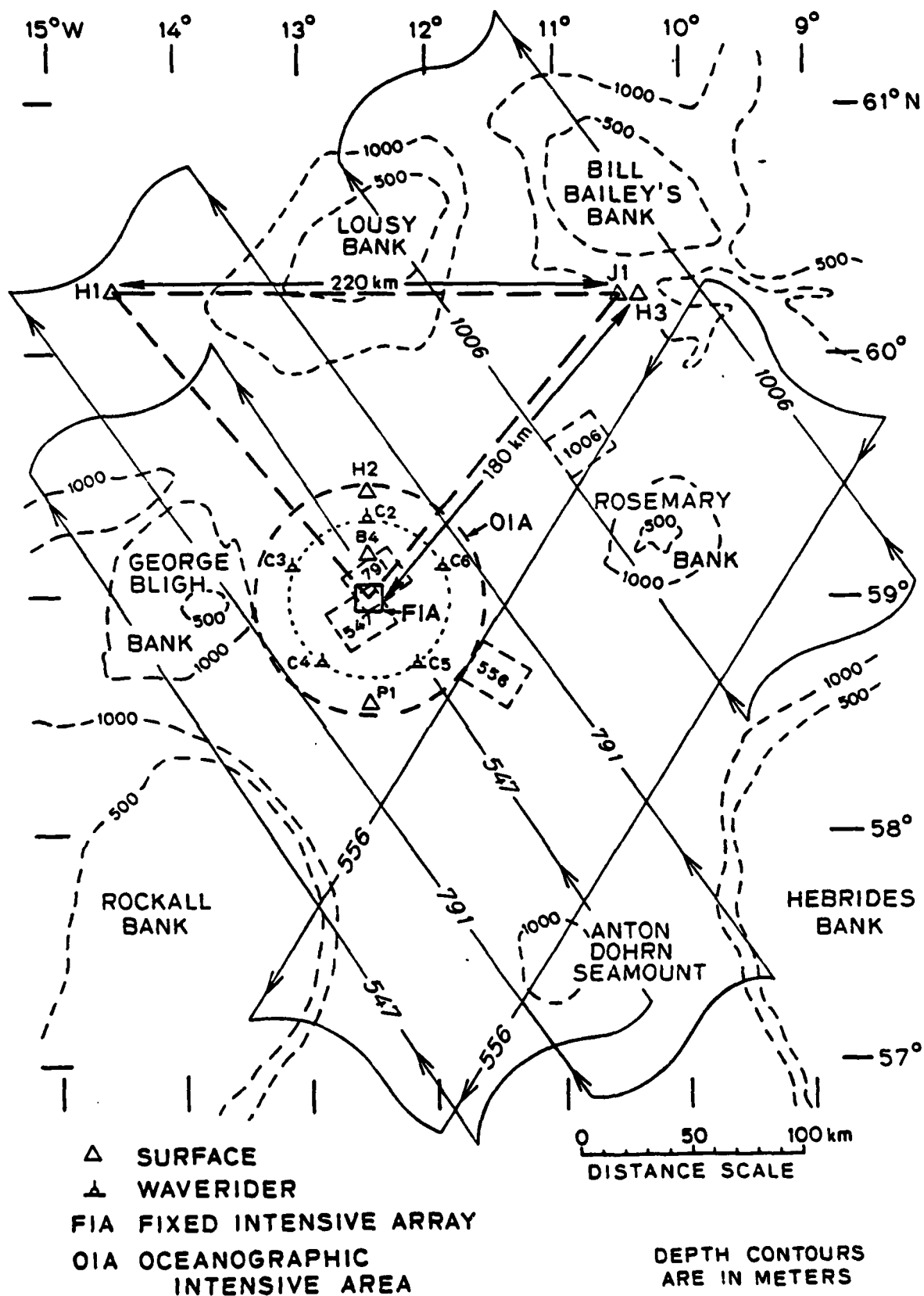


Fig. 1. Joint Air-Sea Interaction (JASIN) experiment area showing typical SEASAT SAR image swaths and sections of images used for wave analysis. Wave rider buoys are denoted by C2, C3, etc. Pitch-roll buoys were generally deployed in the FIA area.

the phase of the radar echo to achieve high azimuthal resolution in the image (i.e. to correctly locate the origin of a given echo) motion of the ocean surface, which introduces a phase shift in the scattered signal, causes points in the image to be displaced from their true position. This misplacement is illustrated in Fig. 5 where moving ships are displaced (along the direction of satellite motion) from their wakes. Spatial modulation of surface roughness and surface motion (giving rise to Doppler shifts) produces the majority of ocean surface features in SAR imagery. Phillips (1981) describes a number of ways in which wind, wave and current can modulate decimeter scale surface roughness.

Wave Visibility during JASIN: Although gravity waves of length ~ 80 to 300 m are often seen in SAR imagery, they are not always seen. In our study we used only images processed optically at Jet Propulsion Laboratory (JPL) and Environmental Research Institute of Michigan (ERIM). We find that three criteria are important in determining wave visibility: wave height, SAR resolution and wind velocity. Alpers, Ross and Reufenach (1981) point out that orbital velocities associated with surface waves produce a smearing effect on SAR imagery increasing resolution cell size especially along the azimuth direction (parallel to the SAR flight path). An expression for the degraded resolution cell length Δy^* along the azimuth direction is given by the above authors as a function of the unsmeared resolution Δy (~ 25 to 40 m for SEASAT), radar wavelength λ , SEASAT orbital velocity V , distance between radar and scattering surface R , ocean wave amplitude A , angular frequency Ω , wavelength Λ and direction relative to the SAR flight path ϕ . Knowing Δy^* and the ocean wavelength along the azimuth direction $\Lambda_y = \Lambda / \cos \phi$, the number of samples per wavelength n_y along the azimuth direction can be calculated. The Nyquist sampling criterion demands $n_y > 2$ in order that

waves be adequately sampled. Jain (1978) and Vesecky et al. (1981) have developed wave visibility criteria along these lines. Because of the roles played by waveheight and/or slope in wave imaging mechanisms (Alpers et al., 1981) one expects wave visibility to decrease with decreasing significant waveheight $H_{1/3}$ and indeed we find waves are seldom imaged for $H_{1/3} \lesssim 1$ m. This waveheight criterion is probably set by the influence of slopes on the modulation. If slopes are the dominant mechanism modulating the normalized radar cross section σ_0 , and if slopes are small, then so too is $\Delta\sigma_0$. If $\Delta\sigma_0$ is less than the noise level, the waves are invisible. The two criterion $n_y \gtrsim 2$ and $H_{1/3} \gtrsim 1$ m are applied to the SEASAT-JASIN data set in Fig. 2. All ocean wave data are drawn from buoy measurements. Interestingly, theory implies that there may be both a minimum $H_{1/3}$ below which waves are not imaged and a maximum $H_{1/3}$ above which waves traveling near the azimuth direction are not imaged because the azimuthal resolution is too degraded by wave orbital velocity.

Since wind produces the 30 cm ocean waves which the radar senses, we expect wave images to disappear when wind velocity falls below about 3.5 m/s and the sea becomes calm. During the SEASAT-JASIN experiment one set of images showed waves while surface winds ranged from 3.5 to 15.2 m/s, and another set of images failed to show waves while surface winds ranged from 6.6 to 12.9 m/s. It is thus apparent that wind speed was not a factor during the SEASAT-JASIN experiment mainly because wind speeds were always above 3.5 m/s.

Comparison of Wave Measurements by SAR and Surface Buoys during JASIN:

During the SEASAT-JASIN experiment (4 August to 11 September, 1978) we made as many buoy wave measurements as possible during periods concurrent with 18 SEASAT passes. These surface measurements included both routine JASIN observations as well as special deployments of pitch-roll buoys. Typical SEASAT

SEASAT JASIN EXPERIMENT, SUMMER 1978

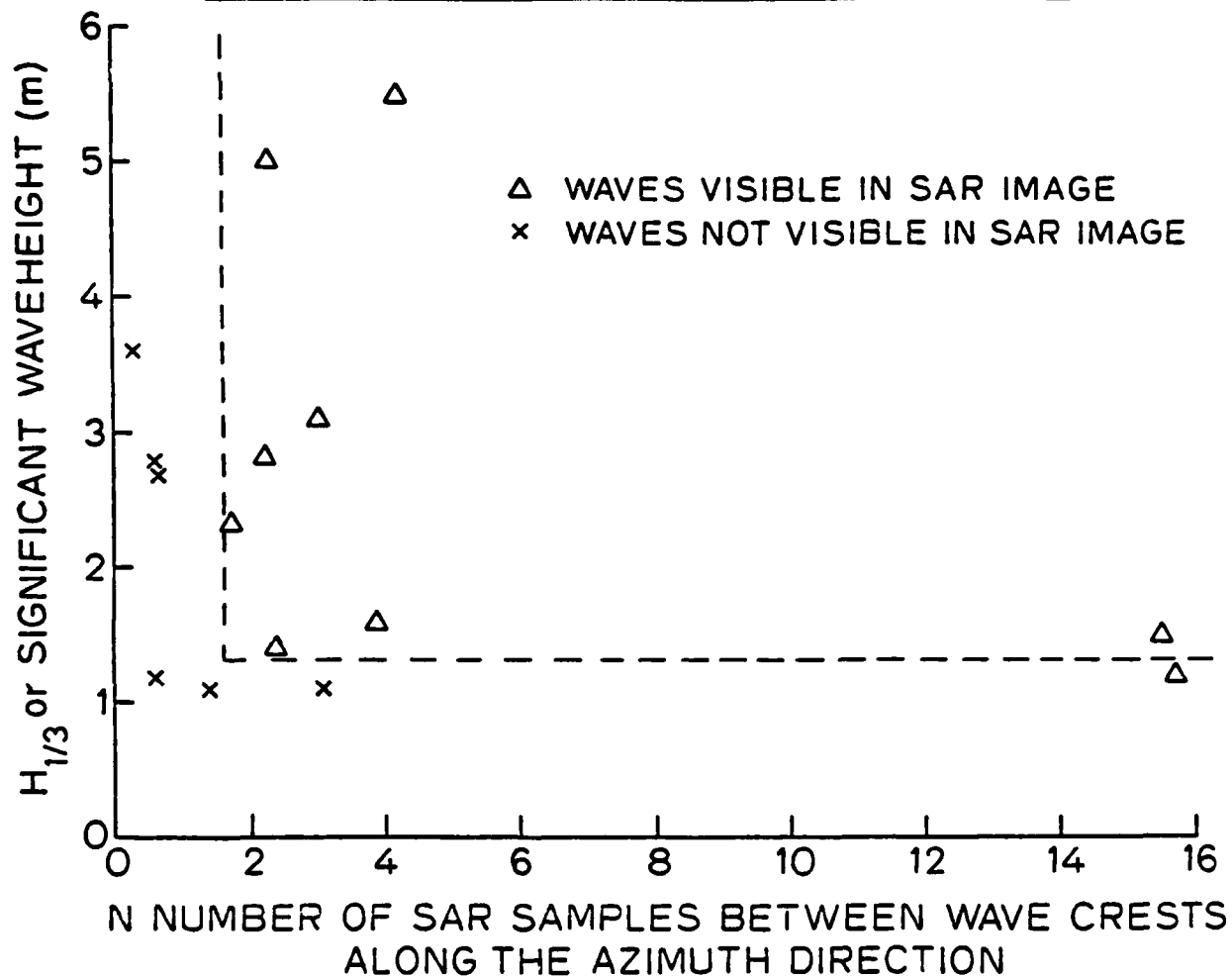


Fig. 2. Data from the SEASAT-JASIN experiment plotted on axes of significant wave height $H_{1/3}$ and n_y the number of SAR resolution cells per wavelength along the azimuth direction. These data fall into two distinct classes according to whether or not waves were visible in SAR imagery.

SAR coverage is shown in Fig. 1 and Table 1 summarizes the proximity of SAP and surface wave measurements.

The waverider buoys (such as C1, C2, etc. shown in Fig. 1) measure only the frequency spectrum of surface height variance. The pitch-roll buoys, deployed from the R.V. Atlantis II and M.V. Discovery, measure directional waveheight spectra $\Psi(f, \theta)$ where f is the frequency and θ the direction of wave travel relative to true north. The spectrum of waveheight variance yields the spatial spectrum of waveheight $\Psi(K, \theta)$ and waveslope $\Psi'(K, \theta)$ variance by a simple calculation (Kinsman, 1965).

The wave measurements from SAR imagery made here are based on a simple assumption, to wit, that fluctuations in SAR image intensity $I(x, y)$ are proportional to ocean wave height fluctuations. Under this assumption $\Psi(K, \theta)$ is simply proportional to the magnitude squared of the two-dimensional Fourier transform of the intensity fluctuations, namely $|F\{I(x, y)\}|^2$. As will become clear below, this assumption is not precisely correct. However, it is not far wrong (Vesecky et al, 1981) and provides a convenient working hypothesis. Although this algorithm is straight-forward, there are numerous variations to its implementation. First, imagery may be produced by either optical or digital processing. Here we have used optically imaged data produced at the Jet Propulsion Laboratory (JPL) and at the Environmental Research Institute of Michigan (ERIM). These images were Fourier transformed, to obtain estimates of the dominant wavelength and direction using the assumption together with the peak of $|F\{I\}|^2$ and its location in the (K, θ) plane.

Fourier transforms of the SEASAT-JASIN imagery were obtained in two ways. In one case the ERIM images were optically Fourier transformed and the results displayed photographically (Kasischke, 1980). In the other case the JPL images were digitized at intervals corresponding to about 20 m and the

DATE (1978)	TIME (UT)	ORBIT NUMBER	*SURFACE BUOY	SEPARA- TION(km)	DOMINANT WAVELENGTH (m)		**DOMINANT WAVE DIRECTION (°T)		WAVE REAM- WIDTH (deg)		WAVE VISI- BILITY (dB)		*** ϕ (DEG)	Hy3 (m)	U (ms ⁻¹)
					SAR ††	SURFACE	SAR ††	SURFACE	SAR	SURFACE	PRR	S/N			
4 AUG.	0615	547	a	0	199	169	266	263	40(S)	32	3.6	5.2	116	1.7	4.5
4 AUG.	2135	556	a	63	147	149	274	280	~40(S)	54	1.8	2.2	248	1.5	3.5
7 AUG.	0622	590	a	15	--	222/89	--	229/329	--	83/77	0	0	83/183	1.3/1.3	7.2
7 AUG.	2143	599	b(C2)	119	69(S)	67	343(S)	--	~90(S)	--	0	.5	--	1.1	6.9
10 AUG.	0629	633	a	58	--	89/53	--	220/220	--	70/40	0	0	74/74	1.1/1.1	9.2
10 AUG.	2150	642	a	210	--	169	--	200	--	29	0	0	168	2.9	12.9
15 AUG.	2235	714	none	--	182(E)	--	276(E)	--	--	--	1.8	0	--	--	--
16 AUG.	0643	719	none	--	160	--	274	--	122(S)	--	1.5	3.2	121	--	7.6
18 AUG.	2240	757	b(C4)	0	275(E)	217	253(E)	--	--	--	2.9	0	--	4.9	15.2
19 AUG.	0641	762	b(C6)	146	264	206	245	--	33(S)	--	5.1	5.1	110	4.4	12.0
21 AUG.	0724	791	b(C2)	35	168	131	252	--	34(S)	--	3.4	4.3	107	3.0	13.0
24 AUG.	0730	834	a	55	151	149	266	~295	--	35	1.8	3.0	~149	2.8	10.2
1 SEPT.	2354	958	c	115	120(E)	149	296(E)	360	--	65	1.6	0	324	1.4	7.2
5 SEPT.	0006	1001	a	75	81(E)	63	125(E)	~146	--	76	2.5	0	~110	2.5	12.6
5 SEPT.	0815	1006	a	122	--	107	--	~69	--	60	0	0	~282	3.6	6.6
8 SEPT.	0018†	1044	c†	20†	336	299	257	262	--	27	6.0	7.8	226	4.1	11.5
8 SEPT.	0827	1049	c	145	318	299	250	262	--	27	5.2	8.0	115	3.6	6.3
11 SEPT.	0030	1087	none	--	301	--	253	--	38(S)	--	4.2	4.2	218	--	13.2

Notes:

*Surface buoys are denoted as follows: a, Atlantis II pitch roll buoy; b, Wave rider buoy moored in OIA--see Fig. 1; c, Discovery Pitch roll buoy.

**The direction from which waves arrive is used here.

***The angle ϕ lies between the direction of satellite velocity \vec{v} and the dominant ocean wave vector \vec{k} .

†Buoy measurement made 0742 - 0755 UT.

††(S) means Stanford measurement only and (E) means ERIM measurement only.

Fourier transform done digitally. The results were then displayed graphically as discussed below and by Vesecky et al (1981). The results obtained by these two methods are shown in Table 1.

Table 1 summarizes comparisons between SEASAT SAR estimates of dominant wavelength and direction and estimates derived from the surface buoys. If we included 2 similar comparisons from the DUCK EX experiment and 15 from the GOASEX experiment (Gonzales, et al., 1981) we find that the SAR estimates agree with the surface buoy estimates with an average error of $\pm 15\%$ and $\pm 11^\circ$ for wavelength and direction respectively. In making the comparison for the SEASAT-JASIN experiment, we have simply averaged the two SAR wave estimates based on JPL or on ERIM processed imagery. SAR estimates of wavelength are biased high by about 10% when compared to buoy measurements.

Wave estimates obtained from SAR imagery on the basis of the simple assumption discussed above contain a 180° ambiguity, i.e., one cannot distinguish waves traveling along direction θ from those traveling in the opposite direction $\theta + 180^\circ$. Shuchman and Zalenka (1978) have shown that this ambiguity can be resolved using SAR data alone by special focusing of the SAR imagery during the imaging process. The difference in the point of sharp focus for waves relative to the point of sharp focus for land reveals the direction of wave travel either away from or toward the radar. By applying this procedure to the JASIN data set, we are freed from relying on ad hoc assumptions (such as waves always traveling toward coasts or down wind) to resolve the 180° ambiguity in dominant wave direction.

The wavenumber spectrum of surface height fluctuations $\Psi(k, \theta)$ provides a good statistical description of ocean wave conditions. Using SAR imagery and surface data collected during the SEASAT-JASIN experiment we can compare SAR and buoy estimates of Ψ . This comparison is made in terms of two statistics,

namely the omnidirectional waveheight spectrum $\Psi(K)$ and the directional distribution $\beta(\theta)$ averaged over some range of wavenumbers ΔK from K_1 to K_2 . Techniques for estimating $\Psi(K)$ and $\beta(\theta)$ from pitch-roll buoy data are described by Longuet-Higgins et al. (1963). For the SAR estimates we have used the aforementioned simple assumption and implemented it on 20 x 20 km sections of JPL optically processed SEASAT imagery. The images were first digitized on a 20 m grid and then processed digitally. Background fluctuations related to the point response of the SAR (Beal, 1981) and to large scale (≥ 1 km) SAR image intensity changes were removed by assuming that the background could be represented by an isotropic transfer function $T_B(K)$. We estimated T_B by letting $T_B(K) = |F\{I(x,y)\}|^2$ where $|F|^2$ was averaged over directions θ more than $\sim 30^\circ$ away from the dominant wave direction. By removing the background we obtain a more realistic estimate of $\Psi(K)$, especially at high wavenumbers where the decreasing response of the SAR system can easily be confused with the $\sim K^{-4}$ decrease expected for the ocean wave spectrum (Phillips, 1977). The corrected spectra are denoted by F_R where $F_I = T_B F_R$ and F_I is the image intensity spectrum before correction. In calculating the SAR estimate of $\Psi(K)$ we have not averaged over all directions to obtain a true omnidirectional spectrum. Rather we have used only data for directions within about $\pm 15^\circ$ of the dominant wave direction depending on the directional distribution. Since, in most cases of a single dominant wave direction, data from directions away from the dominant wave direction contains only background fluctuations, its inclusion would only serve to raise the noise level in our SAR estimate of $\Psi(K)$.

Fig. 3 illustrates a number of features which are typical of comparisons between SAR image intensity spectra $|F_R(K)|^2$ and buoy measurements of ocean waveheight and waveslope spectra. The peak of the SAR spectrum is ~ 3 times

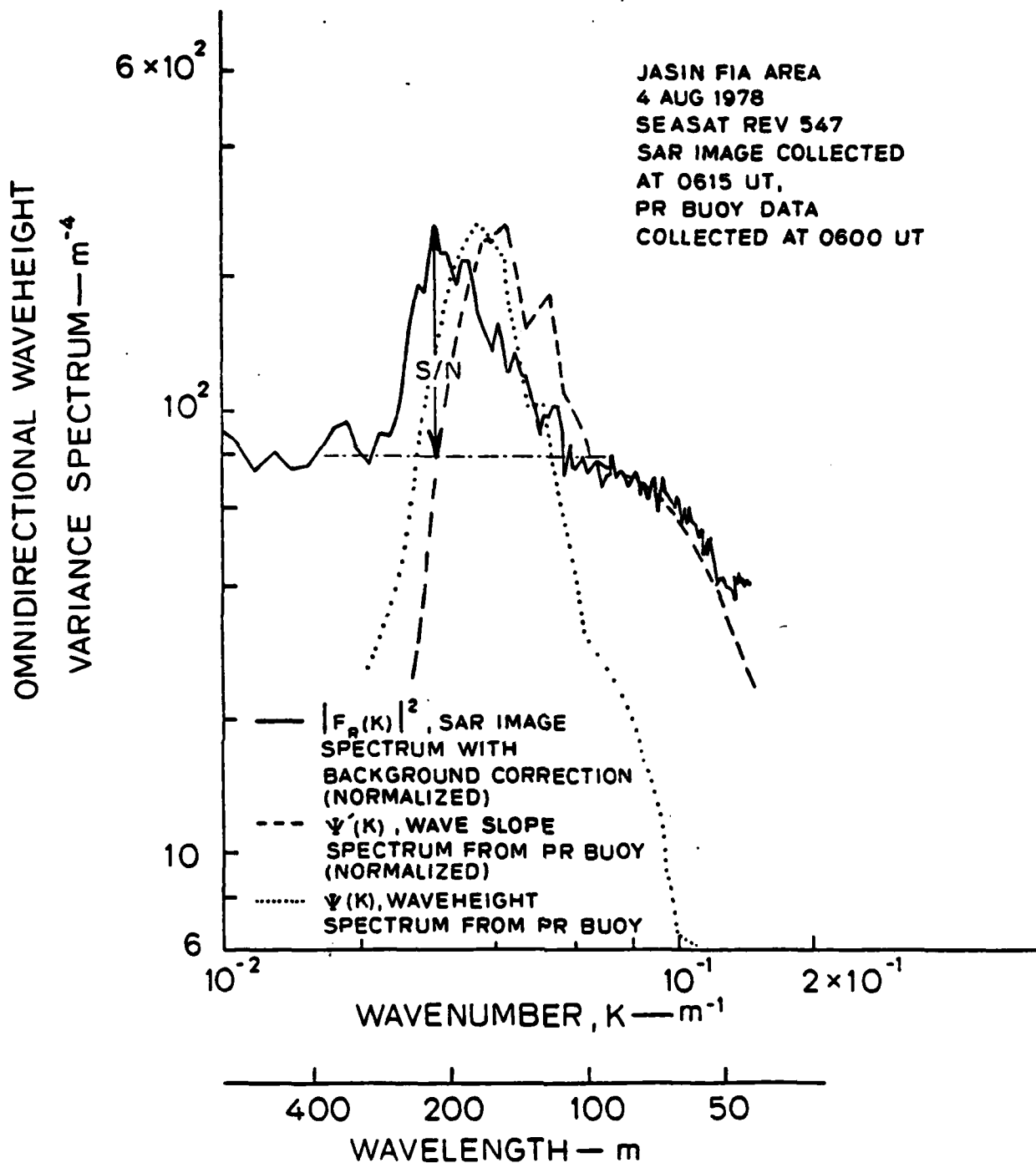


Fig. 3. Comparison of SAR image spectrum corrected for background fluctuations and SAR point response, $|F_R(K)|^2$ with omnidirectional waveheight and waveslope spectra $\Psi(K)$ and $\Psi'(K)$ as measured by pitch-roll buoy. Both $|F_R(K)|^2$ and Ψ' have been normalized along the ordinate.

the background indicated by the horizontal line. The peak of $F_R(K)$ corresponds to a wavelength some 10% above the wavelength of the peak Ψ and 20% above the wavelength of the peak Ψ' . The reason for this bias of F_R (or F_I) toward longer wavelengths is not known. A simple scaling error does not appear to be the cause since the same bias is found in data imaged and analyzed independently by three different research groups -- ERIM, Stanford, and Gonzales et al. (1981). The shape of the SAR spectrum corresponds most closely with the waveheight spectrum. Fig. 4 compares SAR and pitch-roll buoy estimates of the wave directional distribution near the dominant wavelength. Note that the SAR shows more structure than the pitch-roll buoy. Work by Vesecky et al. (1980) suggests that at least some of the SAR distribution structure is real, e.g. bidirectional distributions.

In theory, SAR signals contain information about waveheight, but obtaining this information in useful form tends to be difficult. Jain, Medlin, and Wu (1982) have shown that observations of speckle diversity on a SAR image can be used to estimate waveheight. Our data indicate a perhaps simpler approach. The peak signal to background noise ratio of our data (S/N in Fig. 3) is correlated with significant waveheight ($H_{1/3}$). We find that the data from Table 1 can be fit by a linear law $S/N = -0.17 + 1.73 H_{1/3}$ with a coefficient of determination $R^2 = 0.64$. Thus $H_{1/3}$ can be directly estimated from SAR imagery with a mean error of about $\pm 3/4$ m. Thus the SAR spectrum of Fig. 3 would correspond to $H_{1/3} \approx 3$ m. The $\pm 3/4$ m error compares well with the accuracy of waveheights determined from SAR data using observations of speckle diversity (Jain, Medlin and Wu, 1982). Further, this correlation can be used to produce SAR estimates of the omni-directional waveheight spectrum which yield absolute values along both the ordinate and abscissa of Fig. 3.

Large-Scale Features: The SAR images, although primarily designed to

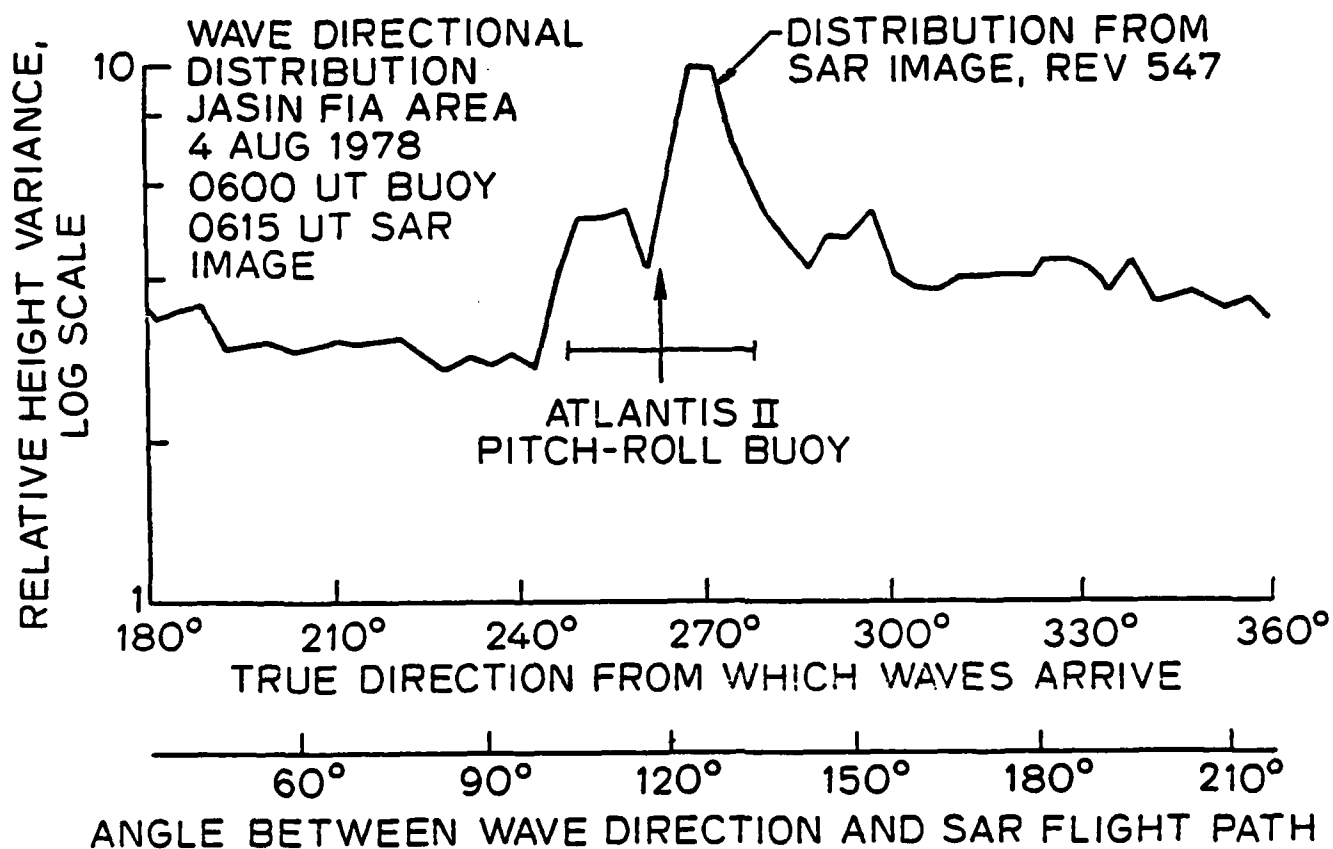


Fig. 4. Comparison of SAR image directional distribution (for a band of wavenumbers $\Delta K = .022 \text{ m}^{-1}$ to $.045 \text{ m}^{-1}$ surrounding the dominant wavenumber) with the mean direction and beam width of the dominant waves as measured by pitch roll buoy.

display ocean waves, often show other perhaps more interesting features. These appear to be internal waves, oceanic fronts, slicks and the spatial variability (gustiness) of the wind speed. Various examples off the U.S. east coast are given by Beal et al. (1981). Visual examination of images collected over the JASIN experiment also revealed a number of interesting features.

To determine if any of the features were due to ocean currents, we looked at successive sets or pairs of images to determine if any feature persisted (on the assumption that the ocean changes slowly). We found that no bold large scale features persisted over times of 8 hours (4 different sets of images) and 15 hours (3 different sets of images). Because the image pairs could not be precisely aligned, small weak features may have persisted, but been overlooked. In four cases land in the image was used to register the images to within ± 1 kilometer. In the other three cases no land was present in the imagery and the superposition was less accurate. The 4 orbits which produced these pairs of images did not have parallel ground tracks and so the boundaries of the image swaths intersect with angles of about 110° . Fig. 1 shows the intersection of images from orbits 547 & 556. Thus the viewing geometry differs considerably between the two images in a pair. From these observations we conclude that either the features were not persistent and hence not oceanic in origin or that the conditions for sensing the phenomenon did not persist.

Features resembling the internal wave patterns seen in LANDSAT images (Apel, et al., 1975) were almost always found over seamounts and at the edge of the continental shelf. The patterns are ephemeral, and probably depend on the stage of the tide.

The image from orbit 1006, shows rows of streaks separated by either 1.3 or 2.6 km extending over an area of at least 100 x 200 km. The streaks are

aligned along the wind direction, and the surface wind speed was approximately 12 ms^{-1} . Jones and Schroeder (1978) show conclusively the L-band radars are sensitive to wind speed, and we identify the changes in SAR image brightness over a large area with variations in wind velocity (c.f. also Valenzuela, 1978). This then is the first clear observation of roll vortices in the surface boundary layer over the ocean.

On orbit 556 an area roughly 50 km in size appeared very dark (very low radar reflectivity). Several sources of data including ship logs, infrared satellite imagery and weather synopses indicated that a thunderstorm was in the area. Apparently rain falling in the area smoothed the sea and damped out the ~ 30 cm waves which scatter the radar signal.

Ships: A perusal of SEASAT SAR imagery (e.g. see Beal et al., 1981 or Fig. 5) reveals many images of stationary ships as well as moving ships with their attendant wakes, which can extend ~ 20 km. In only a few cases have searches been made for ships with known positions. We have searched for oceanographic ships involved in the JASIN experiment on orbits 547 and 590 using imagery which was optically processed at JPL. The ships that should be imaged and their approximate lengths are: R.V. Atlantis II (66 m), M.V. Gardline Endurer (53 m), R.V. Meteor (82 m) and H.R. M.S. Tydeman (89 m). The ship locations in latitude and longitude at the times of SEASAT SAR imagery are known to an accuracy of a few km or less. Without special processing we are usually able to locate points in SEASAT imagery to within about 5 km. Allowing an additional 10 km for unknown systematic error, we expect to find ship images within 15 km of their estimated position in the imagery.

On orbit 547 only the Atlantis II was within the SAR swath and a ship image was found 12 km from the estimated position on the image. None of the

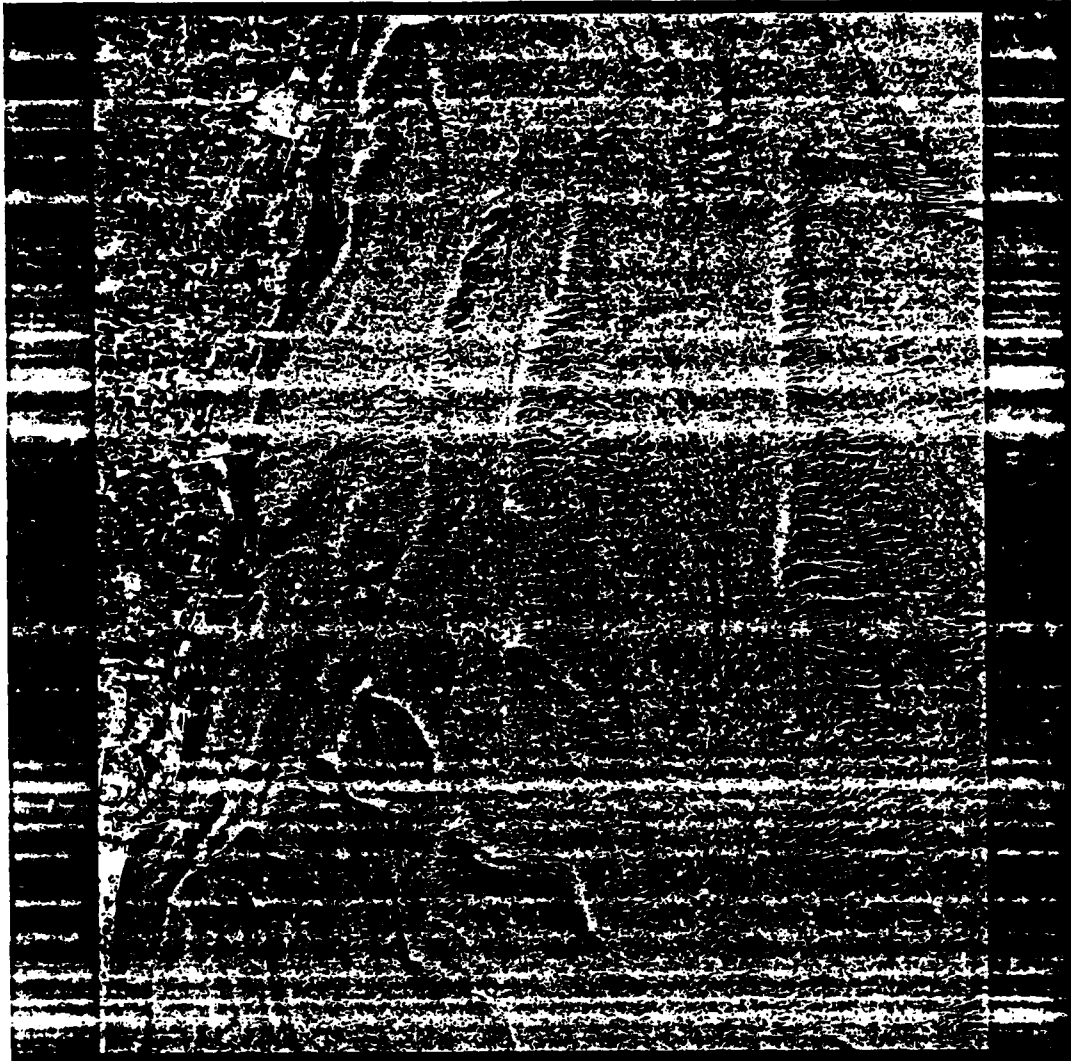
other JASIN ships mentioned above were within the SAR swath and no other ship images were found within ± 100 km along the same 25 km wide subswath. Near the Atlantis II position the dominant swell was of wavelength $\lambda \approx 170$ m out of 250° with $H_{1/3} \approx 1.6$ m while the wind was out of 15° at 3.6 ms^{-1} .

On orbit 590 all four ships were within the SAR swath. However, only the largest ship (H.R.M.S. Tydeman) can even be tentatively identified -- a weak target some 7 km from the estimated position. Near the positions of all the ships, save the Gardline Endurer, the dominant swell had a wavelength of 222 m coming from 250° and a height of 1.2 m. The wind was out of 10° at 6.6 ms^{-1} . At the position of the Gardline Endurer some 180 km to the NW the wave conditions were approximately the same while the wind speed was 5.2 ms^{-1} .

This evidence, taken with an unsuccessful search for the R.V. Oceanographer during the GOASEX experiment, lends us to conclude that images of stationary or slowly moving ships (no significant wakes) are difficult or impossible to detect in SEASAT imagery (optically processed at JPL) for moderate seas and wind speeds greater than about 3.5 ms^{-1} . Thus such SAR imagery cannot be routinely used to determine ship positions as an aid to performing research at sea. We emphasize that the imagery used in these searches was the standard data product. Improvements in resolution and focussing by either specialized optical or digital techniques may presumably improve detection. Fig. 5 illustrates ship images as well as other features as they appear in a high quality, digitally processed SEASAT SAR image. The wakes of faster moving ships make them more evident.

SCALE 1:330000

AZIMUTH



DIGITALLY PROCESSED BY THE NORWEGIAN DEFENCE RESEARCH ESTABLISHMENT

Fig. 5. SAR image of the English Channel off Ostend, Belgium from orbit 762. Several ship images are apparent, both stationary and moving. Note how the ship's velocity relative to the relatively stationary ocean surface causes the ship image to be displaced from its wake. The image was collected on 19 August 1978 at 0645 UT. Four look digital processing was used to obtain 25 x 25 m resolution. (Image digitally processed and kindly provided by the Norwegian Defense Research Establishment).

ACKNOWLEDGEMENTS

We gratefully acknowledge Herbert Carlson of the Deutsches Hydrographisches Institut and Trevor Guymer and David Webb of the Institution of Oceanographic Sciences (IOS) U.K. for supplying wind and wave data collected during the JASIN experiment. Bernhard Gravdal of the Norwegian Defence Research Establishment kindly supplied the image of Fig. 5. Kurt Graf, Dennis Douglas and Dennis Tremain at SRI International provided valuable help by digitizing the JPL imagery. We also thank Harriet Smith, Martha Smith and Sara Zientek for help in preparing the manuscript. The authors gratefully acknowledge financial support from the Office of Naval Research (Physical Oceanography Branch), the National Oceanic and Atmospheric Administration (Ocean Sciences Branch) and the National Aeronautics and Space Administration.

REFERENCES

- Alpers, W.R., D.R. Ross and C.L. Renfenach, On the detectability of ocean surface waves by real and synthetic aperture radar, J. Geophys. Res., **86**, 6481-6498 (1981).
- Apel, J.R., H.M. Byrn, J.R. Proni and R.L. Charnell, Observations of oceanic internal and surface waves from the Earth Resource Technology Satellite, J. Geophys. Res., **80**, 865-881 (1975).
- Beal, R.C., P.S. DeLeonibus and I. Katz (eds.), Spaceborne Synthetic Aperture Radar for Oceanography, Johns Hopkins University Press, Baltimore (1981).
- Beal, R.C., Spatial evolution of ocean wave spectra in Beal et al. (1981), 110-127.
- Bragg, W. L. A General Survey, vol. 1 of The Crystalline State, (Sir. L. Bragg, ed.) Bell and Sons, London (1933).
- Gonzales, F.I., R.H. Shuchman, D.B. Ross, C.L. Reufenach & G.F.R. Gower, Synthetic aperture radar wave observations during GOASEX, in Oceanography from Space (G.F.R. Gower, ed.) Plenum, NY, in press (1981).
- Gower, G.F.R. (ed), Oceanography from Space, Plenum, NY, in press (1981).
- Jain, A., Focusing effects in the synthetic aperture radar imaging of ocean waves, Appl. Phys. **15**, 323-333 (1978).
- Jain, A., G. Medlin and C. Wu, private communications.
- Jones, W. L. and L. C. Schroeder, Radar backscatter from the oceans: dependence on surface friction velocity, Boundary Layer Meteorology, **13**, 133-149 (1978).
- Jordon, R.L., The SEASAT-A synthetic aperture radar system, IEEE J. Oceanic Eng., **OE-5**, 154-163 (1980).
- Kasischke, E., "Extraction of Gravity Wave Information from Spaceborne Synthetic Aperture Radar Data," Masters Thesis, University of Michigan, Ann Arbor, MI (1980).
- Kinsman, B., Wind Waves, Prentice Hall, Englewood Cliffs, N.J. (1965).
- Longuet-Higgins, M.S., D.E. Cartwright and N.D. Smith, Observations of the directional spectrum of sea waves using the motion of a floating buoy, in Conference on Ocean Wave Spectra, Prentice Hall, NY, 111-132 (1963).
- Phillips, O.M., The structure of short gravity waves on the ocean surface, in Beal et al. (1981), 24-31.
- Phillips, O.M., The Dynamics of the Upper Ocean, 2nd Edition., University Press, Cambridge (1977).

Pollard, R.T., coordinator, "Air-Sea Interaction Project: Summary of the 1978 Field Experiment," The Royal Society, Carlton House Terrace, London (1979).

Wright, J.W., Backscattering from capillary waves with applications to sea clutter, IEEE Trans. Antennas & Propagation, AP-14, 749-754 (1966).

Valenzuela, G.R., Theories for the interaction of electromagnetic and ocean waves -- a review, Boundary-Layer Meteorology, 13, 61-85, (1978).

Vesecky, J.F., H.M. Assal and R. H. Stewart, Remote sensing of the ocean waveheight spectrum using synthetic-aperture-radar images, in Oceanography from Space (G.F.R. Gower, ed.), Plenum, NY, in press, (1981).

Vesecky, J.F., S.V. Hsiao, C.C. teague, O.H. Shemdin and S.S. Pawka, Radar observations of wave transformations around islands, J. Geophys. Res., 85, 4977-4986 (1980).

